STUDIES OF TWO-PHASE TURBULENT PIPE FLOW

by

Ow Chee Sheng, B.E. (N.Z.)

A thesis submitted for the degree of Doctor of Philosophy of the University of London and for the Diploma of Membership of the Imperial College.

Mechanical Engineering Department
Imperial College,
London, S.W.7.

May 1980

BIF
LONDON
UNIV.

ABSTRACT

Experimental investigations of the agglomeration and deposition of droplets of mass mean diameter 30 to 40 μm in a horizontal turbulent two-phase air/water pipe rig are reported. Basic instrumentation for a photographic drop-sizing technique is described, including the development of an off-line automatic image analysis system. In its initial application, number frequency spectra from atomiser sprays and a turbulent two-phase pipe flow have been obtained. Preliminary measurements of droplet velocity employing double-flash photography have also been successful. The automatic image analysis system is configured around an existing minicomputer operating system, requiring additionally a conventional, relatively cheap TV camera and a purpose-built digitiser. Image recognition and processing, including rejection of unfocused images, are dealt with by software, based on detection at eight grey levels. The system and its calibration are described and comparisons made with manual sizing.

A horizontal two-phase air/water pipe rig has been designed and constructed for the purpose of studying the simultaneous effects of turbulent agglomeration and deposition processes on the evolution of drop number frequency and concentration. Air-blast atomisers capable of producing a narrow mass frequency spectrum at a high water to air mass ratio were designed, and used to introduce water droplets into the turbulent air stream. The average inter-drop spacing at injection was less than ten-drop diameters.

Experiments to assess the relative effects of re-entrainment, deposition and agglomeration on drop-size distribution and number concentration in turbulent flow at Reynolds number $\sim 10^5$ in a straight pipe are described. Droplet mass frequency spectra were found to be satisfactorily described by the Upper Limit Distribution Functions (ULDF). A heterogeneous ULDF is proposed to describe bimodal mass frequency spectra encountered in the studies. Photographic studies of the drop-size distribution at four axial positions along the eight metres length test section indicated preferential depletion of drop sizes larger than 90 μm from relatively polydispersed spectra resulting in predictably high values of deposition velocity determined from measurements of deposited mass.

Employing a simplified analytic equation to describe the simultaneous effects of deposition and agglomeration on number concentration, the influence of both processes was found to be equally important for an average inter-drop spacing of up to twenty drop diameters. Williams(9) numerical predictions of combined agglomeration and deposition in the rig are compared with the experimental data. Numerical values of Sauter mean diameter were found to increase with pipe length at a rate comparable with that in experimental measurements.

CONTENTS

			Page
ABSTRACT			2
CONTENTS			4
ACKNOWLEDGEMENTS			12
		NOMENCLATURE	13
CHAPTER	1	INTRODUCTION	19
	1.1	Outline of Work	24
	1.2	Layout of Thesis	27
CHAPTER	2	EXISTING THEORETICAL AND EXPERIMENTAL STUDIES	28
	2.1	Introduction	28
	2.2	Agglomeration	29
		2.2.1 Theoretical Models	29
		2.2.2 Experimental Work	34
	2.3	Deposition	39
		2.3.1 Theoretical Models for Turbulent Deposition	39
		2.3.2 Experimental Studies on Turbulent Deposition	44
	2.4	Re-entrainment	51
CHAPTER	3	DROP SIZING TECHNIQUES	58
	3.1	Introduction	58
	3.2	Intrusive Methods	59
		3.2.1 Impaction on Coated Surface	59
		3.2.2 Immersion Sampling	61
		3.2.3 Mechanical Sampling Probe	62

	3.2.4	Electrical Methods	63
		3.2.4.1 Pulse Counting Technique	63
		3.2.4.2 Charged Wire Technique	64
		3.2.4.3 Heated Probes	65
		3.2.4.4 90° Scattering Probe	67
3.3	Non-Intrusive Techniques		69
	3.3.1	Optical Methods	69
	3.3.2	Photography	76
	3.3.3	Holography	78
	3.3.4	Photography-Related Techniques	79
3.4	Sizing by High-Speed Shadow Photography		83
CHAPTER 4	DATA ACQUISITION BY HIGH SPEED SHADOW PHOTOGRAPHY		86
4.1	Introduction		86
4.2	Relevant Instrumentation		89
	4.2.1	Camera	89
	4.2.2	Lenses	90
	4.2.3	Spark/Sources	92
	4.2.4	The Pulse Generator	94
	4.2.5	Photographic Emulsions and Development	94
	4.2.6	Continuous Air Purge for Lens	96
	4.2.7	The Optical Bench	98
	4.2.8	Miscellaneous	99
4.3	Experimental Methods		101
	4.3.1	Experiments with Atomisers	101

		4.3.2 Experiments in the Two-Phase Rig	105
		4.3.3 Depth of Field Studies	108
	4.4	A Note on Droplet Velocity Measurement	110
	4.5	Sizing Methods	113
		4.5.1 Manual Analysis	113
		4.5.2 Automatic Analysis	115
CHAPTER	5	BASIS OF AUTOMATIC SIZING TECHNIQUE	116
	5.1	Introduction	116
	5.2	Hardware	118
		5.2.1 The Digitiser	118
		5.2.1.1 Existing Unit	118
		5.2.1.2 Modifications	120
		5.2.1.3 Software Support Package	123
		5.2.2 The Light Source	124
		5.2.3 TV Camera and Lenses	125
		5.2.4 Auxiliary Equipments	126
		5.2.5 Operating Procedure	126
	5.3	Software	129
		5.3.1 Introduction	129
		5.3.2 TV Image Characteristics	129
		5.3.2.1 Repeatability	129
		5.3.2.2 Image Segmentation	130
		5.3.2.3 Peak Video Amplitude	130
		5.3.2.4 Contrast Uniformity	131
		5.3.2.5 Linked Images	131
		5.3.2.6 TV Screen Edge Errors	132
		5.3.2.7 Photographic Depth of Field	132

5.3.3	Principles of Image Recognition and Focus Discrimination		133
		5.3.3.1 Aims	133
		5.3.3.2 Techniques Considered for Image Recognition	134
		5.3.3.3 Definition	135
		5.3.3.4 Method Employed for Recognition	136
		5.3.3.5 Method Employed for Rejecting "Out-of-Focus" Images	138
5.3.4	Programs and Data Structure		140
		5.3.4.1 Data Organisation	140
		5.3.4.2 Overlay Description	142
		5.3.4.3 Overlay Builder and Run Time Limitations	151
		5.3.4.4 Non-Overlay Version	154
5.3.5	Concluding Remarks		154
5.4	Calibration and Performance		156
5.4.1	General Description		156
5.4.2	Repeatability of Digitised Measurements		157
5.4.3	Screen Position Errors		158
5.4.4	Effect of Altering Peak Video and Grey-Level 7 Settings on Measured Diameters		159
5.4.5	Establishment of a Focus Discrimination Criterion		160
5.4.6	Simulation of Varying Contrast		162
5.4.7	Typical Results		164
5.4.8	Additional Errors		165

		5.4.9 Discussions and Recommendations	168
CHAPTER	6	TREATMENT OF DROPLET SIZE DISTRIBUTION	170
	6.1	Introduction	170
	6.2	Converting a Number Count to Volume Distribution	171
	6.3	The Upper Limit Distribution Function (ULDF)	174
	6.4	The Heterogeneous ULDF	178
	6.5	Number Count Statistics	183
CHAPTER	7	TWO-PHASE FLOW RIG AND MEASUREMENTS	185
	7.1	Major Rig Components	185
	7.2	Droplet Generation	188
		7.2.1 Basic Considerations	188
		7.2.2 Commercial Atomisers	190
		7.2.2.1 The Conventional Pneumatic Atomiser	190
		7.2.2.2 The Ultrasonic Atomiser	192
		7.2.3 The Air-Blast Atomiser	194
		7.2.3.1 Design and Construction	194
		7.2.3.2 Assembly of the Air-Blast Atomisers	196
		7.2.3.3 Performance of the Prototype Atomiser	197
		7.2.3.4 General Performance of the Air-Blast Atomiser	198
		7.2.3.5 A Note on Electrostatic Charging During Atomisation	200
		7.2.4 Atomiser Assembly for Injection into Turbulent Air Stream	201
		7.2.4.1 Injection Through the Pipe Walls	201

		7.2.4.2 Axial Injection	202
	7.3	Fluid Supply and Metering Equipment for the Two-Phase Rig	204
		7.3.1 Air Circuit	204
		7.3.2 Water Circuit	205
	7.4	Humidification	206
	7.5	Liquid Film Extraction Units	207
	7.6	Measurement of Wall-Static Pressure	211
		7.6.1 Single-Phase Flow	212
		7.6.2 Two-Phase Flow	214
	7.7	Experimental Procedure	217
CHAPTER	8	EXPERIMENTAL STUDIES	218
	8.1	Introduction	218
	8.2	Entrainment from the Annular Wall Film	220
		8.2.1 Experimental Procedure	221
		8.2.2 Deductions	222
		8.2.3 Estimation of Re-Entrained Fraction in Experiments Involving Deposition Rate Measurements	223
		8.2.4 Re-Entrainment Effects on Drop-Size Distribution	225
	8.3	Deposition Measurements	227
		8.3.1 Theoretical Consideration	227
		8.3.2 Procedure	229
		8.3.3 Result Analysis and Discussion	230
	8.4	Photographic Experiments	233
		8.4.1 Test Procedure	233
		8.4.2 Analysis of the Photographs	234

8.4.3 Results and Discussion 235
8.4.3.1 Condition A 238
8.4.3.2 Condition A1 240
8.4.3.3 Condition B 241
8.4.3.4 Condition C 242
8.5 Macroscopic Analysis 244
8.5.1 Theoretical Considerations 244
8.5.2 Analysis 246
8.5.3 Discussion 248
8.6 Comparison with a Numerical Model 250
8.6.1 Numerical Technique 250
8.6.1.1 Coagulation 251
8.6.1.2 Radial Diffusion 254
8.6.1.3 Deposition 255
8.6.1.4 Parameters for Gas Phase 256
8.6.2 Results and Discussions 257
CHAPTER 9 CONCLUSION AND RECOMMENDATION 261
REFERENCES 268
APPENDIX A1 COMMON ARRAY CONTENTS 297
APPENDIX A2 OUTLINE FLOWCHART FOR OVAL 298
APPENDIX A3 ROUTINE OVL1 299
APPENDIX A4 ROUTINE OVL2 302
APPENDIX A5 ROUTINE OVL3 308
APPENDIX A6 ROUTINE OVL4 316
APPENDIX A7 PROGRAM LISTINGS FOR PATTERN RECOGNITION AND FOCUS DISCRIMINATION 319

APPENDIX A8 PROGRAM FOR CONVERTING A NUMBER COUNT TO VOLUME DISTRIBUTION BY REF. (193) 356

APPENDIX A9 NON-LINEAR LEAST SQUARE REGRESSION TECHNIQUE 359

APPENDIX A10 ON THE CRITICAL WEBER NUMBER FOR COARSE WATER FORMATION IN STEAM TURBINES 365

APPENDIX A11 RELEVANT SUBROUTINES FOR HETEROGENEOUS ULDF FIT 369

APPENDIX A12 RELATIVE MAGNITUDES OF COAGULATION CONSTANTS FOR A MONODISPERSED SPECTRUM OF 40 μm DIAMETER WATER DROPS IN 102 mm DIAMETER PIPE FLOW AT REYNOLDS NUMBER OF 10^5 372

APPENDIX A13 ESTIMATION OF ERRORS IN $\bar{x}_{30}$ AND $\bar{x}_{32}$ USING THE CENTRAL LIMIT (CL) THEOREM 376

TABLES

FIGURES

ACKNOWLEDGEMENTS

I am most grateful to Dr. R.I. CRANE for providing guidance and encouragement during the course of the work. Special thanks are also due to Messrs. R.D. BLOXHAM and W. LAMBURN for their invaluable help and advice on technical matters. The contributions in one way or another of the staff and students of the Mechanical Engineering Department, in particular Dr. C.B. BESANT for his permission to use the minicomputer and TV camera and Mr. D. THOMPSON in the initial stages of development of the automatic image analysis system are gratefully acknowledged.

Finally, I am also grateful to the MARA Institute of Technology (Malaysia) for providing financial assistance. The work was funded by a Science Research Council grant.

NOMENCLATURE

(Except otherwise stated, the following definitions apply)

A	photographic depth of field (mm)
a	Upper Limit Distribution Function (ULDF) parameter
$a_1 = \exp(\delta_1 m_1)$ $a_2 = \exp(\delta_2 m_2)$	heterogeneous ULDF parameters
B_{ij}	coagulation rate between particles of size i and size j defined in Eqn. 2.1 ($m^{-3}s^{-1}$)
b	scaling factor in heterogeneous ULDF
C_{r_1, r_2}	Collision constant for drop classes r_1 and r_2
c	correlation coefficient defined in Eqn. 7.3
D	pipe diameter (m)
d	diameter of the image of a drop or calibration disc. (μm)
$d_{e,n}$	equivalent circular diameter at grey level n (where n is any integer between 1 and 7)
F	deposition velocity defined as (drop number flux ÷ core concentration) (m/s)
$F^+ = \frac{F}{u}$	dimensionless deposition velocity
f	focal length of lens (mm)
G	total drop number count
g	gravitational acceleration (m/s^2)
ΔH	manometric head (mm)
h	halo width (μm)
h'	halo width for focus discrimination (μm)
I	image intensity; video voltage representing intensity.

$I_R = \frac{I_{1A} - I_D}{I_A - I_D}$ intensity ratio

i weighing factor used when converting a number count to surface or volume distribution

$J = \frac{Q_w \, We_c E}{Q_g \left[\frac{dP}{dL}\right]_g}$ entrainment factor

j offset parameter in heterogeneous ULDF

K coagulation coefficient (s^{-1})

k equivalent sand roughness parameter (m)

L pipe length (m)

l total number of discreet size ranges

M mass concentration at time t (kg/m^3)

M_o initial mass concentration at t = 0 (kg/m^3)

M_E homogeneous mean droplet concentration (kg/m^3)

MP Martinelli parameter (84) defined as $\left(\left[\frac{dP}{dL}\right]_w \Big/ \left[\frac{dP}{dL}\right]_g\right)$

m, m_1, m_2 constants in heterogeneous ULDF

m_f mean liquid film thickness (m)

N(t) drop number concentration at time t in given size interval in numerical computation (m^{-3})

N_∞ Total number concentration at station 2 averaged over the whole cross section (m^{-3})

n number concentration at time t (m^{-3})

n(x)dx number frequency in class interval x to x + dx

n_L average number concentration at distance L from station 2. (m^{-3})

n_o	initial average number concentration (or when L = 0) (m^{-3})
$n[\eta,t]$	number frequency of drops having mass η at time t
P	pressure (N/m^2)
$\left(\frac{dP}{dL}\right)$	pressure gradient (N/m^3)
ΔP	pressure drop (N/m^2)
p	fractional penetration as defined in Eqn. 8.2 a
Q	volumetric flow rate (m^3/s)
q_1	mean mass of drops entrained in the flow (kg)
q_2	mean mass of drops deposited on the walls (kg)
R	pipe radius (m)
Re_D	pipe Reynolds number $\bar{u}D/\nu$
r	radial position measured from pipe or atomiser axis (m)
S	specific gravity of manometric fluid
s	skewness factor in ULDF
SF	shape factor defined as (Perimeter^2/Area)
T_L	Lagrangian integral time scale (s)
t	time (s)
U	Instantaneous air velocity (m/s)
$\bar{U}$	bulk air velocity (m/s)
$\bar{u}$	time mean axial air velocity (m/s)
u	rms fluctuating velocity of gas phase (m/s)
u_*	friction velocity (m/s)
V	drop velocity relative to surrounding fluid (m/s)
$V_t = g\tau$	terminal velocity (m/s)
$V_i(x_1)$	weighted fraction of droplets larger than size x_1

v	rms fluctuating velocity of particle or drop (m/s)
W	magnification factor
w	rms relative velocity of two particles or drops (m/s)
X	coordinate along TV scan line
X'_a	distance from entry plane of test section (m)
$\Delta X'_a$	short length of pipe in the X'_a direction (m)
X_{in}	start coordinate of a transition
X_{out}	end coordinate of a transition
X_L	last transition coordinate along a TV scan line.
X_F	first transition coordinate along a TV scan line.
x	diameter of a particle, drop or a calibration disc.
$\bar{x}$	mean diameter
x_η	diameter of the smallest drop in the spectrum (μm)
x_o	drop diameter less than the smallest observed size
Y	coordinate normal to a TV scan line
y	diatance from the pipe wall or solid surface (m)
Z	standard normal variate
z	normal variate

GREEK CHARACTERS

α	mass loss constant
β	deposition coefficient
γ	longitudinal turbulent integral scale

δ	a ULDF shape parameter
δ_1, δ_2	shape parameters in heterogeneous ULDF
Δ	degree of blur
ε	turbulent energy dissipation rate (W/kg or m^2/s^3)
$\zeta = (\varepsilon \nu)^{\frac{1}{4}}$	microscale eddy velocity (m/s)
η	average mass of smallest drop (kg)
η_i	average mass of drops in size range i.
θ	angle measured from the vertical plane
Λ	population variance
$\lambda = (\nu^3/\varepsilon)^{1/4}$	Kolmogorov microscale
μ	absolute viscosity (kg/sm)
ν	kinematic viscosity (m^2/s)
ξ	diameter of spark image
Π	relative aperture or f-number
ρ	density (kg/m^3)
σ	surface tension (N/m)
$\tau = \frac{\rho_p \chi_p^2}{18 \mu_g}$	particle or drop relaxation time (s)
$\tau^+ = \frac{\tau u_*^3}{\nu}$	
τ_f	interfacial shear stress (N/m^2)
τ_w	wall shear stress (N/m^2)
$\Phi = \frac{\tau}{T_L}$	
ψ	cumulative volume or mass
Ω	numerical constant in coagulation rate expression
ω	population mean

SUPERSCRIPT

+	dimensionless quantity

SUBSCRIPTS

a	axial direction
A to D	intensities defined in text or Fig. 5.24
¢	value at centre of finite element
c	centreline (or pipe axis)
g	air (of gas)
i	particle or drop in size class i
ie	value at inner surface of finite element
j	particle or drop in size class j
L	pipe length
M	measured value
m	maximum drop size
n	arbitrary grey level value (from 1 to 7)
ot	value at outer surface of finite element
p	particle
r	radial direction
w	water (or liquid)
W	wall region
1A	intensity at grey level 7
30	volume or mass mean
31	surface mean
32	Sauter mean
500	mass median
999	corresponding to 99.9% cumulative volume
ave	average value
nett	nett spectrum

CHAPTER 1

INTRODUCTION

The present study originated from the need to understand the processes affecting the size distribution and quantity of entrained water droplets in the cross-over pipes between the high-pressure (HP) steam turbine and the moisture separators of a typical water-cooled nuclear power plant. Unlike the conventional fossil-fired power plants, the steam generated by a pressurised-water reactor (PWR) or boiling water reactor (BWR) is saturated or slightly wet at entry into the HP turbine. The steam which leaves the exhaust of the HP turbine has a wetness fraction typically 12% (1), with further direct expansion in the low-pressure (LP) turbine clearly unacceptable from the viewpoint of thermodynamic and aerodynamic efficiency of LP turbine stages operating with wetness fraction up to 25%. Such a wet steam environment would additionally introduce severe practical problems of blade erosion and possibly fatique fractures at the root of turbine blades (221) due to additional vibrations induced by the non-uniform wetness distribution at the inlet to the LP blades.

To prevent excessive LP exhaust wetness and to improve reheating efficiency using live steam, the practice has been to use expensive and bulky external water separators (e.g. (2)) to "dry" the steam prior to reheating and further expansion in the LP turbine. Whilst information on the drop size distribution in the cross-over pipes separating the HP exhaust and the water separators, on which the efficiencies of the mechanical separators clearly depend, is sparse, separation efficiencies

of more than 95% have been reported (3). However, it is not known whether this high efficiency is a result of correct assumptions about the HP exhaust drop sizes or of effects in the pipe work which may modify the drop-size distribution. A knowledge of the major processes which influence the evolution of number concentration and size-distribution of drops in the cross-over pipes would therefore be extremely useful.

Assuming the validity of the theory of Hutchinson et al. (4) for drop deposition by turbulent impaction and of the results of Crane and Evans (5) for inertial deposition in bends, Crane (6) demonstrated that an HP exhaust wetness fraction of 10% could be reduced in a typical pipe geometry (20m of pipe with four right angle bends) to 3% and 1% for an effective drop diameter of 5 μm and 40 μm respectively. This raises the possibility of "drying" the wet steam by suitable choice of pipe geometry alone (incorporating drainage devices to prevent re-entrainment of deposited water), hence avoiding the need for mechanical water separators which introduce an additional pressure drop in the steam flow, reducing the overall efficiency of the plant.

Steam flows in the cross-over pipes are extremely turbulent with Reynolds number of the order of 10^7 and pipe lengths for which drop residence times of 0.1s to 1s are expected, during which significant droplet agglomeration is possible. The entrained drops are made up of the fraction of those formed from direct condensation, which avoid deposition on the HP turbine blades, and the coarse drops which originate from rivulets of deposited water stripping from the trailing edge of the blades

to be re-entrained into the flow. The maximum diameter of the latter drops may be estimated from a critical Weber number criterion (see Chapter 6). Measurements from scale model HP turbines (7) indicated a near monodispersion of 1.5 μm diameter fog drops after the fourth stage of a 14 stage unit whilst at full scale the maxium diameter of the coarse drops has been estimated (7) as 11 μm and 5 μm at 5 and 10 bar respectively at exit from the final HP blade row. Amongst the three major processes re-entrainment, deposition and agglomeration which influence the evolution of number concentration and size-distribution of drops, the role of agglomeration has been least studied.

Agglomeration or coagulation is described as the process of adhesion or fusion of adjacent drops upon contact with one another. Several agglomeration mechanisms have been identified for aerosol particles (8). When the approach and contact of particles is due to Brownian motion alone, the mechanism is known as thermal coagulation. Agglomeration may also be promoted by the presence of inner force fields such as Van der Waals (molecular) forces, electrostatic attractive forces and forces arising from electric and magnetic dipoles, whereas the influence of external force fields include gravity, electrical and magnetic; finally, intense sound and laminar or turbulent flow field induce coagulation described as acoustic, shear and turbulent respectively.

For electrically and magnetically neutral spherical particles entrained in a turbulent fluid the mechanisms of turbulent and, for heavy particles, gravitational agglomeration predominate. A particle entrained in an accelerated fluid will

move relative to the fluid if the particle and fluid densities differ whereas two such particles with the same density but different diameters will move relative to each other due to unequal inertia. Particles wholly entrained in the fluid would move relative to each other due to velocity gradient in the shear flow.

On a more general note, a better understanding of the agglomeration process is useful in the field of pneumatic transport of powders, design of cyclone separators, etc. whilst general studies of turbulent two-phase pipe flow systems are important in the design of gas-liquid pipe lines in chemical and nuclear reactors, the handling and treatment of dispersions in many engineering systems, the design of gas cleaning and sampling devices and the prediction of dry out on heat transfer surfaces.

The aims of the present work are therefore:

(i) to design and construct an air/water rig for studying droplet agglomeration in turbulent pipe flows.

(ii) to develop a photographic droplet sizing technique for use in the rig, including a minicomputer-based image analysis system.

(iii) to assess experimentally the effects of agglomeration, deposition and entrainment on droplet-size distribution and concentration, attempting to identify the contribution of each process and

(iv) to provide data against which to test a numerical model of turbulent agglomeration.

Owing to the inevitable influence of deposition and re-entrainment processes on the drop-size distribution and number concentration of the entrained flow, experiments which attempt to assess the effect of agglomeration have to be carried out with appropriate allowance for the other two processes. Whereas the process of re-entrainment may be minimised by reducing the thickness of the wall-film, the processes of deposition and agglomeration have to be examined as an integral phenomenon. The numerical model against which data are to be compared was developed by Williams (9) who carried out in parallel with the present work a theoretical study of the agglomeration and deposition processes as well as experimental measurements of relevant turbulence parameters of single-phase flow in the rig as required by the model.

1.1 Outline of Work

A major aspect of the work was concerned with the selection and/or design and construction of relevant instrumentation for the photographic study of drop-size distribution in a horizontal-turbulent two-phase pipe flow rig, with plans for drop velocity measurements at a future date. Practical problems associated with dense spectra and contrast deterioration of the photographs were examined and a technique developed to overcome them. A major time factor in any photographic experiment was the period needed to align the optics for which 2 to 3 hours was typical. Hence a robust traversing optical bench was designed and constructed, enabling a reduction in operating period by up to an order of magnitude when photographs of the radial variation of size distribution across a section of the pipe were needed.

Data extraction in a photographic method is usually done manually or more recently by use of automatic image analysers (10). The manual method is both subjective and tedious whilst dependence for all processing needs on remote installations having a suitable automatic image analyser is both unsatisfactory and impractical for development work. Hence a software-based, off-line, automatic image analysis system capable of detection at eight grey levels was configured around an existing minicomputer operating system with minimal additional instrumentation. Software for feature detection and focus discrimination (since a large number of the images are "out-of focus") was written largely in Fortran IV so that transfering the system to a new computer and operating system should not

be a problem. The feature detection program permits additional measurements of suqh attributes as area, perimeter and shape factor of well-defined images of all shapes and sizes at a relevant grey-level.

An important requirement in the study of droplet agglomeration was the need for high number concentrations of, preferably, a monodispersed spectrum in the entrained flow. A mass mean diameter in the range of thirty to forty microns had been selected for the study. For the flow conditions used in the test, the rate of droplet generation needed was in excess of 10^9 drops/s. Commercial pneumatic atomisers of the twin-fluid type were considered, including performing some suitability tests on them. Eventually, four units of pneumatic ("air-blast") atomiser of the author's design were used.

In view of the need to determine the rate of droplet deposition i.e. measurement of film flow rate, development of a slot-type wall film extraction unit was carried out. The fluid supply and metering equipments were arranged so that treatment of the liquid phase e.g. altering its viscosity or surface tension prior to entry into the two-phase rig at a future date was possible.

Drop-size distributions were adequately described by the Upper Limit Distribution Function (ULDF) (11). Due to the possible presence of two well defined sets of spectra, e.g. re-entrained drops from the wall film and the originally injected mist, a heterogeneous ULDF was proposed to account for the bimodal shape of certain mass frequency distributions.

Test results for three major experimental conditions for flow in a straight section are reported, and the contribution of each of the three major processes present assessed. For one of the experimental conditions, the test results are compared with the numerical predictions of Williams.

1.2 Layout of Thesis

Chapter 2 reviews the existing theoretical and experimental work on the processes of turbulent agglomeration, deposition and re-entrainment with special reference to pipe flow. A review of the existing drop sizing techniques relevant to the determination of drop sizes in the diametral range 10 μm to 300 μm is included in Chapter 3. Whereas Chapter 4 deals mainly with the practical aspect of the photographic drop sizing technique, Chapter 5 reports on the development of a software-based off-line automatic image analysis system.

Chapter 6 describes the method of analysing and empirically correlating drop number counts including the formulation of a heterogeneous distribution function to describe multimodal mass frequency spectra. The two-phase rig instrumentation is described in Chapter 7 including the design and tests of a new twin-fluid pneumatic atomiser for use in the rig. The different contributions of the processes of agglomeration, deposition and re-entrainment to the evolution of drop-size distribution and number concentration are assessed in Chapter 8 including a comparison of the experimental measurements with a numerical model. The main conclusions and recommendations for further work are reported in Chapter 9.

CHAPTER 2

EXISTING THEORETICAL AND EXPERIMENTAL STUDIES

2.1 Introduction

The present study may be conveniently classified under the category of adiabatic, annular two-phase flow in which droplet deposition and agglomeration processes are predominant. Whereas most existing experimental and theoretical work on annular two-phase flow systems has been concerned with understanding of the interactions between the gas core and wall film, relating pressure drop measurements with thickness of annular film and/or film flow rate amongst others, studies which include the effect of droplet agglomeration in a turbulent pipe flow are relatively rare. Whilst most theoretical work on droplet agglomeration is not concerned with pipe flows, a review of such work is nevertheless important. A brief review of the various deposition and re-entrainment studies relevant to the present work will also be included, although in most of these studies the mechanism of agglomeration is excluded.

The existing theoretical and experimental studies of the three processes which affect the evolution of size distribution and number concentration are best reviewed under the headings of agglomeration, deposition and re-entrainment with special emphasis on turbulence-induced processes in pipe flow.

2.2 Agglomeration

2.2.1 Theoretical models

An important aspect of all theoretical studies on droplet agglomeration, or more generally, particle coagulation, is the derivation of the coagulation rate per unit volume between particles of two particular sizes using a suitable physical model of the collision mechanism. Particle collision and coagulation lead to a reduction in the total number of particles in the aerosol accompanied by an increase in the average size. When two arbitrary particles collide, most theoretical models assumed that they coagulate. The rate of coagulation between the two different-sized particles is obviously a function of the number concentration of each size in the aerosol as well as the collision frequency. The collision process is mainly non-linear and the expression which describes the change with time of the size distribution and number concentration of an aerosol is often analytically insoluble, requiring instead a numerical solution. The different numerical techniques or simplified analytic solutions of the coagulation equation will be excluded from this review but are dealt with by Hidy and Brock (12), who discussed some analytic and numerical solutions present in the literature, and by Williams (9).

The kinetics of an assembly of small spherical particles which coalesce on collision was first studied by Smoluchowski (13, 14) for both shear and non-shear conditions. For flow without shear, Smoluchowski assumed that the particles collide and coagulate due to Brownian motion. Assuming the centres of the particles to follow the stream lines of the continuous

phase with zero slip velocity, he found, for the shear condition, that the coagulation rate between two particles was directly proportional to the laminar velocity gradient.

Camp and Stein (15), recognising that the coagulation rate inside a mixing tank may be estimated using Smoluchowski's theory, derived the coagulation rate for turbulent flow, replacing the laminar velocity gradient term in Smoluchowski's equation by an average turbulent velocity gradient which was further expressed (16) as $(\varepsilon/\nu)^{\frac{1}{2}}$ where ε is the average turbulent energy dissipation rate per unit mass inside the mixing tank and ν is the kinematic viscosity of the continuous phase. The resulting expression which describes the coagulation rate a_{ij} between particles of size i and size j within the spectrum is given by

$$B_{ij} = \Omega n_i n_j x_{ij}^3 (\varepsilon/\nu)^{\frac{1}{2}} \quad \ldots\ldots 2.1$$

where n_i, n_j are respectively the number concentration of particles having size i and size j ; x_{ij} (sum of radii) is the distance which separates the centres of the two coagulating particles; Ω is a numerical constant which has the value of 4/3.

Levich (17) considered the turbulent coagulation process as a diffusion of particles towards a "sink" particle and derived, for particle sizes smaller than the Kolmogorov micro-scale (18) a collision rate expression similar to Eqn. 2.1 except for Ω which is an order of magnitude higher than that of Camp and Stein.

Beal (19), following Levich's treatment, included the effect of Brownian motion in his analysis, showing that collisions due to Brownian motion are generally important for particle sizes

less than 1 μm diameter, in air under atmospheric conditions. For particle diameters larger than 1 μm, Brownian diffusion may be neglected compared with turbulent diffusion even when the energy dissipation rate is as low as 1 W/kg.

Particles with different inertia (i.e. different sizes for constant density) entrained in an accelerating fluid "packet" would be accelerated by the fluid at different rates. The resulting relative motion (within the same fluid packet) between the particles can lead to collision hence coagulation. Such a coagulation mechanism arising from particle motion relative to the fluid was examined by East and Marshall (20) for the growth of water droplets in clouds. A consequence of this collision mechanism is that droplets having the same size do not collide with each other within the same fluid packet. East and Marshall considered the distribution of accelerations in the turbulent fluid to be important, and included the effect of gravitational coagulation in their model as due to an additional accelerational term.

Saffman and Turner (21), on the other hand, identified two separate collision mechanisms for particle sizes smaller than the turbulent microscale. In the first mechanism the particles are assumed to be wholly entrained by a turbulent eddy, moving with the eddy, and collision takes place due to spatial variations of turbulent motion. The second mechanism is similar to that described by East and Marshall, in which particles having the same size do not collide. For the first collision mechanism, Saffman and Turner derived a coagulation rate equation which has the same functional relationship as

Eqn. 2.1 but with $\Omega = 1.3$.

Sedunov (22), noting that the numerical constant in Levich's derivation of coagulation rate was an order of magnitude higher than that of Saffman and Turner, attributed the discrepency to the fact that Levich has incorrectly applied the diffusional theory to the relative motion of particles when their separation was less than the mean free path of the particles. He went on to show that the coagulation coefficient is dependent on the collision efficiency within a kinetic space (when particle separation is less than $2.4\ x_{ij}$ (see Eqn. 2.1)) in which particle collision may be modelled using statistical considerations by analogy with the kinetic theory of gases deriving a value of 1.7 for Ω.

In an attempt to describe the formation of unusually large salt fallout particles in debris from a sea-water-surface nuclear explosion, Huebsch (23) used a dimensional analysis and an order of magnitude argument, deriving a coagulation rate equation (for particles smaller than the microscale) which is reducible to Eqn. 2.1 except for the numerical constant ($\Omega = 1.21$) when the diameters of the colliding particles differ by $\frac{2\lambda\rho}{\rho_p}$ where λ is the turbulent microscale, ρ density of continuous phase and ρ_p is the particle density. In deriving the equation, Huebsch introduced the concept of a resonant (or maximising) eddy for which the speed of the entrained particle relative to the characteristic eddy speed (which for the turbulent microscale is given by $(\varepsilon\nu)^{\frac{1}{4}}$) is maximum. Extending the treatment to particle sizes larger than the microscale, Huebsch showed that the maximising eddies have a

characteristic eddy time equal to the particle relaxation time. Particle relative velocities needed in the coagulation expression were determined in terms of the characterictic length and velocity scales of the maximising eddies. Huebsch further deduced that for turbulent coagulation to exceed gravitational coagulation, (for particle sizes smaller than λ) the microscale Froude number, defined as $\frac{\zeta^2}{g\lambda}$ where ζ is the microscale eddy velocity scale, and g is the gravitational acceleration, must be larger than unity.

For very energetic turbulence, particles may be expected to acquire sufficient momentum in one or more eddies to be projected into a neighbouring eddy. The concept of an "independent particle velocity" collision mechanism was used by Abrahamson (24) to derive the coagulation rate equation where the continuous phase is highly turbulent with energy dissipation rates in the range 200 to 5000 W/kg. To satisfy the condition of independent particle velocity, Abrahamson's theory requires that particle sizes be relatively large, the lower limit on particle diameter, x_p given by $x_p^2 = 15\mu\frac{u}{\varepsilon\rho_p}$ where u and μ are respectively the rms fluctuating velocity and the absolute viscosity of the continuous phase. The coagulation rate equation has been derived in terms of particle rms fluctuating velocity v which is related to the rms fluctuating velocity of the continuous phase by $v^2 = \frac{u^2}{1 + 1.5\tau\varepsilon/u^2}$, where τ is the particle relaxation time.

Finally Friedlander (25) usefully compared the relative importance of Brownian, turbulent shear (21) and differential sedimentation coagulation mechanisms for 2 μm diameter particles

interacting with a range of particle sizes (from 0.2 μm to 20 μm diameter). At an energy dissipation rate of approximately 0.0005 W/kg (corresponding to free atmosphere conditions), Brownian and differential sedimentation (the sweeping out of small particles by larger ones due to gravity) mechanisms play an important role.

2.2.2 Experimental Work

Experimental studies on coagulation in pipe flows are few. The coagulation of hydrosols of 0.871 μm diameter polystyrene latex particles in the presence of simultaneous laminar shear and Brownian movement was examined by Swift and Friedlander (26) theoretically and experimentally. A suspension of polystyrene latex particles was destabilised by the addition of sodium chloride solution and allowed to coagulate in an annular shear field generated by a Couette type apparatus, consisting of an inner rotating cylinder located concentrically within an outer stationary cylinder. Experiments were carried out with the latex dispersion subjected to shear rates ranging from 1 to 80 sec^{-1} and agreement with theoretical computation for the rate of change of total particle concentration based on Smoluchowski's shear flow theory, was good. There was further experimental support for the assumption of addivity of the individual coagulation rates by shear and Brownian motion when deriving the rate of change in total particle number concentration.

Yoder and Silverman (27) studied the effect of air turbulence on the simultaneous deposition and agglomeration of

electrically neutralized polystyrene latex particles having 0.26 μm and 0.8 μm diameters. Flow Reynolds number (Re_D) through the 26 mm diameter copper pipe test section was varied from 5×10^3 to 8.5×10^4. The fraction of particles in agglomerates (mainly doublets) and the particle number concentration at the upstream and downstream end of the test section were determined, the former from microscopic examination of drawn-off samples and the latter from photographs of the two-phase flow spectra. Employing a simplified relationship to describe the rate of decrease of number concentration due to the simultaneous effects of deposition and coagulation and assuming that all agglomerates are present in doublets, Yoder and Silverman found that the coagulation and deposition coefficients increased with Reynolds number to the power 1.53 and 1.74 respectively for the 0.8 μm particles, and to powers 1.48 and 1.66 respectively for the 0.26 μm particles.

Arundel et al.(28) used a special design of null comparator optical densitometer to measure the mean particle density of a polydispersed suspension of 0 to 40 μm diameter zinc particles flowing vertically upwards in a 76.2 mm diameter tube at Re_D of 3.5×10^4. They found a marked increase in dispersion density on approaching the wall region. The operational characteristics of the optical densitometer permitted them to deduce that whilst only a limited degree of particle agglomeration occurred at the pipe axis, significant agglomeration was present near the wall. The large increase in particle density near the wall appeared to be a consequence of electrostatic charging, causing the particles to move radially outwards from the pipe

axis. However only a qualitative analysis of the measurements is possible.

More recently, Delichatsios and Probstein (29) carried out a theoretical and experimental study of the turbulent agglomeration process for particle sizes smaller than the turbulent microscale. Applying simple binary collision mean free path concepts for non-interacting particles and the statistical nature of turbulent flow, they derived a coagulation rate expression similar to Eqn. 2.1 with $\Omega = 0.81$. They further solved Mueller's (30) analytic equation governing the temporal evolution of mass frequency distribution for an arbitrary spectrum, showing that the polydispersity of the spectrum resulted in a reduction in the particle-number-density coagulation rate in comparison with the rate for a monodispersed spectrum having the same volume fraction. Experiments to measure the coagulation rate of a monodispersion of 0.6 μm destabilised latex particles in water were carried out for Re_D in the range 2×10^4 to 5×10^4. Samples of the mixture were withdrawn at five stations along the test section and analysed using a Coulter counter which provided information on number density as well as particle size distribution. The experimental results showed excellent agreement with theoretical predictions for the coagulation rate. Experiments in which the dispersed particle sizes were larger than the Kolmogorov microscale were attempted, but were unsuccessful because of simultaneous break-up of the agglomerates. Deposition of the latex particles onto the pipe walls (if any) was not reported implying that it did not feature strongly in their experiments.

Finally, Okuyama et al.(32) solved, numerically, the equation which describes the change with time of the size distribution of aerosols, using the coagulation rate equation derived by Saffman and Turner, via the Runge-Kutta-Merson method for differentiation and Simpson's rule for integration. A log-normal form of the initial particle number frequency distribution with a geometric mean at 0.4 μm was used. They usefully compared the effects of turbulent and Brownian coagulation on the evolution of size distribution for various levels of polydispersion of the initial spectrum and for several values of energy dissipation rate. Whilst the effect of Brownian coagulation relative to turbulent coagulation is small for ε as low as 1 W/kg (in line with Beal's results) the rate of decrease of total number concentration of an initially polydispersed spectrum is more rapid than that of a monodispersed aerosol. Experiments to determine the change in number concentration of aqueous ammonium chloride aerosols having a mean diameter in the range 0.3 to 0.75 μm for Re_D in the range 5×10^3 to 2.2×10^4 were also carried out. The aerosol at the upstream and downstream ends of a test section (for different lengths of the test section,) were isokinetically sampled; the sampled aerosol number concentration and size distribution were determined using an ultramicroscope method (33) based on the principles of sedimentation. Agreement between experimental measurements and theoretical predictions in which an additional term of deposition was included was good for the 0.3 μm diameter particles but poor for the 0.75 μm particles.

Zebel (8) and Hidy and Brock (12) provide information regarding other coagulation mechanisms e.g. coagulation due to internal force fields arising from electrostatic charging of particles or external influence from sonic or electric field.

2.3 Deposition

2.3.1 Theoretical Models for Turbulent Deposition

In general, for electrically neutral particles larger than 1 μm in diameter entrained in a turbulent flow field, the deposition process due to inertial forces predominates compared with deposition due to Brownian diffusion (neglecting the influence of gravitational or thermophoretic forces).

The theory for turbulent deposition (for particle size exceeding 1 μm in diameter) based on the eddy-diffusion-impaction model was independently proposed by Friedlander and Johnstone (34) and later by Owen (35). The model assumes that particles are transported by turbulent diffusion to the Boundary layer on an adjoining surface until one "stopping distance" from the depositing surface. At this position the particles are independently projected towards the surface (executing a "free-flight" to the surface) by eddies near the edge of the viscous sublayer.

Major differences exist in the determination of the initial free-flight velocity between the models of Friedlander and Johnstone and Owen and later those of Davies (36), Beal (37) and Sehmel (38). Friedlander and Johnstone, applying their model to pipe flows, assumed a value of ninety per cent of the friction velocity for the initial free-flight velocity and a stopping distance dependent on the particle inertia. Owen, on the other hand, derived an equation for predicting the deposition velocity, F (defined as the number flux of particles deposited divided by the average core concentration) which was independent of particle inertia; the dimensionless stopping distance $y^+ = \frac{yu_*}{\nu}$

for all particles was further assigned a value of 1.6.

Whereas the models of Owen and Friedlander and Johnstone assumed particle motion by eddy-diffusion from a uniform core concentration at $y^+ = 30.0$ to within a free-flight distance of the depositing surface, Davies treated particle motion by eddy-diffusion from the pipe axis and a free flight velocity which is equal to the rms fluctuating velocity of the fluid at the position where free flight begins. Comparison of Davies' prediction with the experimental results of Liu and Agarwal (39) was poor.

In the model by Beal an initial free flight velocity equal to half the axial velocity at the point where free-flight begins is used. Beal's model predicts an increase in the initial free-flight velocity with particle size. This was contradictory to experimental measurements by Sehmel (38) and Friedlander and Johnstone in which the initial free-flight velocities are larger than in Beal's assumptions and in fact tend to decrease as particle size increases when the influencing parameter changes from particle inertia to particle diffusion.

Sehmel proposed instead an empirically correlated dimensionless free flight velocity given by $1.49\ (\tau^+)^{-0.49}$. However this equation opposes the intuitive idea for the variation of dimensionless free-flight velocity with dimensionless particle relaxation time as discussed by Cleaver and Yates (40). Noting that the assumption of equality between particle eddy diffusivity with fluid eddy diffusivity in the models of ref. (34) to ref. (36) was unsatisfactory, Sehmel proposed a semi-empirical deposition model based on separate sets of equations to define

an effective particle eddy diffusivity parameter in terms of dimensionless distance parameter y^+ and the dimensionless particle relaxation time τ^+ corresponding to well defined regimes of y^+ from the deposition surface.

Liu and Ilori (41), favouring Sehmel's concept, analytically derived an effective particle eddy diffusivity parameter, relating it to the fluid eddy diffusivity within the turbulent boundary layer and the product $u_r^2\tau$ where u_r is the rms fluctuating velocity of the fluid in the radial direction (i.e. normal to the deposition surface). The particle eddy diffusivity (for τ^+ in the range 1 to 10) was further shown to be larger than the corresponding fluid eddy diffusivity by several orders of magnitude at a dimensionless distance y^+ less than 5 from the deposition surface. The deposition velocities based on Liu and Ilori's model are in general agreement with the diffusion-impaction model of ref. (34) for τ^+ in the range 0.1 to 100.

Rouhiainen and Stachiewicz (42), arguing that the deposition model based on a Stokes stopping distance is untenable under most practical conditions, showed that the passage of a dense particle through the viscous sublayer could be assisted by a shear-flow-induced transverse lift force and that a smaller particle radial velocity is present at the edge of the viscous sublayer than the 0.9 u_* value used by Friedlander and Johnstone.

A statistical random walk model for turbulent deposition, free of the assumptions and limitations of earlier methods and which provides for any difference between fluid and particle eddy motion, was proposed by Hutchinson et al. (4). In this

model particles entrained in a turbulent pipe flow are assumed to execute a random walk in the plane normal to the pipe axis as they travel downstream at the same velocity as the gas phase. For those particles which approach the wall region, eventual deposition onto the wall is further treated as a stochastic process with particle velocities described by a Gaussian distribution function. The theory was satisfactorily tested against the experimental data of Alexander and Coldren (43) Cousins and Hewitt (44) and Friedlander and Johnstone covering a wide range of particle sizes, Re_D, particle to fluid density ratio and tube diameters. The predicted peak in the dimensionless deposition velocity was however an order of magnitude higher than the experimental results of Liu and Agarwal.

Gardner (45) correlated the numerical results of the theory of Hutchinson et al. for the turbulent impaction regime i.e. $\tau^+ > 30$ (in which particle inertia is so large that its response to the turbulent eddies is sluggish) into a more readily applicable form. For the eddy diffusion-impaction deposition regime ($0.1 < \tau^+ < 30$) and the diffusion deposition regime ($\tau^+ < 0.1$) Gardner further derived a semi-empirical relationship for computation of the deposition velocity.

Cleaver and Yates (40), following Owen's (46) suggestion, assumed that the particles are convected to the wall from the region of energetic turbulent motion outside the viscous sublayer by the occasional large eddy that encroaches on it. The turbulent burst/downsweep model satisfactorily describe the data of Friedlander and Johnstone, Alexander and Coldren and Sehmel (amongst others) for τ^+ in the range 0.1 to 10^3. The

model also predicts a dimensionless deposition velocity, F^+ which is independent of particle relaxation time for τ^+ exceeding 10^2.

Reeks and Skyrme (47) considered the deposition of large particles as being controlled by a turbulent diffusion process and an inertial penetration through the viscous sublayer both processes being dependent on particle inertia. They solved Tchen's (48) equation of motion (without the external force term) for the particle rms fluctuating velocity, using a suitable description of the Eulerian spectral density of the fluid. Evaluation of the fractional penetration of particles into the sublayer is similar to the stochastic method employed by Hutchinson et al. The predictions were compared with the experimental results of Liu and Agarwal, requiring the adjustment of certain constants in their equations in order to describe the experimental results satisfactorily, especially in the turbulent-impaction regime ($\tau^+ > 30$).

The deposition of particles onto a rough surface was investigated by Browne (49). His results indicate that whilst deposition velocities of particle sizes less than 1 μm diameter in the diffusional deposition regime ($\tau^+ < 0.1$), are significantly affected by surface roughness and Re_D, larger particles which operate in the inertial deposition regime ($\tau^+ > 0.1$) are not.

Finally, James and Hutchinson (50), treating droplet deposition as basically a diffusion process, derived an expression for the mass transfer coefficient for droplet deposition in the presence of an annular wall film in flow through an

annulus. The mass transfer coefficient for deposition onto an annular surface was further found to depend mainly on the film thickness.

2.3.2 Experimental Studies on Turbulent Deposition

Numerous experimental studies on deposition from a turbulent flow have been carried out for vertical as well as horizontal pipe geometries; the values of τ^+ and Re_D varied over a wide range. Two different methods have been used to correlate the mass rate of deposition per unit area, depending on whether the number concentration or entrained mass flow rate is taken as the driving force for deposition; the two transfer coefficients are related uniquely.

Alexander and Coldren (43) investigated the mass transfer characteristics of water droplets entrained in a horizontal 47.2 mm I.D. duct, the two-phase flow being generated by injecting atomised water (27 μm mass mean diameter) into a turbulent air stream (Re_D in the range 10^5 to 10^6). Radial droplet mass concentration profiles were measured at several axial positions downstream of the atomiser using a collection rake consisting of nine 2 mm I.D. impact tubes arranged across a diameter of the duct at the exit of the test section. Deposition rate in the fully developed flow region was lower than that in the undeveloped region, due to the high initial radial velocity imparted to droplets by the atomiser. The main resistance to the transfer of water droplets from the airstream to the duct wall was in a relatively thin layer of gas adjacent to the wall. However, no photographic study of the drop-size distribution

in the entrained flow was carried out.

In the experiments of Friedlander and Johnstone (34), 0.8 to 2.63 μm diameter iron particles and 5 μm diameter aluminium powder were separately entrained in turbulent air flow in the vertical direction. Deposition rates of particles on the walls of the glass or brass tubes were determined by counting at least 100 particles deposited in a known area of the tube wall over a fixed time interval. Particle concentration was regulated by adjusting the amount of powder fed to the atomising nozzle, and core concentration was determined using an isokinetic sampling device located at the pipe axis. Deposition velocity results were correlated with a reduced stopping distance showing reasonable agreement with their theory for eddy-diffusion impaction deposition mechanism.

The deposition of 1 to 28 μm diameter uranine particles in lengths of 5.3 mm to 71.4 mm I.D. aluminium tubes for Reynolds numbers in the range 2×10^3 to 6×10^4 was examined by Sehmel (51). To evaluate deposition rate, a mass balance of particles deposited on the walls and on a filter placed across the tube was made from fluorometric analyses of system washings. The uranine particles were generated by a spinning disk generator and transferred into a holding chamber before passing vertically up one or two parallel lengths of the test section, the inner walls of the tubes in certain cases made tacky to simulate a perfect particle sink. However, no pressure drop measurements or estimation of the extent of aerosol charging during generation (shown by Montgomery and Corn (52) to be significant) were made. For particle diameters larger than

8 μm, deposition velocity was found to be independent of particle size where Re_D = 4200. At Re_D = 21,000 deposition velocity increased rapidly with particle size. Perhaps the most useful result in Sehmel's analysis of the data is the indication that large eddies do penetrate into the viscous sublayer to re-entrain the larger diameter particles. Comparison of the results with the theories of Friedlander and Johnstone, Sehmel and Davies was fair.

Montgomery and Corn (52) investigated the deposition of uranine-methylene-blue aerosol particles in relatively large (152.4 mm I.D.) pipes for Re_D in the range 5×10^3 to 3.67×10^5. A horizontal pipe geometry was used with particle sizes in the range 0.44 to 2.16 μm in diameter. Analysis of deposited mass was essentially similar to the technique by Sehmel (51). Aerosol charge neutralisation was incorporated in the instrumentation. Montgomery and Corn compared their measurements with the theories of Beal, Davies, Friedlander and Johnstone and concluded that the theoretical approaches of Davies and Beal were satisfactory although they underpredicted the measured deposition velocities. The range of τ^+ in Montgomery and Corn's investigations fall in the region where diffusional deposition velocity and inertial deposition velocity are at their minimum.

The deposition of entrained water drops following the removal of a liquid film in vertical annular two-phase flow was investigated by Cousins and Hewitt (44). The gas-droplet mixture was created by entrainment from a liquid film injected around the periphery of the tube; the film was subsequently removed by suction through a porous sinter. Droplet deposition

velocity (or mass transfer coefficient as referred to by the authors) was relatively high in the region immediately downstream of the film removal point, reducing asymptotically with distance further downstream. Deposition velocity further appeared to be independent of gas velocity, pressure, tube diameter and upstream flow conditions. Photographic studies (using cinephotography and microsecond spark photography with diffused rear lighting) provided information on droplet size distribution, velocities and impingement rate. Examination of this data suggested that elutriation of large drops with high radial velocity but low axial velocity may have contributed to the initial high deposition velocity near the first film removal position.

Farmer et al. (53) investigated the deposition of large water drops (mass mean diameter in the range 92 μm to 262 μm) onto the vertical walls of a 12.5 mm I.D. tube coated with a thin layer of magnesium oxide. Where a drop struck the wall, a crater was formed in the oxide layer. The number of such impacts at various distances below an axially located water injection needle was visually counted. Deposition velocity was found to be inversely proportional to τ^+ in line with the intuitive idea that the response of the larger drops to the turbulent eddies is more sluggish than that of the smaller sizes over the size range of particles for which τ^+ exceeds 10^3. If an initially polydispersed spectrum were released, Farmer et al. further predicted that a relatively coarse spectrum would be formed downstream due to preferential deposition of the smaller sizes, an effect referred to as "spectral hardening".

The deposition of 0.1 to 28 μm diameter uranine particles onto the upper and lower surface of a 600 mm by 600 mm square duct at Re_D in the range 9.2×10^4 to 5.5×10^5 was investigated by Sehmel (54) in a separate study. The deposition surface used was a strip of electrically earthed brass shim stock placed either on the floor or ceiling of a wind tunnel. Deposition flux was determined from a fluorometric analysis. Particle concentration in the core flow adjacent to the deposition surface was determined by using thin wires coated with petroleum jelly to sample the uranine particles, and the local air velocity by using a hot wire. Tests with and without a thin layer of sticky deposition surface were carried out. For particle diameters having $\tau^+ < 0.1$ the Brownian diffusion deposition mechanism predominates although the contribution of eddy-diffusion in increasing the measured deposition velocities was significant. Particles were found to re-entrain more readily from the ceiling surface than a floor surface. A semi-empirical eddy diffusivity model was used to correlate the results.

Perhaps one of the most widely quoted experimental studies on turbulent deposition and regarded as generally more accurate than others, is that of Liu and Agarwal (39). Monodispersed, charge-neutralised, olive oil drops (diameter range from 1.4 μm to 21 μm), tagged with uranine particles for fluorometric analysis of the deposited mass, were passed vertically down a 12.7 mm I.D. glass deposition tube for $Re_D = 10^4$ and 5×10^4. The experiments cover a τ^+ range of 0.21 to 774. The results highlighted a linear relationship between F^+ and τ^+ for τ^+ in the range 0.2 to 10, with F^+ reaching a maximum at $\tau^+ \simeq 30$ after

which F^+ seemed to show only moderate dependence on τ^+. However, as with other studies, no data on the actual number concentrations used in the experiments were quoted and the droplets were assumed not to agglomerate.

Forney and Spielman (55) examined the deposition of Lycopodium spores (30.9 μm diameter) in vertical downflows through a range of different diameter glass tubes, the smallest and largest I.D. being 13 mm and 44 mm respectively. Perfect sticking conditions were promoted by coating the inside surface of the test section with a mixture of petroleum jelly and paraffin oil. No pressure drop measurements were made but Re_D varied over the range 4×10^3 to 6×10^4. Microscope counting of the deposited spores provided information on deposition flux whilst particle concentration in the core region was obtained using an isokinetic sampling probe. Deposition velocity exhibited a peak at $Re_D = 10^4$ for the uncoated tubes. Satisfactory correlation for F^+ and the ratio of particle stopping distance to tube diameter was obtained using a modified form of Friedlander's (56) expression; the results further showed general agreement with those of Sehmel (51) and Alexander and Coldren.

McCoy and Hanratty (57) critically examined the existing experimental deposition rate measurements with regard to the ability to predict this quantity for annular two-phase flow. For vertical flows and τ^+ exceeding 10^4, F^+ was found to be inversely related to particle diameter and for τ^+ in the range 10 to 10^4, F^+ remained essentially constant at 0.17; finally the relationship $F^+ = 3.25 \times 10^{-4} \tau^{+2}$ described that range of particle size having τ^+ between 0.1 and 10. They further

deduced that deposition rates for horizontal flows may be estimated from vertical flow measurements provided that the ratio of vertical flow deposition velocity to drop terminal velocity, V_t exceeded 10.

Recently, Papavergos and Hedley (58) modified the deposition model of Hutchinson et al. by treating the fraction of particles which diffused towards the wall region and which failed to deposit as being subjected to the additional deposition mechanism due to turbulent upsweep/downsweep, rather similar to the analysis by Cleaver and Yates. Papavergos and Hedley further included the mechanism of Brownian deposition resulting in an expression for the nett deposition velocity consisting of three independently additive terms. Measurements of the deposition velocities of di-2-ethyl-hexyl-sebacate aerosol particles (size range 0.5 to 4.0 μm diameter) were carried out in a 101.6 mm I.D. glass tube for Re_D ranging from 1.33×10^4 to 7.66×10^4. The entrained aerosol concentration was determined by isokinetic sampling. Deposited particles adhering to the inside walls of the glass tube were counted using an in-situ, non-imaging, near-forward laser scattering technique (59), the surface of the glass tube being scanned helically by the laser beam. The values of τ^+ investigated ranged from 10^{-3} to 1 corresponding to the transition from diffusional deposition to the eddy-diffusion impaction regime. Agreement between theory and experimental measurements was good.

2.4 Re-Entrainment

The subject of re-entrainment, or generally entrainment, from a wall film has been reviewed by Hewitt and Hall-Taylor (60) and in a more recent book by Hewitt (61), under a wider study of annular two-phase flow systems. In contrast with deposition experiments, unidirectional drop entrainment experiments involving the removal of entrained drops from the gas core are simply impractical. In addition, estimates of the rate of entrainment based on measurements of the initial rate following the smooth wall injection of a continuous liquid film would be highly misleading since a build up of surface waves from which most droplets are generated takes place after a considerable number of pipe diameters downstream. Whilst various theories for describing interfacial and wall shear stress, film flow rate, pressure drop, film thickness and mass transfer between film and core of annular two-phase flows have been proposed by Wallis (62, 63) Russel and Lamb (64), Fisher and Pearce (65) and Hutchinson et al. (66) amongst others, a suitable theory for predicting entrained drop sizes and number frequency and their relationship with gas and liquid flow parameters has yet to be formulated.

Existing experimental studies on entrainment in annular two-phase flows may be classified into two main categories. The first category involves understanding the fundamental behaviour of interfacial waves (surface ripples and larger disturbance waves with fairly distinct wave velocity, frequency and amplitude). The existence of large disturbance waves has been shown (67) to be a necessary but insufficient criterion for the formation of entrained drops. Since ultimately the successful

prediction of the rate of entrainment and/or entrained drop sizes depends on understanding the entrainment mechanism from these disturbance waves, experimental investigations of the characteristics of interfacial waves have been carried out by Hall-Taylor et al. (68) Nedderman and Shearer (69), Tomida and Okazaki (70), Thwaites et al. (71) and Hori et al. (72).

Hall-Taylor et al. have identified four categories of annular air/water flow: (a) non-wetting region in which the water fails to wet the whole tube surface but with water flowing over the dry surface in streams or drops; (b) region of ripple waves only in which the tube surface is covered by a complete liquid film with small surface waves; (c) disturbance wave region in which large waves are superimposed on the ripple waves; and (d) the pulse region in which intermittent "pulses" of large disturbance waves are observed. (The disturbance waves do not exist immediately downstream the liquid injector but needed time to grow to a stable form.) There was also strong evidence that the transition to disturbance waves is accompanied by the initiation of entrainment. Measurements of mean velocity of disturbance waves for the vertical annular flow geometry indicated that it is insensitive to changes in film flow rates but increases rapidly with increasing gas flow. The frequency of the waves was insensitive to gas rate but increased in proportion to liquid rate.

Nedderman and Shearer (69), extending the work of ref. (68) over a wider range of variables, noted that when two waves combined, the resultant wave usually has a higher velocity than that of either component waves. Wave velocities determined in their experiments were similar to those of Hall-Taylor et al.

indicating that the disturbance wave, once formed, was unaffected by the geometry of the apparatus. The occurrence of disturbance waves on the liquid film was further suggested to be analogous to the transition from laminar to turbulent flow which exists in single-phase pipe flow.

Measurements of wave velocity, film thickness and wave separation were also carried out by Tomida and Okazaki (70) for a vertical annular flow of air/water. The velocity of disturbance waves was found to be several times the mean film velocity whilst the maximum and minimum film thickness were found to be two to three times and half the mean film thickness respectively.

Thwaites et al. (71) found that the addition of a drag-reducing agent to the liquid film stabilised the film, delaying the transition to disturbance waves to higher Re_D in addition to decreasing the frequency of these waves.

Hori et al. (72) investigating the effect of liquid viscosity on the characteristics of interfacial waves and friction factor for upward annular flow of an air-glycerol aqueous solution, found that whilst liquid film thickness and wave height increased with liquid viscosity, wave frequency exhibited the opposite trend.

On analysing axial view cinephotographs of vertical annular air-water flows, Hewitt (73) noted that the growth of disturbance waves was due to coalescence of ripples and liquid entrainment only occurred when the disturbance waves were established. Drops were released explosively from the disturbance waves and possessed considerable radial velocity at formation. Although the disturbance wave amplitude was circumferentially

non-uniform at any instant, velocity and frequency were independent of the distance travelled (from analyses of normal view cinephotographs). The ratio of wave amplitude to mean film thickness was approximately constant and independent of flow conditions.

The second category of entrainment studies includes those experiments which determine the entrained fraction (or rate of mass transfer between the liquid film and the gas core) by a mass balance involving the local film flow rate and the total mass flow rate of the liquid introduced through the pipe walls further upstream. Several methods have been used to determine the extent of liquid entrainment. Film extraction using suction through a porous sinter (74) or a slot (75) in the pipe wall has been used to provide measurements of local film flow rate. Whilst Simpson (76) concluded that the porous sinter technique gave less consistent results than did the slot method, Hewitt (61) on the other hand was in favour of the porous sinter, stressing that it is more likely to provide a true film-measurement compared with the slot method provided that in a steam/water system there are no dry patches on the wall. Alternatively, direct measurement of the entrained mass flow rate using a sampling or isokinetic probe has been reported in the experiments by Gill et al. (77), Wicks and Dukler (78) and Adorni et al. (79). The total entrained flow rate may be determined by integration of the mass velocity profile. Another method would be to analyse axial view cinephotographs for droplet flux measurements as reported by Mayinger et al. (80). Although useful information on entrained drop sizes and drop

velocity may also be established by this method, it is rather tedious. A method for determining the rate of mass interchange between the gas core and wall film based on measurements of salt or dye concentration in the liquid film following wall injection (further upstream) of a known flow rate of salt or dye has been investigated, first by Quandt (81) and subsequently by Cousins et al. (74), Cousins and Hewitt (82) and Jagota et al. (83). The main limitation of this technique is that mixing of the dye within the liquid film is not instantaneous, resulting in a non-uniform radial concentration of the dye leading to serious measurement errors as discussed in ref. (74) and (83). In addition there is the problem of non-uniform concentration of entrained salt or dye in the gas core as highlighted by Cousins and Hewitt (82).

Wicks and Dukler (78) correlated their experimental results using an entrainment parameter J defined as $Q_w We_c E / Q_g \left(\frac{dP}{dL}\right)_g$ where Q_w and Q_g are respectively the volumetric flow rate of water and air, We_c the critical Weber number (as defined in Chapter 6), E the total entrained mass flow rate of water and $(\frac{dP}{dL})_g$ is the pressure gradient which would exist if gas phase were flowing alone in the pipe. J was correlated with a Martinelli parameter (84) defined as $\left[(\frac{dP}{dL})_w / (\frac{dP}{dL})_g\right]^{\frac{1}{2}}$, where $(\frac{dP}{dL})_w$ is the pressure gradient which would exist if the liquid phase were flowing alone in the pipe. For sudden-shock exposure of the liquid phase to a fast moving air stream, Hinze (85) suggested a value of 13 for We_c and for gradual acceleration, a value of 22. Values of 13 and 16 for We_c have been used in the experimental correlations of Wicks and Dukler. Other

authors who have used the Wicks and Dukler technique for correlation of entrainment data include Jagota et al., Collier and Hewitt (86) and Gill et al. (87).

A different and more promising correlation of the entrainment data is that proposed by Hutchinson and Whalley (88). Arguing that the rate of entrainment may be characterised by the dimensionless group $\frac{\tau_f m_f}{\sigma}$ where τ_f is the interfacial shear stress, m_f the mean film thickness and σ the surface tension of the liquid, they correlated the entrained mass concentration at hydrodynamic equilibrium, M_E, (i.e. when the mass rate of droplet deposition is equal and opposite to the mass rate of entrainment) with $\frac{\tau_f m_f}{\sigma}$ for the experimental data of ref. (74), (87), and (82), and also Gill et al. (89), Cousins and Hewitt (44) and Truong Quang Min and Huyghe (90). A general trend was observed supporting their description of entrainment as arising from the local disruption of the liquid film.

Whalley et al. (91) investigating the entrainment characteristics of annular vertical flow of air/water as well as air/"Genklene" mixtures found that their results (for entrainment rate defined as mass entrained per unit area of tube wall per unit time) compared favourably with the experimental data for pressurised steam/water of Keeys et al. (92) and Singh et al. (93) when the equivalent wall roughness parameter, k, (94) is used instead of m_f, in the dimensionless entrainment group, i.e. $\frac{\tau_f k}{\sigma}$

Recently Ueda (95) investigated the entrainment rate and size of entrained droplets for vertical annular flow of air/liquid mixtures. The surface tension and viscosity of the liquid

used were varied over an order of magnitude. Correlation of their results by the method of Hutchinson and Whalley indicated considerable scatter in their data. This was attributed to the fact that whereas the entrained fraction increased with increasing air velocity the product $\tau_f m_f$ was not sufficiently sensitive to variations in the air velocity. The entrainment rate E was subsequently found to correlate well with the parameter $\frac{\tau_f}{\sigma}(\frac{U_f}{\sigma})^{0.6}$ where U_f is the superficial liquid velocity for the film flow. The drop number frequency distribution may be described by the gamma function and the mass mean diameter was found to be insensitive to total liquid flow rate or liquid viscosity.

Until a satisfactory entrainment model capable of predicting number concentration and mass frequency of entrained drop sizes is formulated, dependence on empirical correlations in estimating the entrainment rate is inevitable for the present.

CHAPTER 3

DROP SIZING TECHNIQUES

3.1 Introduction

A wide range of droplet sizing techniques has been reported (see for example recent reviews by McCreath and Beer (96), Jones (97), Azzopardi (98), and Hewitt (61)). The aim in this chapter is to present a brief review of the methods relevant to the determination of drop-size distributions from a dense atomiser spray and/or in a turbulent two-phase pipe flow. Interest is therefore focussed on those techniques suitable for sizing water droplets in the 10 μm to 300 μm, diameter range encountered in the present studies. The existing methods may be conveniently divided into two main categories according to their operational characteristics, i.e. intrusive and non-intrusive techniques. The following sections present details of each category listing the advantages and limitations in each method.

3.2 Intrusive methods

This category of sizing methods involves the inevitable need to interfere with the droplet-laden flow by the sensing equipment. It relies on an efficient collection and/or detection of droplets and a complete absence of factors which may modify the results before useful information is extracted. The methods belonging to this category include (i) impaction on coated surfaces, (ii) immersion sampling, (iii) mechanical sampling probe, (iv) electrical techniques, and (v) 90° scattering probe (refering to a special case in which the instrumentation is such that an optical probe arrangement is used).

3.2.1 Impaction on coated surfaces

Droplets to be sized are first collected on a glass slide coated either with lamp black (99), white vaseline (100) or magnesium oxide (101, 102). The size of the craters formed by the impaction of individual drops on the coating material (the film thickness just exceeding the largest diameters encountered) may be determined from microscope measurements. Correction factors relating the actual droplet diameters to the measured crater diameters from a previous calibration permit the size distribution of any polydispersed spectrum be accurately determined.

May (101) found the ratio of droplet to crater diameter for the magnesium oxide film to vary from 0.86 for all diameters in the range 20 μm to 200 μm to 0.75 for the 10 to 15 μm range. Stoker (103) used an empirically-determined correction factor (for soot coating) given by $0.77\ We^{0.2}$ where We is the Weber

number (defined in sec. 6.3) of the drop. Houghton and Radford (100) quoted a flattening coefficient of 0.8 for water drops resting on a coating of white vaseline.

Some advantages with this method include the indefinite retention of the craters, no errors arising from drop coalescene after impact and simplicity of the method. The major disadvantages are restrictions on impact angle, fragmentation of heavier drops upon impact, an upper limit on the measured diameter determined by the thickness of the film used and the bypassing of the narrow slides by the smaller drops. Sampling efficiency of water drops for a slide mounted on a cassette held on a trolley with a shutter mechanism which permitted uniform exposure of the whole slide when positioned perpendicularly to the direction of a wet steam flow was estimated by Kolb (102) to range from 60% for a 15 μm drop to 100% for a 100 μm diameter. However, no details of the physical dimensions of the slide used were reported. The dependence of collection efficiency on the ratio of drop diameter to slide width was highlighted by Ryley and Fallon (104). A slide with a narrow width was reportedly more efficient at capturing smaller diameter drops than one having a larger width. Ryley and Fallon further introduced several correction factors including that for evaporation effects, limited penetration and sedimentation effects to the observed drop-size distribution. The use of liquid coating to retain the captured droplets has also been reported. Dunskiy et al (105) used a silicon oil coating to determine the size distribution of satellite droplets during the atomisation of liquids by a rotating disk. Some properties required of the liquid coating include (i) immiscibility with

sampled droplets, (ii) lower density than the droplets to prevent them from rising to the surface, thereby spreading, (iii) discouragement of coalescence within the medium and (iv) ability of the mixture to remain stable over the period of measurements. An advantage of the liquid film over the solid coating is the absence of any need to relate the size of an impression to that of the impacting droplet.

3.2.2 Immersion sampling

This method is an extension of the liquid-coated slide technique. An immersion cell containing a suitable immiscible liquid is temporarily exposed to the drop-laden flow stream. Due to the low density of the capturing medium, the droplets sink through the cell and remain suspended as practically perfect spheres. Photographs of the captured droplets, which remain stationary at the bottom of the glass cell, can be made and analyed either manually or by an automatic image analyser (see for example Adler et al.(106)), additional properties required of the immersion fluid include low surface tension, high viscosity, a different refractive index from the captured droplets and transparency. For sampling water droplets, silicon oil (107) and Stoddard solvent (108) have been used. Adler and Marshall (108) coated the bottom of the cell (made of optically flat glass) with a non-wetting agent to prevent flattening of the drops. Tate (109) dyed the spray with 3% nigrosine to enhance contrast when photographs of the captured droplets were made.

Limitations of this method include (i) the requirement for low concentration of drop population to prevent appreciable

coalescence after capture, (ii) drop fragmentation upon impact due to high velocity contact with the surface of the immersion fluid and (iii) failure of the very small drops to impact on the collection cell due to lateral deflection of the flow over the cell. On the other hand, well focussed images may be photographed permitting the use of simple automatic image analysers e.g. flying spot scanner (106) for fast and accurate measurements. In addition, correction factors for flattening, etc., are not needed since the captured droplets retain their spherical shape. Alternatively microscopic examination of the collected droplets may be carried out immediately.

3.2.3 Mechanical sampling probes

Whereas most isokinetic aerosol sampling probes are meant for solid particles, liquid droplets could equally be sampled provided that they are adequately solidified before reaching the inner regions of the sampling probe. The method therefore involves the use of a compatible freezing agent which solidifes the drops at the inlet to the probe. Rao and Levebvre (110) and Ballal (111) employed such a technique in the study of size-distribution from a fuel spray (Fig. 3.1). The probe is mounted with its inlet facing the incoming two-phase flow. Gaseous nitrogen at approximately 140 K, injected into the incoming flow sample, through a narrow annular slot located near the inlet, rapidly freezing all droplets which are then collected in a pre-cooled perspex pot or passed through a set of standard sieves (112) for direct analysis. Alternatively the collected sample may be microphotographed

to be analysed later. In-situ measurements under the microscope is not possible with this method because of the low temperature involved, resulting in a dense atmosphere of condensed moisture from the surrounding environment. In addition, measured diameters have to be corrected for freezing effects. The probe collection efficiency has to be separately determined if further information on local number density is required. An advantage of this technique is that the collected sample provides a temporal size distribution.

3.2.4 Electrical methods

The detection of electronic signals arising from droplet interference with an electrically operated probe introduced into a droplet laden flow provides the basis of operation of these methods. The type of signals recorded may be classified into one of the following methods: (i) Wicks - Duckler pulse counting technique, (ii) the charged wire technique and (iii) heated probe technique.

3.2.4.1 Pulse counting technique

Originally developed by Wicks and Dukler (113) and subsequently examined by Pye (114), McVean and Wallis (115), Jones (116) and Jones and Sargeant (117) the technique is based on the criterion that when a gap separating a pair of electrically conducting needles, across which a potential is applied, is momentarily bridged, a voltage pulse may be recorded. By varying the gap between the needles (Fig. 3.2) a relationship between an average count rate and gap width provides a method of establishing the drop size distribution.

The method therefore relies on the conductivity of the droplet fluid and hence is limited to those fluids with low electrical resistance. Pye concluded that the technique is suitable for droplets in the range 5 μm to 1000 μm as well as being capable of detecting temporal variations in size distributions. However, Jones and Sargeant encountered difficulties with the method when the apparent resistance across the bridged needles depended upon droplet velocities, surface conditions of the needles and the degree of needle immersion into the drop.

3.2.4.2 Charged wire technique

The principle of this method is that when a drop of conducting liquid comes into contact with a charged wire, some charge is transferred to the drop; the amount of charge drawn from the wire is given by the integral of charge density over the surface of the drop (Fig. 3.3). If a number of drops were to impinge on the wire in succession, a series of step changes of charge density on the wire would occur. These changes could be electronically differentiated giving rise to a train of pulses. A relationship between the charge loss (i.e. pulse size) and drop diameter could be established thus enabling measurements of drop-size distributions to be made.

Guyton (118) reported the pulse size as varying with the square of the drop diameter. However this is disputed by Giest et al. (119) who found that the pulse size varied with the diameter to the 1.6 power. Gardiner (120) noted that the pulses arising from water droplets are similar in shape to those obtained from nuclear scintillation equipment.

Consequently, there is available commercially a range of single or multi-channel pulse size analysers which are capable of accepting and classifying a train of different pulse heights. When calibrating the measurements, water drops of known size are allowed to strike the charged probe and in the case of multi-channel analysers the channel number in which the pulses are stored is noted. Gardiner therefore avoided the need to determine the charge/drop size relationship.

Due to charge concentration at the tip of the wire as drop impinging at this position would remove more charge from the wire than at any other position on the wire hence leading to erroneous results. Gardiner remedied this problem by masking a short length of the wire, from the open end, with a plastic sleeve.

An undesirable feature of the method is the effect on pulse height of drop impact velocity. There is also an upper limit to drop arrival rate which just avoid superimposing two consecutive pulses, restricting its use to flows having a low number concentration.

3.2.4.3 Heated probes

The thermal effects of a water drop on a heated surface forms the basis for this category of size measurements. When a drop falls onto a heated surface, the surface temperature at the impact area decreases sharply if the heat conducted to that point is at a lower rate than that required to maintain a constant contact temperature. Van Paasen (121) presented a technique in which the hot junction of a thermo-

couple is exposed to the droplets. A drop impinging on the hot junction alters the surface temperature momentarily as it evaporates (Fig. 3.4). A relationship between drop diameter and the temperature signal from the thermocouple could be established hence providing a means of determining size distribution. However, the performance of the so called droplet detecting thermocouple relies on no splashing at contact and under a turbulent flow situation, such requirements are difficult to meet.

Alternatively a thin electrically-heated wire (hot-wire) may be exposed to the droplet laden flow stream. A drop impinging at a section of the wire therefore causes local cooling, altering the wire resistance at that point. If the current through the wire is kept constant, changes in the resistance of the wire could be measured as voltage fluctuations with a sensing network such as a Wheatstone bridge (Goldschmidt (122)). Alternatively, a"constant temperature" technique may be used (Moore and Bragg (123)) in which changes in the wire temperature are immediately compensated via a corresponding increase or decrease in the current flowing through the wire. The voltage pulses arising from thesechanges may be calibrated against a range of standard drop sizes. In a test involving a monodispersed spray, Moore and Bragg found that a wide range of pulse height and duration was registered for the same size drop. The abnormality was due to the incomplete retention on the wire of drops moving at speeds exceeding a critical Weber number of 2.5. In a further study Moore (124) found that the height of the voltage pulse produced by a drop of a given size depended on the position

of the drop on the wire. He concluded that for drops larger than a critical size, the pulse duration provided a sensitive measure of drop size and for sizes smaller than the critical diameter, the pulse height was suitable. Medecki and Magnus (125) using a constant current method employed the pulse height to characterise drop size and quoted a size range from 1 μm to 600 μm for which satisfactory performance of their equipment was possible. The time of evaporation for a 10 to 100 μm drop is quoted by Moore as several milliseconds. This may cause practical problems of superimposed pulses when droplet arrival intervals are less than this value. Bragg and Tevaarwerk (126) in a similar study determined the time of evaporation of an 80 μm water drop to be approximately 80 milliseconds in an air stream of 3 m/s. In addition, droplet rate of evaporation and temperature are found to be dependent on ambient air velocity, temperature and relative humidity. On the basis of their results Bragg and Tevaarwerk concluded that the outlook for the hot-wire anemometer as a water drop sampler is rather pessimistic.

3.2.4.4 90° Scattering Probe

Although more than one property of the scattered light may be used to determine size distribution (as is highlighted in sec. 3.3.1) the concern here is with the property of scattered light intensity at 90° to the incident beam. Fig 3.5(a) illustrates the optical arrangement for this technique. A high-intensity light beam is focussed at an adjustable scattering volume, V, determined by aperture sizes B_1 and B_2. A spherical drop moving across V scatters the light. The

scattered intensity at right angles to the original beam is detected by a photomultiplier which outputs a voltage pulse to a pulse height analyser. To improve signal-to-noise ratio the photomultiplier may be cooled permanently down to 253K whilst in operation. Based on light scattering theory (127), a relationship between drop diameter and the scattered intensity (indicated by the pulse height) could be established via a calibration experiment. Ederhof and Dibelius (128) using a light probe shown in Fig. 3.5(b) successfully applied the technique to the determination of size distributions of coarse drops behind the last row of moving blades in a low-pressure steam turbine. A unique feature of the method is the ease with which the scattering volume may be altered to suit the operating environment. Values for V ranging from 20 mm^3 for the measurements of large drops in cooling tower sprays to 10^{-6} mm^3 for small droplets in turbines have been used.

However, some undesirable characteristics of the technique include the need of correction factors for (i) coincidence errors caused by two or more droplets moving simultaneously through the scattering volume, (ii) fringe errors caused by droplets passing the edges of the scattering volume, (iii) multiple scattering errors and (iv) variation of incident light intensity. A less serious error is the dependence on drop refractive index of the measurements.

3.3 Non-intrusive techniques

Optical, photographic, holographic and photography related methods comprise the main bulk of non-intrusive techniques used in drop sizing. The common advantage of these methods lies in their non-interference with the sampled or measurement volume. However, except for single particle measurements, only spatial rather than temporal drop-size distributions are directly determined. For the optical techniques, those methods unsuitable for the determination of drop sizes in the range 10 μm to 300 μm are omitted in the review.

3.3.1 Optical methods

Measurements of the light scattering properties of particles have been widely used to determine such properties as particle size, concentration, refractive index and shape. The independent scattering of light by a single, homogeneous, spherical particle of arbitrary size and refractive index has been examined by Mie (127) as early as 1908 on the basis of electromagnetic theory. Until the development of electronic computers, numerical solutions of Mie's formulae were scarce and limited to small size parameters for which infinite series in the amplitude functions converged rapidly. For particle sizes above 1 μm, computations of the Mie theory became extremely lengthy. As development of digital computers accelerated, many solutions for larger particles were produced, a summary of which is given by Penndorf (129).

For particle sizes larger than the wavelength of incident light, simpler theoretical approaches through geometric

optics have been made. A method which utilised the angular variation of intensity of forward scattered light at very small angles in the determination of size distribution of a polydispersion larger than 10 μm is presented by Chin et al. (130, 131). They related measurements of angular variation in forward light intensity to the size distribution of a polydispersion and found satisfactory agreement between the optical technique and a manual analysis.

However, the work of Chin et al. is disputed by Dobbins et al. (132) who found the angular distribution of light intensity for a polydispersion distributed according to the Upper Limit Distribution Function (ULDF) (see Chapter 6 for definition) to lack the sensitivity necessary to permit determination of size distribution. Instead Dobbins et al. found the volume-to-surface mean diameter, $\bar{x}_{32}$, to be directly dependent upon angular distribution of intensity for a wide variety of shapes of the ULDF. Roberts and Webb (133) extended the treatment to a greater range of skewness and spread and found the least deviation between an experimental $\bar{x}_{32}$ and theoretical $\bar{x}_{32}$ to occur at one-tenth normalised intensity in the generalised illumination profile. The technique has been widely used by several workers including Rizkalla and Lefebvre (134), Bryan et al. (135) and Lorenzetto and Lefebvre (136) in the determination of fuel atomisation characteristics without the need for actual information on size distribution.

Abbis (137) on the other hand, using a numerical technique, studied the feasibility of determining size distribution from measurements of forward scattered light intensity and concluded on an optimistic note. The basis of Abbis's technique was the ability to invert the integral equation of

classical diffraction theory which expressed the scattered light intensity in terms of an arbitrary size distribution function so that the distribution function could be re-expressed in terms of measured intensity of the scattered light. Values for the angular variation of scattered intensity were initially numerically generated for a known size distribution function. Using only information of scattered intensity over a small angle in the forward direction and the inversion equation, the original distribution function was readily reproduced demonstrating the feasibility of the technique. For the fundamental diffraction formula used to remain valid, the smallest particle sized in the spectrum must not be less than 5 μm. The upper limit was less well defined with possible values in the range 50 μm to 100 μm. Pozharnov (138) and Zimon et al. (139) amongst others have used the small-angle method to determine drop-size distributions from respectively a pneumatic atomiser and wet steam.

Since the theoretical basis of the method described above, depends on independent scattering of light intensity, restrictions of this technique include the need for low particle number concentration so that multiple scattering is absent. In addition there is a need to limit optical depth so that all particles are equally illuminated. In practice this is normally done by "slicing" the flow volume, the optical axis passing perpendicularly across a thin "slice" of two-phase flow. Measurements of absolute light intensities in practice require a stable light source and an equally stable detector circuitry.

Other methods based on light scattering include a laser

diffraction technique described by Switenbank et al.(140) and Cornillault (141). In this technique a parallel beam of monochromatic light passes through the sampled volume and forms for each particle within the sample volume, a diffraction pattern which can be observed at the focal plane of a lens (see Fig. 3.6) placed in the light path just beyond the sample volume. If the particles are monodispersed and of the same spherical shape, the diffraction pattern consists of a series of alternate light and dark concentric rings (Fraunhofer diffraction pattern) the diameters of which are inversely proportional to the particle size and independent of particle position and movement within the sample volume. If the particles are polydispersed, the nulls in the diffraction pattern are filled in giving rise to a continuous radial energy distribution. The light energy contribution at any annular ring in the focal plane is simply the sum of all the contributions from each individual particle (of all sizes). Hence a measurement of the radial variation of light energy distribution at the focal plane of the Fourier transform lens (Fig. 3.6) provides a suitable method for deducing the size distribution. The detection of radial variation of light energy distribution could be automated. Coupled with a suitable choice of a minicomputer, a fast automatic analysis of size distribution may be configured (see for example Switenbank et al.). To avoid multiple scattering effects, a low number concentration is required by this method.

Whereas the Laser diffraction technique employs a single beam passing through the flow volume to provide a size distribution for a cloud of particles, the simultaneous measurement

of velocity and size of a single particle crossing a set of spatially well-defined interference fringes, generated by two (see Fig. 3.7) crossed laser beams, has been examined by Farmer (142), Jones (143), Hong & Jones (144), Yule et al. (145) and Ungut et al.(146). The light scattered by movement of the particle across the fringed volume has an AC component, the frequency of which may be interpreted in terms of the rate at which the particle centre crosses the alternate bright and dark interference fringes. Measurement of the AC frequency and fringe spacing therefore yields the local particle velocity, the now well-established laser Doppler anemometry technique (see, for example, Durst, Melling & Whitelaw (147)). For size measurements, Farmer examined the relationship between signal visibility (defined as the ratio of the AC to DC components of the scattered intensity) and the particle diameter to fringe spacing parameter, and concluded that even for a constant diameter to fringe spacing ratio, signal visibility is dependent on the shape of the particles. For spherical particles visibility measurements may be correlated with particle size over a limited range of diameters for a given fringe spacing.

A rigorous wave-theory solution for the scattered intensity in the plane of the incident light beams due to a sphere was given by Jones in an attempt to predict optimum angles for light collection. Extending this work, Hong and Jones found that the relationship between signal visibility and particle size is insensitive to refractive index but affected by the choice of fringe spacing and measuring angle, θ, (see Fig. 3.7) relative to the axis bisecting the two incident beams.

In order that the fringe spacing and θ be chosen so that the whole particle size distribution lie within the sensitive region of visibility - size curve, a priori knowledge of the diametral range of the particles to be analysed is needed. Experimentally the following theoretical conditions must also be met: (i) equal intensity for both laser beams, (ii) perfect temporal and spatial coherence, (iii) the two beams to be polarised in the same plane, (iv) 100% beam polarisation (v) infinite plane waves and (vi) no mechanical vibration. The method is therefore confined to measurement of single particles within the fringe volume and in particular for diameters smaller than the fringe spacing. Another disadvantage of this method is that particles which do not pass through the centre of the fringe volume produce signal visibility which significantly differs from the theoretical value.

For particle diameters larger than the fringe spacing it is apparent that some characteristics in the forward scattering signal may be measured although there is no general agreement on precisely which parameters best reflect the size distribution. It is likely that more than one approach is valid. Yule et al. made measurements of signal amplitudes for spherical particles larger than the sizes for which full Mie theory computations for the light scattered have so far been made, using the optical arrangement illustrated in Fig. 3.8. Note that the photodetectors are positioned on the axis which bisects the 2 laser beams as opposed to the geometry employed by Farmer and Hong and Jones for particles smaller than the fringe spacing. Traversing transparent glass particles at approximately 1 m/s across fringe intervals

of 5.32 μm, Yule et al. found that (i) the scattered pattern became unsymmetrical when the particle motion was not centralised, (ii) the Doppler signal amplitude was always a maximum when the centre of the fringe volume was traversed, (iii) particle shape affected scattered pattern, i.e. dust particles would affect measurements and (iv) the laser output and photomultiplier must be closely monitored during the experiment since variations in their performance seriously alter signal amplitude. They concluded that a monotonically increasing relationship between the peak signal amplitude and size of transparent particles existed for a range of diameters determined by the geometry of the optics. (in particular the collection angle ϕ in Fig.3.8). The problem of particles not passing through the centre of the fringe volume was examined by Ungut et al. They introduced a gate photomultiplier at right angles to the optical axis (see Fig. 3.9) to select measurements only for these particles which passed through the centre of the fringe volume. A disadvantage of the method is its dependence on the optical properties of the particle.

In conclusion, the accuracy required of optical measurements relies heavily on the stable performance of the electronic equipment used, including the need for stringent operating conditions e.g. isolation from external vibrations. In addition it is difficult to interpret data for particles having an arbitrary shape and in certain instances the results are also dependent on the particle refractive index. Perhaps the single major drawback of any optical method is the need to avoid multiple scattering effects, restricting its

usefulness to flows with low particle concentration.

3.3.2 Photography

The method by photography involves the capture of droplet images on a photographic emulsion via a single flash illumination, the duration of which is adjusted to freeze all movement of droplets within the field of view of the camera lens. The direction of illumination inevitably depends on the type of information sought. In the determination of size distributions of droplet-laden flow, the direct-shadow optical arrangement (Fig. 3.10) is usually employed (see for example Moore et al. (148), McCreath et al. (149) and Mellow et al. (150)). Usage of a parallel light beam gives rise to diffraction rings around each drop image as well as limiting the total available light energy received at the focussing screen of the camera. An alternative method is to focus a point source onto the aperture of the camera lens, eliminating Fresnels fringes as well as increasing the total light energy received by the photographic emulsions.

Exposure of the photographic emulsion is usually accomplished by the use of mechanical shutters and a well illuminated object field. For extremely short exposure periods, e.g. < 1 μs, two methods may be considered. The first involves the use of an electrically operated "Kerr-cell" shutter in which the duration of exposure is controlled by the period of an electronic pulse whilst the second is to limit exposure by the duration of the flash (e.g. an argon-stabilised spark discharge or the use of a pulsed laser beam), using "open-shutter" photography. Drop velocity and the amount of

tolerable blur of its image determine the exposure period and hence the selection of the photographic technique.

The main source of error with the photographic method lies in the analysis of the photographs for information on size distribution. Where all drop images are sharply defined (the flow volume well within the depth of field of the optics) the error is minimal. When the depth of field is less than the width of the drop laden flow, analysis, manual or otherwise, must be confined to those images which are well focussed. Subjectiveness in a manual analysis is inevitable. More recently, automatic analysis of droplet photographs has been made possible by the use of sophisticated image analysing computers (151, 10) and a suitable scheme for discrimination between well focussed and poorly focussed images.

The photographic technique is also capable of providing information on droplet velocity. This is usually accomplished via the use of double flash photography (152), stereophotogrammetry (153) or streak photography (154), the details of which will not be included here.

Variations to the above theme include the use of a fluorescence technique described by Benson et al. (155) in which a plane "sheet" of light was used to irradiate droplets, previously dyed with a fluorescing chemical, in the plane of best focus of the camera lens.

Concluding, the art of photography is well established. Simultaneous information on velocity, shape and particle size are provided in a photographic technique without the sort of restriction on number density which limits the effectiveness of other techniques.

3.3.3 Holography

Whereas conventional photography only records the reflected or transmitted light intensity and wavelength from an object in the light path, a holographic record freezes the phase content of the transmitted or reflected light with the help of a second reference beam. Fig. 3.11 illustrates the formation of a hologram. A coherent monochromatic beam is divided into two parts; one part illuminates the object, the scattered light from which is then mixed with the other part, the reference beam, in the recording plane. The resulting intensity pattern of bright and dark fringes is recorded on a photographic emulsion (i.e. hologram). A real image of the recorded features can be reconstructed by illuminating the hologram with the reference beam in the same direction as when the hologram was recorded. The hologram acts as a diffraction screen for the reference beam and the wave pattern behind the hologram is exactly similar to those due to the real object. Chubb and Abbis (156) satisfactorily employed an in-line Fraunhofer (far field) system for sizing freely falling plastic spheres and concluded that the system is especially suitable for particle diameters in the 5 to 500 μm range, provided the maximum recording distance does not exceed certain limits set by the smallest diameters. However, dense artificial sprays cannot be satisfactorily measured by this technique. Webster (157) set the maximum permissible movement of the subject, (during an exposure) using in-line holography, at 10% of the subject diameter for reconstructable images and made measurements of drop sizes in the range 20 to 500 μm travelling at up to 70 m/s.

Because of the coherent properties of the beam, diffraction patterns at every inteference point and dust specks are encountered so that the resulting beam often contains considerable background noise. Multiple scattering effects reduce hologram quality, limiting the technique to low density droplet laden flows. Measurements of holographic records can either be manual or automated involving the use of an image analysing computer. Bexon et al.(158) employed the vidicon target of the Quantimet 720 (without any imaging lens) to capture the reconstructed image and arranged a sizing procedure which automatically scans the image volume, hence increasing the speed and accuracy of analysis. Other advantages of holography include : a large depth of field for all particle diameters; size, spatial and velocity distributions obtained in one recording; and no dependence on particle shape and refractive index.

3.3.4 Photography-related techniques

Direct determination of drop-size distribution by replacing the photographic emulsions with a 2-D array of photodetectors have been reported by Simmons and Lapera (159), Toner et al.(160) and Sadowski and Byckling (161). The main aim of such systems is to bypass the need for intermediate data storage on photographic emulsions and to speed up data processing by coupling information from the photodetectors directly to a minicomputer or microprocessor in an on-line configuration. However, a scheme to distinguish between "in-focus" and "out-of-focus" features is needed when the optical depth of field of the imaging lens is less than the

two-phase flow width.

Sadowski and Byckling avoided the need to consider "out-of-focus" features by reducing the flow geometry to a "thin-slice", the width of which is less than the depth of field of the lens used. A silicon imaging device (of a TV camera) having a 512 x 320 element sensor to produce electronic signals from a visual input is used to detect features from a stationary or moving system; the motion of the latter may be frozen by a short-duration flash. Using only two grey levels (i.e. black or white) to discriminate between background and well-defined features, analogue signals from the TV camera were first digitised and subsequently fed into a minicomputer programmed for feature extraction and computation of such attributes as area or perimeter of each identified feature. The discrimination level at which a positive detection of a feature was made was determined from a previous calibration experiment. The obvious drawback with this technique when considering its use in the present studies on two-phase flow is the need for a thin, laminar stream.

Toner et al.described a system which used the vidicon target of a standard TV camera (without its imaging lens) to detect shadows of droplets illuminated by a parallel light beam. Using Direct Memory Access (DMA) facilities and a microprocessor, feature extraction was carried out as the information from the TV camera was fed into the processor memory. The system therefore operated in real time without the need for intermediate data storage on peripheral units. However, it should be realised that the scheme by Toner et al. is strictly restricted to two-grey-level discrimination,

providing an almost instantaneous readout of detected features on a lineprinter. The system relies on a good choice of a preset discrimination level forminimal deviation from the mean values measured. In practice, measurements are likely to be affected by non-uniform light intensity received by the vidicon target due to local variations in the number concentration of the droplet laden flow stream. To minimise the number of overlapping images drop number concentration has to be low or the width of the flow reduced.

A less flexible system which uses hardwired logic for feature extraction and determination of areas, perimeters etc. is described by Simmons and Lapera. Also using the vidicon target of a standard TV camera for image detection, the vertical trace mode was altered to remove interlaced tracing while retaining an effective 525 horizontal line scans. Droplet motion was frozen by $\frac{1}{2}\,\mu$s flash illumination. Discrimination between in- and out-of-focus drops was carried out by monitoring changes in the scanning line voltage. Once a drop was classified as being in focus, it was electronically identified to the counting circuits which sized and placed the drop in the proper storage group. The technique suffers from drift in the operation of electronic circuitry requiring periodic cross-checks on the measurements. Since important information on e.g. correction techniques for partial images at the edge of the screen and the number of grey levels used as well as the grey-level at which diametral measurements are made are absent, it is difficult to compare the performance of this system with those described above. However, the general impression conveyed is that it is an extremely fast

real-time droplet image analyser, belonging to the category of instrumention which is "one-off" and perhaps ideal for the determination of drop sizes.

3.4 Sizing by high-speed shadow photography

Amongst the various techniques reviewed, droplet photography remains the most feasible choice for the following reasons: (i) droplet population at the test volume unaffected by the measurements, (ii) provides information on size distribution, (iii) permits the determination of size distribution at specific locations within the two-phase volume rather than averaging across a section as encountered in certain optical methods, (iv) data from a dense population may be effectively extracted, (v) optical properties of particles or droplets do not seriously affect the measurements, (vi) relatively cheap instrumentation with extreme flexibility in operation, (vii) provides information for multimodal distributions and over a wide range of shapes and sizes and (viii) more recently (151, 10) photography - related automatic image analysis systems are available for size measurements if needed.

As highlighted in section 3.3.2 the basic principle of the method is illustrated schematically in Fig. 3.10. The nature of the subject under study, namely a fast moving stream of entrained droplets, is such that front or side illumination will result in inadequate exposure of the emulsion for image formation. To avoid the appearance of diffraction rings (if a parallel light beam is used), a condenser lens focusses the spark image onto the operture of the camera lens. Any, increase or decrease of the camera aperture relative to the diameter of the spark image only causes deterioration of the uniform illumination across the focussing screen of the camera. Droplets travelling across the converging light path at the plane of best focus of the lens therefore appear as sharp silhouettes

against a uniform bright background. An additional central bright spot is observed on each "transparent drop" image, a phenomenon due mainly to light rays passing uninterrupted through the centre of the drop.

The limits of the depth of field of an optical system may be defined with respect to a circle of confusion i.e. the smallest diffused image of a point which is indistinguishable from a point. For hand-held cameras, the equation relating the depth to relevant optical parameters is given by Cox (162) as

$$A = \frac{2f\Pi\ (W + 1)}{100\ W^2} \qquad \ldots.3.1$$

where f is the focal length, Π the relative aperture used, W the magnification and A is the required depth of field. Eqn. 3.1 assumes a value of 1% of the focal length of the lens for the diameter of the circle of confusion. This criterion is adequate for most hand-held cameras, the notion being that the further away a photographer is from the object field (determined by the focal length on the camera) a correspondingly larger diffused image diameter of a point is tolerated as indistinguishable from a point by the human eye. However, Eqn. 3.1 quoted by Jones (97), Azzopardi (98) and McCreath (96) is inapplicable when technical measurements of small drop diameters are involved.

For the present optical arrangement, Ramshaw's (163) simplified analysis for depth of field given by Eqn. 3.2. below is preferred. Hence

$$A = \frac{2f\Delta\,(W + 1)}{\xi \quad W^2} \qquad \ldots.3.2$$

where ξ = diameter of spark image or alternatively the aperture opening which just accepts the spark image,

Δ = the degree of blur (an absolute value) at the perimeter of the image, defined in Fig. 4 of ref (163).

For a fixed degree of blur Δ, the depth of field is therefore directly proportional to the focal length f, inversely proportional to the aperture diameter ξ and decreases as the magnification, W, increases. Therefore each drop size, based on a sharpness criterion e.g. 2% on the image diameter, has a different depth of field. Alternatively, a fixed depth of field may be defined (with the other parameters unaltered) for all sizes if an absolute degree of "blur" is tolerated irrespective of size.

The use of mechanical shutters to limit exposures largely depends on the speed of motion of the droplets photographed. In most studies (148, 149) similar to the present investigations, open shutter photography is employed, the total exposure being determined by the flash duration and energy output available.

Further details of developmental work and instrumentation used in perfecting this technique are presented in Chapter 4.

CHAPTER 4

DATA ACQUISITION BY HIGH SPEED SHADOW PHOTOGRAPHY

4.1 Introduction

Development work on the high speed shadow photographic data acquisition technique is described in this chapter. Very often the selection of relevant instrumentation for any photographic work is governed by considerations of several factors, some of which are highly incompatible. A typical example is the triangular relationship between depth of field, magnification, and illumination. The need for high magnification which inevitably reduces the depth of field is often dictated by the requirement for adequate resolution of the smaller sizes in the spectrum in which the extreme diameters differ by an order of magnitude. In practice, to avoid the need of many photographs in establishing a reasonable number count for the spectrum, a large depth of field is preferred. These two conflicting requirements may be satisfied when the focal length of the lens used is sufficiently long, requiring an even longer image distance on the camera. However, since light intensity varies inversely as the square of the distance separating a constant power light source from the camera focussing screen, image definition on the photographic emulsion may be poor when the needs for depth and magnification are satisfied.

Two distinctive types of drop-size distributions may be defined for any two phase flow stream; the distinction (where it exists) lies mainly in the method employed in

sampling. The photographic data acquisition technique provides a spatial rather than a temporal size distribution. However, if all droplets were travelling at the same speed across the photographic test volume at all times, this distinction does not exist. A method for converting the spatial distribution to a temporal distribution lies in the accurate determination of average velocities for each drop size in the spectrum under the assumption that similar practical operating conditions are maintained. The technique presently employed involved photographing repeatedly at each point in space and at more than one position radially across the flow. The net spectrum from these results may be regarded as derived from a random spatial sampling of an infinitely large volume. Although the present instrumentation will form the basis for measurements of droplet velocities, no such measurement has been made in the present work. Consequently, the spatial size spectra determined for the atomiser spray would most likely have a larger volume mean diameter in their temporal distributions, owing to a preponderance of smaller drops near the nozzle exit, a fact highlighted by Lewis and Walker (164). Conversely, a temporal drop size distribution in the droplet laden pipe flow would result in a smaller mean diameter than that currently measured since the smaller drops would be moving relatively faster than the larger ones. However, results from Finlay and Welsh (152) indicated that the maximum difference in the velocities of a 5 μm water drop and a 300 μm drop entrained in 30 m/s air flow,under test conditions rather similar to the present investigations does not exceed 10%.

The error between a spatial and temporal size distribution is therefore not considered significant.

Included in this chapter is a description of the photographic aspect of the experiments conducted in Chapter 7 and 8 to study respectively the size distributions of the atomiser sprays and the two-phase pipe flow spectra. Initial attempts to employ double-flash photography for droplet velocity measurements are also discussed.

4.2 Relevant Instrumentation

4.2.1 Camera

From considerations of the need to expose and develop a single photographic frame for contrast checks before a batch of photographs is taken, the overall magnification required and the need for an adequately large photographic field of view, an MPP Photographic Products Ltd. monorail technical camera (see Fig. 4.1) with a maximum bellows extension of approximately 762 mm was acquired for the present work. The camera houses a standard 5 inch by 4 inch (127 mm x 102 mm) double-sided black slide at its back plate whilst a "blank" front plate was modified to house the lens. The maximum distance separating the focussing screen at the rear and the nodal plane of the lens in front is approximately 902 mm including the extra 76 mm length afforded by the conical lens mount unit and the 32 mm fine-focus movement at each end of the camera. In practice (using a 50 mm focal length lens) the required magnification of up to 14x is readily met without the need to make use of the extra 32 mm fine-focus extension at the rear of the camera. At a magnification of approximately 10x, for example, the 5 inch x 4 inch format captures a two-dimensional field of view measuring about 13 mm x 10 mm which is approximately fifteen times the viewing area available from a non-technical 35 mm camera for the same magnification. Whilst a 35mm camera may yet be suitable for the present work except for this reduced viewing area, the need to expose completely a roll of 24 mm x 36 mm rectangular frames before it could be processed is an unfavourable feature for developmental work. The additional accessories

used with the MPP camera are 25 double-sided cut-film holders enabling a total of 50 cut-films to be exposed in any batch job, and a heavy-duty tripod.

4.2.2 Lenses

The choice of a suitable lens depends primarily on the application intended. In the present work, a lens designed for "macro" work involving a significant amount of magnification is needed. In general the focal length of the selected lens is dictated by the following considerations: (a) the overall magnification required; (b) the depth of field which in turn is determined by the need to minimise the total number of overlapping images arising from the presence of a dense spray; (c) whether or not there is a need for the lens to remain outside the two-phase flow stream or relevant spray chamber; (d) the total amount of light energy eventually received by the photographic emulsion after passing through the two-phase flow stream; (e) the overall extension available on the camera, although in practice this is limited by the physical size of the laboratory which houses the experimental equipment; (f) the need to minimise interference with the two-phase flow at the plane of best focus (or photographic test section) arising from the inevitable intrusion in certain circumstances of the lens into the flow stream.

From considerations of the physical dimensions of the two-phase flow rig (see Chapter 7) in which 102 mm I.D. pipes are used, a lens having a focal length not much less than 51 mm is needed so that the pipe axis may be photographed

with minimum intrusion by the lens into the flow stream. Accordingly, a 50 mm focal length, f/2.8 aperture Leitz-Photar macro lens was used (where the f-number or relative aperture provides a measure of the light gathering power of the lens; a numerically small f-value means a large aperture diameter and vice versa. f/2.8 therefore refers to the largest aperture diameter available from the lens which in the present case is approximately 18 mm). The Leitz lens provided a maximum overall magnification of approximately 14x on the 762 mm MPP camera with its bellows fully extended

Although the Leitz lens usefully established drop size distribution from the fairly dense spectra of a double air jet pneumatic atomiser which shall be referred to as the air-blast atomiser and a single air jet (Delawan-Watson Ltd.) pneumatic atomiser which shall be termed D-W atomiser (see sec. 7.2), when photographing across a two-phase flow downstream of the injection section (see sec. 4.3.2) the 14x magnification employed resulted in relatively few images on a 5 inch x 4 inch photographic negative. A denser image field may be photographed if the depth of field is increased by reducing the magnification as given in Eqn. 3.2, and accepting a larger "cut-off" size dictated by resolution requirements. However, a better alternative was implemented, involving the use of an 80 mm f/5.6 Sneider-Componon lens which was a part of the hardware of the automatic image analysis system described in Chapter 5. A two-fold increase in the depth of field was expected since the overall magnification had decreased to 9x with the camera setting geometrically un-altered, in addition to an increase in focal length of the

lens from 50 mm to 80 mm (see Eqn. 3.2). The depth of field may further be increased by decreasing the relative aperture i.e. an increase in the f-number setting on the lens but it has the adverse effect of diminishing the total amount light energy falling on the photographic emulsion. This in turn affects the choice of a suitable emulsion for the images as well as further limiting the total distances separating the light source from the camera.

4.2.3 Spark sources

A 200 μm diameter droplet travelling at a speed of 15 m/s requires an exposure period not exceeding 0.27 μs to "freeze" its motion if a displacement of 2% on its diameter may be tolerated. Such short durations preclude the use of any mechanical shutters, requiring instead open-shutter photography with exposure periods determined by the flash. Accordingly, a $\frac{1}{4}$ μs argon-stabilised single-electrode spark unit Optical Works Ltd. Model 7 was used initially. Satisfactory photographs of droplet spectra from the air-blast atomiser (see sec. 7.2.3) were taken with no blurred edges detected on any "in-focus" drop image (see Fig. 4.2).

In view of the need to determine droplet velocities at a later stage of experimentation, a double-electrode spark unit would have been preferable. Subsequently, such a unit manufactured by Pulse (Instrumentation and Controllers) Ltd., became available and was additionally acquired. The two spark units may be suitably combined to give a chain of triple flashes for measurements of droplet acceleration if the need arises (for example, in verification of certain

features of a coagulation theory).

The design of the Pulse unit is such that the power pack is separated from the flash head. This permitted ease of operation, the light weight flash head being readily moved around during the initial stages of alignment. The single-electrode Optical Works spark unit has the flash head and power pack housed in an integral unit; its design results in unnecessary loss of light intensity due to the small condenser lens employed. A significant increase in the amount of light available from the Pulse unit was a further reason for its acquisition; this is attributed mainly to the large condenser lens located in front of the electrode assembly. Owing to the longer focal length of the Pulse condenser lens (600 mm) the camera would have to be located further from the source to permit the focussing of the spark image onto the camera lens aperture. This also resulted in unnecessary loss of overall light intensity. To overcome this unfavourable feature, a 152 mm diameter plano-convex lens was integrated with the existing Pulse condenser lens resulting in an equivalent focal length which is about half the original value. An additional unsatisfactory feature of the Pulse unit lies in its focussing lamp. This consists of a 2.5 W torch bulb, its total output barely adequate to form a discernible image of a microscale, for example, on the focussing screen of the camera. The Optical Works unit, on the other hand, has a 60 W focussing lamp. When attempting to focus the image of the microscale onto the focussing screen when using the Pulse spark source, a 60 W articulated table lamp located immediately in front of

the flash head was employed to illuminate the object.

Both spark units were operated under a continuous supply of argon gas at a delivery pressure of approximately 5 psig (35 kPa gauge), without which uniform spark intensity and regulated spark discharge may be difficult to achieve.

4.2.4 The pulse generator

To provide the firing pulse for the spark units, a Malden Electronics Ltd. Model 738 pulse generator was used. It has two separate signal channels, each of which is capable of delivering consecutive triggering pulses set at various combinations of pulse widths, frequencies and amplitudes. A manual operation which delivers a single or a pair of consecutive pulses (with adjustable delay periods) each time a switch is operated is also available. Each channel has independently adjustable delayed triggering facilities; the delay periods may be varied from microseconds up to a maximum of one second. It must be remembered that although the delay period may be accurately generated by the pulse unit, it may not reflect the actual interval between the appearance of two consecutive flashes from the spark source. A separate measurement of the flash intervals ought to be made with each delivery of a pair of consecutive pulses when droplet velocities are needed.

4.2.5 Photographic emulsions and development

A complete photographic process usually involves a physical process of recording the image of an object onto a

photosensitive material followed by a chemical process of development of the latent image to produce a permanent record. It should be realised that at every stage of the photographic process, image details can be diminished or accentuated according to the specifications of the operator. Incorrect mating of the photosensitive emulsion to the spectral composition of the light source and in the present study, the total amount of illumination available, may accentuate or completely eliminate image formation. The choice of a suitable photographic emulsion therefore depends on (i) f- number or relative aperture range available on the camera lens (since it limits the total amount of light energy falling on the photosensitive material), (ii) contrast requirement for the images, (iii) total available incident light energy from the limited duration of the flash, and (iv) the spectral sensitivity of the emulsions to the flash source.

High contrast emulsions are generally slow to react and therefore require relatively longer exposure periods compared with medium contrast films for the same incidence of light energy. Early attempts to use high contrast films in the photography of a dilution of 20 μm diameter polystyrene latex spheres provided satisfactory results when an ordinary electronic flash source was employed. However, with the spark source, the Kodaline Reprographic film used was inadequately sensitised due mainly to the shorter flash duration limiting exposure of the emulsion.

Certain photographic emulsions are capable of having their film speeds altered by the use of a suitable developer

(e.g. Ilford FP4 emulsion with Ilford Perceptol reduces its normal ASA specification from 125 to 65). Additional attempts (employing different combinations of emulsions and chemical developers e.g. Kodak D-8) at photographing the 20 μm polystyrene latex spheres as well as atomised droplets from the D-W atomiser were made. Ilford FP4 films developed in Ilford Contrast FF for 3 minutes at 20°C under a dilution of one part of concentrated solution with four parts of water provided the most satisfactory results. The resolving power of the FP4 films is approximately 100 lines/mm. Ilford FP4 films were therefore used in all subsequent photographic work. After development, the films were adequately fixed in Ilford Amfix diluted 9x at 20°C for at least 3 minutes.

4.2.6 Continuous air purge for lens

When photographing at the innermost region of a dense atomiser spray, image definition was often masked out by the presence of droplets in the space separating the front face of the camera lens and the photographic test section. Droplet images were further degraded if the front face of the lens was wet when intrusion into the spray volume was inevitable.

To overcome these problems a lens cover encompassing a continuous air purge device was built; the assembled camera lens and purge unit are shown in Fig. 4.3. The length of the air purge duct used was such that it avoided causing interference to the flow at the plane of best focus and simultaneously improved image quality through the masking out of a major section of the intervening droplets. As seen

in Fig. 4.4, purge air is directed at the microscope slide which shields the camera lens. The internal geometry of the prototype purge duct was that of a converging nozzle with the purge air leaving the exit at a relatively high velocity. However the 30 mm length of the prototype "converging section" used was extremely unsatisfactory. Despite the relatively fast exit velocity of the purge air, heavier droplets which possessed sufficient inertia strayed into the duct wetting the microscope slide. Modifications to the prototype duct included the addition of a diverging section as shown in dotted lines in Fig. 4.4. Since the exit of the extended unit now approaches the plane of best focus of the camera lens the diffusing action of the diverging section reduces the exit velocity of the purge air flow sufficiently to avoid causing interference to the photographic test section. In addition, an inner nozzle with an exit diameter large enough to avoid interfering with the edges of the incoming converging light beam was introduced, providing a fast inner jet of purge air which eventually left the purge duct at a relatively low velocity as illustrated in Fig. 4.4. The continuous air purge unit for the lens provided extremely satisfactory image definition even when photographing in the densest sprays. Additional extension to the air purge duct is possible by fitting the present assembly into a larger diameter duct. The air mass flow rate through the purge unit is negligibly small compared with the two phase air flow.

4.2.7 The optical bench

The average time needed to align the spark source and camera unit in a typical photographic session was approximately 2 hours. When photographing across different sections of the conical spray of an atomiser, the method employed which avoided the need to realign the optics with each new position photographed was to shift the atomiser assembly relative to the plane of best focus of the camera lens as described in section 4.3.1. However, when similar attempts to photograph radially across a section of the two-phase rig (in either the horizontal or vertical direction) were made, the optics had to be repositioned with each new photographic field of view. This was an extremely slow procedure owing to the need to re-align the optics each time a new position was photographed. Since moving the 10 metres length of 102 mm I.D. piping of the two-phase rig relative to the optics was not practicable, an alternative method employing a purpose-built optical bench was implemented.

An optical bench on which the spark source and the monorail camera may be mounted to slide as an integral unit was designed and built. As illustrated in Fig. 4.5 it houses the Pulse flash head at one end and the monorail camera at the other, the two axes located at the same height in the vertical plane which passes through the axis of the optical bench. The total length of the bench is approximately 2 m, governed by the separation needed to focus the spark image onto the aperture of the camera lens. The task of aligning the optics on the bench was relatively easy since pre-specified locations were defined for the flash head and

camera units. The assembled unit therefore provided a photographic plane of best focus which could be shifted horizontally through a maximum distance of 254 mm and vertically through 127 mm when photographing at various positions across the two-phase flow stream. A graduated scale on the bench enabled an accurate positioning of the photographic plane of best focus near the wall of the two-phase duct when the wall spectra were needed. In addition, the arrangement reduced, by an order of magnitude, the time required to complete a series of exposures. It enabled drop-size spectra across several radial positions be photographed on the same day under the same atmospheric conditions, avoiding the need to complete the experiment on another day as was experienced prior to the introduction of the bench. The bench design avoided the use of a heavy base plate and is readily assembled from its five basic components, none of which is too heavy for a single operator to lift.

4.2.8 Miscellaneous

To enable a direct determination of all magnifications employed in the photography, a precision microscope reticle (Ealing-Beck Ltd) containing a 10 mm length scale graduated in 0.02 mm intervals was used. For maximum magnification factors, the camera was always operated with its bellows fully extended and the front-end fine-focus adjustment set at a maximum value. A magnification factor for each lens could first be determined from a calibration experiment in which the microscale was photographed in the plane of best focus. With the camera geometry unaltered, photographs

of the two-phase spectra are therefore under the same magnifications.

A comparison reticle containing black discs of nominal diameters ranging from 10 to 1000 microns (Ealing-Beck Ltd) was acquired for use in the calibration of the automatic image analysis system described in Chapter 5. An optical bench having a rack and pinion mechanism for saddle traverse was used to position the reticle in this application.

A fully equipped darkroom located near the test laboratory was made available for any immediate photographic development work needed. Batches of up to twelve 5 inch x 4 inch cut-films may be held in a developing tank during each development.

4.3 Experimental methods

Initial attempts at perfecting the high-speed shadow photographic technique involved the use of a modified micro-technical MPP camera (an earlier model of the MPP monorail described in sec. 4.2.1) and a 55 mm focal length enlarger lens to photograph a dilution of 20 micron diameter poly-styrene latex spheres. A twelve-inch square section exten-sion was fitted to the front face of the camera, the original wide-angled camera lens being first replaced by a 55 mm focal length enlarger lens. An overall maximum magnification of approximately 11x was possible with the modifications imple-mented. Useful information on the spectra of the D-W atomiser were derived using this photographic arrangement prior to the arrival of the main instrumentations.

The following subsections describe the photographic procedures employed in the determination of drop-size dis-tributions from experiments with atomisers as well as in the two-phase flow rig. In addition, a brief description is given of the method for producing a set of photographs for use in the calibration of the automatic image analysis system (see Chapter 5). Open shutter photography in a darkened room was employed in all the experiments though Jones (10) and Mellor et al. (150) successfully used mechanical shutters synchronised to the spark discharge in their operation, thus enabling photography in a bright environment.

4.3.1 Experiments with atomisers

Photographic determination of the drop-size distri-bution of the Delavan-Watson pneumatic atomiser and the

author's air-blast atomiser (see Chapter 7) were carried out. Fig. 4.6 (a) illustrates the schematic arrangement of the optics involved. The Optical Works spark source was employed in these experiments. A 90 mm focal length condenser lens focussed the spark image onto the aperture of the camera lens, the distance FCL separating the condenser lens and the front face of the light source being determined by the need for the spark image to just "fill-up" the camera lens aperture. From Fig. 4.6 (a), the distance separating the plane of best focus, f, of the camera lens from the front face of the atomiser is maintained at 70 mm, a choice which best satisfied the need to minimise the total number of overlapping images. The relative aperture of the 50 mm focal length Leitz lens was set at f/11, consistent with the amount of illumination available from the spark source located at approximately 440 mm (FCF distance in Fig. 4.6 (a)) from the camera lens, a choice dictated by the overall geometry of the atomiser test rig (see Fig. 7.4). The corresponding value for FCL was then best set at approximately 100 mm.

An experiment was carried out to determine the section of the conical spray which best represented the overall spray spectrum without having to photograph at every position within the spray. Fig. 4.6 (b) shows the three different directions attempted. Owing to variations in number concentration of droplets with radial position, photographic results from direction A overestimated the true mean diameters of the spray. Direction B was not satisfactory due mainly to the limited depth of field photographed at each selected radial position. Photographs along the Y axis i.e. direction C,

indicated a possibility for staggering the fields of view across the full range of radial positions from the axis of the spray downwards to the outermost periphery of the spray. Under an overall magnification of 14x, the 5 inch x 4 inch image format of the camera permitted a series of rectangular 9 mm x 7 mm object fields to be staggered (lengthwise) along the vertical plane passing through the axis of the conical spray. From assumptions of symmetry, only the lower half of the spray along the Y-axis needed be photographed. In practice, this is equivalent to displacing the axis of the atomiser upwards by a fixed value relative to a stationary plane of best focus of the optics. The diameter of the conical spray at the axial position of 70 mm from the atomiser outlet (which defined the apex of the spray cone) was approximately 144 mm hence requiring exactly eight staggered (lengthwise) rectangular fields of view.

The sequence of events in a typical photographic experiment therefore involved the following: (a) alignment of the optics so that the plane of best focus is located in the vertical plane passing the axis of the conical spray and displaced 70 mm from the face of the atomiser; (b) adjustment of required atomiser operating condition; (c) continuous air purge and 5 psig (35 kPa gauge) argon supply turned on and a required number of photographs taken in a temporarily darkened laboratory; (d) atomiser assembly displaced vertically by a predetermined value relative to the plane of best focus of the optics and step (c) repeated; (e) steps (c) and (d) repeated until the outer periphery of the conical spray is detected

or a fixed number of radial positions previously established are photographed.

To ensure good image quality on the FP4 emulsions the continuous air purge duct was extended to within 5 mm of the plane of best focus. Owing to the net radially outward motion of the droplets, interference at the photographic test section by the partial intrusion of the continuous air purge duct into the spray volume was minimal.

Details of the atomiser test rig, atomiser operating conditions used in the experiments and results of the photographic analysis are presented in Chapter 7.

4.3.2 Experiments in the two-phase rig

A major aim in the design of the two-phase rig was to be able to establish the number concentrations and drop-size distributions of the entrained droplets at various radial positions across each selected axial location downstream of the liquid injection section. Since the working pressure in the two-phase flow duct was marginally above atmospheric, the method selected involved photographing the flow as it left a specific length of horizontal ducting to discharge into a 305 mm diameter flexible tubing which drained the main portion of deposited liquid and the remaining entrained flow from the pipe exit as illustrated in Fig. 4.7.

Fig. 4.5 illustrates the optical arrangement to photograph the flow as it leaves the pipe exit; the corresponding schematic diagram for the optics is shown in Fig. 4.8. The purpose-built optical bench allowed the plane of best focus to be moved in either the horizontal or vertical plane across the pipe exit. From observations of flow recirculation at the entrance of the 305 mm drainpipe and subsequent re-entrainment of the recirculated flow into the outer layers of the jet issuing from the open end of the pipe, the plane of best focus of the camera lens had to be located preferably immediately upstream of the pipe exit (i.e. inside). To facilitate such an arrangement, two diametrically opposite 32 mm wide slots were cut 40 mm lengthwise into the open end of the 102 mm I.D. Durapipe section to allow for the inevitable partial intrusion of the continuous air purge duct into the pipe wall when photographing at the axis of the flow although

the 80 mm focal length Sneider-Componon lens used in the photography, at all radial positions photographed remained outside the duct walls. Droplet spectra at different radial positions across the flow stream were therefore photographed in the horizontal direction perpendicular to the axis of the flow.

When radial variations of size spectra in the vertical direction are needed, the plane of best focus has to be located at approximately 20 mm axially from the duct exit to permit unobstructed movement of the continuous air-purge duct in the vertical plane. However, re-entrainment of the re-circulated flow into the outer layers of the jet meant that only radial positions well within the flow unaffected by re-entrainment may be photographed (the furthest position photographed was at 35 mm from the axis).

Fig. 4.7 illustrates the arrangement of the optical equipment in a typical photographic session. A compressed air bottle delivered a 3 psig (21 kPa gauge) continuous supply of air for the purge device. With the optics properly aligned, the sequence of events involved in a typical photographic session is similar to the atomiser experiments. The exception in this case is that the spark source and camera unit move as an integral unit on the optical bench (hence keeping their correct alignment at all times) relative to the flow stream.

The radial positions (in the horizontal direction) photographed at the first axial location (extraction station 2 in Fig. 8.7) were 2 mm, 16 mm, 30 mm and 44 mm measured radially outwards from the flow axis and towards the camera

side of the flow stream. Extraction stations 4 and 5 in Fig. 8.7 were photographed at two radial positions namely 2 mm and 44 mm. For extraction station 3, only the 2 mm radial position was photographed. The various flow parameters used in the photographic experiments are described in Chapter 8. To improve image quality at the first axial position, where the droplet loading is denser than at the remaining 3 positions downstream, the distance separating the plane of best focus from the exit of the continuous air purge duct was set at approximately 20 mm, leading to the inevitable partial projection of the front end of the purge duct into the flow stream when the 2 mm and 16 mm radial positions were photographed. However, no significant interference to the flow stream at the plane of best focus was noticed (visually) whilst a photographic test indicated no major difference between the spectra determined from photographing the 2 mm position with or without the intrusion of the air purge unit into the flow stream, apart from some contrast deterioration in the photographs of the latter.

4.3.3 Depth of field studies

To enable an "in-focus" criterion be applied in the automatic image analysis system described in Chapter 5, a comparison reticle having black discs of various diameters between 10 and 1000 μm was photographed at several positions relative to the plane of best focus. Fig 4.9 illustrates the optical arrangement used. A stage plate fitted with spring clips and capable of 360° rotary movement was used to hold the comparison reticle, presenting a vertical column of disc sizes to the camera. For the magnifications used in the photography (i.e. 9x and 14x) only a limited number (~ 4 or 5) of disc images may occupy the 5 inch x 4 inch format of the cut-films. The stage plate was therefore mounted on an optical saddle with adjustments for vertical movement so that a different batch of discs could be brought into the field of view of the camera without upsetting the optical arrangement. The rack and pinion mechanism for saddle traverse along the optical bench permitted $\frac{1}{2}$ or even $\frac{1}{4}$ mm intervals be used as suitable measurement units when defining the depth of field of the optics. Finer intervals are to be avoided since a small tilt in the vertical plane of the object field is significant to offset any benefits obtained with a finer graduation.

The sequence of events in a photographic session therefore included (a) an initial visual assessment (at the camera focussing screen) of the relative positions of the plane of best and worst focus; (b) starting at an out-of-focus position driving the comparison reticle in $\frac{1}{2}$ or $\frac{1}{4}$ mm intervals across

the depth of field of the lens until an equal amount of blurness was visually identified at the other position, (c) at each intermediate position, photography of the full range of disc sizes; (d) with the movement reversed, taking of a second set of photographs on the return traverse. The two sets of photographs were visually examined under a slide projector. It was concluded that the photographs in one direction were adequate for the calibration of the image analyser for depth of field and in fact a calibration test for the set of return traverse photographs showed similar results (for the 14x magnification only) as those in the forward traverse.

4.4 A note on droplet velocity measurement

When using double flash photography in the determination of droplet velocity the two quantities sought are the distance separating each image pair and the time interval between the two flashes. Owing to the nature of electronic circuitry in the flash unit, the period between the appearance of two consecutive flashes is never equal to the period set by the pulse generator which inputs the two triggering pulses. A separate measurement of the flash interval is therefore needed and a suitable method would be to employ a photodiode detector which generates a pulse with each detected flash. The leading edge of each pulse may be used to start and stop a timer hence registering the interval between two separate flashes. A Racal Universal counter-timer set up to measure the interval between two consecutive input pulses was used for preliminary investigations (an improvement over reliance on the pulse generator setting, giving an approximation to the interval between flashes).

The signals from an RS Components Ltd. type 305 - 462 photodiode, placed at various positions in front of the flash unit condenser lens, were examined. Double flashing of the pulse flash head unit highlighted the following: (i) the first flash is always brighter than the second flash (attempts to generate uniform intensity flashes by careful setting of electrode gaps were unsuccessful); (ii) the use of a single photodetector of extremely good rise time (1 μs) in the detection of both flashes is to be avoided due to non-uniform pulse peaks arising from (i) and hence extreme difficulty arises

in selecting an appropriate gain factor on the photodiode amplifier for both pulse amplitudes; (iii) in order to avoid premature triggering due to variations in ambient light intensity the photodiode had to be housed in a tube which pointed in the direction of the converging light beam; this arrangement was highly unsatisfactory requiring the photodiode tube to partially interfere with the light path in front of the camera lens; (iv) housing the photodiode in the front end of the flash head permanently damages its response to the spark discharge; (v) there appears to be a minimum operational distance ($\sim$ 500 mm) beyond which the detector circuitry is unaffected by the electric field of the spark discharge.

The following remedies are proposed:

(i) Separate detectors and circuitry are needed for the detection of each flash, the counter-timer operated to start and stop counting at the leading edge of each pulse which enters the counter via a separate channel.

(ii) To avoid discharge effects, two lengths (approx. 1 m) of optical fibre should be used to "pipe" light to each photodiode detector.

(iii) The gain on each detector amplifier should be set to match the light intensity transmitted by the optical fibre, hence avoiding any need of a compromise gain factor when a single detector is used. Suitable optical fibres (Barr & Stroud Ltd.) were acquired but no further development work has yet been possible*.

*Footnote: Although at the time of writing, double flash photography was not attempted, the two lengths of fibre-optic probes have recently been mounted in the pulse flash head unit. Double-flash photographs (Fig. 4.10) of the spectra at r/R = 0.04 at

*Footnote (contd.) station 2 (Fig. 8.7) employing test condition A (Table 8.2) were successfully taken. The results indicated that most droplets were travelling at a mean velocity equal to the free stream velocity $\bar{U}$, of the gas phase over the size range (10 to 200 μm) encountered in the present studies.

4.5 Sizing methods

4.5.1 Manual analysis

One of the earliest and most convenient forms of size analysis is to magnify the images to be sized under a microscope, or via projection onto a suitable screen, followed by a subjective classification of the sizes into appropriate groups. Although histogram widths may be refined with perfectly circular images, in practice the need to describe highly distorted and/or elliptical shapes further coarsens the histogram widths when classification is simply based on the upper and lower limits of linear dimensions e.g. the major and minor axes of an ellipse or the vertical and horizontal Feret or Martin (165) statistical diameter (see Fig 4.11). Herdan (166) concluded that when classifying non-circular images of objects, the most consistent results are those in which the diameters of circles having the same areas as the irregular image area sized are employed. However, a quick review of the manual alternatives available for area measurements together with the need to determine areas for more than 500 images at each location are sufficient to discourage anyone from attempting such measurements manually. When dealing with drop images, it is fortunate that the majority of the well-focussed images are either circular or slightly elliptical in shape, a consequence of surface tension forces, and that a manual analysis is therefore feasible although the process is subjective and tedious. Attempts to determine the degree of human bias when sizing well-defined, irregularly-shaped and elongated particle profiles have been reported. Heywood (165) quoted an overestimation of the mean diameter, by 5.7% averaged over 10

independent observers when standard opaque circles placed next to the particle profiles are used, the figure reducing to 1.9% when transparent circles are used instead. Watson and Mulford (167) reported bias estimates ranging from + 13% to - 10% of the true mean value for 9 different observers.

When dealing with images which are nearly circular the subjective bias examplified above is not serious compared with the subjective decision between an in-focus and an out-of-focus image. Various methods are proporsed to minimise this error. Moore et al. (168) used the criterion of an agreement between two observers to minimise subjectiveness in analysing similar photographs. Yorks and Stubbs (169) employed "standard in-focus images" which are projected onto the screen along with the images to be sized to coordinate the judgements from various operators over a period of time. The job of sizing would then be reduced to merely comparing the "in-focus" images with a set of standard images which also defines the limits of the depth of field. This method is currently adopted in all manual analysis of droplet size distribution sampled from the two phase flow rig as well as the atomiser spectra.

Manual sizing can be extremely tedious with a high density of images on a slide but at a low number density the need to analyse more slides, to provide the confidence required to describe a spectrum, could be equally demanding.

4.5.2 Automatic Analysis

Tedium and subjectiveness accompanying any manual analysis may be avoided through the use of an automatic image analyser of the type commercially available (e.g. Imanco "Quantimet", currently manufactured by Cambridge Instruments Ltd.). Such image analysing computers consist basieally of purpose - built detectors (e.g. TV vidicon) which scan the image, and hardwired logic elements which assign to each "picture point" (on a two-dimensional grid covering the image) a "grey level" (light intensity value); additional modules analyse this digitised information to produce a limited number of attributes (e.g. area, perimeter, etc.) for each detected feature. Whilst the problem of identifying in-focus images in a manual analysis is overcome almost subconsciously, the basic image analysing computer is incapable of such a discrimination; instead it requires a precise mathematical definition of the kind described in section 5.4.

Advantages of automatic analysis includes consistent results, speed of operation (with hardwired logic), non-subjective analysis and the ability to refine histogram widths of highly distorted images via a suitable mathematical criterion. A major operational requirement experienced by many users, for example, Jones (10) is the need for good contrast films or negatives for best results. Other requirements include the need for films or photographic negatives with a high number count of probable "in-focus" images and the minimum number of overlapping images. As with most measurements, an accurate calibration of the system with respect to magnifications used in the photography is first needed.

CHAPTER 5

BASIS OF AUTOMATIC SIZING TECHNIQUE

5.1 Introduction

The basic image analysing computer is incapable of discriminating between in-focus and out-of-focus photographic images of droplets, i.e. those within or outside a given depth of field determined by magnification requirements and the focal length of the lens used. Though automatic image processing systems of the type described by Yule (151) and Jones (10) are capable of such discrimination, they involved respectively the need for extensive software control via a peripheral computer or important internal modifications to the image analysing computer itself. Since no such system was available at Imperial College, the possibility of hiring time elsewhere was considered. It was found to be impractical to rely on remote installations for all processing work, for several reasons including the inevitable need to recalibrate a set of measurements with each new setting of magnification, costs, access and problems associated with developmental work. Accordingly, an existing 2-grey-level (i.e. black or white) digitising system (170) has been developed into an 8-level system with the following advantages: (a) immediate availability "in-house"; (b) major components existing (and likely to exist in most laboratories where automatic image analysis is being contemplated for the first time); (c) rejection of unwanted images handled entirely by software, giving much more flexibility than hardwired proprietary equipment; (d) additional data processing needs readily added to the

algorithms without an intermediate data transfer between image analyser and a separate computer; (e) costs of additional instrumentation not excessive.

The following subsections describe the hardware development, software for image recognition and focus discrimination and the calibration and performance of the present 8-level system. It must be stressed that the present scanning instrumentation is meant for processing information from photographic negatives or similar object fields in which transmitted light is employed in the definition of bright images against a dark background. The program for feature detection and software discrimination between well-focussed and poorly focussed images has been written in Fortran IV with an overall architecture related to a mini-computer operating system (DOS-BATCH on the D.E.C. PDP-11/45).

5.2 Hardware

5.2.1 The digitiser

5.2.1.1 Existing Unit

A digitising system capable of detection at 2-grey-levels had been designed and configured around a standard TV camera and an existing minicomputer operating environment in the Nuclear Power Section (N.P.S.) laboratory of the Dept. of Mechanical Engineering at Imperial College. Full descriptions of the circuit design of the existing digitiser hardware with its corresponding functions are given by Qaqish (170). A circuit diagram (with the modifications described in sec. 5.2.1.2 included) describing important functions of this digitiser is shown in Fig. 5.1. To elucidate the format under which the digitiser operates, a brief description of the operation of a standard TV camera is first described in the following paragraph.

Fig. 5.2 shows a standard 625-line interlaced scan pattern of the Sony TV camera used in the current work. Two field scans are needed for a complete picture, the interchange between odd and even field scans (Fig. 5.2) occurring at a fixed frequency. Fig. 5.3 further illustrates how a complete picture is constructed from the odd and even field scans. At the end of each scan line, a repositioning ("flyback") of the electron beam to the start of the next scan line takes place, any visual display of the "flyback" being effectively suppressed by means of a blanking pulse. Similar blanking pulses are also generated at the end of each odd or even field scan, the line and field scan pulses being distinguishable by the different pulse widths assigned

to each.

The main functions of this digitiser are to divide each horizontal scan line (Fig. 5.3, X-direction) into, in this case, 384 picture points of which 380 are currently used and to transmit for each point a binary digit (bit) representing a grey level, in this case black or white. Since a minimum of 9 bits is needed to represent a decimal value of 625 or 380, outputs from the digitiser are designed to have a parallel logic transfer of at least 10 bits of X-coordinate and 10 bits of Y-coordinate (defined by scan lines) information in addition to the 2 bits needed to describe the grey level (black or white) and an odd or even field scan. When information for all 380 X- and 625 Y-coordinates is read, an end of data flag may be set by switching on (by the hardware) all 10 bits of X or Y, thus representing a value so large (1023 in decimal) that software would recognise as the end of information. Relevant data from the digitiser is fed to a PDP 11/45 minicomputer via the CAMAC (171) interface modules. For each shift in the X-coordinate a vertical column of 625 Y-coordinate (in practice only 580 are effectively used) grey levels is fed into the computer. Since interlaced scan is present, an initial set of odd Y-coordinates is read into the buffer (or dynamic memory region of the computer) to be immediately followed by a set of even Y-coordinates, with each increment in the X-direction. It therefore requires exactly 380 repeated odd/even field scans to build up a complete picture array having 380 X-coordinate columns (Fig. 5.3). The CAMAC interface has up to 24 bits of parallel logic input. For a

2-grey-level system only 22 of the 24 bits are used; one bit to signify whether the field scan is odd or even; another for the grey level i.e. black or white and 10 bits for X and 10 bits for Y-coordinates. The early PDP-11 software support package developed in conjunction with the hardware structure therefore simply tests the black or white information bit as well as the odd or even bit and sets up a black and white (i.e. zeros and ones) "bit-map" in core making use of the X- and Y- coordinate information. On a 24K memory PDP-11 machine with 16-bits word length, sixteen "grey levels" may be packed into each word since in this early version only one bit signifies "grey-level". An array of 625 Y- and 380 X- picture points will therefore require a buffer size of approximately 15K which a 24K memory machine adequately accommodates.

5.2.1.2 Modifications

Upon expanding to 8 grey levels (numbered 0 to 7), software manipulation of incoming data was slow owing to the need for every (X,Y) coordinate pair to be accompanied by 3 bits of grey level information. As a result, every other incoming data position was not recorded. Further, a new buffer size of 45K (see sec. 5.2.1.3) was needed to accommodate a single transfer of digitized 3-bit grey levels. (This corresponded to packing five 3-bit units of information into each PDP-11 word, the most significant bit (M.S.B.) left as a spare bit). In view of buffer size limitation on a 24K machine it was decided to make three repeated transfers, each transfer embracing a third of the total number of 3-bit

information units from a complete picture array of (X,Y) coordinate pairs. To do this, additional logic was incorporated into the Sequence Control Logic block of Fig. 5.1. When X-coordinate position indicated by the Odd Frame Counter (Fig. 5.1) reaches either 128 or 256 a pulse generated by Sequence Control Logic is passed onto the Data Control Line which immediately stops the reading operation. PDP-11 software instruction later restarts the reading from where it left off, having first emptied the buffer for the earlier transfer.

A new criterion for software was also needed. It was decided to ignore, in the software, the available bits of X and Y coordinates but to test the odd-or-even bit for a repeated sequence (172). Since each shift in the X-coordinate was accompanied by a set of consecutive odd and even Y-coordinates, it was therefore possible to decode the relative positions of the 3-bits of grey level information by the following method. Fig. 5.4 illustrates the pattern in which the odd or even scan bit was read into the computer. An increment in the X-coordinate value (in software) occurred whenever a complete set of odd and even scan bit was detected. The structure of 3-bit grey level information in each PDP-11 word was such that the odd scans were packed with a space between them to allow for subsequent even scan 3-bit grey levels to be positioned. Fig. 5.5 illustrates this point. One main limitation to this method was the presence of a half line scan at the beginning of one of the two field scans needed to describe a picture. Its presence destroyed the reference position of the X-coordinate and hence the Y-

coordinate values as well, since for a half line scan, X no longer starts from 1. This problem was solved by masking out, using hardware, the first half line scan so that each starting line scan of a new field was from X-coordinate 1.

A further modification was the addition of an adjustable peak setting for the highest grey level (i.e. level 7) so that photographic negatives having poor contrast (hence generating a low useful signal to noise ratio) may be adequately digitised via a corresponding adjustment of the grey level 7 setting to equal or come close to the peak video levels arising from well defined images on the photographic negative. In Fig. 5.1 the relevant control unit is "Front Panel Manual Video Comparator Threshold Control". Its setting influences the digital output from the Video Comparator, a device which converts an analogue signal to the equivalent digital information by assigning a relevant grey-level value to the video signal magnitude encountered.

To summarise, hardware modifications to the existing black and white digitiser included the following:

(1) Introduction of seven grey levels (3 bits for grey level).
(2) Masking out of first half line scans where they appeared.
(3) Automatic stoppage of data transfer by hardware when data read-in reached an X-value of either 128 or 256.
(4) Addition of an adjustable 7 grey level "window" to allow for less contrasting pictures to be meaningfully digitised.

Fig. 5.6 is a block diagram of hardware structure of the present automatic image analysis system. In the circuit diagram

of Fig. 5.1 all above mentioned modifications are shown in dotted lines.

5.2.1.3 Software support package

Description of the operational characteristics of the modified digitiser would be incomplete if the software support package developed in connection with the hardware design is not included here. A "Macro" assembly language programme called CAMERA (subsequent version renamed as MARK1) was written to correctly arrange incoming grey level information in the form of a 2-dimensional "bit-map" in the dynamic memory zone (or buffer) of the computer. When the buffer is full, its contents are transferred onto disk for permanent storage, leaving the dynamic memory zone free to receive another batch of information read by the TV camera. The following paragraphs describe the major functions and data organisation of this support package.

Routine CAMERA

The original CAMERA (173) routine written for the 2-grey-level (i.e. black or white) system was modified to read data from the 8-grey-level system. This program used the 10 X and 10 Y information bits to set up a binary map of grey levels. Due to an overall decline in the speed of execution of the program (mainly because of addition of extra instructions) every other data item coming from the camera (at intervals of 52 microseconds) is missed.

A new version of this routine renamed MARK1 (coupled with hardware masking of the first half line scan of a field scan) was therefore written, incorporating a new structure

which simply tests the odd or even scan bit and decodes the coordinates from a sequence of these bits in setting up a grey level binary map as described in sec. 5.2.1.2.

The storage requirement for the 8-grey-level system may be computed as follows:

Total number of picture points used = 380(X) x 580(Y)

Number of grey level bits = 3

PDP-11 word length = 16 bits

Compressing 5 sets of grey level data into each word, buffer size needed is approximately 44K. On a 24K PDP-11/45 machine (since updated to 64K for RSX-11 multiuser operating environment) it therefore needs 3 passes of approximately 15K each.

As for data storage on RK05 disk cartridges used in the PDP-11 system, 180 sectors (approximately 46K) are required to hold information from each complete digitisation. The maximum number of data files which may be written onto each RK05 disk cartridge is therefore 25, based on its total storage capacity of 1.2 Megawords.

5.2.2 The light source

Early attempts to digitise photographic negatives employing the detection of transmitted light (see Fig. 5.7 for schematic layout) from an AC-powered light source failed to generate reproducible "bit-maps" (see definition in sec. 5.2.1.1) due mainly to electronically significant cyclic oscillations in light intensity levels. It was therefore essential to have a steady output of light intensity, preferably from a DC light source. A disused photographic enlarger device was internally modified to accept a twelve-

volt fifty-watt DC quartz-iodine light bulb powered by a compatible 12V DC transformer. This provided a suitable source for the illumination of photographic negatives. Fig. 5.8 shows the arrangement of the optical components used in the digitising system; its corresponding schematic layout is illustrated in Fig. 5.7. A diffusing screen is located immediately above (Fig. 5.7) the condenser lens to reduce inherent non-uniformity of light intensity emerging from the quartz-iodine bulb. A front silvered mirror deflects the vertical light path through 90° into a photosensitive detector (vidicon target) housed in a TV camera mounted horizontally.

5.2.3 TV camera and lenses

The TV camera used is a Sony Video Camera AVC-4600CE and has two components: (a) head unit and (b) camera control unit. With a monitor built into the rear of the camera head unit and a choice of either remote (control unit) or local (head unit) operation, it provided a flexible arrangement for signal tuning. From considerations of the need for adequate resolution and reasonable magnifications it was decided to replace the general purpose TV zoom lens with an 80 mm. focal Componon macro lens mounted on six-inch maximum extension Novoflex bellows which fitted into the front end of the camera head unit. The distances e_1, e_2 and e_3 (Fig. 5.7) are adjustable so that for a given distance e_3 which separates the 80 mm. lens from the photosensitive TV vidicon target, a choice of magnification or reduction of images of the photographic negative onto the vidicon target may be achieved by means of suitable combinations of e_1, e_2

and the focal length of the lens used. Various settings for e_2 are made possible through clamping the camera head unit onto a suitable framework supported by saddles mounted on an optical bench (see Fig. 5.8).

5.2.4 Auxiliary equipments

The remaining equipment used in the digitising system already exist in the N.P.S. laboratory. These included a Digital Equipment Corporation or DEC PDP-11/45 minicomputer, a Tektronix 611 display unit, a DEC teletypewriter, a line printer, magnetic tape units and an oscilloscope which has delayed sweep facility. Except for the oscilloscope and the Tektronix 611 which is presently used to display the digitised information at and above a given grey level, the above-mentioned units form the basic operating environment for any computing system.

5.2.5 Operating procedure

Fig. 5.9 shows the hardware arrangement when executing a digitisation experiment. With the photographic negative in place and the selected field of view visually displayed on the monitor in the camera head unit, a typical run initially involves suitable assessment of the video signal displayed on the oscilloscope. An example of the video signal variation along a single scan line passing through the centre of one large image is shown in Fig. 5.10 (a); successive scan lines in (b) show how the intensity falls as the outer edge of an image is approached; a typical scan line across a drop photograph passing through several images is shown in (c). Grey

level 7 is then set according to a predetermined choice relative to the video amplitude displayed. The "reset" button on the digitiser (or interface unit) is depressed and the command "RUN XXX" entered on the teletype, bringing programme "XXX" into execution. At the end of each run, the interface unit must be reset prior to the execution of the next run. To make sense of the results any distortion introduced as a consequence of optical misalignment must first be corrected. This may be done either by digitising a square grid and checking the "squareness" of the digitised counterpart on the Tektronix 611, or through a calibration process such as digitising an image of a microscale shifted in parallel across the length and width of the TV screen, providing simultaneously an appropriate scale factor for the measurements.

Although the actual data transfer period (during which three lots of buffered data are emptied onto disk) never exceeds fifty seconds, a larger time factor is introduced in manually selecting an appropriate field of view and reassessing the video signal displayed on the oscilloscope between runs. Since direct transmitted light is received by the TV vidicon target, surrounding ambient light reflected or otherwise, does not significantly affect the digitised results. A copy of the digitised information may also be selectively displayed on the Tektronix 611 at any one of the available 8-grey levels. A warming up period of approximately 30 minutes for the TV camera, digitiser and oscilloscope units is necessary before the start of any fresh digitising session. An important precaution to be noted when reselecting another

field of view is to avoid the accidental exposure of the vidicon target to excessive direct light.

5.3 Software

5.3.1 Introduction

The aim here is to describe in detail the algorithms used in the detection of discreet features present in a 2-dimensional grey-level bit-map described in sec. 5.2. Included is a scheme for discrimination between in-focus and out-of-focus images present in photographs of droplets passing a given depth of field. A multi-grey level system may be regarded as a combination of several individual black and white systems each at a different level of greyness. However, in practice, grain coarseness of photographic emulsions, light uniformity, quality of lenses used, vidicon resolution and stability of electronic circuitry affect the quality of video output. Section 5.3.2 deals with seven main characteristics of digitised and analogue signals arising from images on photographic negatives of discreet objects scattered over a contrasting background. The discussion refers to a particular application, the sizing of liquid drops in gas-liquid flows. Section 5.3.3 describes the recognition and discrimination algorithms and section 5.3.4 presents details of the program structure (at the time of writing).

5.3.2 TV image characteristics

5.3.2.1 Repeatability

Repeated digitisation of an image at intervals of ten minutes, under the same lighting conditions often indicates that a given edge of the image does not remain in exactly the same position on the 580 x 380 grid of picture points covering the masked TV frame. A small shift of the

order of one picture point, at this edge of an image is noticed in the present digitising system. In addition, repeatability of area measurement is further degraded when the light source used is not DC operated. However with a DC light source, initial measurements of image area in picture point units of several repeated scans of the same image do not show significant change in area (less than 1% on an image occupying approximately 2% of the screen area).

5.3.2.2 Image segmentation

One feature of an "in-focus" image of a transparent drop is the presence of a black spot in the middle of the white image (and vice versa on a photographic positive). Any TV scan line bisecting such an image will be segmented, to at least two sections. Segmentation occurs more at higher grey levels, (Fig. 5.11) as well as towards the perimeter of an "out-of-focus" image. (Note that the numerical values assigned to grey levels increase with video amplitude). Extreme segmentation resulting in several (see Fig. 5.12) small dots representing the original image often appears at the video peak of the image.

5.3.2.3 Peak video amplitude

Maximum video amplitude for a large image and a small image is different, even with uniform light intensity emerging from the source (see Fig. 5.10 (c)). Fig. 5.13 illustrates the requirement to alter the uppermost relevant grey level setting for two images. Where the video peak of the smaller image is lower than the highest grey level

originally set, no image at this grey level is detected. For the larger image, detection is possible at both settings. The uppermost relevant grey level should be set just below the video peak of the small images where a mixture of large and small images are present.

5.3.2.4 Contrast uniformity

In the present study of two-phase flow, owing to the random statistical distribution of droplet concentration across a section of the flow, uniformity of background light falling on the photographic negative is affected by concentration gradients in the flow. A certain amount of non-uniform contrast is anticipated. However, by setting the lowest relevant grey level to be just above the brightest background (in the case of a photographic negative) it is possible to eliminate the effect of non-uniformity in contrast provided that the non-uniformity between bright and dark zones is not excessive within the TV frame.

5.3.2.5 Linked images

The problem of identifying and separating linked image pairs is readily managed by software. A common technique employed (174) is the combination of image erosion and dilation. Photographs obtained during sampling of the dropsize distribution produced by an air-blast atomiser do not show a high frequency of linked images. With an occurrence of less than 1% of total drops sized, their exclusion is preferred.

5.3.2.6 TV screen edge errors

Current practice is to apply a manual masking of incomplete pictures at the edge of a TV frame, hence analysing only whole images. No software is written for correcting incomplete picture areas and perimeters at the edge of a TV frame. When considering a complete automatic analysis with use of stepping motors to drive a photographic negative across the field of view of the TV camera, edge errors have to be included in the software. A statistical method for analysing and correcting edge errors is given by Bockstiegel (175).

5.3.2.7 Photographic depth of field

For a preset degree of blur (say 1% of the diameter of the image) the optical depth of field changes with the object size. When considering a photographic volume hence a fixed depth of field, percentage blur is much higher for a small image than a large one (see Eqn. 3.2). Calibration of percentage blur for each size group over the require depth of field is needed to prevent unfair bias towards sizing more large drops than small ones. Consequently, it is true that manual drop sizing by eye can lead to an overestimation of the larger sizes, for a preset depth of field. However if and only if sharply defined images are to be sized, irrespective of the size group, consistency is possible with manual sizing.

5.3.3 Principles of image recognition and focus discrimination

5.3.3.1 Aims

The main aims of the software are to:

(a) identify individual detected image; linked images are regarded as one large image and subsequently discarded by a shape factor test ;

(b) assign a number to each image, hence "counting" them;

(c) store up, for each image, all digitised information on that image, hence needing,

(d) to repeat image identification at several grey levels;

(e) compute area and perimeter of each image in picture point units, from which a shape factor defined as $(\text{perimeter})^2/\text{area}$ is derived;

(f) also determine the horizontal and vertical feret diameter of each image for each grey level;

(g) compute an "equivalent diameter" of a circle having the same image area in picture points or scaled units;

(h) compute the halo width between each grey level determined by $\frac{1}{2}(d_{e,n} - d_{e,n+1})$ where $d_{e,n}$ = equivalent circular diameter at the lower grey level n and $d_{e,n+1}$ = equivalent circular diameter at one grey level up, n+1;

(i) discard "out-of-focus" images by a halo width criterion, based on an earlier calibration, with standard images for a given depth of field;

(j) finally classify by number count against equivalent circular diameter, all "in-focus" images.

5.3.3.2 Techniques Considered for Image Recognition

Two distinct methods are available, one introduced by Sato (176) in which only two scan lines of data are dynamically managed by the computer at any time, gradually building up the identified cells by applying mapping tests across these lines; the other is more commonly known as coded chain search (see Rintala & Hsu (177),) in which a set of linked number codes traces out the entire perimeter of a cell in the 2-dimensional array of picture points. Merits from both methods have been extracted, resulting in a scheme which best serves the present purpose. Sato's method (also used by Toner (160) in his on-line system) is initially employed but certain limitations appear when video characteristics described in sec. 5.3.2 complicate repeatability of analysis. These limitations are overcome here by introducing a subprogram which further refines the cell properties determined from the first analysis. The sub-program was subsequently found to be adequate in itself to complete the entire pattern recognition work. It is currently implemented in the PDP-11 version (178). The method used in the sub-program can be regarded as a chain search technique, employing run end coding (see definition below) as in Sato's program as well as cross linking in a manner similar to the

coded chain technique.

5.3.3.3 Definitions

To understand the chain search technique, it is best to define some terminology used in the description.

(a) A "picture point" is defined as an element of the 2-dimensional array which defines the entire picture. Its position in the array is determined by a (X, Y) coordinate pair.

(b) A "picture function" is that digitised grey level value associated with a particular picture point. Mathematically, a picture function can be described as a real valued function of two real variables (Rosenfeld (179)).

(c) "Run end coding" means only parameters at both ends of a repeated sequence of picture functions (satisfying a given criterion), are recorded.

(d) A "cell" is made up of a set of physically adjacent picture points (determined by an image) whose picture functions satisfy a given grey level criterion. The shape of each cell is determined by a shape factor (see sec. 5.3.3.1).

(e) Each cell "Transition" is defined as that segment of a TV scan line along which consecutive picture functions satisfy a grey level criterion. Thus a TV line divided into 380 picture points has a maximum of 190 individual transitions belonging to different cells; each would in that case be represented by one picture point only (see Fig. 5.14).

(f) "Voids" are regions in the 2-dimensional array in which the picture functions fail to satisfy a set criterion.

(g) A "closed" void is one which resides within a cell and

which is completely surrounded by the cell transitions.

(h) An "open" void is one which originates from within a cell but the enclosure by cell transitions is incomplete. This void therefore merges with background transitions which surround the cell transitions.

(i) "Background transitions" are void transitions which surround each cell. They originate from the outermost perimeter of the TV frame and are never inside a cell.

(j) "Cell lines" refer to those parts of TV scan lines which actually bisect the cell. Each cell line may have more than one transition (Fig. 5.15).

(k) "Cross link" establishes a relationship between two or more adjacent transitions appearing in 2 consecutive TV lines. Where transitions are cross-linked according to Fig. 5.16, individual cells are defined.

5.3.3.4 Method employed for recognition

(a) Cell Generation

The initial aim of the algorithm is to identify, on a TV line-by-line basis, all transitions which satisfy a given grey level criterion (see 4.3 of ref.(178)). Owing to the rectangular character of the picture point matrix in the present system, adjacent transitions in one direction (Y-direction) less than two picture points apart are merged into one in an attempt to "square" the representation.

A cross link of all adjacent transitions over the entire picture is next carried out, resulting in a number of separate cells each having its own identity. Starting with the first relevant line, each separate transition is given

an identity to which subsequent transitions in the next line are cross-linked (Fig. 5.17). Where a transition fails to attach to any of the existing cells, a new identity is assigned to this transition. Two different identities may link to the same transition at a later stage, e.g. Fig. 5.17 line 3 for Cells 1 and 2. In this case transitions having identity 2 are reset to 1, thus extinguishing cell 2. The procedure is repeated until all lines are analysed and all transitions suitably indexed. The algorithm is complete here if not the need to "fill-in" voids of certain cells.

(b) Voids detection and extinction

Each cell is tested for voids by the presence of three or more cell lines together with at least one line having more than one transition (Fig. 5.18). Its presence is subsequently confirmed by performing a "closed void" test. The test involves initially identifying the void transitions of a cell, followed by cross linking these transitions, ensuring that each outermost void transition had to terminate at a cell transition in order to be considered a closed void (Fig. 5.19).

Consider a set of identified cell transitions drawn in Fig. 5.19 (a) and (b). Background transitions which surround each cell are indicated as "o"s whilst void transitions originating from inside each cell are labelled "x"s; cell transitions represented as solid black lines. The use of run end coding reduces data handling considerably by altering the need for linkage of picture points to that of picture transitions only. A cell void transition is imminent whenever any cell line has more than one transition. Void

transition occupies the space between two successive cell transitions. The initial task is to index each probable void transition as it appears along the cell lines. These void transitions are cross-linked in a manner similar to that described in identifying individual cells except that it is now applied to voids within each cell. More than one "void within the cell" may be present in each cell. Whenever a "void cell" has adjacent to itself a background transition, its transitions are re-indexed to that of the background voids, i.e. it is a part of the background transitions. Where the outermost transitions of the "void cell" terminate at the cell transitions, the void is therefore completely enclosed and is termed closed void (Fig. 5.19). All detected "closed void" transitions are subsequently converted to cell transitions, i.e. they are "filled in".

The present algorithm is capable of detecting a cell within a cell (Fig. 5.20) and separating them. It is applicable to any shape provided dimensioned array size in the software is not exceeded.

5.3.3.5 Method employed for rejecting "out-of-focus" images

At each relevant grey level, the cells generated as described in sec. 5.3.3.4 are individually processed to determine their area and perimeter as well as the horizontal and vertical (relative to the TV screen) feret diametral coordinates. Any well defined cell at a low grey level can, at a higher grey level, fragment into a number of smaller cells, all originating from the same cell. Hence, rather than attempting to describe a drop image by a cell having

its source at a high grey level (e.g. level 7) followed by tracing subsequent area and perimeter values of the cell, down the grey level scale, it is preferred to describe the drop image by a cell with its source at the lowest relevant grey level, (e.g. level 4), the choice of which depends on whether or not the cell lies just above the background intensity. Any cell in the higher grey level having diametral coordinates (horizontal and vertical feret diameters) mapping into the diametral coordinates of the lower grey level source cell, is treated as a continuation of the source cell at this higher grey level. At this higher grey level, the areas of all cells belonging to the same source cell are summed and an equivalent diameter of a circle having the same total area is assigned to represent the source cell.

Hence there is only one description of shape factor for a cell, namely that value determined for the cell at the relevant lowest grey level. An equivalent diameter of a circle having the same area as the source cell at this level is also assigned. An inter-grey-level halo width h can be defined from these diameters as $h_{n,n+1} = (d_{e,n} - d_{e,n+1})/2$ corresponding to grey levels n and n+1 and equivalent circular diameters $d_{e,n}$ and $d_{e,n+1}$. If it were necessary to have an idea of the degree of fragmentation at higher levels, another factor defined by Eqn. 5.1 could be computed.

This is the fragmentation factor F, defined as

$$F = \left[\frac{\sum_{1}^{m} (SF \times Area)_i^{\frac{1}{2}}}{\sum_{1}^{m} (Area)_i} \right]^2 \qquad \ldots\ldots 5.1$$

where m = total number of fragmented cells
SF = shape factor of individual cells
Area = cell area in picture point units
i = cell number

The most extreme fragmentation possible (isolated cells consisting of one picture point each, at the most dense spacing which just avoids the formation of larger cells) leads to an upper limit value of F equal to SF for a cell of one picture point (at present, a rectangle with SF = 18). However, for the present application there is no need to use the fragmentation factor.

A calibrated value of halo width over a pre-specified grey level range is currently employed to test for an in-focus image; this is derived from digitization of photographs of a calibration graticule containing discs of varying diameters. An image is rejected from further processing when $h_{n,n+1}$ exceeds the calibrated value. The procedure resembles those recently described for use with Quantimet image analysers by Yule et al.(151) and Jones and Sargeant (10); further details are given in sec. 5.4.

5.3.4 Programs and Data Structure

5.3.4.1 Data Organisation

On a 24K PDP-11 under DOS-BATCH operation with two fixed RK-11 disk drives (identified as disk 0 and disk 1), memory organisation plays a vital role in achieving speed and efficient use of available resources. Digitised information stored is thus confined to the first 4320 sectors (corresponding to 24 files, see sec. 5.2.1.3) of disk memory space. The remaining 360 sectors are assigned for

dynamic data transfer between core and disk memory.

Main parameters describing the location of each transition in the digitised 2-D grey level bit map are the line number (Y), start (X_{in}) and end (X_{out}) of the transition. As there are effectively only 380 lines to be considered (scanning the picture in the vertical direction) 380 consecutive words of 2 adjacent sectors on the disk (each sector has 256 words) are used to store a 'variable' representing the current total of X_{in}'s and X_{out}'s encountered up to the present line. In Fig. 5.21, Word 1, also signifying line Y_1, has the value 4 stored in it representing the total X_{in}'s and X_{out}'s for Y_1 i.e. parameters of two transitions in that line. In the next word representing the line Y_2 only one transition is encountered and the cumulative total of X_{in}'s and X_{out}'s is 6. The maximum cumulative value possible is 8192 equivalent to storage capacity in 32 sectors for 4096 transitions. The maximum possible number of separated transitions on the 380 by 580 (reduced to 290 when every other value is considered) picture point array is 17550 in the present operation. This can only happen when individual transition-dots are uniformly spaced across the entire frame.

Subroutines DATRIN and DATOUT are specifically written for such data transfer between disk and core. Owing to memory limitations, present software structure is made up of four separate programs, namely:

(a) OVL1 - identical to LOCATE in ref.(178)), identifies transition parameters and stores them on disk as described above (using 34 sectors).

(b) OVL2 - cell generating software, stores cell identity information in another 16 sectors immediately following the first 34 sectors used by OVL1.

(c) OVL3 - void identification and extinction software which does not need storage space on disk 1, but cell parameters written to the system disk, disk 0, in file-structured format.

(d) OVL4 - retrieves cell information from files written by OVL3 for in-and-out-of-focus image discriminations.

Hence the total number of sectors for data storage per grey level is 50 and for 7 grey levels, 350 sectors are made available in data files 25 and 26 (having a total of 380 sectors) of disk 1. (Files 1 to 24 being used earlier for storage of digitised image information).

5.3.4.2 Overlay Description

(a) Overlay tree

Fig. 5.22 shows the structure of the Overlay Files. A common array is set up between the Resident Program and the overlaid files OVL1, etc. to transmit information about total levels searched, maximum number of cells determined for each grey level and some Fortran error return parameters. To get a particular overlaid file into execution the statement "CALL LINK ('Name')" is issued anywhere from either the Resident Program or its subroutines. 'Name' is the name given to the load module of the overlaid file. At the end of execution of each overlay file, a CALL RETURN state-

ment is introduced in it to return control to the calling resident program.

The following subsections contain a brief description of each overlay file and its usage together with limitations if any. All integer variables involved in common block transmission between resident and overlaid files are listed in Appendix A1.

(b) Routine RES

RES is the resident program in MACRO assembly language. It calls subroutine OVAL (in Fortran) through which all links to overlaid files are issued. The reason for this configuration is that DOS-Batch operating system generates an error if both resident and Overlaid main programs are written in Fortran. During compilation, a default name MAIN is assigned to every Fortran main program. Since the Resident Program is in core over the period of execution of the overlaid routines, an ambiguity in identity appears whenever e.g. OVL1 is called to execute. By having RES in MACRO, it can be renamed to RES as in this instance and therefore does not carry the default name 'MAIN'.

OVAL is a Fortran subroutine directing the execution of the overlaid modules. A flow chart for its operation is found in Appendix A2.

(c) Routine OVL1

This is essentially the LOCATE routine described in ref.(178). One modification to it is the merging together of a pair of transitions less than two picture points apart. Flow chart is as shown in Appendix A3 together with a list

of variables used. Subroutines called are DELFIL ('File Name', IERR), which deletes files as named in 'File Name' and IERR is an error return code; DATOUT and DATRIN (see 5.3.4.2 (g)).

The array IXI (8572) is a consecutive combination of 380 words for line identity and the X_{in}'s/X_{out}'s for 4096 transitions. Data structure and transmission is as described in sec. 5.3.4).

Another modification added to it is the selective line search at higher grey levels. Briefly, the program only analyses those lines which contain transitions in them which are detected in the lowest grey level scan.

(d) Routine OVL2

OVL2 is the cell-generating routine in which the array KM (4096) is used to identify each transition. Flow chart and list of variables are shown in Appendix A4. OVL2 limits the maximum number of transitions analysed to 4096. However, it does not write any error messages if 4096 is exceeded.

SETFIL, a subroutine in the Fortran Compiler of DOS.BATCH, is used to generate linked files, with a choice of names. Before OVL2 returns execution to the calling program , it writes onto files 'FIL1', 'FIL3', 'FIL5' and 'FIL7' one for each grey level, the cell number together with the line in which its first transition appears. A series of pointers to cell information is thus made available for the next program, OVL3.

OVL2 starts by determining the first of the 380 lines which contains information and probes the following

lines for an empty line. As soon as it arrives at an empty line, OVL2 begins to identify cells within this first range or "sector" of data lines since the presence of the terminating empty line automatically separates the cells in the remaining lines from these first set of cells. As soon as the cells in this first sector are suitably indexed, the program continues to look for the next line which is not empty and notes that line as the starting line for the next range of data lines (Fig. 5.23). It then looks for the next empty line to appear and notes this as the terminating line for the second sector of data lines to be analysed. Isolated cells within this sector are indexed via the same cell generation routine, the algorithm of which is described in sec. 5.3.3.4 part (a).

In this manner, only lines with information are analysed hence gaining in speed of execution apart from the physical separation of cells which are indexed in separate batches.

(e) Routine OVL3

In relation to the other routines, OVL3 is the most time consuming routine, analysing data from each cell at a time owing to lack of computer memory. It calls subroutine PSORT to determine area, perimeter and shape factor of each cell at a single grey level.

It reads the total number, M, of detected cells and the maximum number of transitions, I6, encountered, (from files 'FIL1' etc.) for the particular grey level, by OVL2. It subsequently reads the cell index NM for the first cell as well as the line in which its earliest transition appears.

Subroutine DATOUT is called to access entry and exit co-ordinates and index for those transitions appearing in the scan lines across which this cell straddles. A transition index which agrees with the cell index is noted and appro-priate transition parameters transfered to cell arrays KVI, KXI and KXO. The arrays KVI, KXI and KXO are 2-dimensional, the first element being the line number whilst the second represents the transition number. If any one cell line has more than ten separate transitions, an error message, "DIMENSION EXCEEDED", is printed and that cell is rejected from further analysis. Since the digitisation process limits X-coordinates to 380 the largest cell can only have 380 lines. Thus by dimensioning the arrays KXI, KXO and KVI to (380, 10) information overflow can be avoided. Under the present system (200, 10) is found to be adequate.

With the cell transition parameters suitably re-stored, picture point elements lying between consecutive transitions of a cell line are individually tested for either, belonging to a "closed" or "open" void. The tech-nique involves identification of "void cells" made up of individual void transitions, within the cell matrix (see sec. 5.3.3.4 part (b). The flow chart in Appendix A5 as well as a list of variables used in OVL3 provides details of its execution.

Individual cell area, perimeter, shape factor, and coordinates of both horizontal and vertical feret diameters are written onto 'FILE 1', 'FILE 2', 'FILE 3', and 'FILE 4', one file corresponding to each of the four grey levels 4 to 7 on which subsequent analysis is based (see sec. 5.3.4.2 (f))

before OVL3 returns control to Resident Program.

(f) Routine OVL4

Routine OVL4 retrieves information of individual cell area, perimeter, shape factor and end coordinates of both the horizontal and vertical feret diameters from data files (written by OVL3) 'FILE 2', 'FILE 3' and 'FILE 4', each file corresponding to a grey level which is above the lowest relevant level. (A list of variables used in OVL4 together with its flow chart can be found in Appendix A6). Arrays ISAM (3,700), SFACT (3,700), ILI (3,700), etc. (see Appendix A6) are assigned to contain the above information for up three relevant grey levels and a total of seven hundred individual cells per grey level. Due to the amount of storage needed, OVL4 uses the most memory space. In-and out-of-focus discrimination is carried out on an individual source cell (see sec. 5.3.3.5) basis, with data supplied by file 'FILE 1'. Into each pair of source cell diametral feret coordinates read from 'FILE 1', corresponding pairs of diametral feret coordinates, at each of the higher grey levels, are mapped. Where more than one cell (at each higher grey level) successfully maps into the source cell data, their areas are summed, scaled and an equivalent circular diameter computed. OVL4 is written to cope with analysis of image parameters for up to four grey levels. An inter-grey-level halo width is computed and compared with a standard value (for the cell) determined from a previous calibration experiment. Where the computed halo width (see sec. 5.3.3.5 and 5.4.5) exceeds the standard value, the image is not within a specific depth of field, i.e. out-of-

focus and is discarded.

When more than seven hundred cells are detected at any grey level, an error message is written to indicate memory overflow. In the present system, grey levels 4 and 5 are used for halo width computation and detection of out-of-focus images, the in-focus diameters being derived from grey level 4. Shape factors determined at grey level 4 are also used in discarding irregular images.

Before returning control to the main program, OVL4 at present outputs on the line printer, the file number (from 1 to 24) shape factors and equivalent circular diameters of both the in-focus and the out-of-focus images, with an asterisk preceeding the latter.

(g) Subroutines

(i) PSORT (M1, M2.....M12)

A Fortran subroutine which returns the area, perimeters shape factor and both end coordinates of the horizontal and vertical feret diameters, in picture point units where relevant, to the calling program. It computes area by summing up all picture points belonging to the cell whilst perimeter is computed by summing only picture points which lie at the periphery of the cell. However, as the area of the TV frame representing one picture point in the present system is a rectangle of 2:1 aspect ratio, shape factors determined from perimeter values arrived at by simply summing picture points at the periphery would be orientation dependent when the image is non-circular. A scheme was devised to reduce this source of error by "squaring" the area element for each detected feature before computing the

shape factor. Since the X-direction intervals are in magnitude twice the Y- intervals, the area representing one picture point may be "squared" by ignoring every other picture point in the Y- direction. A reduced number of picture points each representing a new area of aspect ratio 1:1 is used for calculating shape factors (see sec. 5.3.3.1 (e)). Due to the need to ignore a picture point in the Y- direction in which the total counted is not an exact multiple of 2, shape factors computed for a circle occupying an effective screen area of approximately 2% experienced numerical values in the range 11 to 14 with a mean at 12.5 (compared with the exact value of 4π, = 12.57).

(ii) LEVEL (LEV, IX, JY, NFILE)

An assembly language routine (173) which accesses the binary grey level map on disk for a given set of arguments namely, X-, Y- coordinates (denoted as IX, JY respectively) and NFILE, the data file number, returning a value of grey level LEV, for the (IK, JY, NFILE) set of arguments. LEVEL is only suitable for the present storage structure of grey level information in which five 3-bit values are packed into a 16-bit PDP11 word.

(iii) DATOUT (NN, VAR1, VAR2, STBLK, SEG)

An assembly language subroutine which returns the content of the word pointed to by "SEG" via "VAR1" whereas "VAR2" contains the content of the following word. The reason for returning a pair of consecutive word content is clear when the main program retrieves the entry and exit coordinates of each transition with one call to DATOUT. DATOUT is also used to access the content of one word in

which case "VAR2" is also returned is ignored. "STABLK" is the internal word offset which has one of the following values: 0, 380 or 8572 depending on whether the program requires - the contents of the first 380 words only - i.e. cumulative index or the (4096 x 2) entry and exit coordinates of the transitions or the transition indices stored in words 8572 onwards.

The present method of accessing data involves a transfer of a block (256 words) of data at each call. When consecutive pairs of word contents are needed, an error arises at the block boundary, i.e. when "SEG" points to the 256th word of the transferred block,the next word, 257th is in essence, the first word of the next data block, which is not yet in core. A correction is applied to block boundary data transfer in the main program by testing "SEG" for a 256 value when "SEG" is incremented for another CALL DATOUT (NN, VAR2, IJK, STBLK, SEG), IJK thus returned is ignored, and then decremented to its original value.

(iv) DATRIN (NN, VAR, STBLK, WORDS)

Mainly used to transfer data arrays to files 25 and 26 of disk 1. NN is the grey level value, VAR - the name of the first element of the array to be transferred and WORDS is the absolute total number of words or array to be entered.

(v) DELFIL ("DEV: FILNAM (UIC), DEV: FILE2 (UIC)", IERR)

An assembly language subroutine (173) which deletes files generated by a CALL SETFIL command.

DEV: device type on which file resides

FILNAM (UIC): name of the data file together with the User Identifier Code

IERR: error status

(vi) DOT2 (X, Y)

Another assembly language subroutine which returns a dot to the Tektronix 611 display screen for a given (X, Y) coordinate pair. Execution mode is CALL DOT2 (X, Y). However, its operation is supported by several other subroutines which manipulate and display incoming information on the Tektronix 611. These routines are part of a complete package of functional routines written and used by the Computer Aided Design group in the N.P.S. laboratory. DOT2 is useful but rather slow in displaying a binary map. In a general mini-computer installation, it would be preferable to use instead a standard graphics package with a suitable visual display unit.

(h) Routine DIS2 (X, Y, LEV)

DIS2 is a Tektronix 611 display routine. It simply displays the bit map (on disk unit 1) on the Tektronix screen at any one of the 7-grey levels. Subroutines needed to feed this program are LEVEL and DOT2. The program actually displays all points having grey levels at and above a required level.

5.3.4.3 Overlay builder and run time limitations

The following commands are issued during compilation linking and execution of the non-overlay (see sec. 5.3.4.4) and overlay version. After editing the source program named as, for example, "Filname. Ftn" the "Run

Fortran" command is issued to compile its object module identified as "Filname. Obj." as shown in the following teletype printout.

```
$RU FORTRN
FORTRN  V09.02
#OVL4.OBJ<OVL4.FTN/CK/ON/SU
#^C
.KI
```

The switch, /CK, checks for overflowed dimensions and returns an error message during program execution.

/ON switch restricts integer variable to <u>one word</u> representation (its default value is two words) thus saving memory space.

/SU suppresses line headers when a listing file is output onto the line printer, another effort to confine useful memory to the main program.

When all source files are suitably compiled, the assembly language compiler command being as shown below, "Run Link" is next issued to link up all relevant subroutines and Fortran library routines to each of the source program to create a corresponding load module which is the executable module.

```
$RU MACRO
MACRO V06-04A
#LEVEL.OBJ<LEVEL
#^C
.KI
```

```
$RU LINK
LINK  V03-03A
#LOCATE.LDA<LOCATE.OBJ,LEVEL.OBJ,DATOUT.OBJ,DATRIN.OBJ,FTNLIB/U/E
#^C
.KI
```

The above "Run Link" command do not create an overlay version. Each load module is therefore a stand alone executable module as described in sec. 5.3.4.4 for the non-overlay version.

The following command generates an overlay file for all the source programs:

```
$RU LINK

LINK  V03-03A

#RES.LDA,MAP,RES.STB<RES.OBJ,OVAL.OBJ,FTNLIB/E

#OVL1.LDA<RES.STB,OVL1.OBJ,LEVEL.OBJ,DATOUT,DATRIN,DELFIL,FTNLIB/E

#OVL2.LDA<RES.STB,OVL2.OBJ,DATOUT,DATRIN,FTNLIB/E

#OVL3.LDA<RES.STB,OVL3.OBJ,DATOUT,PSORT,DELFIL,FTNLIB/E

#OVL4.LDA<RES.STB,OVL4.OBJ,FTNLIB/E

#^C
.KI
```

The program to run is "RES". The main limitations at run time are:

(1) Dimension overflow - halts entire program.

(2) Disk drives 1 and 0 must be used simultaneously.

(3) When a program halts in the middle of an execution,

all locked files must first be unlocked and deleted before re-running the program. Otherwise, an error message appears indicating that a file cannot be opened because it is already present. This error message is prompted by "SETFIL" routine. "RUN PIP" to delete and unlock file. For further information on PIP as well as operation on DOS BATCH, ref(180) should be consulted.

5.3.4.4 Non-overlay Version

A non-overlay version for the above routines is also available. Each of the routines namely OVL1, OVL2, OVL3 and OVL4 are written for stand alone use (OVL1 renamed as LOCATE, OVL2 as GENERATE, OVL3 as REFINE and OVL4 as FOCUS), with relevant intermediate information written back onto disk 0. To maintain continuity in execution, the programs must be sequentially run viz: LOCATE, GENERATE, REFINE and FOCUS. For a single grey level (black and white system) analysis, execution can be halted at REFINE and relevant information output on the line printer.

5.3.5 Concluding Remarks

Flow charts drawn for the different routines are on a broad outline only, mainly intended to guide the reader in understanding the listings enclosed (see Appendix A7). In the overlay version the "production run" only analyse two grey levels determined from a previous calibration experiment which makes use of all grey levels. If this software is to be adapted for use with a 16-grey-level digitizer now coming into use in Nuclear Power Section (having

1024 picture point per TV scan line but not incorporating the DC threshold setting facility of the present digitizer), a subroutine to search automatically for the grey level just above the main background could be written.

For the present application, the DC threshold setting facility (i.e. positioning grey level 7 relative to the video peak) is essential unless the number of usable grey levels were expanded to at least 64, approaching the number available on commercial analysers.

The area of the TV frame representing one picture point in the present system is a rectangle of 2:1 aspect ratio. It is recommended that any future digitizer should utilize a square picture point, possibly based on the technique used by Toner (160).

5.4 Calibration and Performance

5.4.1 General description

To be compatible with descriptions used in related work (10, 151), Fig. 5.24 shows the notation employed in the common definition of the distribution of light intensity and hence video amplitude across a well-focussed and a poorly-focussed image. According to Fig. 5.24, I_B and I_C, located between the background level I_D and peak level I_A, thus define the intensity gradient at the edge of an image. If I_D may be translated (by subtraction of a constant value from the video voltage) it may be used as the reference level which defines level 0 on the grey scale. I_{1A} denotes that intensity which corresponds to grey-level 7 of the 8-grey-level scale. Obviously if I_{1A} is variable so that it may have values larger or smaller than I_A (see sec. 5.2.1.2), the "digitised" grey level value assigned to, for example, I_B, will vary accordingly. This additional flexibility of being able to "stretch" or "compress" the grey level scale relative to a fixed image intensity pattern allows the digitisation of "average" contrast films with only eight well-defined, uniformly spaced levels of greyness. A typical commercial image analyser without this flexibility requires an order of magnitude more fixed grey-levels to cover the same intensity range. The two extremities of light intensity levels represented by I_A and I_D, in practice fall between zero and one volt. I_D may be set to correspond to grey-level zero by suitable adjustment of camera controls. Typically the range of useful signal amplitude varies from 0.1 to 0.6 volts depending on the contrast of the film used,

or in the case of testing with pin-holes, the quantity of light received by the vidicon target (via appropriate setting of aperture on the lens). The voltage setting I_{1A} representing grey-level 7 may also be varied over the full range from zero to 1 volt. However, at a given grey-level 7 voltage, V_7, the voltage which corresponds to grey-level 4, for example, is 4/7 of V_7 with similar linear fractions, describing the other levels below level 7.

5.4.2 Repeatability of digitised measurements

Table 5.1 summarises values for the digitised diameter, d_M of three well-defined, sharp edged, circular holes of nominal diameter 2.5 mm, repeated at time intervals of 20 mins and 5 mins. Each image is represented by approximately 2250 picture points, equivalent to a TV screen area of approximately 1%. The video peak voltage is set at 0.3 volts and the grey-level 7 voltage, I_{1A}, adjusted to give I_R defined as $(I_{1A} - I_D)/(I_A - I_D) = 0.5$ and 0.9 respectively; the intensity level, I_D, is translated so as to equal the voltage at grey-level zero. The two measured diameters separated by 5 or 20 minutes are within one percent of each other. Fig. 5.25 illustrated graphically, one of the three sets of results. It is obvious that d_M at any grey-level is always larger for the 0.5 setting of I_R than its corresponding value for the 0.9 setting, since the diameters at the former setting are located towards the lower, i.e. I_D, end of the intensity scale illustrated in Fig. 5.24 In addition d_M at nearly all grey-levels, except level 7, at the 0.9 intensity ratio setting, overestimates the true

diameter. This indicates that a satisfactory measurement procedure would be to set I_R at 0.9 and use level 7 to define the diameter of such images. The same procedure may equally be used to calibrate the image analysis system for measurements in which the object occupies a larger or smaller percentage of screen area.

5.4.3 Screen position errors

To assess the TV camera manufacturer's claim of up to 2% geometrical and linearity error on diameters measured within the TV frame, a sharp-edged circular hole, having an effective area on the screen of 2% of the total screen area was digitised with I_D set at grey-level zero, at various positions across the screen as illustrated in Fig. 5.26.

Table 5.2 summarises the results. The best screen position for calibration measurements, based on the measured diameter having a value which is closest to the average value from the nine (Table 5.2) measurements, appears to be at position 2. The standard error of the measurements as a percentage of this mean value just exceeds two percent for both settings of the intensity ratio, I_R. At a given intensity ratio, the measured diameters appear to be independent of peak video voltage setting.

The present results also indicate an over estimation of true diameters (see sec. 5.4.2). The unusually large error in the microscope measurement is due to imperfections in the object.

It would be appropriate that all calibration measurements should be carried out with relevant features located

at screen position 2 to avoid the need for correction factors (assuming that images to be sized on the basis of the calibration are randomly positioned within a TV frame).

5.4.4 Effect of altering peak video and grey-level 7 settings on measured diameters

50 μm and 150 μm nominal diameter black discs on a comparison reticle in the plane of best focus were photographed with a magnification of approximately 14x. The photographic images were digitised using an approximately 1:1 magnification with grey-level 7 and peak video voltage set according to Table 5.3, which summarises the measured diameters at the best screen position (see sec. 5.4.3). Fig. 5.27 is a graphical version of Table 5.3. It appears that for I_R = 0.75, the measured diameter at level 4 provides the best comparison with the actual diameter x whereas the same diameters for I_R = 1.0 underestimate the true value by approximately 4% for the 50 μm diameter disc and 2.8% for the 150 μm diameter disc. It is further noted, in line with findings in sec. 5.4.3, that for a given I_R, the measured diameters appear to be largely independent of peak video voltage settings. Hence, if these disc images adequately represent droplet images, when determining diameters from photographs of droplets the appropriate value to use for the intensity ratio, I_R would be 0.75 and the required d_M would be at level 4. However, in practice variations in contrast on the photographic negative, coupled with non-uniformity in light intensity across the TV frame, affects I_A or peak video voltage, making it dependent upon

TV screen position. If these variations in I_A distribute statistically about a mean and have a small standard error (i.e. good contrast films with uniform background) the net effect on a histogram presentation of size data would be minimal. It must be emphasized that for the present results the total error in the value of d_M consists of errors from two sources: a photographic translation process and the digitisation process. No attempt is made to isolate these two "errors" since in a "production run" all of the measured diameters are determined from results generated by the photographic process which is inherently imperfect.

5.4.5 Establishment of a focus discrimination criterion

A comparison reticle having discs of various diameters between 10 and 1000 μm was photographed with an overall magnification of 9x and 14x (consistent with magnifications employed in sec. 4.3 on the photographic determination of drop-size distributions). The photographic negatives were subsequently analysed by the digitising system under the following video settings: peak video voltage of any image set at 0.25 volts; relative intensity level I_D translated so that it corresponds with grey-level zero voltage; grey-level 7 then set at 0.19 volts i.e. ~75% of the peak video voltage.

The focus criterion adopted here is similar to that described by Yule (151) and Jones (10) in which a relationship between the measured diameter and the width of the blurred region, known as the halo, is first established for each position relative to the plane of best focus.

Conforming with the notation specified in section 5.4.1, it implies that for each photographic negative being analysed, I_B and I_C may be set as a fixed proportion of $I_A - I_D$ determined from a calibration. "In-focus" images may then be defined by

$$h < h' \qquad \ldots\ldots 5.2$$

where halo width h is given by

$$h = \tfrac{1}{2}(d_C - d_B) \qquad \ldots\ldots 5.3$$

d_C and d_B are respectively the measured diameters at levels I_C and I_B. A value of h' may be determined for a chosen depth of field which gives measured diameter (for a single size) within an acceptable percentage error of the time value.

Figures 5.28 to 5.31 summarise results from such a calibration for the 9x magnification. In Fig. 5.29 the halo width between grey-levels 4 and 5 defined by $\frac{1}{2}(d_{e,4} - d_{e,5})$ is plotted against position relative to the plane of best focus. Fig. 5.28 is a similar plot except that the average halo over three grey-level intervals lying between grey-levels 4 and 7 defined by $(d_{e,4} - d_{e,7})/6$ is plotted. Both figures exhibit similar trends; the halo width increases as the object is positioned further away from the plane of best focus. Fig. 5.30 illustrates the relationship between the measured diameter, d_M determined at grey-level 4 and halo width given by $\frac{1}{2}(d_{e,4} - d_{e,5})$. It is evident that as the object is shifted away from the plane of best focus, the measured diameter underestimates the true value.

From Fig. 5.29, a maximum halo width in the region of

2 μm could be taken, with reasonable accuracy, to represent a fixed depth of field, regardless of drop diameter. This corresponds with Ramshaw's (163) simplified theory, enabling subsequent analysis to be carried out, without the need for weighing or correction factors referred to in (10) and (151). Focus discrimination may therefore be based on a constant h' with h defined by grey-levels 4 and 5. If these represent I_C and I_B respectively, then

$$h = \tfrac{1}{2}(d_C - d_B) \quad \text{where} \quad \frac{I_B - I_D}{I_{1A} - I_D} = \frac{5}{7} \qquad \ldots\ldots 5.4$$

and $d_M = d_{e,4}$. Values of h' determined for photographs with approximately 14x and approximately 9x magnifications are respectively 1.5 μm and 2.0 μm, the corresponding depths of field being approximately 0.25 mm and approximately 0.5 mm.

Fig. 5.31 illustrates the overall accuracy of the combined photographic and image analysis system, the measured diameter determined from photographs in the best focal plane, the corresponding values being summarised in Table 5.4. This compares d_M for different values of I_R with the actual microscope measurement.

5.4.6 Simulation of varying contrast

Fig. 5.32 shows examples of how d_M and h are related when I_A is altered (via TV camera lens aperture and pedestal control which subtracts a fixed value from the video voltage) to simulate photographs with varying contrast. Fig. 5.33 illustrates various settings of peak video voltage (i.e.

intensity level I_A) relative to a fixed grey-level 7 voltage represented by I_{1A}. I_B and I_C therefore respectively represent voltages given by $(I_D + 5/7(I_{1A} - I_D))$ and $(4/7(I_{1A} - I_D) + I_D)$ where I_D has the voltage corresponding to grey-level zero. I_R increases beyond 0.75 as the image video peaks sink lower through the grey scale, reaching 1.33 for the smallest d_M values shown for each disc; this covers the range found for "in-focus" drop images in practice. Although the images analysed are from objects which lie in the best focal plane, the results indicate that whereas the halo width under "normal" conditions should be less than 2 μm, the sinking of peak video voltage, I_A relative to grey-level 7 voltage I_{1A}, as experienced by poor contrast images, meant an inevitable loss of data even though the measured diameter d_M only marginally underestimates the true value (see Fig. 5.34 and Table 5.4). While measurements at grey-level 3 would appear a suitable remedy for the loss of data, in practice it is found that the total number of detected features at this level increases suddenly (compared with those at grey-level 4) probably caused by random background fluctuations or "contrast noise" having their signal peaks at this level. Though the electronic noise to signal ratio is much smaller than these fluctuations the usage of grey-level 3 as a measurement level is possible only when extremely uniform and good contrast negatives are employed. In the manual translation of video signal so that I_D is set at grey-level zero, excessive signal voltage subtraction must be avoided because attenuation of I_A would occur since a negative translation is not possible.

Measured diameters at grey-level 4 would always underestimate the true values when I_A is attenuated.

In a "production run" in which the value of I_A varies according to TV screen position as well as image diameter, loss of "in-focus" data is inevitable. A suitable compensation would be to increase the halo width criterion h' to e.g. 2.5 μm with a corresponding improvement in the photographic process aimed at minimising the proportion of poor contrast features present. Whilst usage of 2.5 μm for halo width h' meant a corresponding increase in depth of field, the true depth of field may never be accurately determined in practice due to the presence of some degree of non-uniformity in I_A arising from non-uniform illumination and/or localised contrast variations on films.

5.4.7 Typical results

Photographic images of droplets, magnified approximately 14x, from an air-blast atomiser (a description of which is found in sec. 7.2) are analysed with I_R set at 0.6 corresponding to the brightest image found in the TV screen. This setting, as opposed to the ideal value of 0.75, was found suitable in the light of non-uniformity in I_D over the entire range of in-focus images. Scratches on photographic negatives and images of dust particles (readily separated by their irregular shapes) which settle on the negative before exposure are excluded via a suitable shape factor test. In-focus images with shape factor values less than 25 are presently treated as relevant information, this upper limit being determined

from a survey of all shape factor values encountered in the earlier trials when the system was calibrated.

Results of processing the drop photograph part of which is shown in Fig. 4.2 are plotted in Fig. 5.35. This compares the size distribution with those obtained manually by two different observers and indicates the very satisfactory performance of the system in the present application, although the total number counted in each case differs fairly significantly. It also demonstrates the subjectiveness in a manual analysis.

Fig. 5.36 illustrates another set of results determined from an analysis of photographs of droplet spectra(magnified approximately 9x) across a section of two-phase flow immediately downstream of the atomiser injection unit described in Chapter 7. The contrast on this set of photographs is unfortunately poorer than those from which results for Fig. 5.35 are derived. The agreement between the two observers and the image analysing system is as good as the data permit with the scatter in the upper or larger diameter end of the mass frequency spectrum due mainly to the small sample size (approximately 350 "in-focus" images from 10 negatives).

In general, poor contrast films give rise to more disagreement between independent observers and the total number counted from an automatic analysis may be in doubt because of possible "loss of information" discussed in section 5.4.6.

5.4.8 Additional errors

An important source of uncertainty in the measured

diameters may be attributed to errors arising from scaling the image analysis system so as to provide consistent results.

Before each set of negatives is analysed, a well-focussed photographic image of a microscale, having the same magnification as the images of droplets is digitised with the scale positioned horizontally across the centre of the TV screen in the X-direction. Fig. 5.37 presents a Tektronix 611 display of the digitised microscale at a relevant grey-level over the full range of 380 X- and 580 Y- picture point positions. The interval between two consecutive picture points in the X- direction may be computed from the ratio $(X_L - X_F)/(380-1)$ defined as the X-scale factor where X_L and X_F are the scale readings at X=380 and 1 respectively. Since a small uncertainty accompanies each read value at either end of the scale, a fixed amount of error may be computed for the scale factor. The scaling error for the 9x magnification is approximately 2% in the determination of the area represented by a picture point. In addition, an across screen error of the type described in sec. 5.4.3 gives rise to a small difference in the scale factors independently determined for the upper and lower half of the TV screen. This effect may be reduced by scaling the TV screen at 3 positions; namely, upper half, centre and lower half and averaging the factors so determined. It should be remembered that the above discussions refer to scaling the TV measurements using results from a photographic translation process which in itself has inherent errors, e.g. focussing accuracy, optical distortion, etc. With a good quality lens and accurate optical arrange-

ment these errors may further be minimised.

Superimposed upon the above irregularities, is the 1 to 2% random variation in line scanning speed, which affects picture point scaling since the points are defined by the pulses from a stable oscillator. As sec. 5.4.2 indicated a repeatability error of less than 1% in the measured diameter, this effect is therefore not serious.

Since image areas are computed by summing rectangular areas the overall error in sizing increases as the image size is reduced. (In a typical case, a 300 μm drop photograph at 9x magnification is televised to give an image area of just over 3000 picture points so that a 30 μm drop would be represented by about 30 points only). There is another source of error which is inversely proportional to the measured diameter, reducing to insignificant value the larger the measured diameter. This is the "quantization" approximation associated with any analogue to digital conversion of signals. In quantization the analogue signal is approximated by a finite set of values or "quantization levels" by replacing the actual value at each prespecified (X,Y) point by the quantization (or grey) level closest to it. In the present image analysis system, detected features described by less than eight picture points are discarded as unrepresentative of droplet images. This corresponds to a limiting droplet diameter of about 10 μm for the 14x magnification results. Further reduction of this limit is possible if higher magnification of droplets are undertaken.

5.4.9 Discussions and recommendations

Although individual estimates of error resulting in an overall error for the image analysing system may be rigidly quoted, the errors due to the photographic process are not readily deduced since exposure period, light intensity, development time, developer used, bath temperature, etc. affect image quality. It is therefore not practicable to assess the overall error from consideration of all the contributing factors; only the end results from a calibrated system such as Fig. 5.35 can indicate the degree of confidence which can be placed in the analyses.

The speed of operation of the present software-based feature detection system depends on the total number of features analysed. Fragmentation of drop images near their peak intensity and background intensity fluctuations give rise to typically four to five times as many detected features at grey-level 5 as at 4 . Although the minimum analysis time for one TV frame is about 10 minutes, an improved recognition algorithm to eliminate irrelevant features at an earlier stage may help to further reduce processing time. Comparisons of the present speed of operation with those of purpose-built image analysing computers, e.g. Quantimets, are therefore not yet meaningful. However, the present software structure is such that the accumulated digitised information may be continuously processed in an overnight run without operator intervention. The use of cartridge discs for intermediate data storage has an extremely adverse effect on running time; a computer with suffi-

cient core or semiconductor memory would solve this problem. A larger memory computer will also help to do away with the need for program overlays, hence avoiding the need to transfer data to and from storage disks with each exchange of overlaid programs. Programming in Macro assembly language will also reduce processing time but at the expense of the interchangeability which a Fortran program provides. A finer grid of picture points with a matching higher resolution TV camera would allow larger areas of negatives be televised in one frame without losing accuracy and resolution, hence further improving analysis time since the total number of data transfers between disk storage and computer memory would be reduced(189).

Additional subroutines which analyse double exposure photographs for velocity measurements may readily be added, incorporating an algorithm for linking each original image with its counterpart in the second exposure. (An example of such a technique is given by Jonas and Kent (222)).

One disadvantage of the optical arrangement is the need to use photographic negatives as the only input material. However, converting the entire system to analyse prints or pictures should be relatively easy. The algorithm developed for the present work is equally applicable to work involving the need to identify features within features, for example, solid and hollow regions in a cross section of an engine block which in Computer Aided Design work, automatic meshing of identified solid features for stress analysis could be considered (181), and at as many "depths" as necessary.

CHAPTER 6

TREATMENT OF DROPLET SIZE DISTRIBUTION

6.1 Introduction

The many different applications of liquid atomisation and importance of an accurate representation of droplet size distribution have often been noted (182-185). In the presentation of experimental data, several equations involving one or more parameters have been used. Amongst them, e.g. Nukiyama-Tanasawa (181), Rosin-Rammler (185), Log-Probability, Square-Root Probability (187), Logistic (183) and others, perhaps the most satisfactory equation, from the viewpoint of attaching useful physical descriptions to the parameters, is the Upper Limit Distribution Function (ULDF) of Mugele and Evans (11). The aims of this chapter are four fold, viz :- (a) where droplet size distribution inevitably has to be deduced from a number count as in the present work, to highlight the importance of an accurate conversion from number to volume distribution; (b) application of the ULDF to existing experimental data together with a comparison of a manual ULDF fit with that of a numerical technique; (c) introduction of a heterogenous ULDF to describe data for which the ULDF of Mugele and Evans is unsatisfactory and (d) to list some important considerations when selecting a suitable sample size to represent an unknown parent distribution.

As a consequence of work done in (b) a short paper on critical Weber number for coarse water formation in steam turbines has been published (188).

6.2 Converting a number count to volume distribution

A distribution of number frequency with respect to droplet diameter is often highly skewed towards the smaller end of diameter range but a volume frequency with respect to a transformed diameter may often be approximated by the normal distribution function (11). When dealing with droplets it is extremely inconvenient to size by volume although methods using molten wax (190) have been employed to simulate atomisation of fuel by selecting waxes having similar physical properties to the fuel. Whilst other similar solidification processes such as nitrogen freezing have been tried, generally the sampling process involved some kind of physical intrusion into the droplet flow. Sizing by number count via a non-intrusive photographic technique is a good alternative but it introduces additional errors when converting a number count to a volume distribution. Very often the largest droplets are present in statistically small numbers and large errors can arise when converting number to volume distribution for stochastically small samples.

Assuming that a given sample is stochastically large enough to represent the population, converting a number count to volume distribution can either be carried out according to Lapple's (191) method (as shown by Seldon (192)) in which a suitable mean diameter of a size interval is cubed and multiplied by the total number counted in that interval, or by a more accurate method presented by Wise (193). The method by Wise involves an "integration by parts" of Eqn. 6.1 below.

$$V_i(x_1) = \frac{\int_{x_1}^{x_m} x^i\, n(x)\, dx}{\int_{x_0}^{x_m} x^i\, n(x)\, dx} \qquad \ldots.6.1$$

where $V_i(x_1)$ is the weighted proportion of droplets with diameters larger than x_1 ; $n(x)$ is the number probability function so that $n(x)dx$ is the total number counted in the interval x to x+dx ; x_m is a diameter larger than the largest observed diameter; x_0 is less than the smallest diameter observed; i is a weighing factor having a value of 3 for volume and 2 for surface area. Integrating Eqn. 6.1 by parts, we have

$$V_i(x_1) = \frac{x_1^i\, P^{-1}(x) + i \int_{x_0}^{x_m} x^{i-1}\, P^{-1}(x)\, dx}{x_0^i + i \int_{x_0}^{x_m} x^{i-1}\, P^{-1}(x)\, dx} \qquad \ldots.6.2$$

where $P^{-1}(x_1) = \int_{x_1}^{x_m} n(x)\, dx$ is defined as the proportion by number of droplets larger than x_1 in diameter. The term $\int x^{i-1}\, P^{-1}(x)\, dx$ can easily be integrated to good numerical accuracy using the Trapezoidal rule. The resulting volume or surface distribution is as accurate as the data permit.

Wise's method may also be applied to the computation of relevant mean diameter. A summary of the equations used by both methods in determining the Sauter mean diameter $\bar{x}_{32}$, surface mean $\bar{x}_{31}$ and volume mean $\bar{x}_{30}$ is listed in Table 6.1.

Table 6.2 is a summary of $\bar{x}_{32}$, $\bar{x}_{31}$ and $\bar{x}_{30}$ computed from equations in Table 6.1 for two sets of droplet spectra.

Lapple's method overestimates $\bar{x}_{32}$ severely; the error is shown to increase with a coarser interval. It may further be shown (see sec. 6.3) that $\bar{x}_{32}$ computed from the parameters of a ULDF fit to the data agrees well with Wise's method of deriving $\bar{x}_{32}$ from the original data. The method of "integration by parts" is therefore adopted in all number-to-volume conversion calculations. A computer programme written for the transformation and computation of $\bar{x}_{32}$, $\bar{x}_{31}$ and $\bar{x}_{30}$ is listed in Appendix A8 together with a list describing the variables used.

6.3 The upper limit distribution function (ULDF)

The ULDF is basically a normal distribution of volume or mass frequency with respect to a transformed drop diameter. It may be written as

$$\frac{d\psi}{dz} = \frac{\delta}{\sqrt{\pi}} e^{-\delta^2 z^2} \qquad \ldots.6.3$$

where ψ is the cumulative volume, δ a shape parameter and $z = \ln\left[\frac{ax^s}{(x_m^s - x^s)}\right]$, the transformed drop size. Constants a, x_m and s are respectively a skewness factor, maximum drop size and an arbitrary positive number usually taken as unity unless there is experimental evidence to substantiate another choice. The Sauter (or volume to surface) mean diameter, $\bar{x}_{32}$ is then given by

$$\frac{\bar{x}_{32}}{x_m} = \left[1 + ae^{1/(4\delta^2)}\right]^{-1} \quad \text{for } s = 1 \qquad \ldots.6.4$$

and

$$\frac{\bar{x}_{32}}{x_m} = \left[1 + 2ae^{1/(4\delta^2)} + a^2 e^{1/\delta^2}\right]^{-1} \quad \text{for } s = \tfrac{1}{2} \qquad \ldots.6.5$$

while the volume median diameter x_{500} is given by

$$\frac{x_{500}}{x_m} = (1 + a)^{-1/s} \qquad \ldots.6.6$$

A summary of equations describing $\bar{x}_{31}$ and $\bar{x}_{30}$ is listed in Table 6.3 for s=1 and s=$\frac{1}{2}$.

Contrary to the comments of Roberts and Webb (133) on the difficulty of physically interpreting the parameters a and δ, it is obvious from Eqn. 6.6 that parameter a highlights the importance of volume or mass median diameter as a measure of the fraction of total volume contribution from coarse drops, whilst δ indicates the degree of polydispersity of the spectrum.

Fitting of the ULDF is normally done graphically (168,11) with x_m and a determined by plotting x versus ψ on log-probability axes and δ by fitting a straight line to a similar plot of $ax^s/(x_m^s - x^s)$ versus ψ.

Alternatively, Marquardt's (194) algorithm for least squares estimation of non-linear parameters may be employed to determine optimum values of x_m , a and δ . The widely quoted (1) data of Moore et al.(168) were reanalysed as a test of this improved method of fitting the ULDF.

Appendix A9 contains a synopsis of Marquardt's algorithm together with relevant subroutines needed by the optimising programme (195) to compute the dependent variable as well as partial derivative values of this variable with respect to each parameter. Analytic partial derivatives of the volume frequency with respect to each parameter are hence derived for the cases when s=1 and $s=\frac{1}{2}$.

In a study of the detachment and breakup of water from the trailing edges of cascade blades in steam conditions matching those in low-pressure turbines, Moore et al. derived size spectra for three experimental conditions listed in

Table 6.4. Considerations of the mechanism of atomisation process in a blade wake suggested a probable existence of a well-defined maximum stable drop size. This may be characterised by a critical Weber number, We_c, defined as the ratio of aerodynamic disruptive force to the surface tension force simultaneously acting on a droplet, i.e.

$$We_c = \frac{\rho V^2 x_m}{\sigma} \qquad \ldots.6.7$$

where ρ = density of the continuous medium, V = relative velocity between droplet and suspending medium, x_m = maximum stable drop size and σ = interfacial surface tension.

For a particular steam condition, the value for We_c depends mainly on the value determined for x_m, the maximum drop diameter present in the spectrum. Moore et al. derived values for We_c having an average value of approximately 22 for subsonic and supersonic flow past the trailing edges of blades in cascades.

Table 6.4 summarises the optimum values obtained for δ, x_m and a (for s=1 and s=$\frac{1}{2}$) for all three experimental conditions quoted in ref.(168). Non-linear confidence limits for x_m are also listed. $\bar{x}_{32}$ computed by method of Wise from the original data is tabulated together with the value determined from Eqn. 6.4 using the optimised parameters. On the basis of x_m thus determined, it is shown (188) that optimisation of the ULDF fit increases maximum drop diameter and hence the critical Weber number considerably in the case

of supersonic blade exit flow (corresponding to Condition 3). Despite coarseness of the histogram intervals, $\bar{x}_{32}$ computed from the original data by Wise's "integration by parts" method agrees reasonably well with that determined from Eqn. 6.4. Further analysis of the spectra (ref.(188)) indicated that a better definition for We_c would be to use the diameter which corresponds to 99.9% of cumulative mass since in practice the 0.1% of the mass at the upper end of the spectrum would not be expected to contribute much towards damage of blade surfaces. The critical Weber number for the supersonic flow steam condition (see Table 6.4) would then be close to 22 as for the other two conditions. Further discussion on We_c is found in Appendix A10 which is a copy of ref.(188).

6.4 The heterogeneous ULDF

Although the ULDF adequately describes most droplet size spectra encountered in the present work, it fails to describe a multimodal distribution subjected to similar physical constraints on a maximum drop diameter. Droplet size distributions from two-phase flow systems or spray nozzles do exhibit multimodal shapes indicating the existence of heterogeneity. The infrequent but significant occurrences of droplets an order of magnitude larger than the volume of mass mean in the course of a typical photographic analysis is often neglected under the assumption that if a large enough number count is analysed its effect is negligible.

However in the event that large droplets are evidently present, e.g. re-entrained droplets from the walls in an annular two-phase flow commencing as an extremely fine mist (e.g. injected further upstream) or through uneven thicknesses in the liquid film of an air-blast atomiser, the upper limit criterion can still be effectively enforced by rewriting Eqn. 6.3 as a heterogeneous distribution of, for example, two normal distributions resulting in

$$\frac{d\psi}{dz} = \frac{\delta_1}{\sqrt{\pi}} e^{-\delta_1^2 z^2} + \frac{\delta}{\sqrt{\pi}} e^{-\delta_2^2 (z + j)^2} \qquad \ldots.6.8$$

where j represents a constant displacement between the means of the two normal distributions making up the heterogeneous spectrum. Together with a need to account for the volume contributed from each distribution, the final form of Eqn.

6.8 may be written as

$$\frac{d\psi}{dz} = \frac{1}{b+1}\left[b\frac{\delta_1}{\sqrt{\pi}} e^{-\delta_1^2 z^2} + \frac{\delta_2}{\sqrt{\pi}} e^{-\delta_2^2 (z + j)^2} \right] \qquad \ldots.6.9$$

where b is a suitable weighing factor. Writing $j = -m(\delta_1 + \delta_2)$, a constant represented by a multiple, m, of the sum of the standard deviations of each distribution, Eqn. 6.9 as a function of droplet diameter, x, may then be written as

$$\frac{d\psi}{dx} = \frac{x_m}{(b+1)\sqrt{\pi}\,(x_m - x)x}\left[b\,\delta_1 e^{-\delta_1^2 z_1^2} + \delta_2 e^{-\delta_2^2 z_2^2} \right] \qquad \ldots.6.10$$

where $z_1 = \ln\left(\frac{ax}{x_m - x}\right)$ and $z_2 = \ln\left(\frac{ae^{-m(\delta_1+\delta_2)}x}{x_m - x}\right)$

It is emphasized here that Eqn. 6.10 provides a better description for non-unimodal distributions and has an inherent assumption of a single maximum diameter for the net spectrum. This assumption is especially valid as in the example of a two-phase flow situation (currently studied) with a re-entrained spectrum.

To attempt a graphical fit of Eqn. 6.9 to experimental results is a rather formidable task. It is in this application that Marquardt's algorithm is most useful although a "good" initial guess of a set of parameters is first needed to set-up the optimising process. Early attempts to optimise values for the parameters of Eqn. 6.10 resulted in extremely slow convergence indicating that the equation may be ill-conditioned. A detailed scrutiny of the transformation functions, z_1 and z_2, indicated that a more suitable heterogeneous equation would be

$$\frac{d\psi}{dx} = \frac{x_m}{(b+1)\sqrt{\pi}\,(x_m-x)x}\left[b\,\delta_1 e^{-\delta_1^2(\ln(\frac{x}{x_m-x})+m_1\delta_1)^2} + \delta_2 e^{-\delta_2^2(\ln(\frac{x}{x_m-x})+m_2\delta_2)^2}\right] \quad \ldots.6.11$$

where the product $m_1\delta_1$ (or $m_2\delta_2$) represents a multiple of its standard deviation. The relevant Sauter mean, $\bar{x}_{32}$, and volume median, x_{500} are respectively (for s=1),

$$\frac{\bar{x}_{32}}{x_m} = (b+1)\left[b(1 + e^{\{(1/4\,\delta_1^2) + m_1\delta_1\}}) + (1 + e^{\{(1/4\,\delta_2^2)+m_2\delta_2\}})\right]^{-1} \quad \ldots.6.12$$

and

$$\frac{x_{500}}{x_m} = \frac{1}{(b+1)}\left[b(1 + e^{m_1\delta_1})^{-1} + (1 + e^{m_2\delta_2})^{-1}\right] \quad \ldots.6.13$$

In the absence of $m_1\delta_1$ and $m_2\delta_2$, the normal variate of Eqn. 6.11 reduces to $z = \ln\frac{x}{x_m-x}$ (corresponding to a = 1 of the unimodal ULDF) which has a mean, $\bar{z}$, equal to zero and the original volume frequency distributed with respect to diameter is unskewed. The addition of either $m_1\delta_1$ or $m_2\delta_2$ to z offsets $\bar{z}$ from its zero position. A positive or negative displacement of $\bar{z}$ from its zero position respectively introduces a skew towards the smaller or larger end of the diameter range of the original volume frequency versus diameter spectrum. Eqn. 6.11 thus describes a heterogeneous distribution of two spectra; the degree of skew experienced by each depends on its relevant $m_1\delta_1$ or $m_2\delta_2$ displacement of $\bar{z}$ from zero.

Appendix All contains a set of analytic partial derivatives of the distributed quantity with respect to each of the parameters present in Eqn. 6.11. Also included is a Fortran subroutine to compute values for these partial derivatives as well as another subroutine to calculate values of the dependent variable (Eqn. 6.11) for use by the main program.

Fig. 6.1 is a plot of the optimised mass frequency curve and the original data of an atomiser spectrum (data batch AK). Table 6.5 summarises the parameters of the heterogeneous ULDF fit. Although a certain amount of scatter is present in Fig. 6.1, the correlation emphasized the presence of lowest order heterogeneity in the net spectrum. A similar attempt to fit the data using unimodal ULDF was wholly unsuccessful giving rise to a "forced off" (see ref.(195)) failure, its 95% non-linear confidence limits ranging from zero to 10^8 for x_m.

It must be emphasized that although the ULDF or the heterogeneous ULDF offers a suitable description for drop size spectra resulting from an atomisation process in which the balance between aerodynamic disruptive forces and surface tension forces highlights the existence of a stable maximum drop size (85), the parameters and hence Sauter and other mean diameters computed from the optimised values must be viewed with caution. Where there is a need to employ e.g. Sauter mean in further correlating experimental results, the Sauter mean computed from the original data

via Wise's (193) method is preferred. In the absence of an adequate theory capable of describing the atomisation process, ULDF or similar distributions, having inherent stochastic assumptions of normality of some quantity, must never be treated as the governing model, although it is a useful guide in deciding a suitable stochastic sample size (see sec. 6.5) in experimental work.

6.5 Number count statistics

Any experimental study which involves statistical sampling in order to determine the characteristics of an infinite population often requires a suitable choice of a stochastic sample size which best represents the population. Where a variable or its transformation function is normally distributed and is in a form not containing parameters which have to be estimated from the sample, the estimates of the two inherent quantities mean and variance can readily be computed. However, the ULDF type of transformation introduces two additional parameters (x_m and a) into the distributed quantity. These have to be estimated from the sample unless their values have been given a priori, in which case a statistical sample size can be computed for a required set of confidence limits on, for example, the arithematic mean. Since the most important "tests" presuppose normality, it is not possible, using standard confidence limit tests, to estimate a best sample size where no a priori assumption can be made of the additional parameters such as x_m and a which may depend on sample fluctuations.

Under the assumption of log-normal behaviour of number frequency distributed with respect to particle diameter (in which the number to volume conversion merely follows Kapteyn's transformation (166)), Jackson et al.(196) showed the order of magnitude of sample size induced errors in samples with number counts ranging from 500 to 50,000 per sample. They concluded that number distribution data can be converted to mass distribution data with reduced errors only when a large

sample of narrow size ranges is considered. The above is an example involving a priori assumptions and its result should be cautiously used as a guide in deciding a suitable sample size.

It is the aim here to employ a non-linear least squares ULDF fit to the experimental data with "sufficient" number count for the optimised parameters to have 95% confidence limits within an acceptable range of uncertainty. The sample size needed cannot therefore have a preassigned value since it depends on how "variable" the measurements are relative to the describing function. In practice, a number count of between five hundred and one thousand is adequate although there are instances in which even a number count as high as one thousand does not provide a satisfactory least squares fit to the describing function. When faced with such a situation, two possible solutions are available. The sample size may be enlarged by increasing the number of readings i.e. number counts, or if the problem persists the proposed correlating equation is unsuitable or incapable of describing the data satisfactorily.

CHAPTER 7

TWO-PHASE FLOW RIG AND MEASUREMENTS

7.1 Major Rig Components

Major considerations in selecting a pipe geometry were: (i) a fully developed turbulent pipe flow should exist over several tens of pipe diameters (constrained by the available laboratory space); (ii) the rate of turbulent agglomeration should exceed that of thermal or velocity gradient rates by more than an order of magnitude; (iii) air flow rates should provide sufficient droplet residence time (e.g. a few hundred milliseconds) to permit studies on agglomeration effects. 'Durapipe' (ABS plastic) of 102 mm inside diameter was selected for the construction of the test rig. The unobstructed and useful length in the laboratory was approximately 10 m. Hence, allowing 30 pipe diameters (198) for the flow to become fully developed and 1 m for upstream location of a blower, mixing chamber and other relevant instrumentation , 6 m of useful length were left for experimental measurements. To satisfy conditions (ii) and (iii) simultaneously, a flow Reynolds number of 10^5 (see Appendix A12) was chosen. Accordingly a Secomak ½ HP single-phase centrifugal blower was used, capable of a maximum air flow rate of up to 20 m^3/min (corresponding to Reynolds number of 2.7×10^5 in the absence of friction and other losses) under atmospheric pressure conditions. To measure the air mass flow rate, a 2 m length of 102 mm I.D. 'Durapipe' having a 76 mm diameter orifice plate (with D and D/2 tapping arrangement) to BS1042 specification

(199) was attached to the inlet of the blower. A sliding valve at the open end of this 2 m section was used to vary the air flow rate through the rig. (Fig. 7.1)

Initial measurements by Williams (9) of the single-phase flow turbulent energy spectra (using a hot-wire anemometer) exhibited discernible peaks at 50 Hz or its harmonics, introduced by the blades of the centrifugal blower (which was arranged to force rather than to draw air through the rig in order to avoid operating in a wet two-phase atmosphere). A baffle tank which adequately dampened these pressure and velocity fluctuations was connected (9) to the outlet of the blower via a flexible hose which further isolated the downstream test section from blower vibrations. The blower assembly was additionally mounted on vibration dampers on the test bench.

The accuracy of the 76 mm diameter orifice plate for measuring fan air flow rate was checked against pitot tube measurements of the air velocity at 10 diameters downstream of the entry plane (Fig. 7.1). The average velocity across the 102 mm diameter test section agreed with the orifice plate value within limits of measurement errors (9).

A 168 mm diameter droplet injection chamber was connected to the outlet of the baffle tank (Fig. 7.1). The atomised liquid was injected axially downstream to mix with the fan air which flowed past the injection unit. As described in Sec. 7.2.4 the atomisers were housed in a "bullet" shaped casing (Fig. 7.15) located concentrically in the mixing chamber; the cross-sectional area of the annular space was

such that it was marginally larger than the cross-sectional area of the 102 mm I.D. pipes in the test section. The mixing chamber was connected to the inlet of the test section via a 305 mm length converging section. A drain hole was suitably located at the bottom of the mixing chamber to remove deposited liquid on the walls of the chamber.

The overall length of the test section was selected by suitable combinations of a series of shorter sections. A male and female flange were fitted to opposite ends of the shorter pipe sections. At each flange joint, the open ends of the two pipe sections matched end-on (Fig. 7.2) minimising discontinuity to the flow and preventing accumulation of liquid at the flange joints. Pipe lengths of 2 m, 1 m and $\frac{1}{2}$ m were prepared; the number of units of each type was such that all relevant permutations needed for a range of different experiments were met. In addition to the above, several liquid film extraction units were built for measurements of droplet deposition rate (see sec. 7.5).

At the outlet of the two phase flow rig, a length of 304 mm diameter flexible tubing was positioned to drain off deposited as well as entrained droplets from the flow. The open-loop flow configuration was therefore adopted with saturated air exhausted into the laboratory.

7.2 Droplet Generation

7.2.1 Basic Considerations

The radial variation of non-dimensional energy dissipation rate ε^+ (defined as $\varepsilon R/u_*^3$) in a turbulent pipe flow, taken from Fig. 20 of Laufer's (200) work, is summarised in Table 7.1 for four non-dimensionalised radial positions, (ignoring the extremely high values close to the pipe wall) and for Reynolds number (henceforth Re_D) equal to 5×10^5 and 5×10^4. Based on initial measurements of friction velocity in the present rig for Re_D equal to 10^5, the Kolmogorov microscale, λ , defined as $(\nu^3/\varepsilon)^{\frac{1}{4}}$ is also shown for each radial position in Table 7.1. The aim here was to select drop sizes preferably smaller than these values of microscale so that existing theories (21, 29) might be used to predict the measurements with regard to evolution of size spectra due to turbulent agglomeration.

As seen from Table 7.1, since an isotropic turbulence condition is very nearly met in the pipe centreline, a good choice of drop spectrum appears to be to use the centreline microscale to limit the maximum drop size. However, since energy dissipation rate increases radially towards the wall i.e. a decreasing microscale, a drop-size spectrum with a mass mean diameter of about 40 μm seems appropriate assuming for the moment that the presence of entrained drops in the flow does not significantly alter the dissipation scale.

Whilst the best choice of drop-size distribution is that of a monodispersed spectrum with diameter at 40 μm or less, in practice this requirement is very difficult to meet.

Spinning disc or cup atomisers (108, 111) which generate a fairly monodispersed spectrum are an obvious choice. However, for droplet agglomeration to be significant a high number concentration is needed. Whereas number concentrations of the value 10^6 (27) and 10^9 (29) submicron particles per cm^3 have been used in other studies, much uncertainty remains as to the best number concentration to select for studies of the present nature. An average interparticle spacing of around 10 diameters may be calculated (1) as the typical distance separating drops at the exit of a HP turbine and this value has been adopted as a guide in computing the rate of droplet generation required.

Based on the above particle spacing, the water to air mass ratio required was 0.43 and for an air mass flow rate of 0.15 kg/s (at $Re_D^- = 10^5$) the droplet production rate needed was of the order of 2×10^9 drops/s at a mass mean diamter of 40 μm. Such high droplet production rates are not readily met by spinning disc or cup type atomisers of compatible physical dimensions. Commercial atomisers of the pressure or twin-fluid type which satisfy the above requirement of droplet throughput often produce extremely polydispersed spectra. Nevertheless, attempts to use commercial pneumatic atomisers of both conventional and ultrasonic types were made (see sec. 7.2.2). The ideal atomiser for the present work is one which produces a monodispersed cloud of droplet diameter less than or equal to 40 μm without the need for atomising air so that Re_D in the two-phase flow is attributed solely to fan air. However, a pneumatic atomiser designed by the author was

eventually selected, as described in sec. 7.2.3.

7.2.2 Commercial Atomisers

7.2.2.1 The Conventional Pneumatic Atomiser

In order to establish the suitability of the Delavan-Watson GC390109 atomiser (hereafter referred to as the D-W atomiser) for use in the two-phase rig, a photographic analysis of its drop-size distribution under two sets of air to liquid mass flow ratios was carried out. It should be emphasised that an "in-depth" study of atomisation characteristics was not planned. The qualitative results from the present tests would be used to decide whether or not the atomiser was satisfactory for further experimental work. Fig. 7.3 illustrates the main dimensions of this atomiser including the manufacturer's specification on spray length and diameter. Atomisation takes place when an annular air jet disrupts a conical film of water issuing under pressure from the small opening of a central liquid nozzle.

Fig. 7.4 illustrates the atomiser test rig used. The schematic arrangement for air and water supply is shown in Fig. 7.5. A 6.35 mm diameter orifice plate device with corner tappings in accordance with ref. (200) provided readings for air mass flow rates. Water flow rate was read from a calibrated rotameter. Atomised liquid was collected and drained from the photographic test section via a suitably large drain pipe, its inside lined with a short length of honeycomb section to enhance droplet deposition. To make room for the photographic equipment, the drain pipe inlet was located 300 mm from the face

of the atomiser.

The D-W atomiser air circuit was operated at 20 psig (137 kPa gauge) consistent with keeping the total air mass flow rate low as well as to avoid a large spray width in view of its intended application in a 102 mm I.D. pipe. Table 7.2 summarises the two sets of experimental conditions (DW1 and DW2) selected for the photographic study. The sequence of events in a typical photographic experiment are as described in sec. 4.3.1). The photographic plane was sufficiently close (70 mm) to the atomiser outlet to minimise any effect which droplet evaporation might have had on its size distribution.

The photographs were manually sized (see sec. 4.5.1) since the automatic image analysis system was not available when this aspect of the work was carried out. Conversion from number to mass frequency distribution was by Wise's(193) method (see sec. 6.2). When computing the net mass frequency distribution for the entire spray, a scaling factor equal to the annular area occupied by the radial element photographed (see Fig. 4.6) was first applied to the number counts over all drop sizes at the corresponding radial position.

Fig. 7.6 (a) and (b) illustrate the number and mass frequency distributions for experimental conditions DW1 and DW2 respectively. The mass frequency spectra indicated bimodal distributions if sufficiently large number counts were made instead of the current total number counts of respectively 740 and 1200 for DW1 and DW2. A likely explanation for this behaviour is the uneven distribution of liquid film thickness produced by the inner liquid nozzle. Fig. 7.7 illustrates the

normalised radial distribution of Sauter mean diameter, $\bar{x}_{32}$, and the ratio of number count to average count per negative for both test conditions. The heavier drops are concentrated on the outer periphery of the spray. In a temporal size distribution their presence would be even more significant. The peak number density is at approximately 20 mm radially from the liquid nozzle axis. In addition, approximately 55% of the mass of the spray is contained in 10% of the number count at the largest diameter end of the spectrum. Although the mass mean diameter centred around 50 μm (Table 7.2), the polydispersity of the drop-size distribution made it unacceptable as typical starting spectrum for the present studies if the aims highlighted in sec. 7.2.1 were rigidly adhered to.

To meet the requirement of 10 diameters interparticle spacing at Re_D of 10^5, the total liquid volumetric flow rate required would be 4 l/min, assuming no deposition on the pipe walls. The maximum liquid flow rate used in the test was 0.8 l/min, so that 5 atomisers operating in this condition would be needed to meet this criterion even if the size distributions were satisfactory. Increasing the atomiser liquid throughput was not an alternative solution since this would lead to a coarser spectrum.

The conclusion was that the D-W atomiser, whilst physically small as well as producing a relatively small spray diameter, was unsuitable for the above reasons.

7.2.2.2 <u>The Ultrasonic Atomiser</u>

Whilst development work was carried out on a new twin-fluid nozzle design, an air-operated ultrasonic atomiser

(manufuctured by Ultrasonics Ltd.) was tested. It could handle a maximum water flow rate of 3.2 l/min with a corresponding 50 μm maximum drop size, (manufacturer's specification) at an air to water mass flow ratio of 0.7. This atomiser appeared to be ideal for the present studies in view of its compactness (Fig. 7.8). A series of tests to determine its suitability was planned, accepting at the time the quoted value for maximum drop diameter.

Since no information on the spray width was included in the manufacturer's literature, as a first test its operation in the two-phase rig with regard to initial droplet deposition rate onto pipe walls was examined. The atomiser was mounted concentrically at the converging section of the two-phase rig so that the front end of the nozzle was in line with the entry plane (see Fig. 7.9) to the test section. The bulk air flow through the test section was adjusted so that Re_D equalled 10^5. Atomiser operation was set at the recommended values of 60 psig (413 kPa gauge) for air and 3.2 l/min for water and the amount of water deposited $\frac{1}{2}$ m downstream was measured. (see sec. 7.5 for deposition measurement technique).

More than 60% of the injected water was deposited on the pipe wall, indicating a spray diameter much wider than than 102 mm pipe diameter. Similar results were noted even when the operating air pressure and liquid flow rates were halved.

The ratio of the atomiser air mass flow rate to total air flow rate was approximately 26% when operating at 3.2 l/min water flow rate making the influence of atomiser air velocity

on bulk air velocity relatively significant. Visual observations of coarse drops stripping from a continuous liquid film in the wake region of the resonance chamber raised doubts on the validity of a 50 μm maximum drop diameter in the spectrum as claimed by the manufacturers.

Since the spray cone angle and hence spray diameter could not be readily altered for this type of atomiser, it was decided to use this atomiser as a final alternative in the event that modifications to the D-W atomiser proved unsuccessful. No photographic analysis of the ultrasonic spray spectra was therefore contemplated.

7.2.3 The Air-Blast Atomiser

7.2.3.1 Design and Construction

From the previous D-W atomiser test results it is obvious that the formation of a uniform thin sheet of water is essential (201) for narrow drop-size distributions and small drop diameters at moderate operating pressures. An air-blast atomiser,as defined here, is one in which the liquid is spread into a continuous thin sheet (over a prefilmer) and then exposed on both sides to high velocity air. However, most commercial air-blast atomisers are designed for use in the field of fuel combustion where the total air-to-fuel mass ratio is greater than 2 (135). In the present studies, the air-to-liquid mass ratio must be less by more than an order of magnitude. Hence the inner and outer air mass flow rates, in any new design, should be minimised without adversely affecting its performance.

An obvious choice of design would be to replace the liquid nozzle of the D-W atomiser by a twin-fluid nozzle retaining the outer annular air jet of the D-W atomiser. The resulting air-blast atomiser would have similar physical geometry to the D-W atomiser except that the conical liquid film would be replaced by a more uniform thin sheet of water.

A prototype twin-fluid nozzle was designed and constructed. Referring to Fig. 7.10 the major components were an outer liquid nozzle, an inner air nozzle and an axial deflector. Noting that large volumetric axial air flow rates (mainly for complete combustion purposes) were used in commercial air-blast atomisers, the prototype unit was designed to reduce this flow without losing its basic function of spreading and accelerating the liquid film. To ensure that the inner air nozzle was concentric with the axial deflector a helical spacer (which also imparted a tangential velocity component to the axial air flow) was soldered onto the axial deflector. Similarly, three short lengths of spacers, located circumferentially on the outer surface of the air nozzle at 120° apart, prevented misalignment between the liquid nozzle and air nozzle. The curvatures selected for the liquid prefilmer at the front end of the liquid nozzle and the axial deflector were such that fluid acceleration through the annular gap was enhanced under the correct setting.

The operation of the atomiser may be envisaged as follows: An axial air jet flowing through the helical passage is deflected radially outwards before striking the inner surface of a liquid film flowing over the prefilmer. The liquid,

supplied through 3 equispaced circumferential inlets, flows into a weir from which it spills over the prefilming surface before being uniformly spread as it leaves the prefilmer at approximately 90° to an outer coaxial air jet.

7.2.3.2 Assembly of the Air-Blast Atomisers

Since several combinations of the relative displacements between the three major components (Fig. 7.10) of the twin-fluid unit were possible, a scheme for systematic assembly of the nozzles, to repeat the settings, was devised. The optimum settings were first determined from a series of trials involving photographic and/or visual assessment of spray quality for various combinations of liquid and air flow rates through the respective annuli. The following optimum dimensions were selected: (i) a 0.5 mm annular liquid gap between the inner air nozzle and the liquid nozzle and (ii) a 0.6 mm wide axial air annulus measured from the outer edge of the liquid prefilmer to the inside edge of the axial deflector.

In practice the liquid annulus may be adjusted by first closing it and then turning the air nozzle counterclockwise for 180° (or half a turn) relative to the liquid nozzle. Similarly, the axial air annulus may be set by rotating the axial deflector counterclockwise for two turns from its fully shut position. As a guide the axial air annulus was correctly set when, in the absence of liquid flow over the prefilmer, the total air mass flow rate through the annulus was 7 kg/min under 20 psig (137 kPa gauge) delivery pressure. The dimension of the outer coaxial air annulus was unaltered and was therefore

equal to the original D-W atomiser value of 1 mm annular gap.

7.2.3.3 Performance of the Prototype Atomiser

The atomising characteristics of the prototype unit were studied photographically for two sets of experimental conditions summarised in Table 7.3. Using only one orifice plate device to meter both the coaxial and axial air flow rates (the actual proportion which flowed into each was therefore an inverse function of the resistance to air flow), the sequence of events during each test were as described in sec. 7.2.2.1 except that the air pressure was set at 30 psig (206 kPa gauge). The results were similarly derived.

Fig. 7.11 and 7.12 illustrate the number and mass frequency distributions for the net spectra. The total air-to-liquid mass ratio used was less than 0.3. Referring to Table 7.3 the total number counts for data batch AG and AH were respectively 1511 and 1583. At the higher liquid flow rate (i.e. batch AH), the shift in the unimodal spectrum towards the large sizes was of the order of one additional size interval. Although the spectra number frequency modal diameters were in the range 40 to 50 μm the mass mean diameter was less than 44 μm for both conditions. A non-linear least squares fit to the Upper Limit Distribution Function, ULDF (see sec. 6.3 for both spectra indicated a maximum drop size less than 75 μm.

The cone angle of 80° of the air-blast atomiser was also smaller than the D-W unit, requiring only 6 or 7 radial photographic positions instead of 8. Due to fluid leakage through the locknut threads of the prototype unit no attempt

to examine its performance at higher flow rates was made. Based on the above results, four additional units were constructed, having first redesigned the liquid nozzle to incorporate a rubber O-ring seal which corrected the leakage problem. (see Fig. 7.10)

7.2.3.4 General Performance of the Air-Blast Atomisers

Each of the four atomisers was individually assembled in accordance with the settings of sec. 7.2.3.2. Two of the four atomisers were randomly selected for further photographic analysis. The test conditions for atomisers number 1 and 3 are summarised in Table 7.4. An additional orifice plate device using D and D/2 tappings (12.7 mm orifice diameter) to BS1042 specification (200) was used to determine the coaxial air mass flow rate. The test rig used was similar to that described in sec. 7.2.2.1 with the addition of an extra air circuit. The water mass flow rate for all test conditions was set at 1.3 kg/min. The axial air and coaxial air mass flow rates were independently adjusted, so that the ratios listed in Table 7.4 for test conditions AI to AK were met. An important parameter in the tests was the ratio of total air to water mass flow rate which was kept at 0.2. The sequence of events in each test was similar to that described in sec. 7.2.2.1. However, the highest air pressure encountered was 30 psig (206 kPa gauge). Four photographs were taken at each radial position and the spray width at 70 mm from the face of the nozzle was such that seven photographic positions were required.

The total number of drops counted for each test

condition averaged 4000. Figs. 7.13 and 7.14 illustrate the mass frequency distribution of the spray spectra. Results from atomiser unit 1 in which the axial to coaxial air mass ratio was varied from 1 : 1 to 1 : 3, suggest that the best condition was 1 : 1. As the axial air mass flow rate was reduced, uneven thickness in the liquid sheet reappeared, as seen in data batch AK in which a second peak was just discernible.

To check the consistency of atomiser operation given the same physical settings, atomiser unit 3 (data batch AL) was tested under exactly similar flow rates as data batch AI of unit 1. The drop-size spectrum is illustrated in Fig. 7.13 showing reasonably good agreement in the operational characteristics amongst the atomisers. A ULDF fit gave maximum drop sizes of 85 μm and 81 μm for AI and AL respectively. The mass mean diameters are the same at 33 μm.

It was therefore decided not to carry out tests at higher liquid flow rates but to use an integral assembly of the four units as the droplet generator for the two phase rig. At liquid injection rates of 1.3 l/min for each atomiser, the required 4 l/min water rate for 10 diameters droplet spacing was readily met. The advantages of the air-blast atomisers include (i) narrow spray diameter (ii) low air-to-liquid mass flow ratio (iii) suitably small drop diameters and (iv) narrow mass-frequency spectra.

Based on a mass mean diameter of 33 μm and a liquid flow rate of 1.3 l/min, droplet production rate from each air-blast atomiser exceeded 10^9 drops/s.

It is worth mentioning that the mass frequency spectrum illustrated in Fig. 5.35 of Chapter 5 belonged to the spray spectra of atomiser number 4 operating under the same test conditions as AI and AL.

7.2.3.5 Electrostatic Charging During Atomisation

Depending on the technique employed to generate aerosol particles, significant electrostatic charging of the particles has been reported (202). A possible mechanism for drop charging in pneumatic atomisation of water would be the presence of ion concentrations in the drops during liquid separation. Spray electrification of pure water has been investigated by Chapman (203) using a brass pneumatic nozzle. The average charge measured for a 3 μm and a 10 μm diameter droplet was respectively 0.6×10^{-7} esu and 2.88×10^{-7} esu. The author has been unable to obtain any data on electrostatic charging of droplet sizes larger than 10 μm. Woods (204) determined the collision efficiency between equal size droplets (carrying opposite charges) using a streak photographic technique and concluded (for drop sizes smaller than 80 μm diameter) that drop coalescence rate increased linearly with drop charge when a threshold value of about 5×10^{-5} esu is exceeded whilst charges of the same sign totally inhibited coalescence. For drop sizes 80 μm diameter and larger, an additional wake capture coalescence mechanism as reported by Telford et al. (205) was present. In contrast Krasnogorskaya and Neizvestnyy (206) found that the threshold charge (above which collision efficiency increased sharply) is directly proportional to droplet

mass. The value of the proportionality constant was, however, not determined.

For the present studies it is assumed that the effect of electrostatic charging on coagulation rate would be small relative to inertial forces. No instrumentation either for the measurement of electrostatic charges and/or neutralisation of any charged droplets was therefore planned.

7.2.4 Atomiser Assembly for Injection into Turbulent Air Stream

7.2.4.1 Injection through the Pipe Walls

In view of the high air velocity (15m/s at $Re_D = 10^5$) in the 102 mm diameter test section, an attempt to introduce droplet into the turbulent air stream at 90° to the pipe axis was carried out.

The velocity profiles in the test section immediately downstream and at 6 diameters downstream of the test section, in which one and subsequently two diametrally opposite air-blast atomisers were mounted, were measured. The atomisers were operated in the "dry" condition where water injection was suppressed. The measurements indicated that disturbance to the fan air velocity near the wall region, although significant immediately downstream of the injection section, did not seriously affect the velocity profile after 6 diameters downstream.

The atomisers were subsequently operated with water feed and the amount of water deposited approximately 4 diameters downstream was metered. The ratio of the deposited to injected

water rate exceeded 60% indicating that the droplets possessed sufficient inertia at injection to reach the opposite wall of the 102 mm pipe over downstream distances less than 4 pipe diameters. The 90° wall injection technique was therefore unsuitable.

7.2.4.2 Axial Injection

An axial injection technique was attempted. The four air-blast atomisers were housed in a "bullet" shaped casing mounted concentrically in a short length of 168 mm I.D. mixing chamber (Fig. 7.15).

A method for feeding axial air, coaxial air and water to the 4 atomisers simultaneously was devised. The total axial (or coaxial) air mass flow through all four atomisers was measured using one orifice device. For each axial or coaxial air feed, a primary air supply was further redistributed to four secondary air feeds inside the casing, each to the corresponding air inlet of an atomiser. The nett resistance to air flow through each of the redistributed secondary air feeds would influence the fraction of total inlet supply into each atomiser. Hence care was therefore exercised to ensure that the lengths of the secondary feed lines were approximately equal and not kinked.

Since each atomiser had three circumferentially equi-spaced water inlets, a total of twelve secondary water outlets was required at the redistribution chamber fed by a single inlet. The design of the water redistribution chamber is illustrated in Fig. 7.16. The 3 water feeds needed by each atomiser were

tapped from circumferentially equispaced secondary outlets.

The water and air redistribution chambers as well as the four air-blast atomisers were mounted on a common framwork which will be referred to as the "atomiser assembly". Referring to Fig. 7.17, the atomisers were located at the front end of the assembly. Behind the atomisers were the air redistribution chambers followed further back by the water redistribution chamber.

The encased atomiser assembly, having a total length of 204 mm, was fed with three main fluid lines: two for air and one for water. The front face of the atomiser assembly was located at the entry plane of the converging section. With the atomiser spray axes arranged parallel to the pipe axis, initial measurements (at $Re_D = 10^5$) of water deposited immediately downstream of the droplet injection chamber indicated deposited water rates of up to 60% of injection rates (for liquid flow rates in the range 2 to 6 l/min). The atomisers were then inclined so that each spray axis was parallel to the walls of the converging section. The amount of injected water which deposited reduced to 45% and could not be further minimised. The initial high percentage deposition may be attributed to the high number concentration at the converging section in addition to the radial velocity component imparted to the droplets as they left the atomisers. The axial injection technique was therefore used in subsequent two-phase experiments.

7.3 Fluid Supply and Metering Equipment for the Two-Phase Rig

Fig. 7.1 illustrates the arrangement of the air and water feeds for the atomiser assembly in the injection and mixing chamber.

7.3.1 Air Circuit

The required coaxial and axial air mass flow rates were independently monitored from separate air circuits fed by a common supply of filtered laboratory air capable of a maximum delivery pressure of 80 psig (552 kPa gauge). Each air circuit was pressure regulated and the maximum operating pressure needed for atomisation never exceeded 45 psig (311 kPa gauge). Mass flow rates through each air circuit were individually metered from separate sets of D and D/2 orifice plates (using 16 mm orifice diameter) fitted in a 30 mm duct according to BS1042 specification (200). The pressure difference across each orifice plate was measured by a U-tube water manometer. Since the gauge pressure in the manometer was fairly high (311 kPa gauge) all manometric joints were tested for leakage using soap solution. A Bourdon type pressure gauge and a mercury thermometer provided the other readings necessary for the computation of air mass flow rates. The pressure head indicated by the water manometer could be read to an accuracy of $\pm$ 0.5 mm and the corresponding maximum error in the measurements of atomiser air mass flow rate was within $\pm$ 2% of the mean for test conditions used in the present studies. (see sec. 7.7)

7.3.2 Water Circuit

A Beresford 3-phase, 3/4 HP, single-stage, 25 mm, self-priming pump having a nett maximum capacity of 7 l/min at a delivery pressure of 40 psig (276 kPa gauge) at the exit of the air-blast atomisers was used. Water flow rate was metered by a calibrated rotameter and a water filter removed all solids larger than 5 μm from the water circuit, an essential requirement in view of the fact that the performance of the air-blast atomiser depended on a uniform circumferential water feed for a near monodispersed spectrum. To permit treatment of water (e.g. altering the surface tension or viscosity of the liquid fed to the atomisers) at a future date, a 1 m^3 fibreglass tank was used as a water reservoir.

Two rotameters having maximum readings of 5 l/min and 10 l/min respectively were used in the experimental studies over different periods. To check the accuracy of the manufacturer's graduation, measurements of flow rates at several settings were made using a stopwatch and measuring cylinder. Fig. 7.18 illustrates the relationship between measured value (averaged over five repeated trials) and the graduated scale (for the 5 l/min maximum flow unit). The measured flow rates were generally lower than the graduated values with a maximum deviation of 1.5% from the graduated reading. The second rotameter was similarly calibrated and a maximum deviation of 1.7% lower than the graduated readings was detected.

7.4 Humidification

Drop evaporation in an unsaturated environment can significantly alter the sizes of the 10 or 20 μm drops within the residence period of the drops in the test section.

To monitor the change in room relative humidity (RH) due to drop evaporation, a hair hygrometer (Fisher Ltd.) was used. In most of the two-phase experiments drop evaporation was expected to have been significant over the first fifteen minutes from start-up, as was indicated by fairly sharp rises in RH reading over this period. Since the two-phase rig was housed in an enclosed environment the recurring use of saturated air leaving the exit of the drain pipe frequently raised RH readings to the 90% mark after a continuous operating period of approximately one hour.

The experiments were therefore conducted in a fully saturated environment, recording the first reading after an initial saturation period. The effect of droplet evaporation on size distribution was therefore not serious.

7.5 Liquid Film Extraction Units

The extraction of deposited liquid film from the pipe walls may be carried out either by the use of suction through the walls of a porous sinter (91, 95) (which inevitably removes a portion of the gas phase as well) or via a slot in the pipe wall (75). The method selected should preferably have a minimal effect on the flow ambient conditions as extraction takes place. For the horizontal arrangement of the two-phase rig the decision was to use a simple slot extraction method (without external aid). The technique therefore makes used of the slight positive pressure within the pipe and gravitational effect to force the liquid out of the system. However, the gas phase must not be permitted to leave with the liquid since it would alter the static pressure of the flow at each extraction station.

Fig. 7.19 (a) illustrates the extraction slot used. A 60° chamfer at the leading edge of the downstream pipe section was used on the basis of Yablonik and Khaimov's (207) work. The major dimensions which govern the performance of the extraction unit were (i) the slot width which must be wide enough to avoid liquid crossing over the gap, (ii) the size of the intermediate collection chamber which should be adequately large to avoid over-flowing, requiring (iii) a compatible drain-pipe, the performance of which was determined by (iv) a constant pressure head weir arrangement for the eventual removal of liquid from the system without any loss of the gas phase from the flow.

In the initial design of the extraction unit a 26 mm wide

square-edge slot (Fig. 7.19 (b)) was used. The equal lengths of the two pipe sections were such that the overall length of the extraction unit was ½ m and the depth e, of the collection chamber was arbitrarily set at 15 mm. To test the extraction efficiency of the prototype unit, Reynolds number of air flow in the rig was set at 10^5. A similar extraction unit was located immediately upstream of the test unit; the distance separating the extraction slots was exactly ½ m. Water, injected into the flow stream via the drain pipe of the upstream unit, flowed along the bottom of the horizontal pipe and into the downstream extraction slot. The open end of the extraction drain pipe was located approximately 76 mm below the surface of a weir arrangement; the liquid which spilled over was collected in a measuring cylinder over fixed time intervals. A small amount of entrained gas (bubbles) was noticed leaving with the water at the open end of the immersed drain pipe. The "immersed drainage" arrangement was tested for liquid flow rates of up to 3 l/min. At each liquid flow rate, five repeated measurements of extracted liquid rate were made over suitable time intervals and averaged.

Fig. 7.20 illustrates the relationship between extracted and injected liquid rates. For liquid flow rates less than 2 l/min, the extraction unit appeared to work satisfactorily but significant departure from linearity at higher values occurred. A visual examination at the collection slot indicated that the collection chamber was over flowing. This was confirmed when the weir arrangement was removed allowing the collected liquid to be drained directly, aided by the slight

positive pressure head in the air flow and as indicated in Fig. 7.20 the linear relationship was sustained over all liquid injection rates up to 3 l/min.

Operation of the extraction unit in a dense two-phase annular flow was qualitatively examined. Experimental condition C (see Table 8.2) was set up. With the help of an intense light source, the extraction slot located at ¼ m from the open end of the test section was visually examined. The relatively thick liquid film flowing along the bottom of the pipe occasionally crossed over the 26 mm slot width in sudden bursts. At the "ceiling" of the circular section, rivulets of water were seen stripping off from the sharp edge of the slot to be reentrained into the flow stream.

Hence although the extraction unit was satisfactory under a simple flow test the flow characteristics in a dense two-phase environment were rather different with a faster flowing liquid film. With the rig in operation, the upstream section of the extraction unit was gradually moved further away from the downstream edge and at a slot width of 36 mm no cross-over was observed. To minimise the effect of reentrainment, a diffuser was introduced, its lower end suitably slotted (Fig. 7.19 (a)) to permit collection of the thick bottom film. The liquid film at the "ceiling" of the pipe was trapped by the leading edge of the downstream section as it left the edge of the diffuser as illustrated in Fig. 7.19 (a).

To enable the immersed drainage technique to be used for all film flow rates encountered in the present studies, the depth of the collection chamber was increased to 30 mm. The

modified unit was tested in the simple flow situation and Fig. 7.21 illustrates the relationship between extracted and injected liquid rates using the overflowing weir arrangement. A qualitative examination for cross-over effects in a two-phase flow environment was repeated. Flow cross-over problems highlighted earlier were absent.

The volume of liquid collected in a 2 litre measuring cylinder may be read to an accuracy of ± 2 cc and the stop-watch to ± 0.5 s. Based on a collected volume of 1.5 l over the shortest period encountered in the experiments, that is, 30 s, the maximum reading errors amounted to $\pm 1.7\%$ at the highest liquid collection rate. However, due to variations in the liquid flow rates and random collection errors by the operator, the maximum standard error of the repeated measurements encountered was $\pm 3\%$ of the average value (when measuring deposition rates as described in sec. 8.3).

The results of the present tests in Figs. 7.20 and 7.21 also indicate the presence of liquid entrainment into the air stream. Referring to Fig. 7.21 the amount entrained appeared to remain constant over all liquid injection rates.

7.6 Measurement of wall-static pressure

The apparatus used in the determination of wall-static pressure along the pipe is illustrated in Fig. 7.22. Dimensions of the wall-static pressure tappings used were in accordance with BS1042 specification (200). Each of the four $\frac{1}{2}$ m pipe length components of the test section was converted so that four equispaced static pressure holes were located circumferentially at its mid-section.

A micromanometer enabled wall-static pressure measurements relative to local atmospheric pressure in the laboratory be made. Although the atmospheric pressure varied from one period to another by as much as 25 mm of mercury head, the local variations over the period when wall-static pressure measurements were made never exceeded 0.5% of the ambient value.

The static pressure head (in mm of manometric fluid) plotted against pipe length permitted computation of pressure drop per unit length and hence wall shear stress given by (208)

$$\tau_W = \frac{\Delta P}{L} \frac{D}{4} \qquad \ldots 7.1$$

where τ_W = wall shear stress (N/m^2)

ΔP = pressure drop over length L (N/m^2)

D = pipe inside diameter (m)

assuming linear variation of pressure over length L. Hence, if ΔH mm is the pressure head reading, S the specific gravity of the manometric fluid, Eqn. 7.1 reduces to

$$\tau_W = \left(\frac{\Delta H}{L}\right) \frac{D}{4} \rho_w S g \qquad \ldots 7.2$$

where ρ_w = density of water (kg/m^3)

g = gravitational acceleration (m/s^2)

7.6.1 Single-Phase Flow

Fig. 7.23 illustrates the geometry of the test section used. Using only one set of pressure tappings (since preparations of another 3 sets were not ready) and relocating it at ten different axial pipe positions via suitable combinations of the different pipe lengths, wall-static pressure was determined for Re_D in the range 8×10^4 to 12×10^4. The experimental procedure was straight forward; noting the initial manometer reading with the static pressure lines isolated (using the two-way valve see Fig. 7.24) and a new reading with the static pressure lines connected to the manometer (having first levelled the micromanometer bench). The difference in the 2 readings gives the pressure head above atmospheric pressure. The measurements were repeated thrice to ensure consistency and the values averaged.

The air mass flow rate through the atomisers was kept constant at exactly 10.7% of the total air mass flow rate for Re_D of 10^5 in order to satisfy the two-phase flow operational requirement of atomiser air flow rate. It therefore required that the fan air mass flow rate for the other Re_D be altered so that the total air mass flow rate (atomiser plus fan air) equalled that needed for a particular flow Re_D.

Fig. 7.25 illustrates the relationship between wall-static pressure head with the number of pipe diameters downstream of the entry plane (Fig. 7.23). The relationship between friction velocity and pipe Re_D is plotted in Fig. 7.26. Using Moody's (210)

diagram, the equivalent sand roughness parameter, k/D of the pipes used in the test section was found to be 6×10^{-4} where k is the absolute roughness and D the pipe diameter. (see Table 7.5). The inside surface of the Durapipes were untreated (e.g. polishing etc.) and the roughness of the various sections should be the same order of magnitude based on the quality of the manufacture.

The linear least squares correlation coefficient c, included in Table 7.5 and subsequent tables is defined as

$$c = \frac{\sum_{k=1}^{N} (\hat{x}_k - \bar{\hat{x}}) (\hat{y}_k - \bar{\hat{y}})}{\left(Var(\hat{x}) * Var(\hat{y}) \right)^{\frac{1}{2}}} \qquad \ldots.7.3$$

where $Var(\hat{x}) = \sum_{k=1}^{N} (\hat{x}_k - \bar{\hat{x}})^2$

$$Var(\hat{y}) = \sum_{k=1}^{N} (\hat{y}_k - \bar{\hat{y}})^2$$

and $\bar{\hat{x}}$ and $\bar{\hat{y}}$ are respectively the mean values of N pairs ($\hat{x}$, $\hat{y}$) measurements made on two random variables. It provides a measure of the degree of association between the various data pairs described by a straight line fit, the best fit (when all points lie on the straight line) having $c = \pm 1$.

Two further experiments at Re_D of 10^5 only using the same set of static pressure tappings relocated at 6 downstream axial positions were carried out with 3 extraction units included in the test section as shown in Fig. 7.23. In one of the test, no atomiser air was injected; instead, fan air

mass flow rate was increased to provide the required Re_D.

Table 7.6 summarises the results. For flow with atomiser air injection. The friction velocity with extraction units was 3.7% greater than the corresponding results without extraction units. However, with no atomiser air flow, the friction velocity decreased significantly indicating that the injection of atomiser air to mix with 90% of the total mass flow increased the turbulence intensity at the inlet to the test section, i.e. a turbulent flow which gradually decayed to its fully developed value further downstream. Hot-wire measurements by Williams(9) confirmed this trend.

7.6.2 Two-Phase Flow

The geometry of the test section used in the two-phase flow pressure drop measurements was similar to the single-phase measurement except for the presence of extraction station 1 in Fig. 7.23 which removed the wall film immediately downstream of the mixing chamber. Experimental conditions A, C and T (see Table 8.2) were used.

For annular flow with a continuous wall film, a liquid purging technique described by Hewitt et al.(211) may be used for measuring pressure drop. However, the observed flow two diameters downstream of extraction unit 1 (Fig. 7.23) even at the highest liquid injection rate (condition T) did not have a continuous annular liquid film. Instead, a relatively thick layer flowed along the bottom of the pipe whilst intermittent streams of accumulated wall deposits flowed circumferentially (with a superimposed axial velocity), due to gravity down the

channel walls; the thickness of the bottom layer increased with distance downstream. In view of this observation, measurement of wall-static pressure using a continuous air-purge manometric system (which was momentarily interrupted when noting the readings) was considered, making use of the existing single-phase flow pressure drop instrumentation.

Referring to Fig. 7.24, a 5 psig (35 kPa gauge) continuous supply of purged air kept the manometric lines and the four pressure tappings free of liquid when no measurements were made. The supply of purge air was momentarily cut off simultaneously connecting the micromanometer to the static pressure lines (using the 2-way valve) when a pressure reading was required. The time interval between stopping the purge air flow and recording the reading on the manometer was sufficiently short (less than 30s) to avoid problems with liquid ingress into the static holes. For each pressure head, four repeated measurements were made. The maximum error in the repeatability of the measurements was ±4% of the averaged value.

Liquid ingress into the pressure tapping located at the bottom of the pipe was visible, with liquid in the transparent plastic tubing connection, but did not seriously affect repeatability of the measurements. In view of this observation measurements using only the three tappings which avoided the bottom stream were carried out. The two results agreed within limits of repeatability error mentioned above. Hence only three of the four tappings were used in subsequent measurements.

Fig. 7.27 illustrates the change in wall-static pressure with pipe length for the two-phase flow with no intermediate

extraction stations. Friction velocity (Table 7.7) increased over that for single-phase flow by 20.2%, 21.4% and 22.6% respectively for conditions A, C and T, neglecting the small contribution, if any, due to the presence of extraction station 1. In addition, for conditions C and T, the pressure drop correlation (see Fig. 7.27) indicated on increasing roughness effect due to the thickening bottom liquid film. Considering test condition T, the slope, $(\frac{\Delta P}{L})$ of the pressure-drop graph at the downstream end increased over that at the upstream end by approximately 20%, corresponding to a change in the friction velocity of 4.5% of the upstream value.

The determination of friction velocity for two-phase flows with intermediate extraction stations will be reported in Chapter 8.

7.7 Experimental Procedures

In view of the different experiments carried out (see Chapter 8), a general description of the "common" procedures involved will be provided here. More specific test procedures will be included in the relevant studies described in Chapter 8.

The sequence of events in each experimant included :

(i) setting up a suitable length of test section for the relevant study (e.g. photographic, deposition or entrainment) ensuring that it was horizontal (using a spirit level device);

(ii) noting the atmospheric pressure, temperature and room relative humidity;

(iii) in-situ computation of manometer and pressure settings required for specific air mass flow rates dictated by the test conditions, using the data from (ii);

(iv) adjusting the mass flow rates for (a) fan air, (b) atomiser axial and coaxial air and (c) atomiser water flow rate in that sequence, as required;

(v) permitting saturation of the laboratory atmosphere as described in sec. 7.4 prior to carrying out the experiments and

(vi) making frequent checks on relevant flow readings to avoid departures from required flow rates.

CHAPTER 8

EXPERIMENTAL STUDIES

8.1 Introduction

In order to study the effect of turbulence on droplet agglomeration it is essential that the additional effects of droplet deposition and re-entrainment be isolated from or integrated with the experimental measurements. Droplet deposition as well as agglomeration affects both the number concentration and size distribution, especially when preferential deposition of certain size ranges takes place resulting in a downstream spectrum much coarser than the original spectrum (see, for example, Farmer et al.(53)). Droplet re-entrainment can significantly alter the size distribution of the downstream spectrum in addition to causing an underestimation of the true deposition rates. However, in practice, reduction of the annular film flow rate may help to minimise the problems associated with re-entrainment.

The aims in the present studies are therefore (i) to experimentally assess the extent of re-entrainment at different film flow rates (ii) based on the results from (i) to select a suitable test-section geometry so that deposition and agglomeration effects are predominant, (iii) to determine the relative magnitudes of deposition and agglomeration on the evolution of size distribution in a turbulent two-phase horizontal pipe flow using a macroscopic analysis and (iv) to compare the experimentally determined spectra with those predicted by a numerical model for the same upstream starting spectrum.

A horizontal pipe geometry was selected in view of the ease of measurements and instrumentation compared with a vertical flow arrangement. The influence of pipe orientation on agglomeration, deposition and re-entrainment is dealt with in sec. 8.2 onwards. The combined effect of gravity and turbulence on the spatial distribution of drops over the pipe cross section may be estimated by considering the flow of a dilute suspension between two parallel planes separated by a distance equal to the diameter D of the pipe. Following the method of Kubie and Gardner (212), a dispersion coefficient may be defined as the ratio of drop concentrations at $z = +D/2$ and $z = -D/2$, with $z = 0$ defining the plane which contains the pipes axis; it may be estimated using Gardner's (45) simplification of the theory of Hutchinson et al.(4) for the determination of drop eddy diffusivity. For a mono-dispersion of 30 μm drops in the test section at $Re_D = 10^5$, the dispersion coefficient is 0.85. Hence the spatial distribution of drops for the horizontal flow does not appear to depart significantly from that in vertical flow for the operating conditions used in the present studies. In addition, the radial variations of drop-size distribution were photographed along a horizontal plane which passed through the pipe axis thus avoiding gravitational effects when comparing the radial spectra.

8.2 Entrainment From the Annular Wall Film

Amongst the existing work on entrainment, the empirical correlation by Hutchinson and Whalley (88) offered most promise. They correlated, for vertical annular flow, the homogeneous mean droplet concentration, M_E in the gas core at hydrodynamic equilibrium with a dimensionless term $\frac{\tau_f m_f}{\sigma}$ as discussed in sec. 2.4. However, in order to estimate M_E, measurements of film thickness and interfacial shear stress would have to be carried out, assuming that the correlations remained valid for horizontal annular flow as well. The presence of an axisymmetric horizontal annular film with maximum thickness at least 20 times the mean thickness (65) and the obvious effect of gravity on the entrained droplets would unfortunately limit the usefulness of Hutchinson and Whalley's correlation in solving horizontal flow problems.

To carry out a series of experiments for the horizontal pipe flow employing the above correlation technique may require pipe lengths of several hundred diameters in order to establish a fair degree of flow equilibrium. This, however was beyond the scope of the present work. Since the local entrainment rate over the eighty-five pipe diameters was the main concern here it would therefore be appropriate, as a preliminary investigation, to estimate the order of magnitude of the entrained fraction from an annular wall film formed by injection water directly into the pipe wall (at $Re_D = 10^5$) via an annular slot.

8.2.1 Experimental Procedure

Fig. 8.1 illustrates the geometry of the test section used. An extraction unit was modified so that the width of the annular slot was 2 mm as illustrated in Fig. 8.2. The injection slot was located at axial position 1 in Fig. 8.1 and the introduction of water into the turbulent air stream could either be made from above (top injection) or below (bottom injection) the pipe axis via the unit's liquid inlet pipe. Since gravity would significantly aid entrainment from the wall film at the roof of the circular duct (i.e. θ between 0 and $\pm 90^{o}$ in Fig. 8.2) top injection was employed in the tests. Fan air was set to give approximately 15 m/s mean velocity, with water flow rates in the range 1.4 l/min to 3.4 l/min. Film flow rates at 15, 25, 45 and 65 diameters downstream of the injection slot were measured using a second extraction unit. Pressure drop between the injection and extraction units was also measured for each of the test condition. Table 8.1 summarises the measurements and entrained fractions.

A qualitative examination of the annular film at the injection slot revealed the following:

(i) at all injected liquid rates, a single liquid crest at θ equal to 180° (see Fig. 8.2) marked the start of the bottom liquid layer.

(ii) for liquid injection rates less than 2 l/min, a wavy liquid film which covered the upper half of the pipe wall immediately downstream of the slot, flowed circumferentially downwards to join the bottom stream over axial distances of less than 2 pipe diameters from the injection slot.

(iii) at higher injection rates a local build-up of liquid at θ equal to 0° was noticed; the build-up intermittently disintegrated when it became extremely unstable. This provided sudden bursts of entrained coarse drops in the airstream which redeposited onto the lower liquid layer further downstream.

8.2.2 Deductions

Referring to Table 8.1 although a qualitative study of liquid film behaviour at the injection slot indicated significant entrainment over certain liquid flow rates the fraction of entrained liquid in the gas core at 65 diameters downstream never exceeded 8% of injected liquid rate. Since there was an additional maximum error in the rotameter readings of +1.5%, the net entrained fraction was therefore less than 8%. The maximum error in the measurements of film flow rate was of the order of $\pm$2% of the mean values. Since the errors in the measurements were relatively large compared with the percentage determined for the entrained fraction the effect of re-entrainment on film flow rate measurements in unidirectional deposition studies should be small provided that the currently encountered entrainment mechanism remained valid.

Pressure drop measurements for test condition T81 to T86 and T91 to T96 indicated an increase in friction velocity (see Fig. 8.3) with injected liquid rate, highlighting an increase in the equivalent wall roughness. The relationship between friction velocity and axial position of the extraction unit for a fixed total length of the test section is illustrated

in Fig. 8.4. Except for an initial high value near the injection unit, the general trend indicated an increase in friction velocity with axial distance due probably to the increasing waviness of the bottom stream. The initial high value may be attributed to liquid-air interaction immediately downstream of the injection slot.

The effect of gravity on re-depositing most of the initial "bursts" entrained droplets further downstream may be deduced from result pairs. T63 & T73, T64 & T74, T65 & T75 and T66 & T76, each pair referring to a common value of liquid injection rate more than 2.0 l/min. The four pairs of results indicated the same trend of a reduction of entrained fraction between 15 and 25 pipe diameters from the injection slot.

An experiment involving the introduction of liquid at θ equal to 180° and a length of 65 pipe diameters separating the injection and extraction unit was carried out. The entrained fractions for the different liquid injection rates were of the same magnitude as in batch T9. (see Table 8.1). Hence the effect of gravity on the main fraction of entrained drops was to eventually re-deposit them onto the bottom stream within 65 pipe diameters from their initiation.

8.2.3 Estimation of Re-Entrained Fraction in Experiments Involving Deposition Rate Measurements

Whereas the previous tests were carried out with the gas core free from the effects of a dense entrained spectrum, an attempt was made to determine the degree of re-entrainment in an experiment for which deposition measurement was intended.

The total length of the test section was 83 pipe diameters with extraction stations 1, 2 and 3 located at 2.0, 14.5 and 24.5 pipe diameters respectively from the entry plane. The method involved making film flow rate measurements at extraction stations 2 and 3 simultaneously on one occasion; then, with extraction station 2 plugged, the film flow rate at extraction station 3 was measured under the same test condition. Any re-entrainment from the flowing liquid film between 2 and 3 would imply a lower value in the extracted film flow rate at 3 alone compared with the total extracted from 2 and 3 simultaneously. By varying the distance which separated 2 and3 a relationship between re-entrainment fraction and pipe length (i.e. film thickness) could be deduced.

Contrary to the above prediction, an experiment involving test condition A and the test section geometry described above gave a net increase in deposition rate when station 2 was plugged. Referring to sec. 7.5 the maximum error in the measurements of the extraction unit has been quoted as $\pm 3\%$ of the mean value. The difference in the film flow rate measurements in this test was less than 3% of the liquid extracted with station 2 plugged.

A further experiment was carried out with extraction stations 2 and 3 located twenty pipe diameters apart. The difference was similarly undetectable, remaining well within the $\pm 3\%$ error margin.

Therefore the total error in the measurements alone were of the order of magnitude of the entrained fraction to be detected The method was intrinsically incapable of detecting the required

changes, but the results indicated that entrainment rates were much lower than deposition rates.

8.2.4 Re-Entrainment Effects on Drop-Size Distribution

Although the percentage of re-entrained volume was small relative to the deposited volume, it could still have a significant effect on drop-size distribution of the entrained flow in the gas core. A photographic test was carried out to determine the effect, if any, of re-entrainment on size distribution.

Fig. 8.5 illustrates the test section used, with test condition A (Table 8.2). With extraction station 1 in full operation thirty-four photographs of the core spectrum were taken at extraction station 2; the photographic procedure was as described in sec. 4.3.2 A separate set of thirty-four photographs was taken with extraction station 1 plugged allowing a relatively thick liquid layer to flow across stations 1 and 2. Thirty photographs in each case were analysed, as described in sec. 8.4; the results are summarised in Table 8.3.

Fig. 8.6 compares the two mass frequency spectra showing the considerable variation from one flow situation to another. The averaged number of in-focus drop images counted per photograph for the data batch when no liquid extraction at 1 was made was 30% higher than with continuous liquid extraction implying a relatively higher number concentration as well.

Hence although the percentage of re-entrained flow, from previous measurements, could not be satisfactorily determined the presence of a relatively thick (especially at the bottom of the circular cross section) wall-film certainly

modified the spectrum in the gas core. The mass mean diameter without upstream extraction was 18% larger than the spectrum with continuous extraction. Thus the thickness of the wall-film and the subsequent exchanges between the entrained flow and the liquid layer across a wavy surface i.e. the history of this interaction had unfortunately influenced the shape of the drop-size distribution downstream.

An important consideration when organising the test-section geometry for deposition and agglomeration studies was the need to minimise the thickness of the annular film (by providing preferably an infinite sink for deposition) so that the influence of flow history on the downstream spectra due to the above process was not serious. A reduced cross-sectional area (due to the presence of a relatively thick annular film) would also result in higher mean air velocities through the annular core resulting in further departures from the computed mean flow velocities from measured values of volumetric air flow rates at the inlet.

8.3 Deposition Measurements

8.3.1 Theoretical Considerations

The conservation of drop number applied to an elementary pipe length dL yields

$$\frac{dn}{dL} = -\frac{4F}{D\bar{U}}n \qquad \ldots.8.1$$

$$\text{i.e.} \quad \ln \frac{n_L}{n_o} = -\frac{4FL}{D\bar{U}} \qquad \ldots.8.2$$

where n_L = average concentration at distance L (m^{-3})

n_o = initial concentration (m^{-3})

D = pipe diameter (m)

L = pipe length over which flow parameters remain constant (m)

F = Deposition velocity defined as the number of drops depositing in unit time per unit area divided by the average number concentration in the gas core (m/s)

$\bar{U}$ = mean air velocity (m/s)

Defining the fraction of particles which failed to deposit, i.e. the fractional penetration p, as $\frac{n_L}{n_o}$, eqn. 8.2 becomes

$$\ln p = -\frac{4FL}{D\bar{U}} \qquad \ldots.8.2a$$

$$\text{or} \quad F = \frac{Q}{\pi DL} \ln \frac{1}{p} \qquad \ldots.8.3$$

where Q = volumetric air flow rate (m^3/s)

$$= \frac{\pi D^2}{4}\bar{U}$$

Eqn. 8.3, used by Liu&Agarwal (41) and Sehmel (51) for the computation of experimental deposition velocities, has the following assumptions:

(i) No circumferential variation in number concentration

(ii) Where only mass measurements of deposited drops were made rather than number counts, the weight per particle was assumed equal and time-invariant, implying

(iii) the absence of any form of drop agglomeration and

(iv) an infinite sink i.e. no re-entrainment possible.

From (ii) Eqn. 8.2 may be re-written using the concept of mass concentration i.e.

$$\ln \frac{M}{M_o} = - \frac{4FL}{DU} \qquad \ldots.8.4$$

Eqn. 8.4 implies a governing equation of the form

$$\frac{dM}{dt} = - \alpha M \qquad \ldots.8.5$$

where $\alpha = \frac{4F}{D}$

M = average mass concentration (kg/m^3), a function of time, t.

Hence a plot of entrained mass versus pipe length on a log-linear graph should yield the required deposition velocity F.

The method for measurement therefore involved the extraction of film flow at several axial positions downstream of an axial injection of atomised water and relating the extraction mass flow rate of each station to the entrained mass at the inlet of the pipe section over which deposition measurement was made.

8.3.2 Procedure

Taking account of the final note of sec. 8.2.4 and the need for adequate film flow rates to minimise the effect of measurement errors, the geometry selected for the study of drop deposition and subsequently agglomeration is illustrated in Fig. 8.7.

From previous discussions on axial injection in which about 40% by volume of the atomised liquid was deposited immediately downstream of the injection chamber, the important task would be to remove this initially high film flow rate to reduce re-entrainment effects. It was also clear that the required 10 diameters inter-particle spacing would not be met unless a higher atomiser throughput was employed in the tests. It was therefore appropriate to determine droplet deposition rates for 3 separate liquid flow rates but with the air mass flow through the atomiser at 10.7% of the total air flow. Table 8.3 summarises the test conditions employed. (Condition T, although not used in the deposition experiments, is listed for common referencing from sec. 7.6.2.on measurement of pressure drop characteristics in two-phase flow.)

The sequence of events in each experiment is described in sec. 7.7. Pressure drop measurements were made from 4 axially located (Fig. 8.7) sets of static-pressure tappings, the method as described in sec. 7.6. Simultaneous measurements of film flow rates at 3 adjacent extraction stations at a time were made. An important precaution was that pressure drop measurements up stream of an extraction station must not be carried out when measurements were made at the extraction

station. The continuous air-purge of the static pressure holes not only distort the velocity profile downstream but also aided the re-entrainment of any liquid film which approach the static holes. The wall-static pressure tappings were capped when not in use. The results of the deposition measurements are summarised in Table 8.4.

Data batches T11A, B and C were obtained using only 5 extraction stations rather than 6, during an early part of the work in which unit 1a was not present.

8.3.3 Result Analysis and Discussion

Using Eqn. 8.3, deposition velocities for the 5 sections (I to V in Fig. 8.7) were computed; an example of the computation is illustrated in Table 8.5, and the results are summarised in Table 8.6.

Fig. 8.8 illustrates the relationship between dimensionless deposition velocity and position of extraction station. Refering to Fig.8.8(a), the deposition velocities for test condition A are very well repeated over the 4 separate measurements. The results for test condition A1 are similarly included (data batch T14) and the good agreement between results at different flow Reynolds number (using the same upstream spectra) indicated that the deposition mechanism was a function of pipe turbulence with friction velocity as a useful non-dimensionalising parameter. For data batch T18, extraction station 5 was located 15 pipe diameters nearer to station 4 than the other results. The aim was to determine whether or not the reduction in deposition velocity at pipe section V (Fig. 8.7) was due to the relatively large distance

(35 pipe diameters) which separated stations 5 from 4 across which re-entrainment effects could have been significant. The results with a shorter deposition section (in fact approximately equal to that of section IV) indicated the same general trend of a reduction in deposition velocity from section IV to section V.

In Fig. 8.8 (b) the averaged deposition velocities from more than one trial for test conditions A, B and C are plotted. For pipe sections I and II, deposition velocities decreased sharply for all 3 test conditions reaching a minimum at section III. At section IV, an increase was experienced in test conditions B and C, with a much higher value for the latter. At section V, although the deposition velocities were lower than IV for each condition, a difference in the absolute values between the test conditions exists which suggests an increase in deposition velocity with injected liquid rate.

The initial high deposition velocities over pipe sections I and II were probably due to the radial velocity component imparted on the droplets during atomisation as well as the unequal acceleration of droplets to the freestream velocity resulting in a preponderence of heavier drops in the first two pipe sections. The elutriation of heavy drops from the core spectrum as reported in ref. (44) may be another factor contributing to the high initial deposition velocities. However, an additional factor may be attributed to the relatively high turbulence intensity present at the entry plane, due mainly to drop-air interactions. Measurements of solid particle-liquid interaction on turbulence intensities in a two-phase pipe flow

by Zisselmar and Molerus (213) have indicated strong mutual influence of the 2 phases when the particle sizes are of the order of the turbulent microscale, resulting in an increase in turbulence intensities when the solid concentration is less than 3% by volume. The maximum liquid concentration by volume in the present test conditions assuming no deposition on the wall was only 0.11% by volume and the larger diameters end of the drop-size distribution especially at the higher injection rates were probably approaching the order of magnitude of the turbulent microscale.

The significant increase in deposition velocities at section IV for higher liquid rates may be the consequence of droplet agglomeration and/or unequal deposition rates of different sizes. Since the computation of deposition velocities was based on measurements of mass, the gravitational deposition of the heavier drops alone would account for the discrepency provided that the drop size distribution at each of the extraction stations indicated the presence of a coarser spectrum than those determined in sec.7.2.34 for the atomisers. Hence a photographic determination of the size spectra at each extraction station should provide additional information on this deviation.

8.4 Photographic Experiments

8.4.1 Test Procedure

A photographic determination of the two-phase flow spectra at relevant extraction stations was carried out. In view of the results of the previous section on deposition measurements, it seemed appropriate that the starting spectrum for the study of simultaneous effect of agglomeration and deposition on the evolution of drop-size distribution be determined at station 2 where the deposition velocity approached a minimum value for all 4 test conditions studied. The spectra at 2 therefore contained the history of upstream flow which would be predominantly the simultaneous effects of agglomeration and deposition on the inlet spectra at the entry plane to the test section.

The radial positions photographed at axial stations 2, 3, 4 and 5 as described in sec. 4.3.2 were mainly for test condition A in which a detailed study was planned. For conditions A1, B and C, only the core spectra were photographed and for a limited number of axial stations as summarised in Table 8.7.

To assess the repeatability of the photographic results, the photographic experiments to establish the core spectra at station 2 for all test conditions were each repeated on separate occasions.

The number of photographs required to establish a representative sample for the size-distribution was increased for stations 3, 4 and 5 to match the reduction in number density per 5 inch x 4 inch negative. Accordingly, the total number of photographs taken at stations 2, 3, 4 and 5 for each experimental run were 34, 51, 68 and 102 respectively. The actual

number of photographs eventually analysed varied from one batch to another depending on the counting statistics needed for a comfortably representative sample size as well as to avoid the analysis of randomly double exposed photographs (due to occasional flaws in the flash discharge.)

8.4.2 Analysis of the Photographs

A visual examination of the photographic negatives indicated an extremely low number of in-focus drops per negative with a maximum of approximately 30 at the first axial position photographed (i.e. extraction station 2) reducing to under 5 counts for station 5 which was also the reason for taking 102 photographs at that position. Such low number counts per negative were obviously unsatisfactory for an automatic analysis since most of the 22 TV frames required to analyse completely a 5 inch x 4 inch negative would be unproductive. To present selectively those regions on the negative most likely to have an in-focus image to the TV camera would retain the subjectiveness of a manual analysis hence defeating the original aim of the TV system.

In view of the above, it was therefore decided to carry out a manual analysis of all the photographs based on the method highlighted in sec. 4.5.1 accepting some subjectiveness in the results. The in-focus images were therefore sorted into size groups followed by calculation of volume distribution by the method of Wise (193). It is very difficult to define an absolute value for the subjective error in any photographic analysis since several factors including the quality of the photographs,

repeatability of photographic contrast in a complete batch of photographs and the experience of the operator affect the outcome of the analysis. However, if the results from an automatic analysis may be treated as a reference spectrum the subjectiveness of a manual analysis by two independent observers may be assessed from Fig. 5.35 for a sample size of approximately 500 counts; the spectra in Fig. 5.36 indicate more discrepency when the sample size is reduced to under 400 counts with correspondingly poorer contrast negatives. The contrast of the negatives from which most data were derived was of the quality from which Fig. 5.35 was deduced and since the average number count per spectrum was in excess of 500, Fig. 5.35 would be representative of the subjective error in a typical analysis.

8.4.3 Results and Discussions

Table 8.9 summarises the computed mean diameters $\bar{x}_{32}$, $\bar{x}_{31}$, and $\bar{x}_{30}$ from the original number count statistics shown in Table 8.8. For the results at extraction station 2, the core spectrum for each of the four test condtions was derived from two separate spectra obtained to assess the repeatability of the results. Referring to Fig. 8.9 (a) to (d), the shapes of the mass frequency spectrum of the repeated experiments are well matched for each test condition. The mean diameters of the repeated measurements are compared in Table 8.10 showing a maximum difference between the two sets of results of 6.4 μm; the total number counts averaged 760 for each spectrum.

The 95% confidence limits for each of the mean diameters

$\bar{x}_{30}$, $\bar{x}_{31}$ or $\bar{x}_{32}$ of each spectrum (the number count statistics as listed in Table 8.8) may be directly estimated from the numerous photographic samples which made up the spectrum. Treating the number frequency data from each photograph as an independent random sample of the unknown population having a fixed variance Λ^2 and mean diameters ω, the Central Limit theorem may be applied (as described in Appendix A13) to determine the 95% confidence limits for the relevant mean diameter. It is worth remembering that the number count statistics from each individual photograph are influenced by the nett effect of random variation in number counts (from one photographic sample to another) and the error due to a subjective analysis. As long as the subjective error is unbiased but randomly distributed amongst the photographs, the confidence limits estimated above should reflect the true range within which the population mean ($\bar{x}_{32}$, $\bar{x}_{31}$ or $\bar{x}_{30}$) lies.

Fig. 8.10 illustrates the empirical distribution of a typical set of 98 values of two relevant mean diameters (results are from condition A, station 5 at radial position r/R = 0.04) highlighting the near normal distribution of x_{30} and x_{32} (computed from local number frequency distribution of each of the 98 photographs) as predicted by the Central Limit theorem. The maximum range of the 95% confidence limits for $\bar{x}_{30}$ and $\bar{x}_{32}$ for all the data batches listed in Table 8.9 was further found to be within 7% of their respective mean values.

Applying the ULDF fit to each set of results, the least squares parameters thus determined are summarised in Table 8.11.

The heterogeneous ULDF fit was needed for certain data batches inview of the bimodal nature of the mass frequency results. Whilst the parameter correlation coefficient defined in (195) averaged 0.95 for the ULDF fits, the corresponding values for the heterogeneous fit were generally poorer due to an increased number of parameters relative to the total number of data pairs to be fitted. Although the least squares fit indicated satisfactory confidence limits for the maximum drop size x_m, for most of the data and good agreement between $\bar{x}_{32}$ computed from the optimised parameters and the original data, the optimised values of x_m varied a great deal from one data batch to another without any obvious trend. Nevertheless, the satisfactory ULDF fits and the good confidence limits estimated for $\bar{x}_{32}$ or $\bar{x}_{30}$ using the CL theorem seem to suggest that a sample size having a total number count between 500 and 1000 would be representative of the population spectrum for the present purpose.

Whereas the process of drop break-up is not relevant in the present studies, the use of x_m to establish, for example, a critical Weber number to describe the forces which control drop deformation and break-up due to turbulence in studies of drop dispersion in gas-liquid or liquid-liquid systems should, in general, be treated with cautiżon, even when the data are adequately described by the ULDF with good confidence limits for x_m. An alternative definition of a maximum diameter, for example, x_{999} (see Appendix A10) is sometimes better when attempting to further correlate the data.

8.4.3.1 Condition A

For this test condition, the mass median diameter, x_{500}, computed from the optimised parameters, increased with distance from the entry plane with a consistently large value near the wall compared with the core (see Fig. 8.11). The radial variation in mass median diameter of the spectrum at station 2 is illustrated in Fig. 8.12 including the variation of $\bar{x}_{32}$ and $\bar{x}_{30}$. A plot of the radial variation of normalised number count is also included. Referring to Fig. 8.12, although the number concentration decreases radially towards the wall, $\bar{x}_{30}$ and x_{500}, on the other hand, increase as the wall is approached. Fig. 8.13 illustrates the radial variation in the mass frequency distribution (as described by the ULDF least squares parameters) highlighting the coarser wall region spectrum compared with the core. The corresponding axial speotra are plotted in Fig. 8.14 for core flow and Fig. 8.15 for the wall flow.

Of particular interest is the bimodal wall spectrum at station 4 which may be attributed to drop re-entrainment and/or a preferential depletion of certain drop sizes from a coarse spectrum. Referring to Table 8.8, although the total number of large drops which described the second mode of the bimodal wall spectrum at station 4 was less than five, the frequent encounters with such sizes as out-of-focus images in most of the fifty-one photographs analysed certainly confirm their presence.

The spectra at r/R = 0.7 at $\theta = 0$ and 180° at station 2 were photographically examined and compared with the spectrum

at the core. Thirty photographs were analysed for each spectrum; the total number counted averaged 622. Table 8.12 summarises the computed mean diameters which are of comparable magnitudes with the mean diameters at $r/R = 0.6$ and 0.88 in Table 8.9 under the same test condition. Fig. 8.16 compares the mass frequency spectra with the core spectrum indicating the trend towards a coarser spectrum on moving radially towards the wall. In addition at $r/R = 0.7$ the spectrum at $\theta = 0$ is coarser than the corresponding spectrum at $\theta = 180^{o}$. Though possible drop re-entrainment from the "ceiling" of the pipe may have affected the upper spectrum $\theta = 0$, circumferential homogeneity of the drop-size distribution was not expected owing to the action of gravity.

The wall spectra are generally coarser than the core spectra at the three axial stations studied. The effect of re-entrainment from the wall film is sufficient to account for this difference. However, the number count statistics for $r/R = 0.88$ in Table 8.8 indicated the presence of 150 μm and 160 μm drops at station 5 and the complete lack of such sizes at station 2 even though the film flow rate immediately upstream of each station is considerably more for station 2 compared with that for station 5. Whilst this discrepancy may be attributed to more photographs being analysed for the wall spectrum at station 5 than at station 2, the very presence of a generally coarser wall spectrum relative to the core spectrum (not due to sampling re-entrained drops) would account for the observed trend. The increase in turbulence intensity radially towards the wall (200) would also enhance the rate of interaction

between droplets as they travel towards the wall under the influence of turbulent diffusion. However there is insufficient evidence to suggest whether one or the other effect is predominant beyond observing that the rate of increase in drop sizes near the wall region is more rapid than the rate of increase of the corresponding sizes in the core spectra axially downstream.

The general trend towards a coarser spectrum on moving axially downstream implies that droplet agglomeration was significant. There is no reason to believe that the preferential depletion of the smaller drops due to turbulent deposition (53) is causing this change since the dimensionless relaxation time, τ^+, of most droplets in the core spectra is well below 10^3, above which the inverse relationship between deposition velocity and drop diameter determined by Farmer et al. (53) (for vertical pipe flow) operates. As will be shown in the next section, the inverse relationship between deposition velocity and drop diameter would be seriously modified by the influence of gravity in a horizontal pipe flow system.

8.4.3.2 Condition A1

For condition A1, the number concentration at station 2 was higher than the corresponding results for condition A as indicated in both the averaged number count per slide (Table 8.8) and the measured entrained mass flow rate (Table 8.4). The spectra at stations 2 and 5 are compared with the corresponding condition A results in Fig. 8.17. A relatively coarser spectrum was registered at both stations. The spectrum

at station 5 implied an increase in the agglomeration rate relative to the corresponding condition A results. The spectrum at station 2 further confirmed the need to establish drop-size distributions independently for each new flow condition even though the spectra at the entry plane to the test section were the same and measurements of dimensionless deposition velocities showed similar results for two separate flow Reynolds numbers. The history of droplet interaction upstream of station 2 cannot be neglected in a photographic study.

8.4.3.3 Condition B

For this test condition, although the mass mean diameter, $\bar{x}_{30}$ increased downstream of station 2, the mass median, x_{500}, diameter appeared to decrease between stations 2 and 3 and then increase (Tables 8.9 and 8.11) for stations 4 and 5. A ULDF fit to the data at station 5 indicated poor confidence limits for x_m. This was expected in view of the low total number count of approximately 380 from the 96 photographs. Since a detailed photographic study for condition B was not planned, no further data to improve the confidence limits of the ULDF fit were contemplated.

The axial variation of mass frequency spectra is illustrated in Fig. 8.18 which indicated a preferential depletion of the 90 to 150 μm sizes over pipe sections III and IV of Fig. 8.7. The more polydispersed spectrum at station 2 (compared with the corresponding condition A spectrum) appeared to have preferentially shedded its heavier drops due either

to gravity alone or the combined effect of gravity and drop agglomeration in the axial and radial direction.

8.4.3.4 Condition C

The axial variation of drop-size distribution for test condition C is illustrated in Fig. 8.19 for stations 2, 3 and 4 only. In view of the extremely low number density at station 5 from the test results of condition B, no photographs were taken for condition C at station 5. The preferential depletion of the 90 to 150 μm size range, similar to the results of condition B was again apparent. The spectrum at station 2 was more polydispersed than for conditions A and B with a relatively high percentage mass of the large diameter range of sizes. The mass mean diameter increased linearly with axial distance downstream.

Comparing Fig. 8.8 (b) with Figs. 8.18 and 8.19, there is an obvious relationship between preferential depletion of certain large diameter sizes and the increase in measured deposition velocities across pipe sections III and IV. The main factor which influence this behaviour is gravity although the additional role of droplet agglomeration in enhancing deposition rate cannot be overruled. Table 8.13 lists some values for drop relaxation time and terminal velocities. For the effect of gravity and hence droplet sedimentation to be insignificant, the ratio V_t/u_* should be less than about 0.2 (Soo (209)), where V_t is the terminal velocity of the droplet and u_* is the friction velocity. The measured friction velocity was 0.77 m/s. Hence, drop sizes 70 μm and larger would be affected by gravity

and gravitational sedimentation cannot be avoided. In fact a 100 μm diameter drop would traverse the distance of the pipe radius in under one hundred and fifty milliseconds based on its terminal velocity. If it were released from rest at the "ceiling" of the pipe at station 2 it would, travelling with an axial velocity of 15 m/s have enough space/time to reach 99.9% of its terminal velocity on landing, under the influence of gravity, on the bottom stream at an axial distance of 4.6 m downstream of station 2 (i.e. pipe section IV) assuming the validity of Stokes law (214).

Had the present tests been carried out in a vertical pipe, the increase in drop sizes axially downstream of the entry plane would, for conditions B and C be more rapid than those currently observed since the effect of gravity in removing the heavier drops from the spectra would be absent. The measured deposition velocity computed on a mass basis would for conditions B and C be less than that for condition A over pipe sections III, IV and V. The dimensionless deposition velocity over pipe section V would vary in a similar way to the results of Liu and Agarwal (39) if plotted against dimensionless relaxation time of a drop having the diameter $\bar{x}_{30}$ of the polydispersed core spectrum.

8.5 Macroscopic Analysis

The aim in this section is to provide an estimate of the relative magnitudes of deposition and agglomeration effects on the rate of decrease of the entrained drop number concentration assuming that the influence of re-entrainment is negligible and that inertial deposition predominates.

8.5.1 Theoretical Considerations

The equation which describes the rate of loss of number concentration due to simultaneous deposition and coagulation (215) may be written as

$$\frac{dn}{dt} = -(Kn^2 + \beta n) \qquad \ldots 8.6$$

where n = drop number concentration, function of time, t,

K = constant coagulation coefficient for all sizes

β = constant deposition coefficient for all sizes.

The rate of loss of particles to surfaces is thus proportional to the number concentration n in the gas-core.

i.e. $$\left(\frac{dn}{dt}\right)_L = -\beta n \qquad \ldots 8.7$$

or $$(\Delta n)_L = \beta \int_o^t n\, dt \qquad \ldots 8.8$$

over time intervals in which β remains constant. Therefore a plot of $(\Delta n)_L$, the number deposited over a certain pipe surface area (hence length) determined by time t, against $\int_o^t n\, dt$ will yield β from the slope of the graph. To determine K , Eqn. 8.6 is rewritten as

$$\frac{dn}{dt} = - n(Kn + \beta)$$

or $$\int \frac{dn}{n} = - \int (\beta + Kn)dt$$

i.e. $$\ln n - \ln n_o = - \beta t - K \int_o^t n\,dt$$

over time intervals for which K is constant, and from Eqn. 8.8,

$$\ln n + \beta t = - \frac{K}{\beta} (\Delta n)_L + \ln(n_o) \qquad \ldots 8.9$$

where n_o = number concentration at $t = 0$.

Thus a plot of $\ln n + \beta t$ versus $(\Delta n)_L$ will yield the ratio $\frac{K}{\beta}$ from the slope of the graph and hence K.

The above treatment refers strictly to drop number concentrations for which K and β are assumed constant with time and between different drop sizes. In practice, K and β are functions of particle sizes and fluid flow parameters.

For the computation of rate of loss of entrained mass, a mass loss constant, a, (see Eqn. 8.5) averaged over the full length of the test section may be derived. The value of a is proportional to the deposition velocity F computed using mass measurements rather than number count values and given by $a = \frac{4F}{D}$

If the mean mass of drops in the entrained flow and of those deposited on the pipe walls at a given time be denoted by q_1 and q_2 respectively then,

the entrained mass concentration, $M = n\,q_1$

whilst $$\frac{dM}{dt} = q_2 \left(\frac{dn}{dt}\right)_L$$

Hence from Eqn. 8.5 and Eqn. 8.7,

$$\frac{\alpha}{\beta} = \frac{q_2}{q_1}$$

It can further be shown that the ratio $\frac{\alpha}{\beta}$ represents the ratio of deposition velocity F computed on a mass basis to that on a number count basis.

In an ideal situation where the sizes of all droplets are equal and have the same mass, α should be equal to β since the computations are essentially similar. However, for a polydispersed spectrum, since a 100 μm drop has a mass equivalent to eight 50 μm drops or one hundred and twenty five 20 μm drops, the ratio $\frac{\alpha}{\beta}$ should provide a good indication of the extent of preferential deposition of certain drop sizes from the entrained spectra within limits of the simplifications used in the analysis.

8.5.2 Analysis

The estimation of number concentration from an actual number count was not feasible since an accurate estimate of the depth of field in a manual analysis was not readily deduced; the problem was further complicated by the small depth of field used in the photography. However, the value of $\bar{x}_{30}$ may be estimated with some degree of confidence as discussed in sec. 8.4.3. In addition, the value of $\bar{x}_{30}$ from two independent sets of experiments for all the four test

conditions at the core region of station 2 was within $\pm$ 3% of the mean value of each pair of results.

Hence the variation of the total entrained number concentration with axial distance $\frac{X'_a}{D}$ may be established from information on entrained volume flow rate at each extraction station and the local value of $\bar{x}_{30}$ at the core. The core spectrum was chosen in view of the circumferential and radial inhomogeneity of the drop-size distribution.

To estimate the "equivalent" number of drops deposited on the walls of pipe sections III to V when droplet agglomeration in the gas core constantly altered the value of $\bar{x}_{30}$, the deposited volume was divided by the volume of a spherical drop having diameter $\bar{x}_{30}$ estimated from Fig. 8.22 at the mid-section of the deposition length.

Table 8.14 summarises a set of computations for test condition A; the relevant values are plotted in Fig. 8.20 to illustrate the relationship between $\int_o^t n dt$ and $\ln n + \beta t$ with $(\Delta n)_L$. Although the linear least squares correlation coefficients defined in sec. 7.6.1 for the plots of $\int_o^t n dt$ against $(\Delta n)_L$ were good, the linearity of the relationship between $\ln n + \beta t$ and $(\Delta n)_L$ was less satisfactory.

Fig. 8.21 illustrates the relationship between entrained mass and pipe length for all three test conditions. The mass loss constant α is determined from the slope of a least square fit to each set of data. The correlation coefficient for α exceeded 0.99 for the three sets of results.

The parameters α, β and K determined for test conditions A, B and C are summarised in Table 8.15. Since the core spectrum

at extraction station 5 for test condition C was not photographed, an extrapolation of Fig. 8.22 for the required value was employed. Values of Kn^2 and βn at stations 2, 3, 4 and 5 are summarised in Table 8.16.

8.5.3 Discussion

Referring to Table 8.15, it is worth noting that the ratio of $\frac{\alpha}{\beta}$ which provided a direct indicator for the ratio of deposition velocities determined using mass measurements to that using number count technique is very much larger than unity and as expected increases progressively with conditions B and C for which the photographic study highlighted preferential deposition of the larger drop sizes.

Although for test condition A (where the effect of gravity on deposition results was not significant), the dimensionless deposition velocity plotted against dimensionless drop relaxation time (using the diameter $\bar{x}_{30}$ at the pipe axis) compares favourably with Liu and Agarwal's (39) results for vertical flow system (see Fig. 8.23), the deposition velocity computed on an average number count basis was approximately 20% of the value computed on mass basis. From Figs. 8.23 and 8.8(a) there is further evidence of a gradual trend towards a constant deposition velocity computed on mass basis with much reduced agglomeration effects as the number concentration decreases further.

A plot of the ratio of $Kn^2/\beta n$ against axial position downstream of station 2 in Fig. 8.24 for the three test conditions yielded three curves which seemed to converge to a value of 0.2 at station 5. Of special interest is the axial position

at which the agglomeration term Kn^2 and deposition term, βn are equal. At this position, approximately forty pipe diameters downstream of the entry plane, the inter-drop spacing is approximately 20 diameters (using estimated values for the entrained mass rate and mass mean diameter at the gas core) for the three test conditions. At station 2, (18 diameters from the entry plane), the averaged agglomeration rate is two to three times more significant than deposition rate, the ratio increasing with a generally more polydispersed spectrum.

For test condition C the linear least squares correlation coefficient for the slope $\frac{K}{\beta}$ was 0.89 indicating that the assumption of a constant K was an oversimplification. However, the lack of adequate data points prevented further detailed analysis of the trend for K .

8.6 Comparison with a Numerical Model

Drop-size distribution data for test condition A were also intended for comparison with the numerical model of Williams (9), which for an initial input spectrum would predict the evolution of size-distribution of the droplets at various axial and radial positions downstream of the starting spectrum. A brief treatment of Williams numerical model will be given and the predicted and measured spectra compared.

8.6.1 Numerical Technique

Assuming homogeneity of the drop and gas parameters in the circumferential but not in the axial and radial directions, Williams divided the circular pipe section into a finite number of annular elements each having the same cross-sectional area and bounded in the axial direction by prespecified spatial intervals. Gas motion parameters within each cylindrical element were assumed constant.

As the droplets traverse axially through an element, coagulation effects would alter the shape of the drop spectrum within the element. The change in the spectrum after a time interval Δt defined as the time an average drop traverses the axial length of one element, downstream may be determined from a set of coagulation equations. A separate set of equations enabled the radial exchange of droplets between two adjacent cyclindrical elements be determined. For the outermost radial element adjacent to the pipe walls, the deposition of drops onto the pipe walls was computed using a third set of equations.

Since the rate of coagulation and deposition of droplets depended on drop size and local fluid parameters, separate subroutines were written to compute these values for the different dropsizes within each element.

Brief details of the equations used in the numerical computation will be included in the following subsections.

8.6.1.1 Coagulation

The equation which describes the change with time of the size distribution of aerosols due to coagulation alone was derived by Muller (30) as

$$\frac{\partial n(r,t)}{\partial t} = \int_0^{r/2} C_{r,r-r_1} n(r_1,t)\, n(r-r_1,\, t)\, dr_1 - n(r,t) \int_0^{\infty} C_{r,r_1}\, n(r_1,\, t)\, dr_1 \quad \ldots\ldots 8.10$$

where $n(r,\, t)$ is the size distribution function at time t, C_{r_1,r_2} is the effective coagulation frequency between drops of mass η_1 and η_2.

Eqn. 8.10 is often rewritten, replacing the continuous size spectrum by discreet size ranges, as

$$\frac{dN_i(t)}{dt} = \tfrac{1}{2} \sum_{j=1}^{i-1} C_{j,i-j}\; N_j(t)\, N_{i-j}(t) - N_i(t) \sum_{j=1}^{l} C_{i,j}\, N_j(t) \quad \ldots\ldots 8.11$$

where $N_i(t)$ is the number of drops having an average mass η_i (i.e. in size-range i) at time t, l the total number of discreet size ranges and $C_{i,j}$ as defined above.

To avoid dealing with a large number of arithmetic size ranges for which

$$\eta_i = \eta_{i-1} + \eta \quad \ldots\ldots 8.12$$

where η is the mass of the smallest drop present, Williams classified droplets by volume such that a drop with volume in the range $2^{i-3} \times 3V_o$ to $2^{i-2} \times 3V_o$ is assigned to class i. V_o is the smallest volume in the spectrum. An average collision between an i drop with a j drop for the discreet distribution was further deduced to produce p drops of class i and q drops of class i + 1 where

$$p = \left[1-\frac{3}{2}\,2^{j-1}+\frac{\eta_i}{16}\left(1+\frac{7}{2}2^{2j}-\frac{9}{4}2^{j+i}\right)\right]\frac{1+2^{j-i}}{1+\frac{3}{2}2^{j-i}-\frac{\eta_i}{16}\left(1+\frac{7}{2}2^{2j}-\frac{9}{4}2^{i+j}\right)} \qquad \ldots. 8.13$$

and

$$q = \left[\frac{3}{2}2^{j-i}-\frac{\eta_i}{16}\left(1+\frac{7}{2}2^{2j}-\frac{9}{4}2^{j+i}\right)\right]\frac{1+2^{j-i}}{1+\frac{3}{2}2^{j-i}-\frac{\eta_i}{16}\left(1+\frac{7}{2}2^{2j}-\frac{9}{4}2^{i+j}\right)} \qquad \ldots. 8.14$$

where $\eta_i = \left[\dfrac{N_{i+1}-4N_{i-1}}{N_{i+1}+4N_{i-1}}\right] t$; N_{i+1} is defined below.

Using a small time step Δt, the temporal difference equations for drop number concentration N_i are:

$$\left.\begin{aligned}
(N_i)_{t+\Delta t} &= (N_i - N_iN_j P_{ij}(1-p)\Delta t)_t \\
(N_j)_{t+\Delta t} &= (N_j - N_iN_j P_{ij}\Delta t)_t \\
(N_{i+1})_{t+\Delta t} &= (N_{i+1} + N_iN_j P_{ij} q\Delta t)_t
\end{aligned}\right\} \quad i>j$$

and

$$\left.\begin{aligned}
(N_i)_{t+\Delta t} &= (N_i - 2N_i^2 P_{ii}\Delta t)_t \\
(N_{i+1})_{t+\Delta t} &= (N_{i+1} + N_i^2 P_{ij}\Delta t)_t
\end{aligned}\right\} \quad i=j \qquad \ldots. 8.15$$

where $P_{ij}(t,\ t+\Delta t) = C_{ij}\ \dfrac{1-\exp\left\{-(B_i(t) + B_j(t)\Delta t)\right\}}{B_i(t) + B_j(t)}$

and $B\ (t) = \sum_{j=1}^{1} C_{ij}\ N_j(t)$

The value of C_{ij} derived in (9) is

$$C_{ij} = 11.455\ \frac{\rho_p}{\rho\nu}\ \gamma(\sqrt{\Phi_i} + \sqrt{\Phi_j}\ )^2\ \ \frac{w}{u}\ \tan^{-1}\left[0.2669\frac{\rho_p}{\rho}\ \ \frac{u\gamma}{\nu}\ \frac{\Phi_i\ \Phi_j}{(\sqrt{\Phi_i} + \sqrt{\Phi_j}\ )^2}\ \left(\frac{w}{u}\right)^2\right] \quad \ldots\ 8.16$$

where $\left(\frac{w}{u}\right)^2 = \dfrac{\Phi_i^2+\Phi_j^2+2\Phi_i\ \Phi_j-4\Phi_i\ \Phi_j\left[\frac{1+\ \Phi_i\ \ +\Phi_j}{(1\ +\Phi_i)(\ 1+\Phi_j)}\right]^{\frac{1}{2}}}{(\Phi_i+\Phi_j)(1+\Phi_i)(1+\Phi_j)}$

γ = longitudinal integral space scale defined as

$u\int_o^\infty f(x)\ dx$ where $f(x) = \dfrac{U(X_a') \ U(X_a'+ x)}{u_a^2}$

i.e. $f(x) = \dfrac{U(t_1+ t)\ U(t_1)}{u_a^2}$ by Taylors(219)

hypothesis if $\bar{u} \gg u$ and $x = \bar{u}t$

$\Phi = \tau/T_L$ where T_L = Lagrangian integral time scale of fluid

w = rms relative velocity of two particles(or drops)

The main assumptions in deriving C_{ij} were:

(i) Infinite domain of turbulence.

(ii) Drop is spherical and Stokesian.

(iii) Drop is small compared with the smallest turbulent eddy and

(iv) No gravitational coagulation (valid in the rig provided that drop diameters are $<<$ 200 μm)

Eqn. 8.16 was derived by first solving simplified form of Tchen's (48) equation of motion of a particle in a spatially and temporally inhomogeneous fluid velocity field; the validity of the simplification was first assessed using a Monte Carlo simulation. The statistical parameters which described the motion of a drop were next derived in terms of the energy spectrum of the gas for which a more suitable empirical form of the wave-number spectrum was tested. Droplet rms relative velocity which was a determining factor of collision between two adjacent drops was derived and a functional form for the coagulation rate deduced assuming unity collision efficiency. (i.e. on close approach, the trajectory of one drop was not influenced by the flow field round the other) and unity coalesence efficiency (i.e. no bouncing or shattering on impact).

8.6.1.2 Radial Diffusion

Considering the nett flux of drops radially into and out of a cylindrical element (b,l) where b and l denote the centre of the element (relative to an upstream position) in the radial and axial direction, the change in number concentration along the element due to radial diffusion was deduced as

$$\dot{N}(b,l) = [\, Q_{ie}(b,l) - Q_{ot}(b,l) \,] \frac{1}{\pi \Delta X_a' (r_{ot}(b) - r_{ie}(b))^2}$$

where $Q_{ie}(b,l) = -D_r(b-1,l)\,[\, N(b,l) - N(b-1,l) \,] \frac{2\pi \Delta X_a' r_{ie}(b)}{r_c(b) - r_c(b-1)}$

$$Q_{ot}\ (b,1\ ) = -D_r(b,1\ )\ [\ N(b+1,\ 1\ ) - N(b,1\ )\ ]\ \frac{2\pi \Delta X'_a r_{ot}(b)}{r_c(b+1) - r_c(b)}$$

; $D_r(b,1)$ representing the local value of diffusivity of element(b,1). The concentration at the upstream face of element (b, 1+1) is

$$N(b,\ 1+1) = N(b,1\ ) + N(b,1\ )\ \Delta t\ (b,1\ ) \qquad \ldots\ 8.15$$

where $\Delta t\ (b,1\ ) = \frac{\Delta X'_a}{\bar{u}(b,1)} = \frac{\text{length of element}}{\text{local mean axial flow velo. through element}}$

Eqn. 8.15 was solved independently for each drop-size class using the local value of diffusivity D_r given as

$$D_r = u_r^2\ T_L$$

where u_r = rms velocity of gas phase in radial direction

$$\text{or } D_r = u_r \gamma \quad \text{since } T_L = \frac{\gamma}{u_r}$$

8.6.1.3 Deposition

The deposition of drops on the pipe wall will cause a change in number concentration of each size class within the outermost radial element (n_{re} , 1) where n_{re} was the total number of radial elements. This change was deduced, assuming no re-entrainment, as

$$\dot{N}(n_{re},\ 1\ ) = -2\pi \Delta X'_a r_{ot}(n_{re}) \left[\frac{v_r(n_{re},\ 1\ )}{\sqrt{2\pi}}\ N(n_{re},\ 1\ ) - \tfrac{1}{2} D_r(n_{re},\ 1\ ) \cdot \frac{N(n_{re},\ 1\ ) - N(n_{re}-1,\ 1\ )}{r_c(n_{re}) - r_c(n_{re}-1)} \right] Pr_{dep}(1)$$

where $v_r(n_{re}, 1) = {}_{\ell}u_a \left[1 + \Phi \right]^{-\frac{1}{2}}$

and $Pr_{dep}(1)$ = deposition probability for element $(n_{re}, 1)$ which is also a function of drop size deduced as

$$\text{erfc} \left[113 Re_D^{-0.9} \left(\frac{u_{rW}}{{}_{\ell}u_r} \right) \left(\frac{\gamma_W}{R} \right)^{-1} \cdot \frac{(1 + \Phi_W)^{\frac{1}{2}}}{\Phi_W} \right]$$

where u_{rW} = rms radial velocity fluctuation of gas phase near the sublayer assumed equal to the axial component i.e. u_{aW}

${}_{\ell}u_r$ = rms radial velocity fluctuation of the gas phase at the pipe axis assumed equal to the axial component i.e. ${}_{\ell}u_a$ from isotropy.

v_r = rms radial velocity fluctuation of the drops

γ_W = Longitudinal integral scale near the wall region.

8.6.1.4 Parameters for gas phase

For the numerical model, additional measurements of single-phase flow parameters in the rig at several axial and radial positions were required, the values being the local mean and fluctuating axial velocity, the longitudinal turbulent integral scale γ and the turbulent microscale. For the mean air velocity, a pitot tube traverse mechanism was used whilst rms value was deduced from hot-wire anemometer measurements. The logitudinal integral scale was deduced from measurements of the autocorrelation function i.e. $\overline{U(t)U(t+\Delta t)}$ where U(t) was

the air velocity at time t and U(t+Δt) the velocity after an interval Δt at the same position. Measurement of the energy dissipation rate via a technique by Lawn (216), based on the Kolmogorov-Bradshaw hypothesis, provided the value of turbulent microscale. For the range of drop sizes encountered in the present study, Williams excluded the microscale term from the final form of the numerical model having first checked the validity of its exclusion.

8.6.2 Results and Discussions

For the purpose of comparison, the arithmetic size intervals of the initial spectrum were converted to the geometric classification by Williams and the number count within each class-size per unit volume normalised using the averaged number concentration at station 2. An average value of $\bar{x}_{30}$ over the four radial positions at station 2 was used in the computation of initial number concentration N_∞ using information on the entrained mass flow rate across that station. The total error in N_∞ based on errors in the determination of entrained flow rate and the 95% confidence limits for $\bar{x}_{30}$, was of the order of $\pm$ 20%. The statistical scatter in the number frequency results in 95% confidence limits was about $\pm$ 10% at the modal value according to Selden's (217) method of analysis; this is valid provided the sample size n, is such that $nq > 5$ when q is < 0.5, q being the fraction of total count at the modal diameter.

The initial entrained liquid mass flow rate through each of the five radial elements used in the numerical model

was further assumed uniform in the comparison. Number density for each class-size was therefore computed making use of a fifth of the entrained mass flow rate across the relevant extraction station and the local value of $\bar{x}_{30}$ for the radial element, the local time step Δt selected so that the length of each element was 25 mm. The spectra at station 2 were used as input data for the numerical model and the predicted and measured number densities for each class size are compared in Fig. 8.25 and Fig. 8.26 for the core and wall spectra respectively at two downstream positions.

The predicted number densities for $\frac{X'_a}{D}$ equal to 30 (at station 4) and 65 (at station 5) relative to station 2 for the axis and wall spectra are consistently lower than the measured value. In addition, the measured value of deposition velocity computed on mass basis was found to be consistently lower than the predicted value by about 23% over pipe sections III, IV and V. Suspecting that this discrepancy may partly be the cause of the poor comparison, an additional set of analytical results was derived reducing the predicted deposition velocity artificially to near the measured value. The reduction was brought about by reducing the radial rms air velocity by 25% in the deposition equations. The results with a reduced analytic deposition velocity are shown in Fig. 8.27 and Fig. 8.28 for the core and wall spectra respectively showing a much better comparison than before.

Since comparisons of the number frequency distribution are not ideal for showing the effect of agglomeration the predicted and experimentally determined values of $\bar{x}_{32}$ are

compared in Fig. 8.29 and Fig. 8.30 for the core and wall spectra respectively. Included in the figures are the analytic results for the variation of $\bar{x}_{32}$ due to coagulation and deposition effects alone. Though $\bar{x}_{32}$ for the core spectra in the prediction is consistently higher than for the measured spectra, the change with axial distance downstream is of the same order of magnitude as the experimental results. $\bar{x}_{32}$ of the wall spectra on the other hand compares favourably with the measured values. The initial steep rise in $\bar{x}_{32}$ in Fig. 8.29 is due to the significant difference between the mass frequency spectra at $\frac{r}{R} = 0.04$ and 0.88 at station 2. A rapid reduction in this difference due to radial diffusion of drops is predicted by the model and which accounts for the consistently higher values of predicted $\bar{x}_{32}$ at the core compared with the measured value.

The errors in the analytical values of drop number density arise from three sources: error in the determination of turbulence parameters for the coagulation, diffusion and deposition equations; error in the initial spectrum and assumption of initially uniform mass flow rates through the five radial elements; and error in the approximations used in the theories. Whilst the total error in the analytic results is difficult to quantify (see Williams (9)) an order of magnitude comparison between the predicted and measured spectra should be adequate for the present. The numerical model although satisfactorily describing the trend in $\bar{x}_{32}$ especially in the wall region generates large percentage error in suspended mass flow rate for a small percentage error in the deposition velocity.

Williams has used a 2-dimensional turbulent deposition model which satisfactorily described the results of Liu and Agarwal (39). Since the deposition velocity of the olive oil drops used in the experiments by Liu and Agarwal was computed assuming uniform mass of all deposited drops and the absence of agglomeration, any error in the results as a consequence of those assumptions would affect the present comparisons.

In conclusion the numerical model does predict the right order of magnitude for the rate of aerosol evolution using turbulence parameters determined for the single-phase flow situation.

CHAPTER 9

CONCLUSION AND RECOMMENDATION

An open-shutter sub-microsecond spark photographic technique has been developed for the sizing of water droplets from an atomiser spray or in a turbulent two-phase pipe flow. The smallest drop size which could be satisfactorily photographed was 10 μm under an overall magnification of 14x. Good contrast photographs of dense sprays having an average inter-drop spacing of 10 drop diameters have been obtained employing an air-purged hood for the camera lens. Though the initial application of the technique has been to determine drop-size distribution in the two-phase rig and atomiser sprays, preliminary measurements of droplet velocity using double-flash photography have also been successful. A special-purpose optical bench was designed to improve the speed of data acquisition when photographing the spectra across a section of the two-phase rig at several radial positions.

In connection with the sizing of droplets, an off-line automatic image analysing system with detection at eight grey levels has been successfully built round a conventional television camera and a minicomputer. Software developed for the automatic system includes a new algorithm for recognising relevant images, regardless of shape, and performing subsidiary operations including "filling-in" of internal voids of a detected feature or separating features within features to as many depths as necessary so extending its usefulness to other research fields e.g. computer aided design. The system has

provided the required resolution and accuracy for sizing liquid drops in the 20-200 μm diameter range from shadow photographs of 9x and 14x magnifications containing a high proportion of "out-of-focus" images. Focus discrimination is based on the results of calibrations, the procedure being similar in principle to those recently reported by other workers. The software-based system may further be developed to include measurements of droplet velocity or acceleration as discussed in sec. 5.4.9 together with other recommendations. As an alternative to double-flash photography for the measurement of droplet velocity, the present software structure may be modified to analyse digitised images from streak photographs providing information on individual streak length and hence velocity. Though the automatic system is presently suitable for analysing photographic negatives only, it is capable of executing the basic functions of a hardwired image analysing computer such as the determination of areas, perimeters, shape factors, or simply counting the number of individual features in a microscope specimen or etched slides (e.g. containing nuclear particle tracks) in which the object field is sharply defined.

On size distribution, when the mass frequency distribution of droplets is required from a number count analysis, minimum conversion error is introduced if the method proposed by Wise (193) is used. Though most of the mass frequency data may be satisfactorily correlated by the ULDF (11), a heterogeneous ULDF is formulated to provide a suitable description for bimodal drop mass frequency spectra whilst retaining the emphasis on the existence of a maximum stable drop size.

Optimum fits of the ULDF (or heterogeneous ULDF) to mass-frequency data are made using a non-linear least squares regression algorithm, avoiding the subjective nature of a graphical fit. The maximum drop diameters determined from an optimised ULDF fit may not necessarily provide a realistic solution to certain practical problems. An effective maximum diameter, for example x_{999} which corresponds to a 99.9 per cent cumulative mass, is sometimes a better alternative to x_m when further correlating the data.

A sample size of between 500 and 1000 counts provided the required confidence limits for the mean diameters and the optimised maximum drop size of most spectra encounted in the present studies.

Equipment for the study of turbulent agglomeration in a horizontal two-phase pipe flow has been constructed. The design of the two-phase rig includes: (i) a slot-type wall film extraction unit which provided satisfactory measurements of droplet deposition velocity; (ii) a fluid supply and metering system which permits the treatment of water, for example, altering certain physical properties of the dispersed phase at a future date; (iii) the use of four units of air-blast atomisers of the author's design to introduce a high number concentration of water drops (approximately ten drop diameters inter-drop spacing) into the air stream. Each air-blast atomiser is capable of generating a narrow mass frequency spectrum with a mass mean diameter around 33 μm under moderate operating pressures; the corresponding liquid-to-air mass ratio is approximately 5 and for a liquid flow rate of 1.5 l/min, the droplet

generation rate exceeds 10^9 drops/s per atomiser. Photographic analysis of the spray spectra indicated that the air-blast atomisers should be operated under a coaxial-to-axial air mass ratio of 1 : 1 for a narrow mass frequency distribution. Conventional commercial pneumatic atomisers were found to be unsuitable for the present study from the point of view of extreme polydispersity in the mass frequency spectra, or the relatively high air-to-liquid mass flow ratios required in their operation.

Experiments to assess the relative magnitudes of deposition and re-entrainment indicated that although the error due to re-entrainment on deposition velocity measurements is small, the interaction between the deposited liquid film and the gas core has a significant effect on the drop-size distribution of the entrained flow when the film flow rate is high. It has not yet been possible to assess the extent to which liquid exchange between the gas core and wall-film occurred although simple measurements have been attempted. Reduction of the film flow rate throughout the full length of the test-section has helped to minimise the effect of re-entrainment on drop-size distribution in the gas core.

Measurements of deposition velocities indicated high initial values at the entry plane to the test section, decaying to a minimum value approximately eighteen pipe diameters downstream beyond which computation of deposition velocities by Liu and Agarwal's technique (39) indicated another peak at approximately 50 diameters from the entry plane when the polydispersed spectrum contains a significant fraction of large drop sizes which are affected by gravity. Deposition velocities

computed from measurements of deposited mass gave predictably high values due to preferential deposition of the heavier drops (larger than 70 μm) from a polydispersed spectrum. Whilst this discrepency is not obvious when the drop-size distribution is less polydispersed with a corresponding mass mean diameter under 40 μm, a photographic experiment indicated coarser spectra near the pipe wall than at the pipe axis, even at low number concentration when the effect of deposition should be predominant.

The dimensionless deposition velocity determined for the test condition in which the effect of gravity is not significant, plotted against dimensionless relaxation time based on the mass mean diameter of the core spectrum, agrees well with the results of Liu and Agarwal in the turbulent-impaction regime.

Employing a simplified analytic equation to describe the simultaneous effects of deposition and coagulation on number concentration, the influence of both processes is found to be equally significant for an inter-drop spacing of up to twenty diameters. Droplet agglomeration rate at eighteen diameters from the entry plane to the test section is further found to be two to three times more significant than the deposition rate, the ratio increasing with a generally more polydispersed spectrum.

Whilst the difference in the number frequency distribution between a numerical prediction and the measurements (for the same upstream spectrum) is rather sensitive to errors between predicted and measured deposition velocities, the

numerical model of Williams indicated the correct order of magnitude variation in Sauter mean diameter of the droplet spectra.

The following additional investigations are recommended:

(a) There is a need for a satisfactory deposition model which accounts for the influence of external force field effects (e.g. gravity) on different drop sizes in a polydispersed spectrum.

(b) The present experiments should be repeated over a wider range of flow Re_D and drop sizes which are not seriously affected by gravity, employing a vertical pipe geometry if necessary.

(c) The effect of pipe bends on the evolution of drop sizes and number concentration should also be examined.

(d) An experimental determination of the drop fluctuating rms velocity employing double-flash photography or laser doppler anemometry (LDA) as described in ref. (219) is highly desirable for improving existing theoretical models for agglomeration as well as deposition. Experiments involving initially a dilute system using the LDA measurements of drop rms velocity should provide some useful preliminary results. For a dense spectrum, the use of double-flash photography would also provide drop rms relative velocity.

(e) The influence of liquid properties e.g. surface tension or viscosity on the rate of droplet agglomeration and deposition should also be investigated. Research into

the effect of surface tension forces on deposition velocity measurements using the existing instrumentation should provide some interesting results which would also add to the present knowledge about re-entrainment.

(f) A means of detecting the amount of interchange between the wall film and gas core is needed as well as information on the extent to which such factors affect the mass frequency spectrum near the wall region, hence providing a definite explaination for the relatively coarse wall spectrum. A qualitative examination employing axial view cinephotography is also recommended.

(g) Measurements of the actual amount of electrostatic charging should be carried out to confirm the present assumption that electrostatic forces are small relative to inertial forces.

REFERENCES

1. GYARMARTHY, G. "Basic notions" in "Two-phase steam flow in turbine and separators", Ed. Moore, M.J. and Sieverding, C.H. 1976, Hemisphere, Washington, 1-58.

2. HOSSLI, W. "The 1160 MW Turbine for 'Donald C. Cook' Nuclear Power Plant of AEP", Brown Boveri Rev., 1972 59 (1), 4-19.

3. USHER, J. "Wet steam turbines for nuclear generating stations - design and operating experience", J. Inst. Nucl. Eng. 1977 18 (5), 141-146.

4. HUTCHINSON, P., HEWITT, G.F. and DUKLER, A.E. "Deposition of liquid or solid dispersions from turbulent gas streams: a stochastic model", Chem. Engng. Sci. 1971 26, 419-439.

5. CRANE, R.I. and EVANS, R.L. "Inertial deposition of particles in a bent pipe", J. Aerosol Sci. 1977 8, 161-170.

6. CRANE, R.I. "Some aspect of wet steam flow in turbine cross-over pipes", Int. J. Mech. Sci. 1978 20, 237-246.

7. SMITH, A. "Wilson point experiments in steam turbines", Reyrolle Parsons Rev. 1974/75 2 (2), 1

8. ZEBEL, G. "Coagulation of aerosols" in "Aerosol science", Ed. Davis C.N. 1966, Academic Press, London, 31-57.

9. WILLIAMS, J.J.E. "Droplet coagulation in two-phase turbulent pipe flows", Ph.D. Thesis, 1980 Univ. of London (Imperial College).

10. JONES, A.R. and SARJEANT, M. "A high speed photographic system for measuring drop sizes and velocities in dense fuel sprays", 1979, Central Electricity Generating Board Rep. No. R/M/N 1049.

11. MUGELE, R.A. and EVANS, H.D. "Droplet size distribution in sprays", Ind. Engng. Chem. 1951 43 (6), 1317-1324.

12. HIDY, G.M. and BROCK, J.R. "The dynamics of aerocolloidal system", 1970, Pergamon Press, Oxford, 296-349.

13. SMOLUCHOWSKI, M. von Phys. Z. 1916 17, 557, 585.

14. SMOLUCHOWSKI, M. von Z. Phys. Chem. 1917 92, 129.

15. CAMP, T.R. and STEIN, P.C. "Velocity gradients and internal work in fluid motion", J. Boston Soc. Civ. Engrs. 1943 30 (4), 219-237.

16. WEBER, W.J. JR., "Physicochemical Processes for water quality control", 1972, Wiley-Interscience, New York.

17. LEVICH, V.G. "Physico-chemical Hydrodynamics", 1962, Prentice-Hall, Chap. III, V.

18. HINZE, J.O. "Turbulence: An introduction to its mechanism and theory", 1959, McGraw-Hill, New York, 184-186.

19. BEAL, S.K. "Turbulent agglomeration of suspensions", J. Aerosol Sci. 1972 3, 113-125.

20. EAST, T.W.R. and MARSHALL, J.S. "Turbulence in clouds as a factor in precipitation", Quart. J. Roy. Met. Soc. 1954 80, 26-47.

21. SAFFMAN, P.G. and TURNER, J.S. "On the collision of drops in turbulent clouds", J. Fluid Mech. 1956 1, 16-30.

22. SEDUNOV, Yu.S. "Certain questions on the coagulation of particles in turbulent flow", Investia A.N. SSSR, Ser. Geophys. 1964 7, 150-156. (p. 80-84 of English translation)

23. HUEBSCH, I.O. "Relative motion and coagulation of particles in a turbulent gas", US Naval Radiological Defense Lab., 4th May, 1967, USNRDL-TR-67-49.

24. ABRAHAMSON, J. "Collision rates of small particles in a vigorously turbulent fluid", Chem. Engng. Sci. 1975 30, 1371-1379.

25. FRIEDLANDER, S.K. "Smoke, dust and haze", 1977, John Wiley & Sons, Chap. 7.

26. SWIFT, D.L. and FRIEDLANDER, S.K. "The coagulation of hydrosols by Brownian motion and laminar shear flow", J. Colloid Sci. 1964 19, 621-647.

27. YODER, J.D. and SILVERMAN, L. "Influence of turbulence on aerosol agglomeration and deposition in a pipe", 60th Annual Air Pollution Control Assoc. Meeting Cleveland, Ohio, 13th June 1967, Paper No. 67-33.

28. ARUNDEL, P.A., BIBB, S.D. and BOOTHROYD, R.G. "Dispersed density distribution and extent of agglomeration in a polydisperse fine particle suspension flowing turbulently upwards in a duct", Powder Technol. 1970/71 4, 302-312.

29. DELICHATSOIS, M.A. and PROBSTEIN, R.F. "Coagulation in turbulent flow: Theory and experiment", J. Colloid and Interface Sci. 1975 51 (3), 394-405.

30. MUELLER, H. Kolloidbeihefte 1928 27, 223. (cited from ref. (31))

31. TOLFO, F. "A simplified model of aerosol coagulation", J. Aerosol Sci. 1977 8, 9-19.

32. OKUYAMA, K., KOUSAKA, Y. and YOSHIDA, T. "Turbulent coagulation of aerosols in a pipe flow", J. Aerosol Sci., 1978 9, 399-410.

33. YOSHIDA, T., KOUSAKA, Y. and OKUYAMA, K. "A new technique of particle size analysis of aerosols and fine powders using an ultramicroscope", Ind. Engng. Chem. Fundam. 1975 14,47-51.

34. FRIEDLANDER, S.K. and JOHNSTONE, H.F. "Deposition of suspended particles from turbulent gas streams", Ind. Engng. Chem. 1957 49 (7), 1151-1156.

35. OWEN, P.R. "Dust deposition from a turbulent airstream" Int. J. Air-Water Pollution 1960 3, 8-25, 50-53. Also in "Aerodynamic captive of particles", Ed. Richardson, E.G., 1960, Pergamon Press, New York, 8-25, 50-53.

36. DAVIES, C.N. "Deposition from moving aerosols" in "Aerosol science" Ed. Davis, C.N. 1966, Academic Press, London, 393-440.

37. BEAL, S.K. "Deposition of particles in turbulent flow on channel or pipe walls", Nucl. Sci. & Engng. 1970 40, 1-11.

38. SEHMEL, G.A. "Particle deposition from turbulent air flow", J. Geophy. Res. 1970 75 (9), 1766-1781.

39. LIU, B.Y.H. and AGARWAL, J.K. "Experimental observation of aerosol deposition in turbulent flow", J. Aerosol Sci. 1974 5, 145-155.

40. CLEAVER, J.W. and YATES, B. "A sublayer model for the deposition of particles from a turbulent flow", Chem. Engng. Sci. 1975 30, 983-992.

41. LIU, B.Y.H. and ILORI, T.A. "Inertial deposition of aerosol particles in turbulent pipe flow" in "Flow studies in air and water pollution" (Meeting, June 1973), Amer. Soc. Mech. Engrs., New York, 103-113.

42. ROUHIAINEN, P.O. and STACHIEWICZ, J.W. "On the deposition of small particles from turbulent streams", J. Heat Trans. (Trans. ASME) 1970 92, 169-177.

43. ALEXANDER, L.G. and COLDREN, C.L. "Droplet transfer from suspending air to duct walls", Ind. Engng. Chem. 1951 43, 1325-1331.

44. COUSINS, L.B. and HEWITT, G.F. "Liquid phase mass transfer in annular two-phase flow: droplet deposition and liquid entrainment", 1968, U.K. Atomic Energy Research Establishment Rep. No. R-5657, Harwell.

45. GARDNER, G.C. "Deposition of particles from a gas flowing parallel to a surface", Int. J. Multiphase Flow 1975 2, 213-218.

46. OWEN, P.R. "Pneumatic transport", J. Fluid Mech. 1969 39 (2), 407-432.

47. REEKS, M.W. and SKYRME, G. "The dependence of particle deposition velocity on particle inertia in turbulent pipe flow", J. Aerosol Sci. 1976 7, 485-495.

48. TCHEN, C.M. "Mean value and correlation problems connected with the motion of small particles suspended in a turbulent fluid", Doctoral Dissertation, Technische Hogeschool, Delft; Mortinus Nijhoff, The Hague, 1947.

49. BROWNE, L.W.B. "Deposition of particles on rough surface during turbulent gas-flow in a pipe", Atmos. Environ. 1974 8, 801-816.

50. JAMES, P.W. and HUTCHINSON, P. "Droplet deposition in an annular geometry", Int. J. Multiphase flow 1979 5, 103-112.

51. SEHMEL, G.A. "Aerosol deposition from turbulent airstream in vertical conduits", Pacific Northwest Laboratory, Richland, Washington, March 1968, BNWL-578.

52. MONTGOMERY, T.L. and CORN, M. "Aerosol deposition in a pipe with turbulent air flow", J. Aerosol Sci. 1970 1, 185-213.

53. FARMER, R., GRIFFITH, P. and ROHSENOW, W.M. "Liquid droplet deposition in two-phase flow", J. of Heat. Transf. (Trans. ASME.) 1970 192, 587-594.

54. SEHMEL, G.A. "Particle eddy diffusivities and deposition velocities for isothermal flow and smooth surfaces", J. Aerosol Sci. 1973 4, 125-138.

55. FORNEY, L.J. and SPIELMAN, L.A. "Deposition of coarse aerosols from turbulent flow", J. Aerosol Sci. 1974 5, 257-271.

56. FRIEDLANDER, S.K. "Deposition of suspended particles from turbulent gases" Ph.D. Thesis, 1954, University of Illinois, Urbana, Ill.

57. McCOY, D.D. and HANRATTY, T.J. "Rate of deposition of droplets in annular two-phase flow", Int. J. Multiphase Flow 1977 3, 319-331.

58. PAPAVERGOS, P.G. and HEDLEY, A.B. "Particle deposition behaviour in fully developed turbulent flows", 2nd Multi-phase Flow and Heat Transfer Symposium-Workship, April 1979, Miami Beach.

59. PAPAVERGOS, P.G. and HEDLEY, A.B. J. Aerosol Sci. (in preparation) (cited from ref. (58)).

60. HEWITT, G.F. and HALL-TAYLOR, N.S. "Annular two-phase flow" (1st Edn.) 1970, Pergamon Press, New York.

61. HEWITT, G.F. "Measurement of two-phase flow parameters", 1978, Academic Press, London.

62. WALLIS, G.B. "Annular two-phase flow: Part 1 - A simple theory", J. Basic Engng.(Trans.ASME) 1970 92, 59-72.

63. Ibid, "Annular two-phase flow: Part 2 - A simple theory", J. Basic Engng.(Trans. ASME) 1970 92, 73-82.

64. RUSSEL, T.W.F. and LAMB, D.E. "Flow mechanism of two-phase annular flow", Canadian J. of Chem. Engng. 1965 43, 237-245.

65. FISHER, S.A. and PEARCE, D.L. "A theoretical model for describing horizontal annular flows", Int. Seminar for Momentum, Heat and Mass Transfer in Two-phase Energy and Chemical System, Sept. 1978, Dubrovnik, Yugoslavia.

66. HUTCHINSON, P., BUTTERWORTH, D. and OWEN, R.G. "Development of a model for horizontal annular flow", 1974, U.K. Atomic Energy Research Establishment Rep. No. R-7789.

67. HEWITT, G.F. "Liquid mass transport in annular two-phase flow", Int. Seminar Momentum Heat Mass Transfer in Two-phase Energy and Chemical Systems, Sept. 1978, Dubrovnik, Yugoslavia.

68. HALL-TAYLOR, N., HEWITT, G.F. an d LACEY, P.M.C. "The motion and frequency of large disturbance waves in annular two-phase flow of air-water mixtures", Chem. Engng. Sci. 1963 18, 537-552.

69. NEDDERMAN, R.M. and SHEARER, C.J. "The motion and frequency of large disturbance waves in annular two-phase flow of air-water mixtures", Chem. Engng. Sci. 1963 18, 661-670.

70. TOMIDA, T. and OKAZAKI, T. "Statistical character of large disturbance waves in upward two-phase flow of air-water mixtures", J. Chem. Engng. Japan, 1974 7 (5), 329-333.

71. THWAITES, G.R., KULOV, N.N. and NEDDERMAN, R.M. "Liquid film properties in two-phase annular flow", Chem. Engng. Sci. 1976 31, 481-480.

72. HORI, K., NAKAZATOMI, M., NISHIKAWA, K. and SEKOGUCHI, K. "On ripple of annular two-phase flow - 3. Effect of liquid viscosity on characteristics of wave and interfacial friction factor", Bull. JSME. 1979 22 (169), 952-959.

73. HEWITT, G.F. "Disturbance waves in annular two-phase flow", Proc. Instn. Mech. Engrs. 1969-70 184 (3C), 142-150.

74. COUSINS, L.B., DENTON, W.H. and HEWITT, G.F. "Liquid mass transfer in annular two-phase flow" Symp. on two-phase flow, 1965, Exeter, paper C4, C401-C601.

75. BENNET, J.A.R. and THORNTON, J.D. "Data on the vertical flow of air-water mixtures in the annular and dispersed flow regions. Part 1: Preliminary study", Trans. Instn. Chem. Engrs. 1961 39, 101-112.

76. SIMPSON, R.L. "A study of adiabatic, fully-developed annular-dispersed two-phase flow in a vertical round tube", GEAP-10094.

77. GILL, L.E., HEWITT, G.F., HITCHON, J.W. and LACEY, P.M. "Sampling probe studies of the gas core in annular two-phase flow - I: The effect of length on phase and velocity distribution", Chem. Engng. Sci. 1963 18, 525-535.

78. WICKS, M. and DUKLER, A.E. "Entrainment and pressure drop in cocurrent gas-liquid flow: 1 air-water in horizontal flow", Amer. Inst. of Chemical Engng. 1960 6 (3), 463-468.

79. ADORNI, N., CASAGRANDE, I., CRAVARDO, L., HASSID, A. and SILVESTRI, M. "Experimental data on two-phase adiabatic flow: Liquid film thickness, phase velocity distribution, pressure drops in vertical gas-liquid flow", 1961, CISE, Rep. R 35.

80. MAYINGER, F., LANGNER, H. and ZETZMANN, K. "Flow pattern of two-phase flow in inside cooled tubes - a generalised form of flow pattern map and entrainment measurements of annular flow", European Two-phase Flow Meeting, June 1976, Erlangen, Paper No. D9.

81. QUANDT, E.R. "Measurement of some basic parameters in two-phase annular flow", Amer. Instn. Chem. Engrs. J. 1965 11 (2), 311-318.

82. COUSINS, L.B. and HEWITT, G.F. "Liquid phase mass transfer in annular two-phase flow: Radial liquid mixing", 1968, U.K. Atomic Energy Research Establishment Rep. No. R-5693.

83. JAGOTA, A.K., RHODES, E. and SCOTT, D.S. "Tracer measurements in two-phase annular flow to obtain interchange and entreainment", Canadian J. of Chem. Engng. 1973 51, 139-148.

84. LOCKHART, R.W. and MARTINELLI, R.C. "Proposed correlation of data for isothermal two-phase, two-component flow in pipes", Chem. Engr. Progr. 1949 45 (1), 39-48.

85. HINZE, J.O. "Fundamentals of the hydrodynamic mechanism of splitting in dispersion processes", Amer Instn. Chem. Engrs. J. 1955 1 (3), 289-295.

86. COLLIER, J.G. and HEWITT, G.F. "Data on the vertical flow of air-water mixtures in the annular and dispersed flow regions. Part II: Film thickness and entrainment data and analysis of pressure drop measurements", Trans. Instn. Chem. Engrs. 1961 39, 127-144.

87. GILL, L.E., HEWITT, G.F. and LACEY, P.M.C. "Sampling probe studies of the gas core in annular two-phase flow - II studies of the effect of phase flow rates on phase and velocity distributions", Chem. Engng. Sci. 1964 19, 665-682.

88. HUTCHINSON, P. and WHALLEY, G.B. "A possible characterisation of entrainment in annular flow", Chem. Engng. Sci. 1973 28, 974-974.

89. GILL, L.E., HEWITT, G.F. and ROBERTS D.N. "Liquid phase mass transfer in annular two-phase flow: Radial liquid mixing", 1968, U.K. Atomic Energy Research Establishment, Rep. No. R-5693, Harwell.

90. TRUONG QUANG MIN and HUYGHE, J. "Some hydrodynamical aspects of annular dispersed flow: Entrainment and film thickness", Sym. on Two-phase Flow, 1965, Exeter, Paper C2.

91. WHALLEY, P.B., HEWITT, G.F. and HUTCHINSON, P. "Experimental waver and entrainment measurements in vertical annular two-phase flow", 1973, U.K. Atomic Energy Research Establishment, Rep. No. R-7521, Harwell.

92. KEEYS, R.K.F., RALPH, J.C. and ROBERTS, D.N. 1970, U.K. Atomiser Energy Research Establishment, Rep. No. R-6293, Harwell. (cited from ref. (91))

93. SINGH, K., ST. PIERRE, C.C., CRAGO, W.A. and MOECK, E.O. "Liquid film flow rates in two-phase flow of steam and water at 1000 psia", Amer. Instn. Chem. Engrs. J. 1969 15 (1), 51-56.

94. NILKURADSE, J., Stromungsgesetze in rauhen Rohren. Forsch. Arb. Ing. - Wes. No. 361 (1933). (cited from ref. (198))

95. UEDA, T. "Entrainment rate and size of entrained droplets in annular two-phase flow", Bull. of Japan Soc. of Mech. Engrs. 1979 22 (171), 1258-1265.

96. McCREATH, C.G. and BEER, J.M. "A review of drop size measurement in fuel sprays", Appl. Energy 1976 2, 2-15.

97. JONES, A.R. "A review of oil droplet size measurement", 1976, Central Electricity Generating Board, Rep. No. R/M/N920.

98. AZZOPARDI, B.J. "Measurement of drop sizes", Int. J. Heat & Mass Transf. 1979 22, 1245-1279.

99. LEE, D.W. "The effect of nozzle design and operating conditions on the atomisation and distribution of fuel sprays", 1932, NACA Rep. No. 425.

100. HOUGHTON, H.G. and RADFORD, W.H. "On the measurement of drop size and liquid water content in fogs and clouds", M.I.T. Papers in Phys. Ocean. & Met. 1938 6 (4), 1-18.

101. MAY, K.R. "The measurement of airborne droplets by the magnesium oxide method", J. Sci. Instrum. 1950 27, 128-130.

102. KOLB, B. "Measuring the size of droplets in wet steam", Brown-Boveri Rev. 1962 49 (7/8), 350-359.

103. STOKER, R.L. "A method of determining the size of droplets dispersed in a gas", J. Appl. Phys. 1946 17, 243-245.

104. RYLEY, D.J. and FALLON, J.B. "Size sampling of steam-borne water droplets", Proc. Instn. Mech. Engrs. 1965-66 180 (30) Paper 25, 23-38.

105. DUNSKIY, V.F., NIKITIN, N.V. and TONKACHEGEVA, N.F. "Satellite droplets forming during atomisation of liquids by a rotating disk", Fl. Mechs.-Soviet Res. 1972 1 (1), 110-113.

106. ADLER, C.R., MARK, A.M. MARSHALL, W.R. and PARENT, R.J. "A scanning device for determining the size distribution of spray droplet images", Chem. Engng. Progress 1954 50 (1), 14-23.

107. NAMIE, S. and UEDA, T. "Droplet transfer in two-phase annular mist flow - Part 1, Experiment on droplet transfer rate and distributions of droplet concentration and velocity", Bull. of Japan Soc. Mech. Engrs. 1972 15 (90), 1568-1580.

108. ADLER, C.R. and MARSHALL, W.R. "Performance of spinning disk atomisers", Chem. Engng. Progr. 1951 47 (10), 515-608.

109. TATE, W.R. "Immersion Sampling of spray droplets", Amer. Instn. Chem. Engrs. J. 1961 7 (4), 574-577.

110. RAO, K.V.L. and LEFEBVRE, A.H. "Fuel atomisation in a flowing air stream", Amer. Inst. Astro. & Aero. J. 1975 13 (10), 1413-1415.

111. BALLAL D.R. "Ignition of liquid fuel sprays", M.O.D. Contr. No. AT/2028/083XR, Mech. Engng. Dept., Cranfield Inst. of Tech., 1975.

112. NELSON. P.A. and STEVENS, W.F. "Size distribution of droplets from centrifugal spray nozzles", Amer. Instn. Chem. Engrs., J. 1961 7 (1), 80-86.

113. WICKS, M. and DUKLER, A.E. "In-situ measurements of drop size distribution in two phase flow - A new method for electrically conducting liquids", Proc. 3rd Heat Transf. Conf. 1966 5, 39-49.

114. PYE, J.W. "Droplet size distribution in sprays using a pulse counting technique", J. Inst. of Fuel 1971 44, 253-256.

115. McVEAN, S.S. and WALLIS, G.B. "Experience with the Wicks - Dukler probe for measuring drop size distributions in sprays", 1969, Dartmouth College Report.

116. JONES, A.R. "Some experimental and analytical considerations of the Wicks-Dukler method for measuring droplet size distribution in sprays", 1976, Central Electricity Generating Board, Rep. No. R/M/N866.

117. JONES, A.R. and SARGEANT, M. "An experimental appraisal of the Wicks-Dukler technique for measuring drop sizes", 1977, Central Electricity Generating Board Rep. No. R/M/N930.

118. GUYTON, A.C. "Electronic counting and size determination of particles in aerosols", J. Indust. Hyg. Toxical. 1946 28, 133.

119. GIEST, J.M., YORK, J.L. and BROWN, G.G. "Electronic spray analyser for electrically conducting particles", Ind. & Engng. Chem. 1951 43 (6), 1371-1377.

120. GARDINER, J.A. "Measurement of the drop size distribution in water sprays by an electrical method", Instrum. Practice 1964, 353-356.

121. VAN PAASEN, C.A.A. "Thermal droplet size measurements using a thermocouple", Int. J. Heat & Mass Transf. 1974 17, 1527-1548.

122. GOLDSCHMIDT, V.W. "Measurement of aerosol concentration with a hot wire anemometer", J. Colloid Sci. 1965 20, 617-634.

123. MOORE, M.J. and BRAGG, G.M. "A preliminary assessment of the hot wire anemometer as a droplet sizing device", 1971, Central Electricity Generating Board, Lab. Note No. RD/L/N10/71.

124. MOORE, M.J. "A theory for the hot-wire anemometer as a droplet sizing device", 1971, Central Electricity Generating Board, Lab. Note No. RD/L/N53/71.

125. MEDECKI, H. and MAGNUS, D.G. "Liquid aerosol detection and measurement", Presented at the 68th Annual Meeting of the Air Pollution Central Association, Boston, Massachusetts, 15th-20th June 1975, Paper 24-1, 1-17.

126. BRAGG, G.M. and TEVAARWERK, J. "The effect of a liquid droplet on a hot wire anemometer probe", Proc. Symp. Flow, Pittsburgh, Vol. 1 - Its measurement and control in science and industry, Dowdell, R.B. (ed.), Part 2 - Flow measuring devices, Wendt, Jr. R.E. (ed.), Instrument Soc. of Ame., Pittsburgh, 1974, 599-603.

127. MIE, G. "Contributions to the optics of turbid media- especially colloidal metal solutions", Ann. Physik 1908 25, 377-445.

128. EDERHOF, A. and DIBELIUS, G. "Determination of droplet sizes and wetness fraction in two-phase flows using a light scattering technique (High pressure live steam of nuclear power plants, low pressure steam turbines; cooling tower plumes)", Inst. Mech. Engrs. Conf. Paper C60/76, 1976, 21-27.

129. PENNDORF, R. "Bibliography of numerical computations on scattering and adsorption of electromagnetic radiation for spherical particles based on the Mie theory", Air force Cambr. Res. Lab., June 1963, Rep. AFCRL-63-668.

130. CHIN, J.H., SLIEPCEVICH, C.M. and TRIBUS, M. "Particle size distributions from angular variation of intensity of forward-scattered light at very small angles", J. Phys. Chem. 1955 59, 841-844.

131. CHIN, J.H. SLIEPCEVICH, C.M. and TRIBUS, M. "Determination of particle size distributions in polydispersed systems by means of measurements of angular variation of intensity of forward-scattered light at very small angles", J. Phys. Chem. 1955 59, 845-848.

132. DOBBINS, R.A., CROCCO, L. and GLASSMAN, I. "Measurement of mean particle sizes of sprays from diffractively scattered light", Amer. Inst. Astro & Aero. J. 1963 1 (8), 1882-1886.

133. ROBERTS, J.H. and WEBB, M.J. "Measurement of droplet size for wide range particle distributions", Amer. Inst. Astro & Aero. J. 1964 2 (3), 583-585.

134. RIZKALLA, A.A. and LEFEBVRE, A.H. "Influence of liquid properties on air-blast atomiser spray characterstics", J. Engng. Power (Trans. ASME) 1975 97 (2), 173-179.

135. BRYAN, R., GODBOLE, P.S. and NORSTER, E.R. "Some observations of the atomising characteristics of air-blast atomisers", Cranfield Int. Symp. Series, Vol 11, "Combustion and heat transfer in gas turbine systems", Ed. Norster, E.R. 1971, 343-359.

136. LORENZETTO G.E. and LEFEBVRE, A.H. "Measurements of drop size as a plain-jet air-blast atomiser", Amer. Inst. Astro & Aero. J. 1977 15 (7), 1006-1010.

137. ABBIS, J.B. "Theoretical aspects of the determination of particles - size distributions from measurements of scattered light intensity", Royal Aircraft Establishment Farnborough (England), 1970, Technical report 70151.

138. POZHARNOV, V.A. "Measurement of droplet-size spectrum in two-phase flows from low-angle light scattering", Fl. Mechs.-Soviet Res. 1975 4 (5), 112-119.

139. ZIMIN, E.P., INOZEMTSEV, O.V., LIVERANT, E.I. and MIKHNEVICH, I.G. "Optical measurements of steam wetness", Teploenergetika 1974 21 (12), 46-49.

140. SWITENBANK, J., BEER, J.M., TAYLOR, D.S., ABBOT, D. and McCREATH, G.C. "A laser diagnostic technique for the measurement of droplet and particle size distribution Amer. Inst. Astro & Aero. - 14th Aerospace Sciences Meeting Washington D.C., 1976, Paper No. 76-69.

141. CORNILLAULT, J. "Particle size analyser", Appl. Optics 1972 11 (2), 265-268.

142. FARMER, W.M. "Measurement of particle size, number density and velocity using a laser interferometer", Appl. Optics 1972 11 (11), 2603-2612.

143. JONES, A.R. "Light scattering by a sphere situated in an interference pattern, with relevance to fringe anemometry and particle sizing", J. Phys.D. Appl. Phys. 1974 7, 1369-1376.

144. HONG, N.S. and JONES, A.R. "A light scattering technique for particle sizing based on laser fringe anemometry", J. Phys.D. Appl. Phys. 1976 9, 1839-1848.

145. YULE, A.J., CHIGIER, N.A., ATAKAN, S. and UNGUT, A. "Particle size and velocity measurement by laser anemometry", Amer. Inst. Astro & Aero. 15th Aerospace Science Meeting, Los Angeles, California, Jan. 24th-26th, 1977, Paper No. 77-214.

146. UNGUT, A., YULE, A.J. TAYLOE, D.S. and CHIGIER, N.A. "Simultaneous velocity and particle size measurements in two-phase flows by laser anemometry", Amer. Inst. Astro & Aero. 16th Aerospace Science Meeting, Jan. 16th-18th, 1978, Huntsville, Alabama, Paper No. 78-74.

147. DURST, F., MELLING, A. and WHITELAW, J.H. "Principles and practice of laser-doppler anomometry", 1976, Academic Press, London.

148. MOORE, M.J., LANGFORD, R.W. and CASTLE, D.A. "Instrumentation developed for the test section of the CERL steam tunnel", 1967, Central Electricity Generating Board, Rep. No. RD/L/N128/66.

149. McCREATH, C.G., ROETT, M.F. and CHIGIER, N.A. "A technique for measurement of velocities and size of particles in flames", J. Phys. E: Scient. Instrums. 1972 5, 601-604.

150. MELLOW, R., CHIGIER, N.A., BEER, J.M. "Pressure jet spray in air stream", Presented at ASME Gas Turb. Conf. & Products Show, Brussels, Belgium, May 24th-28th, 1970, Paper 70-GT-101.

151. YULE, A.J., CHIGIER, N.A. and COX, N.A. "Measurements of particle sizes in sprays by the automated analysis of spark photographs" in "Particle size analysis", Paper 22, Ed. Grooves, M.J. 1978, Heyden, London.

152. FINLAY, I.C. and WELSH, N. "A photographic technique for determining the velocities of liquid droplets flowing in an air stream", J. Photo. Sci. 1968 16, 70-78.

153. REDDY, K.V.S., VAN WIJK, M.C. and PEI, D.C.T. "Stero-photogrammetry in particle-flow investigations", Can. J. Chem. Engng. 1969, 47, 85-88.

154. JONAS, P.R. and KENT, P.M. "Two-dimensional velocity measurement by automatic analysis of trace particle motion", J. Phys. E: Sci. Instrums. 1979 12, 604-609.

155. BENSON, G.M., EL-WAKIL, M.M., MYERS, P.S. and UYEHARA, G.A. "Fluorescent technique for determining the cross-sectional drop size distributions of liquid sprays", Amer. Rocket Soc. J. 1960 30, 447-454.

156. CHUBB, T.W. and ABBISS, J.B. "Particle size measurements by in-line holography", March 1973, Roy. Aircraft Estbl., Tech. Rep. 72229.

157. WEBSTER, J.M. "The application of holography as a technique for size and velocity analysis of high velocity droplets and particles", J. Photo. Sci. 1971 19, 38-44.

158. BEXON, R., GIBBS, J. and BISHOP, G.D. "Automatic assessment of aerosol holograms", J. Aerosol Sci. 1976 7, 397-407.

159. SIMMONS, H.C. and LAPERA, D.J. "A high-speed spray analyser for gas turbine fuel nozzles", ASME Gas Turbine Conf. Session 26, March 12, 1969, Cleveland, Ohio.

160. TONER, M.C., DIX, M.J. and SAWISTOWSKI, H. "A television-microprocesser system for high-speed image analysis", J. Phys. E: Sci. Instrums. 1978 11 (9), 960-966.

161. SADOWSKI, J.W. and BYCKLING, E. "Apparatus for real-time measurement of particle size distribution", Powder Tech. 1978 20, 273-284.

162. COX, A. "Photographic optics" (13th Ed.), 1966 Focal Press, London, (p. 72).

163. RAMSHAW, C. "A technique for drop-size measurement by direct photography and electronic image size analysis", J. Inst. Fuel 1968 41, 288-292.

164. LEWIS, J.D. and WALKER, G. "Drop-size distributions in a liquid spray", The Engneer 1963 216, 512-516.

165. HEYWOOD, H. "A comparison of methods of measuring microscopical particles", Trans. Inst. Mining Metall. 1945 55, 341-404.

166. HERDAN, G. "Small particle statistics", (2nd Edn.), 1960, Butterworths, London.

167. WATSON, H.H. and MULFORD, D.F. "A particle-profile test strip for assessing the accuracy of sizing irregularly shaped particles with a microscale", Br. J. Appl. Phys., Suppl. No. 3 1954, S105-S108.

168. MOORE, M.J., LANGFORD, R.W. and TIPPING, J.C. "Research at CERL on turbine blade erosion", Proc. Instn. Mech. Engrs. 1967-68 182 (3H), 61-68.

169. YORKS, J.L. and STUBBS, H.E. "Photographic analysis of sprays", Trans. of Amer. Soc. Mech. Engrs. 1952 74, 1157-1162.

170. QAQUISH. A. "Alpha-particle detection in nuclear reactors using solid state track recorders", Ph.D. Thesis, Univ. of London (Imperial College), 1978, (Personal Copy).

171. "CAMAC - A modular instrumentation system for data handling", European Atomic Energy Community - EURATOM, Joint Nuclear Research Centre - Ispra Establishment (Italy), ESONE Committee, Luxembourg, March 1969.

172. BLOXHAM, R.D. (Thermal Power Section, Department of Mechanical Engineering, Imperial College, London), private communications, 1979.

173. THOMPSON, D. (Nuclear Power Section, Department of Mechanical Engineering, Imperial College, London), private communications, 1979.

174. MULLER, W. "The Leitz-Texture-Analysing-System", Scientific and Technical Information (Leitz) Suppl. Apr. 1974 4.

175. BOCKSTIEGEL, G. "A calculation technique for the correction of edge errors occuring in determination of size distribution with linear scanning instruments", Prakt. Metallog. 1959 6, 596-602.

176. SATO, M., SHIMIZU, K. and SAKARI, T. "An automatic particle analyser system using an off-line digital computer", J. Inst. of Fuels March 1977 50, 19-22.

177. RINTALA, W.M. and HSU, C.C. "A feature-detection program for patterns and overlapping cells", IEEE Trans. on Systems Science and Cybernetics March 1968 55-4 (1), 16-23.

178. OW, C.S. "Description of hardware and software for an off-line minicomputer based digitising and pattern recognition system", Report TP/C/T802, Thermal Power Section, Department of Mechanical Engineering, Imperial College, London 1978.

179. ROSENFELD, A. "Picture processing by computer", 1969, Academic Press, New York, (p. 16).

180. "Dos-Batch Handbook", Version V9, DEC-11-ODBHA-A-D, Digital Equipment Corp., Maynard, Massachusetts, April 1974.

181. ETELA, D.T. (Nuclear Power Section, Department of Mechanical Engineering, Imperial College, London), private communications, 1979.

182. TURNER, G.W. and MOULTON, R.W. "Drop-size distributions from spray nozzles", Chem. Engng. Progr. 1953 49 (4), 185-190.

183. KIM, K.Y. and MARSHALL, W.R. "Drop-size distributions from pneumatic atomisers", Amer. Instn. Chem. Engrs. J. 1971 17 (3), 575-320.

184. VALHA, J. "Liquid film disintegration on the trailing edges of swept bodies", Strojnicky Casopics 1970 21 (3), 229-238.

185. NUKIYAMA, S. and TANASAWA, Y. "Experiments on the atomisation of liquids in an air stream, Rep. No. 3: - On the droplet size distribution in an at atomised jet", Trans. Soc. Mech. Engrs. (Japan) 1938 5 (18), 62-67. Also available in English translation from N.T.C. ref. AL734.

186. ROSIN, P. and RAMMLER, E. "Law governing the fineness of powdered coal", J. Inst. of Fuel 1933 7 (31), 29-36.

187. SIMMONS, H.C. "The correlation of drop-size distributions in fuelnozzle sprays. Part 1: The drop-size/volume-fraction distribution", J. of Engng. Power (Trans. ASME) 1977 99 (3), 309-314.

188. OW, C.S. and CRANE, R.I. "On the critical Weber number for coarse water formation on steam turbines", J. Mech. Engng. Sci. 1979 21 (5) 353-356.

189. OW, C.S. and CRANE, R.I. "A simple off-line automatic image analysis system with application to drop sizing in two-phase flows", Int. J. Heat and Fluid Flow, 1980 2, 47-53.

190. JOYCE, F.R. "The atomisation of liquid fuels for combustion", J. Inst. of Fuel 1949 22, 150-156.

191. LAPPLE, C.E. "Mist and dust collection in industry and building", Heating Piping and Air Conditioning 1944 16, 635.

192. SELDEN, JR., M.G. "How to mathematically model particle size distributions", Microscope 1976 24, 213-216.

193. WISE, M.E. "Converting a number distribution of particle size into one for volume or surface area", Phillip Res. Rep. 1954 9, 231-237.

194. MARQUARDT, D.W. "An algorithm for least-squares estimation of non-linear parameters", J. Soc. Indust. Appl. Math. 1963 11 (2), 431-441.

195. MARQUARDT, D.W. and STANLEY, R.M. "NLIN 2-least-squares estimation of non-linear parameters", Apr. 1965, Supplement to SDA 3094 (NLIN), mimeo manuscript. IBM SHARE Library, Distribution Number 309401, August, 1966

196. JACKSON, M.R., IGLARSH, H. and SALKOWSHI, M.J. "Sample-size induced errors in the transformation of particle size distributions", Powder Tech. 1969/70 3, 317-322.

197. DRAPER, N. and SMITH, H. "Applied regression analysis", 1966, Wiley-interscience, London, 264-273.

198. SCHLICHTING, H. "Boundary layer theory" (6th Edn.), 1968, McGraw Hill, New York, Chap. 20.

199. BRITISH STANDARD 1042 "Methods for the measurement of fluid flow in pipes - Part 1: Orifice Plates, Nozzles and Venturitubes", British Standards Institution, 1962.

200. LAUFER, J. "The structure of turbulence in fully developed pipe flow", 1954, NACA TN 2954.

201. FRASER, R.P., DOMBROWSHI, N. and ROUTLEY, J.H. "The atomisation of a liquid sheet by an impinging air-stream", Chem. Engng. Sci. 1963 18, 339-353.

202. DENNIS, R. "Handbook on aerosols", 1976 U.S. Energy Research & Development Administration, Technical Information Centre, Tennessee, (p. 44). (Available as TID-26608).

203. CHAPMAN, S. "Spray electrification of liquids", Phys. Rev. 1934 5, 150.

204. WOODS, J.D. "The effect of electric charges upon collisions between equal-size water drops in air", Quart. J. Roy. Met. Soc. 1965 91, 353-355.

205. TELFORD, J.W., THORNDIKE, N.S. and BOWEN, E.G. "The coalescence between small water drops", Quart. J. Roy. Met. Soc. 1955 81, 241-250.

206. KRASNOGORSKAYA, N.V. and NEIZVESTNYY, A.I. "Experimental investigation of collision and coalescence efficiencies of charged drops of equal size", Izvestiya Academy of Sciences, USSR, Atmospheric and Oceanic Physics, 1973 9 (4), 220-225.

207. YABLONIK, R.M. and KHAIMOV, V.A. "The slot channel in the moisture collecting system in a passage", Teploenergetika 1973 20 (4), 65-69.

208. SOO, S.L. "Fluid dynamics of multiphase system", Blaisdell Pub. Co., 1967, (p. 135).

209. Ibid. (p. 147).

210. MOODY, L.F. "Friction factors for pipe flow", (Trans. ASME) 1944 66, 671-694.

211. HEWITT, G.F., KING, R.D. and LOVEGROVE, P.C. "Techniques for liquid film and pressure drop studies in an annular two-phase flow", 1962 U.K. Atomic Energy Autherity, Rep. No. R-3764, Harwell.

212. KUBIE, J. and GARDNER, G.C. "Drop sizes and drop dispersion in straight horizontal tubes and in helical coils", Chem. Engng. Sci. 1977 30, 195-202.

213. ZISSELMAR, R. and MOLERUS, O. "Investigation of solid-liquid pipe flow with regard to turbulence modification", Chem. Engng. J. 1979 18, 233-239.

214. FRIEDLANDER, S.K. "Smoke, dust and haze" John Wiley & Sons 1977, New York, (p. 96).

215. LANGSTROTH, G.O. and GILLESPIE, T. "Coagulation and surface losses in disperse systems in still and turbulent air", Trans. Faraday Soc. 1936 32, 1042-1300.

216. LAWN, C.J. "The determination of the rate of dissipation in turbulent pipe flow", J. Fluid Mech. 1971 48 (3), 477-505.

217. SELDON JR. M.G. "The statistical reliability of particle size distributions", Microscope 1977 26, 127-129.

218. RYLEY, D.J. "The behaviour of nucleation fogs within the nozzle boundary layer in the wet steam turbine", J. Mech. Engng. Sci. 1971 13 (3), 190-199.

219. TAYLOR, G.I. "Statistical theory of turbulence Parts 1 - 4", Proc. Roy. Soc. London 1935 151, 421-478.

220. BACHALO, W.D., HESS, C.F. and HARTWELL, C.A. "An instrument for spray droplet size and velocity measurements", American Soc. of Mech. Engrs. 1979 Paper No. 79-WA/GT-13.

221. HAAS, H. "Operating experience with wet steam circuits-turbines, water separators, piping", VGB Kraftwerkstechnik 1974 54 (12), 791-798. (Central Electricity Generating Board Trans. 6726)

222. JONAS, P.R. and KENT, P.M. "Two-dimensional velocity measurement by automatic analysis of trace particle motion", J. Phys. E: Sci. Instrum., 1979 12, 604-609.

ERRATA

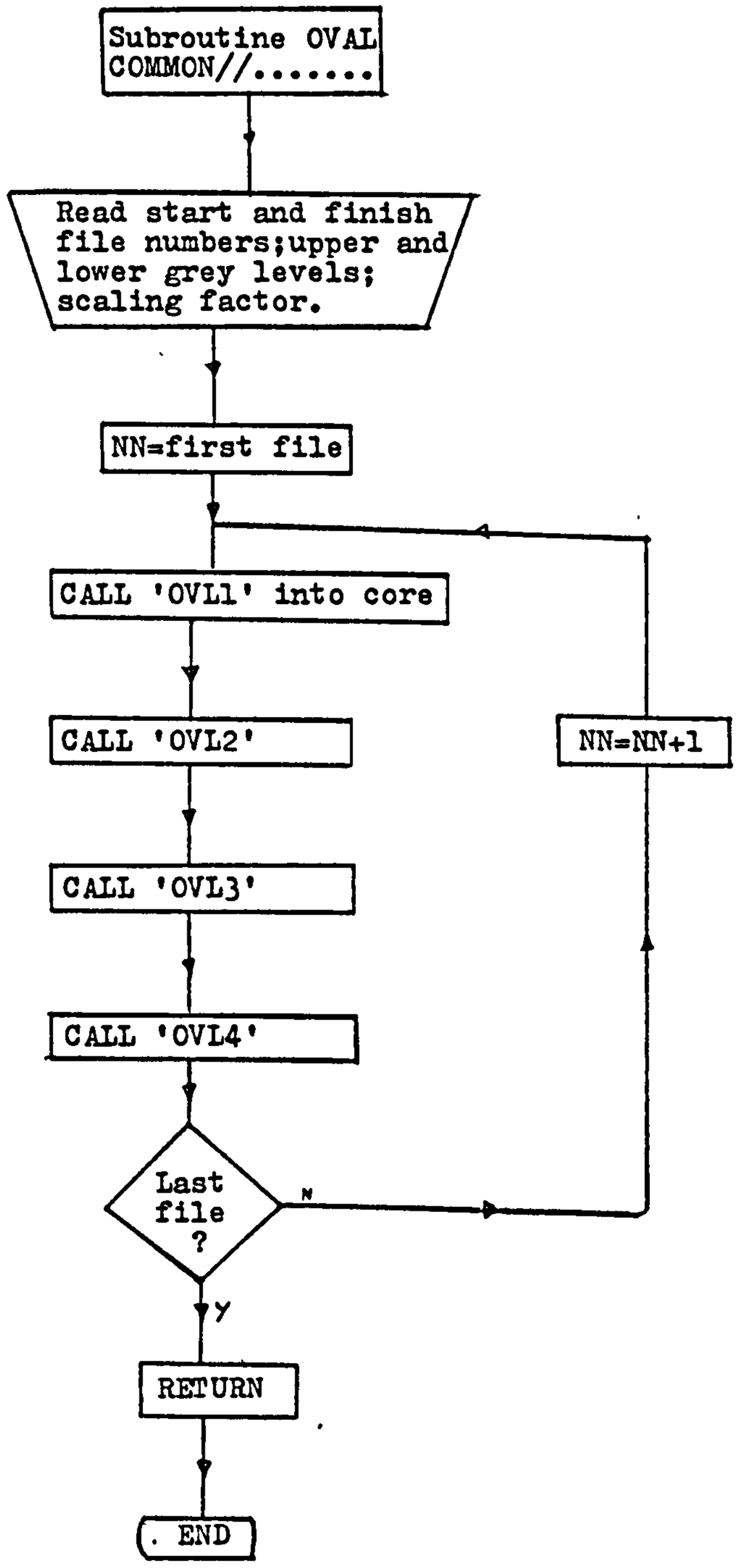
Ref. (154) should read:

DOUGLAS, H.A., HIDE, R. and MASON, P.J. "An investigation of the structure of baroclinic waves using three-level streak photography", Quart. J. Roy. Met. Soc. 1972 98; 247-263.

APPENDIX A1: COMMON ARRAY CONTENTS

Arrays	Elements	Description
COMMON/A/MJ	MJ	Total number of grey levels analysed.
COMMON/B/NFILE,NLAST	NFILE	Current file number.
	NLAST	Terminating file number.
COMMON/C/NE,NB	NE	Highest grey level.
	NB	Starting grey level.
COMMON/D/CS7	CS7	Area scaling factor($\mu m^2/pp^2$)
COMMON/E/M1,M2,M3,M4	M1	Total cells for grey level 4.
	M2	Total cells for grey level 5.
	M3	Total cells for grey level 6.
	M4	Total cells for grey level 7.
COMMON/F/IKK,IRJ	IKK	Error return code for SETFIL calls.
	IRJ	Error return code for SETFIL calls.

APPENDIX A2: OUTLINE FLOWCHART FOR OVAL

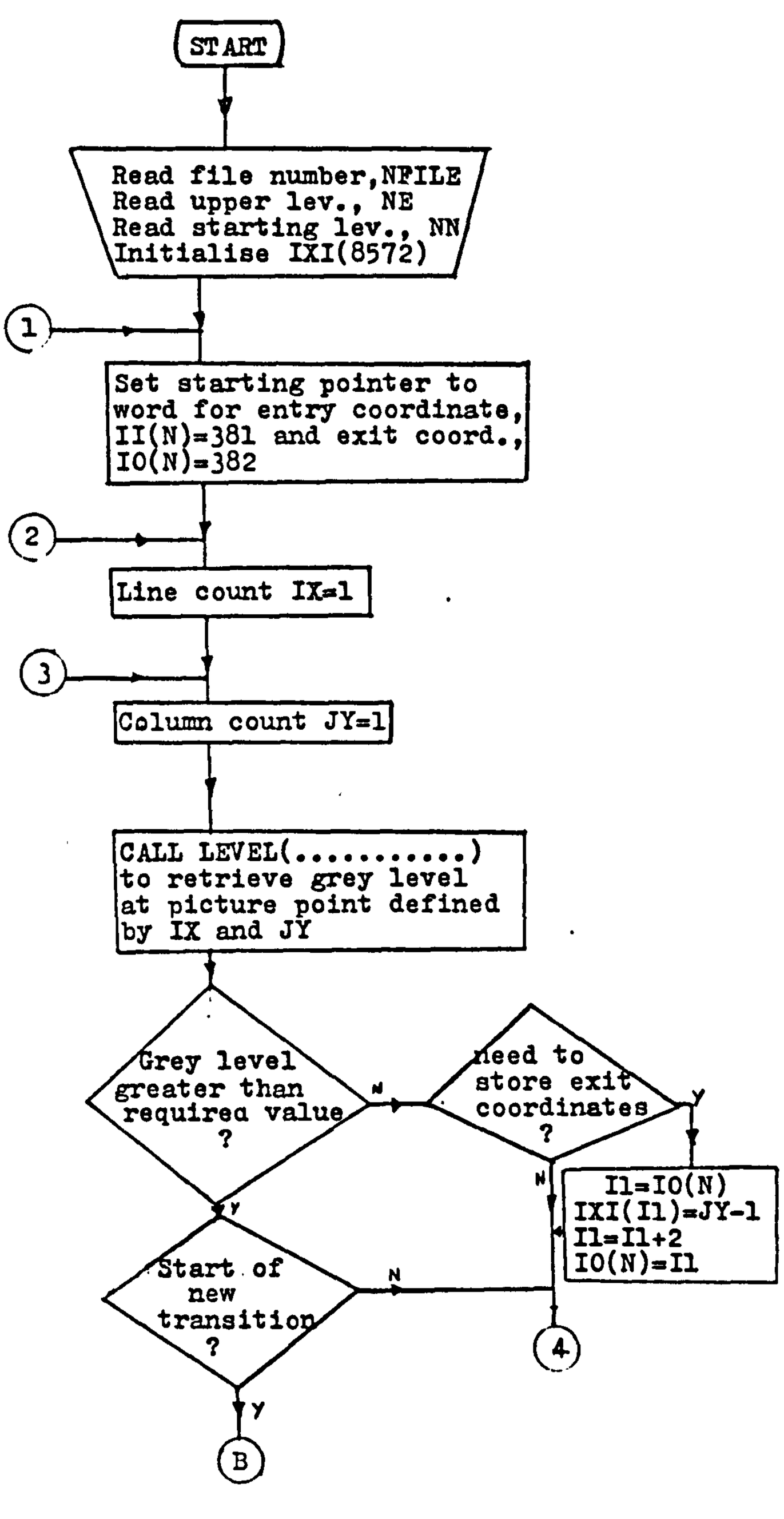


APPENDIX A3: ROUTINE OVL1

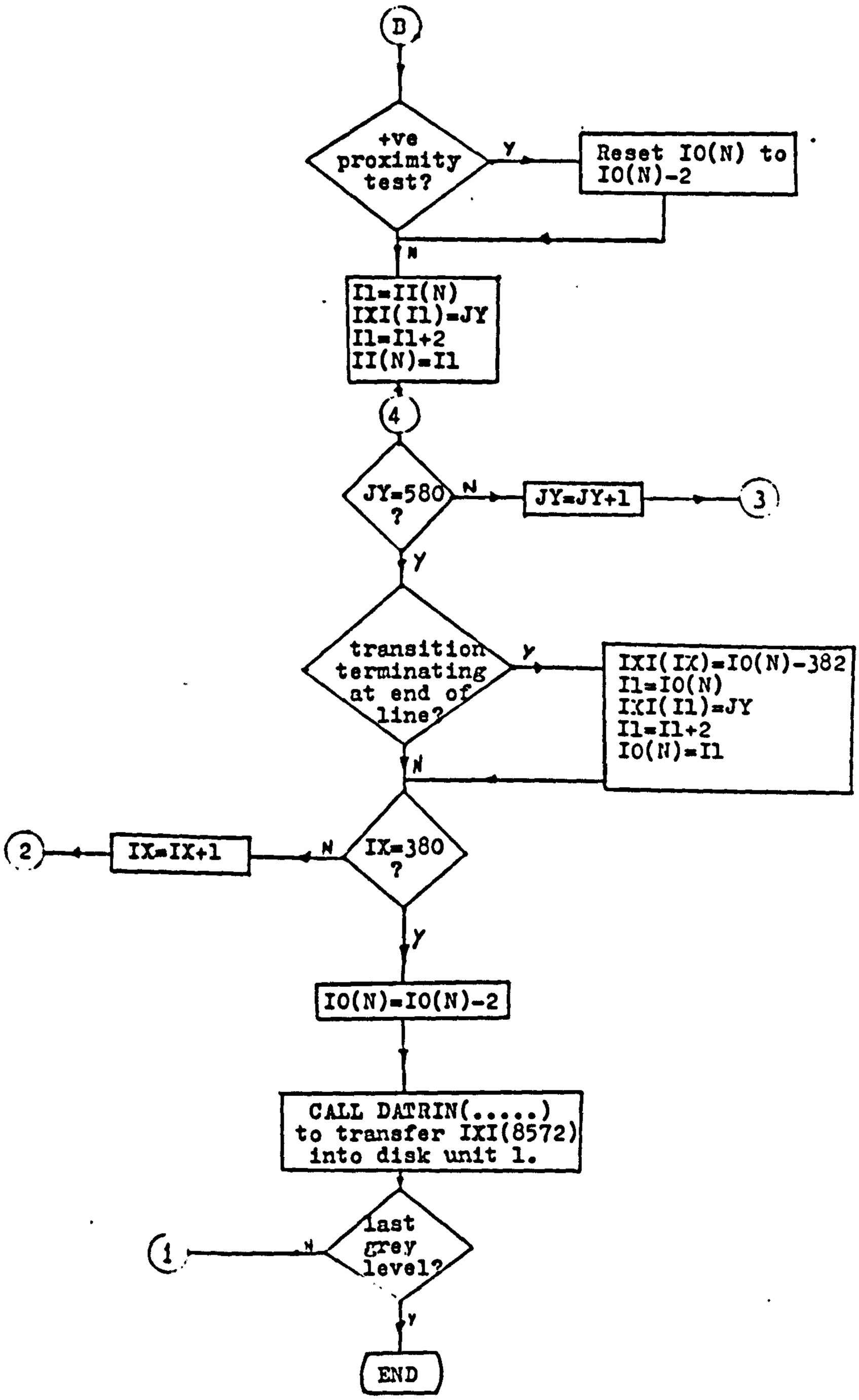
A3.1: List of variables used in OVL1

Variable	Description
IXI(8572)	: A single array for two purposes. The first 380 elements i.e. IXI(1) up to IXI(380) each representing a line, has a cumulative index stored in it. The remaining IXI(381) onwards are used to store the entry and exit coordinate pairs for each transition encountered in the program at a particular grey level .
IO(7)	: Pointer to words containing all exit coordinates only; up to seven grey levels.
II(7)	: Pointer to words containing all entry coordinates only; up to a maximum of seven grey levels.
NFILE	: File number currently analysed
NN	: Grey level at start of analysis (lowest).
NE	: Highest grey level to be analysed.
IFLAG	: When set, indicates that a transition is currently processed and that exit coordinate is next to be determined.

A3.2: Flowchart for OVL1



A3.2 (contd.)


D
+ve proximity test?
Y
Reset IO(N) to IO(N)-2
N
I1=II(N)
IXI(I1)=JY
I1=I1+2
II(N)=I1
4
JY=580 ?
N
JY=JY+1
3
Y
transition terminating at end of line?
Y
IXI(IX)=IO(N)-382
I1=IO(N)
IXI(I1)=JY
I1=I1+2
IO(N)=I1
N
IX=380 ?
N
IX=IX+1
2
Y
IO(N)=IO(N)-2
CALL DATRIN(.....) to transfer IXI(8572) into disk unit 1.
last grey level?
N
1
Y
END

APPENDIX A4: ROUTINE OVL2

A4.1: List of variables used in OVL2

Variable	Description
KM(4096)	: Indexing array for up to a maximum of 4096 transitions.
KY(10), KL(5)	: Arrays for temporary storage of quantities of interest as described below.
NN	: Grey level value.
Element KL(10)	: Initially assigned to zero; subsequently updated to contain "cumulative index" of the last line of the picture sector being analysed.
Element KM( )	: Each represents one transition and into it is stored the transition identity, NM.
NM	: Is the index value of all transition belonging to the same cell.
I6	: Is the dynamic total number of KM( ) transitions starting from KM(1), to be transferred to file 25 of disk unit 1. I6 varies from one grey level to another, depending on the total number of transitions present.
Element KY(1)	: Contains current picture sector's start line number, Y_{start}.

A4.1 (contd.)

Element KY(2) : Contains current picture sector's last line number, Y_{end}.

Element KY(3) : Contains current picture sector's "cumulative index", a pointer to the total number of transition analysed to date.

Element KL(1) : Contains a "cumulative index" for transitions encountered up to the end of the second last line (Y_{end}-1)

M1 : For PDP Fortran operation; (=KY(1))

M2 : For PDP Fortran operation; (=KY(10))

M3 : For PDP Fortran operation;(=KY(9))

L1 : Second last line of current sector being analysed.

N : Line variance in DO loop execution.

Element KY(9) : Contains an accumulating value or cumulative line index for transition parameters at the end of the current line. If this index equals the previous line index, no transition is present in the current line.

Element KL(2) : Contains "cumulative index" for transitions encountered at end of current+1 line.

Element KL(4) : Initially set to 1; subsequently used in CALL DATOUT statement to

A4.1 (contd.)

: access the cumulative index for current line.

Element KL(5) : Contains cumulative index for current +1 line.

M6 : Set equal to KL(4) for PDP Fortran DO-LOOP.

M7 : Set equal to KL(5) for PDP Fortran DO-LOOP.

KY(6) : Contains X_{in} for transition no. J1.

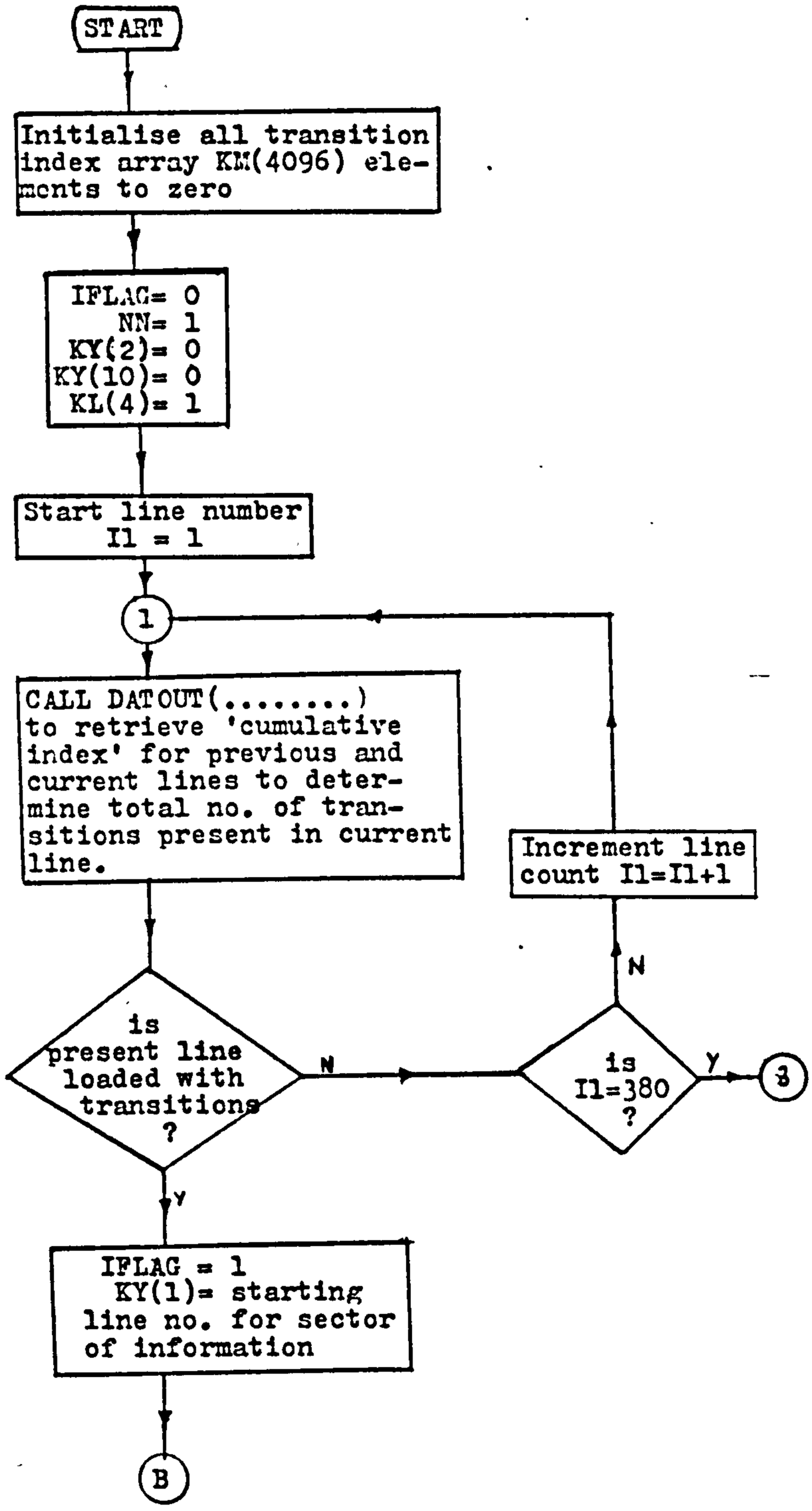
KY(7) : Contains X_{out} for transition no. J1.

J1 : Transition number=(cumulative index J ÷ 2).

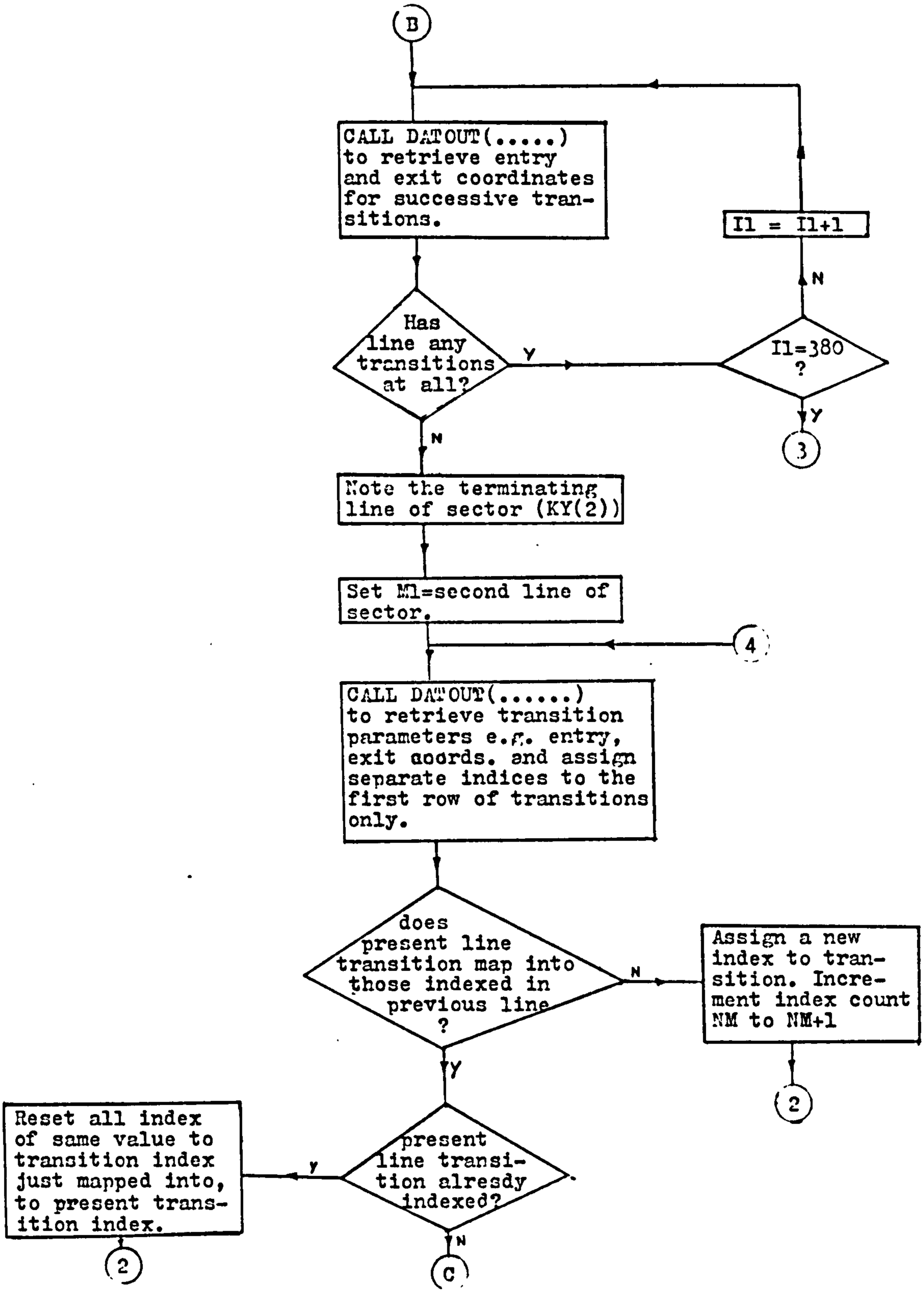
J2 : Equals J-1; is a local variable used by subroutine DATOUT to access X_{in} and X_{out} for transition no. J1.

IS6 : Line index for filtering purposes, used in overlay version to speed up execution by ignoring those cells which only has one cell line.

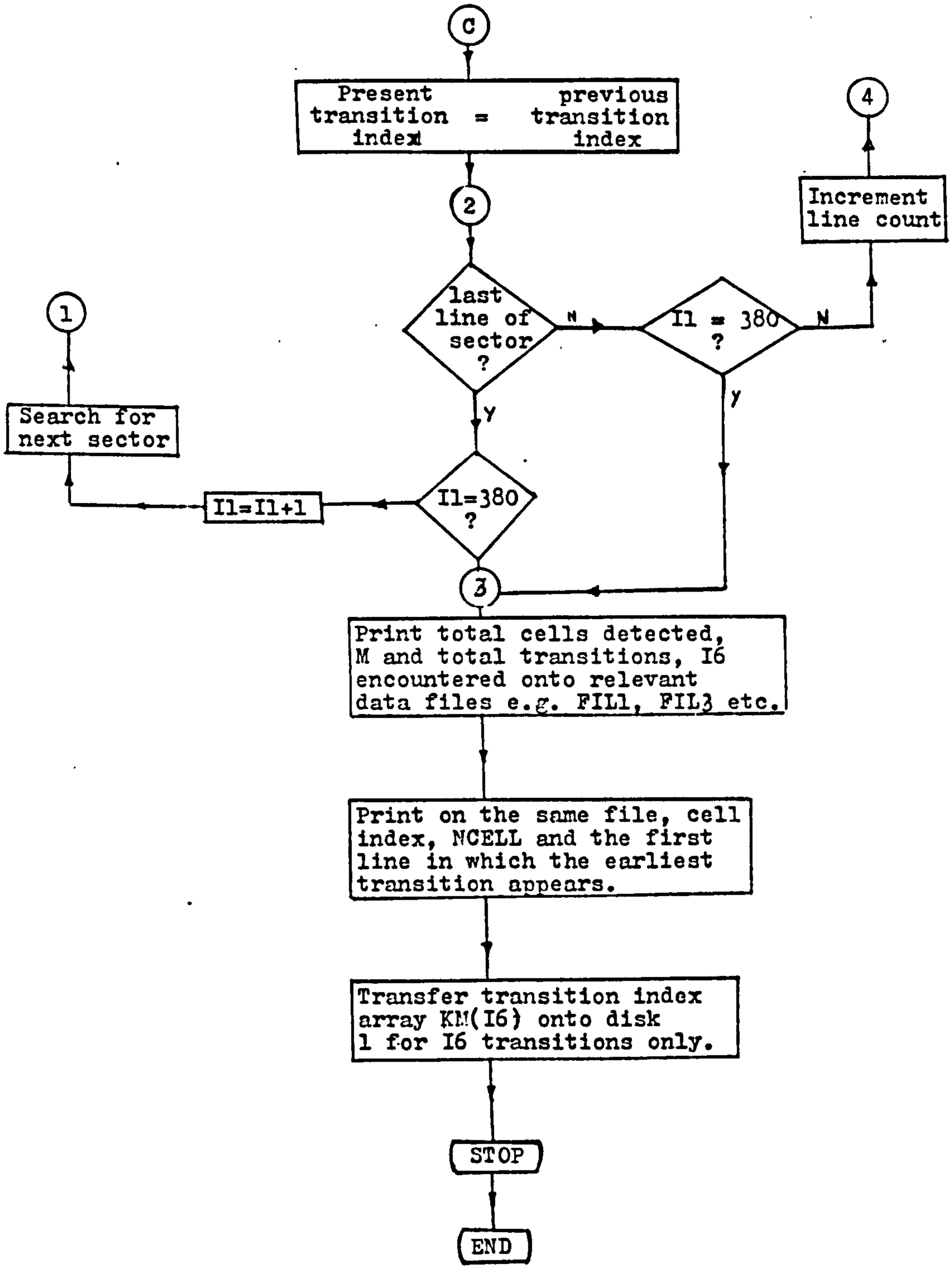
A4.2: Flowchart for single grey level analysis:- OVL2



A4.2 (contd.)


B
CALL DATOUT(.....) to retrieve entry and exit coordinates for successive transitions.
I1 = I1+1
N
Has line any transitions at all?
Y
I1=380 ?
Y
3
N
Note the terminating line of sector (KY(2))
Set M1=second line of sector.
4
CALL DATOUT(.....) to retrieve transition parameters e.g. entry, exit coords. and assign separate indices to the first row of transitions only.
does present line transition map into those indexed in previous line ?
N
Assign a new index to transition. Increment index count NM to NM+1
2
Y
present line transition alresdy indexed?
y
Reset all index of same value to transition index just mapped into, to present transition index.
2
N
C

A4.2 (contd.)


C
Present transition index = previous transition index
2
last line of sector ?
N
I1 = 380 ?
N
Increment line count
4
Y
Y
1
Search for next sector
I1=I1+1
I1=380 ?
3
Print total cells detected, M and total transitions, I6 encountered onto relevant data files e.g. FIL1, FIL3 etc.
Print on the same file, cell index, NCELL and the first line in which the earliest transition appears.
Transfer transition index array KM(I6) onto disk 1 for I6 transitions only.
STOP
END

APPENDIX A5: ROUTINE OVL3

A5.1: List of variables used in OVL3

Variable	Description
KVI(P,Q)	: 2-D array where P represents maximum number of cells lines, Q represents maximum number of transitions allowed in any one line. KVI has one of the following integer value stored eventually: 0:- means to ignore this transition when reassigning cell coordinates into 1-D array e.g. IF, IFI, IFO. 1:- used when indexing void transition to indicate an open void associated with this transition. n:- where 1<n<1000 used for indexing enclosed voids or "void cells". 1000:- when encountered, indicates that this transition is the last transition to appear in the line and no void transition appears after this element.
KXI(P,Q)	: P and Q have the above meaning. KXI are the entry coordinates for all the cell transitions.
KXO(P,Q)	: KXO are the exit coordinates for all

A5.1 (contd.)

: the cell transitions.

MI(P) : P has the above meaning. MI is an array to indicate the total number of transitions present in line number P. At present the maximum allowed is 10.

IF(R) : Array to represent the line coord. of the transition.

IFI(R) : Array to represent the entry coord. of the transition.

IFO(R) : Array to represent the exit coord. of the transition.

R : Total number of transitions describing the cell.

M : Total number of detected cells; value supplied by OVL2.

I6 : Total number of detected transitions; value also supplied by OVL2.

NCELL : Individually confirmed cell index.

KYF : Pointer to the first line of cell NCELL.

I : Absolute cell count.

L : Line counter.

NM : Largest possible number for NCELL.

M1 : Indicator to total number of transitions present in each line describing the cell.

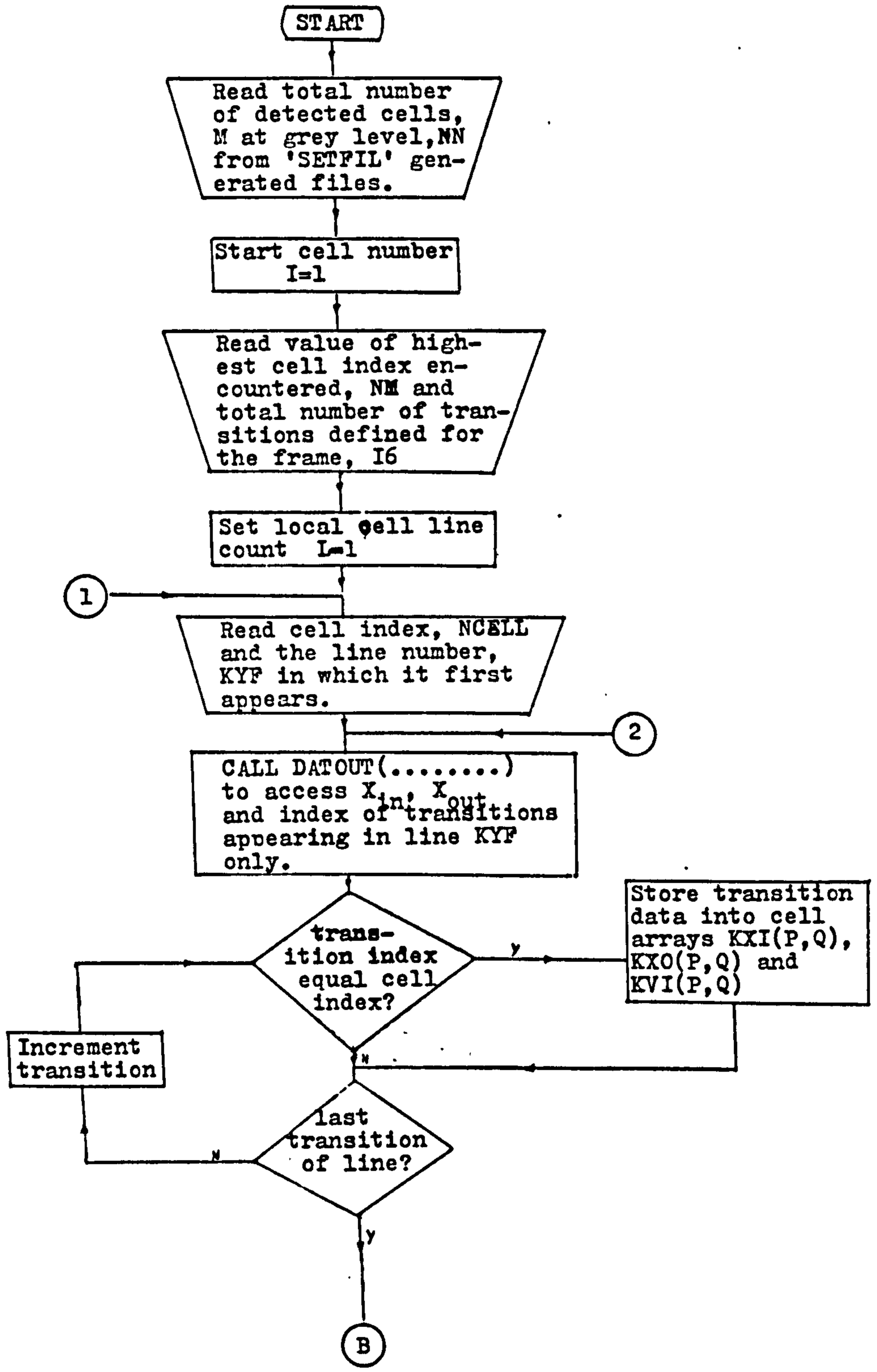
KY(3) : Stores the first transition exit pointer of the line of interest.

KY(4) : Stores the last transition exit point-

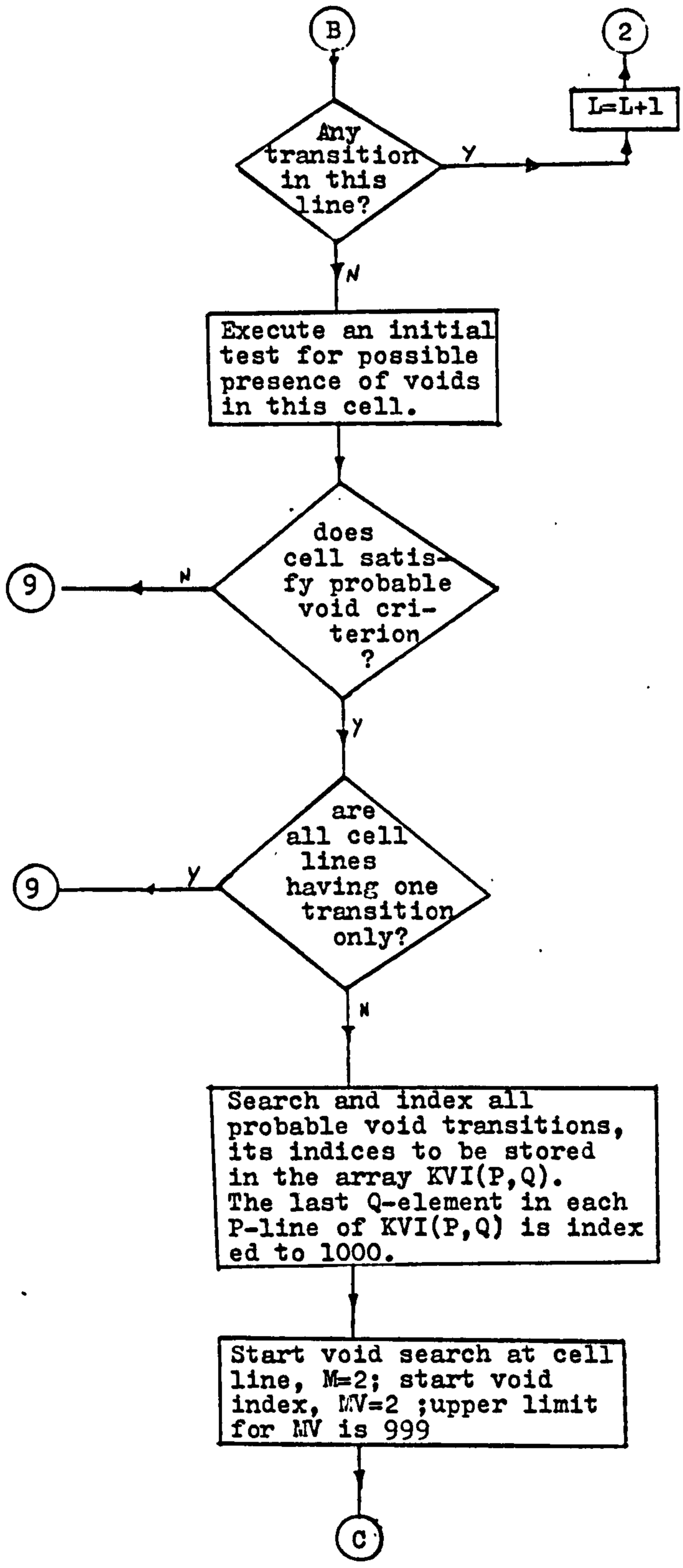
A5.1 (contd.)

	er of the same line above.
J1	: Is pointer to the transition i.e. transition number.
KVL	: Pointer to the last line of cell NCELL
ILINE	: Absolute number of cell lines.
ISEG	: Flag, when set (1) means two or more transitions are present in a cell line ;when all cell lines are analysed and ISEG has the value zero, means each cell line has one transition only.
N	: Local line pointer in void analysis.
MV	: Void index (starting at 2); similar to cell index NM.
IFU	: Flag to enable a jump of execution into an existing DO LOOP.
K2	: Previous line number.
K3	: Current line number.
K5	: Total line transition less 1.
IL	: Total number of transitions in pre - vious line.
IFLAG1	: Set when current void transition maps into a previous void.
ILI	: Pointer to last trans. on current line.
K4	: Pointer to the line's transition (end = K5).

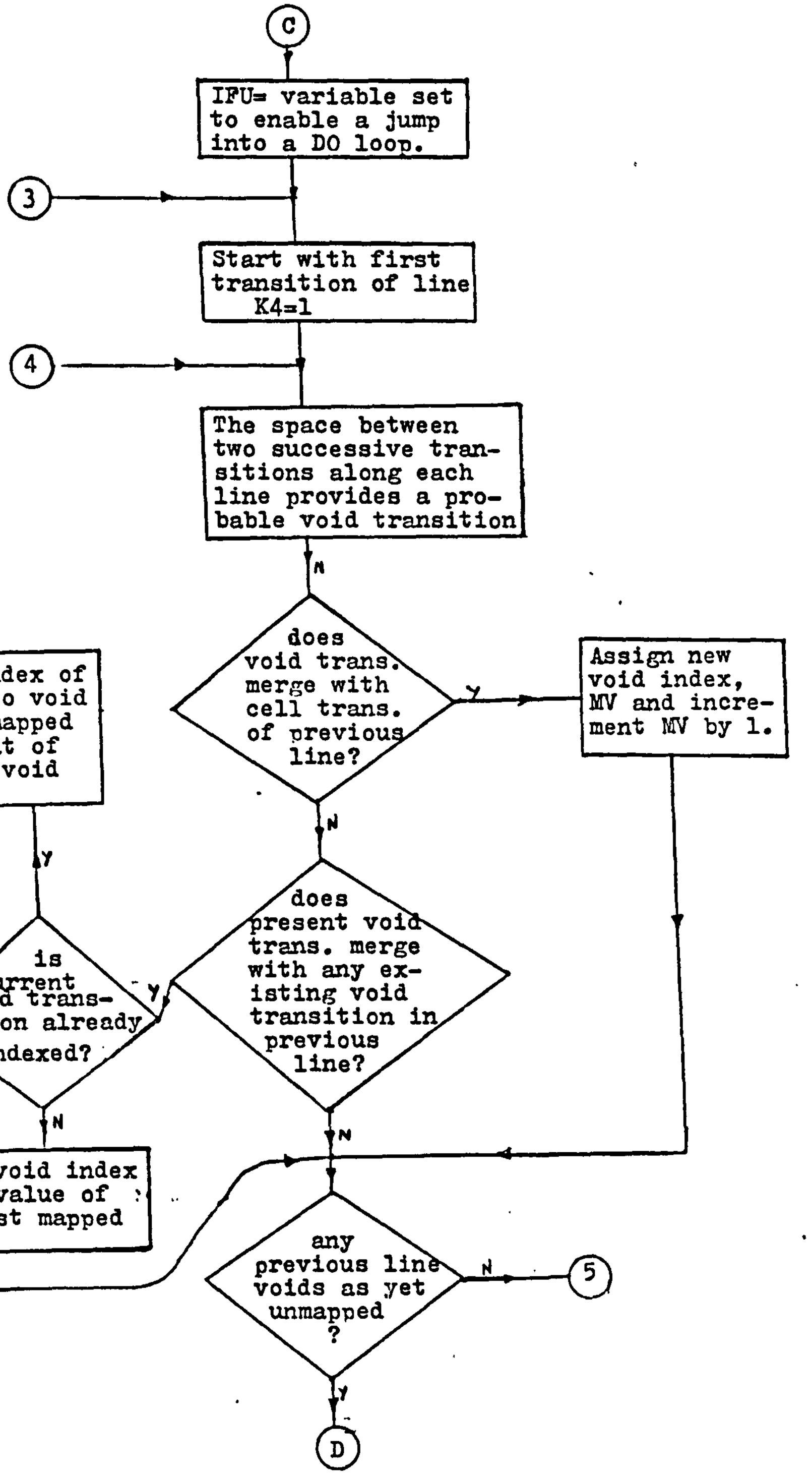
A5.2: Flowchart for single grey level analysis:- OVL3



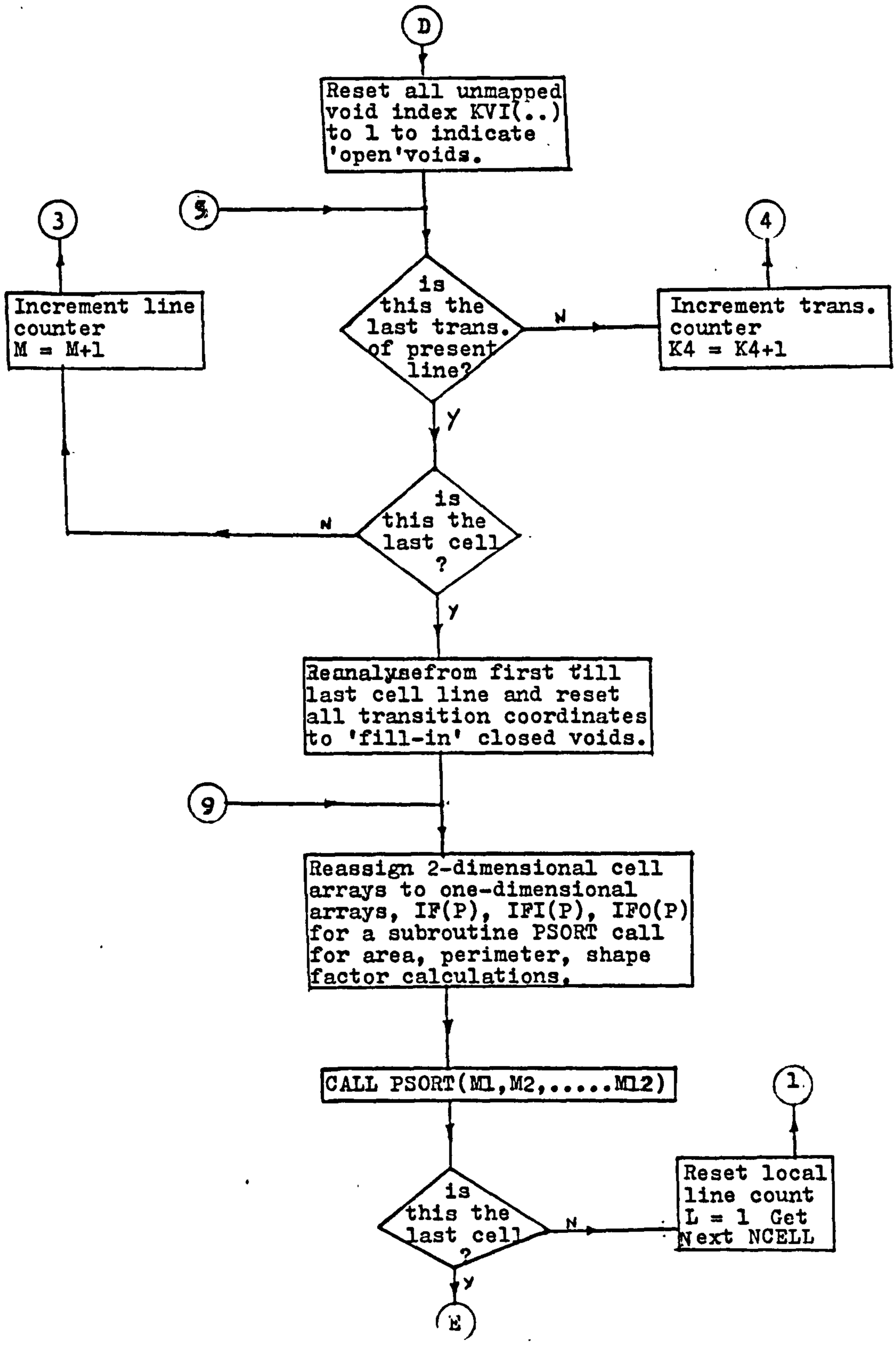
A5.2 (contd.)


B
2
L=L+1
Any transition in this line?
Y
N
Execute an initial test for possible presence of voids in this cell.
does cell satisfy probable void criterion ?
N
9
Y
are all cell lines having one transition only?
9
Y
N
Search and index all probable void transitions, its indices to be stored in the array KVI(P,Q). The last Q-element in each P-line of KVI(P,Q) is indexed to 1000.
Start void search at cell line, M=2; start void index, MV=2 ;upper limit for MV is 999
C

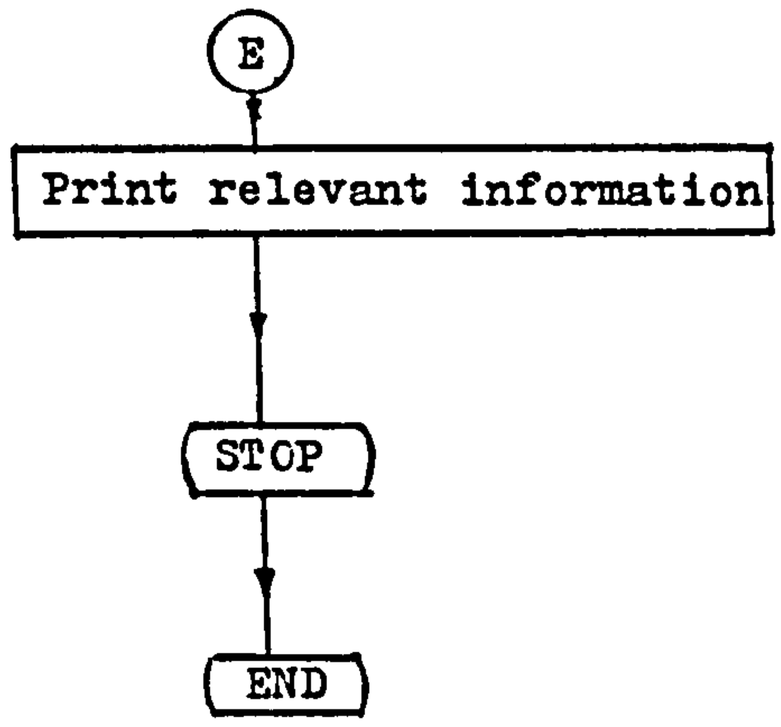
A5.2 (contd.)


C
IFU= variable set to enable a jump into a DO loop.
3
Start with first transition of line K4=1
4
The space between two successive transitions along each line provides a probable void transition
N
does void trans. merge with cell trans. of previous line?
Y
Assign new void index, MV and increment MV by 1.
N
does present void trans. merge with any existing void transition in previous line?
Y
is current void transition already indexed?
Y
Reset all index of same value to void index just mapped into, to that of the present void value.
N
Present void index has the value of index just mapped into.
N
any previous line voids as yet unmapped ?
N
5
Y
D

A5.2 (contd.)


D
Reset all unmapped void index KVI(..) to 1 to indicate 'open'voids.
5
3
4
Increment line counter M = M+1
is this the last trans. of present line?
N
Increment trans. counter K4 = K4+1
Y
is this the last cell ?
N
Y
Reanalysefrom first till last cell line and reset all transition coordinates to 'fill-in' closed voids.
9
Reassign 2-dimensional cell arrays to one-dimensional arrays, IF(P), IFI(P), IFO(P) for a subroutine PSORT call for area, perimeter, shape factor calculations.
CALL PSORT(M1,M2,.....M12)
1
Reset local line count L = 1 Get Next NCELL
is this the last cell ?
N
Y
E

A5.2 (contd.)



APPENDIX A6: ROUTINE OVL4

A6.1: List of variables used in OVL4

Variable	Description
ISAM(P,Q)	: Cell area for level P and cell no. Q.
SFACT(P,Q)	: Cell shape factor for level P and cell number Q.
ILI(P,Q) ILO(P,Q)	: ILO(P,Q)-ILI(P,Q) gives horizontal feret diameter of cell number Q at grey level P.
IYI(P,Q) IYO(P,Q)	: IYO(P,Q)-IYI(P,Q) gives vertical feret : diameter of cell number Q at grey level P.
ICS1	: Cell area on "squared" matrix.
ICS2	: Cell perimeter on "squared" matrix.
ISAM1	: Lowest relevant grey level cell area
SFACT1	: Lowest relevant grey level shape factor.
ILI1 IL01	: (IL01-ILI1) gives horizontal feret dia. at lowest relevant grey level.
IYI1 IY01	: (IY01-IYI1) gives vertical feret dia. of cell at lowest relevant grey lev.
ISAM21	: Cell area on "squared" matrix at lowest relevant grey level.
ISPM21	: Cell perimeter on "squared" matrix at lowest relevant grey level.
NN	: NW+1
NW	: Grey level pointer

A6.1 (contd.)

AIO(1) : Halo width between grey levels 4&5.

AIO(2) : Halo width between grey levels 5&6.

AIO(3) : Halo width between grey levels 6&7.

AIO(4) : Equivalent circular diameter at lev.4

AIO(5) : Equivalent circular diameter at lev.5

AIO(6) : Equivalent circular diameter at lev.6

AIO(7) : Equivalent circular diameter at lev.7

Z1 : (AIO(1)/AIO(4))x100. or percentage halo width based on diameter at grey level 4.

Z2 : Percentage halo width expected of in-focus drop image only.

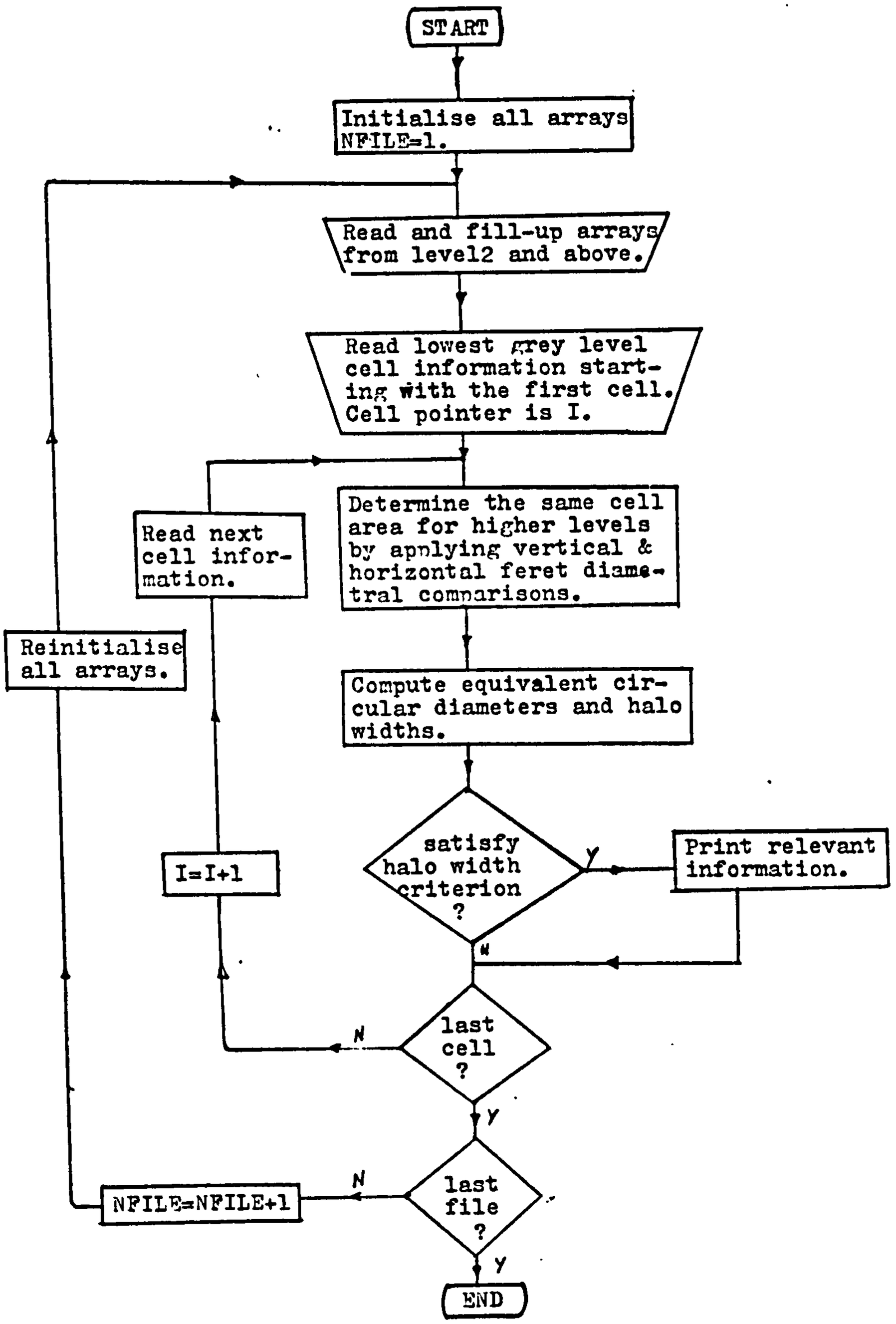
Z3 : Ratio of equivalent circular diameters between grey levels 4&5.

Z4 : Average percentage halo width between grey levels 4&7 based on diameter at grey level 4 ($=(d_{lev4} - d_{lev7})\ 100./6\ d_{lev4}$).

ISUMAM(P) : Total cell area at each grey level P. In the case of a fragmented cell, it represents the sum of all fragmented cell areas.

ISUMPM(P) : Cell perimeter at grey level P.

A6.2: Flowchart for in- and out-of-focus analysis:- OVL4



APPENDIX A7: PROGRAM LISTINGS FOR PATTERN RECOGNITION AND FOCUS DISCRIMINATION.

```
RES     MACRO V06-04A 07-MAY-80 00:50 PAGE 1

1                       .REM@
2
3                       ------------------------------------------------------------
4
5                       RESIDENT PROGRAM: RES
6
7                       CALLS FORTRAN SUBROUTINE OVAL.
8
9                       C.S. OW.
10
11                      ------------------------------------------------------------
12                      @
13
14                              .TITLE RES
15                      ;
16 000000 004567 RES::  JSR R5,OVAL             ;JUMP TO SUBROUTINE OVAL(FORTRN)
           0000006
17 000004 104460        EMT 60                  ;EXIT
18         000000'      .CSECT A                ;COMMON BLOCK A
19 000000 000000 MJ:    0                       ;COMMON BLOCK/A/MJ
20         000030'      .CSECT B                ;COMMON BLOCK /B/NFILE,NLAST
21 000000 000000 NFILE: 0
22 000002 000000 NLAST: 0
23         000006'      .CSECT C                ;COMMON BLOCK/C/ NE,NE
24 000000 000000 NE:    0
25 000002 000000 NE::   0
26         000002'      .CSECT  D               ;COMMON BLOCK /D/  CS7
27 000000 000000 CS7:   0,0
           000002 000000
28         000000'      .CSECT E                ;COMMON BLOCK/E/M1,M2,M3,M4
29 000000 000000 M1:    0
30 000002 000000 M2:    0
31 000004 000000 M3:    0
32 000006 000000 M4:    0
33 000010 000000 IKK:   0
34         000000'      .CSECT F                ;COMMON BLOCK/F/IKK,IRJ
35 000002 000000 IRJ:   0
36         000006'      .CSECT
37         000000'      .END RES


RES     MACRO V06-04A 07-MAY-80 00:50 PAGE 1-1
SYMBOL TABLE

CS7      000000R  005    IKK      000010R  006    IRJ      000002R  007
MJ       000000R  002    M1       000000R  006    M2       000002R  006
M3       000004R  006    M4       000006R  006    NE       000002R  004
NE       000000R  004    NFILE    000000R  003    NLAST    000002R  003
OVAL  = ****** GX       RES      000000RG
. ABS.   000000      000
         000006      001
A        000002      002
B        000004      003
C        000004      004
D        000004      005
E        000012      006
F        000002      007
ERRORS DETECTED:  0
FREE CORE:  13374. WORDS
,LP:<RES
```

```
FORTRAN V09.02                  01:45:12    08-MAY-80    PAGE    1

                C       ------------------------------------------------------------
                C
                C       PROGRAM OVL1
                C
                C       PROGRAM TO REGISTER XIN,YIN AND YOUT AT EACH LEVEL
                C       STARTING AT LEVEL NN UP TO LEVEL NE.
                C       SEARCHING BIT MAP VERTICALLY ALONG X COLUMNS
                C       MAX. NO. OF LEVELS SEARCHED TO BE 1 EACH TIME UP TO 7
                C       DATA FOR EACH LEVEL IS STORED IN FILE 25 AND 26 OF DK1
                C       2 BLOCKS FOR YLINE ACCUMULATING SEG INDICATORFOR IXO'S
                C       ONLY I.E. 2,4,6,ETC ALL EVEN NOS.
                C       16 BLOCKS FOR IXI I.E. (4096)WORDS
                C       16 BLOCKS FOR IXO (4096)ARRAY SIZE
                C       THE 32 BLOCKS CONTAIN ALTERNATE IXI AND IXO'S
                C       /ON AND /SU SWITCHES ARE TO BE USED DURING COMPILATION
                C
                C       C.S.ON
                C
                C       ------------------------------------------------------------
0001                    COMMON/A/MJ
0002                    COMMON/B/NFILE,NLAST
0003                    COMMON/C/NE,NB
0004                    DIMENSION KY(10),KL(5)
0005                    DIMENSION IO(7),II(7)
0006                    DIMENSION IXI(8572)
0007                    CALL DELFIL('F1IL',IRJ)
0008                    CALL DELFIL('F2IL',IRJ)
0009                    CALL DELFIL('F3IL',IRJ)
0010                    CALL DELFIL('F4IL',IRJ)
0011                    CALL DELFIL('FILE1',IRJ)
0012                    CALL DELFIL('FILE2',IRJ)
0013                    CALL DELFIL('FILE3',IRJ)
0014                    CALL DELFIL('FILE4',IRJ)
0015                    MJ=NE-NB+1
0016                    I2=0
0017                    KM=0
0018                    N=NB
0019                    NN=1
0020    1               DO 2 I=1,380
0021                    IXI(I)=0
0022    2               CONTINUE
0023                    IFLAG=0
0024                    IO(N)=382
0025                    II(N)=381
0026                    IF(NN.EQ.1)GO TO 20
0027                    K=0
0028                    KY(2)=0
0029                    KY(10)=0
0030                    KL(4)=0
0031                    MFLAG=0
0032                    M11=1
0033    22              CALL DATOUT(1,K,KL(1),0,M11)
0034                    IF(M11.NE.256)GO TO 23
0035                    M11=M11+1
```

```
0036            CALL DATOUT(1,KL(1),IK,0,M11)
0037            M11=M11-1
0038    23      IF(K.EQ.0)GO TO 24
0039            IF((K.EQ.KY(2)).AND.(MFLAG.EQ.0))GO TO 24
0040            IF(MFLAG.EQ.0)GO TO 25
0041            KY(3)=K
0042            IF(KY(3).EQ.KY(2))GO TO 26
0043            IF(M11.EQ.380)GO TO 27
0044            KY(2)=KY(3)
0045            GO TO 24
0046    25      IF(M11.EQ.380)GO TO 28
0047            MFLAG=1
0048            KY(2)=K
0049            KY(1)=M11
0050    24      IXI(M11)=IXI(J2)
0051            IF(M11.EQ.380)GO TO 29
0052            M11=M11+1
0053            GO TO 22
0054    29      IF(MFLAG.EQ.0)GO TO 30
0055    27      KY(2)=M11
0056            GO TO 31
0057    28      KY(1)=M11
0058            GO TO 27
0059    26      MFLAG=0
0060            KY(2)=M11-1
0061    31      J1=KY(1)
0062            J2=KY(2)
0063            GO TO 21
0064    20      J1=1
0065            J2=380
0066    21      DO 10 IX=J1,J2
0067            DO 9 JY=1,580
0068            CALL LEVEL(LEV,IX,JY,NFILE)
0069            IF(LEV.GE.N)GO TO 4
0070            IF(IFLAG.EQ.0)GO TO 9
0071            I1=IO(N)
0072            I2=IX
0073            IX1(I1)=JY-1
0074            I1=I1+2
0075            IO(N)=I1
0076            IFLAG=0
0077            GO TO 9
0078    4       IF(IFLAG.EQ.1)GO TO 9
0079            IF(I2.NE.IX)GO TO 5
0080            KM=IO(N)-2
0081            K1=IXI(KM)+2
0082            IF(JY.GT.K1)GO TO 5
0083            IO(N)=IO(N)-2
0084            IFLAG=1
0085            GO TO 9
0086    5       IFLAG=1
0087            I1=II(N)
0088            IXI(I1)=JY
0089            I1=I1+2
0090            II(N)=I1
```

```
FORTRAN V09.02                          01:45:12     08-MAY-80    PAGE     3

0091     9          CONTINUE
0092                IF( IFLAG.EQ.0 )GO TO 11
0093                I1=IO( N )
0094                I2=IX
0095                IXI( I1 )=JY-1
0096                I1=I1+2
0097                IO( N )=I1
0098                IFLAG=0
0099     11         IXI( IX )=IO( N )-382
0100     10         CONTINUE
0101                IF( NN.EQ.1 )GO TO 30
0102                KY( 2 )=KY( 3 )
0103                IF( M11.EQ.380 )IXI( M11 )=IXI( J2 )
0104                IF( M11.EQ.380 )GO TO 30
0105                GO TO 24
0106     30         IJ=IO( N )-2
0107                CALL DATRIN( NN, IXI( 1 ), 0, IJ )
0108                IF( N.EQ.NE )GO TO 3
0109                N=N+1
0110                NN=NN+1
0111                GO TO 1
0112     3          CALL RETURN
0113                END


ROUTINES CALLED:
DELFIL, DATOUT, LEVEL , DATRIN, RETURN

OPTIONS =/OP:3

BLOCK          LENGTH
MAIN.     18114  (106604)*
A             2       (000004)
B             4       (000010)
C             4       (000010)

**COMPILER ----- CORE**
   PHASE          USED  FREE
DECLARATIVES   00622 10797
EXECUTABLES    01132 10287
ASSEMBLY       01441 14685
```

```
FORTRAN V09.02                  01:46:53    08-MAY-80    PAGE     1

C
C       ------------------------------------------------------------
C
C       PROGRAM OVL2
C
C       PROGRAM EXECUTES A CHAIN SEARCH OF ALL DATA
C       AND ASSIGNS AN IDENTITY TO EACH CELL THUS DETERMINED.
C
C       PROGRAM MUST BE COMPILED WITH /ON SWITCH
C
C       C.S.OW
C
C
C       ------------------------------------------------------------
C

0001            COMMON/A/MJ
0002            COMMON/E/M1,M2,M3,M4
0003            COMMON/F/IKK,IRJ
0004            DIMENSION KM(4096),KY(10),KL(5)
0005            NN=1
0006    85      K=0
0007            KY(2)=0
0008            KY(10)=0
0009            KL(4)=1
0010            NM=1
0011            IFLAG=0
0012            I1=1
0013            DO 101 I=1,4096
0014            KM(I)=0
0015    101     CONTINUE
0016    100     CALL DATOUT(NN,K,KL(1),0,I1)
0017            IF(I1.NE.256)GO TO 200
0018            I1=I1+1
0019            CALL DATOUT(NN,KL(1),IK,0,I1)
0020            I1=I1-1
0021    200     IF(K.EQ.0)GO TO 99
0022            IF((K.EQ.KY(2)).AND.(IFLAG.EQ.0))GO TO 99
0023            IF(IFLAG.EQ.0)GO TO 98
0024            KY(3)=K
0025            IF(KY(3).EQ.KY(2))GO TO 97
0026            IF(I1.EQ.380)GO TO 95
0027            KY(2)=KY(3)
0028            GO TO 99
0029    98      IF(I1.EQ.380)GO TO 69
0030            IFLAG=1
0031            KY(2)=K
0032            KY(1)=I1
0033    99      IF(I1.EQ.380)GO TO 70
0034            I1=I1+1
0035            GO TO 100
0036    70      IF(IFLAG.EQ.0)GO TO 80
0037    95      KY(2)=I1
0038            GO TO 94
```

```
0039     69       KY(1)=I1
0040              GO TO 95
0041     97       IFLAG=0
0042              KY(2)=I1-1
0043     94       L1=KY(2)-1
0044              L2=KY(2)-KY(1)
0045              IF(L2.EQ.0)GO TO 15
0046              M11=KY(1)
0047              DO 41 N=M11,L1
0048              CALL DATOUT(NN,KY(9),KL(2),0,N)
0049              IF(N.NE.256)GO TO 201
0050              N=N+1
0051              CALL DATOUT(NN,KL(2),IK,0,N)
0052              N=N-1
0053     201      IF(KY(9).EQ.KY(10))GO TO 41
0054              KY(10)=KY(10)+2
0055              M22=KY(10)
0056              M33=KY(9)
0057              DO 30 I2=M22,M33,2
0058              I3=I2/2
0059              IF(KM(I3).GE.1)GO TO 21
0060              KM(I3)=NM
0061              NM=NM+1
0062     21       N1=KL(2)-KY(9)
0063              L5=I2-1
0064              CALL DATOUT(NN,KY(4),KY(5),380,L5)
0065              IF(N1.EQ.0)GO TO 30
0066              N1=KY(9)+2
0067              M44=KL(2)
0068              DO 42 J=N1,M44,2
0069              J2=J-1
0070              CALL DATOUT(NN,KY(6),KY(7),380,J2)
0071              IF((KY(7).LT.(KY(4)-2)).OR.(KY(6).GT.(KY(5)+2)))GO TO 42
0072              J1=J/2
0073              IF(KM(J1).LT.1)GO TO 24
0074              M20=N+1
0075              DO 45 NL=M11,M20
0076              K3=NL-1
0077              IF(K3.EQ.0)K3=NL
0078              CALL DATOUT(NN,KL(4),KL(5),0,K3)
0079              IF(K3.NE.256)GO TO 203
0080              K3=K3+1
0081              CALL DATOUT(NN,KL(5),IK,0,K3)
0082              K3=K3-1
0083     203      IF(K3.NE.0)GO TO 46
0084              IF(KL(4).EQ.0)GO TO 45
0085              KL(5)=KL(4)
0086              KL(4)=0
0087              GO TO 47
0088     46       IF(KL(4).EQ.KL(5))GO TO 45
0089     47       KL(4)=KL(4)+2
0090              M6=KL(4)
0091              M7=KL(5)
0092              DO 23 NI=M6,M7,2
0093              K4=NI/2
```

```
FORTRAN V09.02                          01:46:53     08-MAY-80    PAGE     3

0094                IF(KM(K4).EQ.KM(J1))KM(K4)=KM(I3)
0095     23         CONTINUE
0096     45         CONTINUE
0097     24         KM(J1)=KM(I3)
0098     42         CONTINUE
0099     30         CONTINUE
0100                KY(10)=KY(9)
0101     41         CONTINUE
0102                IF(KL(2).EQ.KY(9))GO TO 18
0103                KY(9)=KY(9)+2
0104                M8=KY(9)
0105                M9=KL(2)
0106                DO 25 K1=M8,M9,2
0107                K2=K1/2
0108                IF(KM(K2).GT.0)GO TO 25
0109                KM(K2)=NM
0110                NM=NM+1
0111     25         CONTINUE
0112                KY(10)=KL(2)
0113                GO TO 17
0114     15         CALL DATOUT(NN,KY(9),KL(2),0,KY(1))
0115                IF(KY(1).NE.256)GO TO 204
0116                KY(1)=KY(1)+1
0117                CALL DATOUT(NN,KL(2),1K,0,KY(1))
0118                KY(1)=KY(1)-1
0119     204        M10=KY(9)
0120                M111=KY(10)+2
0121                DO 16 I=M111,M10,2
0122                I4=I/2
0123                KM(I4)=NM
0124                NM=NM+1
0125     16         CONTINUE
0126     18         KY(10)=KY(9)
0127     17         KY(2)=KY(3)
0128                IF(11.EQ.380)GO TO 80
0129                GO TO 99
0130     80         IF(NM.EQ.1)GO TO 151
0131                CALL DATOUT(NN,I6,I5,0,380)
0132                I6=16/2
0133                CALL DATRIN(NN,KM(1),34,I6)
0134                NM=NM-1
0135                GO TO (160,161,162,163)NN
0136     82         WRITE(7,81)NM,16
0137     81         FORMAT(1H ,14I5)
0138                NLINE=0
0139                NCELL=0
0140                DO 150 M=1,NM
0141                N=1
0142     149        IF(KM(N).EQ.M)GO TO 148
0143                IF(N.EQ.I6)GO TO 150
0144                N=N+1
0145                GO TO 149
0146     160        CALL SETFIL(7,'FIL1',IRJ,'DK',0)
0147                GO TO 82
0148     161        CALL SETFIL(7,'FIL3',IRJ,'DK',0)
```

```
0149            GO TO 82
0150    162     CALL SETFIL(7,'FIL5',IRJ,'DK',0)
0151            GO TO 82
0152    163     CALL SETFIL(7,'FIL7',IRJ,'DK',0)
0153            GO TO 82
0154    148     NSEG=N
0155            I5=1
0156    147     CALL DATOUT(NN,NLINE,NS,0,I5)
0157            IF(I5.NE.256)GO TO 205
0158            I5=I5+1
0159            CALL DATOUT(NN,NS,IK,0,I5)
0160            I5=I5-1
0161    205     NLINE=NLINE/2
0162            NS=NS/2
0163            IF((NSEG.GT.NLINE).AND.(NSEG.LE.NS))GO TO 146
0164            IF((NSEG.LE.NLINE).AND.(NSEG.GT.0))GO TO 145
0165            IF(I5.EQ.380)GO TO 150
0166            I5=I5+1
0167            GO TO 147
        C       FILTER OFF IMAGES WHICH DO NOT HAVE MORE THAN ONE T.V.LINE
0168    146     IF(NN.GT.1)GO TO 174
0169            IS6=I5+1
0170            CALL DATOUT(NN,NLINE,NS,0,IS6)
0171            IF(IS6.NE.256)GO TO 170
0172            IS6=IS6+1
0173            CALL DATOUT(NN,NS,IKK,0,IS6)
0174            IS6=IS6-1
0175    170     NCS=(NLINE+2)/2
0176            NCSL=NS/2
0177            DO 177 IH=NCS,NCSL
0178            IF(KM(IH).EQ.M)GO TO 174
0179    177     CONTINUE
0180            GO TO 150
0181    174     I10=I5+1
0182            WRITE(7,81)M,I10
0183            NCELL=NCELL+1
0184            GO TO 150
0185    145     IF(NN.GT.1)GO TO 175
0186            NCS=(NLINE+2)/2
0187            NCSL=NS/2
0188            DO 176 IH=NCS,NCSL
0189            IF(KM(IH).EQ.M)GO TO 175
0190    176     CONTINUE
0191            GO TO 150
0192    175     WRITE(7,81)M,I5
0193            NCELL=NCELL+1
0194            GO TO 150
0195    150     CONTINUE
0196            END FILE 7
0197            GO TO (164,165,166,167)NN
0198    164     M1=NCELL
0199            GO TO 152
0200    165     M2=NCELL
0201            GO TO 152
0202    166     M3=NCELL
```

```
0203            GO TO 152
0204    167     M4=NCELL
0205            GO TO 152
0206    151     WRITE(5,153)
0207    153     FORMAT(1H0,'BLANK FILE')
0208    152     IF(NN.EQ.MJ)GO TO 154
0209            NN=NN+1
0210            GO TO 85
0211    154     CALL RETURN
0212            END
```

ROUTINES CALLED:
DATOUT, DATRIN, SETFIL, RETURN

OPTIONS =/OP:3

BLOCK	LENGTH	
MAIN.	10100	(047350)*
A	2	(000004)
E	8	(000020)
F	4	(000010)

COMPILER ----- CORE

PHASE	USED	FREE
DECLARATIVES	00622	10797
EXECUTABLES	01374	10045
ASSEMBLY	02057	14069

```
FORTRAN V09.02                  01:37:12    08-MAY-80    PAGE     1

        C       ------------------------------------------------------------
        C
        C       PROGRAM OVL3
        C
        C       PROGRAM TO FILL-IN VOIDS OF CELLS.
        C
        C       PROGRAM MUST BE COMPILED WITH /SU AND /ON SWITHCES
        C
        C       C.S.OW
        C
        C       ------------------------------------------------------------
        C
        C
0001            COMMON/A/MJ
0002            COMMON/E/M1,M2,M3,M4
0003            COMMON/F/IKK,IRJ
0004            DIMENSION KVI(200,10),KXI(200,10),KXO(200,10)
0005            DIMENSION ISUMAM(4),ISUMPM(4)
0006            DIMENSION KY(10),MI(200),IF(300),IFI(300),IFO(300)
0007            EXTERNAL PSORT
0008            NN=1
0009            ISEG=0
0010    87      GO TO (90,91,92,93)NN
0011    88      GO TO (94,95,96,97)NN
0012    89      READ(7,1)NM,I6
0013    1       FORMAT(1X,1415)
0014            I=1
0015            GO TO (98,99,100,101)NN
0016    102     GO TO (103,104,105,106)NN
0017    98      IFLAG=0
0018            DO 16 IB=1,200
0019            MI(IB)=0
0020            DO 16 JB=1,10
0021            KVI(IB,JB)=0
0022    16      CONTINUE
0023            L=1
0024            READ(7,1)NCELL,KYF
0025            KVF=KYF
0026            IF(KYF.GT.1)GO TO 3
0027            IFLAG=1
0028    4       CALL DATOUT(NN,KY(1),KY(2),0,KYF)
0029            IF(KYF.NE.256)GO TO 22
0030            KYF=KYF+1
0031            CALL DATOUT(NN,KY(2),IR,0,KYF)
0032            KYF=KYF-1
0033    22      IF(IFLAG.EQ.1)GO TO 8
0034            KY(3)=KY(1)+2
0035            GO TO 5
0036    90      M=M1
0037            GO TO 88
0038    91      M=M2
0039            GO TO 88
0040    92      M=M3
0041            GO TO 88
```

```
0042    93      M=M4
0043            GO TO 88
0044    94      CALL SETFIL(7,'FIL1',IRJ,'DK',0)
0045            GO TO 89
0046    95      CALL SETFIL(7,'FIL3',IRJ,'DK',0)
0047            GO TO 89
0048    96      CALL SETFIL(7,'FIL5',IRJ,'DK',0)
0049            GO TO 89
0050    97      CALL SETFIL(7,'FIL7',IRJ,'DK',0)
0051            GO TO 89
0052    8       KY(3)=2
0053            KY(2)=KY(1)
0054            GO TO 5
0055    3       KYF=KYF-1
0056            GO TO 4
0057    5       IF(KY(3).GT.KY(2))GO TO 10
0058            M11=1
0059            M9=KY(3)
0060            M8=KY(2)
0061            DO 6 J=M9,M8,2
0062            J1=J/2
0063            CALL DATOUT(NN,KY(4),KY(5),8704,J1)
0064            IF(KY(4).NE.NCELL)GO TO 6
0065            J2=J-1
0066            CALL DATOUT(NN,KY(7),KY(8),380,J2)
0067            KXI(L,M11)=KY(7)
0068            KXO(L,M11)=KY(8)
0069            IF(L.GT.1)GO TO 85
0070            KVI(L,M11)=1
0071    85      M11=M11+1
0072            IF(M11.GT.10)GO TO 800
0073    6       CONTINUE
0074            IF(M11.EQ.1)GO TO 10
0075            IFLAG=0
0076            M11=M11-1
0077            KVI(L,M11)=1000
0078            MI(L)=M11
0079            L=L+1
0080            IF(L.GT.200)GO TO 900
0081            IF(KYF.EQ.379)GO TO 10
0082            KYF=KYF+1
0083            GO TO 4
0084    10      KVL=L-2+KVF
0085            ILINE=L-1
        C       DO INITIAL TEST FOR POSSIBLE VOIDS IN THIS CELL
        C       CRITERION USED IS (ILINE.GE.3).AND.(SEG.LINE.GE.1)
        C       LINE IS SEGMENTED WHEN SEGS.GE.2 IN THE LINE
0086            IF(ILINE.GE.3)GO TO 7
0087            GO TO 9
0088    7       DO 11 L1=1,ILINE
0089            IF(MI(L1).EQ.1)KVI(L1,1)=1000
0090            IF(MI(L1).GE.2)ISEG=1
0091    11      CONTINUE
0092            IF(ISEG.EQ.0)GO TO 9
0093            ISEG=0
```

```
      C       START VOIDS SEARCH
      C       EACH TRUE VOID ALONG A LINE IS ASSIGNED AN INDEX IN KV1.
      C       VOID UPPER AND LOWER COVER AND VOID TO VOID TRANSITION
      C       MAPPING TEST ARE ALSO CARRIED OUT
0094            N=2
0095            MV=2
0096            IFU=0
0097            DO 69 K3=N,ILINE
0098            K5=MI(K3)-1
0099            IF(K5.EQ.0)IFU=1
0100            K4=1
0101   84       IFLAG1=0
0102            IF(IFU.EQ.1)GO TO 64
      C
      C       UPPER VOID TEST.
      C
      C       LOOK FOR UPPER COVER
      C
0103            K2=K3-1
0104            IN=1
0105            IL=MI(K2)
0106            IF((KXO(K3,K4)+2).LT.KXI(K2,IN)).OR.((KXI(K3,K4+1)-2).GT.
               1KXO(K2,IL)))KVI(K3,K4)=1
0107            IF(K3.EQ.ILINE)KV1(K3,K4)=1
0108            IF(MI(K2).EQ.1)GO TO 61
0109            K7=MI(K2)-1
0110            DO 67 K6=1,K7
0111            IF(K2.EQ.1)KVI(K2,K6)=1
0112            IF(((KXI(K3,K4+1)-2).LE.KXO(K2,K6)).OR.((KXO(K3,K4)+2).GE.
               1KXI(K2,K6+1)))GO TO 67
0113            IF(IFLAG1.EQ.1)GO TO 65
0114            IF((KVI(K3,K4).NE.0).AND.(KVI(K3,K4).NE.KVI(K2,K6)))GO TO 65
0115            KVI(K3,K4)=KVI(K2,K6)
0116            IFLAG1=1
0117            GO TO 67
0118   65       DO 63 N9=N,K2
0119            M7=MI(N9)-1
0120            IF(M7.EQ.0)GO TO 63
0121            DO 14 K9=1,M7
0122            IF(KVI(N9,K9).EQ.KVI(K2,K6))KVI(N9,K9)=KVI(K3,K4)
0123            IFLAG1=1
0124   14       CONTINUE
0125   63       CONTINUE
0126   67       CONTINUE
      C         TEST FOR UNMAPPED VOIDS OF PREVIOUS LINE
0127            IF(IFLAG1.EQ.1)GO TO 64
0128   61       IF(KVI(K3,K4).NE.0)GO TO 64
0129            KVI(K3,K4)=MV
0130            MV=MV+1
0131   64       IFLAG1=0
0132            IFU=0
0133            INI=1
0134            ILI=MI(K3)
0135            K2=K3-1
0136            IF(MI(K2).EQ.1)GO TO 13
```

```
0137                M6=MI(K2)-1
0138                DO 62 K6=1,M6
0139                IF((KXO(K2,K6)+2).GE.KXI(K3,IN1)).OR.((KXI(K2,K6+1)-2).LE.
                   1KXO(K3,ILI))GO TO 62
0140                DO 12 N1=N,K2
0141                M5=MI(N1)
0142                IF(M5.EQ.1)GO TO 12
0143                DO 82 N2=1,M5
0144                IF(KV1(N1,N2).EQ.KVI(K2,K6))KV1(N1,N2)=1
0145                KVI(K2,K6)=1
0146      82        CONTINUE
0147      12        CONTINUE
0148      62        CONTINUE
0149      13        IF((K4.EQ.K5).OR.(K5.EQ.0))GO TO 69
0150                K4=K4+1
0151                GO TO 84
0152      69        CONTINUE
                    C
                    C       FILL UP VOIDS IF ANY
                    C
0153                DO 70 L2=1,ILINE
0154                IF(MI(L2).EQ.1)GO TO 70
0155                K9=MI(L2)-1
0156                DO 18 L3=1,K9
0157                IF(KVI(L2,L3).LE.1)GO TO 18
0158                KXI(L2,L3+1)=KXI(L2,L3)
0159                KV1(L2,L3)=0
0160      18        CONTINUE
0161      70        CONTINUE
                    C
                    C       REASSIGN INDIVIDUAL COORDS INTO ARRAYS IF,IF1,IF0
                    C       DETERMINE AREA AND PERIMETER
0162      9         J3=1
0163                J4=1
0164      46        IF(MI(J4).EQ.0)GO TO 47
0165                J6=MI(J4)
0166                DO 20 J5=1,J6
0167                IF(KVI(J4,J5).LT.1)GO TO 20
0168                IF(J3)=KVF+J4-1
0169                IFI(J3)=KXI(J4,J5)
0170                IFO(J3)=KXO(J4,J5)
0171                J3=J3+1
0172      20        CONTINUE
0173      47        IF(J4.EQ.ILINE)GO TO 44
0174                IF(J4.GT.ILINE)GO TO 2
0175                J4=J4+1
0176                GO TO 46
0177      98        CALL SETFIL(8,'F1IL',IRJ,'DK',0)
0178                GO TO 102
0179      99        CALL SETFIL(8,'F2IL',IRJ,'DK',0)
0180                GO TO 102
0181      100       CALL SETFIL(8,'F3IL',IRJ,'DK',0)
0182                GO TO 102
0183      101       CALL SETFIL(8,'F4IL',IRJ,'DK',0)
0184                GO TO 102
```

```
0185     103      CALL SETFIL(1,'FILE1',IRJ,'DK',0)
0186              GO TO 80
0187     104      CALL SETFIL(1,'FILE2',IRJ,'DK',0)
0188              GO TO 80
0189     105      CALL SETFIL(1,'FILE3',IRJ,'DK',0)
0190              GO TO 80
0191     106      CALL SETFIL(1,'FILE4',IRJ,'DK',0)
0192              GO TO 80
0193     44       KY(10)=J3-1
0194              IF(J3.EQ.1)GO TO 2
0195              CALL PSORT(IF,IFI,IFO,KY(10),ISAM,SFACT,IL1,ILO,IY1,IYO,ISP,ISPA
0196              M10=KY(10)
0197              WRITE(8,15)1,KY(10)
0198              WRITE(8,15)(IF(M9),IFI(M9),IFO(M9),M9=1,M10)
0199              WRITE(8,115)ISAM,SFACT,ILI,ILO,IYI,IYO,ISP,ISPA
0200              WRITE(1,115)ISAM,SFACT,ILI,ILO,IYI,IYO,ISP,ISPA
0201     115      FORMAT(1X,I5,F10.2,8I5)
0202     15       FORMAT(1X,15I5)
0203     2        IF(I.EQ.M)GO TO 81
0204              I=I+1
0205              GO TO 80
0206     800      WRITE(5,802)
0207     802      FORMAT(1X,'LINE SEG EXCEEDED-IMAGE IGNORED')
0208     801      IF(NN.EQ.1)M1=M1-1
0209              IF(NN.EQ.2)M2=M2-1
0210              IF(NN.EQ.3)M3=M3-1
0211              IF(NN.EQ.4)M4=M4-1
0212              IF(I.EQ.M)GO TO 81
0213              I=I+1
0214              GO TO 80
0215     900      WRITE(5,901)
0216     901      FORMAT(1X,'LINE ARRAY EXCEEDED-IMAGE IGNORED')
0217              GO TO 801
0218     81       END FILE 7
0219              END FILE 8
0220              END FILE 1
0221              IF(NN.EQ.MJ)GO TO 86
0222              NN=NN+1
0223              GO TO 87
0224     86       CALL DELFIL('FIL1',IRJ)
0225              CALL DELFIL('FIL3',IRJ)
0226              CALL DELFIL('FIL5',IRJ)
0227              CALL DELFIL('FIL7',IRJ)
0228              CALL RETURN
0229              END

         ROUTINES CALLED:
         PSORT , DATOUT, SETFIL, DELFIL, RETURN

         OPTIONS =/OP:3

         BLOCK        LENGTH
         MAIN.    16570  (100564)*
         A        2      (000004)
         E        8      (000020)
         F        4      (000010)
```

```
**COMPILER ------ CORE**
   PHASE        USED  FREE
DECLARATIVES  00622  10797
EXECUTABLES   01774  09645
ASSEMBLY      02481  13645
```

```
FORTRAN V09.02                  01:43:10     08-MAY-80    PAGE     1

C       ------------------------------------------------------------------
C
C       PROGRAM OVL4
C
C       PROGRAM TO MAP HIGHER LEVEL AREAS AND FERET DIAMETERS ONTO
C       EXISTING LOWEST LEVEL CELLS AND TO APPLY THE FOCUS
C       DISCRIMINATION CRITERION.
C       TOTAL CELLS DETERMINED FOR EACH LEVEL ARE STORED IN FILES:
C       FIL2,FIL4,FIL.6AND  FIL8.
C
C
C       C.S.OW
C
C       ------------------------------------------------------------------
0001            COMMON/A/MJ
0002            COMMON/B/NFILE,NLAST
0003            COMMON/D/CS7
0004            COMMON/E/M1,M2,M3,M4
0005            COMMON/F/IKK,IRJ
0006            DIMENSION ISUMAM(4)
0007            DIMENSION ISAM(2,1050),SFACT(2,1050),ILI(2,1050),ILO(2,1050)
0008            DIMENSION IYI(2,1050),IYO(2,1050),MM(4)
0009            DIMENSION A10(7)
0010            WRITE(5,17)NFILE
0011    17      FORMAT(1X,'FILE:',5X,I2)
0012            DO 18 I=1,4
0013            MM(I)=0
0014            ISUMAM(I)=0
0015    18      CONTINUE
0016            NW=1
0017            MM(1)=M1
0018            MM(2)=M2
0019            MM(3)=M3
0020            MM(4)=M4
0021    7       GO TO (9,10,11)NW
0022    15      NN=NW+1
0023            M11=MM(NN)
0024            IF(M11.EQ.0)GO TO 20
0025            DO 12 I=1,M11
0026            READ(1,51)ISAM(NW,I),SFACT(NW,I),ILI(NW,I),ILO(NW,1),IYI(NW,I)
                1,IYO(NW,I),ICS1,ICS2
0027    51      FORMAT(1X,I5,F10.2,8I5)
0028    12      CONTINUE
0029    20      END FILE 1
0030            IF(NW.EQ.MJ-1)GO TO 13
0031            NW=NW+1
0032            GO TO 7
0033    9       CALL SETFIL(1,'FILE2',IRJ,'DK',0)
0034            GO TO 15
0035    10      CALL SETFIL(1,'FILE3',IRJ,'DK',0)
0036            GO TO 15
0037    11      CALL SETFIL(1,'FILE4',IRJ,'DK',0)
0038            GO TO 15
```

```
0039     13       M11=MM(1)
0040              CALL SETFIL(1,'FILE1',1RJ,'DK',0)
0041              DO 80 I=1,M11
0042              IFLAG=0
0043              DO 19 J=1,4
0044              ISUMAM(J)=0
0045     19       CONTINUE
0046              READ(1,51)ISAM1,SFACT1,ILI1,ILO1,IYI1,IYO1,ISAM21,ISPM21
0047              IF(ISAM1.LE.8)GO TO 80
0048              ISUMAM(1)=ISAM1
0049              MJ1=MJ-1
0050              DO 69 I1=1,MJ1
0051              MI=MM(I1+1)
0052              DO 68 I2=1,MI
0053              IF(IYI(I1,I2).LT.IYI1)GO TO 68
0054              IF(IYO(I1,I2).GT.IYO1)GO TO 68
0055              IF(ILI(I1,I2).LT.ILI1)GO TO 68
0056              IF(ILO(I1,I2).GT.ILO1)GO TO 68
0057              I3=I1+1
0058              ISUMAM(I3)=ISUMAM(I3)+ISAM(I1,I2)
0059     68       CONTINUE
0060     69       CONTINUE
0061              DO 64 I3=4,7
0062              IF(ISUMAM(I3-3).EQ.0)GO TO 64
0063              AIO(I3)=SQRT(FLOAT(ISUMAM(I3-3))*CS7*14./11.)
0064     64       CONTINUE
0065              I2=1
0066     67       IF(ISUMAM(I2).EQ.0)GO TO 70
0067              IF(I2.EQ.4)GO TO 55
0068              I2=I2+1
0069              GO TO 67
0070     55       I2=1
0071     66       I23=I2+3
0072              I24=I2+4
0073              AIO(I2)=(AIO(I23)-AIO(I24))/2.
0074              IF(I2.EQ.3)GO TO 65
0075              I2=I2+1
0076              GO TO 66
0077     65       I2=1
0078     61       I23=I2+3
0079              I24=I2+4
0080              I25=I2+5
0081              Z1=(AIO(I2)/AIO(I23))*100.
0082              Z2=(250./AIO(I23))**1.0
0083              Z3=AIO(I23)/AIO(I24)
0084              Z4=((AIO(I23)-AIO(I25))/(AIO(I23)*4.))*100.
0085              IF(Z1.GT.Z2)GO TO 63

0086              IF(MJ.LE.2)GO TO 100
0087              IF((Z4.GT.Z2).AND.(AIO(I23).GT.25.))GO TO 63
0088     100      WRITE(5,21)I,AIO(I23),SFACT1,Z1,Z2,Z3,AIO(4),AIO(5),
                  1AIO(6),AIO(7)
0089     21       FORMAT(1X,I5,2X,9F8.3)
0090              GO TO 80
0091     63       IF(MJ.LE.2)GO TO 79
```

```
0092            IF((Z3.GT.2.0).OR.(I2.EQ.2))GO TO 79
0093            I2=I2+1
0094            GO TO 61
0095    70      IFLAG=I2-1
0096            I2=1
0097            IF(IFLAG.LE.1)GO TO 79
0098            IFLAG=IFLAG-1
0099    71      I23=I2+3
0100            I24=I2+4
0101            AIO(I2)=(AIO(I23)-AIO(I24))/2.
0102            IF(I2.EQ.IFLAG)GO TO 72
0103            I2=I2+1
0104            GO TO 71
0105    72      I2=1
0106    73      I23=I2+3
0107            I24=I2+4
0108            I25=I2+5
0109            Z1=(AIO(I2)/AIO(I23))*100.
0110            Z2=(250./AIO(I23))**1.
0111            Z3=AIO(I23)/AIO(I24)
0112            Z4=((AIO(I23)-AIO(I25))/(AIO(I23)*4.))*100.
0113            IF(Z1.GT.Z2)GO TO 74
0114            IF(MJ.LE.2)GO TO 102
0115            IF((Z4.GT.Z2).AND.(AIO(I23).GT.25.))GO TO 74
0116    102     WRITE(5,21)I,AIO(I23),SFACT1,Z1,Z2,Z3,AIO(4),AIO(5),
                1AIO(6),AIO(7)
0117            GO TO 80
0118    74      IF(Z3.GT.2.0)GO TO 79
0119            IF(I2.EQ.IFLAG)GO TO 79
0120            I2=I2+1
0121            GO TO 73
0122    79      WRITE(5,78)I,AIO(I23),SFACT1,Z1,Z2,Z3,AIO(4),AIO(5),
                1AIO(6),AIO(7)
0123    78      FORMAT(1X,'*',I4,4X,9F8.3)
0124    80      CONTINUE
0125            WRITE(5,101)
0126    101     FORMAT(1X,'*****************************************')
0127            END FILE 1
0128            CALL RETURN
0129            END

        ROUTINES CALLED:
        SETFIL, SQRT  , FLOAT , RETURN

        OPTIONS =/OP:3

        BLOCK       LENGTH
        MAIN.   26660  (150110)*
        A       2      (000004)
        B       4      (000010)
        D       2      (000004)
        E       8      (000020)
        F       4      (000010)
```

```
**COMPILER ----- CORE**
   PHASE       USED  FREE
DECLARATIVES 00913 10506
EXECUTABLES  01343 10076
ASSEMBLY     01991 14135
```

```
FORTRAN V09.02                  00:52:03     07-MAY-00    PAGE     1

        C       ------------------------------------------------------
        C
        C       SUBROUTINE OVAL
        C
        C
        C       CALLS INTO EXECUTION ROUTINES OVL1,OVL2,OVL3 AND OVL4
        C
        C       C.S.OW.
        C
        C       ------------------------------------------------------
0001            SUBROUTINE OVAL
0002            COMMON/A/MJ
0003            COMMON/B/NFILE,NLAST
0004            COMMON/C/NE,NB
0005            COMMON/D/CS7
0006            COMMON/E/M1,M2,M3,M4
0007            COMMON/F/IKK,IRJ
0008            WRITE(6,1)
0009    1       FORMAT('$START')

0010            READ(6,2)NFILE
0011    2       FORMAT(I2)
0012            WRITE(6,3)

0013    3       FORMAT('$FINISH')
0014            READ(6,2)NLAST
0015            WRITE(6,4)
0016    4       FORMAT('$UPPER')
0017            READ(6,5)NE
0018    5       FORMAT(I1)
0019            WRITE(6,6)
0020    6       FORMAT('$LOWER')
0021            READ(6,5)NB
0022            WRITE(6,7)
0023    7       FORMAT('$SCALE(F10.0)')
0024            READ(6,8)CS7

0025    8       FORMAT(F10.0)
0026    9       CALL LINK('OVL1')
0027            CALL LINK('OVL2')

0028            CALL LINK('OVL3')
0029            CALL LINK('OVL5')
0030            IF(NFILE.EQ.NLAST)GO TO 20
0031            NFILE=NFILE+1
0032            GO TO 9
0033    20      RETURN
0034            END

        ROUTINES CALLED:
        LINK

        OPTIONS =/OP:3

        BLOCK           LENGTH
        OVAL    275     (001046)*
        A       2       (000004)
```

```
        B       4       (000010)
        C       4       (000010)
        D       2       (000004)
        E       8       (000020)
        F       4       (000010)

**COMPILER ------ CORE**
   PHASE        USED  FREE
DECLARATIVES  00843  10576
EXECUTABLES   00863  10556
ASSEMBLY      01180  14946
```

```
FORTRAN V09.02                  01:59:15     08-MAY-80    PAGE     1

C       ------------------------------------------------------------
C
C       SUBROUTINE PSORT
C
C       SUBROUTINE ESTABLISHES CELL AREA, PERIMETER AND SHAPE FACTOR.
C
C
C       C.S.OW
C
C       ------------------------------------------------------------

0001            SUBROUTINE PSORT(M1,M2,M3,M4,M5,FM6,M7,M8,M9,M10,M11,M12)
0002            DIMENSION M1(M4),M2(M4),M3(M4)
0003            I4=M4
0004            IFLAG1=0
0005            IFLAG2=0
0006            IFLAG3=0
0007            IFLAG4=0
0008            IFLAG5=0
0009            ISTXLI=1000
0010            ISTXLO=0
0011            LINE=0
0012            ISAM=0
0013            ISAM2=0
0014            ISPM2=0
0015            ISFACT=0
0016            IF(I4.EQ.0)GO TO 100
0017            IF(I4.EQ.1)GO TO 90
0018            J=1
0019    1       IF(M1(J).EQ.M1(1))GO TO 60
0020            IF(M1(J).EQ.M1(I4))GO TO 70
0021            GO TO 3
0022    60      ISPM1=M3(J)-M2(J)+1
0023            ISPM2=(ISPM1-(ISPM1/2)*2)+ISPM1/2+ISPM2
0024            IFLAG1=1
0025            GO TO 3
0026    70      ISPM1=M3(J)-M2(J)+1
0027            ISPM2=(ISPM1-(ISPM1/2)*2)+ISPM1/2+ISPM2
0028            IFLAG2=1
0029    3       IF(J.EQ.1)GO TO 5
0030            IF(M1(J).EQ.M1(J-1))GO TO 7
0031    5       IFLAG3=0
0032    8       IF(M2(J).LE.ISTXLI)ISTXLI=M2(J)
0033            IF(M3(J).GE.ISTXLO)ISTXLO=M3(J)
0034            IF(IFLAG1.EQ.1)GO TO 10
0035            ISPM1=0
0036            ISAM1=0
0037            N=M2(J)
0038    2       LINE=M1(J)
0039            DO 12 K=1,I4
0040            IF(M1(K).NE.(LINE-1))GO TO 12
0041            IF((N.LE.(M3(K)+2)).AND.(N.GE.(M2(K)-2)))GO TO 17
0042    12      CONTINUE
0043            ISPM1=ISPM1+1
```

```
0044    17      IF(N.EQ.M3(J))GO TO 11
0045            N=N+1
0046            IFLAG5=0
0047            GO TO 2
0048    7       IFLAG3=1
0049            GO TO 8
0050    11      ISPM2=(ISPM1-(ISPM1/2)*2)+ISPM1/2+ISPM2
0051            ISAM1=M3(J)-M2(J)+1
0052            ISAM=M3(J)-M2(J)+1+ISAM
0053            ISAM2=(ISAM1-(ISAM1/2)*2)+ISAM1/2+ISAM2
0054            IFLAG4=1
0055            IFLAG5=0
0056    10      IF(IFLAG2.EQ.1)GO TO 20
0057            ISPM1=0
0058            ISAM1=0
0059            N=M2(J)
0060    15      LINE=M1(J)
0061            DO 14 K=1,I4
0062            IF(M1(K).NE.(LINE+1))GO TO 14
0063            IF((N.LE.(M3(K)+2)).AND.(N.GE.(M2(K)-2)))GO TO 18
0064    14      CONTINUE
0065            ISPM1=ISPM1+1
0066    18      IF(N.EQ.M3(J))GO TO 13
0067            N=N+1
0068            IFLAG5=0
0069            GO TO 15
0070    13      ISPM2=(ISPM1-(ISPM1/2)*2)+ISPM1/2+ISPM2
0071            IFLAG5=0
0072            IF(IFLAG4.EQ.1)GO TO 20
0073            ISAM1=M3(J)-M2(J)+1
0074            ISAM=ISAM+ISAM1
0075            ISAM2=(ISAM1-(ISAM1/2)*2)+ISAM1/2+ISAM2
0076    20      IF(IFLAG3.EQ.1)GO TO 30
0077            ISPM2=ISPM2+2
0078            GO TO 40

0079    30      IF((M3(J-1)+5).LE.M2(J))GO TO 25
0080            ISPM2=ISPM2+2
0081            GO TO 40
0082    25      ISPM2=ISPM2+1
0083    40      IFLAG3=0
0084            IFLAG1=0
0085            IFLAG2=0
0086            IFLAG4=0
0087            IF(J.EQ.I4)GO TO 50
0088            J=J+1
0089            GO TO 1
0090    90      ISPM1=M3(I4)-M2(I4)+1
0091            ISPM2=((ISPM1-(ISPM1/2)*2)+ISPM1/2)*2+ISPM2+2
0092            ISAM=ISAM+M3(I4)-M2(I4)+1
0093            ISAM2=(ISAM-(ISAM/2)*2)+ISAM/2+ISAM2
0094            ISTXLI=M2(I4)
0095            ISTXLO=M3(I4)
0096    50      SFACT=((FLOAT(ISPM2))**2.)/FLOAT(ISAM2)
0097            M11=ISAM2
```

```
0098            M12=ISPM2
0099            M9=M1( 1 )
0100            M10=M1( I4 )
0101            M7=ISTXLI
0102            M8=ISTXLO
0103            M5=ISAM
0104            FM6=SFACT
0105     100    RETURN
0106            END

        ROUTINES CALLED:
        FLOAT

        OPTIONS =/OP:3

        BLOCK        LENGTH
        PSORT   987     (003666)*

        **COMPILER ----- CORE**
           PHASE        USED  FREE
        DECLARATIVES 00622 10797
        EXECUTABLES  01023 10396
        ASSEMBLY     01366 14760
```

```
DATRIN  MACRO V06-04A 08-MAY-80 01:51 PAGE 1


                        .REM @
                        ------------------------------------------------------------

                        SUBROUTINE DATRIN(NN,VAR,STBLK,WORDS)

                        SUBROUTINE CREATES AN ARRAY OF VARIABLE BLOCK SIZE IN DK
                        DEPENDING UPON THE ARGUEMENTS FED IN,THE FIRST ARRAY IS
                        LOCATED IN FILE 25 OF DK1 CONSISTENT WITH DIGITISED DATA
                        FROM THE T.V. CAMERA
                        50 BLOCKS ARE ALLOCATED FOR EACH LEVEL.
                        FIRST 2 BLOCKS CONTAINS TOTAL SEGS FOR EACH LINE
                        NEXT 32 BLOCKS CONTAIN ALTERNATE XIN AND XOUT DATA
                        STBLK=BLOCK OFFSET WITHIN EACH GREY LEV
                        NN=BLOCK OFFSET FOR GREY LEVEL

                        MAXIMUM NO OF GREY LEVELS PERMITTED IS 7

                        C.S.OW                                  11-JAN-79


                        ------------------------------------------------------------

                        @
                        ;
                        ;
                                .TITLE DATRIN
                                .GLOBL TRA.
                                .MCALL .INIT,.WAIT,.TRAN,.RLSE
                        ;
000000 017501 DATRIN::  MOV @2(R5),R1                   ;GET GREY LEVEL
       000002
000004 005301 .         DEC R1
000006 070127           MUL #50.,R1                     ;BLOCK OFFSET FOR TRAN
       000062
000012 010104           MOV R1,R4                       ;SAVE IT
000014 062704           ADD #4320.,R4                   ;ADD IN BLOCK OFFSET FOR
       010340
000020 017501           MOV @6(R5),R1                   ;GET INTERNAL BLOCK OFFS
       000006
000024 060104           ADD R1,R4                       ;ADD TO LEVEL OFFSET
000026 017567           MOV @10(R5),CS2                 ;NO OF WORDS TO TRANSFER
       000010
       000070
000034 016567           MOV 4(R5),CS1                   ;START OF BLOCK MAP
       000004
       000060
000042 010467           MOV R4,TRNBLK
       000052
000046                  .INIT #LNKDK
000054                  .TRAN #LNKDK,#TRNBLK
000066                  .WAIT #LNKDK
000074                  .RLSE #LNKDK
000102 000205           RTS R5
000104 104060 ALLDON:   EMT 60                          ;EXIT
000106 000104'          ALLDON
000110 000000 LNKDK:    0
000112 012707           .RAD50/CSO/
```

```
DATRIN  MACRO V06-04A 08-MAY-80 01:51 PAGE 1-1


49 00114     001            .BYTE 1,1
   00115     001                 .
50 00116 015270             .RAD50/DK/
51 00120 000000 TRNBLK:     .WORD 0
52 00122 000000 CS1:        .WORD 0
53 00124 000000 CS2:        .WORD 0
54 00126 000002             .WORD 2,0
   00130 000000
55       000000'            .END DATRIN
```

```
DATRIN  MACRO V06-04A 08-MAY-80 01:51 PAGE 1-2
SYMBOL TABLE

ALLDON  000104R          CS1     000122R          CS2     000124R
DATRIN  000000RG         LNKDK   000110R          TRA.   = ****** G
TRNBLK  000120R          .SYM   = 000027
. ABS.  000000      000
        000132      001
ERRORS DETECTED:  0
FREE CORE:  12722. WORDS
.LP:<DATRIN
```

```
DATOUT  MACRO V06-04A 08-MAY-80 01:50 PAGE 1


                        .REM @
                        ------------------------------------------------------------

                        SUBROUTINE DATOUT(NN,VAR1,VAR2,STBLK,SEG)

                        SUBROUTINE RETRUNS 2 VALUES,VAR1 AND VAR2 CONSECUTIVELY
                        FOR ANY OF THE 3 ARRAYS WITH A GREY LEVEL TO THE CALLING
                        PROGRAM.
                        STBLK NOW HOLDS EITHER 0,380,OR 8572
                        SEG POINTS TO VAR1 ONLY



                        C. S. OW                                11-JAN-79

                        ------------------------------------------------------------
                        @
                ;
                        .TITLE DATOUT
                        .GLOBL TRA.
                        .MCALL .INIT,.WAIT,.TRAN
                ;
000000 017501 DATOUT::MOV @2(R5),R1             ;GET GREY LEVEL
       000002
000004 005301           DEC R1
000006 070127           MUL #50.,R1             ;BLOCK OFFSET FOR GREY LEV
       000062
000012 010104           MOV R1,R4
000014 062704           ADD #4320.,R4           ;24 FILES BLOCK OFFSET
       010340
000020 017501           MOV @12(R5),R1          ;GET REQUIRED SEGMENT
       000012
000024 005301           DEC R1
000026 017503           MOV @10(R5),R3          ;GET INTERNAL WORD OFFSET
       000010
000032 060301           ADD R3,R1               ;TOTAL WORD OFFSET
000034 010100           MOV R1,R0
000036 105001           CLRB R1
000040 000301           SWAB R1
000042 042700           BIC #177400,R0                  ;GET REMAINDER
       177400
000046 060104           ADD R1,R4                       ;ADD IN REMAINING OFFSET
000050 020467           CMP R4,TRNBLK           ;ALREADY IN CORE?
       001110
000054 001422           BEQ NOTRAN
000056 010467           MOV R4, TRNBLK          ;SET UP TRAN BLOCK
       001102
000062 005767           TST INFLG               ;DATA SET INITED?
       001062
000066 001005           BNE INDONE              ;YES BRANCH
000070                  .INIT #LNKDK
000076 005267           INC INFLG               ;FLAG TO SAY INIT DONE
       001046
000102          INDONE: .TRAN #LNKDK,#TRNBLK
000114                  .WAIT #LNKDK
000122 006300 NOTRAN:   ASL R0                  ;CONVERT WORDS TO ADDRESS COUNT
```

```
DATOUT  MACRO V06-04A 08-MAY-80 01:50 PAGE 1-1

48 00124 062700          ADD #BUFFER,R0              ;POINTER TO WORD
         000150'
49 00130 012001          MOV (R0)+,R1                ;GET CONTENTS OF FIRST WORD
50 00132 010175          MOV R1,@4(R5)               ;RETURN FIRST VALUE
         000004
51 00136 012001          MOV (R0)+,R1                ;GET SECOND VALUE
52 00140 010175          MOV R1, @6(R5)              ;RETURN THIS VA;UE
         000006
53 00144 000205          RTS R5                      ;RETURN
54                 ;
55                 ;
56 00146 104060 ERROR:   EMT 60
57 00150        BUFFER:  .BLKW 400
58 01150 000000 INFLG:   0
59 01152 000146'         ERROR
60 01154 000000 LNKDK:   0
61 01156 014736          .RAD50/DEV/
62 01160    001          .BYTE 1,1
   01161    001
63 01162 015270          .RAD50/DK/
64 01164 000000 TRNBLK:  0,BUFFER,400,4,0
   01166 000150'
   01170 000400
   01172 000004
   01174 000000
65       000000'         .END DATOUT
```

```
DATOUT  MACRO V06-04A 08-MAY-80 01:50 PAGE 1-2
SYMBOL TABLE

BUFFER  000150R          DATOUT  000000RG         ERROR   000146R
INDONE  000102R          INFLG   001150R          LNKDK   001154R
NOTRAN  000122R          TRA.  = ****** G         TRNBLK  001164R
.SYM  = 000027
. ABS.  000000     000
        001176     001
ERRORS DETECTED:  0
FREE CORE:  12758. WORDS
,LP:<DATOUT
```

```
MARK1   MACRO V06-04A 08-MAY-80 00:00 PAGE 1


                        .REM @
                        ------------------------------------------------------------
                        PROGRAM  MARK1

                        PROGRAM READS DATA FROM CAMERA IN 7 GREY LEVELS AND STOR
                        ON DK1 IN A NON FILE STRUCTURED FORMAT TO BE ACCESSED BY

                        ROUTINE 'LEVEL'.
                        5 DATA PER WORD

                        MODIFIED VERSION OF D.'  THOMPSON'S  CAMERA PROGRAM
                        ------------------------------------------------------------

                        @
                        .TITLE MARK1
                        .GLOBL MARK1
                        .MCALL .INIT,.RLSE,.WAIT,.TRAN,.WRITE,.READ,.D2BIN
    164010              ACR=164010
    164000              ADR=164000
    164004              DATA=164004
    164000              DATA1=164000
    164000              TEST=164000
                    ;
000000              MARK1:: .INIT #LNKKB
000006                      .WRITE #LNKKB, #BUFTIT          ; ASK FOR FILE NUMBER
000020                      .WAIT #LNKKB
000026                      .RLSE #LNKKB                    ; RELEASE TO ENSURE ALL
000034                      .INIT #LNKKB
000042                      .READ #LNKKB, #BUFTIT           ; READ THE NUMBER
000054                      .WAIT #LNKKB
000062                      .RLSE #LNKKB
000070                      .D2BIN #BUF
00102 012601                MOV (SP)+, R1                   ; GET THE NUMBER
00104 003735                BLE MARK1                       ; NOT IN RANGE
00106 020127                CMP R1, #25.
      000031
00112 003332                BGT MARK1
00114 005301                DEC R1                          ; CALCULATE FILE OFFSET
00116 070127                MUL #180., R1
      000264
00122 010167                MOV R1, NFILE
      000414
00126 005726                TST (SP)+
00130 012767 CAM2:          MOV #10, ACR                    ; DUMMY READ TO CLEAR SY
      000010
      164010
00136 016700                MOV DATA, R0
      164004
00142 012701                MOV #BUFFER, R1                 ; START ADDRESS FOR LINE
      000544'
00146 010102                MOV R1, R2                      ; ADDRESS WITHIN LINE
00150 012703                MOV #3, R3                      ; SHIFT COUNT WITHIN WOR
      000003
00154 012767                MOV #100000, OLDS
      100000
```

```
MARK1   MACRO V06-04A 08-MAY-80 00:00 PAGE 1-1


          000350
49 00162 012767           MOV #12, ACR
          000012
          164010
50 00170 010067           MOV R0, DATA                    ; SET CAMERA GOING
          164604
51 00174 012700 WAIT:     MOV #10000., R0                 ; WAIT LOOP COUNTER
          023420
52 00200 012767 WAIT1:    MOV #12, ACR
          000012
          164010
53 00206 016704           MOV TEST, R4                    ; TEST IF DATA AVAILABLE
          164600
54 00212 032767           BIT #400, ADR
          000400
          164000
55 00220 001006           BNE GOTDAT                      ; YES, GO AND GET IT
56 00222 005767           TST INDAT                       ; NO, HAS DATA STARTED Y
          000310
57 00226 001764           BEQ WAIT1                       ; NO, WAIT FOR START OF
58 00230 077015           SOB R0, WAIT1                   ; CONTINUE TO WAIT
59 00232 000167           JMP ENDDAT                      ; NO DATA FOR 1000 LOOPS
          000146
60 00236 012767 GOTDAT:   MOV #10, ACR
          000010
          164010
61 00244 016704           MOV DATA1, R4                   ; READ THE DATA
          164600
62 00250 016700           MOV ADR, R0
          164000
63 00254 012767           MOV #1, INDAT                   ; WITHIN DATA FLAG
          000001
          000254
64 00262 005100           COM R0                          ; DATA MUST BE COMPLEMEN
65 00264 010005           MOV R0, R5
66 00266 042705           BIC #177437, R5                 ; GET GREY LEVEL ALONE
          177437
67 00272 042700           BIC #177757, R0                 ; GET ODD/EVEN ALONE
          177757
68 00276 020067           CMP R0, OLDS                    ; SEE IF SAME ODD OR EVE
          000230
69 00302 001422           BEQ SAMIND                      ; YES, CARRY ON
70 00304 005700           TST R0                          ; IF 0, X = X + 1, ELSE
71 00306 001403           BEQ NEWX                        ; VALUE BUT NOW ODD SCAN
72 00310 010102           MOV R1, R2                      ; GO TO START OF LINE AG
73 00312 005003           CLR R3                          ; SHIFT COUNT START FOR
74 00314 000413           BR ODDONE
75 00316 005267 NEWX:     INC XREF                        ; MOV TO NEXT X
          000212
76 00322 016701           MOV XREF, R1
          000206
77 00326 070127           MUL #240., R1                   ; START ADDRESS OFFSET I
          000360
78 00332 062701           ADD #BUFFER, R1                 ; R1 = ADDRESS IN BUFFER
          000544'
79 00336 010102           MOV R1, R2
80 00340 012703           MOV #3, R3
```

```
MARK1   MACRO V06-04A 08-MAY-80 00:00 PAGE 1-2


          000003
81 00344 010067 ODDONE: MOV R0, OLDS
          000162
82 00350 010304 SAMIND: MOV R3, R4                      ; CURRENT SHIFT COUNT
83 00352 162704         SUB #5, R4                      ; SHIFT REQUIRED FOR GRE
          000005
84 00356 072504         ASH R4, R5                      ; MOVE TO CORRECT POSITI
85 00360 050512         BIS R5, (R2)                    ; SET INTO MAP
86 00362 062703         ADD #6, R3
          000006
87 00366 020327         CMP R3, #12.                    ; NEW SHIFT WITHIN SAME
          000014
88 00372 003700         BLE WAIT                        ; YES, LOOK FOR MORE DAT
89 00374 005722         TST (R2)+                       ; MOVE TO NEXT WORD
90 00376 162703         SUB #15., R3                    ; RESET SHIFT COUNT
          000017
91 00402 000674         BR WAIT
92                ;
93 00404 016701 ENDDAT: MOV NPASS, R1                   ; WHICH PASS INDICATOR
          000130
94 00410 070127         MUL #60., R1
          000074
95 00414 066701         ADD NFILE, R1           ; OFFSET FOR FILE NUMBER
          000122
96 00420 010167         MOV R1, TRNBLK                  ; START OF SECTION BLOCK
          074132
97 00424                .INIT #LNKDK
98 00432                .TRAN #LNKDK, #TRNBLK
99 00444                .WAIT #LNKDK
100 0452                .RLSE #LNKDK
101 0460 026727         CMP NPASS, #2                   ; ALL PASSES COMPLETE?
          000054
          000002
102 0466 001420         BEQ ALLDON
103 0470 005267         INC NPASS
          000044
104 0474 005067         CLR XREF
          000034
105 0500 005367         DEC XREF
          000030
106 0504 005067         CLR INDAT
          000026
107 0510 012760         MOV #BUFFER, R0                 ; ZERO THE BUFFER FOR NE
          000544'
108 0514 012701         MOV #15360., R1
          036000
109 0520 005020 DELBUF: CLR (R0)+
110 0522 077102         SOB R1, DELBUF
111 0524 000167         JMP CAN2                        ; GO BACK TO START
          177400
112               ;
113 0530 104060 ALLDON: EMT 60                          ; LAST PASS COMPLETE, EX
114               ;
115               ;
116 0532 177777 OLDS:   177777
117 0534 177777 XREF:   -1
118 0536 000000 INDAT:  0
```

```
MARK1   MACRO V06-04A 08-MAY-80 00:06 PAGE 1-3


119 0540 000000 NPASS:  0
120 0542 000000 NFILE:  0
121 0544        BUFFER: .BLKW 15360.
122 4544 000530'        ALLDON
123 4546 000000 LNKDK:  0
124 4550 014736         .RAD50 /DEV/
125 4552    001         .BYTE 1,1
    4553    001
126 4554 015270         .RAD50 /DK/
127 4556 000000 TRNBLK: 0,BUFFER,15360.,2,0
    4560 000544'
    4562 036000
    4564 000002
    4566 000000
128 4570 000530'        ALLDON
129 4572 000000 LNKKB:  0
130 4574 077174         .RAD50 /TIT/
131 4576 000001         1
132 4600 042420         .RAD50 /KB/
133 4602 000024 BUFTIT: 20.
134 4604 000000         0
135 4606 000024         20.
136 4610    124 BUF:    .ASCII/TYPE FILE NUMBER:-  /
    4611    131
    4612    120
    4613    105
    4614    040
    4615    106
    4616    111
    4617    114
    4620    105
    4621    040
    4622    116
    4623    125
    4624    115
    4625    102
    4626    105
    4627    122
    4630    072
    4631    055
    4632    040
    4633    040
137     000000'         .END MARK1
```

```
MARK1   MACRO V06-04A 08-MAY-80 00:00 PAGE 1-4
SYMBOL TABLE

ACR    = 164010          ADR    = 164000          ALLDON  000530R
BUF      074610R         BUFFER  000544R         BUFTIT  074602R
CAMERA= ****** G         CAM2    000130R         DATA   = 164604
DATA1  = 164600          DELBUF  000520R         ENDDAT  000404R
GOTDAT  000236R          INDAT   000536R.        LNKDK   074546R
LNKKB   074572R          MARK1   000000RG        NEWX    000316R
NFILE   000542R          NPASS   000540R         ODDONE  000344R
OLDS    000532R          SAMIND  000350R         TEST   = 164600
TRNBLK  074556R          WAIT    000174R         WAIT1   000200R
XREF    000534R          .SYM   = 000027
. ABS.  000000      000
        074634      001
ERRORS DETECTED:  0
FREE CORE:  12606. WORDS
,LP:<MARK1
```

```
FORTRAN V09.02                  02:03:30   08-MAY-80   PAGE     1
        C       ------------------------------------------------------------
        C
        C       PROGRAM DIS2
        C
        C       PROGRAM TO DISPLAY BINARY MAP ONTO TEKTRONIX SCREEN
        C
        C       C.S.OW
        C
        C       ------------------------------------------------------------
0001    .       WRITE(6,54)
0002    54      FORMAT('$FILE NUMBER  ')
0003            READ(6,55) NFL
0004     55     FORMAT(I2)
0005     579    WRITE(6,1234)
0006    1234    FORMAT('$LEVEL  ')
0007            READ(6,4321) ILOW
0008     4321   FORMAT(I1)
0009     2      DO 1 IX =4,384
0010            DO 1 IY = 1,580
0011            CALL LEVEL(LEV,IX,IY,NFL)
0012            IF(LEV.LT.ILOW) GO TO 1
0013            CALL DOT2(IX,IY)
0014     1      CONTINUE
0015            PAUSE 111
0016            GO TO 579
0017            END

        ROUTINES CALLED:
        LEVEL , DOT2

        OPTIONS =/OP:3

        BLOCK          LENGTH
        MAIN.    180     (000550)*

        **COMPILER ------ CORE**
           PHASE        USED  FREE
        DECLARATIVES  00702 10717
        EXECUTABLES   00783 10636
        ASSEMBLY      01090 15036
```

```
LEVEL.   MACRO V06-04A 08-MAY-80 00:00 PAGE 1


                        .REM @
                        ------------------------------------------------------------

                        SUBROUTINE LEVEL (LEV,IX,IY,IFILE)

                        SUBROUTINE RETURNS IN LEV THE LEVEL (0-7) OF POINT IX,IY
                        IN THE FILE IFILE
                        X AND Y COORDS START FROM 1, IFILE MUST BE IN THE
                        RANGE 1 TO 24


                                        5 DATA PER WORD

                        ------------------------------------------------------------

                        @
                        .TITLE LEVEL
                        .GLOBL TRA,
                        .MCALL .INIT,.WAIT,.TRAN,.RLSE
000000 017501 LEVEL::   MOV @10(R5), R1
       000010
000004 005301           DEC R1
000006 070127           MUL #180., R1
       000264
000012 010146           MOV R1, -(SP)           ; GET THE FILE NUMBER OFFSET
000014 017501           MOV @4(R5), R1          ; X VALUE
       000004
000020 005301           DEC R1
000022 005000           CLR R0
000024 071027           DIV #127., R0           ; FIND WHICH 127 LINE SECTION
       000177
000030 010001           MOV R0, R1              ; 0, 1 OR 2
000032 070127           MUL #60., R1            ; OFFSET FOR TRAN
       000074
000036 010104           MOV R1, R4              ; (AVOIDS INTEGER OVERFLOW)
000040 010001           MOV R0,R1               ; 0, 1 OR 2 AGAIN
000042 070127           MUL #127., R1           ; X OF START OF THIS SECTION
       000177
000046 010100           MOV R1, R0
000050 017501           MOV @4(R5), R1
       000004
000054 160001           SUB R0, R1              ; X RELATIVE TO START OF SECTION
000056 005301           DEC R1
000060 070127           MUL #120., R1           ; WORDS DUE TO X
       000170
000064 017503           MOV @6(R5), R3          ; Y VALUE
       000006
000070 005303           DEC R3
000072 005002           CLR R2
000074 071227           DIV #5, R2              ; WORDS DUE TO Y
       000005
000100 060201           ADD R2, R1              ; OFFSET INTO MAP
000102 070327           MUL #-3, R3             ; SHIFT COUNT, USED LATER
       177775
000106 010100           MOV R1, R0
000110 105001           CLRB R1
```

```
LEVEL   MACRO V06-04A 08-MAY-80 00:00 PAGE 1-1


47 00112 000301          SWAB R1                        ; BLOCKS INTO MAP, DIVIDE BY 256
48 00114 042700          BIC #177400, R0                ; WORDS INTO THAT BLOCK
         177400
49 00120 060401          ADD R4, R1                     ; ADDSECTION OFFSET
50 00122 062601          ADD (SP)+, R1                  ; FILE NUMBER OFFSET
51 00124 020167          CMP R1, TRNBLK                 ; ALREADY IN CORE?
         012110
52 00130 001422          BEQ NOTRAN
53 00132 010167          MOV R1, TRNBLK                 ; SET UP TRAN BLOCK
         012102
54 00136 005767          TST INFLG                      ;DATASET INITED.?
         012062
55 00142 001005          BNE 1NDONE                     ;YES, BRANGH
56 00144                 .INIT #LNKDK
57 00152 005267          INC INFLG                      ;FLAG TO SAY INIT DONE
         012046
58 00156           INDONE: .TRAN #LNKDK, #TRNBLK
59 00170                 .WAIT #LNKDK                   ; READ INTO CORE BUFFER
60 00176 006300 NOTRAN:  ASL R0                         ; CONVERT WORDS TO ADDRESS COUNT
61 00200 062700          ADD #BUFFER, R0                ; POINTER TO WORD
         000224'
62 00204 011001          MOV (R0), R1                   ; GET DATA WORD
63 00206 072103          ASH R3, R1                     ; BRING DATA TO START OF WORD
64 00210 042701          BIC #177770, R1                ; CLEAR OTHER DATA
         177770
65 00214 010175          MOV R1, @2(R5)                 ; RETURN LEVEL
         000002
66 00220 000205          RTS R5
67                 ;
68                 ;
69 00222 104060 ERROR:   EMT 60
70 00224        BUFFER:  .BLKW 5000
71 12224 000000 INFLG:   0
72 12226 000222'         ERROR
73 12230 000000 LNKDK:   0
74 12232 014736          .RAD50 /DEV/
75 12234    001          .BYTE 1,1
   12235    001
76 12236 015270          .RAD50 /DK/
77 12240 177777 TRNBLK:  177777,BUFFER,5000,4,0
   12242 000224'
   12244 005000
   12246 000004
   12250 000000
78       000000'         .END LEVEL


LEVEL.  MACRO V06-04A 08-MAY-80 00:00 PAGE 1-2
SYMBOL TABLE

BUFFER  000224R          ERROR   000222R          INDONE  000156R
INFLG   012224R          LEVEL   000000RG         LNKDK   012230R
NOTRAN  000176R          TRA.  = ****** G         TRNBLK  012240R
.SYM  = 000027
. ABS.  000000      000
        012252      001
ERRORS DETECTED:  0
FREE CORE:  12722. WORDS
.LP:<LEVEL
```

APPENDIX A8: PROGRAM FOR CONVERTING A NUMBER COUNT TO VOLUME DISTRIBUTION BY REF.(193).

A8.1: List of variables used.

Variable	Mathematical symbol	Description
IT		: Total number of data batches.
IB		: Batch number.
Z		: Scale factor.
N		: No. of size classes.
M		: No. of radial positions.
B(J)		: Lower interval for size class J.
U(J)		: Upper interval for size class J.
ZN(J,K)		: No. count in size class J at radial position K.
WN(K)		: Radial scaling factor.
D(I)		: Class size
SW		: Sum of radial scaling factors.
BM(J)		: Mean diameter of size class J
BNTV(J)		: Class interval.
SUP		: Total number counts.
S(J)		: Number counts at radial position J.
SQ		: Cumulative number count.
T(I)		: Number frequency (%) /size class.
SP(J)	$x^3 P^{-1}(x)$	
SR(J)	$x^2 P^{-1}(x)$	
SU(J)	$xP^{-1}(x)$	
A(J)	$(3/2)\Delta x \int x^2 P^{-1}(x)\, dx$	

A8.2: Program Listings

```
      PROGRAM CS(INPUT,OUTPUT,TAPE5=INPUT,TAPE6=OUTPUT)


C
C     CONVERTING A NUMBER COUNT TO VOLUME BY WISES METHOD
C     OVERALL SPECTRUM WEIGHTED ACCORDING TO SPRAY CONE AREA RADIALLY
C     OUTWARDS. DATA SUBMITTED IN THE FORM OF NUMBER PER SIZE RANGE
C     1-2, 2-3, 3-4 ETC
C
      DIMENSION A(70),B(70),BM(70),BNTV(70),S(70),SP(70),SR(70),ST(70),
     1AN(70),U(70),WN(70),ZN(70,70),T(70)
      DIMENSION D(70),SJ(70),SO(70),AM(70)
      DIMENSION SW(70)
C
C     READ IN NO. OF DIFFERENT BATCHES IT
C
      READ(5,1)IT
    1 FORMAT(I5)
  100 DO  200 J=1,70
      D(J)=1.
      AN(J)=0.
      AM(J)=0.
      SR(J)=0.
      SP(J)=0.
      ST(J)=0.
      SW(J)=0.
      A(J)=0.
      BM(J)=0.
      BNTV(J)=0.
      S(J)=1
      SU(J)=0.
       SO(J)=0.
      T(J)=0.
  200 CONTINUE
C
C     READ INDIVIDUAL BATCH INFORMATION MAG.Z, BATCH NO IB, NO OF DATA
C     SETS N, NO OF RADIAL POSITIONS M, ALSO READ INDIVIDUAL CLASS DATA,
C     LOWER INTERVAL, B(J), UPPER INTERVAL J(J), NO. OF COUNTS ZN(J,K),
C     SCALE FACTOR WN(K).
C
      READ(5,2)Z,IB,N,M
    2 FORMAT(F10.0,3I5)
      DO 1000 I=1,N+1
      D(I)=FLOAT(I)
 1000 CONTINUE
      DO 5 I=1,N
      B(I)=J(I)
      U(I)=J(I+1)
      READ(5,4)(ZN(I,J),J=1,M)
    4 FORMAT(8F10.0)
    5 CONTINUE
      READ(5,4)(WN(K),K=1,M)
      SW=0.
      DO 6 L=1,M
      SW=SW+WN(L)
    6 CONTINUE
      WRITE(6,16) IB
   16 FORMAT(1H0,12HDATA BATCH =,I5)
      DO 400 I=1,N
      WRITE(6,401)(ZN(I,J),J=1,M)
  400 CONTINUE
  401 FORMAT(8F10.3)
C
C     COMPUTE CLASS MEAN BM(J) INTV BNTV(J) WEIGHTED PERCENTAGE NO
C     COUNT S(J)
C
      DO 7 K=1,N
      B(K)=B(K)/Z*1000.
      U(K)=J(K)/Z*1000.
      BM(K)=(B(K)+U(K))/2.
      BNTV(K)=U(K)-B(K)
      SUP=0.
      DO 300 J=1,M
      SUP=SUP+(ZN(K,J)*WN(J))
  300 CONTINUE
      S(K)=SUP/SW
    7 CONTINUE
      SQ=0.
      DO 8 L=1,N
      SQ=SQ+S(L)
    8 CONTINUE
      DO 9 I=1,N
      S(I)=S(I)/SQ
      T(I)=S(I)
    9 CONTINUE
```

```
C
C     PERCENTAGE NO COUNT IS IN S(I)
C     NEXT CONVERT TO VOL BY TRAPEZOIDAL RULE BASED ON WISE METHOD
C     NEED TO KNOW CUMULATIVE NO COUNT FROM UPPER END
C
      CALL INVLST(S,N)
      CALL SUM(S,N)
      CALL INVLST(S,N)
      J=N
   10 SP(J)=S(J)*(B(J)**3)
      SR(J)=S(J)*(B(J)**2)
      SU(J)=S(J)*B(J)
      SV(J)=SV(J+1)+S(J+1)+S(J)
      SO(J)=SO(J+1)+SU(J+1)+SU(J)
      ST(J)=ST(J+1)+SR(J+1)+SR(J)
      IF(J.EQ.1)GO TO 18
      J=J-1
      GO TO 10
   18 J=N
   11 A(J)=SP(J)+(1.5*BNTV(J)*ST(J))
      IF(J.EQ.1)GO TO 12
      J=J-1
      GO TO 11
   12 C=0.
      X30=(A(1)**(1./3.))
      X31=SQRT(A(1)/(B(1)+0.5*BNTV(1)*SV(1)))
      X32=A(1)/((B(1)**2)+(BNTV(1)*SO(1)))
      DO 13 J=1,N
      AN(J)=A(J)-A(J+1)


      C=C+AN(J)
   13 CONTINUE
      DO 15 J=1,N
      AN(J)=AN(J)/ C*100.
      AM(J)=AN(J)
   15 CONTINUE
      CALL INVLST(AN,N)
      CALL SUM(AN,N)
      CALL INVLST(AN,N)
      WRITE(6,17)
   17 FORMAT(1H0,10X,10HCLASS SIZE, 10X,5HMEAN,10X,19HPERCENTAGE NO COU
     1NT,10X,17HPERCENTAGE VOLUME)
      WRITE(6,19)(B(J),U(J),CM(J),T(J),S(J),AM(J),AN(J),J=1,N)
   19 FORMAT(1H0,5X,2F7.2,5X,F9.4,F20.4,F11.4,8X,2F10.4)
      WRITE(6,20)X32,X31,X30
   20 FORMAT(1HC,5HX32 =,F10.4,10X,5HX31 =,F11.4,10X,5HX30 =,F10.4)
      E1=0.
      E2=0.
      E3=0.
      DO 21 M=1,N
      E1=E1+(BM(M)**3)*T(M)
      E2=E2+(B(M)**2)*T(M)
      E3=E3+(B(M)*T(M))
   21 CONTINUE
      XX32=E1/E2
      XX31=SQRT(E1/E3)
      XX30=E1**(1./3.)
      WRITE(6,20)XX32,XX31,XX30
      IF(I.LT.IT)GO TO 100
      STOP
      END


      SUBROUTINE INVLST(X,I)
      DIMENSION X(I)
      IP=FLOAT(I)/2.
      DO 2 L=1,IP
      J=L-1
      M=I-J
      N=1+J
      Y=X(M)
      X(M)=X(N)
      X(N)=Y
    2 CONTINUE
      RETURN
      END

      SUBROUTINE SUM(A,I)
      DIMENSION A(I), B(200)
      M=1
      B(M)=A(1)
      NE=I-1
    1 B(M+1)=B(M)+A(M+1)
      IF(M.EQ.NE) GO TO 2
      M=M+1
      GO TO 1
    2 DO 3 K=1,I
      A(K)=B(K)
    3 CONTINUE
      RETURN
      END
```

APPENDIX A9: NON-LINEAR LEAST SQUARE REGRESSION TECHNIQUE

A9.1: Synopsis of Marquardt's Algorithm

Marquardt's method of least squares estimation of non-linear parameters is summarised and compared with two alternative methods, the linearised approximation and steepest descend, each of which has inherent convergence problems (193).

Assume that the model to which data are fitted can be described by

$$E(y) = f(x, \beta) \qquad \ldots.A9.1$$

where f( ) means function of ( );

$x=(x_1, x_2, x_3, \ldots.x_m)$ is a set of m independent variables;

$=(\beta_1, \beta_2, \beta_3, \ldots.\beta_k)$ represents the set of parameters

and E(y) is the expected value of the dependent variable y.

Denoting the data points as $(Y_i, X_{1i}, X_{2i}, \ldots.. X_{mi})$ for i=1,.....n data sets, the general aim is to minimise the error sum of squares given by

$$S(\beta) = \sum_{u=1}^{n} (Y_u - f(x_u, \beta))^2 \qquad \ldots.A9.2$$

In the linearised approximation technique, $f(x, \beta)$ is expanded as a Taylor's series about $f(x, b)$ where b is the initial estimate of β, and truncated after the first derivative term.

i.e. $f(x, b+\delta_t) = f(x, b) + P\delta_t$ A9.3

where δ_t is a "correction vector" and $P = \sum_{j=1}^{k} \frac{\partial f_i}{\partial b_j}$; i=1,....n ; j=1,....k. Hence

$$S(b) = \sum_{u=1}^{n} \left[Y_u - f(x,b) - P\delta_t \right]^2 \quad \text{.... A9.4}$$

The set of δ_t which will optimise S(b) may be derived by setting $\frac{\partial S}{\partial \delta_t} = 0$, i.e. solving the equation

$$A\ \delta_t = g \quad \text{.... A9.5}$$

where $A^{(kxk)} = P^T P$

$g^{(kxl)} = P^T \left[Y - f(x,b) \right]$,

Y being the set of observed dependent variables. A new estimate for β is next derived by expanding $f(x, \beta)$ about $f(x, b')$ where $b' = b + \delta_t$ and a new estimate δ_t' is derived from Eqn. A9.5, the process being repeated until the convergence criterion set is satisfied.

With the steepest descend method, the correction factor b is given by

$$\delta_g = -\left(\frac{\partial S}{\partial b_1}, \frac{\partial S}{\partial b_2}, \ldots\ldots\ldots\ldots \frac{\partial S}{\partial b_k}\right)^T$$

i.e. the direction of negative gradient of the space defined by the error sum of squares, S. In the above form δ_g is infact equal to g (Eqn. A9.5) in orientation, if both could be viewed as vectors, except for a scale factor.

Marquardt's compromise is to estimate the correction

vector δ from a modified form of Eqn. A9.5 , rewritten as

$$(A + \lambda I)\delta = g \qquad \ldots\ldots A9.6$$

where λ is a positive number and I the unit matrix. Marquardt proved that, for $\lambda \geqslant 0$, any solution for δ in Eqn. A9.6 also optimises S(b) and that as λ tends to infinity, the vector δ rotates towards δ_g and the magnitude of δ simultaneously tends to zero. The correction vector, δ is found to lie within the included angle determined by δ_t and δ_g for any positive λ. Thus starting from a point b of the parameter space, the steepest descend method provides a correction vector δ_g for b which may be the best local direction to move to minimise S, but may not be the best overall direction. The best direction, must, however, be within 90° of δ_g otherwise S will diverge. The Taylors series correction vector δ_t, was monitored by Marquardt to be in the range 80° to 90° from δ_g in most practical problems. Eqn. A9.6 therefore provides a correction vector δ which interpolates between these two extremities, thus combining the best features of both while avoiding their inherent limitations. For further details, refs.(194, 195 and 197) should be consulted.

A9.2: Relevant subroutines for ULDF fit.

Ref.(195) requires the provision of additional subroutines from the user in the determination of optimum values for non-linear parameters. Subroutines to be provided include one which inputs the non-linear equation and another which describes the analytic partial derivatives of the distributed quantity with respect to each parameter. Other requirements e.g. data input format are well documented in ref.(195) and not necessarily be repeated here.

Eqn. 6.3 expressed as a function of x is

$$F(x) = \frac{d\psi}{dx} = \frac{s\, x_m^s\, \delta\ e^{-\delta^2 z^2}}{\sqrt{\pi}\, x\, (x_m^s - x^s)} \qquad \text{where } z = \ln\left[\frac{ax^s}{(x_m^s - x^s)}\right]$$

The partial derivatives with respect to the parameters a, x_m and δ are

$$\frac{\partial F}{\partial a} = -\frac{\delta^3 s2\ x_m^s\ e^{-\delta^2 z^2}}{\sqrt{\pi}\ ax\ (x_m^s - x^s)}\ z \qquad \text{....A9.7}$$

$$\frac{\partial F}{\partial x_m} = \frac{\delta s^2 x_m^s\ e^{-\delta^2 z^2}}{\sqrt{\pi}\, x\, (x_m^s - x^s)2}\left[2x_m^s\ \delta^2 z - x^s\right] \qquad \text{....A9.8}$$

$$\frac{\partial F}{\partial \delta} = \frac{s\ x_m^s\ e^{-\delta^2 z^2}}{\sqrt{\pi}\, x\, (x_m^s - x^s)}\left[1-2\,\delta^2 z^2\right] \qquad \text{....A9.9}$$

A9.3: Labels used by subroutines for ULDF fit.

Fortran label	Mathematical symbol	Meaning
B(1)	δ	shape parameter
P(1)	$\frac{\partial F}{\partial \delta}$	Eqn. A9.9
B(2)	x_m	maximum diameter of spectrum

Fortran label	Mathematical symbol	Meaning
P(2)	$\frac{\partial F}{\partial x_m}$	Eqn. A9.8
B(3)	a	skewness parameter
P(3)	$\frac{\partial F}{\partial a}$	Eqn. A9.7
F	$\frac{d\psi}{dx}$	mass frequency as a function of x
Y(I)	$\left(\frac{d\psi}{dx}\right)_{data}$	mass frequency from experimental data
RES	Y(I)-F	residuals
X(I,1)	x	diameter
A	$x_m^s - x^s$	s = 1 or $\frac{1}{2}$
AB	z	
C	$e^{\delta^2 z^2}$	
T	$x_m^s \ln x_m - x^s \ln x$	
H	$\frac{s\ 2\ \delta^3\ x_m^s}{(x_m^s - x^s)}$	

A9.4: Program listings

Listing of subroutines for ULDF in a form suitable for input into the main program of ref.(195) for:-

(a) s = 1

```
      SUBROUTINE FCODE(Y,X,B,PRNT,F,I,RES)
      DIMENSION Y(500),X(500,10),B(50),PRNT(5)
      COMMON/ACSO/A,AB,C,T,H,G
      A=ABS(B(2))-X(I,1)
      AB=0.5*ALOG((B(3)*(X(I,1)))/A)**2)
      C=EXP((B(1)**2)*(AB**2))
      T=(ABS(B(2))*(0.5*ALOG(B(2)**2)))-(X(I,1)*ALOG(X(I,1)))
      H=(2.*(B(1)**2)*(ABS(B(2))))/A
      F=(B(1)*(ABS(B(2)))*(1./C))/(SQRT(22./7.)*X(I,1)*A)
      RES=Y(I)-F
      RETURN
      END
```

```
 SUBROUTINE PCODE(P,X,B,PRNT,F,I)
 DIMENSION P(50),X(500,10),B(50),PRNT(5)
 COMMON/ACSO/A,AB,C,T,H,G
 P(1)=(ABS(B(2))*(1./C))*(1.-(2.*((B(1)*AB)**2)))/(SQRT(22./7.)*
1X(I,1)*A)
 P(2)=(B(1)*(1./C)*((1.+(H*AB))*A-(ABS(B(2)))))/(SQRT(22./7.)*X(I,1
1)*(A**2))
 P(3)=-((B(1)**3)*2.*ABS(B(2))*(1./C)*AB)/(SQRT(22./7.) *B(3)*
1X(I,1)*A)
 RETURN
 END
```

(b) $s = \frac{1}{2}$

```
 SUBROUTINE FCODE(Y,X,B,PRNT,F,I,RES)
 DIMENSION Y(500),X(500,10),B(50),PRNT(5)
 COMMON/ACSO/A,AB,C,T,H,G
 A=(ABS(B(2))**0.5)-(X(I,1)**0.5)
 AB=0.5*ALOG(((B(3)*(X(I,1)**0.5))/A)**2)
 C=EXP((B(1)**2)*(AB**2))
 T=((ABS(B(2))**0.5)*(0.5*ALOG(B(2)**2)))-((X(I,1)**0.5)* ALOG(X(I,
11)))
 H=(2.*(B(1)**2)*0.5)/A
 F=(B(1)*0.5*(ABS(B(2))**0.5)*(1./C))/(SQRT(22./7.)*X(I,1)*A)
 RES=Y(I)-F
 RETURN
 END
```

```
 SUBROUTINE PCODE(P,X,B,PRNT,F,I)
 DIMENSION P(50),X(500,10),B(50),PRNT(5)
 COMMON/ACSO/A,AB,C,T,H,G
 P(1)=(0.5*(ABS(B(2))**0.5)*(1./C))*(1.-(2.*((B(1)*AB)**2)))/(SQRT(
122./7.)*X(I,1)*A)
 P(2)=(B(1)*0.5*(1./C)*(((0.5*(ABS(B(2))**(0.5-1.)))+(H*AB))*A-(0.5
1)))/(SQRT(22./7.)*X(I,1)*(A**2))
 P(3)=-((B(1)**3)*2.*0.5*(ABS(B(2))**0.5)*(1./C)*AB)/(SQRT(22./7.)*
1B(3)*X(I,1)*A)
 RETURN
 END
```

APPENDIX A10 (Reprinted by permission of the Council of the Institution of Mechanical Engineers from the Journal of Mechanical Engineering Science)

RESEARCH NOTES

Contributions intended for publication as Research Notes should preferably be limited in length to 1000 words and two illustrations, and should be addressed to the Manuscript Section, The Institution of Mechanical Engineers, 1 Birdcage Walk, Westminster, London SW1H 9JJ.

ON THE CRITICAL WEBER NUMBER FOR COARSE WATER FORMATION IN STEAM TURBINES

C. S. Ow†‡ R. I. Crane†

The widely quoted experiments of Moore *et al.* indicate that the largest stable drops resulting from atomization behind a blade, in typical low-pressure wet-steam flows, can be described by a constant critical Weber number, We_c, of about 21, obtained graphically by fitting upper-limit distribution functions (ULDF) to measured spectra. A non-subjective re-analysis of these data has been made, using Marquardt's algorithm for the least-squares estimation of nonlinear parameters to improve the fitting. It is shown that optimization of the ULDF fit increases We_c considerably in the case of supersonic blade-exit flow. However, replacement of the computed maximum size by that corresponding to a given cumulative mass is necessary to avoid distortion of the result by the small fraction of total mass contained in the largest drops. A cumulative mass of 99·9 per cent consistently gives We_c values near 21, confirming Moore's result, but indicating the need for further work on the Mach-number dependence of We_c.

Introduction

The ability to predict drop-size spectra is of considerable importance in three aspects of wet-steam turbine design: the prediction of wetness losses and of the erosion hazard, and the design of extraction belts. While the energy loss attributable to wetness is made up from a large number of components, Moore's (1)§ estimate for a hypothetical low-pressure final stage indicates the considerable influence of the so-called coarse water drops (stripped from the water films on blade surfaces); details of their size distributions are required as input to any comprehensive theory for wetness loss. Estimates of the life of a blade or blade shield, subjected to erosion by coarse water drop impact, are dependent upon the drop sizes involved and particularly upon the maximum size in the spectrum (2)–(4). The existence of a well-defined, maximum stable size follows from a consideration of the drop-atomization process in a blade wake, where the balance between surface tension and aerodynamic forces leads to a critical Weber number, $We_c = \rho V_r^2 x_m/\sigma$, which defines the maximum drop diameter, x_m, in terms of the steam density, ρ, the velocity, V_r, relative to the drop, and the surface tension, σ.

Coarse water size measurements in low-pressure turbines (see, for example, (5)(6) for spectra in power-station and laboratory turbines, respectively) are scarce at present, and do not generally refer to the appropriate location in the flow for direct application to erosion or loss predictions. Considerable reliance has therefore been placed on data from laboratory studies of the detachment and break-up of water from the trailing edges of blades in cascades. Frequently quoted data (e.g. in (7)) are those of Moore *et al.* (8)(9), who used a photographic technique with a variety of steam conditions matching those in low-pressure turbines. A maximum diameter being a difficult quantity to estimate from a necessarily limited number of measured drop images, x_m was obtained by fitting to the drop mass distributions the 'upper-limit' equation of Mugele and Evans (10). This equation is superior to many commonly-used theoretical distributions (Rosin–Rammler, Nukiyama–Tanasawa, etc.) in that it emphasizes a maximum diameter. Moore *et al* deduced a critical Weber number of between 19 and 23 for each flow condition, consistent with the 'bag' mode of break-up (11) and towards the upper end of the range of We_c from several studies, presented in (12). Having selected a value for x_m based on this We_c, Moore (13) indicates how a hypothetical spectrum may be constructed using the upper-limit equation, for use in wetness-loss prediction (or for any other purpose). Extensive use of $We_c \approx 22$ has been made in steam-turbine studies, for example by Pouchot *et al.* (14).

In the course of a recent study that involved fitting an equation to measured-size spectra of atomized drops, the data of Moore *et al.* (9)(15) were re-analysed to test an improved method of applying the upper-limit distribution function (ULDF). This paper presents the results of the re-analysis, in which x_m is obtained from a computer-generated optimum fit of the ULDF, rather than by the subjective graphical method used hitherto.

ULDF fit to the data

The ULDF (10) is essentially a normal distribution of mass frequency with respect to a transformed drop

The MS. of this research note was received at the Institution on 26th June, 1978 and accepted for publication on 22nd February 1979.

† *Imperial College of Science and Technology, London.*
‡ *Graduate of the Institution.*

§ *References are given at the end of this note.*

0022-2542/79/1000-0353 $02.00

size, and may be written as

$$\frac{dm}{dy} = (\delta/\pi^{1/2}) \exp(-\delta^2 y^2) \quad (1)$$

where m is the cumulative mass (mass contained in drops of diameter less than x, so that the mass frequency is dm/dx), $y = \ln ax^s/(x_m^s - x^s)$ is the transformed drop size, and δ is a shape parameter. Constants a and δ are related, respectively, to the skewness and half-width of the distribution (16), while s is an arbitrary positive number, usually taken as unity. The Sauter (or surface) mean diameter, x_{32}, is then given by

$$x_{32}/x_m = [1 + a \exp(1/4\delta^2)]^{-1} \text{ for } s = 1$$

and

$$x_{32}/x_m = [1 + 2a \exp(1/4\delta^2) + a^2 \exp(1/\delta^2)]^{-1} \quad (2)$$

for $s = \frac{1}{2}$

while the mass median diameter, x_{500}, is given by

$$x_{500}/x_m = (1 + a)^{-1/s} \quad (3)$$

Fitting is normally done graphically (9)(10), with x_m and a determined by plotting x versus m on log-probability axes (a subjective procedure), and δ by fitting a straight line to a similar plot of $ax^s/(x_m^s - x^s)$ versus m. Here, Marquardt's (17) algorithm for the least-squares estimation of nonlinear parameters has been used to determine the optimum values of x_m, a and δ. Convergence was obtained in less than seven iterations (about 1·5 s on a CDC 6500 computer) for mass frequency histograms of five or six equal drop-size intervals. Two values of s were used: unity, as in (8) and (9); and $\frac{1}{2}$, selected for its similarity to Simmons's (18) correlation of fuel-spray size data, in which a straight line was obtained by plotting x versus m on square root-probability axes. (No obvious physical significance can be attached to x^s when $s = \frac{1}{2}$.)

Results of optimized fitting

The parameters a, δ and x_m of the computed optimum fits (for $s = 1$ and $s = \frac{1}{2}$) are compared in Table 1 with those of the graphical fit ($s = 1$) of Moore *et al.* (9). Condition numbers, shown with cascade exit velocity and Mach number at the head of each column, correspond with those used in (7)–(9). Notwithstanding the coarse intervals of the data histograms, the parameter correlation coefficient defined in (17) exceeded 0·91 in all cases, except for a value of 0·71 for one of the three coefficients of condition 1 ($s = 1$). Critical Weber numbers for conditions 1 and 2 are based on relative velocity, V_r, outside the blade wake. V_r is given by $(V - V_{dl})$, where V and V_{dl} are the steam and drop velocities, respectively, assumed to be in the same direction, and V_{dl} is 15 m/s for all conditions. For consistency with Moore's analysis, V for condition 3 was taken as the wake-trough steam velocity (378 m/s) at the position of secondary atomization, in accordance with the observation that, at the supersonic exit condition, atomization was completed within the wake and not at its edges.

Table 1. Parameters of ULDF fits to the data of (8) and (9). Rows A: graphical fit, (8) and (9). Rows B: present optimized fit for $s = 1$ (Figures in parentheses are for $s = \frac{1}{2}$)

Condition number		1	2	3
Cascade exit velocity (m/s)		282	341	463
Cascade exit Mach number		0·65	0·83	1·17
a	A	0·540	0·867	1·040
	B	0·596 (0·284)	1·010 (0·461)	1·835 (0·974)
δ	A	0·673	0·986	0·942
	B	0·850 (0·990)	1·110 (1·390)	1·235 (1·895)
x_m (μm)	A	310	252	200
	B	327 (337)	261 (275)	270 (371)
95 per cent confidence limits for x_m (μm)	A	—	—	—
	B	270 (281) and 443 (and 429)	233 (251) and 296 (and 307)	253 (346) and 291 (and 406)
x_{32} (μm), from equation (2)	A	160	119	84
	B	177 (172)	117 (114)	85 (85)
x_{32} (μm), from data (no weighting within a size class)		161	112	84
We_r, based on x_m	A	18·7	23·4	21·9
	B	19·7 (20·3)	24·2 (25·5)	29·5 (40·7)
x_{mm} (μm)	A	304	230	181
	B	313 (317)	229 (229)	206 (217)
We_r, based on x_{mm}	A	18·3	21·4	19·8
	B	18·9 (19·1)	21·3 (21·3)	22·6 (23·8)

Although simple one-parameter descriptions of the two ULDFs, such as x_{32} or x_{500}, are in good agreement (x_{32} being compared in Table 1 with the Sauter mean diameter derived from the data), a significant difference is found in x_m for condition 3. This result is further illustrated in Fig. 1, which compares mass frequency spectra with the data and indicates the superiority of the present fit. Specifying $s = \frac{1}{2}$ results in a further large increase in maximum diameter. The range of x_m between the lower and upper 95 per cent confidence limits is rather large for condition 1, but for condition 3 it represents a critical Weber number of between 27·6 and 31·8.

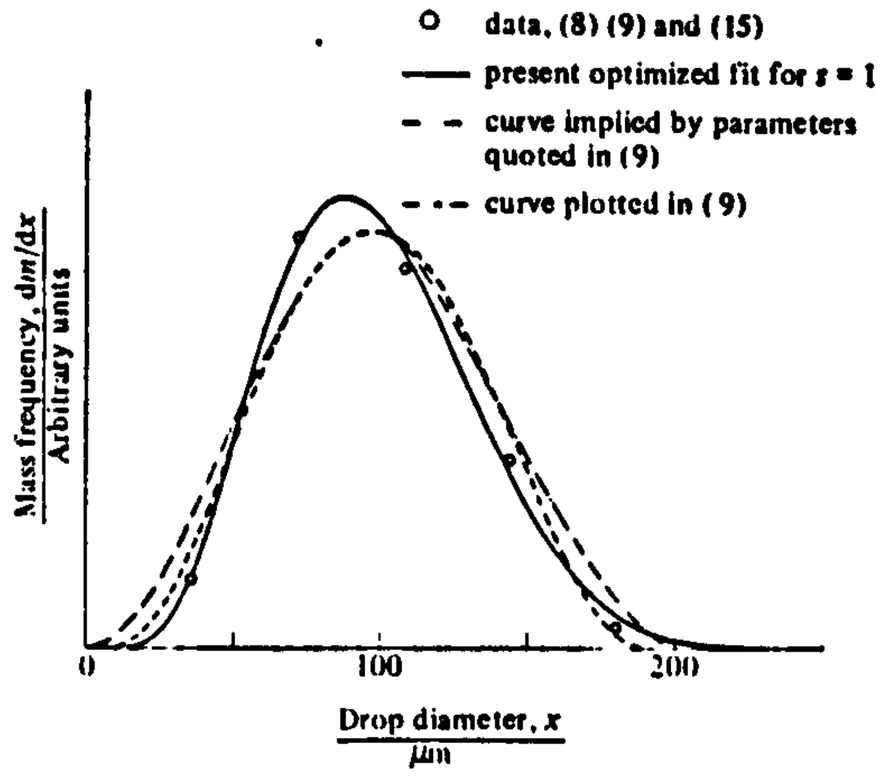


Fig. 1. Mass frequency distribution for condition 3 of (8) and (9)

A source of uncertainty in the experimental distributions is the generally small number count of drops in the size class of largest diameter. To examine the effect of this on the estimate of x_m, the drop number in this class was assumed to be changed by +20 per cent and −20 per cent from the data (9). Optimized fits ($s = 1$) then yielded, for condition 3, We_c values of 30·2 and 28·5, respectively, showing that the bulk of this particular spectrum, rather than the actual number of the largest drops counted, largely determines the estimated maximum size.

The shape of the upper end of each distribution in Fig. 1 reveals a previously unsuspected flaw in the idea of defining x_m via the ULDF. The slope of the optimized curve as it approaches x_m is such that a very small fraction of the total water mass is contained in drops within about 50 μm of x_m. This suggests that the mathematically defined x_m should be replaced by an 'engineering definition', for example the diameter x_{999}, given by

$$x_{999}/x_m = [1 + a \exp(-2{\cdot}185/\delta)]^{-1} \quad (4)$$

which corresponds to a cumulative mass of 99·9 per cent of the total. The bottom row of Table 1 shows the effect on We_c of replacing x_m by x_{999}, the optimized fit for either s no longer giving any We_c values substantially exceeding 22. The need for such a redefinition was not apparent in (8) and (9), because the ULDF parameters happened to give a sharply defined x_m.

Discussion

If the turbine process under study is unlikely to be influenced by 0·1 per cent of the coarse water mass, it is suggested that x_{999} is more appropriate than x_m as the effective maximum diameter. The ULDF then loses its advantage over other distribution functions in which mass frequency tends to zero only as $x \to \infty$, but its form is still more satisfying.

If We_c is based on x_m, the higher value obtained for condition 3 appears to support previous work (e.g. Krzyzanowski and Weigle (19)), suggesting that the concept of a unique We_c of around 20 to 22 for all relevant flow conditions in low-pressure turbines is an oversimplification, even when the appropriate value of V_r can be identified. We_c was treated as a function of Mach number only by Spies *et al.*, quoted in (14), and by Valha (4), whose data (in air flow) are shown in (4) and (19). Values of We_c in (4) and (19) appear to have been obtained by taking x_m as twice the modal value of x in a Gaussian curve fitted to the experimental mass distribution, and V_r as the main stream velocity. This yielded $We_c \approx 40$ for the whole Mach-number range of Moore's investigation, whereas Moore's data give such a high value, based on this V_r, only for condition 3. It is unfortunate that Valha's and Weigle's data are not available in a form which could be analysed by the present method and used to determine any connection between the ULDF parameters and Mach number.

Additional research is required to establish the dependence of We_c on flow conditions, for which a common, non-subjective, data-analysis procedure is needed. The present technique is recommended, since it would reveal any underlying trends in spectrum shape, as well as maximum size, with Mach number, geometry of the surface from which the water was stripped, boundary layer condition on that surface, etc. If the ULDF parameters as well as We_c could be related empirically to the flow conditions, it would be possible to propose a reliable procedure for the synthesis of spectra for design purposes to replace that suggested in (13), which implies $a = 1$ (zero skew) and $\delta = 1$.

Conclusions

An automatic procedure has been used to provide optimum fits of the ULDF to the measured drop mass distributions, which overcomes the subjective nature of the usual graphical method. For the two subsonic cascade exit steam flows, the least-squares estimates of maximum drop size, x_m, are in broad agreement with the graphical values, giving critical Weber numbers, We_c, in the region of 22. No advantage is evident from using $s = \frac{1}{2}$ rather than $s = 1$.

In the supersonic case, the optimized x_m yields $We_c \approx 30$. A sensitivity analysis indicates that this result is determined largely by the bulk of the spectrum rather than by the number count in the largest-diameter drop-size class, which is subject to considerable experimental uncertainty. However, the shape of the optimized mass frequency spectrum shows that ULDF does not always give a realistic maximum size for practical purposes. Taking the effective maximum size to correspond instead with a 99·9 per cent cumulative mass yields $We_c \approx 21$ for all three flow conditions.

The variety of data-analysis methods and definitions of We_c has contributed to the discrepancy in We_c between the widely quoted results of Moore *et al.* and data from East-European sources. The present analysis technique is recommended for further work which is needed to clarify this situation.

REFERENCES

(1) MOORE, M. J. *Two-phase steam flow in turbines and separators* Ed. Moore, M. J. and Sieveding, C. H. 1976, 104–122 (Hemisphere, Washington).

(2) MOORE, M. J. and LANGFORD, R. W. Central Electricity Generating Board Report, 1970 (unpublished).

(3) SOMM, E. 'A means of estimating the erosion hazard in low-pressure steam turbines', *Brown Boveri Rev.* 1971 58 (10), 458–472 (English edition).

(4) VALHA, J. 'Untersuchungen zur Erosion bei Dampfturbinen-Endstufen', *Energietechnik* 1977 27 (10), 404–412.

(5) EDERHOF, A. and DIBELIUS, G. 'Streulichtsonde zur Bestimmung von Tropfengrösse und Feuchte in Zweiphasenströmungen', *VGB Kraftwerkstechnik* 1975 55 (1), 61–66. See also (1), 253.

(6) KIRYUKHIN, V. I., FILIPPOV, G. A., POVAROV, O. A. and DIKAREV, V. I. 'Investigation of the structure of wet steam in a multistage turbine', *Thermal Engineering* 1977 23 (5), 26–29.

(7) GYARMATHY, G. See (1), 51.

(8) MOORE, M. J., LANGFORD, R. W. and TIPPING, J. C. 'Research at CERL on turbine blade erosion', *Proc. Instn mech. Engrs* 1967–68 182 (3H), 61–68.

(9) MOORE, M. J., LANGFORD, R. W. and TIPPING, J. C. Central Electricity Generating Board *Rep. RD/L/N17/67* 1967.

(10) MUGELE, R. A. and EVANS, H. D. 'Droplet size distribution in sprays', *Ind. Engng Chem.* 1951 43 (6), 1317–1324.

(11) LANE, W. R. 'Shatter of drops in streams of air', *Ind. Engng Chem.* 1951 43 (6), 1312–1317.

(12) GYARMATHY, G. See (1), 50.

(13) MOORE, M. J. See (1), 114.

(14) POUCHOT, W. D., KOTHMANN, R. E. and FENTRESS, W. K. 'Basic investigation of turbine erosion phenomena', *NASA CR-1830* 1971.

(15) MOORE, M. J. and LANGFORD, R. W. 1978, private communication.

(16) ROBERTS, J. H. and WEBB, M. J. 'Measurement of droplet size for wide range particle distributions', *AIAA J.* 1964 2 (3), 583–585.

(17) MARQUARDT, D. W. 'An algorithm for least-squares estimation of non-linear parameters', *J. Soc. Ind. appl. Math.* 1963 11 (2), 431–441.

(18) SIMMONS, H. C. 'The correlation of drop size distribution in fuel nozzle sprays', *Trans. Am. Soc. mech. Engrs, Ser. A* 1977 99 (3), 309–314.

(19) KRZYZANOWSKI, J. and WEIGLE, B. 'Toward the criterion of erosion threat of steam turbines blading through the structure of the droplet steam', *Prace Instytutu Maszyn Przeplywowych* 1976 (No. 70–72), 189–201.

APPENDIX A11: RELEVANT SUBROUTINES FOR HETEROGENEOUS ULDF FIT.

A11.1: Partial derivatives.

The partial derivatives of Eqn. 6.9 with respect to the parameters δ_1, δ_2, m_1, m_2, x_m and b are:-

$$\frac{\partial F}{\partial \delta_1} = \frac{x_m b \; e^{-\delta_1^2 z_1^2}}{(b+1)\sqrt{\pi}\; x(x_m-x)}\left[1-2\delta_1 z_1(z_1+m_1\delta_1)\right] \qquad \ldots.A11.1$$

$$\frac{\partial F}{\partial \delta_2} = \frac{x_m \; e^{-\delta_2^2 z_2^2}}{(b+1)\sqrt{\pi}\; x(x_m-x)}\left[1-2\delta_2 z_2(z_2+m_2\delta_2)\right] \qquad \ldots.A11.2$$

$$\frac{\partial F}{\partial m_1} = -\frac{2m_1\; x_m b \delta_1^3 \; e^{-\delta_1^2 z_1^2}}{(b+1)\sqrt{\pi}\; x(x_m-x)}\; z_1 \qquad \ldots.A11.3$$

$$\frac{\partial F}{\partial m_2} = -\frac{2m_2\; x_m \delta_2^3 \; e^{-\delta_2^2 z_2^2}}{(b+1)\sqrt{\pi}\; x(x_m-x)}\; z_2 \qquad \ldots.A11.4$$

$$\frac{\partial F}{\partial x_m} = \frac{1}{(b+1)\sqrt{\pi}\,(x_m-x)^2 x}\left[b\delta_1 e^{-\delta_1^2 z_1^2}(2\delta_1 x_m z_1 - x) + \delta_2 e^{-\delta_2^2 z_2^2}(2\delta_2^2 x_m z_2 - x)\right] \qquad \ldots.A11.5$$

$$\frac{\partial F}{\partial b} = \left[\frac{\delta_1 x_m \; e^{-\delta_1^2 z_1^2}}{(b+1)^2\sqrt{\pi}\; x(x_m-x)}\right] - \left[\frac{\delta_2 \; x_m \; e^{-\delta_2^2 z_2^2}}{(b+1)^2\sqrt{\pi}\; x(x_m-x)}\right] \qquad \ldots.A11.6$$

where $z_1 = \ln\left[\frac{x e^{m_1\delta_1}}{(x_m-x)}\right]$ and $z_2 = \ln\left[\frac{x e^{m_2\delta_2}}{(x_m-x)}\right]$

All.2: Labels used by subroutines for heterogeneous ULDF fit.

Fortran label	Mathematical symbol	Meaning
B(1)	δ_1	shape parameter
P(1)	$\frac{\partial F}{\partial \delta_1}$	Eqn. All.1
B(2)	x_m	maximum diameter
P(2)	$\frac{\partial F}{\partial x_m}$	Eqn. All.5
B(3)	m_1	an offset multiplier
P(3)	$\frac{\partial F}{\partial m_1}$	Eqn. All.3
B(4)	δ_2	shape parameter
P(4)	$\frac{\partial F}{\partial \delta_2}$	Eqn. All.2
B(5)	m_2	an offset multiplier
P(5)	$\frac{\partial F}{\partial m_2}$	Eqn. All.4
B(6)	b	scale factor
P(6)	$\frac{\partial F}{\partial b}$	Eqn. All.6
F	$\frac{d\psi}{dx}$	mass frequency defined by Eqn. 6.10
Y(I)	$\left(\frac{d\psi}{dx}\right)_{data}$	mass frequency from experimental data
RES	Y(I)-F	residuals
X(I,1)	x	diameter
A	$(x_m - x)$	
AB	$\left[\ln \frac{x}{(x_m - x)}\right] + m_1 \delta_1$	normal variate z_1
AB1	$\left[\ln \frac{x}{(x_m - x)}\right] + m_2 \delta_2$	normal variate z_2
C	$\exp(\delta_1^2 z_1^2)$	
C1	$\exp(\delta_2^2 z_2^2)$	
T	$\frac{x_m}{x(x_m - x)}$	
H	22./7.	

All.3: Program listings

Listing of subroutines for heterogeneous ULDF in a form suitable for input into the main program of ref. (195).

```
      SUBROUTINE SUBZ(Y,X,B,PRNT,NPRNT,N)
      NPRNT=0
      RETURN
      END
```

```
      SUBROUTINE FCODE(Y,X,B,PRNT,F,I,FES)
      DIMENSION Y(500),X(500,10),B(50),PRNT(5)
      COMMON/CSO/A,AB,AB1,C,C1,T,H
      A=ABS(B(2))-X(I,1)
      AB=(0.5*ALOG((X(I,1)/A)**2))+(B(3)*B(1))
      AB1=(0.5*ALOG((X(I,1)/A)**2))+(B(5)*B(4))
      C=EXP((B(1)*AB)**2)
      C1=EXP((B(4)*AB1)**2)
      T=B(2)/(X(I,1)*A)
      H=SQRT(22./7.)
      F=(T*((B(6)*B(1)*(1./C))+(B(4)*(1./C1))))/(H*(B(6)+1.))
      FES=Y(I)-F
      RETURN
      END
```

```
      SUBROUTINE PCODE(P,X,B,PRNT,F,I)
      DIMENSION P(50),X(500,10),B(50),PRNT(5)
      COMMON/CSO/A,AB,AB1,C,C1,T,H
      P(1)=(T*B(6)*(1./C)*(1.-(2.*B(1)*AB*(AB+(B(3)*B(1))))))/
     1(H*(B(6)+1.))
      P(2)=((B(1)*B(6)*(1./C)*((2.*(B(1)**2)*B(2)*AB)-X(I,1)))+
     1(B(4)*(1./C1)*((2.*(B(4)**2)*B(2)*AB1)-X(I,1))))/
     2((1.+B(6))*H*((B(2)-X(I,1))**2)*X(I,1))
      P(3)=-(T*2.*B(3)*B(6)*(B(1)**3)*(1./C)*AB)/(H*(B(6)+1.))
      P(4)=((1./C1)*T*(1.-(2.*B(4)*AB1*(AB+(B(4)*B(5))))))/
     1(H*(B(6)+1.))
      P(5)=-(T*2.*B(5)*B(6)*(B(4)**3)*(1./C1)*AB1)/(H*(B(6)+1.))
      P(6)=(T*((B(1)*(1./C))-(B(4)*(1./C1))))/(H*((B(6)+1.)**2))
      RETURN
      END
```

APPENDIX A12: RELATIVE MAGNITUDES OF COAGULATION CONSTANTS FOR A MONODISPERSED SPECTRUM OF 40μm DIAMETER WATER DROPS IN 102 mm DIAMETER PIPE FLOWS AT REYNOLDS NUMBER OF 10^5.

(a) Thermal Coagulation

For drop sizes larger than the molecular mean free path, the thermal coagulation (drop collision due to Brownian motion) equation is given by (8, 218)

$$\frac{dn}{dt} = -\frac{4\alpha\theta}{3\mu} n^2 = -K_\theta n^2 \qquad \ldots\ldots A12.1$$

where n = number concentration of drops

α = Boltzmann's constant (= 1.38×10^{-23} J/k)

θ = absolute temperature

μ = dynamic viscosity of air.

(For θ = 293 K and $\mu = 1.654 \times 10^{-5}$ kg/sm, K_θ is 3.24×10^{-16} m^3/s)

(b) Velocity gradient coagulation

In a sheared flow with velocity gradient $G = \frac{dU}{dy}$, particles may be caused to move with a relative velocity to each other, promoting additional collisions. The coagulation rate for laminar flow is given by Zebel (8), as

$$\frac{dn}{dt} = -\frac{4}{3} r_{12}^3 G n^2$$

$$= - K_G n^2 \qquad \ldots\ldots A12.2$$

where $r_{12} = r_1 + r_2 = x_p$ for monodispersed spectrum and

G = laminar velocity gradient.

Although Eqn. A12.2 is derived for laminar flow velocity gradient an order of magnitude study of this mechanism in a turbulent velocity field may be useful. An empirical velocity profile for pipe flow at Reynolds number of 10^5 is given by (198),

$$\frac{U}{U_{max}} = \left[\frac{y}{R}\right]^{1/7} \qquad \ldots\ldots A12.3$$

where y = distance from the wall, R = pipe radius and U_{max} = centreline velocity.

$$\therefore \quad G = \left|\frac{dU}{dy}\right| = \frac{U_{max}}{7R}\left[\frac{y}{R}\right]^{-6/7} \qquad \ldots\ldots A12.4$$

As y tends to zero, velocity gradient tends to infinity which is not a practical solution. For the Reynolds number currently used, the thickness of the "laminar" sublayer is approximately 88 μm; computation of the velocity gradient at y= 88 μm is unrealistic since the drop size of 40 μm is relatively large compared with the value of y. As a compromise y/R = 0.12 will be used consistent with subsequent computations.

$$\text{Hence} \quad G = \frac{U_{max}}{7R}\left[\frac{R}{0.12}\right]^{6/7}$$

where U_{max} = 1.223 $\bar{U}$ from ref.(198) and $\bar{U} \simeq 15$ m/s at Re_D of

10^5. A typical value for gradient coagulation constant K_G would therefore be 2.1×10^{-12} m^3/s assuming that the coagulation equation remained valid for the turbulent velocity profile.

(c) Turbulent coagulation

(i) Particle size smaller than turbulent microscale

For drop sizes smaller than the Kolmogorov (18) microscale of turbulence, Saffman and Turner (21) among others (17, 19, 29) derived, for droplets moving with the air (see sec. 2.2.1), the coagulation rate as

$$\frac{dn}{dt} = - K_T n^2 \qquad \ldots. \text{A12.5}$$

where $K_T = 1.3 (\varepsilon/\nu)^{\frac{1}{2}} x_p^3$,

ε = turbulent energy dissipation rate (W/kg or m^2/s^3)

ν = kinematic viscosity of gas phase (m^2/s) .

In turbulent pipe flows the dimensionless energy dissipation rate $\varepsilon^+ = (\varepsilon u_*^3)/R$ is a maximum near the wall region, typically $\varepsilon^+ = 19$ for $r/R = 0.88$ (ref. (200)) where r is the radial position.

Hence considering $u_* = 0.77$ m/s

$x_p = 40$ μm

$\nu = 1.35 \times 10^{-5}$ m^2/s

$R = 0.0508$ m

and $\varepsilon^+ = \varepsilon u^3/R = 171$ m^2/s^3,

$K_T = 2.96 \times 10^{-12}$ m^3/s.

(ii) Particle size larger than the microscale.

Abrahamson(24) using a model of independent particle velocities derived a coagulation equation which related parameters of fluid turbulence intensity, energy dissipation rate and particle relaxation time given by (rewritten for a monodispersed spectra);

$$\frac{dn}{dt} = -5.0\, x_p^2\, (2\,\overline{U}_p^2)^{\frac{1}{2}}\, n^2$$
$$= -K_{TA}\, n^2 \qquad \ldots\ A12.6$$

where $\overline{U}_p^2 = \dfrac{\overline{U^2}}{1+1.5\,\tau\,\varepsilon/\overline{U}_p^2}$ (the particle mean square velocity deviation)

$\overline{U^2}$ = mean square velocity deviation of the gas phase

= particle relaxation time (s).

From Laufer's(200) measurements, the turbulence intensity at $r/R = 0.88$ is approximately twice the friction velocity. Hence, using typical values for u_*, ε and $\tau = 5.48\times10^{-3}$ s for a 40 μm water drop in air, $K_{TA} = 13.8\times10^{-9}$ m^3/s.

Hence from the above examples, it is clear that turbulent agglomeration will exceed those of thermal and velocity gradient mechanisms by at least an order of magnitude although the velocity gradient mechanism derived strictly for laminar flow has been used in the computations.

APPENDIX A13: ESTIMATION OF ERRORS IN $\bar{x}_{30}$ and $\bar{x}_{32}$ USING THE CENTRAL LIMIT (CL) THEOREM.

The CL theorem states that if X is a random variable from a non-normal distribution with a definite mean ω and variance Λ^2 then the random variable $Z=({}_N\bar{X}-\omega)\sqrt{N}/\Lambda$ has a distribution that approaches the standard normal distribution as N tends to infinity (${}_N\bar{X}$ is the mean of sample size N).

In practice the more the distribution of X differs from normality the larger N must become to guarantee approximate normality of Z.

The mass frequency distributions in most spray spectra are not as highly skewed as number frequency spectra. Hence an estimate of the confidence limit of say ω_{30} of the nett spectrum is possible provided that the ${}_N x_{30}$'s of a large number (say P) of smaller samples of size N which made up the nett sample size PN are known. Then by the CL theorem,

$$\frac{\Lambda}{\sqrt{N}} = {}_{S,N}\Lambda_x \qquad \text{....A13.1}$$

and

$$\frac{\Lambda}{\sqrt{PN}} = {}_{S,PN}\Lambda_x \qquad \text{....A13.2}$$

where ${}_{S,N}\Lambda_x$ = sample estimate of the normal standard deviation based on P samples each having size N.

and ${}_{S,PN}\Lambda_x$ = sample estimate of the normal standard deviation based on Q samples each size PN.

Therefore,

$${}_{S,PN}\Lambda_x = {}_{S,N}\Lambda_x \sqrt{\frac{N}{PN}} = \frac{{}_{S,N}\Lambda_x}{\sqrt{P}} \qquad \text{....A13.3}$$

from which an estimate of ω is possible using e.g. 95% confidence limit $_{PN}\overline{X} \pm 2\ _{S,PN}\hat{}x$.

Example

Consider the results of a batch of sixty photographs for condition A at r/R = 0.04. Values of x_{30}, x_{31} and x_{32} may be computed for each of the sixty samples and their sample estimate of the population standard deviation is, for example, x_{30},

$$_{S,23}\hat{}x_{30} = 8.54$$ where the average sample size was 23.32 counts,

and $$_{S,1398}\hat{}x_{30} = \frac{8.54}{\sqrt{60}} = 1.1$$ for the total count of 1398 from the 60 samples.

The value of $_{1398}\overline{X}_{30} = 42.5$ μm.

Hench 95% confidence limits for ω_{30} is

$$\omega_{30} = {}_{S,1398}\overline{X}_{30} \pm 1.96\ {}_{S,1398}\hat{}x_{30}$$
$$= 42.5 \pm 2.2\ \mu m.$$

Hole No.	Diameter measured under microscope (mm)	Grey Level	Digitised diameter d_M (mm) at I_A= 0.3V			
			I_R = 0.9		I_R = 0.5	
			t = 0 min.	t = 20 mins.	t = 0 min.	t = 0.5 mins.
1	2.44 ± 0.015	4	2.53	2.52	2.57	2.56
		5	2.50	2.49	2.55	2.53
		6	2.48	2.45	2.52	2.51
		7	2.43	2.42	2.50	2.50
2	2.47 ± 0.015	4	2.58	2.54	2.58	2.60
		5	2.55	2.52	2.56	2.57
		6	2.53	2.48	2.53	2.54
		7	2.50	2.46	2.52	2.53
3	2.50 ± 0.015	4	2.66	2.63	2.69	2.68
		5	2.64	2.59	2.66	2.66
		6	2.60	2.56	2.64	2.63
		7	2.56	2.53	2.63	2.61

Table 5.1: Measured diameters for 3 well-focussed circular holes repeated at 20 mins. and 5 mins. intervals at two settings of intensity ratio I_R.

Microscope diameter (mm)	Screen Position (Fig.5.4)	Digitised diameter for I_A= 0.25V (within brackets I_A=0.3V)							
		I_R =0.75				I_R = 1.0			
		Grey level scale				Grey level scale			
		4	5	6	7	4	5	6	7
3.23± 0.28	1	3.415	3.399	3.380	3.367	3.396	3.382	3.354	3.340
	2	3.348	3.433	3.413	3.406	3.431	3.423	3.410	3.399
	3	3.543	3.523	3.495	3.483	3.506	3.497	3.467	3.456
	4	3.320 (3.333)	3.303 (3.326)	3.295 (3.311)	3.291 (3.305)	3.307 (3.319)	3.302 (3.311)	3.292 (3.295)	3.283 (3.288)
	5	3.364 (3.373)	3.358 (3.366)	3.347 (3.356)	3.337 (3.350)	3.357 (3.355)	3.349 (3.350)	3.334 (3.340)	3.329 (3.332)
	6	3.406 (3.452)	3.398 (3.439)	3.393 (3.432)	3.385 (3.427)	3.440 (3.430)	3.426 (3.426)	3.413 (3.412)	3.407 (3.408)
	7	3.459	3.438	3.424	3.413	3.439	3.428	3.408	3.397
	8	3.472	3.463	3.446	3.438	3.454	3.441	3.422	3.407
	9	3.553	3.540	3.515	3.502	3.531	3.517	3.493	3.479
	Mean	3.442	3.428	3.412	3.402	3.429	3.418	3.399	3.389
	Standard deviation	0.0764	0.0751	0.0690	0.0671	0.0692	0.0670	0.0633	0.0618
	Std. dev. / Mean	2.219%	2.190%	2.020%	1.970%	2.020%	1.960%	1.862%	1.830%

Table 5.2: Vidicon diameters for a single circular hole at across screen positions indicated in Fig. 5.26.

Microscope diameter x (μm)	Grey level	I_A = 0.35V		I_A = 0.25V	
		I_R= 0.75	1.0	0.75	1.0
152.1±0.64	4	152.85	148.1	151.50	147.5
	5	151.38	147.6	150.29	146.7
	6	150.32	145.6	148.10	145.1
	7	149.40	144.1	146.83	143.2
		I_A = 0.35V		I_A = 0.25V	
		I_R= 0.75	1.0	0.75	1.0
51.10±0.64	4	52.13	50.08	51.53	48.97
	5	52.13	49.50	51.06	48.60
	6	50.80	48.20	50.80	46.52
	7	49.83	46.52	50.57	46.00

Table 5.3: TV diameters from in-focus photographs of black discs on a comparison reticle. Nominal diameters photographed are 50 μm and 150 μm under a magnification of 14x. x is the actual diameter of graticule circle under the microscope.

Actual Diameter x (μm)	Measured diameters d_M (halo width, $_4h_5$) with I_{1A} set at 0.2V and I_R at the following values:-			
	0.57 i.e. I_A = 0.35V	0.75 0.265V	1.0 0.2V	1.33 0.15V
21.0	23.32 (0)	24.73 (0.71)	20.20 (2.96)	Less than 8 picture points
31.5	36.41 (0.96)	32.98 (1.91)	30.29 (2.11)	27.96 (0.62)
41.0	44.01 (0)	39.97 (0.65)	38.23 (2.37)	34.98 (3.82)
51.1	51.82 (1.87)	48.07 (0)	47.00 (1.30)	45.16 (4.20)
61.3	64.39 (0.81)	63.59 (1.50)	59.45 (2.33)	54.06 (3.53)
70.2	72.58 (1.43)	69.96 (1.83)	64.92 (2.80)	63.06 (3.57)
80.9	81.62 (1.16)	76.90 (1.46)	76.00 (2.91)	72.10 (5.09)
91.5	91.99 (1.12)	91.06 (1.71)	86.66 (0.99)	84.68 (3.67)
100.0	101.64 (0.84)	99.79 (1.65)	97.37 (2.14)	93.00 (3.92)
202.3	199.83 (0.94)	198.64 (1.73)	195.20 (2.42)	191.67 (4.54)
302.3	297.94 (1.17)	295.42 (1.68)	293.00 (1.99)	289.30 (4.26)
398.1	394.57 (1.45)	392.80 (1.56)	390.00 (2.18)	382.00 (3.15)
506.2	491.49 (1.63)	487.60 (1.68)	482.10 (2.28)	479.00 (4.51)
753.6	748.00 (1.57)	742.20 (2.07)	738.00 (7.50)	733.30 (5.27)

Table 5.4: Simulation of poor contrast effects.

Results within bracketts are halo widths between grey levels 4 and 5.

Mean Diameter	Relevant Equations	
	Lapple's Definition	Wises's Definition
$\bar{x}_{32} =$	$\dfrac{\sum_{i=1}^{G} N_i x_i^3}{\sum_{i=1}^{G} N_i x_i^2}$	$\dfrac{x_0^3 + 3\int_{x_0}^{x_m} x^2 P^{-1}(x)\, dx}{x_0^2 + 2\int_{x_0}^{x_m} x\, P^{-1}(x)\, dx}$
$\bar{x}_{31} =$	$\dfrac{\sum_{i=1}^{G} N_i x_i^3}{\sum_{i=1}^{G} N_i x_i}$	$\dfrac{x_0^3 + 3\int_{x_0}^{x_m} x^2 P^{-1}(x)\, dx}{x_0 + \int_{x_0}^{x_m} P^{-1}(x)\, dx}$
$\bar{x}_{30} =$	$\dfrac{\sum_{i=1}^{G} N_i x_i^3}{\sum_{i=1}^{G} N_i}$	$\dfrac{x_0^3 + 3\int_{x_0}^{x_m} x^2 P^{-1}(x)\, dx}{1}$

Table 6.1: Lapple's and Wise's equations in the determination of $\bar{x}_{32}$, $\bar{x}_{31}$ and $\bar{x}_{30}$
The integral within Wise's notation is numerically solved by Trapezoidal Rule

Mean Diameter (μm)	Atomiser data batch AK 6.7 μm intervals		Moore et al.(168) Condition 1 50 μm intervals	
	Lapple's	Wise's	Lapple's	Wise's
$\bar{x}_{32}$	51.53	42.32	252.64	161.39
$\bar{x}_{31}$	41.00	38.40	162.89	130.30
$\bar{x}_{30}$	35.07	34.95	111.86	109.69

Table 6.2: $\bar{x}_{32}$, $\bar{x}_{31}$, and $\bar{x}_{30}$ computed for droplet spectrum from atomiser data batch AK as well as the Moore et al.(168) condition 1 results, by Lapple's and Wise's methods.

$$s=1\begin{cases}\dfrac{x_{31}}{x_m}=\left[\dfrac{1}{1+2ae^{1/(4\delta^2)}+a^2e^{1/\delta^2}}\right]^{\frac{1}{2}}\\[2ex]\dfrac{x_{30}}{x_m}=\left[\dfrac{1}{1+3ae^{1/(4\delta^2)}+3a^2e^{1/\delta^2}+a^3e^{9/(4\delta^2)}}\right]^{\frac{1}{3}}\end{cases}$$

$$s=\tfrac{1}{2}\begin{cases}\dfrac{x_{31}}{x_m}=\left[\dfrac{1}{1+4ae^{1/(4\delta^2)}+6a^2e^{1/\delta^2}+4a^3e^{9/(4\delta^2)}+a^4e^{4/\delta^2}}\right]^{\frac{1}{2}}\\[2ex]\dfrac{x_{30}}{x_m}=\left[\dfrac{1}{1+6ae^{1/(4\delta^2)}+15a^2e^{1/\delta^2}+20a^3e^{9/(4\delta^2)}+15a^4e^{4/\delta^2}+6a^5e^{25/(4\delta^2)}+a^6e^{9/\delta^2}}\right]^{\frac{1}{3}}\end{cases}$$

Table 6.3: $\bar{x}_{31}$ and $\bar{x}_{30}$ as described by ULDF for s=1 and $s=\frac{1}{2}$.

Condition Number		1	2	3
Cascade exit velo.(m/s)		282	341	463
Cascade exit Mach number		0.65	0.83	1.17
a	A	0.540	0.867	1.040
	B	0.596(0.284)	1.010(0.461)	1.835(0.974)
δ	A	0.673	0.986	0.942
	B	0.850(0.990)	1.110(1.390)	1.235(1.895)
x_m (μm)	A	310	252	200
	B	327(337)	261(275)	270(371)
95% confidence for x_m (μm)	A	-	-	--
	B	270 & 443 281 & 429	233 & 296 251 & 307	253 & 291 346 & 406
$\bar{x}_{32}$ (μm) from Eqn. 6.3.2 (Eqn.6.3.3)	A	160	119	84
	B	177(172)	117(114)	85(85)
$\bar{x}_{32}$ (μm) from data by Wise's definition	A B	161	112	84
Critical Weber No. based on x_m.	A	18.7	23.4	21.9
	B	19.7(20.3)	24.2(25.5)	29.5(40.7)

Table 6.4: Parameters of ULDF fits to the data of ref. (168). Rows A : graphical fit, (168)
Rows B : present optimised fit for s=1 (figures in brackets for s=½)

Parameter	Value
m_1 (a_1)	0.212 (1.518)
δ_1	1.97
x_m (μm)	106
δ_2	0.632
m_2 (a_2)	-0.142 (0.914)
k	0.724
$\bar{x}_{32}$ from Eqn. 6.12	39.02
$\bar{x}_{32}$ from original data by Wise's method.	42.33
95% non-linear confidence limits on x_m.	97 & 118

Table 6.5: Parameters of heterogeneous ULDF fit to atomiser data (batch AK) for s=1 only. a_1 or a_2 is defined as $e^{m_1\delta_1}$ or $e^{m_2\delta_2}$ respectively in the normal variates $y=\ln(\frac{a_1 x}{x_m-x})$ and $\ln(\frac{a_2 x}{x_m-x})$

r/R	ε^+		λ (μm)
	$Re_D = 5x10^5$	$Re_D = 5x10^4$	$Re_D = 1x10^5$
0.88	20	18	61.6 (mean value)
0.60	6	6	82.1
0.32	3.5	3.5	94.0
0.04	2	2	108.1

Table 7.1: Non-dimensional turbulent energy dissipation rate ε^+ at four radial positions from ref. (200) and corresponding Kolmogorov microscale λ for Re_D of 10^5.

Test condition	DW1	DW2
Total air to water mass ratio $\dot{m}_a/\dot{m}_w$	0.53	0.24
Water flow rate (kg/min.)	0.37	0.82
Number of radial positions photographed.	8	8
Number of photographs per position.	2	2
$\bar{x}_{32}$ (μm)	64	69
$\bar{x}_{31}$ (μm)	57	62
$\bar{x}_{30}$ (μm)	49	55
Average counts per photograph	46	75

Table 7.2: Delavan-Watson atomiser test conditions and results.

Test condition	AG	AH
Total air to water mass ratio $\dot{m}_a/\dot{m}_w$	0.289	0.233
Axial to coaxial air mass ratio	unknown	unknown
Water flow rate (kg/min.)	0.886	1.090
Number of radial positions photographed.	7	6
Number of photographs per position	3	4
$\bar{x}_{32}$ (μm)	43.9	45.4
$\bar{x}_{31}$ (μm)	42.8	46.7
$\bar{x}_{30}$ (μm)	41.5	43.9
Average counts per photograph	72	66

Table 7.3: Prototype air-blast atomiser test conditions and results.

Test condition	AI	AJ	AK	AL
Atomiser unit number	1	1	1	3
Total air to water mass ratio $\dot{m}_a/\dot{m}_w$	0.2	0.2	0.2	0.2
Axial to coaxial air mass ratio	1:1	1:2	1:3	1:1
Water flow rate (kg/min.)	1.3	1.3	1.3	1.3
Number of radial positions photographed.	7	7	7	7
Number of photographs per position	4	4	4	4
$\bar{x}_{32}$ (μm)	37	40	42	40
$\bar{x}_{31}$ (μm)	35	37	38	37
$\bar{x}_{30}$ (μm)	33	34	35	33
Average counts per photograph	116	148	160	178
Total number counts	3241	4140	4470	4926

Table 7.4: Test conditions and results for two randomly selected air-blast atomisers.

Parameters	Re_D ($x10^4$)				
	8	9	10	11	12
Corr. coeff. c	-0.998	-0.998	-0.999	-0.999	-0.999
τ_w (N/m^2)	0.492	0.593	0.698	0.809	0.953
$u_*=\sqrt{\tau_w/\rho}$ (m/s)	0.643	0.706	0.765	0.828	0.894
$\bar{U}$ (m/s)	11.86	13.33	14.82	16.30	17.79
Friction fact. $f=8(\frac{u_*}{\bar{U}})^2$	0.0234	0.0223	0.0212	0.0205	0.0201

Table 7.5: Single-phase turbulent pipe flow measurements and friction factor f for the determination of equivalent sand roughness parameter.(without extraction units but with atomiser air)

	With 10% atomiser air	Without atomiser air
Corr. coeff. c	-0.999	-0.999
τ_w (N/m^2)	0.758	0.644
u_* (m/s)	0.794	0.732
$\bar{U}$ (m/s)	14.82	14.82
% change in u_* compared with that without extraction units (Table 7.5)	3.7%	-

Table 7.6: Single-phase flow with 3 intermediate extraction stations for Re_D of 10^5.

Test condition	A	C	T
Correlation coeff. c	-0.999	-0.999	-0.999
Wall shear stress τ_w (N/m^2)	1.019	1.039	1.059
Friction velo. u_* (m/s)	0.920	0.929	0.938
Friction factor $f=8(\frac{u_*}{\bar{U}})^2$	0.0313	0.0319	0.0326
Mean velocity $\bar{U}$ (m/s)	14.82	14.82	14.82

TABLE 7.7: Two-phase flow measurements and friction factor with one extraction unit located immediately downstream of mixing chamber.

Run No.	Distance between injection and extraction slots n/D	Injected liquid rate (Rotameter reading) l/min.	Extracted liquid rate l/min.	Entrained fraction %
T61	15	1.4	1.310	6.43
T62		1.8	1.716	4.67
T63		2.2	2.091	4.95
T64		2.6	2.477	4.73
T65		3.0	2.880	4.00
T66		3.4	3.298	3.00
T71	25	1.4	1.309	6.50
T72		1.8	1.706	5.22
T73		2.2	2.104	4.36
T74		2.6	2.510	3.85
T75		3.0	2.938	2.07
T76		3.4	3.314	2.53
T81	45	1.4	1.306	6.71
T82		1.8	1.710	5.00
T83		2.2	2.106	4.27
T84		2.6	2.509	3.50
T85		3.0	2.928	2.40
T86		3.4	3.307	2.74
T91(T91')	65	1.4	1.301(1.313)	7.07(6.21)
T92(T92')		1.8	1.702(1.702)	5.44(5.44)
T93(T93')		2.2	2.111(2.111)	4.05(4.05)
T94(T94')		2.6	2.500(2.506)	3.85(3.62)
T95(T95')		3.0	2.933(2.944)	2.23(1.87)
T96(T96')		3.4	3.322(3.313)	2.29(2.59)

Table 8.1: Summary of preliminary investigations of re-entrainment from wall-film flows. Results in ' are for bottom injection only.

Test condition	A	A1	B	C	T
Re_D ($x10^5$)	1	1.16	1	1	1
Atomiser liq. rate(l/min.)	4	4	5	6	8
Atomiser $\dot{m}_a/\dot{m}_w$ mass ratio	0.23	0.23	0.19	0.15	0.13
Coaxial/Axial air mass ratio.	1	1	1.5	1.9	2
Atomiser air to total air mass ratio.	10.7%	9.2%	10.7%	10.7%	10.7%

Table 8.2: Experimental test conditions for deposition and agglomeration studies. (Condition T included for common referencing from another section.

Extraction station 1	Operating	Not operating
Test condition	A	A
$\bar{x}_{32}$ (μm)	51.3	65.8
$\bar{x}_{31}$ (μm)	46.3	54.5
$\bar{x}_{30}$ (μm)	42.4	46.4
Average counts per photo.	22.2	30.6
Film flow rate at stn. 2 (l/min.)	0.74	3.14

Table 8.3: Results for photographic study of re-entrainment effects.

Distance from entry plane(m) (Pipe section)	Test condt. Run No.	A						A1	B			C		
		T11A	T13	T16"	T18'	T19	Ave.	T14	T11B	T16	Ave.	T11C	T17	Ave.
	Injected liquid rate(l/min)	3945	3945	3945	3945	3945	3945	3945	4930.8	4930.8	4930.8	5899.4	5899.4	5899.4
	Extraction stn. No.													
-0.457	0	3758.5	3776.9	3790.0	3819.4	3856.1	3029.0	3915.2	4694.9	4719.4	4707.2	5651.6	5677.3	5664.5

0.223 (I)	1a	----	1806.6	1853.3	1897.0	1921.6	1869.6	2060.2	----	2329.3	2329.3	----	2899.2	2899.2
0.432 (II)	1b	1335.7	1323.4	1389.0	1430.2	1458.7	1387.4	1622.0	1582.4	1697.3	1639.9	1988.1	2103.9	2046.0
1.768 (III)	2	582.9	658.8	647.6	690.9	722.3	660.5	922.9	706.6	805.3	756.0	879.0	966.1	922.5
2.810 (IV)	3	423.3	504.1	461.1	499.3	518.2	481.2	696.0	500.8	574.9	537.9	616.6	679.0	647.8
4.825 (V)	4	243.2	301.6	----	279.0	295.8	279.9	408.4	250.6	287.1	268.8	279.8	274.9	277.4
8.292	5	119.0	161.6	----	170.9'	140.0	140.2	212.3	98.4	127.5	112.9	100.6	87.7	94.1

Table:8.4: Summary of deposition measurements indicating entrained rate at each extraction station. ' indicates a shorter length test section with station 5 at 6.792m from entry plane. " indicates a photographic batch at extraction station 4.

L relative to previous station (m) (pipe section)	Extraction station No.	Deposited liq. rate (cc/min)	Cumulative liq. rate (cc/min)	Fraction deposited	Fractional penetration p	$F = \frac{Q}{\pi DL} \ln \frac{1}{p}$ (m/s)	F^+ for $u_* = 0.79$m/s
--	0	88.88	3945.00	0.023	0.977	--	--
-- (I)	1a	1934.51	3856.12	0.502	0.498	--	--
0.209 (II)	1b	462.87	1921.62	0.241	0.759	0.486	0.615
1.336 (III)	2	736.48	1458.74	0.510	0.495	0.179	0.227
1.042 (IV)	3	203.85	722.26	0.282	0.718	0.120	0.151
2.015 (V)	4	222.65	518.41	0.429	0.571	0.106	0.134
3.467	5	155.82	295.76	0.527	0.473	0.079	0.100

Table 8.5: Computation of deposition velocity by Eqn. 8.3 for condition A

Run No.	Test Condt.	u_* (m/s)	$\bar{U}$ (m/s)	Distance relative to entry plane (m)					ν ($\times 10^{-5}$) (m^2/s)
				stn. 1b 0.432	stn. 2 1.768	stn. 3 2.810	stn. 4 4.825	stn. 5 8.292	
T11A	A	0.75	14.65	--	0.208 (0.278)	0.106 (0.142)	0.102 (0.136)	0.077 (0.102)	1.339
T13	A	0.76	14.48	0.548 (0.719)	0.178 (0.233)	0.097 (0.127)	0.094 (0.123)	0.066 (0.087)	1.361
T14	A1	0.85	17.02	0.488 (0.571)	0.167 (0.196)	0.119 (0.139)	0.113 (0.132)	0.081 (0.095)	1.361
T19	A	0.79	15.03	0.486 (0.615)	0.179 (0.227)	0.120 (0.151)	0.106 (0.134)	0.079 (0.100)	1.361
T18	A	0.78	14.99	0.497 (0.634)	0.186 (0.237)	0.118 (0.150)	0.106 (0.136)	0.084 (0.107) 6.796 m	1.335
Ave. excluding T14		0.77	14.79	(0.635)	(0.234)	(0.142)	(0.132)	(0.096) excld. T18.	1.351
Std. dev.(% of mean)		2.5%	1.8%	(9.8%)	(12.6%)	(6.9%)	(4.0%)	(7.05%)	0.98%
T16	B	0.76	14.81	0.557 (0.773)	0.190 (0.250)	0.122 (0.161)	0.127 (0.167)	0.086 (0.113)	1.352
T11B	B	0.77	14.55	--	0.203 (0.263)	0.114 (0.147)	0.127 (0.165)	0.100 (0.130)	1.379
Ave.		0.77	14.68	(0.733)	(0.257)	(0.154)	(0.166)	(0.122)	1.366
T17	C	0.77	14.81	0.564 (0.730)	0.199 (0.257)	0.128 (0.165)	0.165 (0.213)	0.121 (0.156)	1.352
T11C	C	0.77	14.65	--	0.205 (0.269)	0.118 (0.154)	0.145 (0.189)	0.109 (0.142)	1.361
Ave.		0.77	14.73	(0.730)	(0.262)	(0.160)	(0.201)	(0.149)	1.357

Table 8.6: Deposition velocity with respect to pipe length for all conditions studied. (Values within bracketts are non-dimensionalised). For run number T18 the deposition length for extraction station 5 is shortened by 1.6m.

Radial position r/R	0.04	0.32	0.60	0.88
Axial station No.				
2	A, Al, B, C	A	A	A
3	A, B, C	-	-	A
4	A, B, C	-	-	A
5	A, Al, B, C	-	-	A

Table 8.7: Axial and radial positions photographed for various test conditions.

Extraction station	2				3		4		5	
Radial position r/R	0.04	0.32	0.60	0.88	0.04	0.88	0.04	0.88	0.04	0.88
No. of slides / Size range μm	60	30	30	30	51	--	48	51	102	102
10-20	81	100	32	41	171	--	43	68	98	71
20-30	548	308	266	179	259	--	114	103	133	106
30-40	386	147	138	136	216	--	147	98	104	71
40-50	187	52	82	75	103	--	84	80	72	36
50-60	82	33	41	48	90	--	42	36	31	26
60-70	57	29	19	30	42	--	25	24	28	17
70-80	24	16	19	25	23	--	17	19	9	14
80-90	16	9	5	12	8	--	6	10	13	5
90-100	7	4	3	5	4	--	3	3	4	4
100-110	5	3	5	5	4	--	2	2	6	5
110-120	2	1	1	2	1	--	-	1	2	3
120-130	1	-	1	-	1	--	-	2	1	3
130-140	-	-	-	1	-	--	-	1	-	2
140-150	-	-	-	-	-	--	-	1	-	1
150-160	-	-	-	-	-	--	-	-	-	2
160-170	-	-	-	-	-	--	-	-	-	1
170-180	-	-	-	-	-	--	-	-	-	-
Ave. counts /slide	23.3	23.4	20.4	18.6	18.1	--	10.1	8.9	4.9	3.6

Table 8.8: Summary of number count statistics for test condition A

Test condition	A1		B				C		
Station number	2	5	2	3	4	5	2	3	4
No. of slides / Size range μm	60	93	60	51	68	96	60	51	68
10-20	231	12	427	46	-	8	192	103	9
20-30	422	60	495	197	86	57	428	322	85
30-40	380	86	294	260	147	81	332	305	151
40-50	237	68	175	203	88	64	199	213	112
50-60	156	69	81	136	116	63	124	170	115
60-70	74	31	68	69	36	36	66	86	34
70-80	43	24	31	43	20	24	45	54	28
80-90	34	16	23	19	7	17	32	25	15
90-100	10	7	14	11	5	3	17	19	7
100-110	10	6	9	8	3	10	17	8	7
110-120	3	2	5	2	1	1	7	8	2
120-130	1	3	2	1	1	5	2	4	1
130-140	-	1	1	1	-	1	3	1	2
140-150	-	1	-	1	1	-	-	1	2
150-160	-	1	-	-	-	-	2	2	1
160-170	-	-	-	-	-	-	2	-	-
170-180	-	-	-	-	-	-	-	2	-
Ave. counts/slide	26.7	4.2	27.1	19.6	7.5	3.9	24.6	25.9	8.4

Table 8.8(contd.) Summary of number count statistics for test conditions A1, B and C at radial position r/R= 0.04 only.

Test condition	A					Al	B	C
Extraction station No.	Mean dias.	r/R=0.04	0.32	0.60	0.88	0.04	0.04	0.04
2	$\bar{x}_{32}$	51.5	52.4	54.4	60.3	56.4	57.3	66.0
	$\bar{x}_{31}$	46.4	46.2	48.5	54.0	50.8	49.6	57.4
	$\bar{x}_{30}$	42.5	41.3	43.9	48.7	45.9	43.2	50.4
3	$\bar{x}_{32}$	53.5					60.2	66.5
	$\bar{x}_{31}$	48.0					55.3	59.0
	$\bar{x}_{30}$	43.3					51.0	52.8
4	$\bar{x}_{32}$	53.3			63.3		60.0	67.2
	$\bar{x}_{31}$	49.0			56.0		55.3	61.0
	$\bar{x}_{30}$	45.3			49.8		51.8	56.0
5	$\bar{x}_{32}$	60.8			80.6	71.9	71.0	
	$\bar{x}_{31}$	53.6			67.4	65.3	65.0	
	$\bar{x}_{30}$	47.2			56.2	59.4	59.6	

Table 8.9: Computed mean diameters from original data by Wise's(193) definition (see also Table 6.1).

No. of slides analysed	First trial				Repeated		
	30				30		
Mean diameters (μm)	$\bar{x}_{32}$	$\bar{x}_{31}$	$\bar{x}_{30}$		$\bar{x}_{32}$	$\bar{x}_{31}$	$\bar{x}_{30}$
Test condition							
A	47.6	46.4	42.5		53.9	48.8	44.8
A1	56.0	49.9	44.6		56.6	51.6	47.0
B	58.3	50.3	43.6		56.0	48.8	42.8
C	67.3	58.1	50.6		64.0	56.3	50.0

Table 8.10: Computed mean diameters by Wises's(193) definition for two sets of repeated measurements at r/R=0.04 at station 2 for test conditions as shown.

Test condition		A				A1	B	C
Radial position r/R=		0.04	0.32	0.60	0.88	0.04	0.04	0.04
Station No.	Parameters							
2	a or (m_1, m_2)	3.37	1.11	2.93	2.35	2.02	1.40	3.36
	δ or (δ_1, δ_2)	1.15	0.78	1.04	1.18	1.12	0.85	1.07
	x_m or (x_m, k)	251	134	253	224	195	166	344
	95% limits	240&284	118&157	153&334	230&280	182&218	155&180	320&416
	$\bar{x}_{32}$ (μm)	49.5	50.1	53.9	64.0	56.2	55.9	66.4
	x_{500} (μm)	57.4	63.5	64.4	72.8	64.5	69.3	78.9
3	a or (m_1, m_2)	3.66	/	/	/	/	0.79,0.66	0.55,-0.94
	δ or (δ_1, δ_2)	1.35					1.60,1.21	1.31, 0.50
	x_m or (x_m, k)	284					265, 1.40	2.02,-1.91
	95% limits	212&320					220&306	177&242
	$\bar{x}_{32}$ (μm)	54.6					60.7	64.0
	x_{500} (μm)	60.9					68.5	85.9

Table 8.11: ULDF and heterogeneous ULDF least squares parameters for s=1 of all test conditions. Results at station 2 at r/R=0.04 consists of nett from two separate spectra.

Test condition		A				A1	B	C
Radial position r/R=		0.04	0.32	0.60	0.88	0.04	0.04	0.04
Station No.	Parameters							
4	a or (m_1, m_2)	2.24			0.39, -1.08		0.44, -2.34	-0.04, 0.50
	δ or (δ_1, δ_2)	1.21			1.12, 1.36		1.76, 0.48	0.78, 1.65
	x_m or (x_m, k)	194			165, 4.47		185, 2.98	204, 0.90
	95% limits	182&223			142&204		160&242	138&278
	$\bar{x}_{32}$ (μm)	53.2			63.7		61.8	67.8
	x_{500} (μm)	60.0			77.5		78.9	81.8
5	a or (m_1, m_2)	1.04			0.68	0.36, -1.10	2.89	
	δ or (δ_1, δ_2)	0.79			0.57	1.26, 0.70	1.32	
	x_m or (x_m, k)	150			182	178, 1.84	370	
	95% limits	127&197			169&219	159&218	0&549	
	$\bar{x}_{32}$ (μm)	58.6			73.6	72.0	73.4	
	x_{500} (μm)	73.3			108.2	87.5	82.2	

Table 8.11 (contd.)

Diameter (μm)	r/R=0.7	
	θ =0°	θ=180°
$\bar{x}_{32}$	68.5	55.1
$\bar{x}_{31}$	57.7	48.5
$\bar{x}_{30}$	48.6	43.3
Ave. counts per slide	22.6	18.8

Table 8.12: Mean diameters for condition A at station 2 for two radial positions in the vertical plane.

Droplet diameter (μm)	Relaxation time $\tau = \frac{x_w^2 \rho_w}{18 \mu_g}$ x10^3 (s)	Terminal velocity $V_t = \frac{\rho_w g x_w^2}{18 \mu_g}$ x10^3 (m/s)	V_t/u_* (u_*=0.77m/s)
30	3.081	30.22	0.04
40	5.480	53.76	0.07
50	8.560	83.97	0.11
60	12.330	120.96	0.16
70	16.780	164.62	0.21
80	21.910	214.94	0.28
90	27.330	268.11	0.35
100	34.240	335.89	0.44
110	41.430	406.43	0.53
120	49.300	483.63	0.63

Table 8.13: Relaxation times and terminal velocities for water drops in air.

Time t s x10^2	Station No.	Entrained volume cc/min.	$\bar{x}_{30}$ (Fig.8.20) (μm)	Deposited volume cc/min.	A Entrained No. based on $\bar{x}_{30}$ at each stn. x $10^{-9}/m^3$	$\int_0^t ndt$	Deposited No. x $10^{-8}/m^3$	$(\Delta n)_L$ x$10^{-8} m^3$	ln A	ln A+ βt
0	2	660.5	42.5		2.28				21.55	
			42.9	179.3		0.71	6.02	6.02		21.61
7.04	3	481.2	43.3		1.57				21.17	
			44.3	201.3		1.48	6.14	12.16		21.34
20.66	4	279.2	45.3		0.797				20.50	
			46.3	139.0		1.93	3.73	15.89		20.86
44.08	5	140.2	47.2		0.354				19.68	

Table 8.14: Sample calculation for $\int_0^t ndt$, $(\Delta n)_L$ and ln n+βt for Fig. 8.20 for condition A

Test condition	A	B	C
Slope $(-\alpha/\bar{U})$	0.235	0.291	0.353
Corr. coeff. c for $\alpha/\bar{U}$	-0.995	-0.996	-0.998
α (based on $\bar{U}$=14.73m/s)	3.462	4.292	5.200
Slope β (s^{-1})	0.821	0.709	0.779
Corr. coeff. c for β	0.999	0.997	0.999
Ratio α/β (or $4F/\beta D$)	4.217	6.057	6.680
Slope $(-K/\beta)$ x 10^{-9}	0.797	1.547	1.344
Corr. coeff. c for K/β	-0.953	-0.912	-0.892
K x 10^{-10} (m^3/s)	6.543	10.960	10.470

Table 8.15: Summary of parameters K,β and α for test conditions A,B and C

Test condition	A			B			C		
Extraction station	Kn^2 x10^{-8} (s^{-1})	βn x10^{-8} (s^{-1})	$Kn^2/\beta n$	Kn^2 x10^{-8} (s^{-1})	βn x10^{-8} (s^{-1})	$Kn^2/\beta n$	Kn^2 x10^{-8} (s^{-1})	βn x10^{-8} (s^{-1})	$Kn^2/\beta n$
2	34.00	18.71	1.82	47.74	14.79	3.23	38.60	14.96	2.58
3	16.13	12.89	1.25	18.24	9.14	2.10	14.33	9.11	1.57
4	4.16	6.54	0.64	2.82	3.59	0.79	1.76	3.19	0.55
5	0.82	2.91	0.28	0.22	1.00	0.22	0.10	0.77	0.13

Table 8.16: Summary of Kn^2, βn and the ratio ($Kn^2/\beta n$).

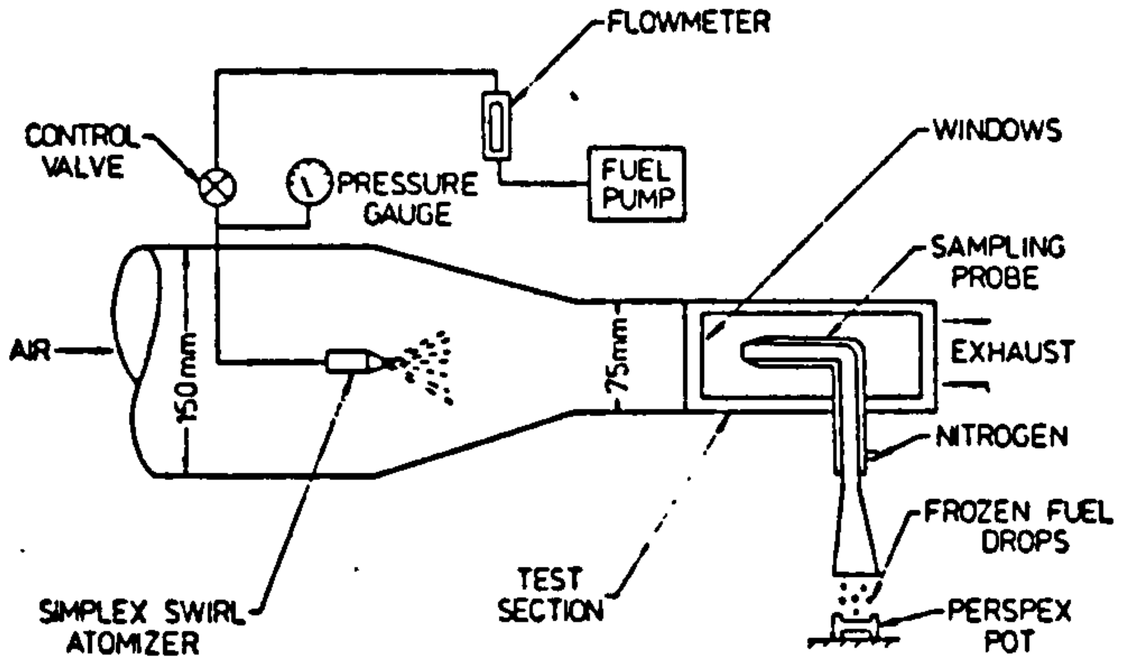


FIG. 3.1 Illustration of mechanical sampling probe (reproduced from ref.(110)).

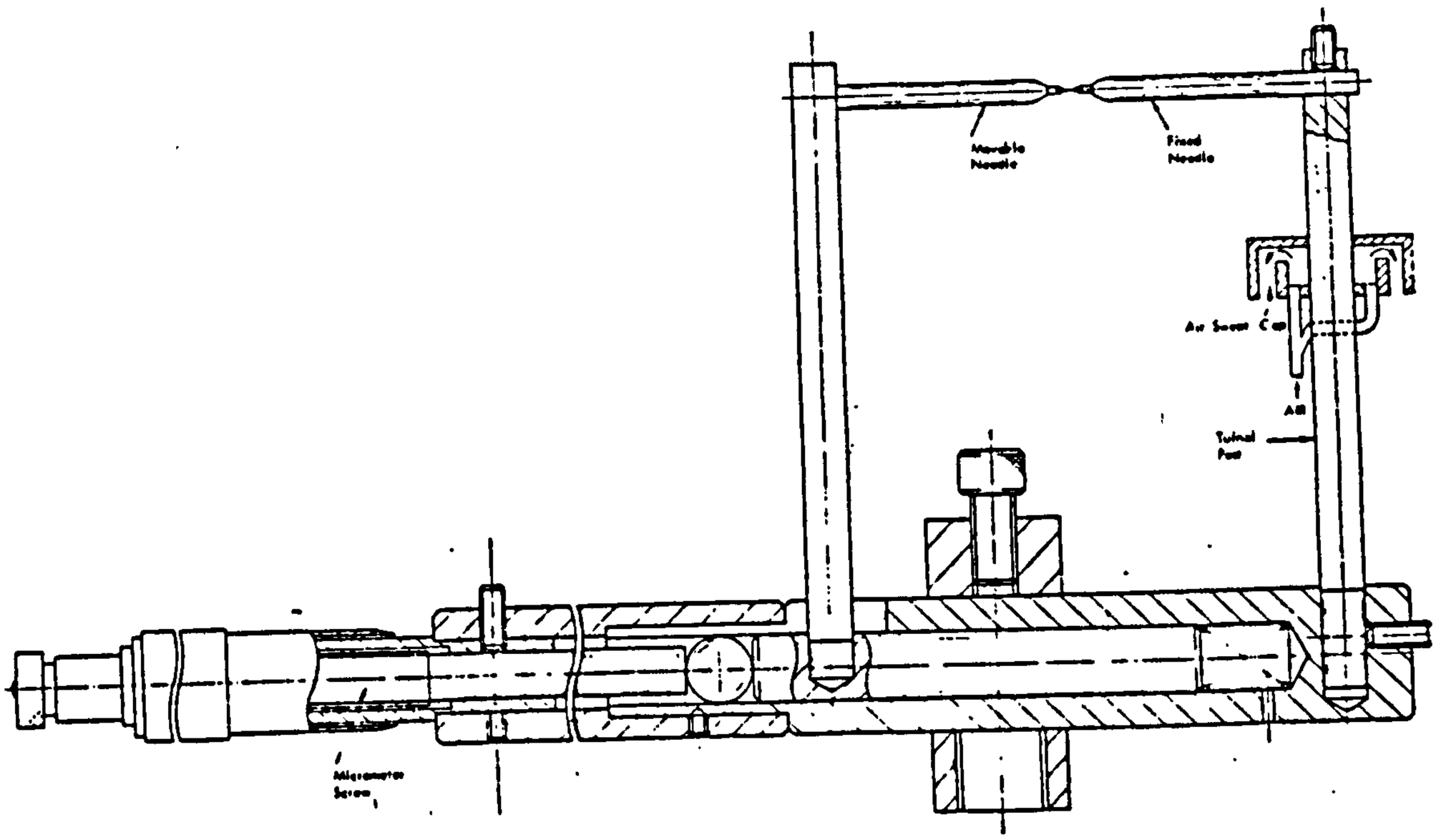


FIG. 3.2 Pulse counting technique (reproduced from ref.(114)).

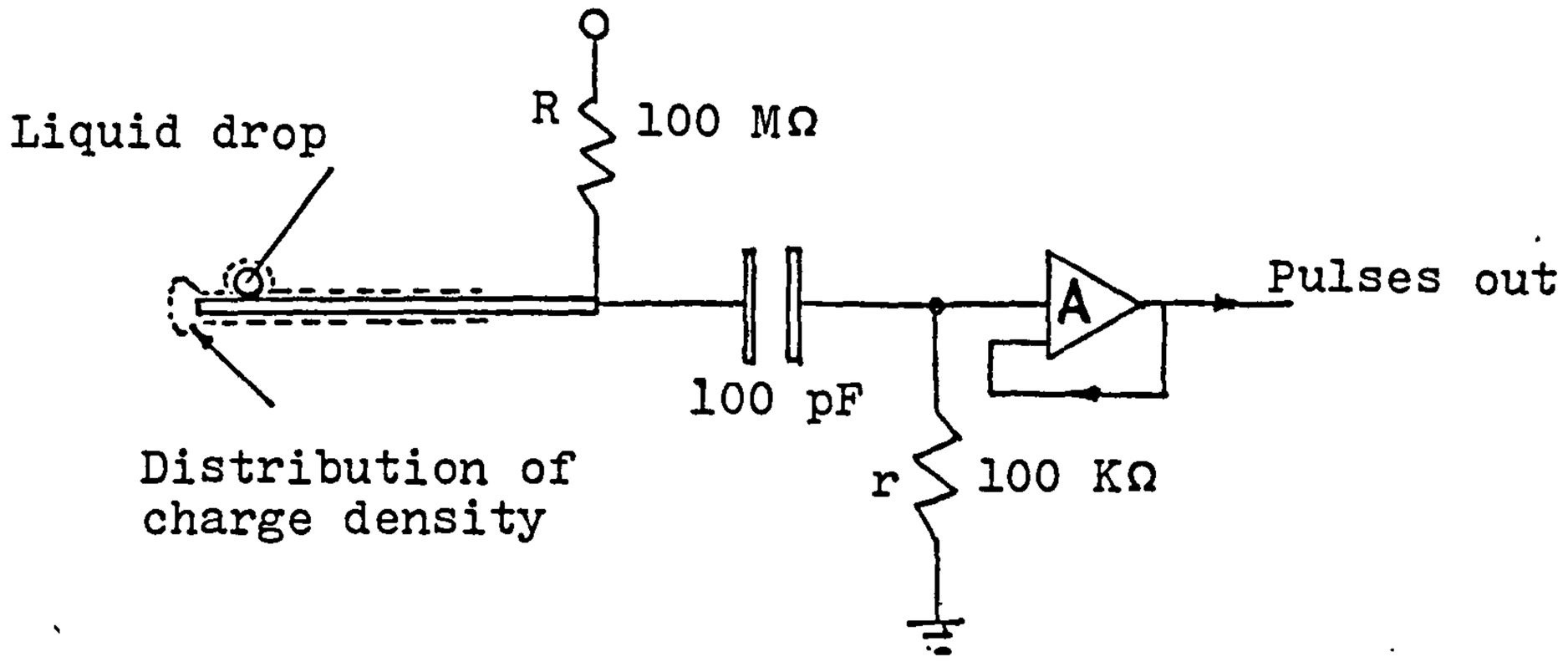


FIG. 3.3 Charged wire probe technique

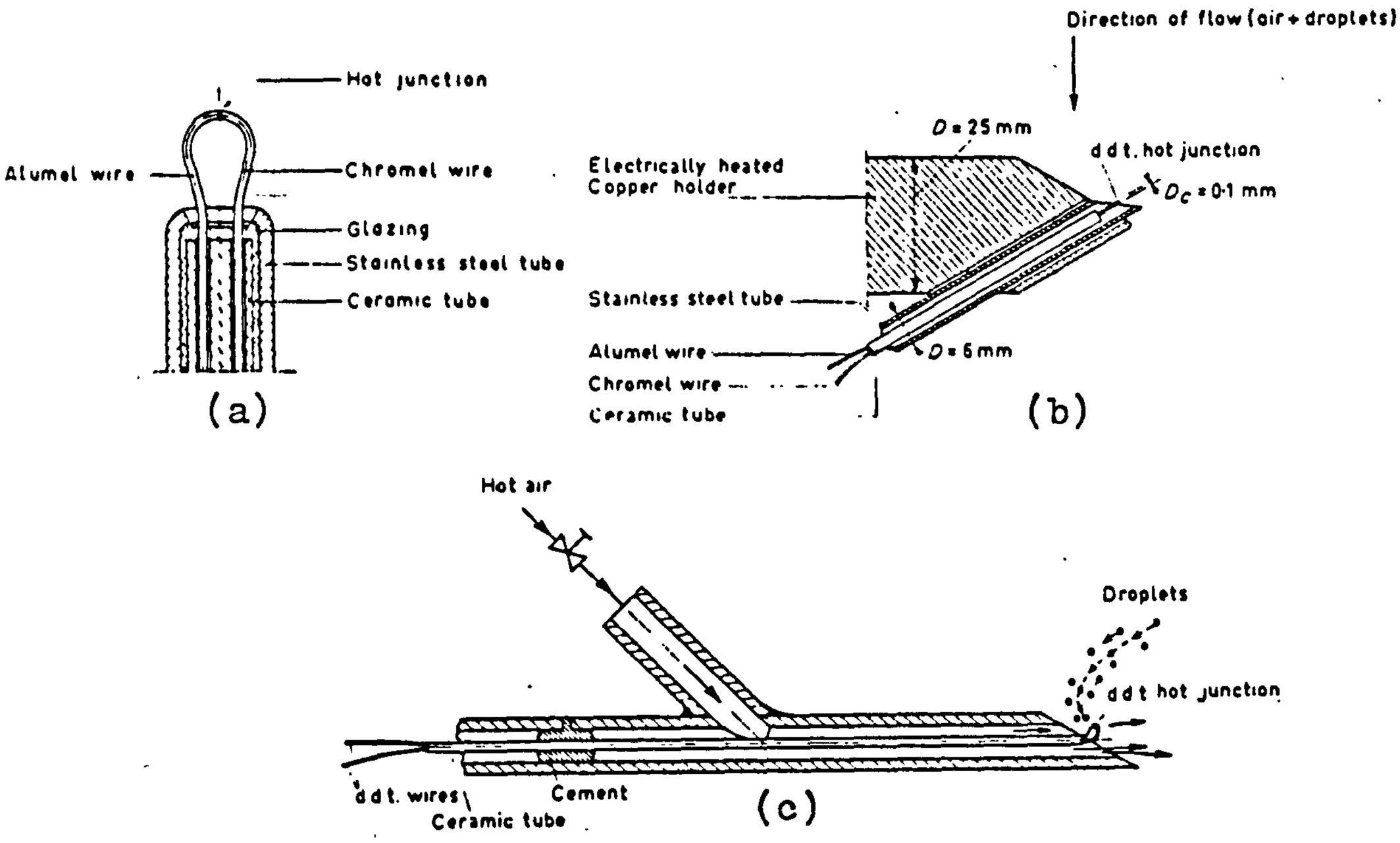
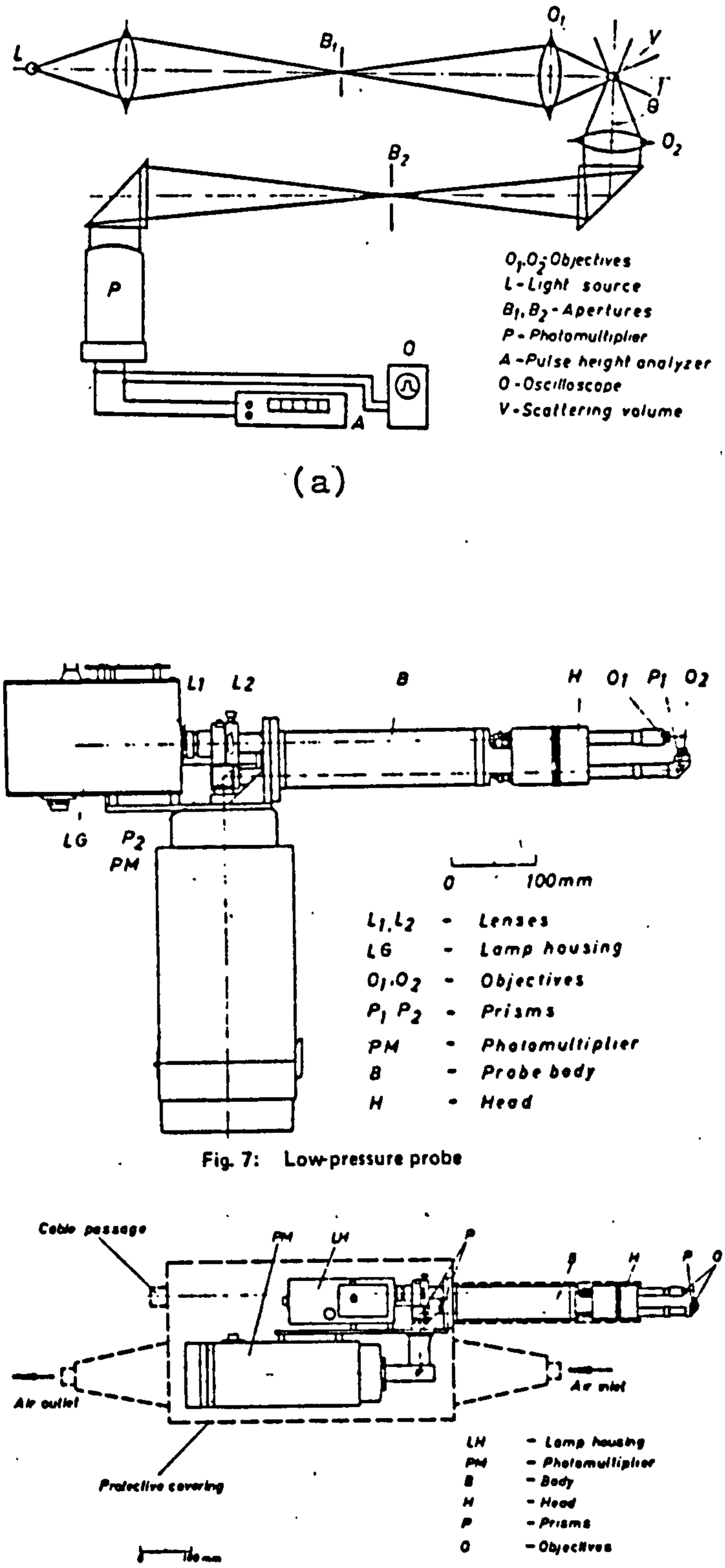


FIG. 3.4 Droplet detecting thermocouple(d.d.t.) (a) bare d.d.t.; (b) hot junction electrically heated; (c) hot junction heated by hot air. (reproduced from ref. (121))



(a)

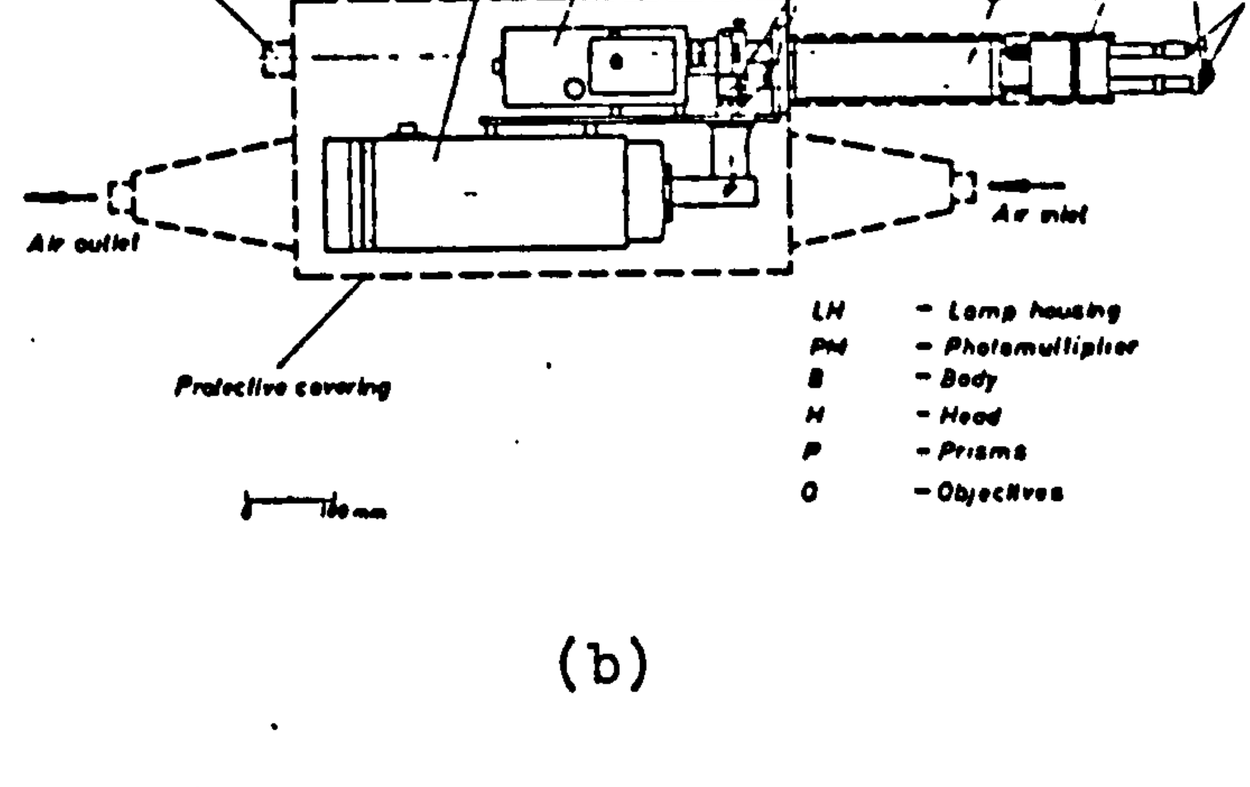


Fig. 7: Low-pressure probe

(b)

FIG. 3.5 Light scattering probe.
(a) Optical arrangement.
(b) Typical probe geometry.
(reproduced from ref.(128)).

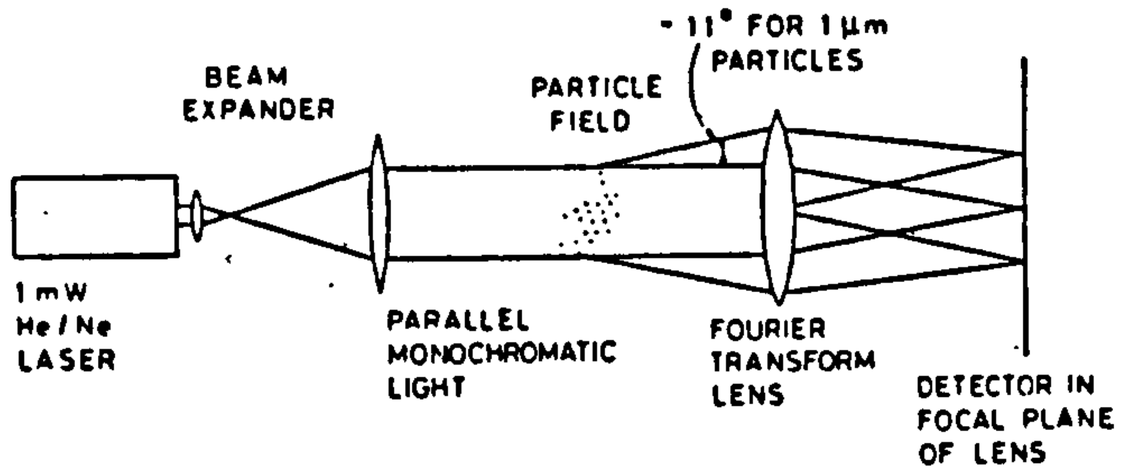


FIG. 3.6 Laser diffraction technique (reproduced from ref. (140)).

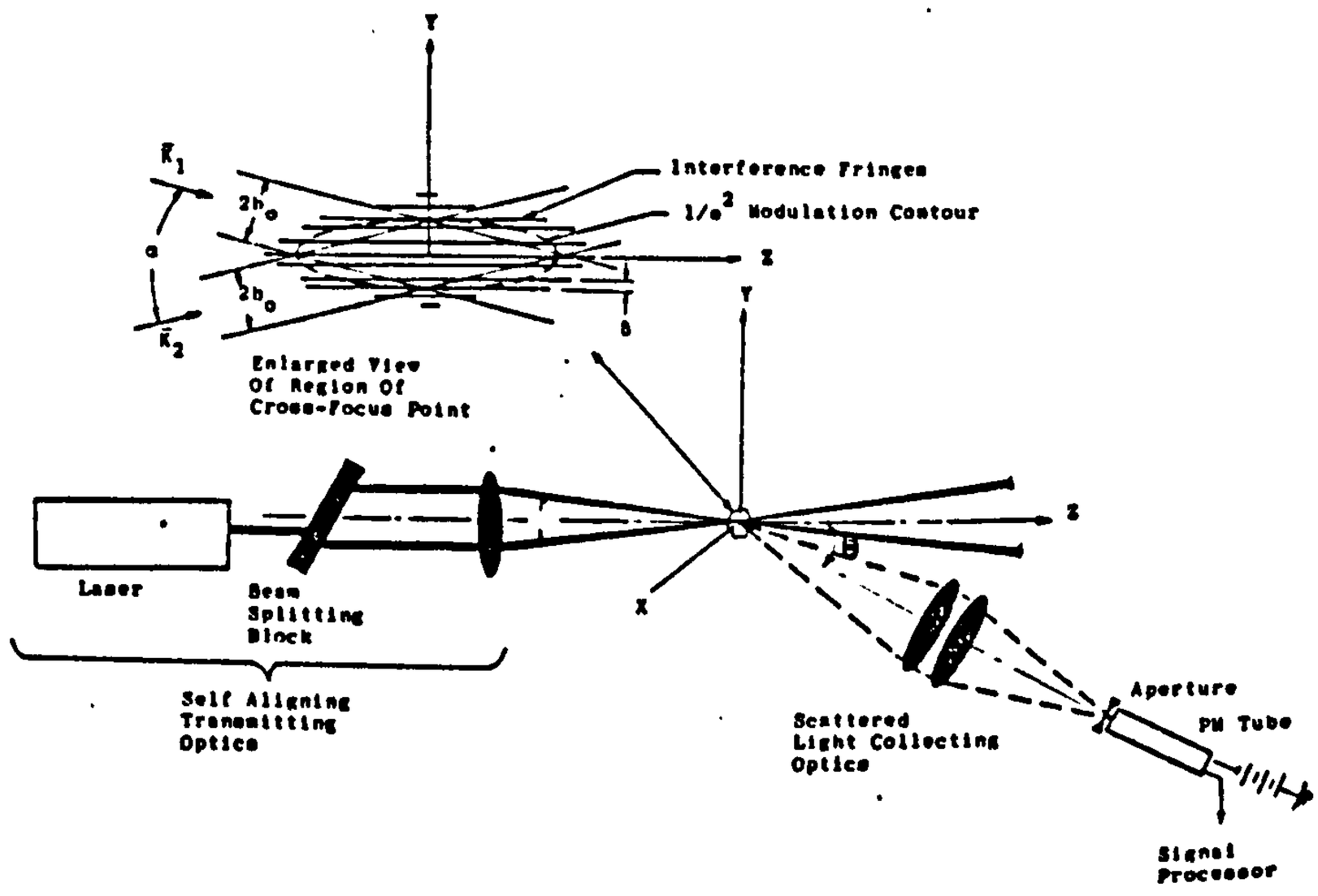


FIG. 3.7 Interference fringe technique as examined by Farmer (142).

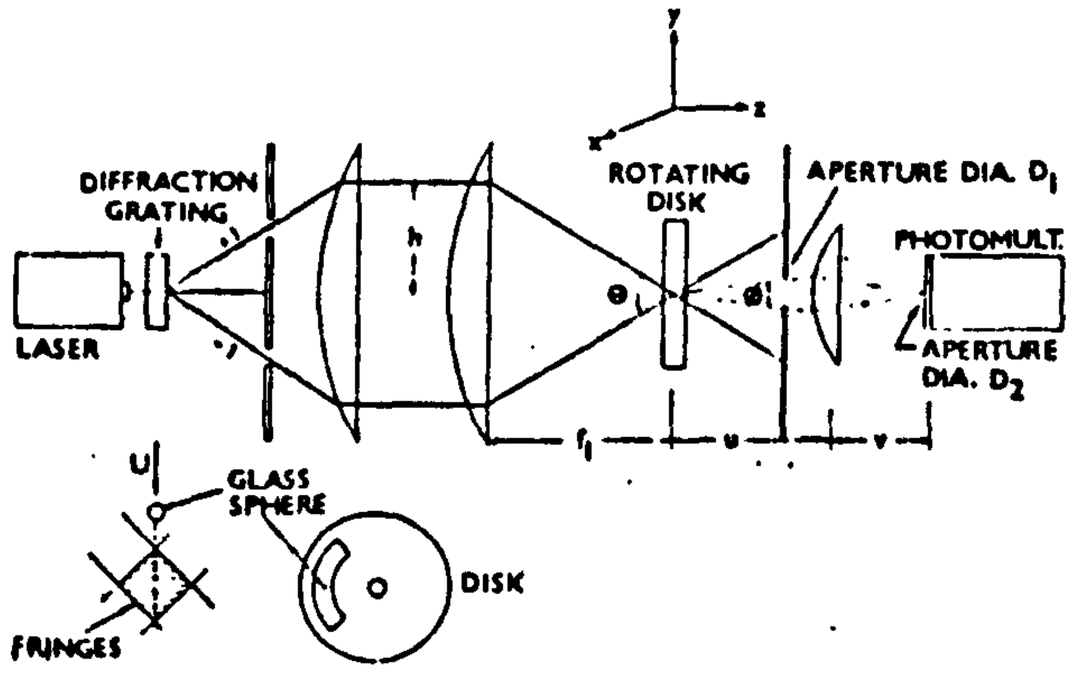


FIG. 3.8 Laser Doppler Anemometry (LDA) for particle size measurement. (reproduced from ref. (145)).

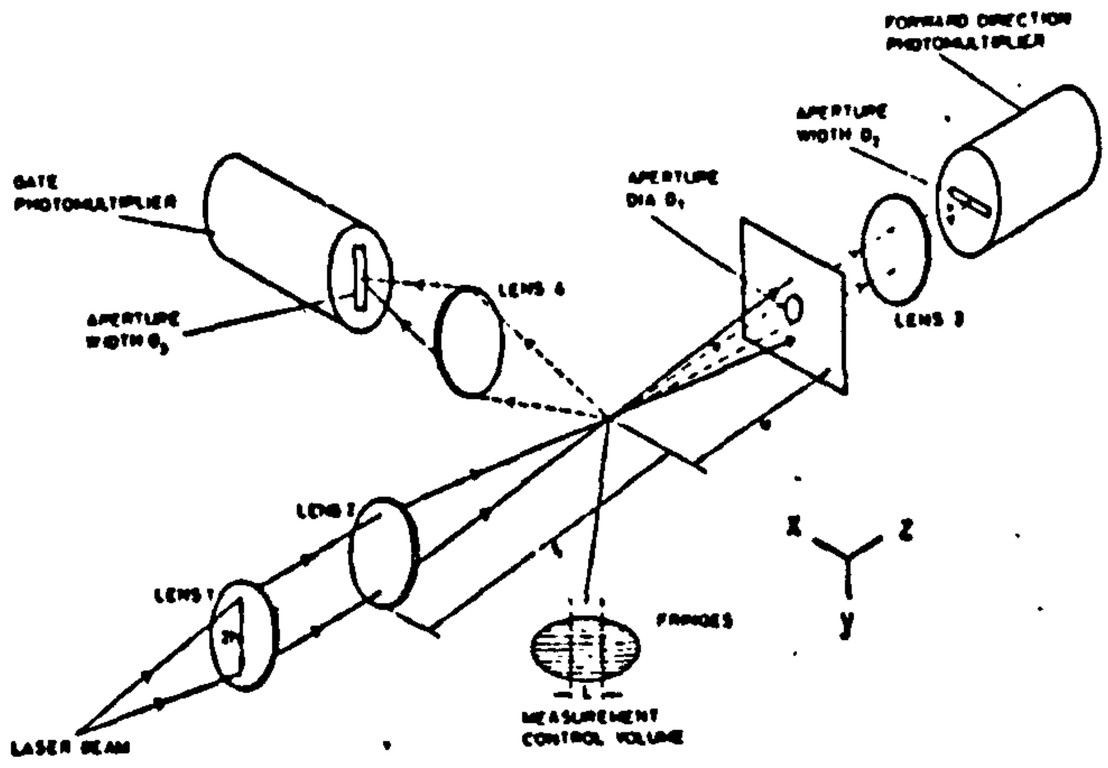


FIG. 3.9 Laser Doppler Anemometry (LDA) for particle sizing used by Ungut et al. (146).

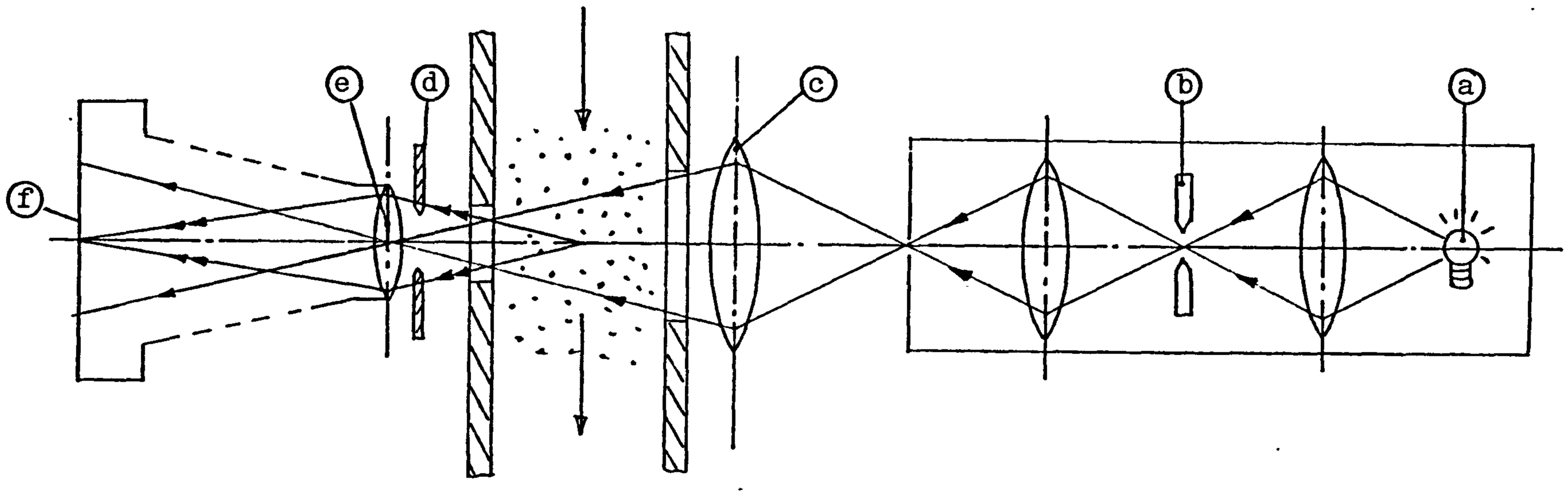


FIG. 3.10 Illustration of shadow photography method.
(a) focussing lamp ; (b) spark source ;
(c) condenser lens ; (d) camera shutter/aperture ;
(e) camera lens ; (f) focussing screen.

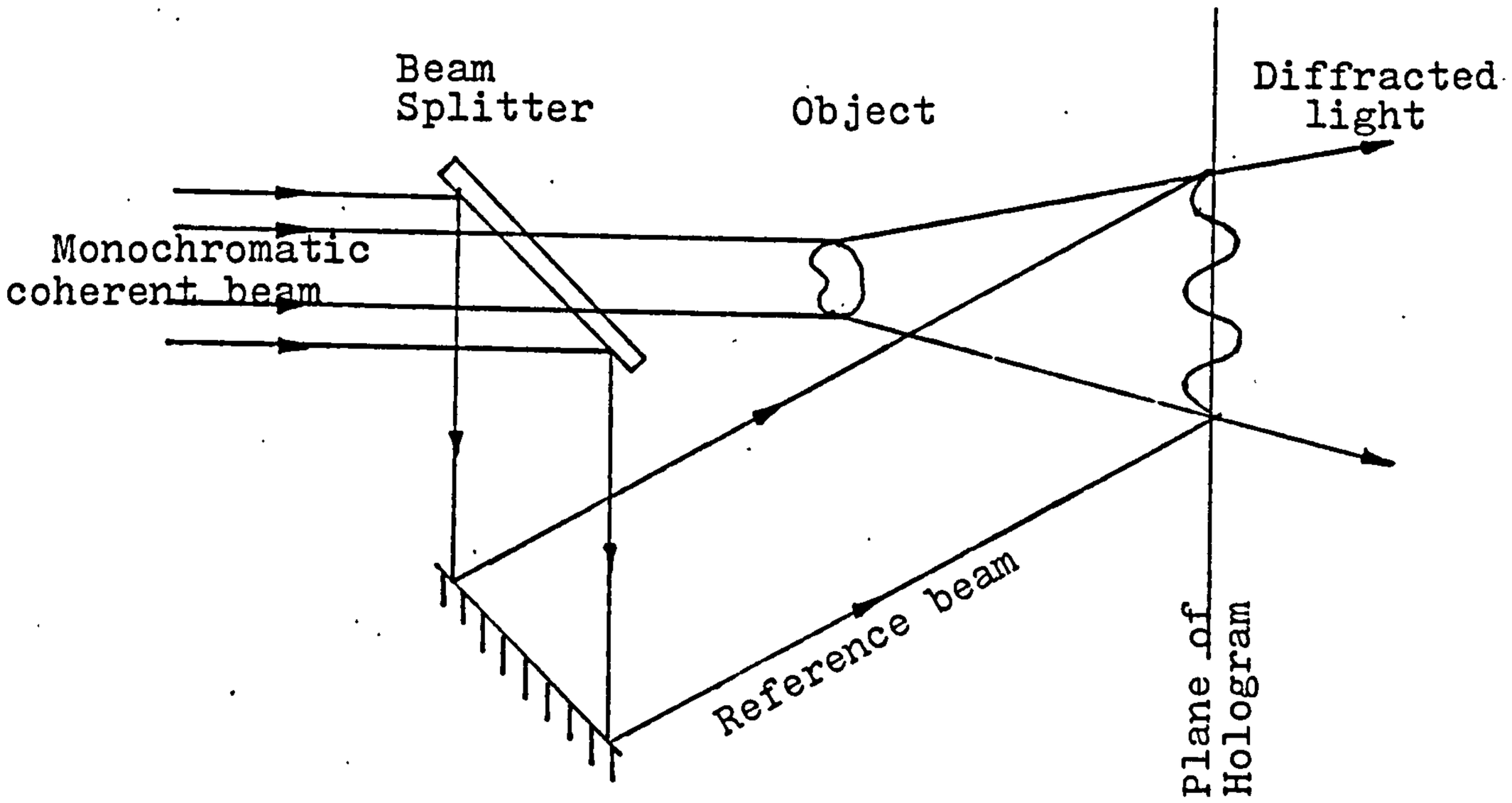


FIG. 3.11 Holography - formation of diffraction patterns

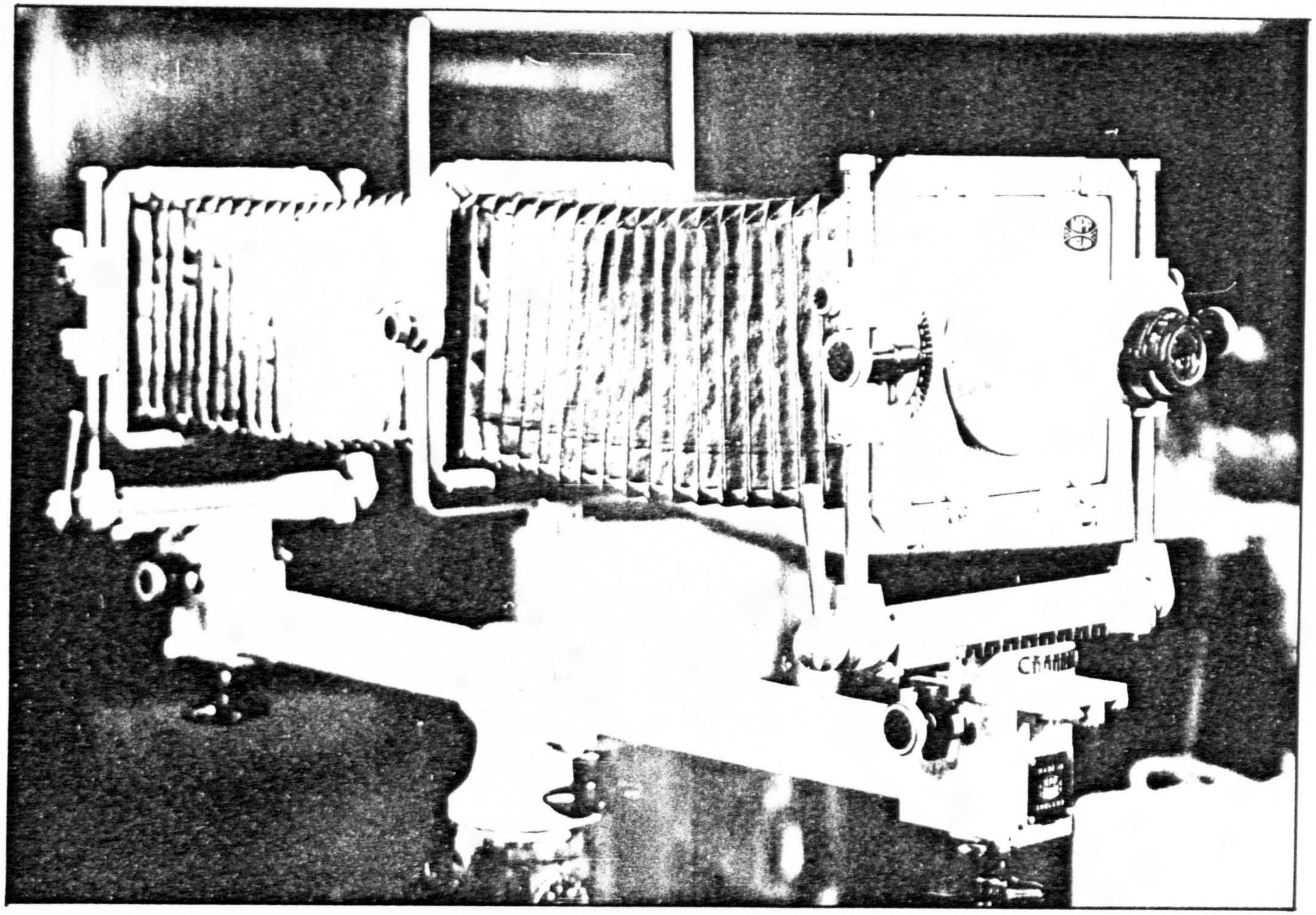


FIG. 4.1 The MPP monorail camera with bellows fully extended.

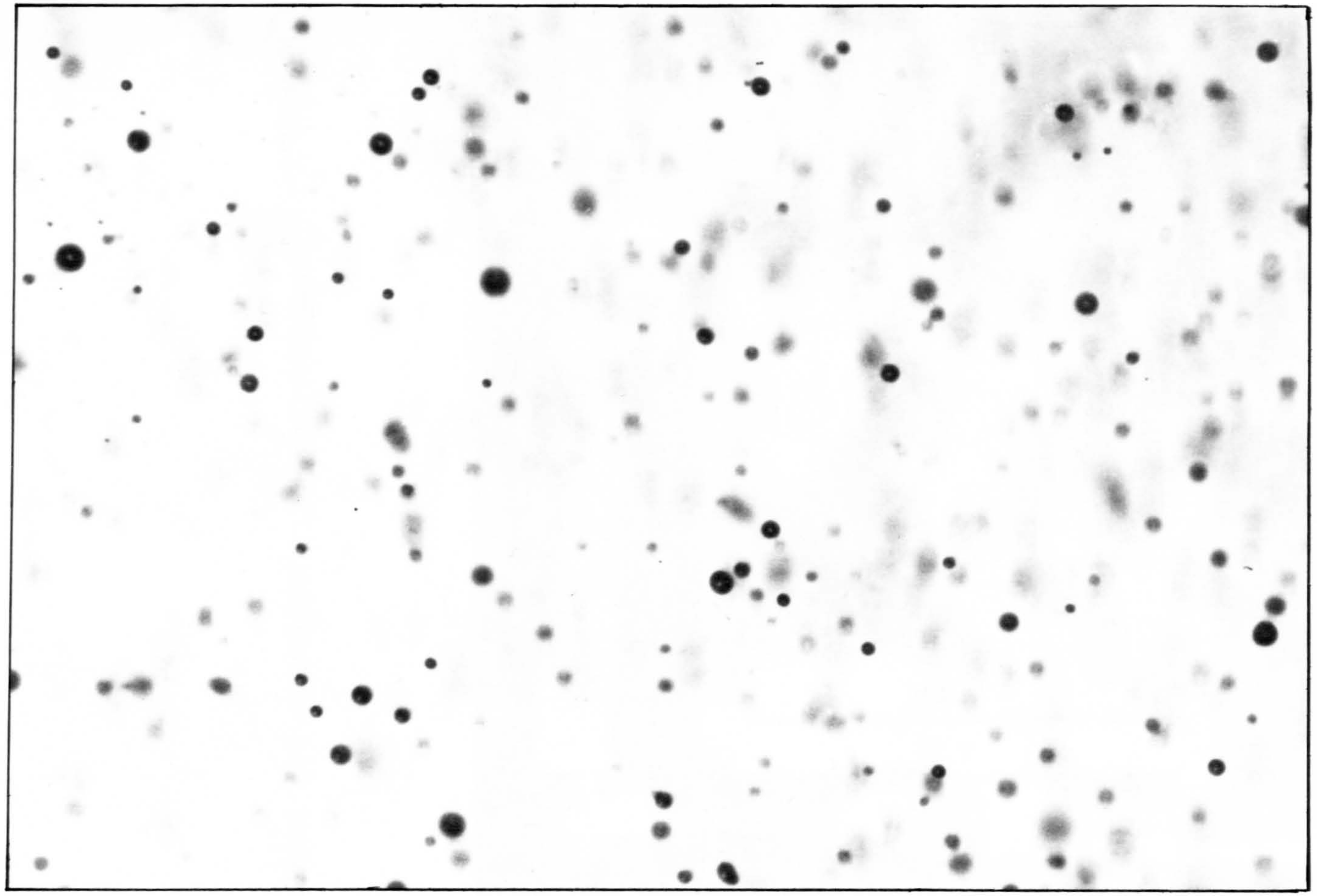


FIG. 4.2 Typical photograph of an air-blast atomiser spray spectrum. Overall magnification approx. 70x. (Area=approx. 6% of complete negative.)

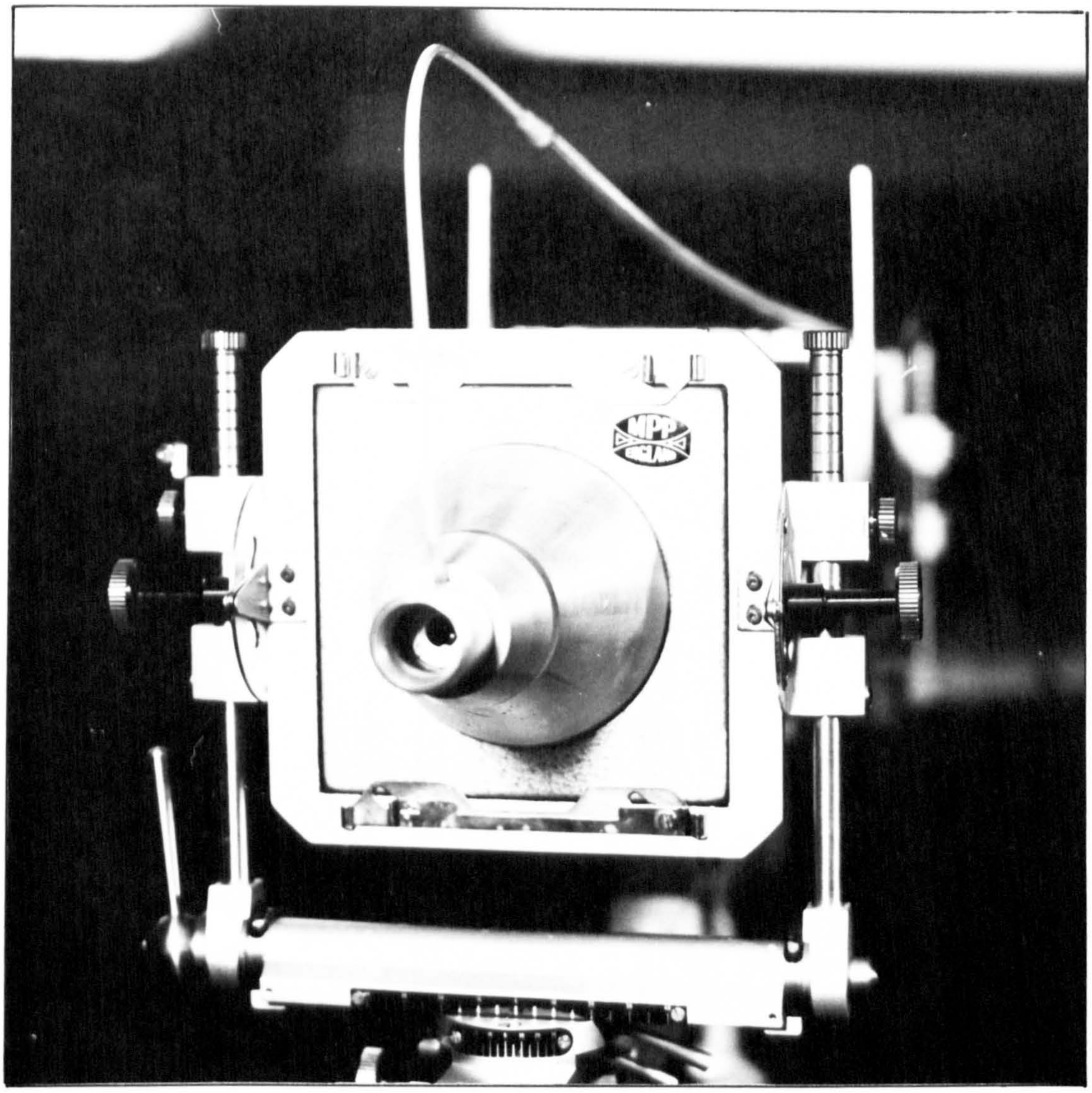


FIG. 4.3 Illustration of continuous air purge assembly for lens.

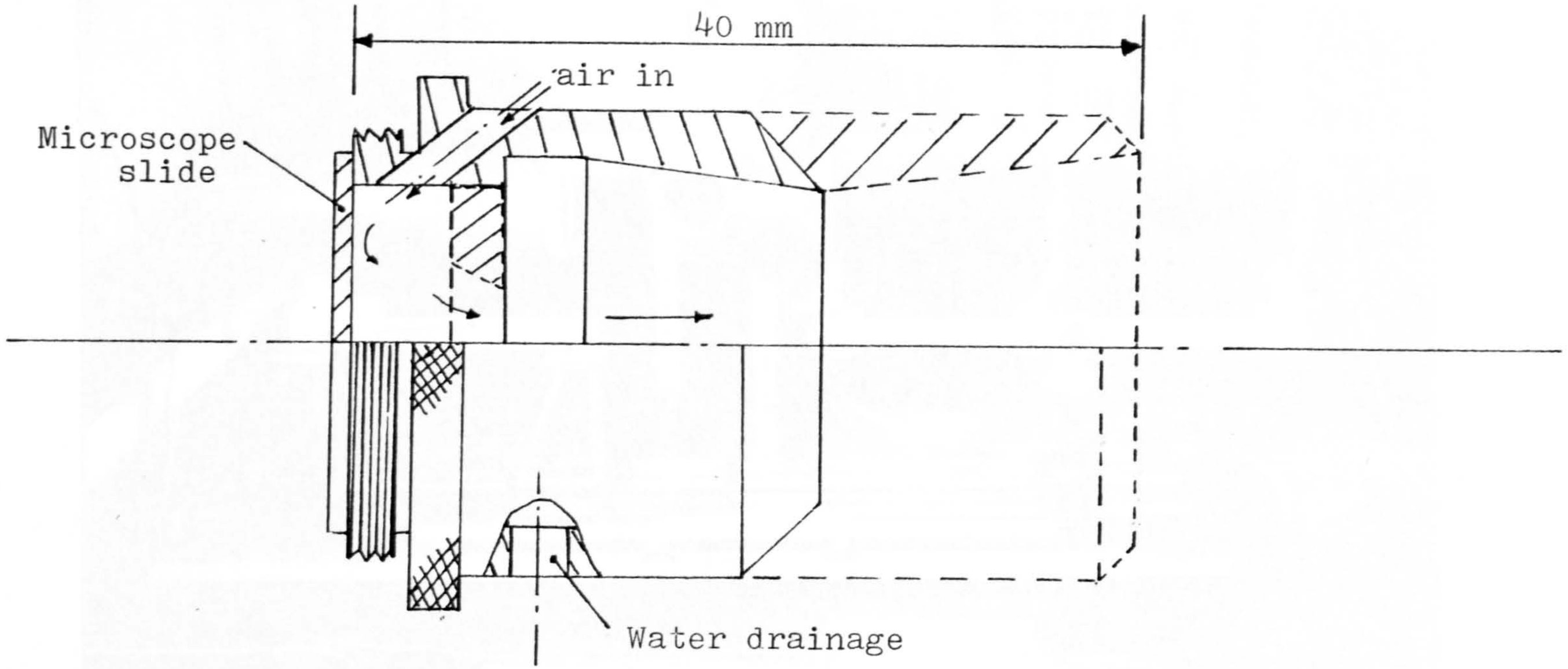


FIG. 4.4 Schematic of air purge hood. Dotted lines indicate modifications to the original unit.

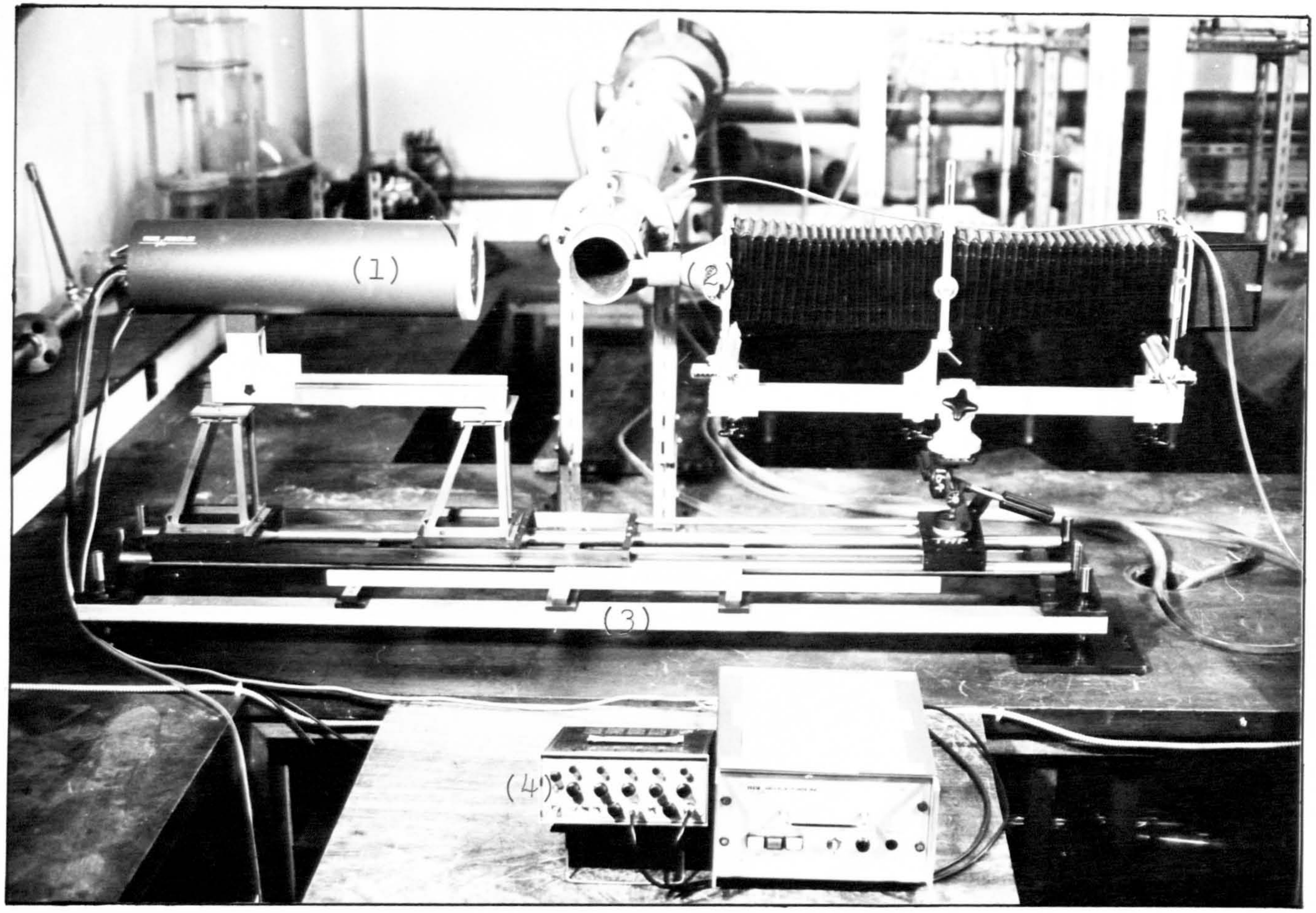
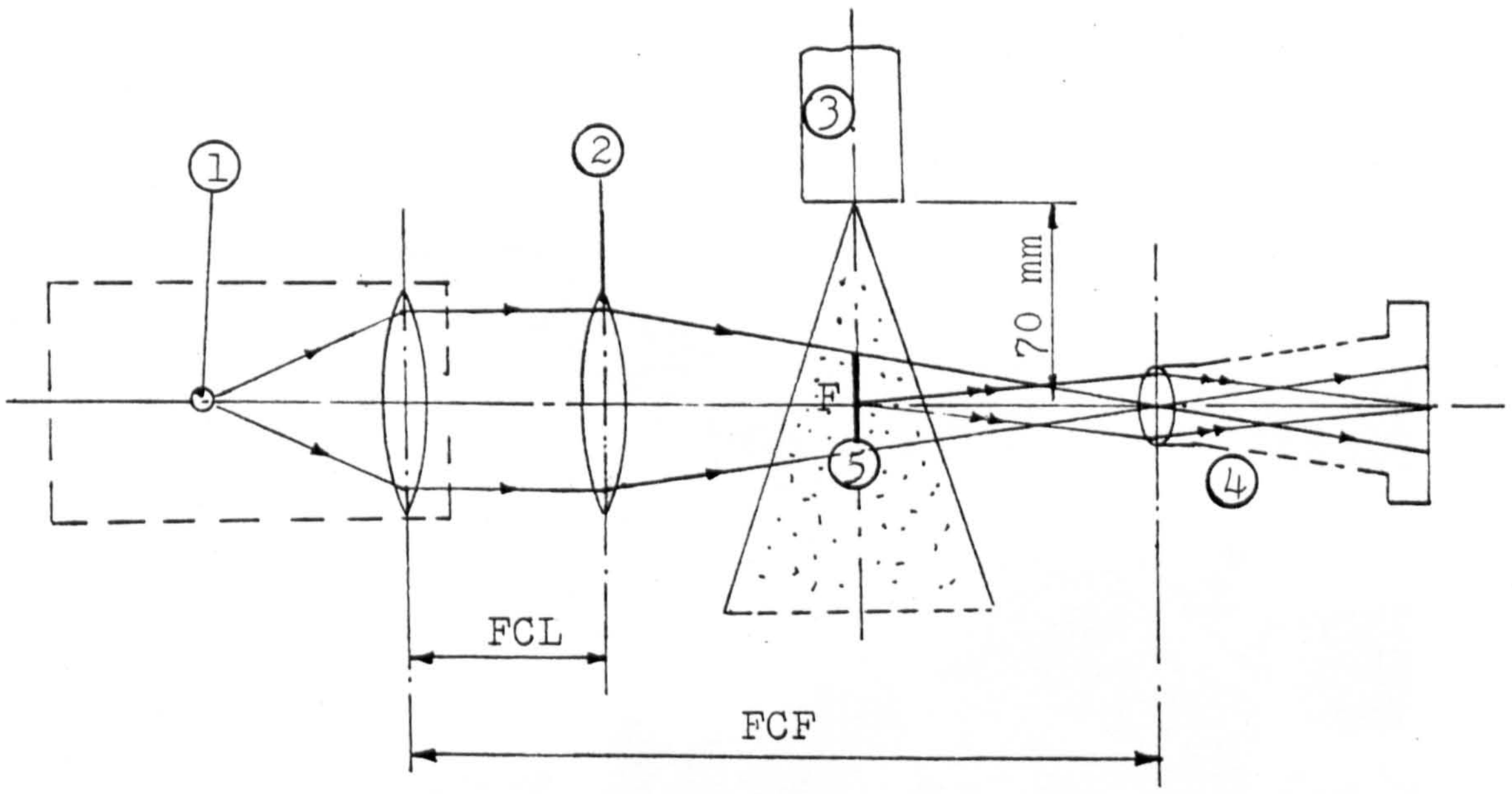
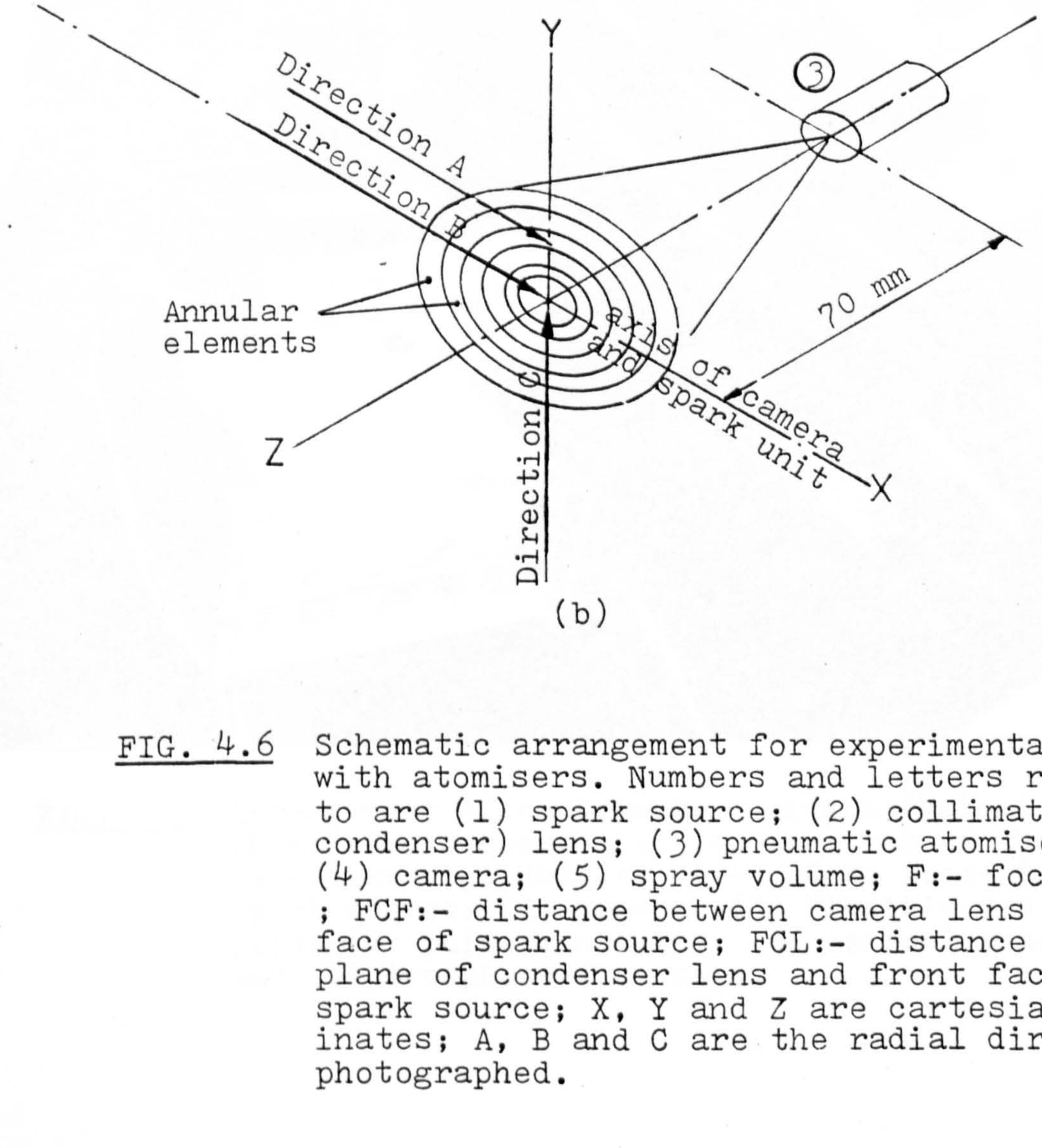


FIG. 4.5 Illustration of optical bench with camera and light source in position at exit of two-phase rig. Numbers referred to are:- (1) spark unit; (2) camera; (3) optical bench and (4) pulse generator.



(a)



(b)

FIG. 4.6 Schematic arrangement for experimentation with atomisers. Numbers and letters referred to are (1) spark source; (2) collimating (or condenser) lens; (3) pneumatic atomiser; (4) camera; (5) spray volume; F:- focal plane ; FCF:- distance between camera lens and front face of spark source; FCL:- distance between plane of condenser lens and front face of spark source; X, Y and Z are cartesian coordinates; A, B and C are the radial directions photographed.

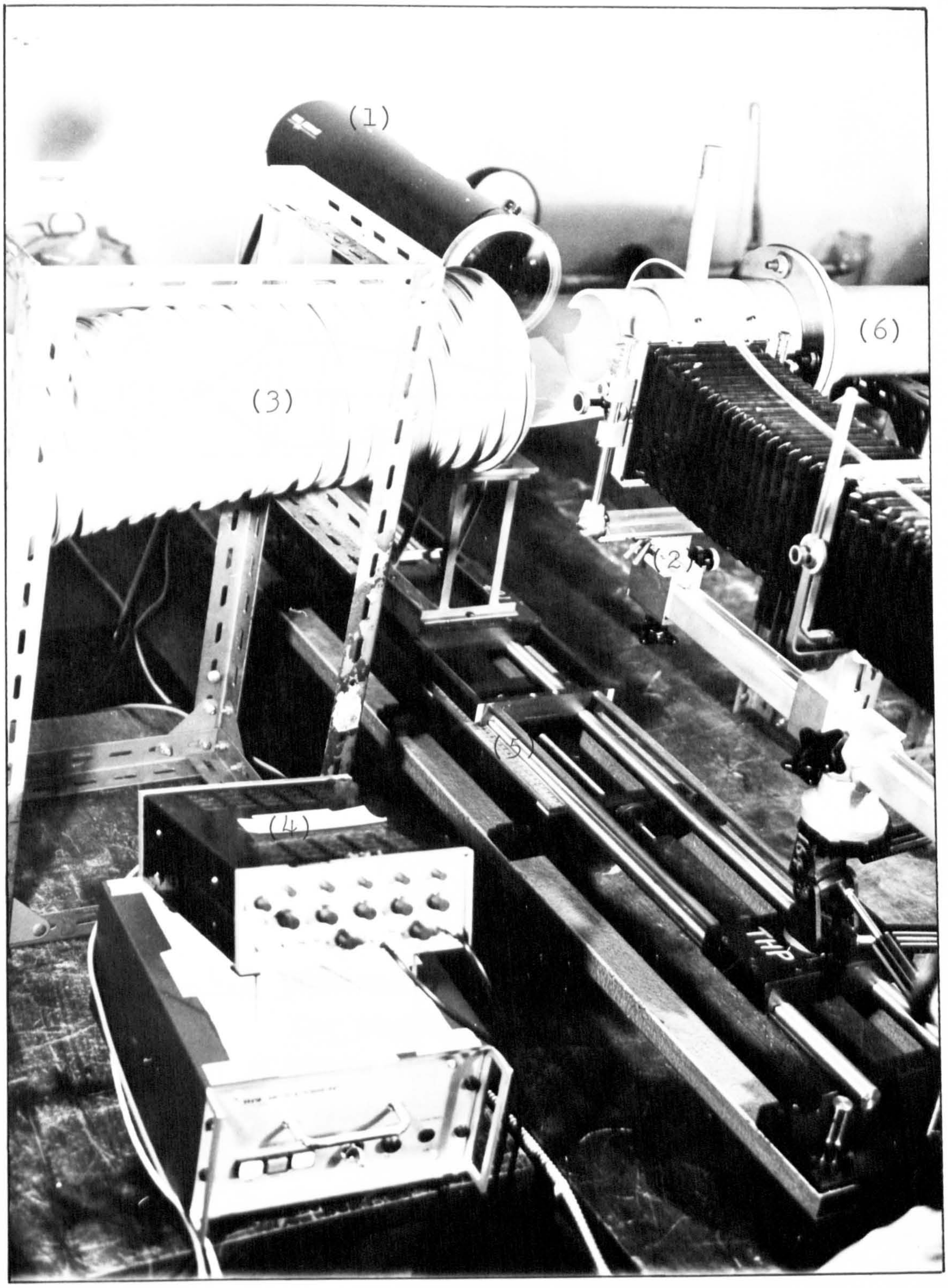


FIG. 4.7 Arrangement of equipments during a typical photographic session at the open end of the two-phase rig. Numbers referred to are:- (1) spark source; (2) camera; (3) flexible drain pipe; (4) pulse generator; (5) optical bench and (6) two-phase flow pipe.

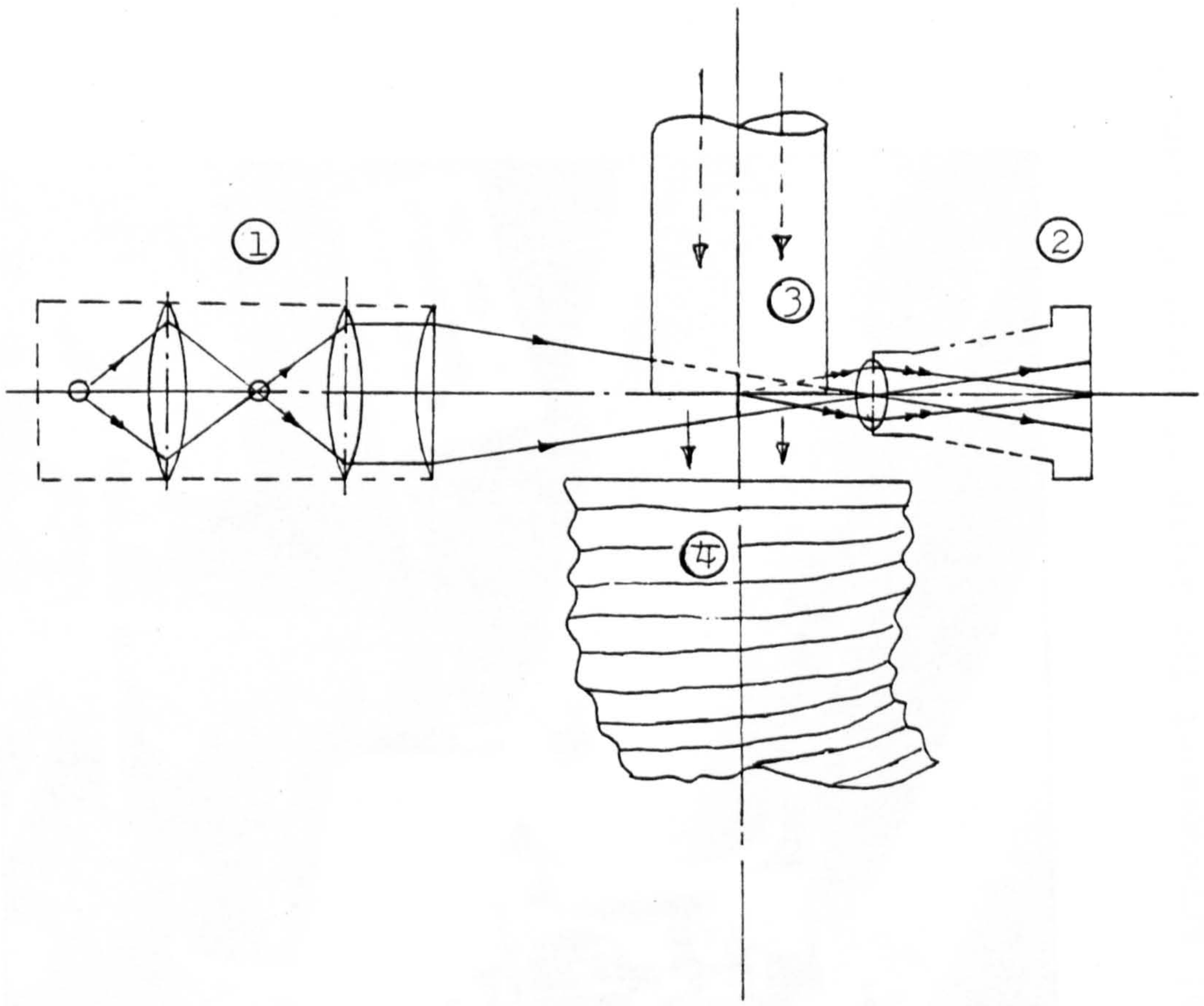


FIG. 4.8 Schematic diagram of optical arrangement for photography at the exit of the two-phase duct. Numbers referred to are:- (1) spark source; (2) camera; (3) two-phase duct; (4) flexible drain pipe.

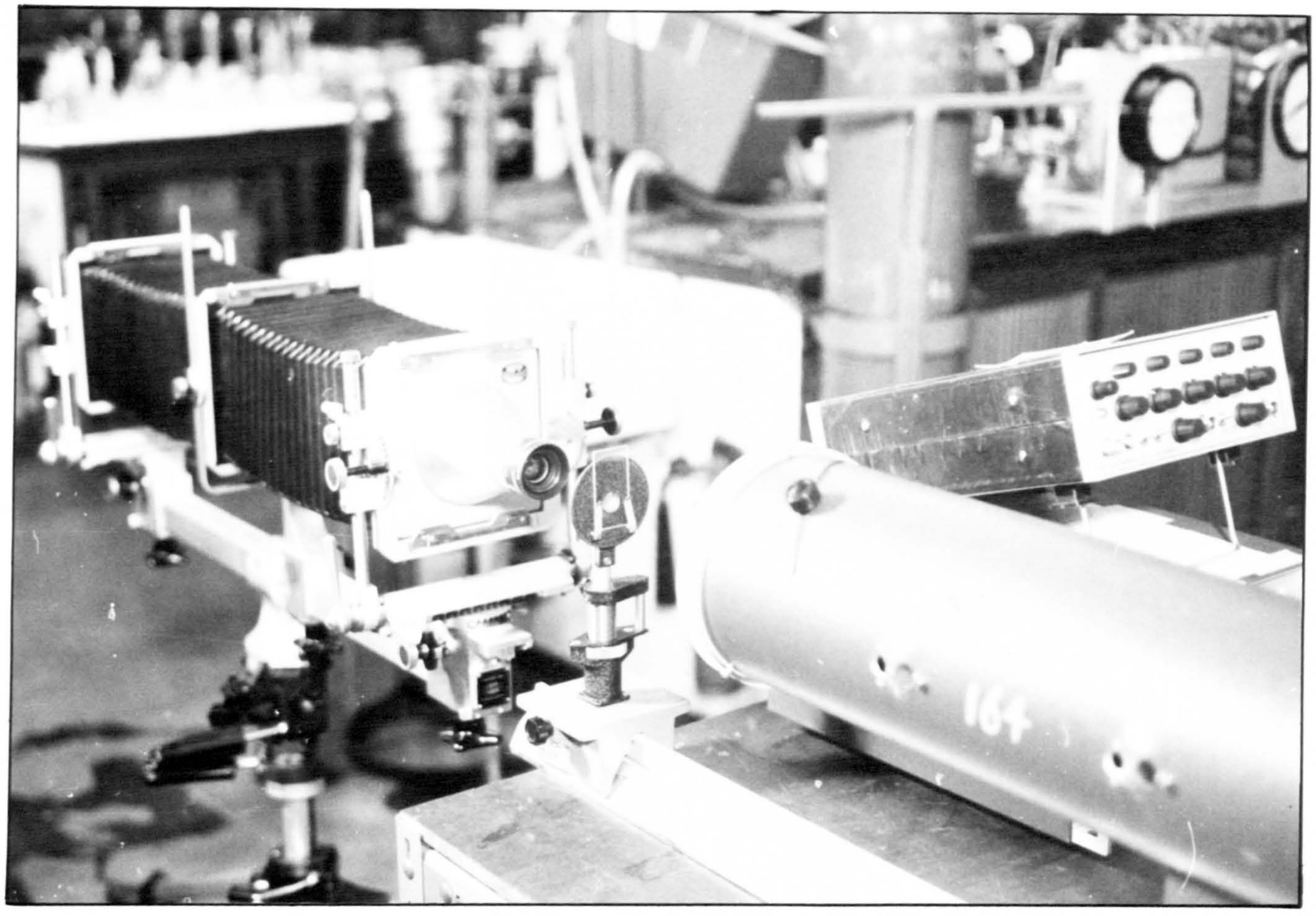


FIG. 4.9 Illustration of optical arrangement for depth of field studies.

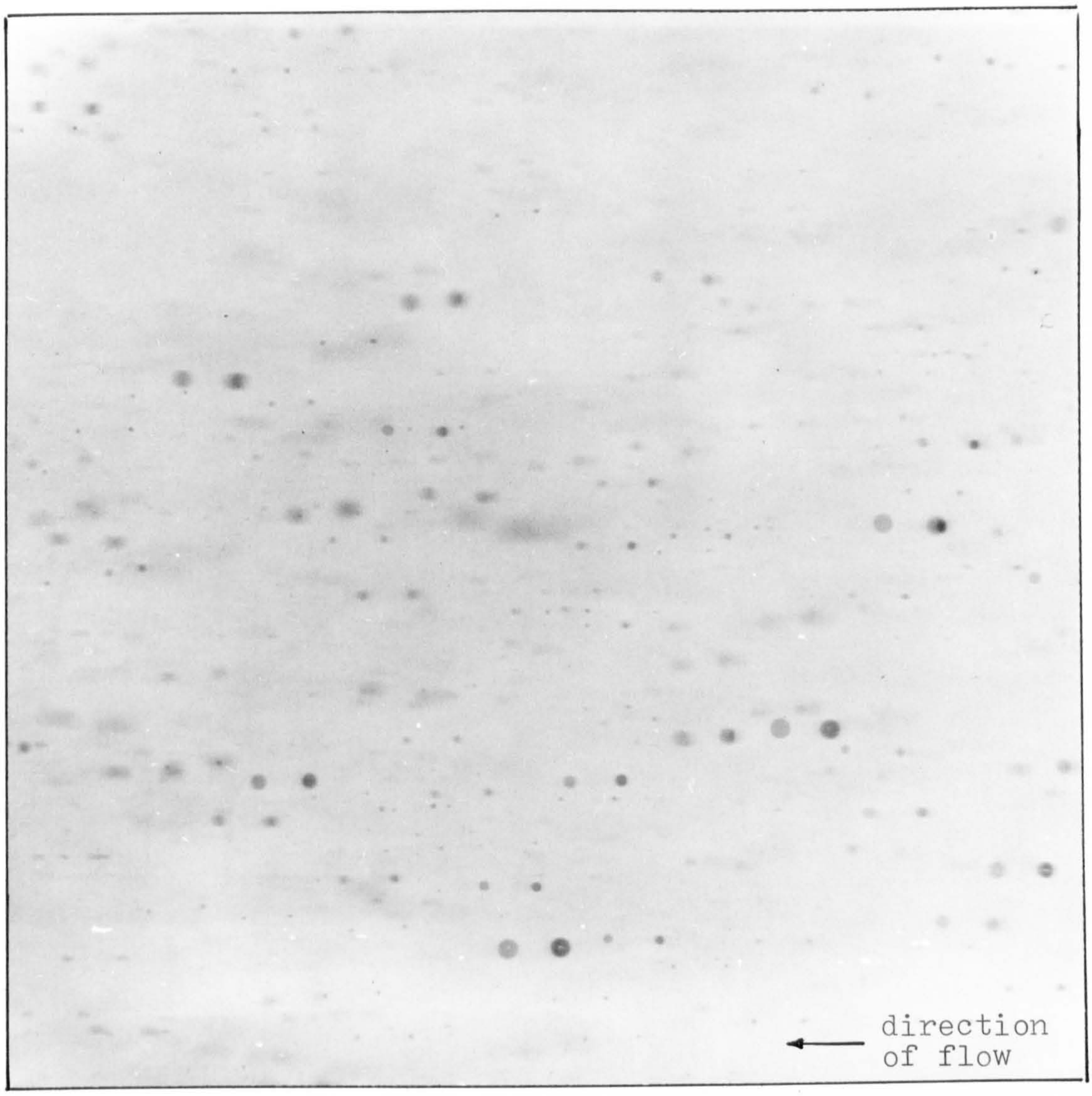


FIG. 4.10 Typical double flash photograph. (Magnification approx. 15x and flash interval approx. 31 μs)

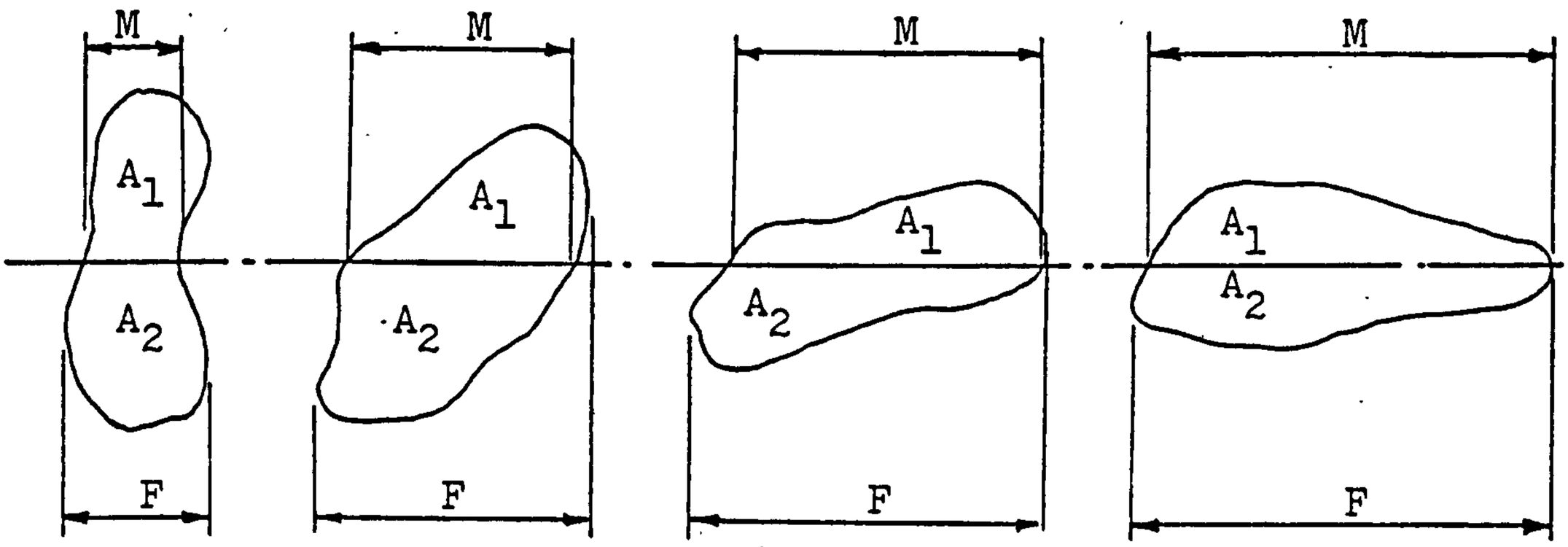


FIG. 4.11 Illustration of horizontal Martin's (M) and Feret's (F) statistical diameters. Areas A_1 and A_2 (which determine Martin's diameter) are equal.

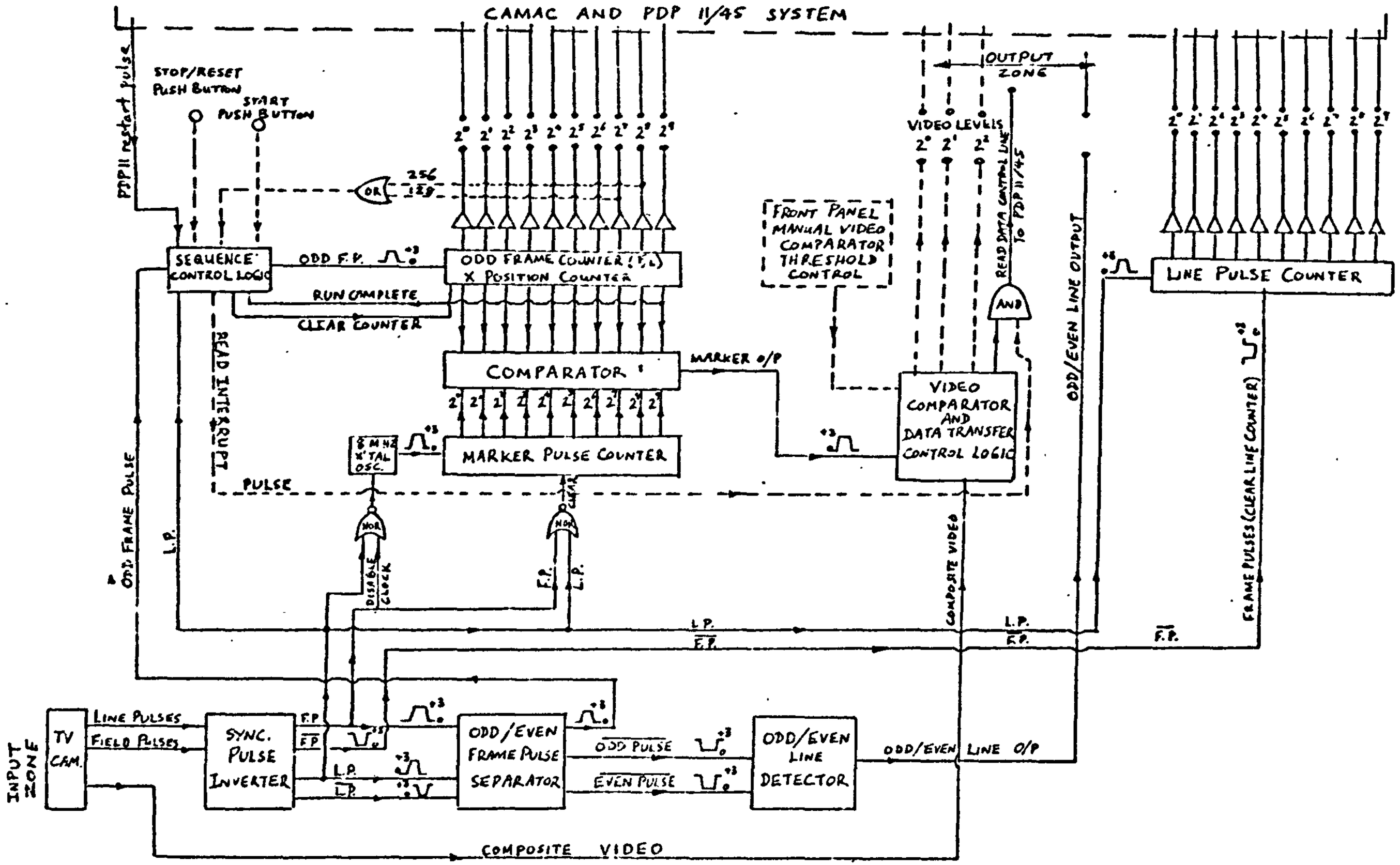


FIG. 5.1 Digitiser circuit design (modifications illustrated in dotted lines).

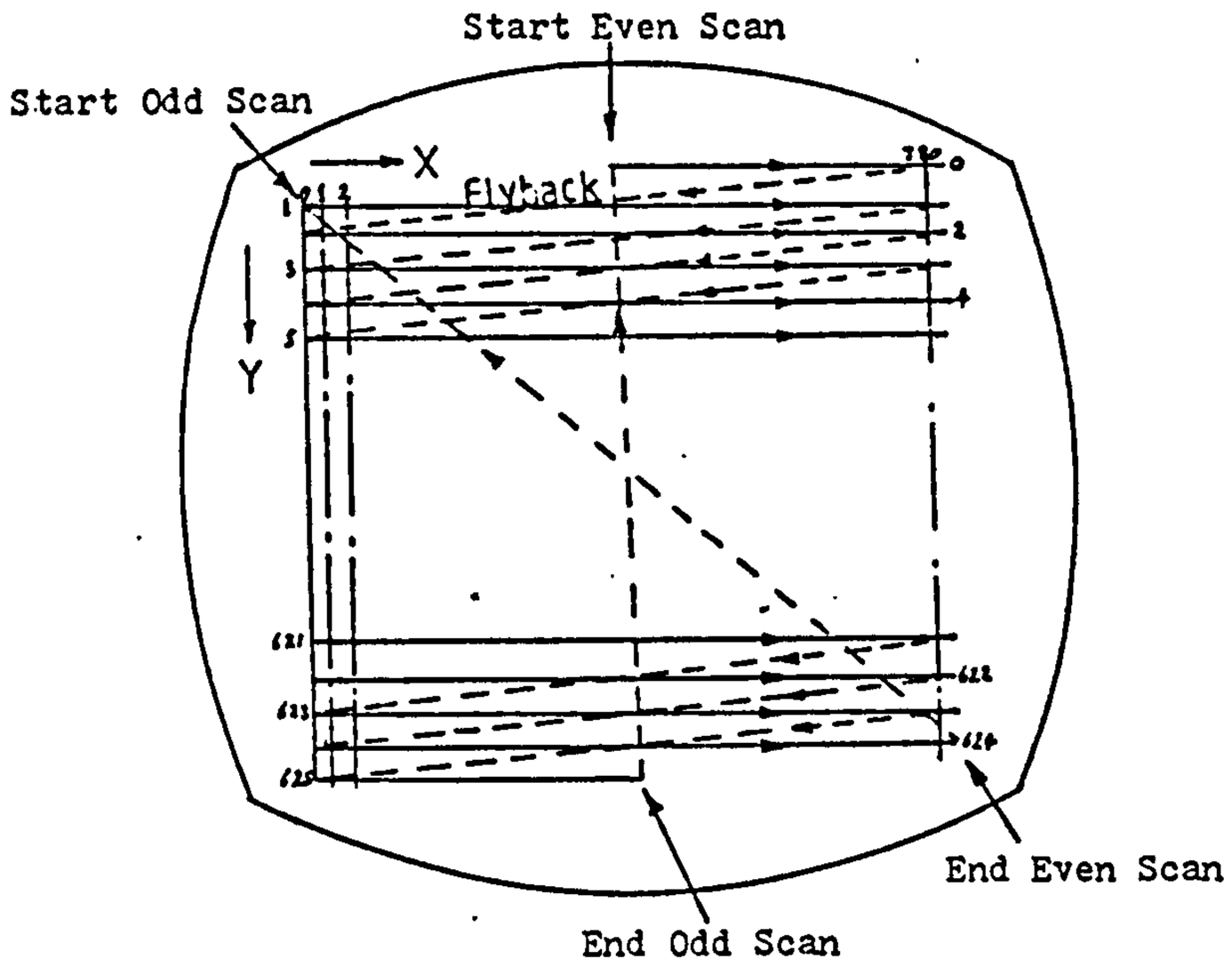
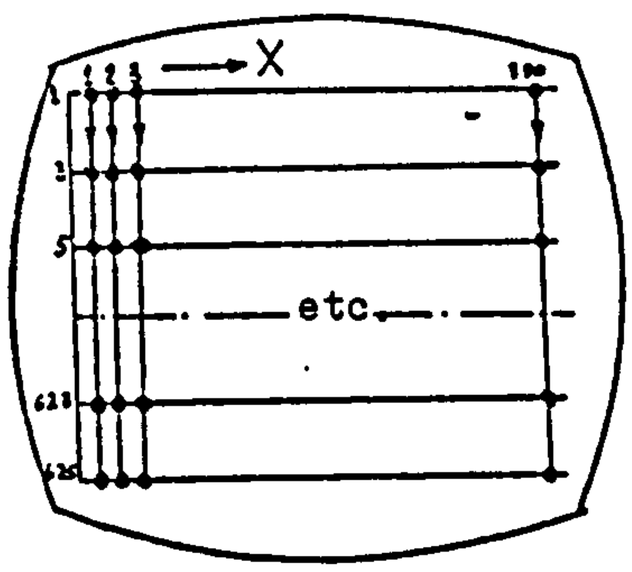
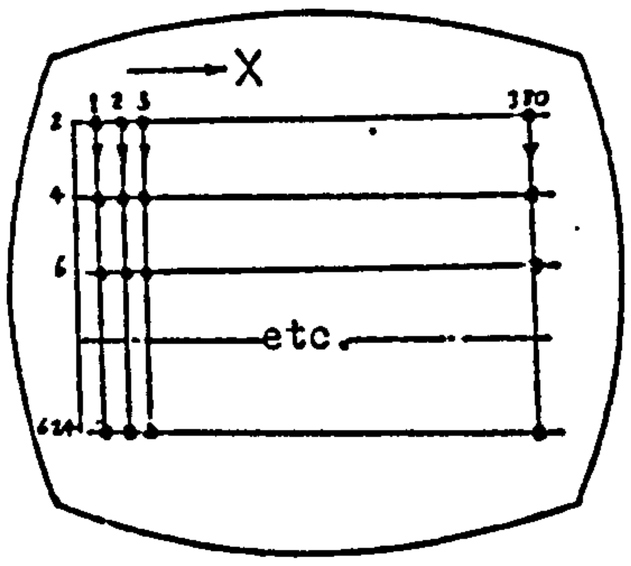


FIG. 5.2 TV Scanning system



Field 1: Odd lines



Field 2: Even lines

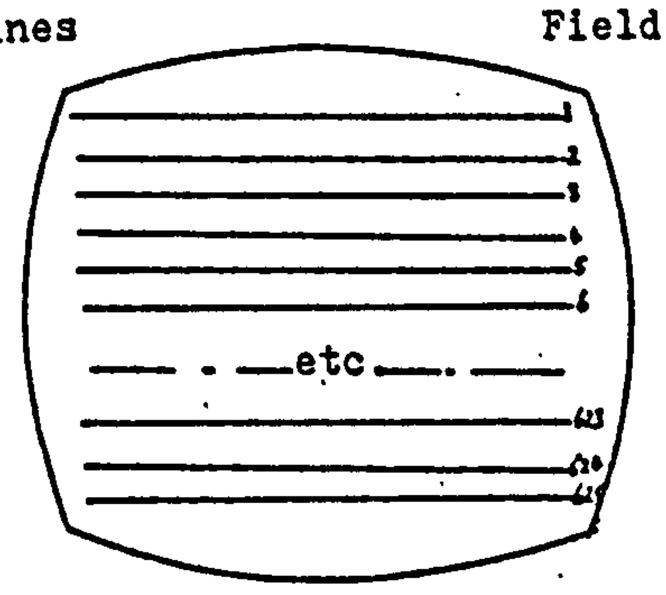


FIG. 5.3 Complete picture: Field 1 + Field 2

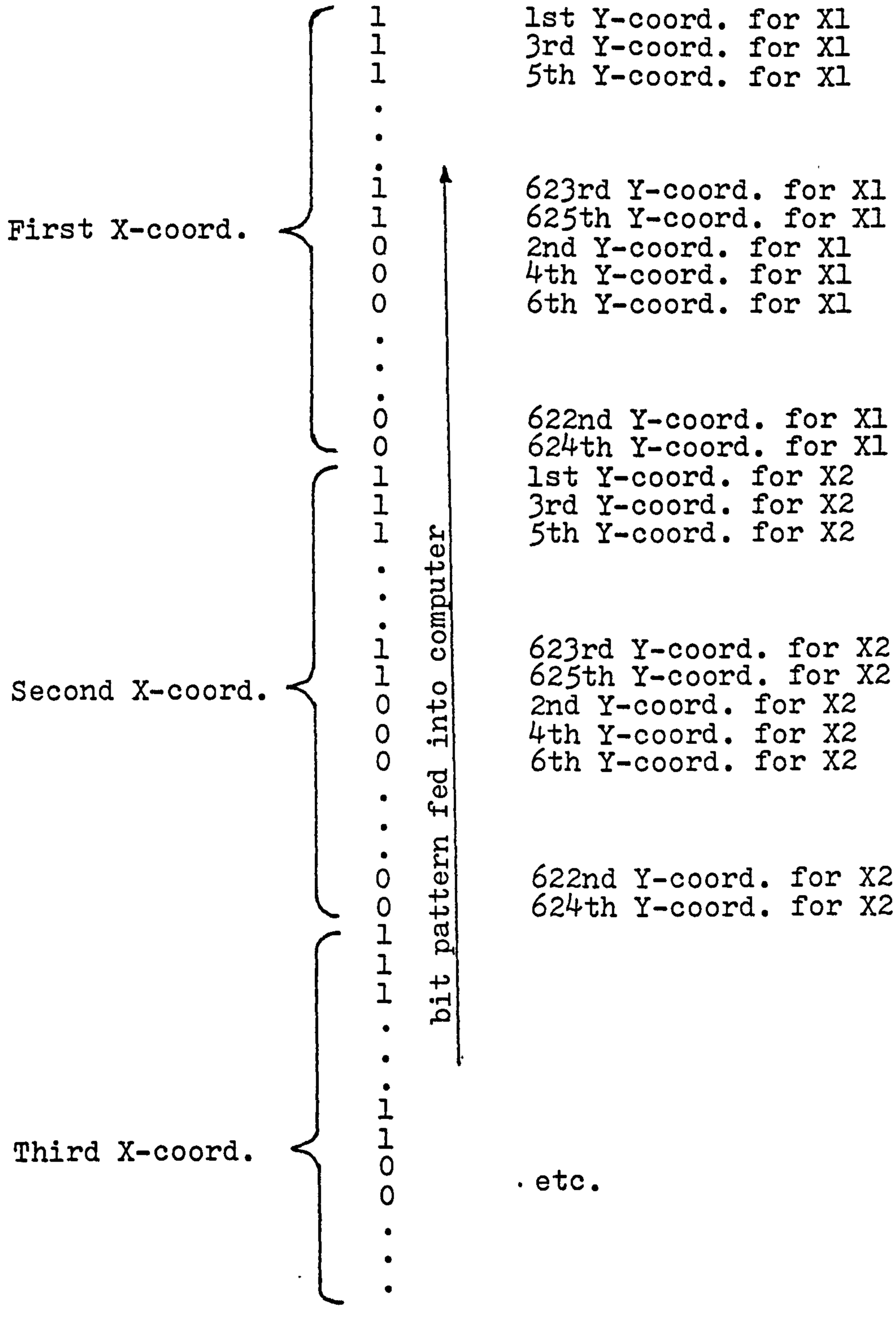
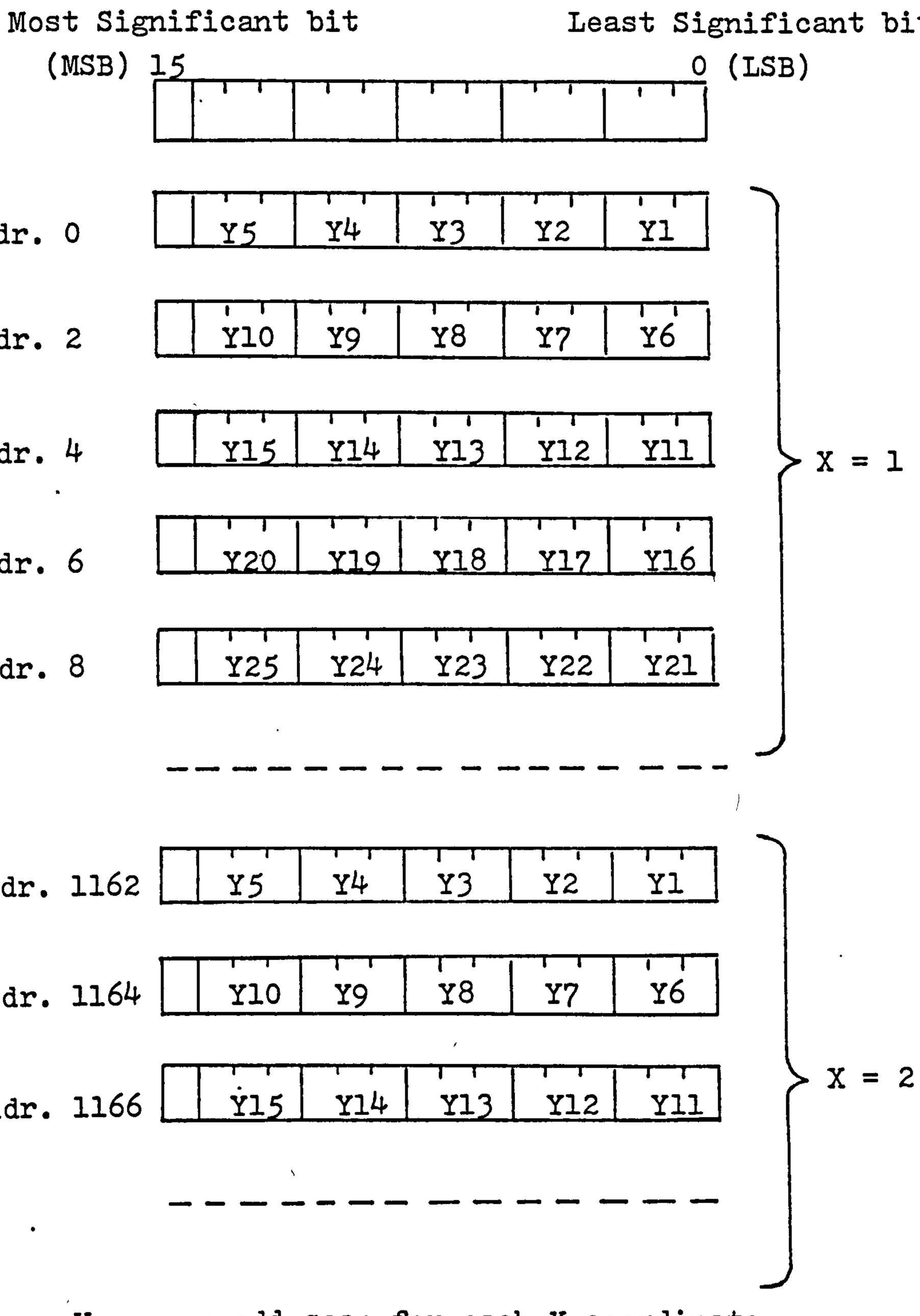


FIG. 5.4 Odd/even scan bit pattern



$Y_{1,3,5}$ = odd scan for each X-coordinate
$Y_{2,4,6}$ = even scan for each X-coordinate
Addr. :- Arbitrary word address in computer memory.

FIG. 5.5 Data arrangement in a PDP11 word

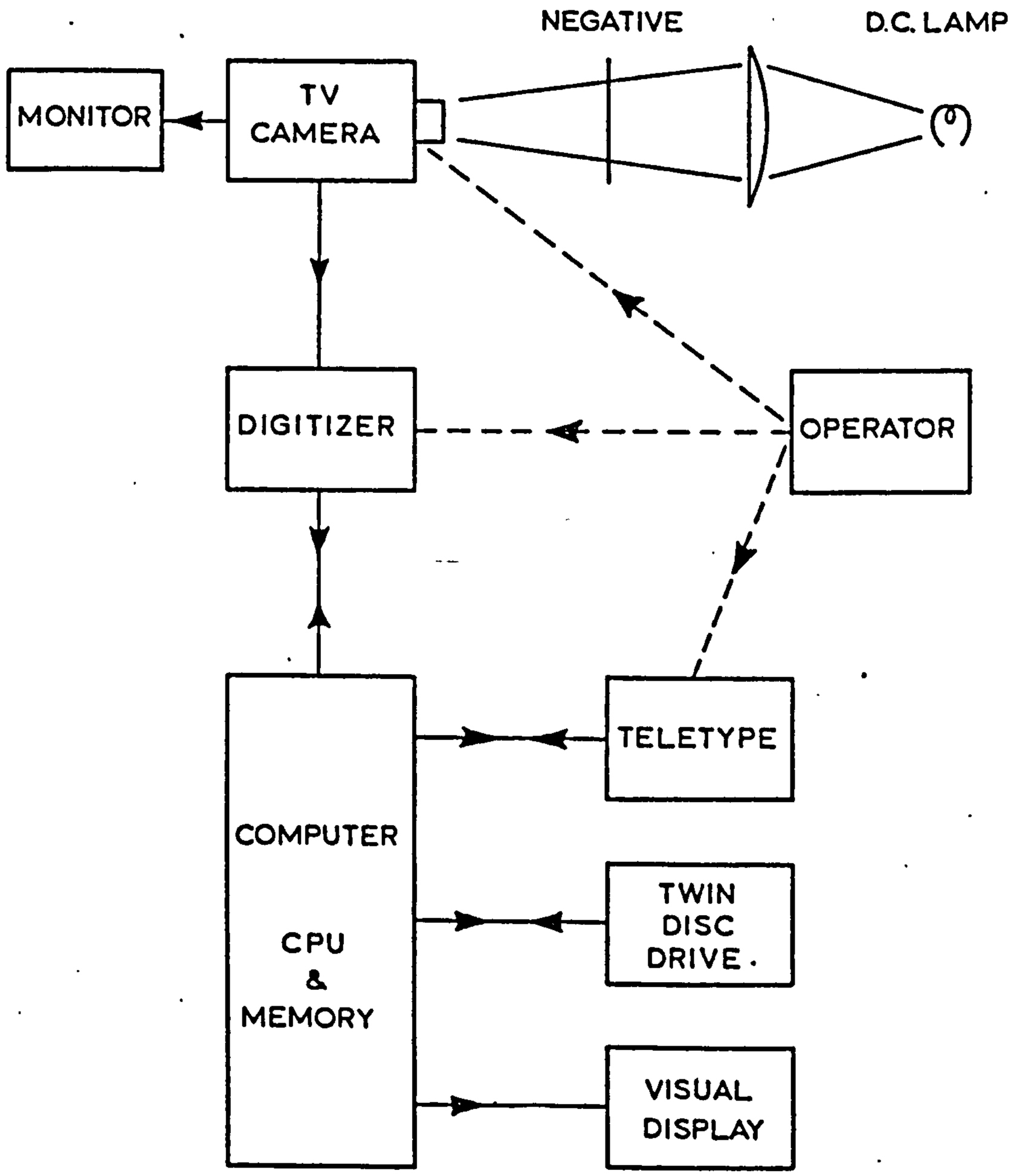


FIG. 5.6 Hardware arrangement for off-line image analysis.

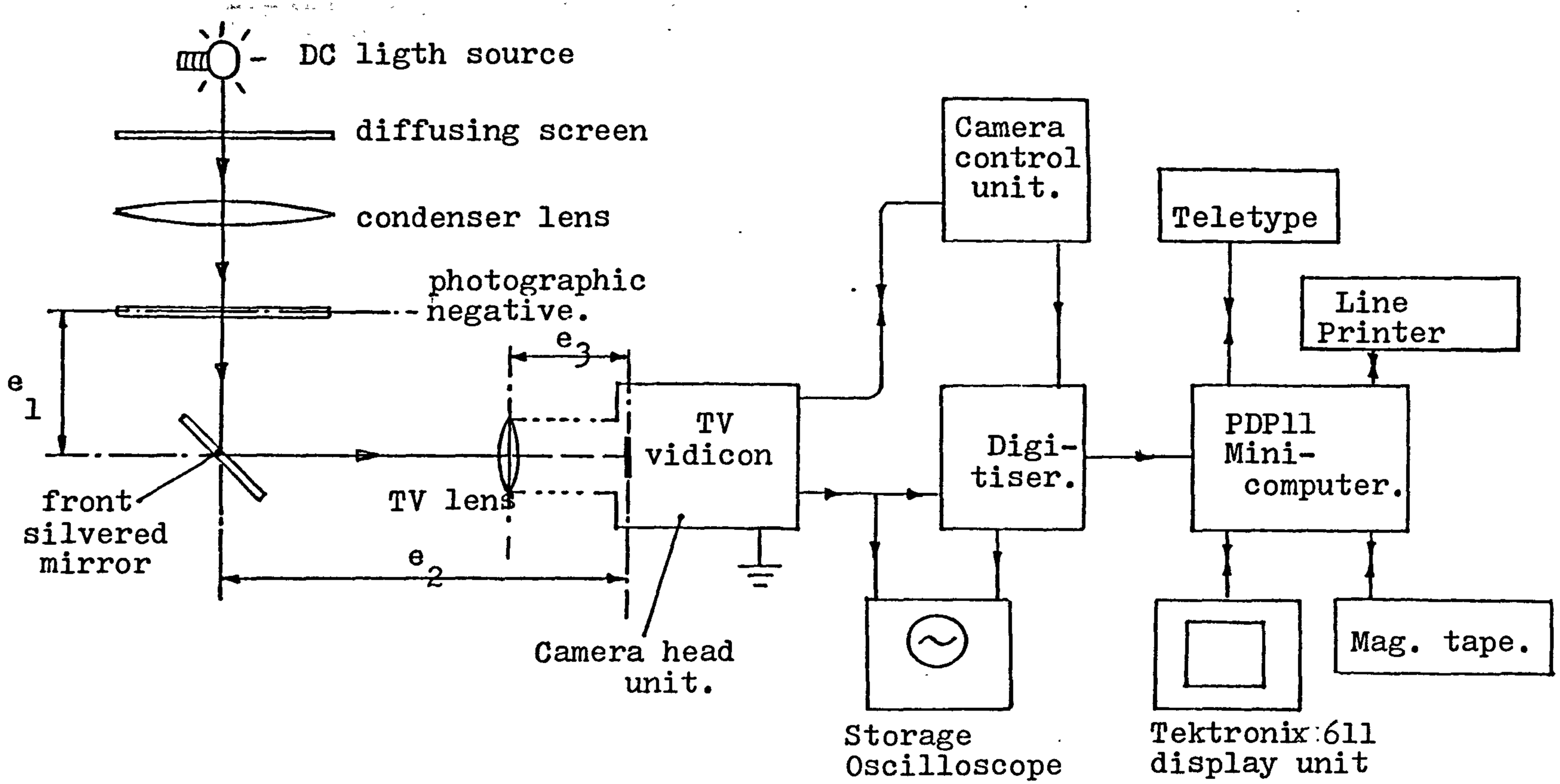


FIG. 5.7 Schematic layout of digitising optics relative to minicomputer and its peripheral units.

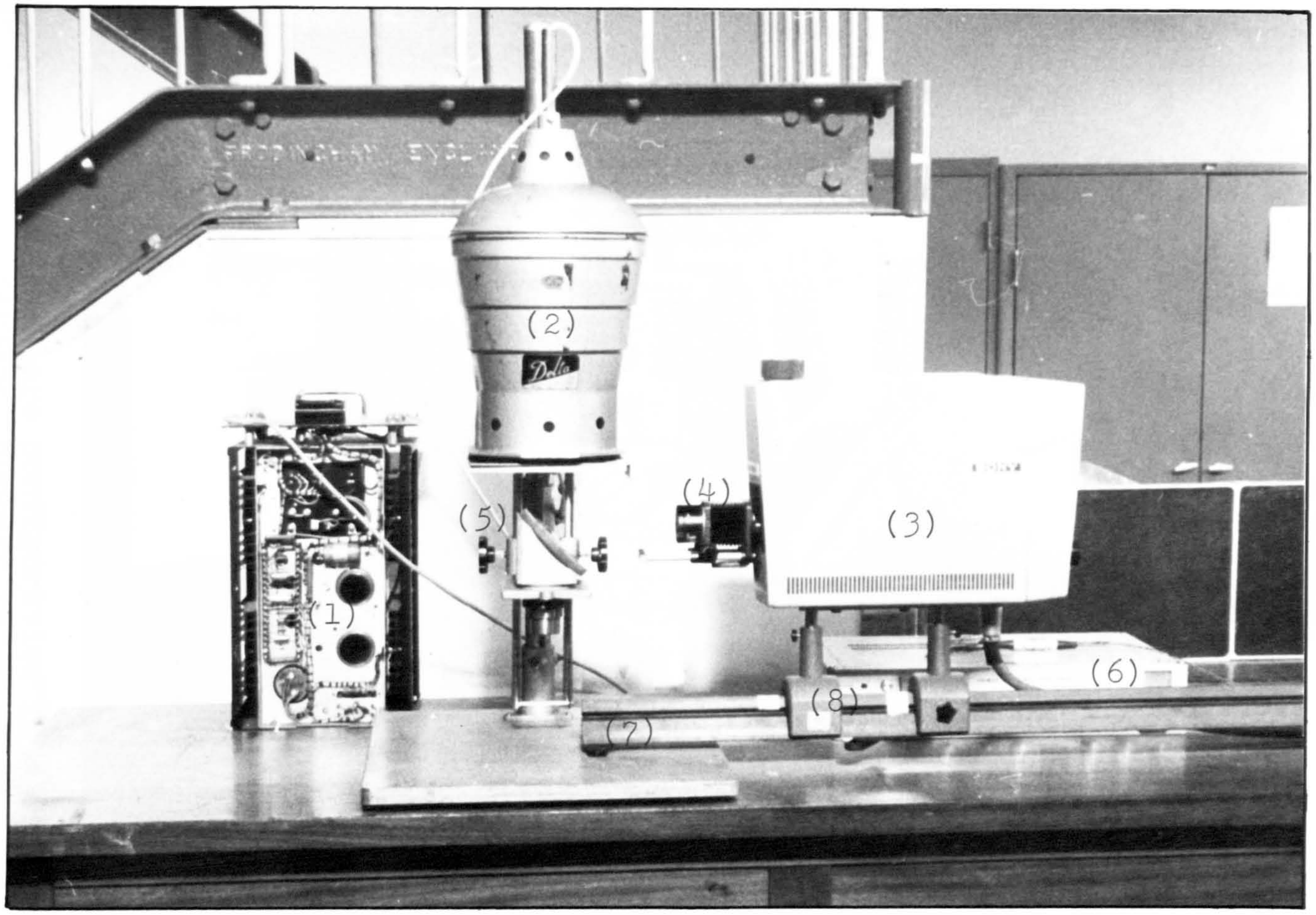


FIG. 5.8 Illustration of optical arrangement for image analysis system. Numbers referred to are:- (1) 12V D.C. transformer; (2) D.C. light source; (3) TV camera head unit; (4) Componon lens and bellows; (5) front-silvered mirror; (6) TV camera control unit; (7) optical bench; (8) optical saddles.

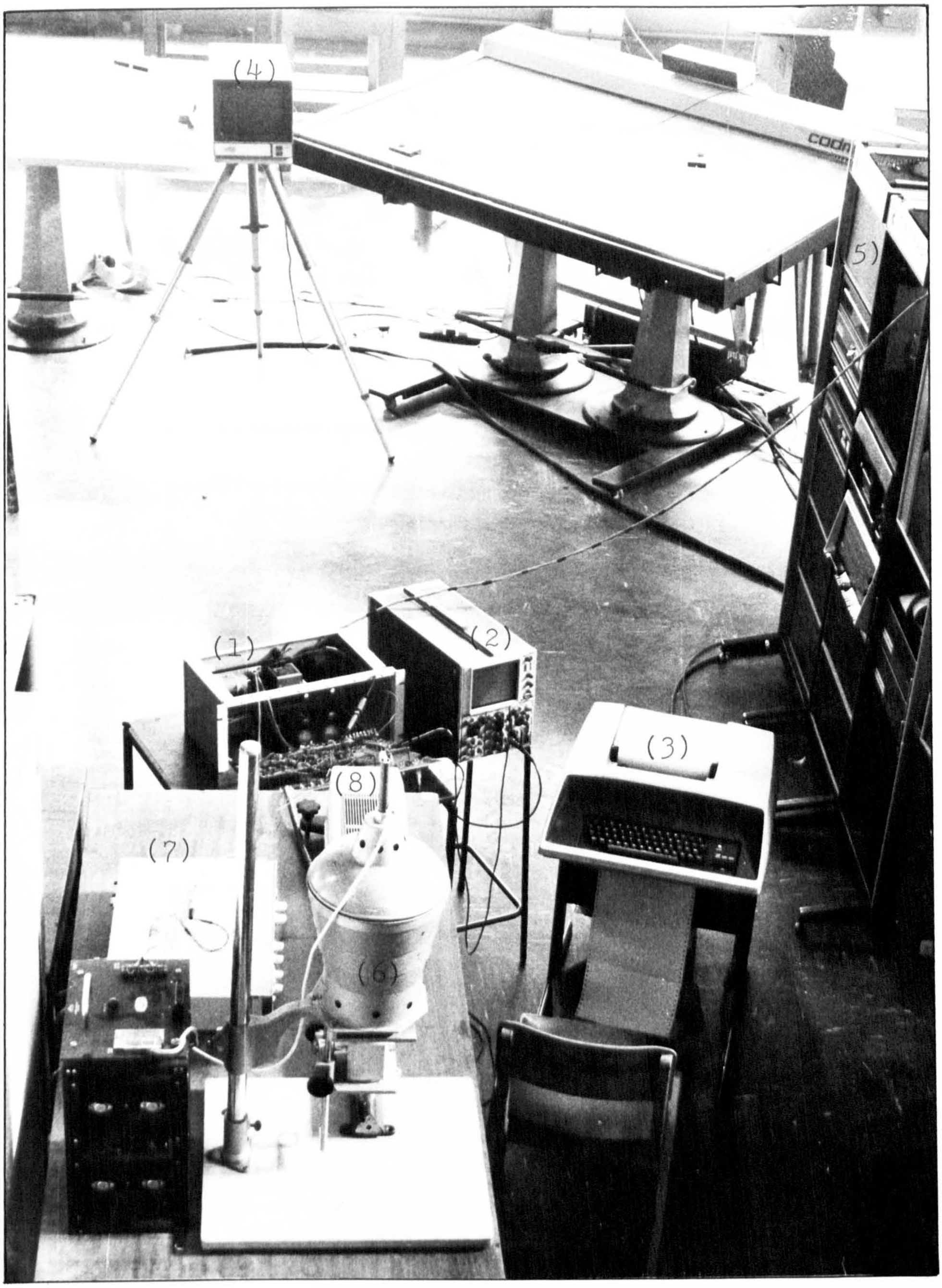


FIG. 5.9 Hardware configuration in a digitising session. Numbers referred to are:- (1) digitiser interface unit; (2) oscilloscope; (3) DEC teletypewriter; (4) Tektronix 611 display unit; (5) PDP 11/45 minicomputer; (6) light source; (7) TV camera control unit and (8) TV camera head unit.

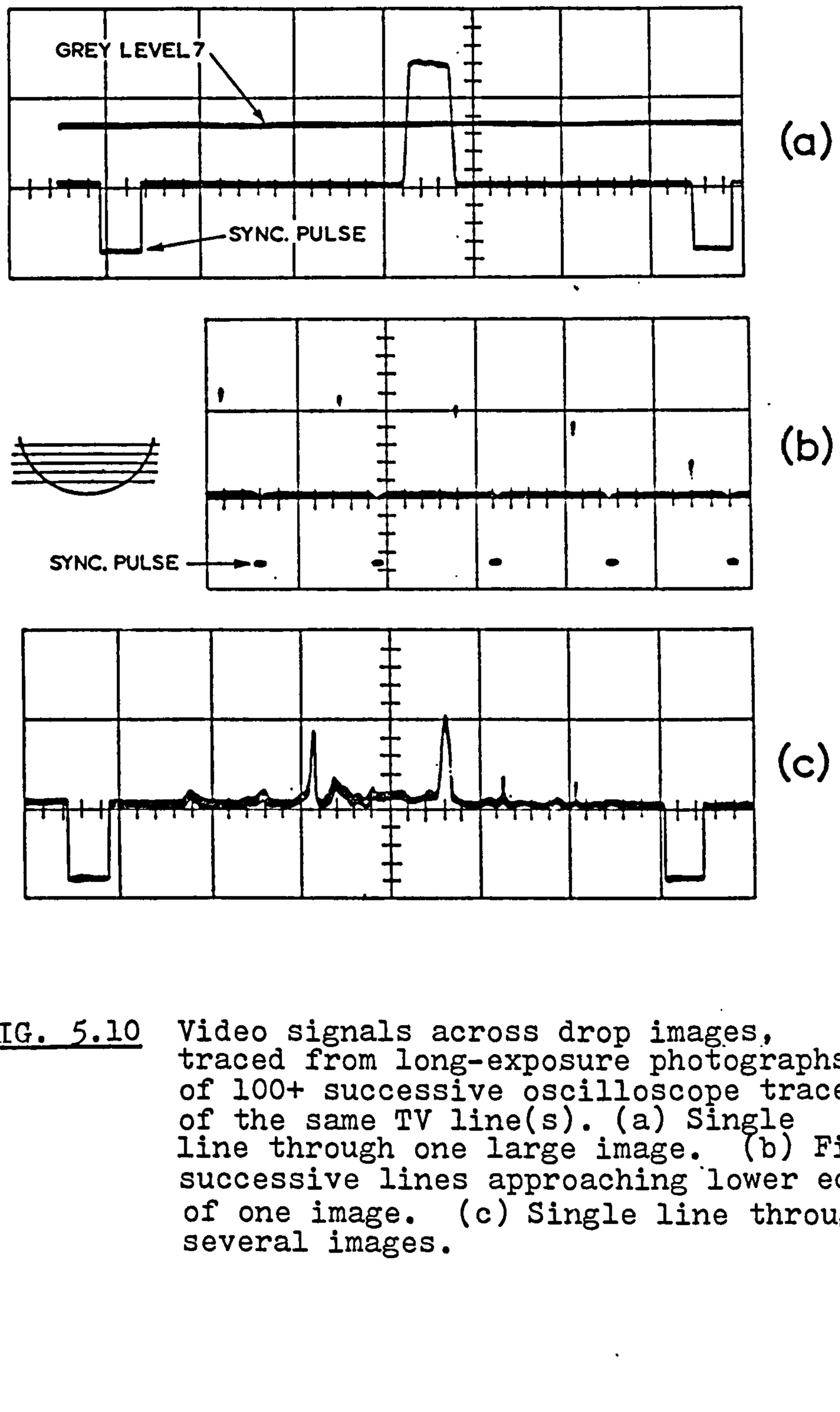


FIG. 5.10 Video signals across drop images, traced from long-exposure photographs of 100+ successive oscilloscope traces of the same TV line(s). (a) Single line through one large image. (b) Five successive lines approaching lower edge of one image. (c) Single line through several images.

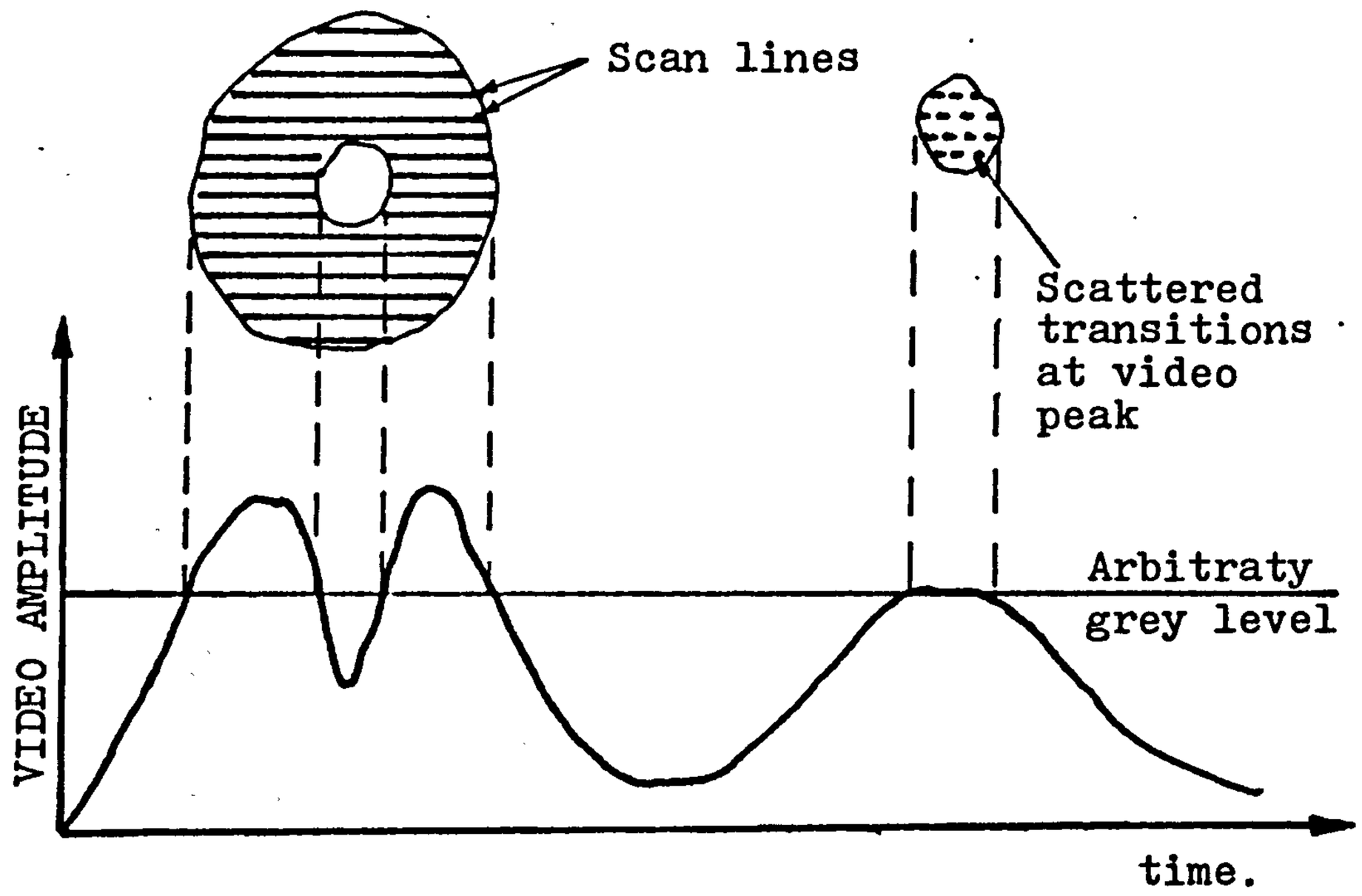
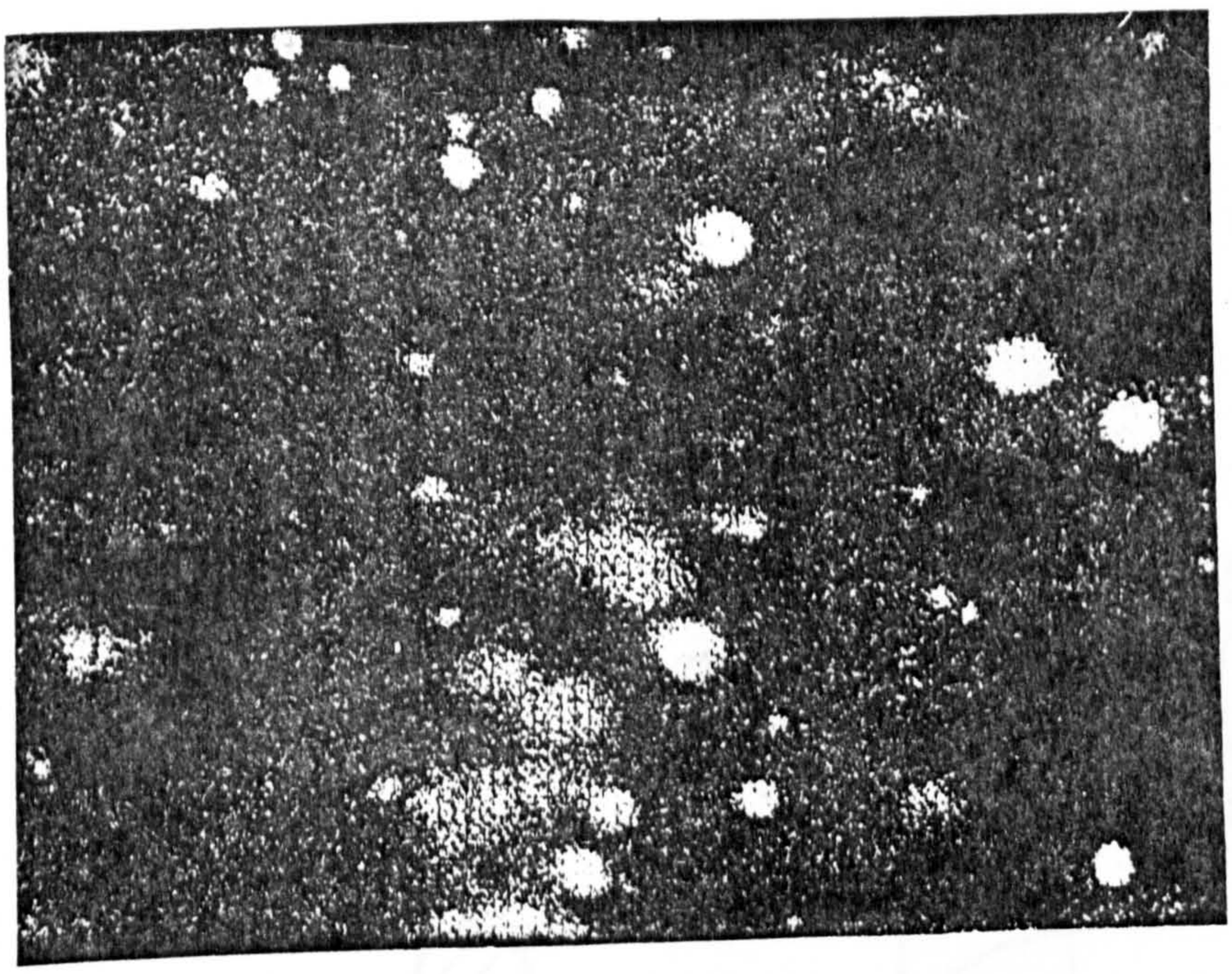
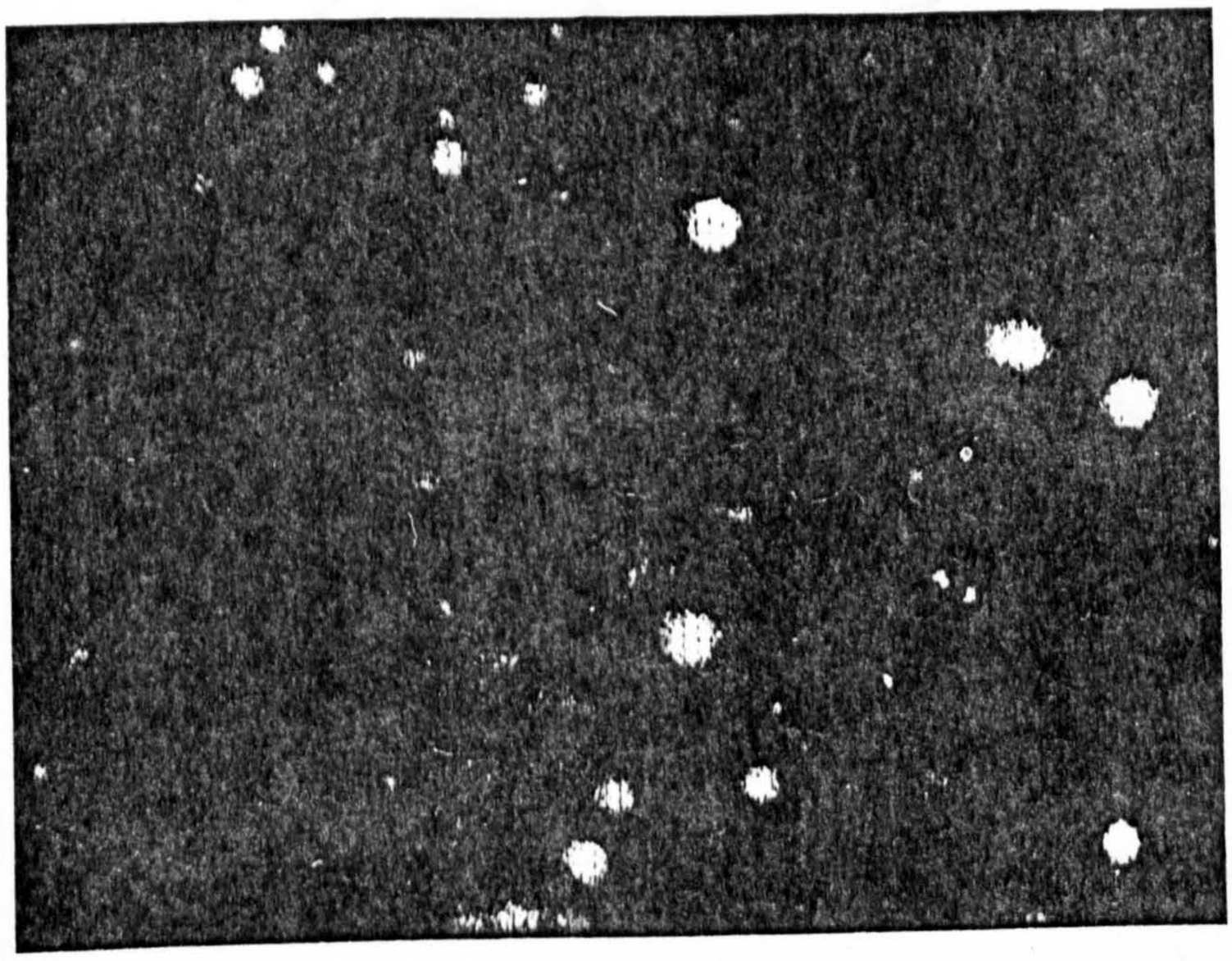


FIG. 5.11 Segmentation of detected images



(a)



(b)

FIG. 5.12 Typical displays of detected features in a complete frame at grey levels 4 (a) and 6 (b).

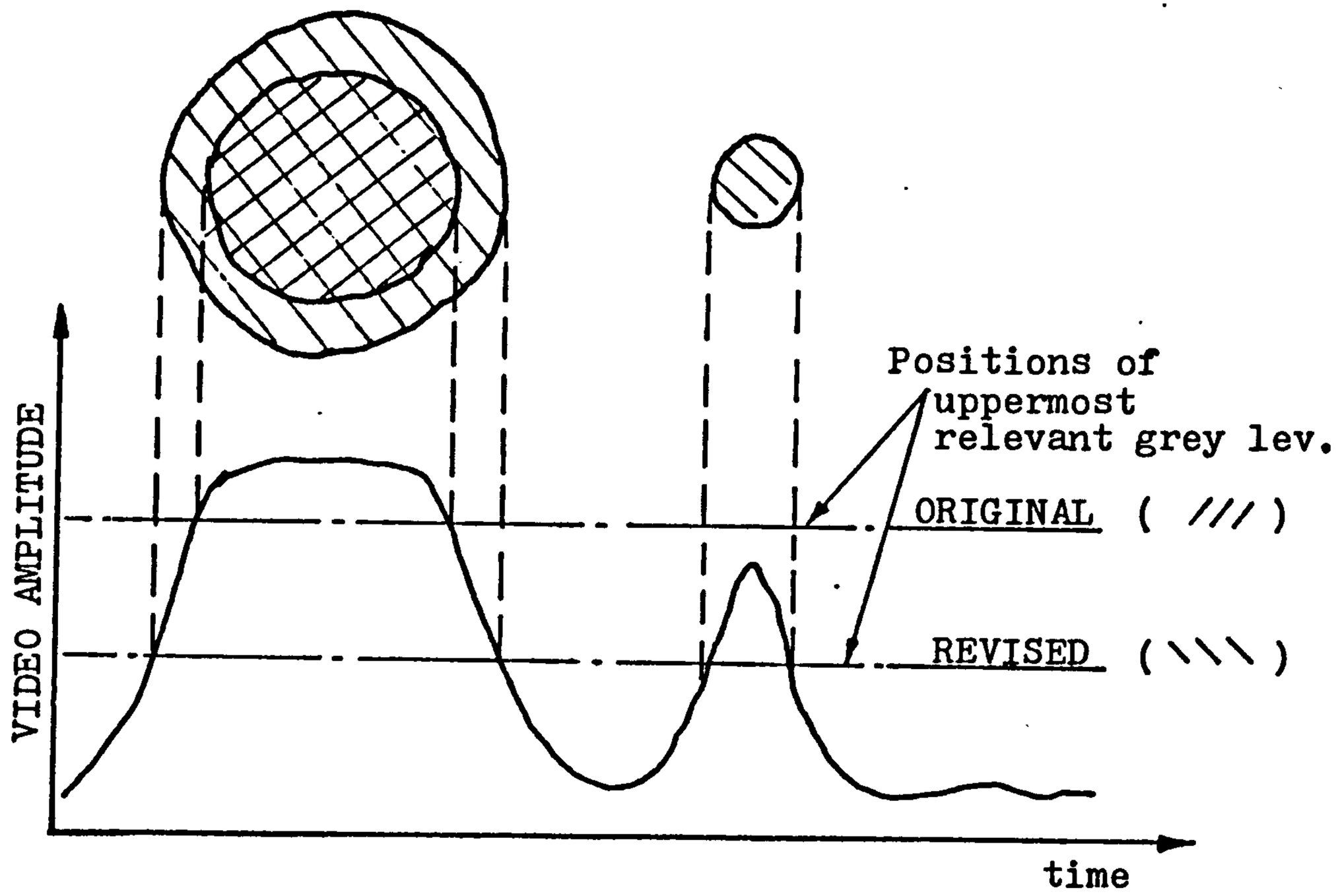


FIG. 5.13 Effect of altering grey level setting on image area

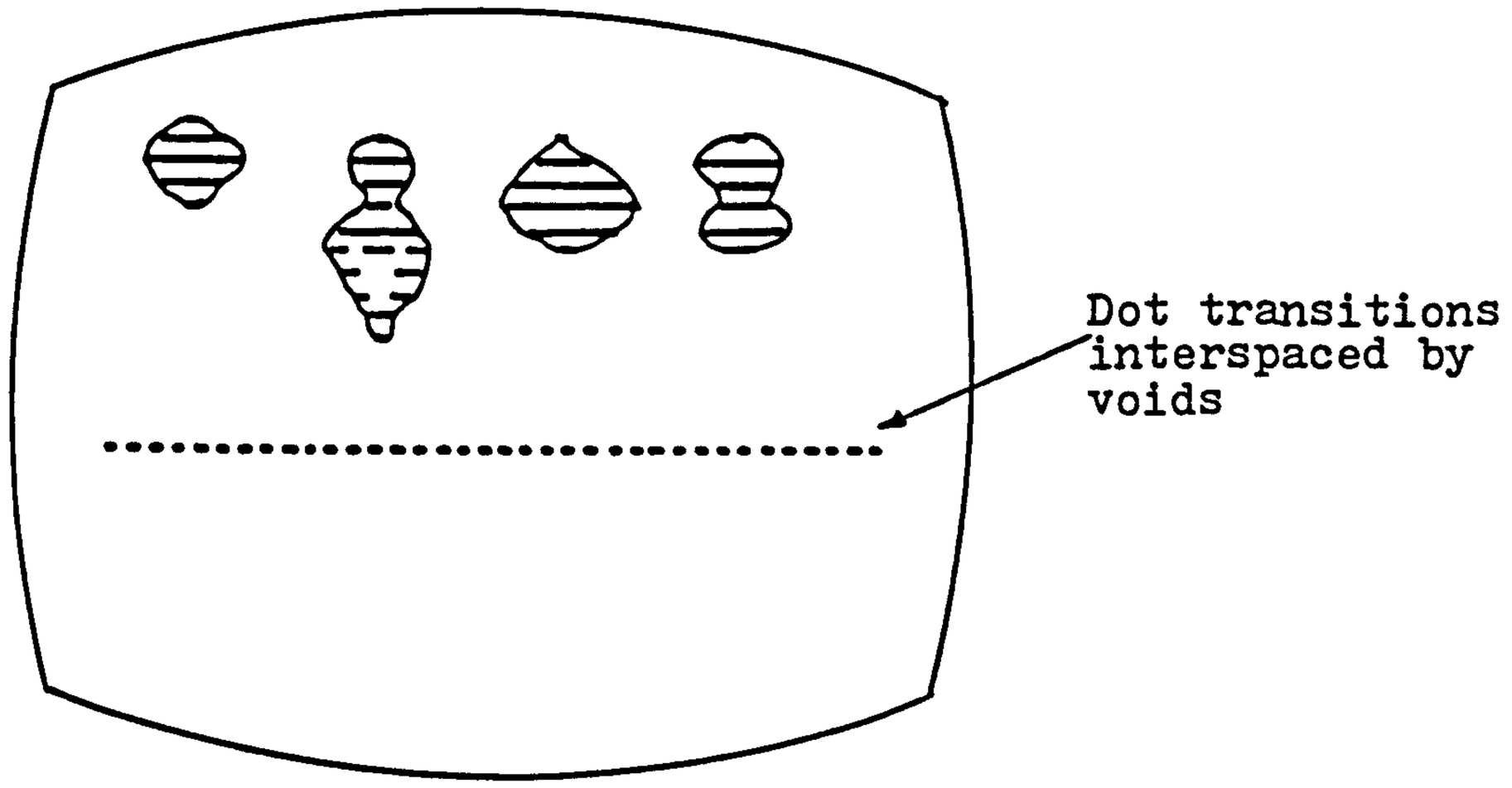


FIG. 5.14 Illustration of cell transitions

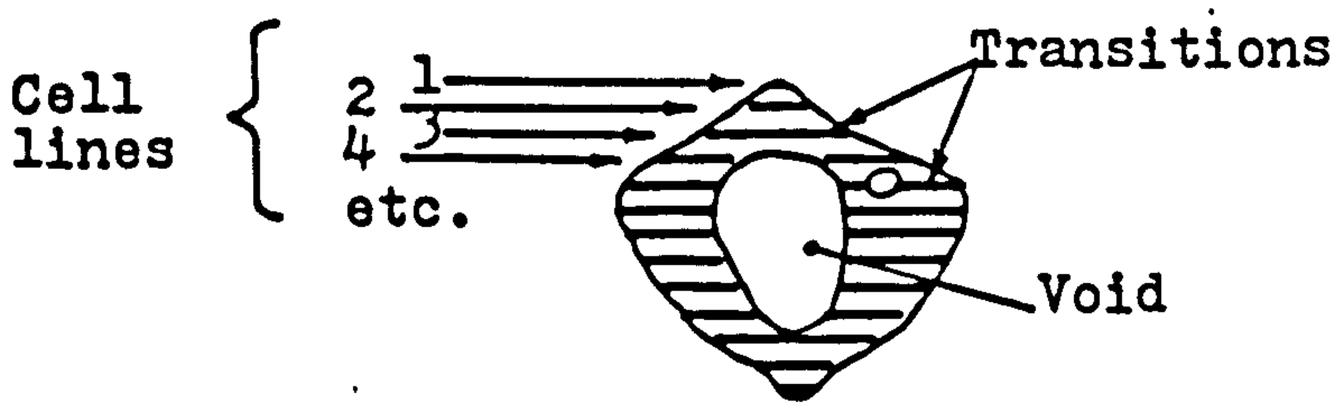


FIG. 5.15 Illustration of cell lines

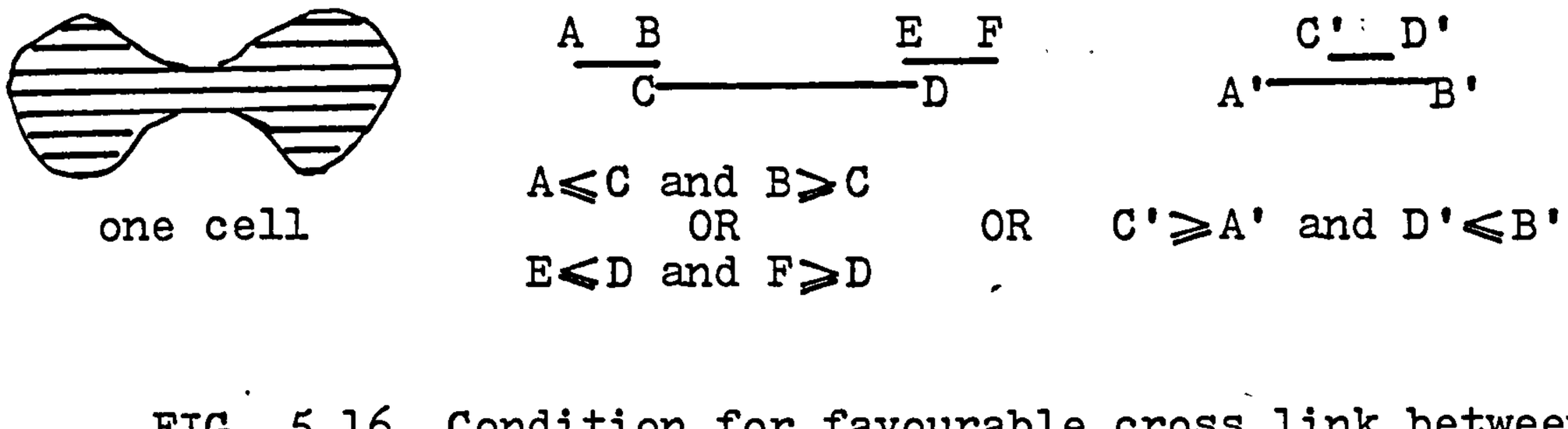


FIG. 5.16 Condition for favourable cross link between cell transitions (A, B, etc. refers to X-coordinates of those run-end positions, along a scan line).

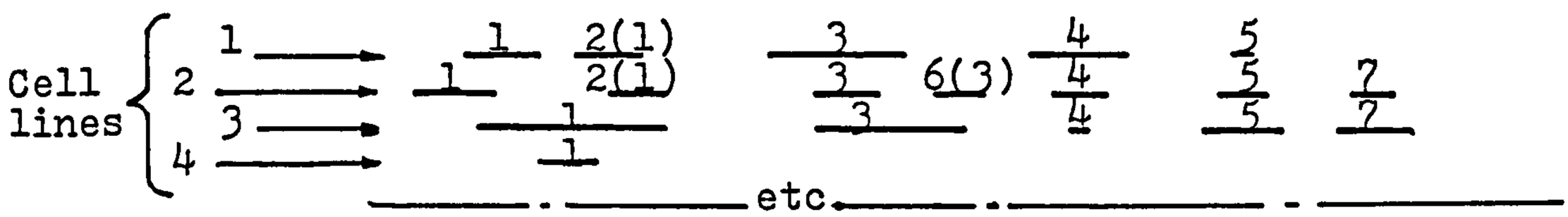


FIG. 5.17 Illustration of cell identification process

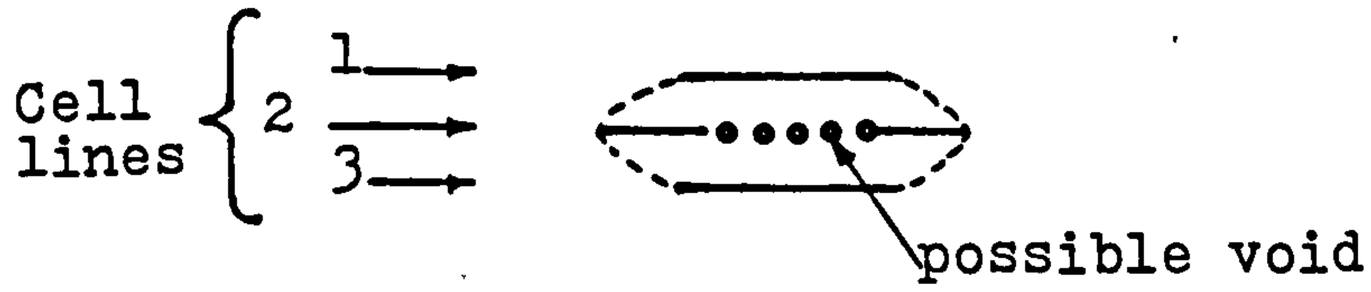
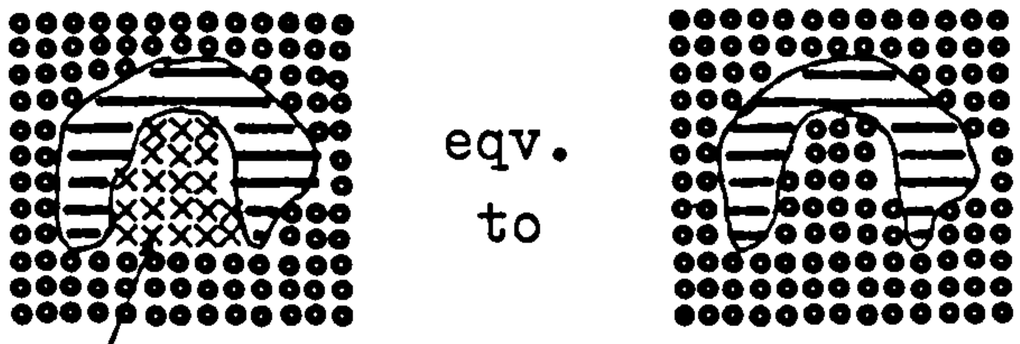


FIG. 5.18 Illustration of void test

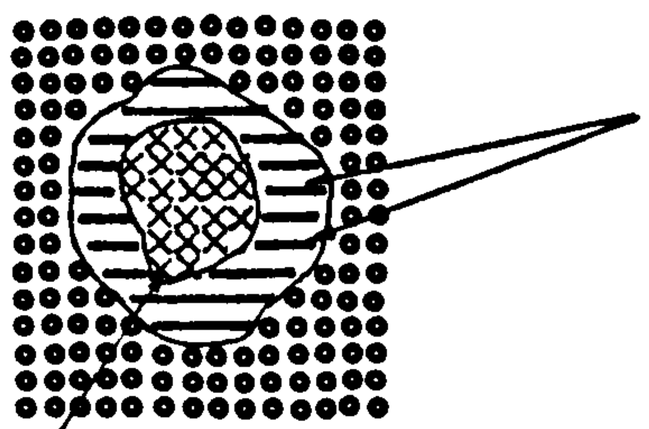
(a)



eqv. to

Outermost void transition merging with background transitions and not with cell transitions, hence an "open void."

(b)



cell transitions

Outermost void transitions terminated by cell transitions. Hence a "closed void". Background transition completely separated from void transition.

FIG. 5.19 Detection of closed or open voids

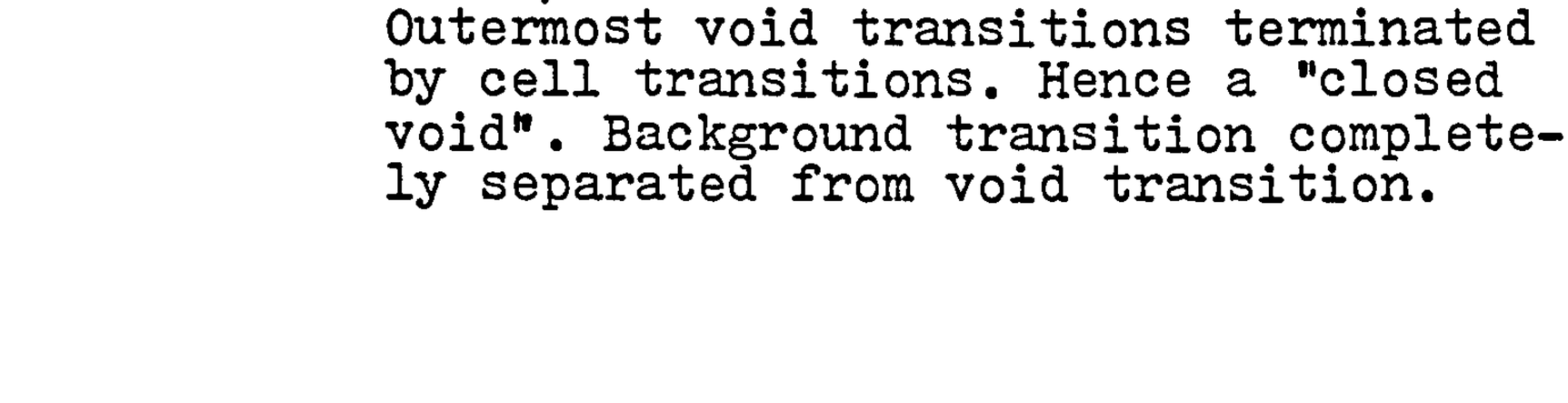
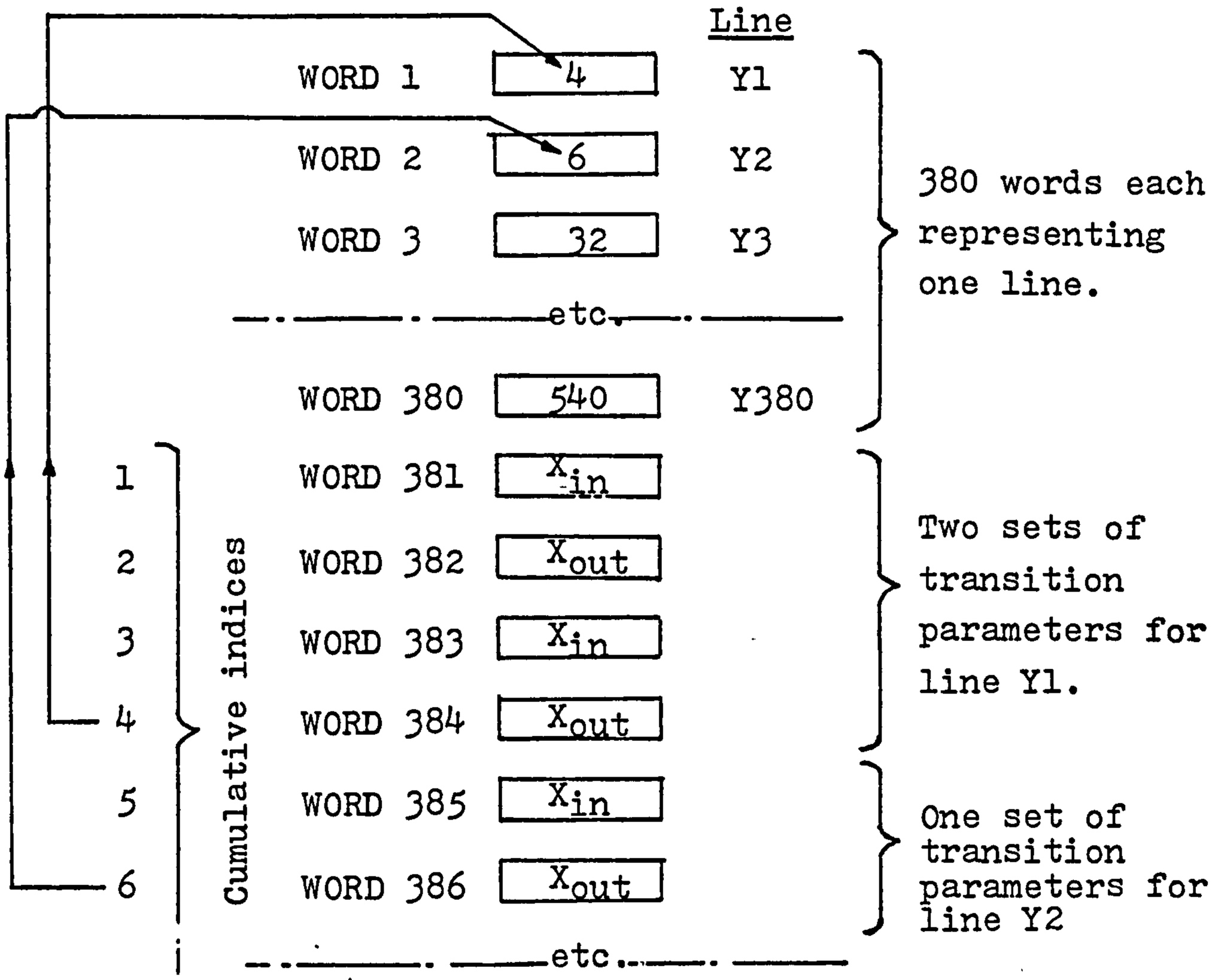


FIG. 5.20 Treatment of cells within cells



for 50 sectors altogether.

FIG. 5.21 Data storage for transition parameters

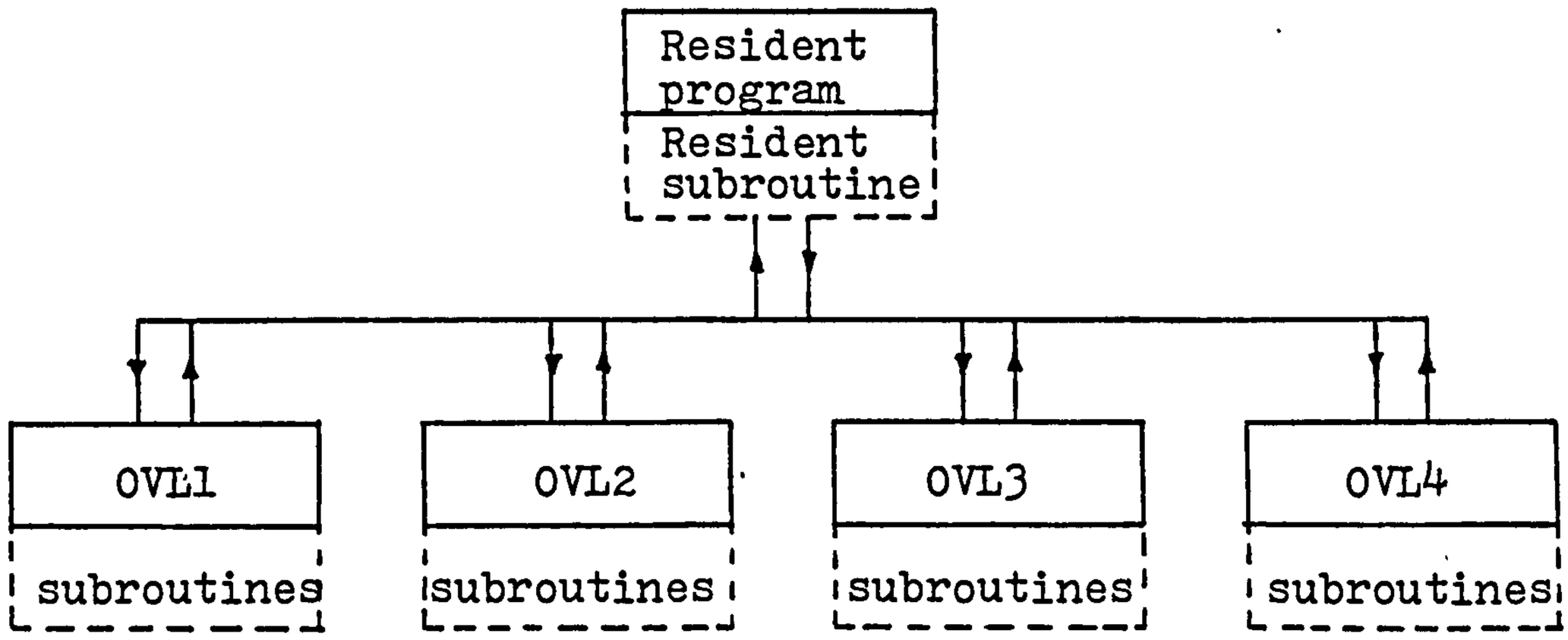


FIG. 5.22 Overlay structure for "RES"

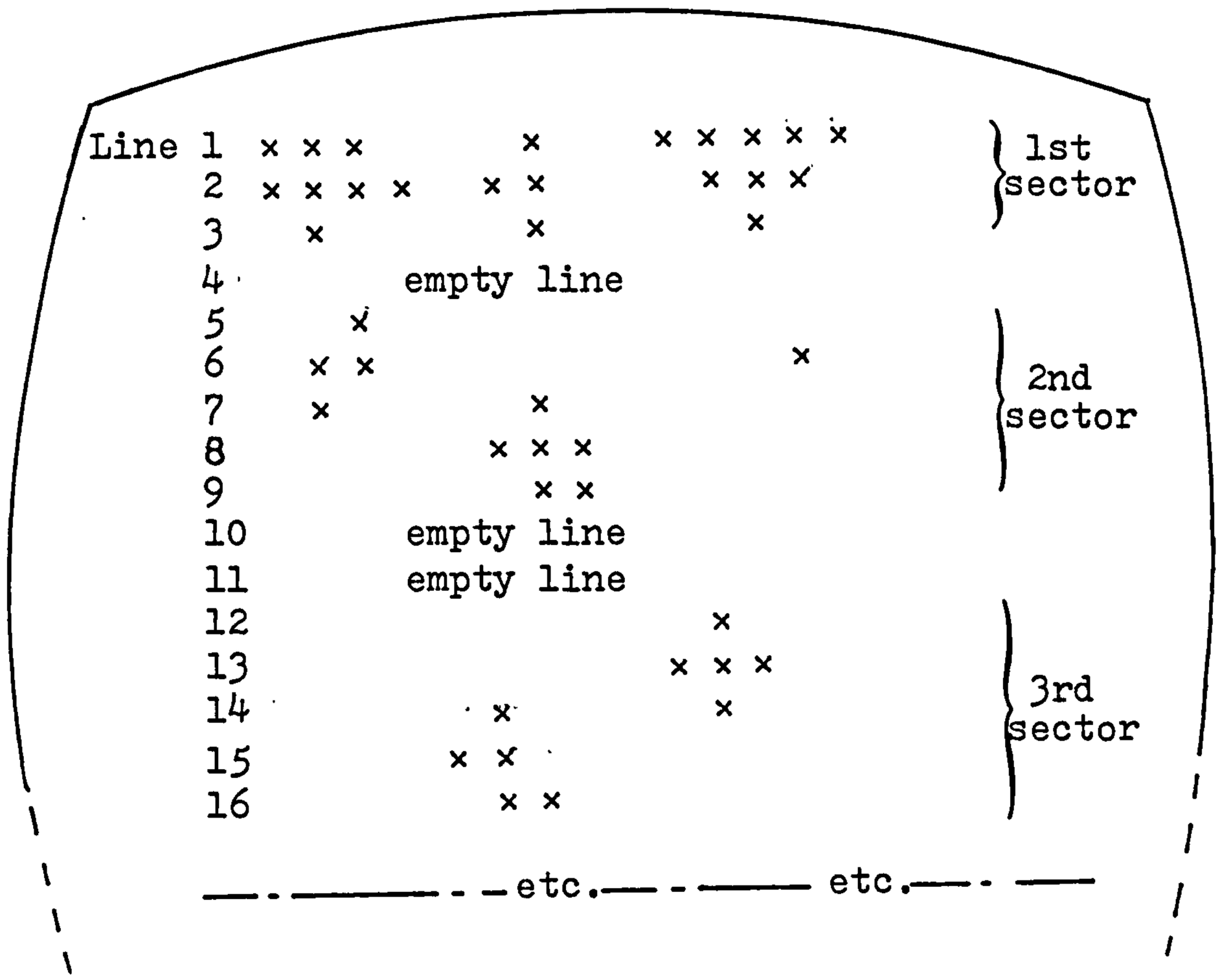


FIG. 5.23 Illustration of "data sectors" for cell identification routine OVL2.

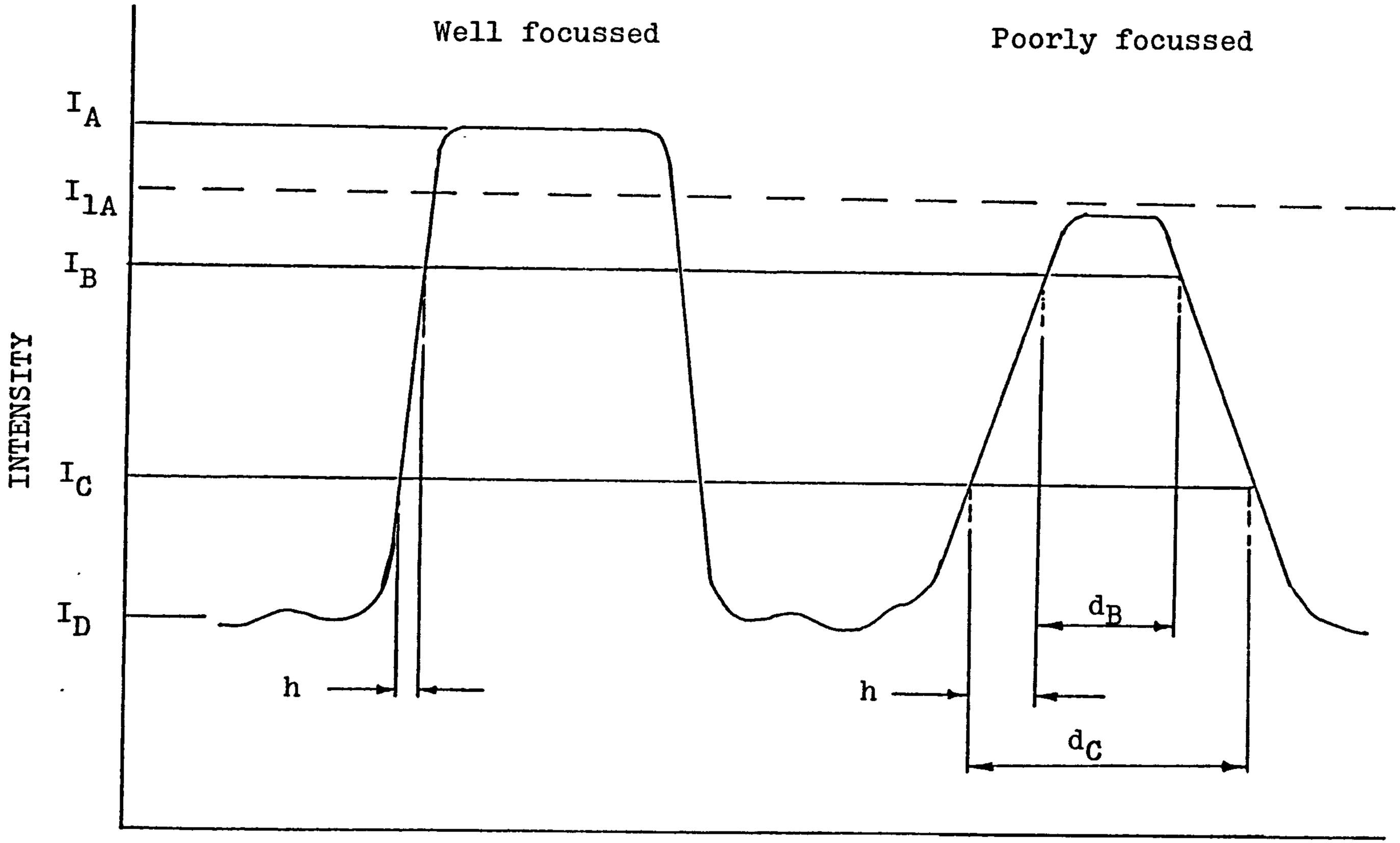


FIG. 5.24 Effect of degree of focus upon intensity variation across a drop image. Dotted line represents grey-level 7 setting.

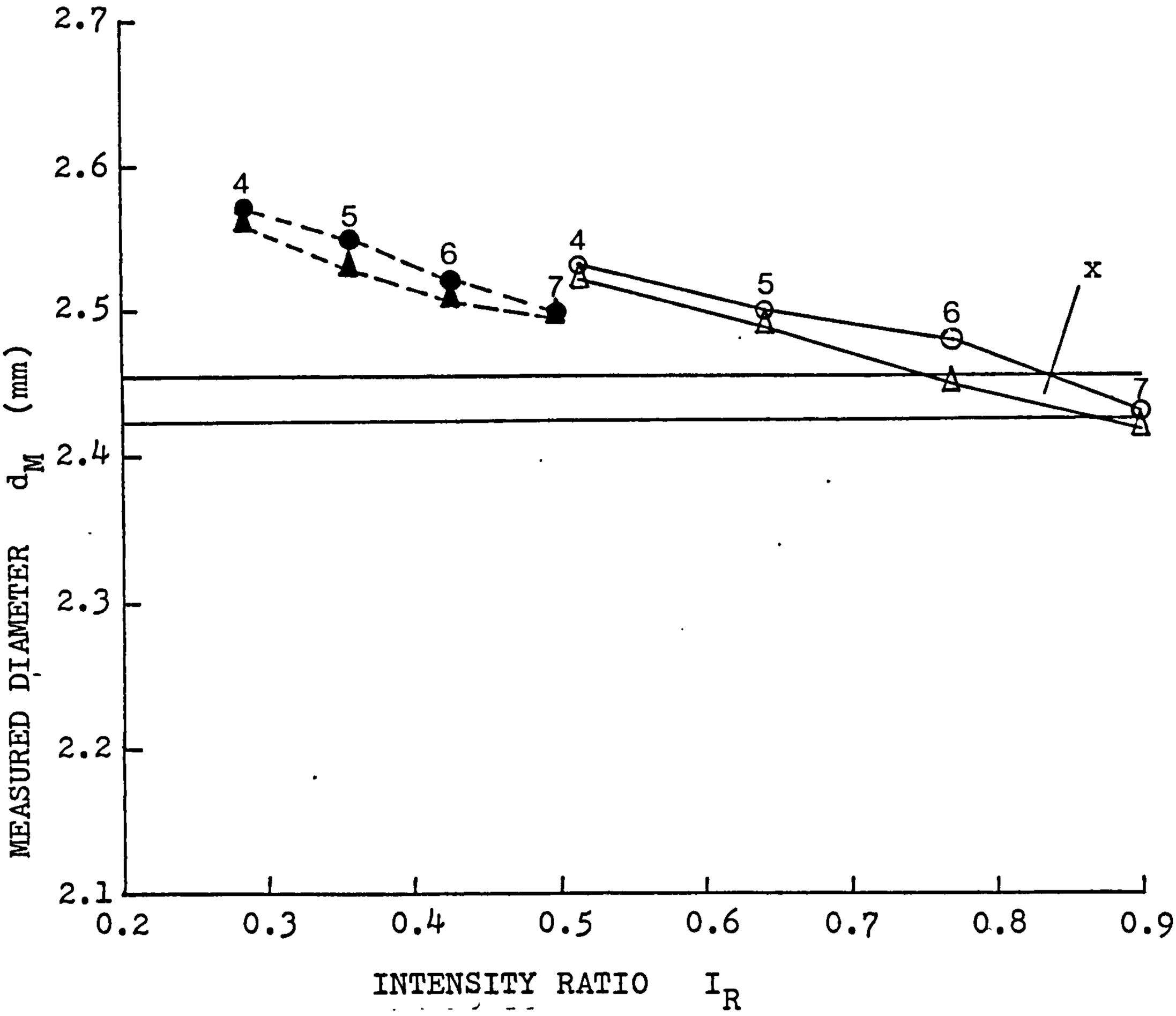


FIG. 5.25 Illustration of repeatability of measured diameter, d_M, of a circular hole (No. 1) with sharp edges at two settings of grey level 7 voltage, I_{1A}. Numbers beside data points denote level on grey scale. I_R = 0.9 (○ at t=0 and Δ at t=20 mins) and 0.5 (● at t=0 and ▲ at t=5 mins). Horizontal lines represent uncertainty in actual diameter, x, determined under the microscope.

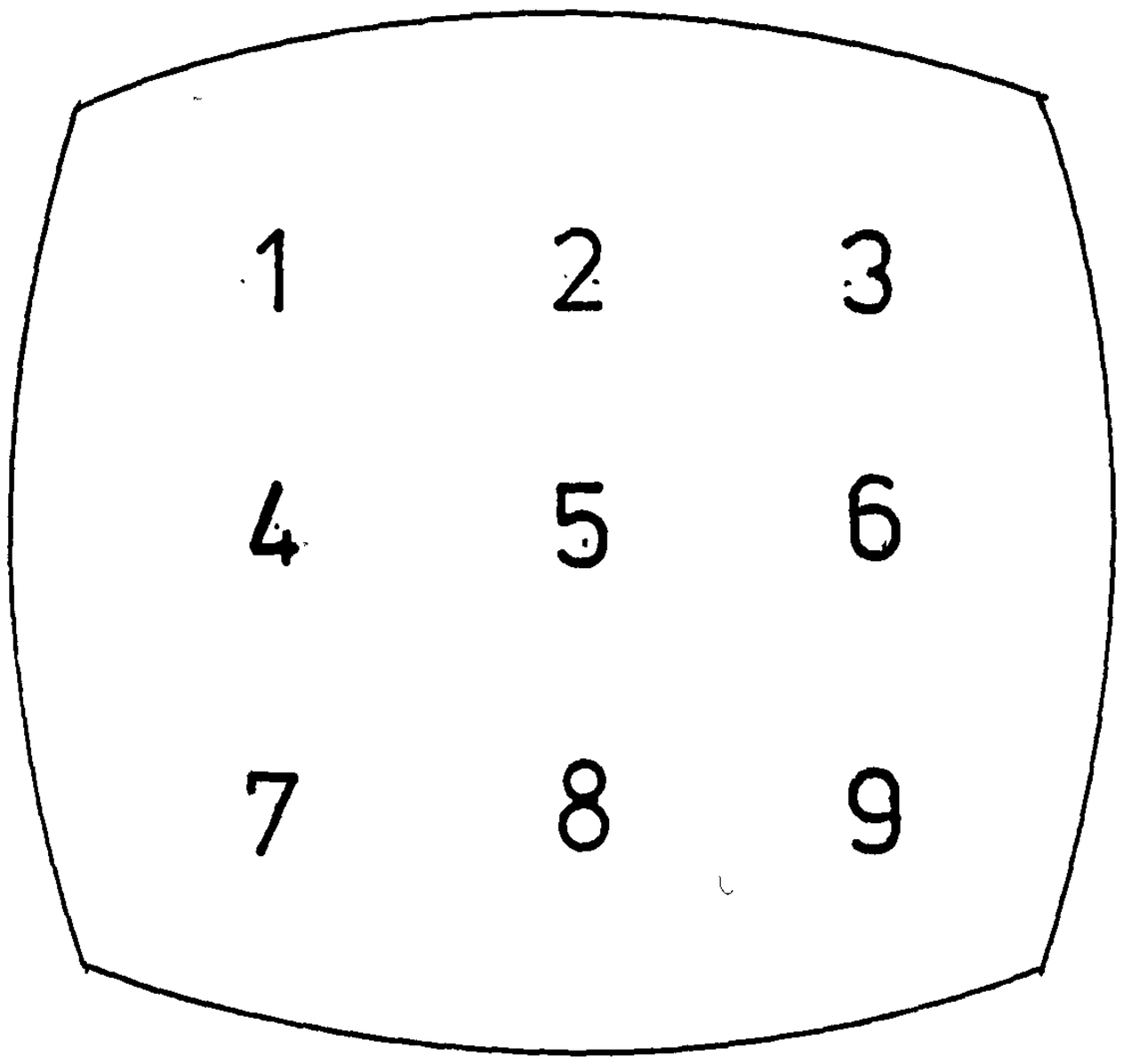


FIG. 5.26 TV screen positions for pin-hole diameters indicated in Table 5.2

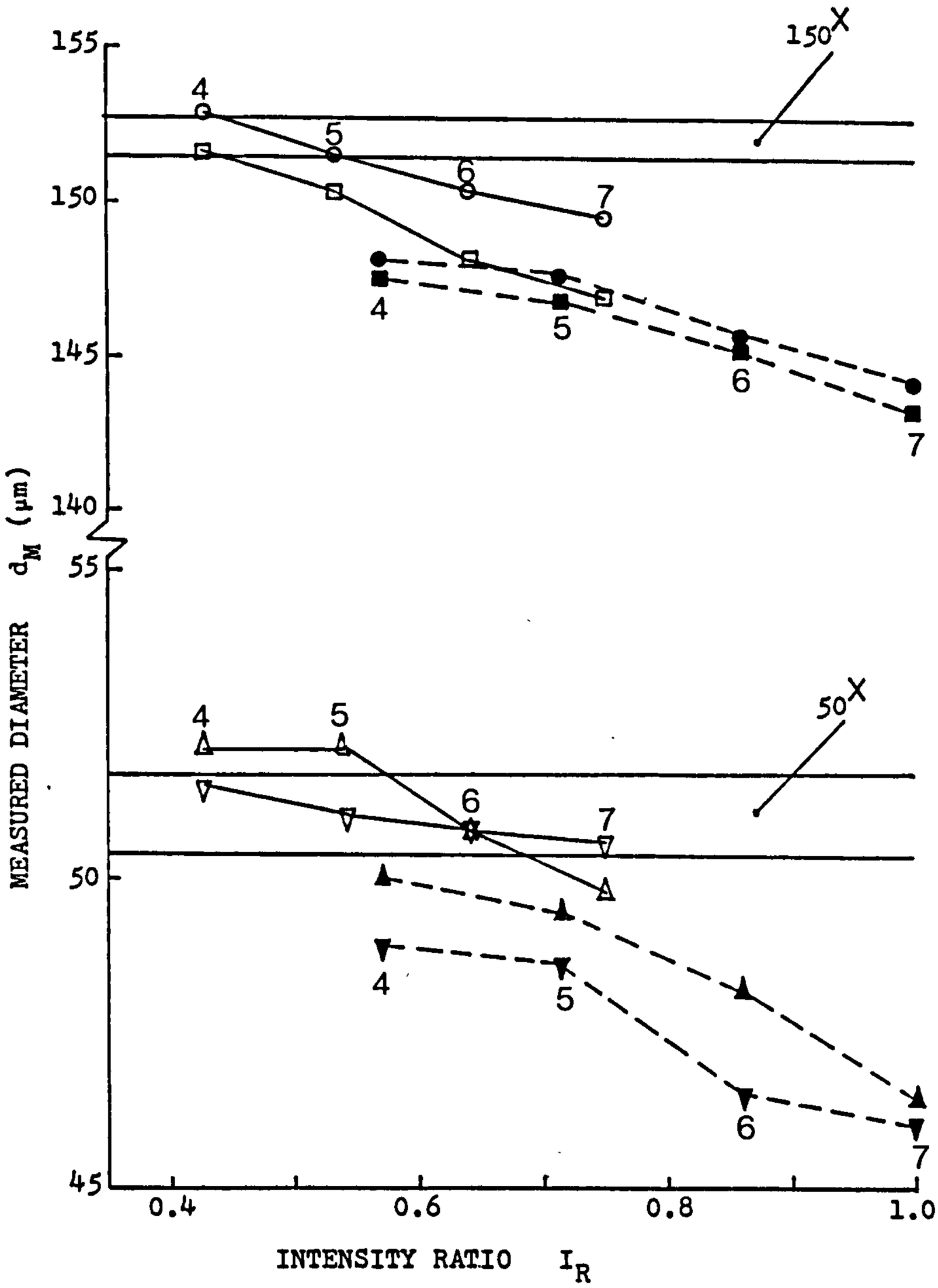


FIG. 5.27 Effect of peak video voltage, I_A, and grey level 7 voltage, I_{1A}, upon measured diameter, d_M (at intensity I) for image of a reticle disc of nominal diameter 50 μm and 150 μm. x = actual disc diameter (horizontal band denotes uncertainty in microscope measurement. Numbers beside data points denote level on grey scale. I_A = 0.25V (□,Δ); 0.3V (▽) and 0.35V (○). I_R = 0.75 (○,□,Δ,▽) and 1.0 (●,■,▲,▼).

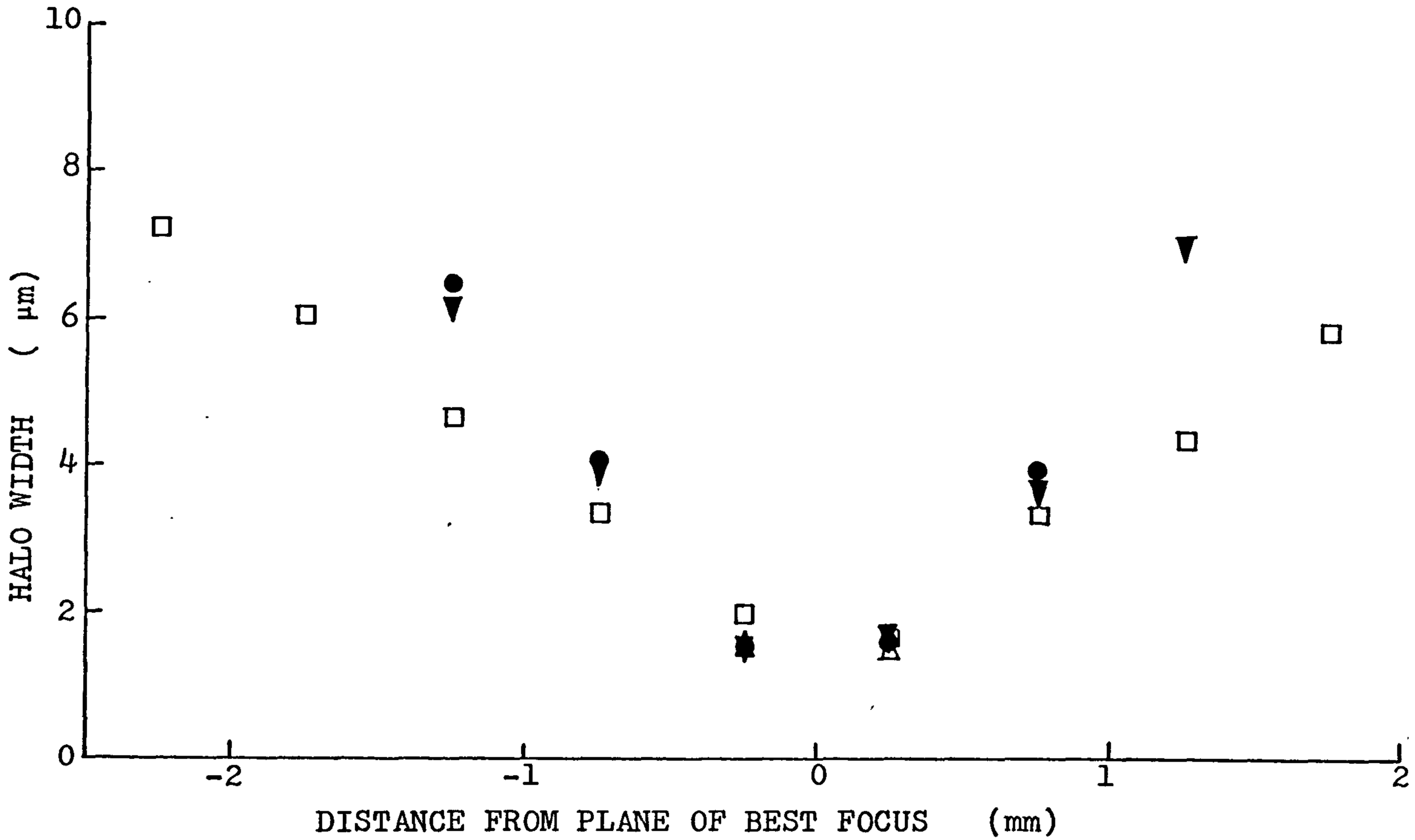


FIG. 5.28 Variation in halo width (averaged over 3 intervals between level 4 and 7) with position of reticle in field for magnification 9x. Disc diameters in µm: □ 506, ▼ 92, ● 61 and Δ 21.

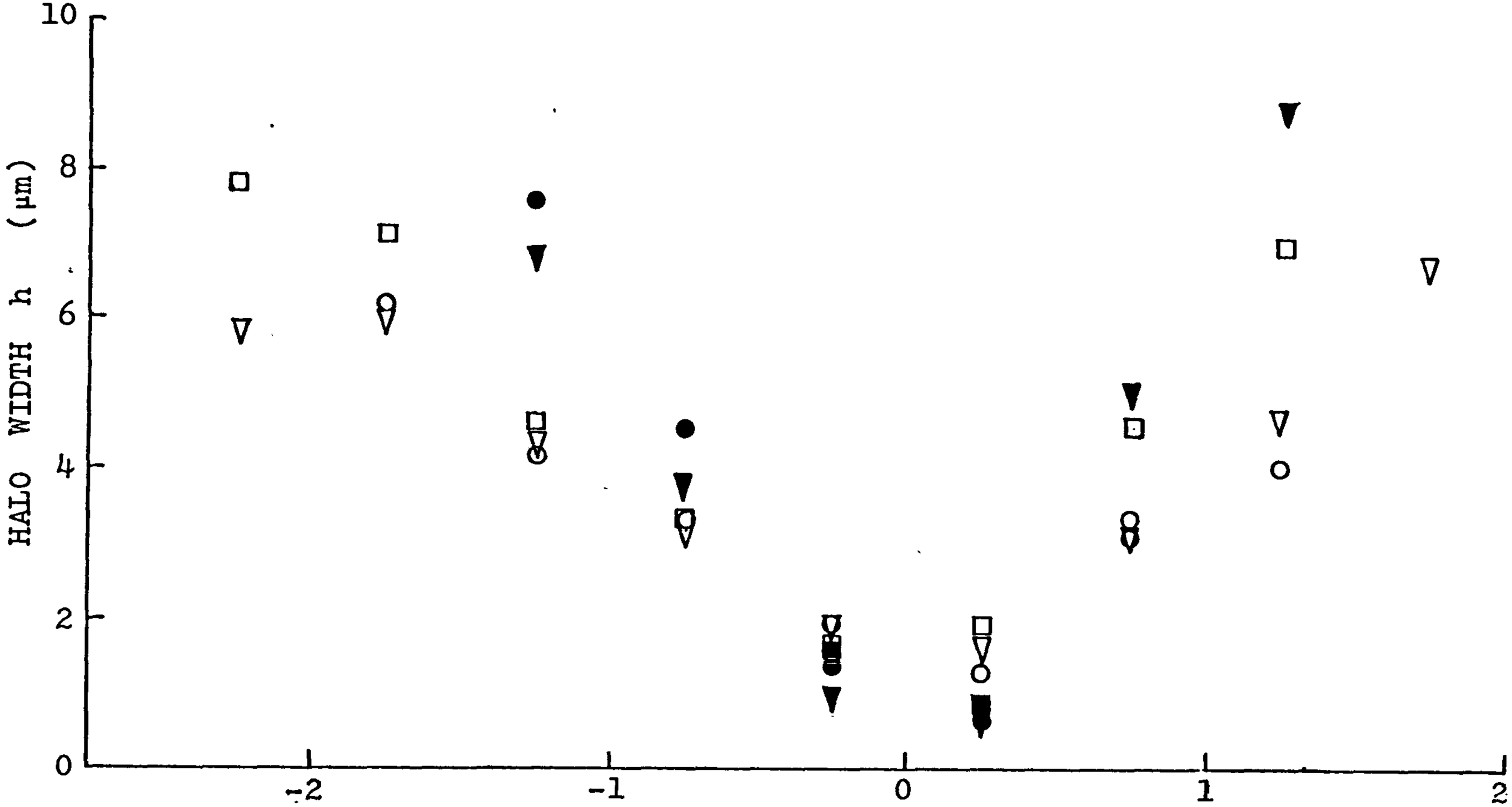


FIG. 5.29 Variation of halo width h (between grey levels 4 & 5) with position of reticle in field for magnification 9x. Disc diameters in μm : ■ 32, ● 61, ▼ 92, □ 202, ○ 398, ▽ 754.

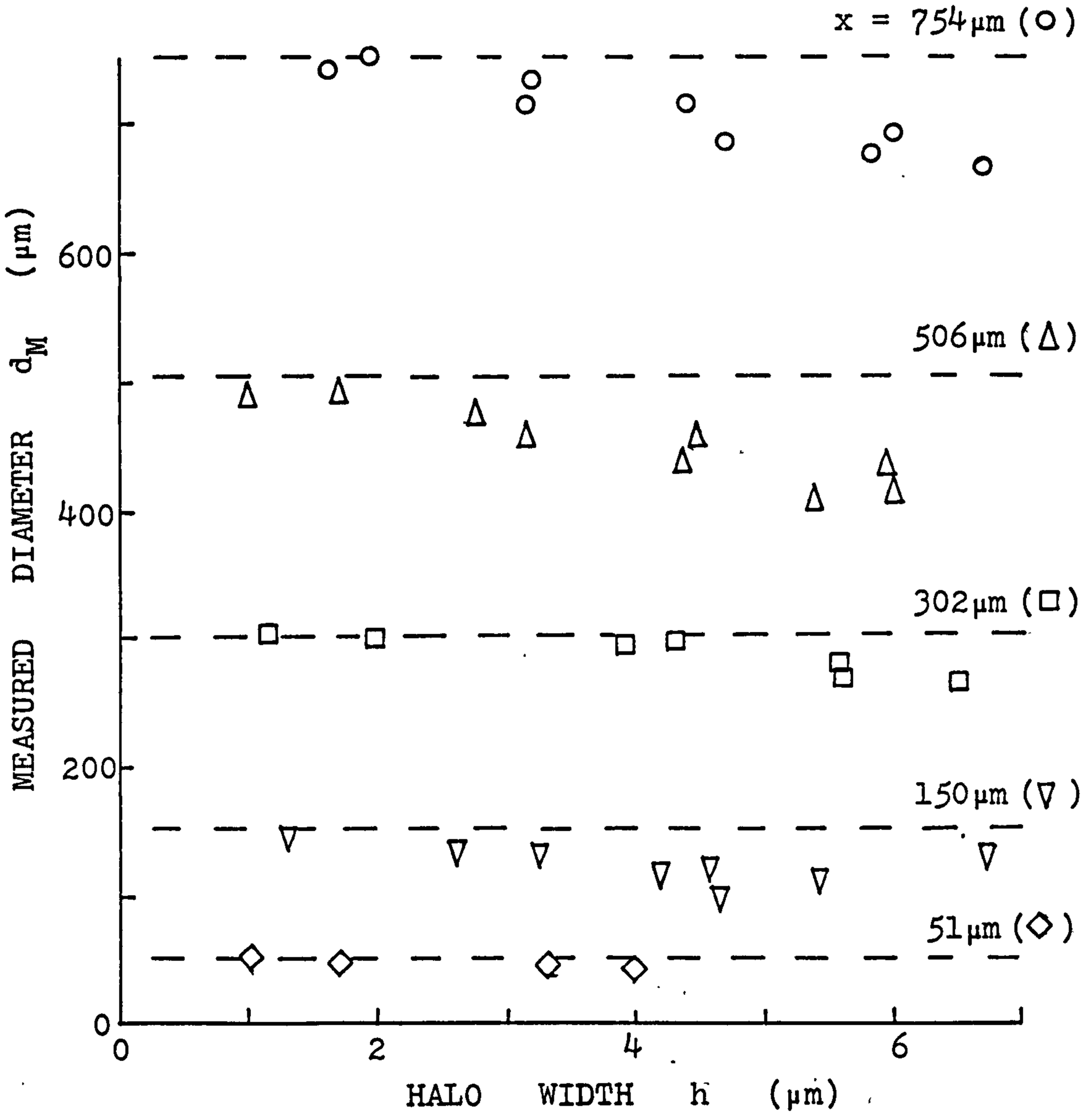


FIG. 5.30 Relationship between measured diameter, d_M (at grey level 4) and halo width h (between levels 4 and 5) as reticle is moved relative to plane of best focus. x = actual diameter of disc.

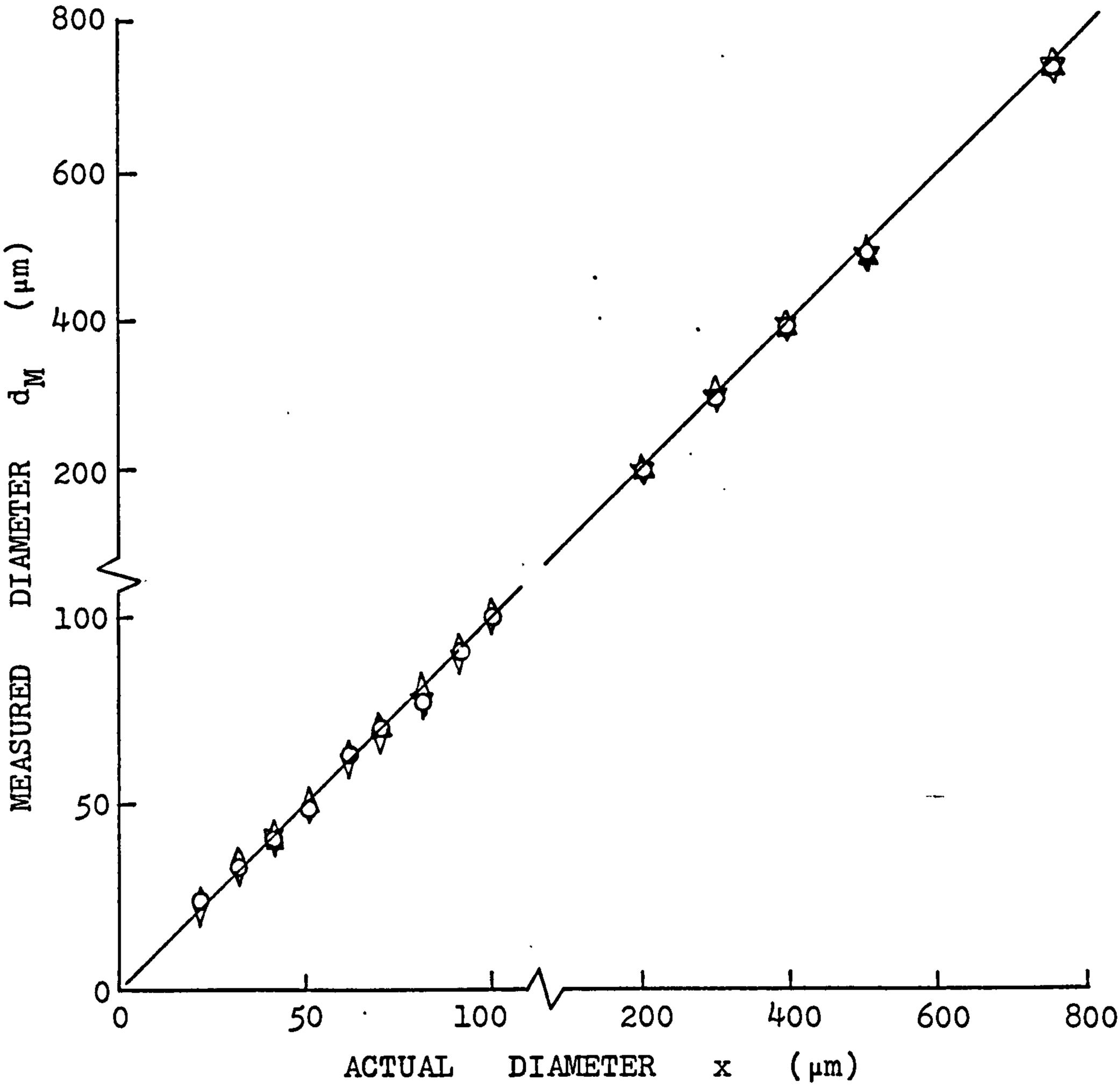


FIG. 5.31 Comparison of measured and actual diameters for in-focus photograph of reticle discs. (x = diameter of disc, not its photographic image; plotted points indicate accuracy of complete measurement process, not the image analysis system alone.)
I_R : Δ 0.57, O 0.75, ∇ 1.00.

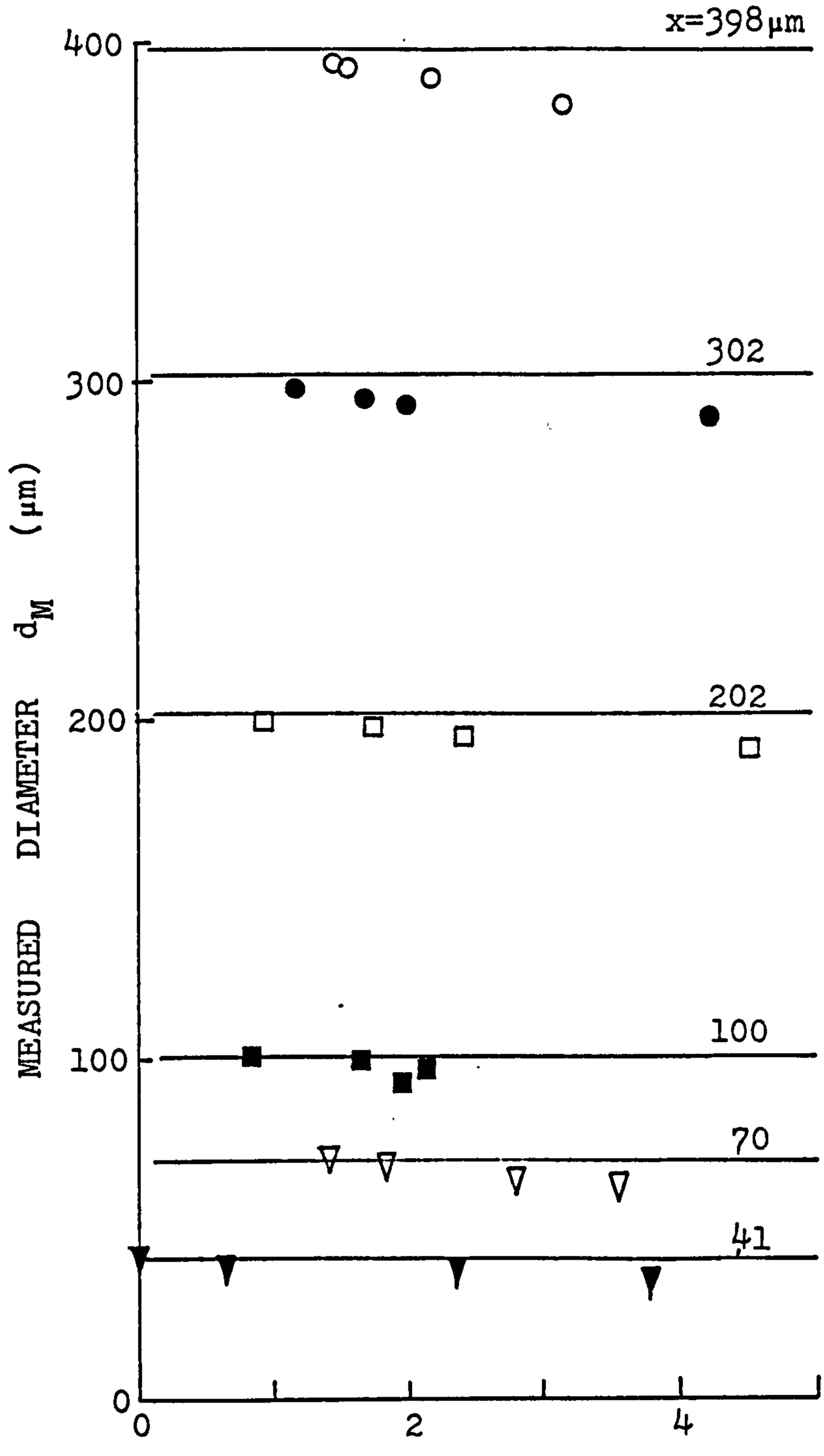


FIG. 5.32 Results of simulating a poor contrast photograph by adjustment of peak video voltage I_A relative to fixed grey scale. (Halo width increases as I_A decreases.) x = actual diameter of reticle disc.

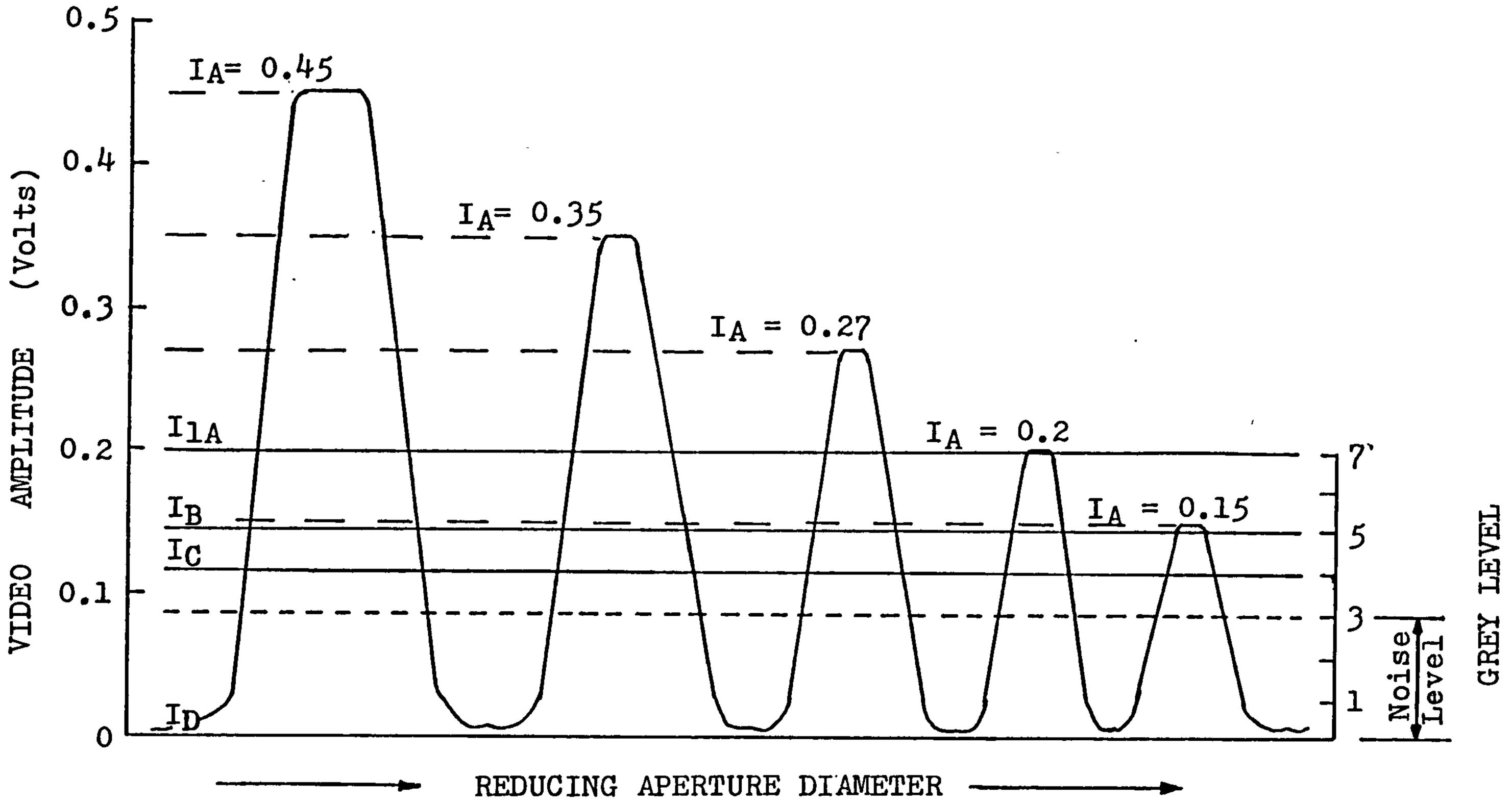


FIG. 5.33 Relationship between I_{1A}, I_B, I_C and I_D and peak video level I_A when the latter is altered by suitable adjustment of camera aperture.

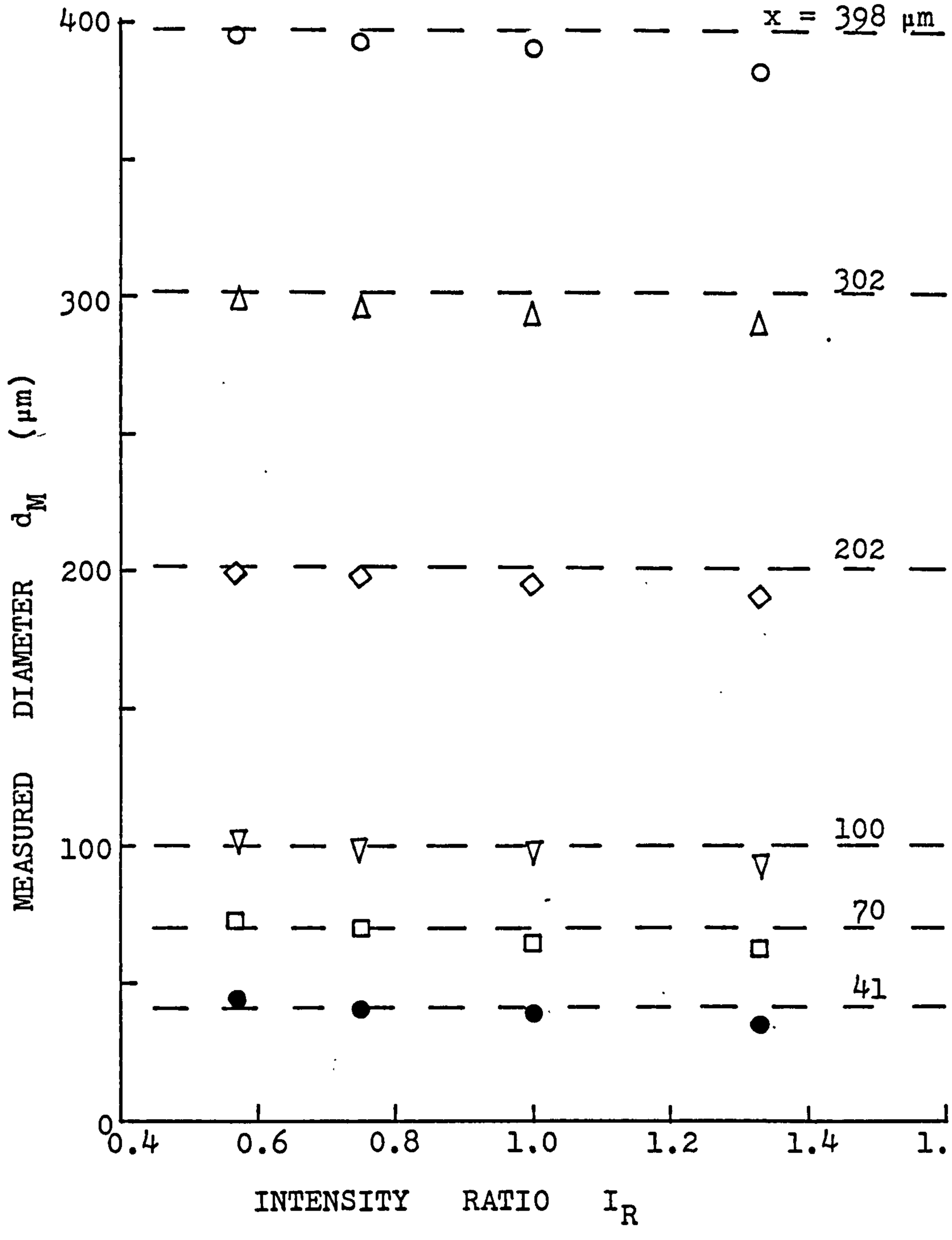


FIG. 5.34 Additional poor contrast effects. Measured diameter, d_M at different values of I_R. x is actual disc diameter.

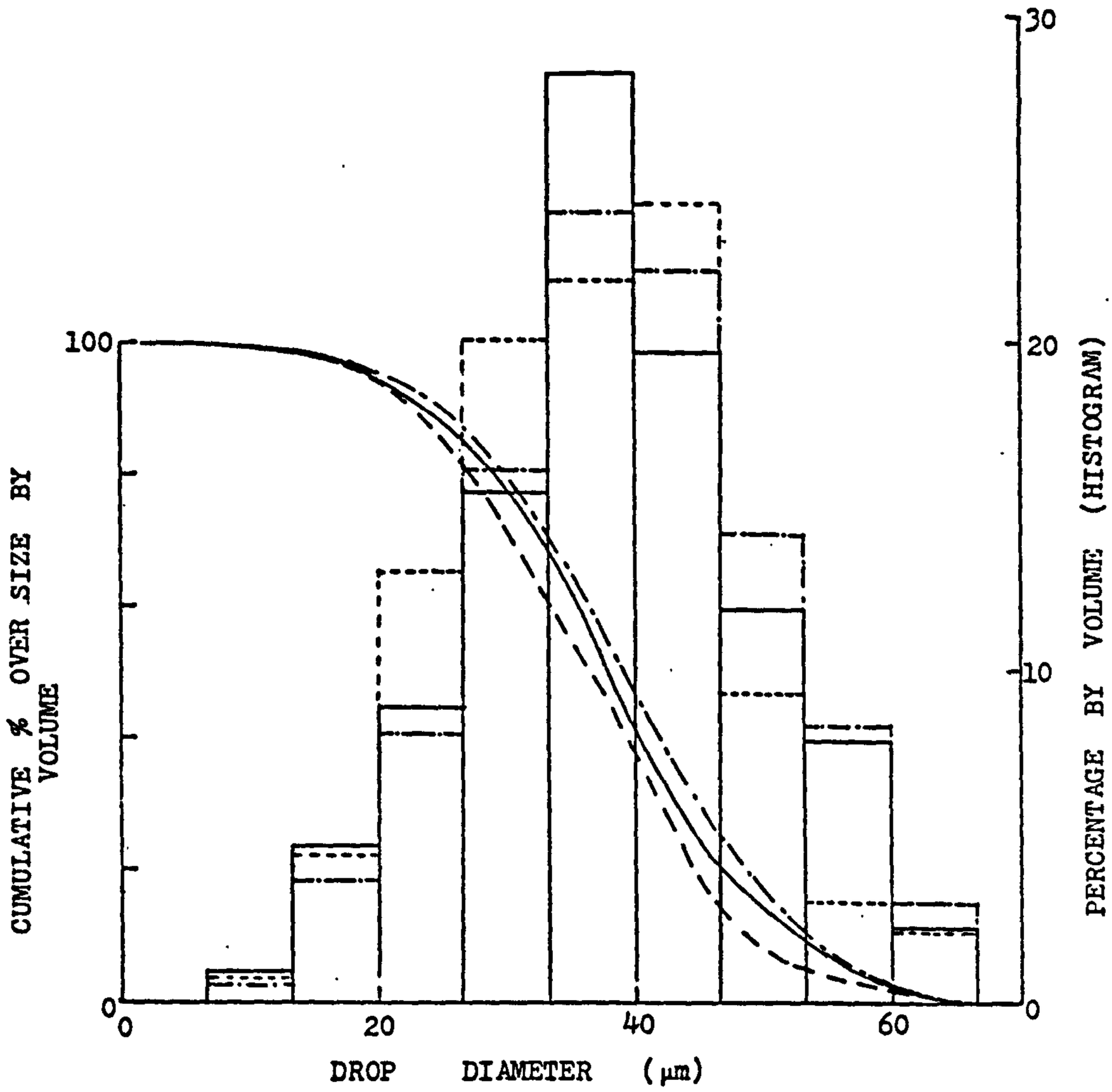


FIG. 5.35 Drop size distributions from photograph shown in part in Fig. 4.2. (Approx. 500 'in focus' images).

——— automatic analysis

- - - - - manual analysis (observer A)

—·—·— manual analysis (observer B)

(Manual sizing was by sorting images into size groups only, followed by calculation of refined distributions by the method of Wise (193)).

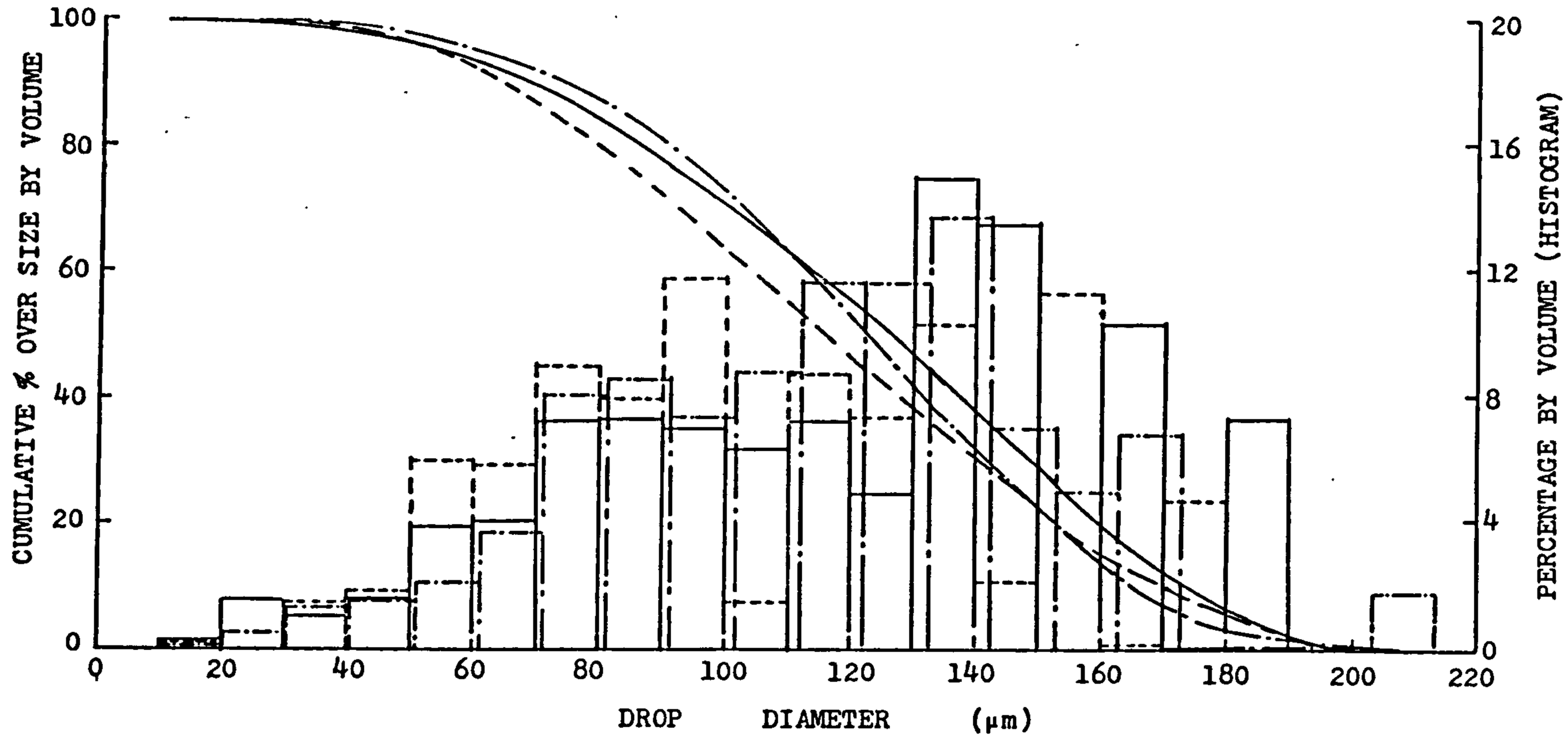


FIG. 5.36 Drop size distribution from photographs of two-phase flow spectra.

——— automatic analysis

- - - - - - - manual analysis (observer A)

—·—·— manual analysis (observer B)

(The shift in histogram width arises from a different setting of magnification used.)

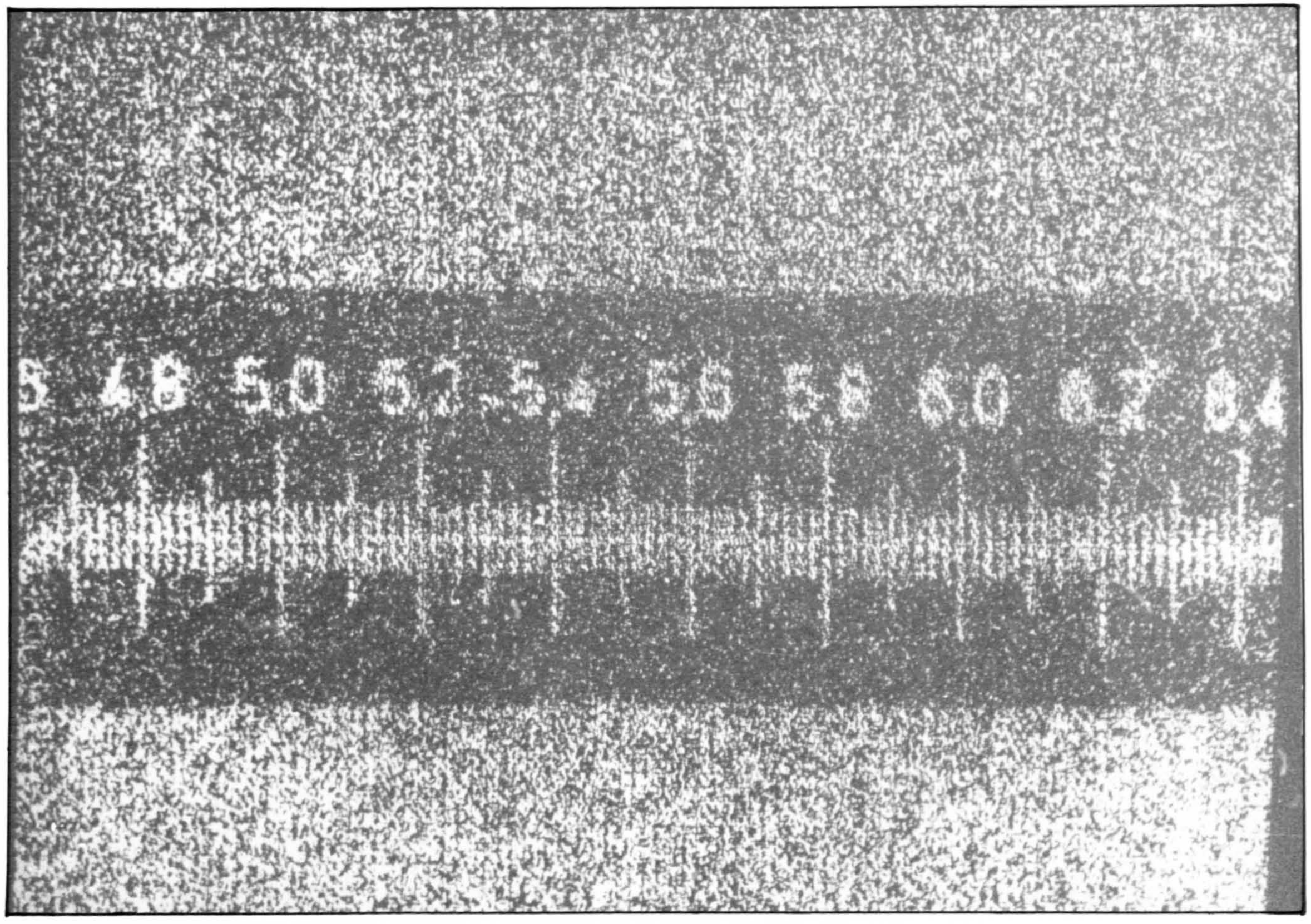


FIG. 5.37 Tektronix 611 display of digitised image of a scale at grey level 3.

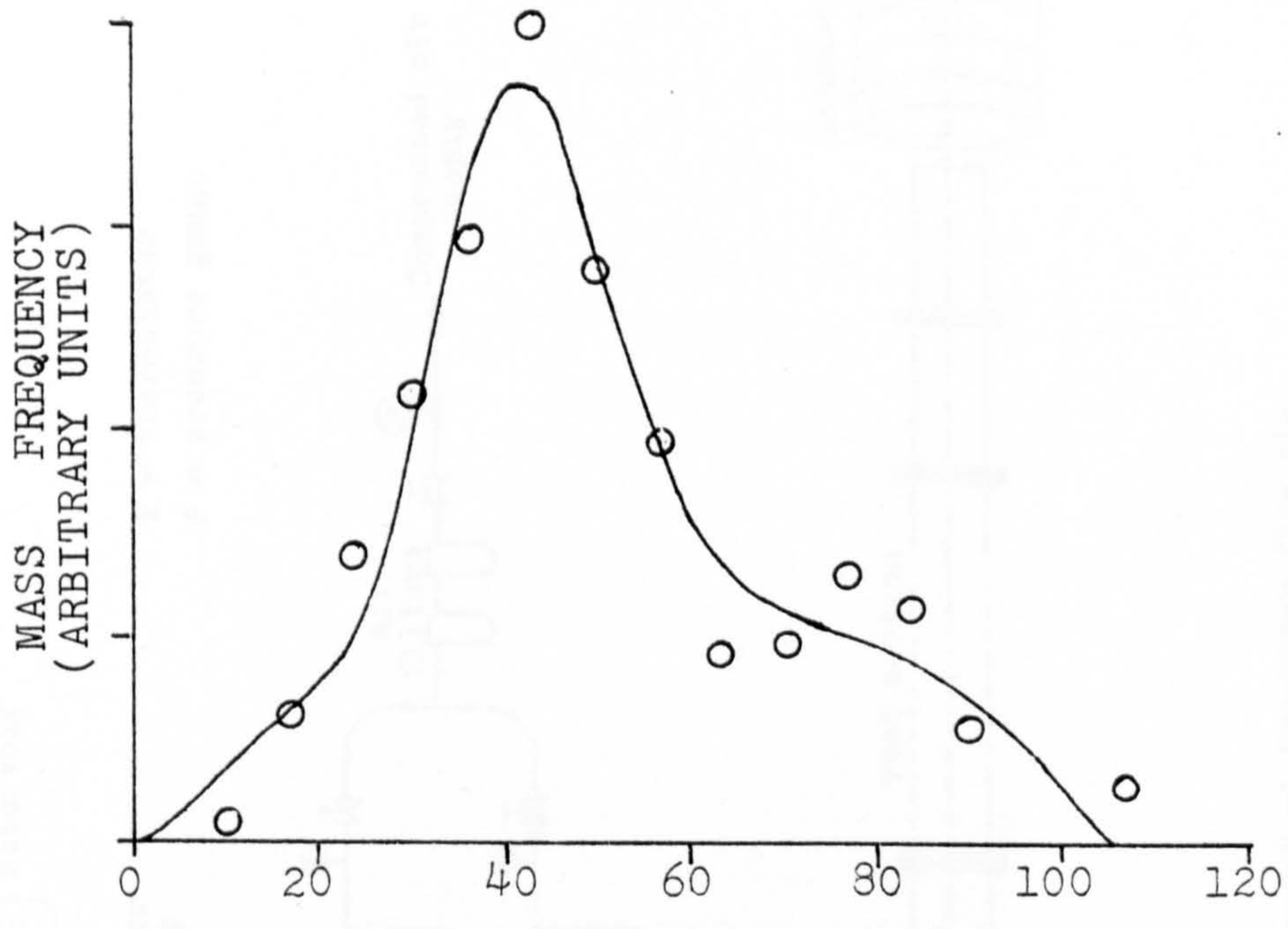


FIG. 6.1 Mass frequency distribution for atomiser data batch AK.

——— optimised fit for s=1

o experimental data

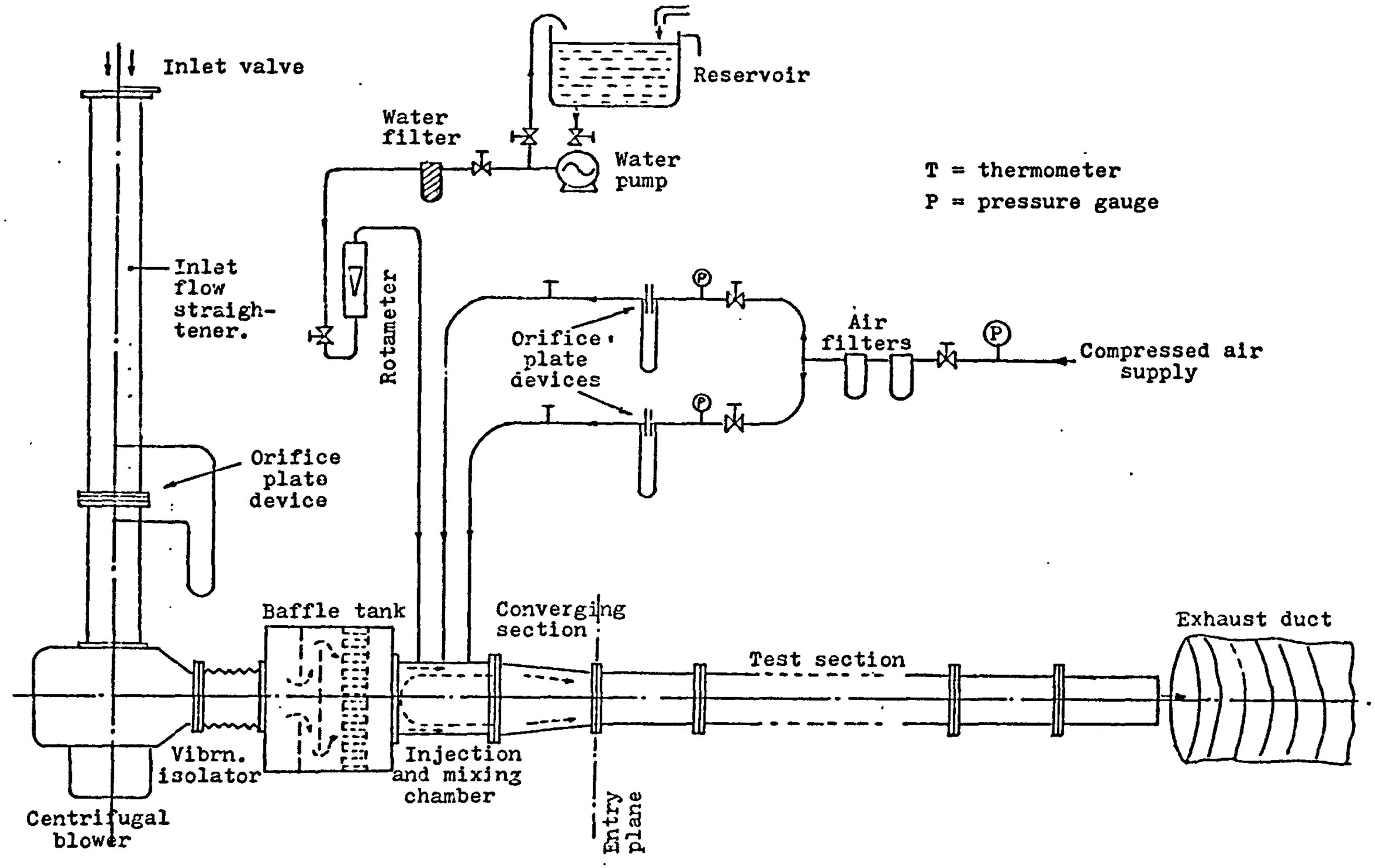


FIG. 7.1 Schematic arrangement of two-phase flow rig.

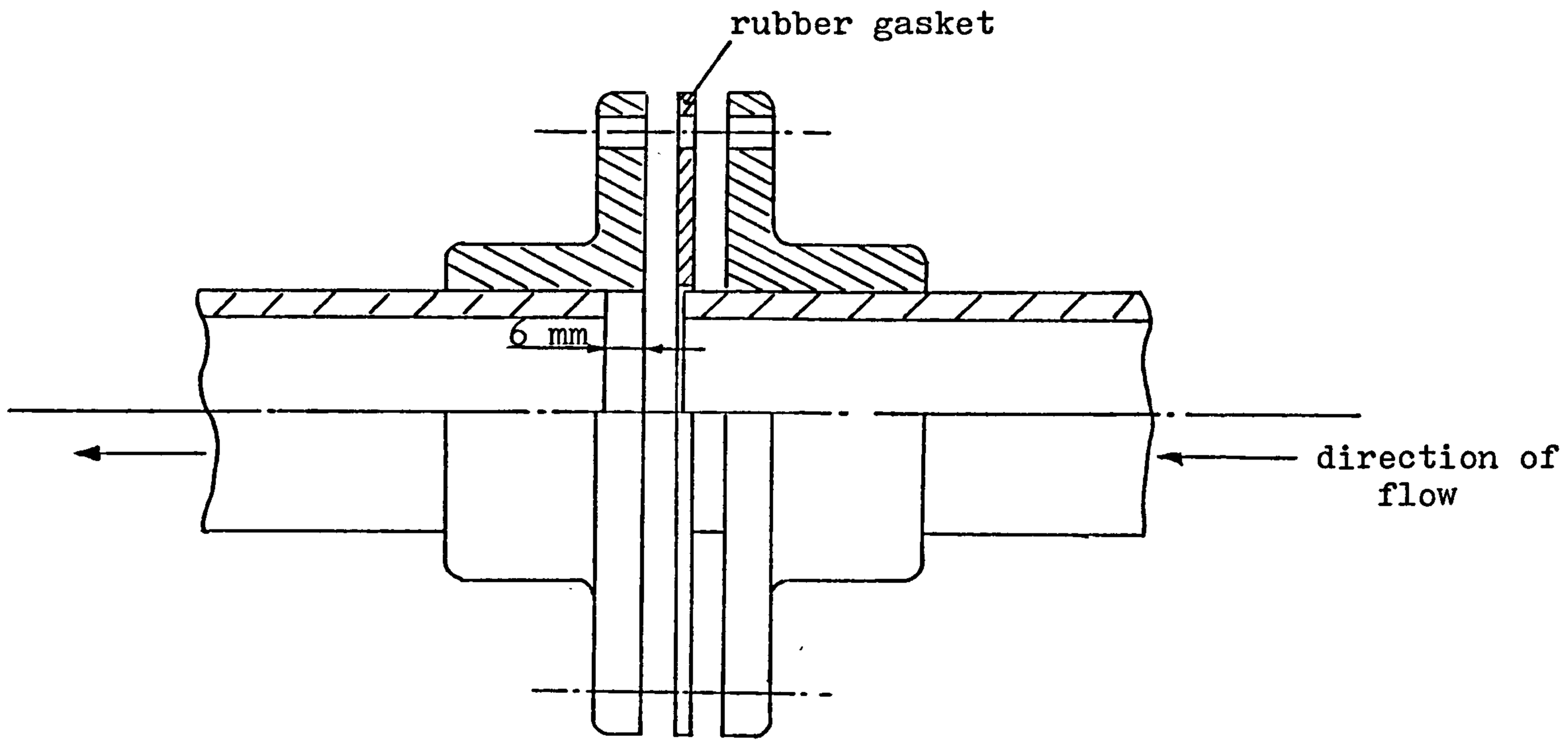


FIG. 7.2 Illustration of flange joint

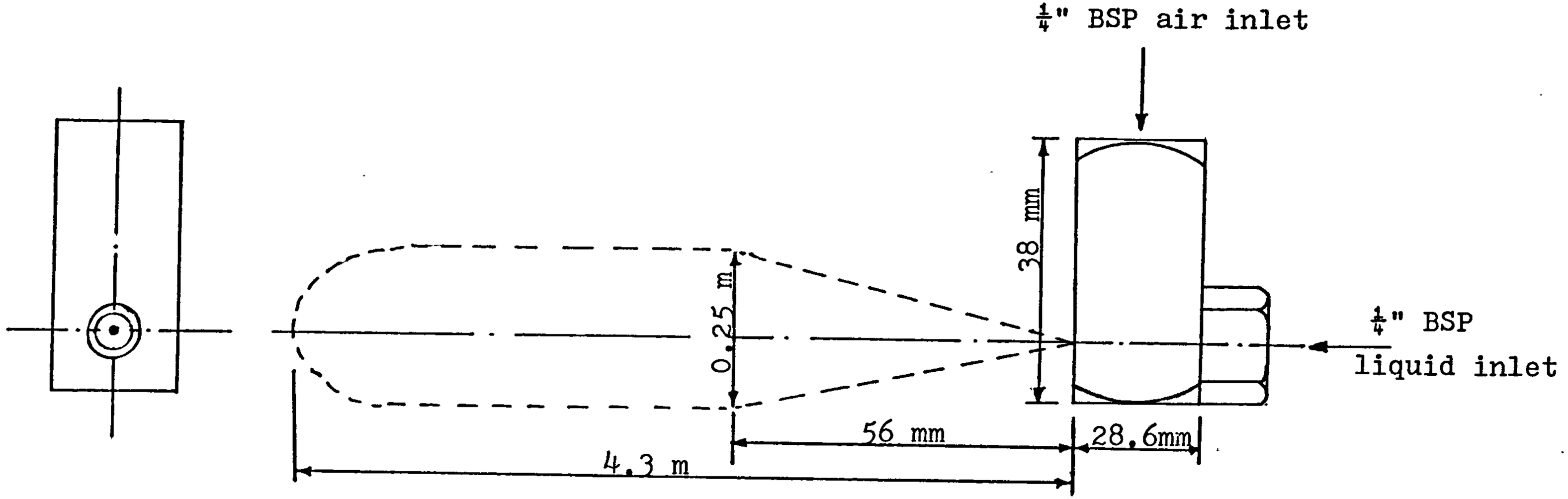
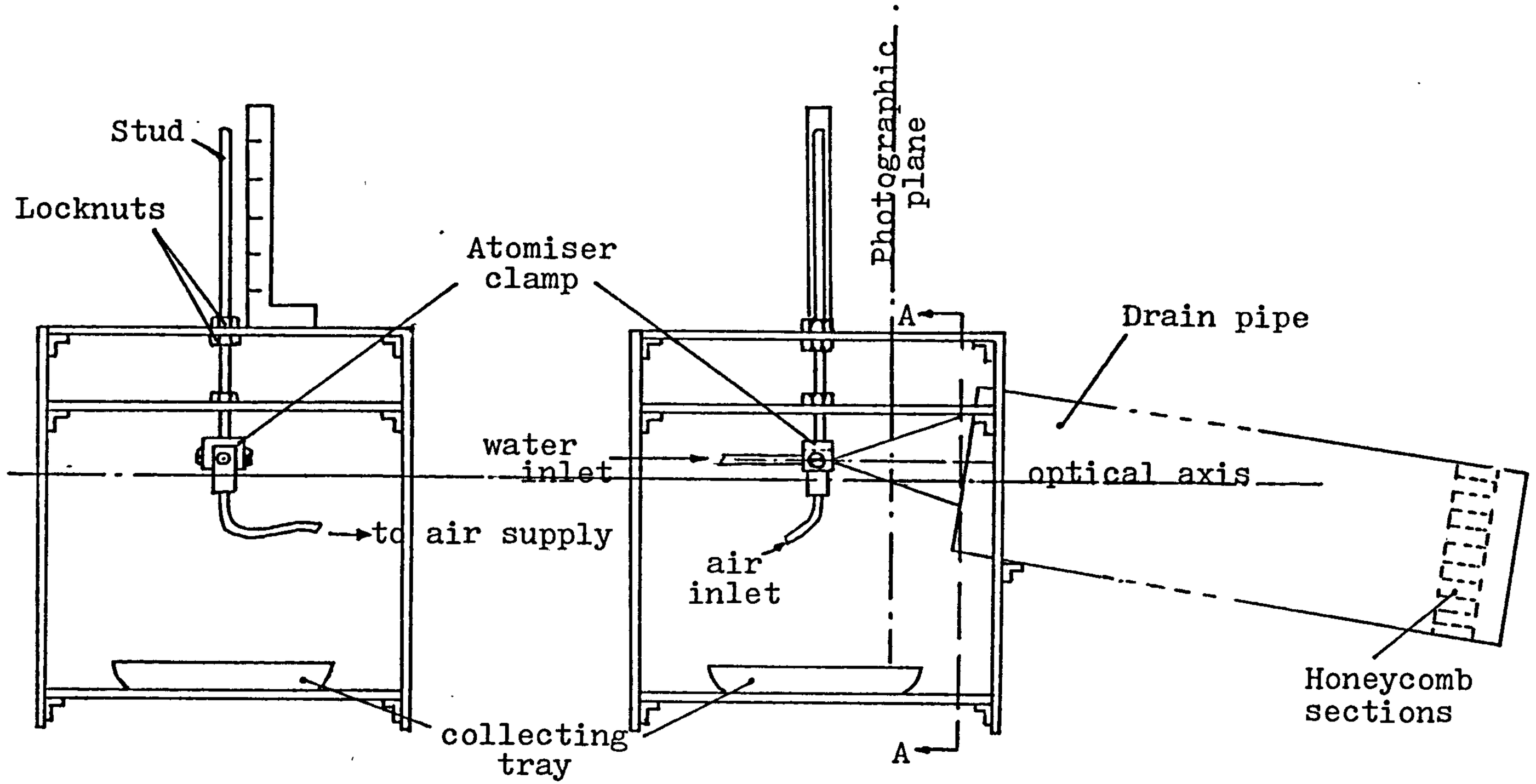


FIG. 7.3: The single air jet pneumatic atomiser (Delavan-Watson's Ltd.)



VIEW AA

FIG. 7.4: Illustration of atomiser test rig without the optics.

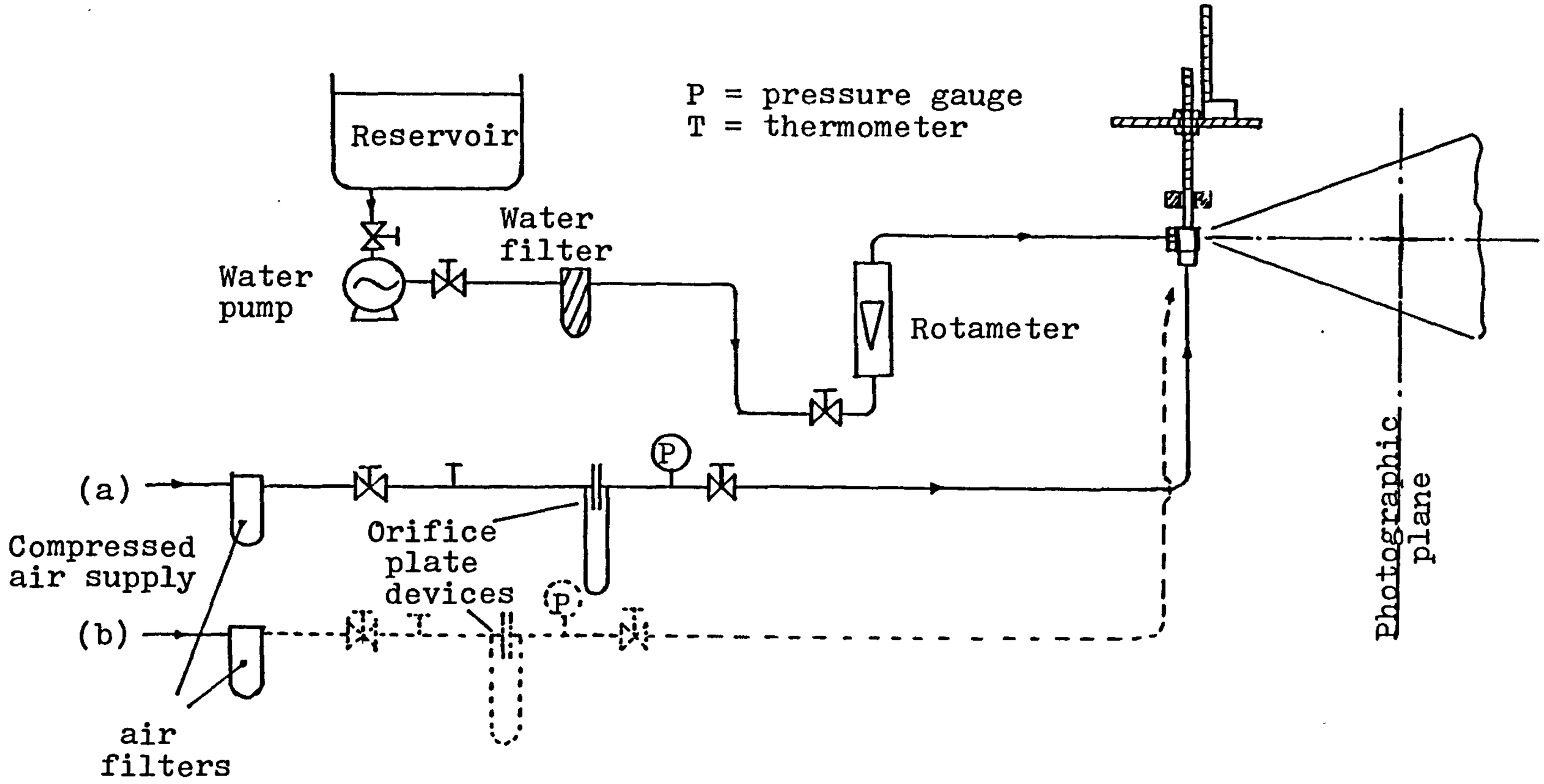


FIG. 7.5 Schematic arrangement for fluid supply to atomiser in the photographic studies of spray spectra. Air circuit (b) needed for air-blast atomisers.

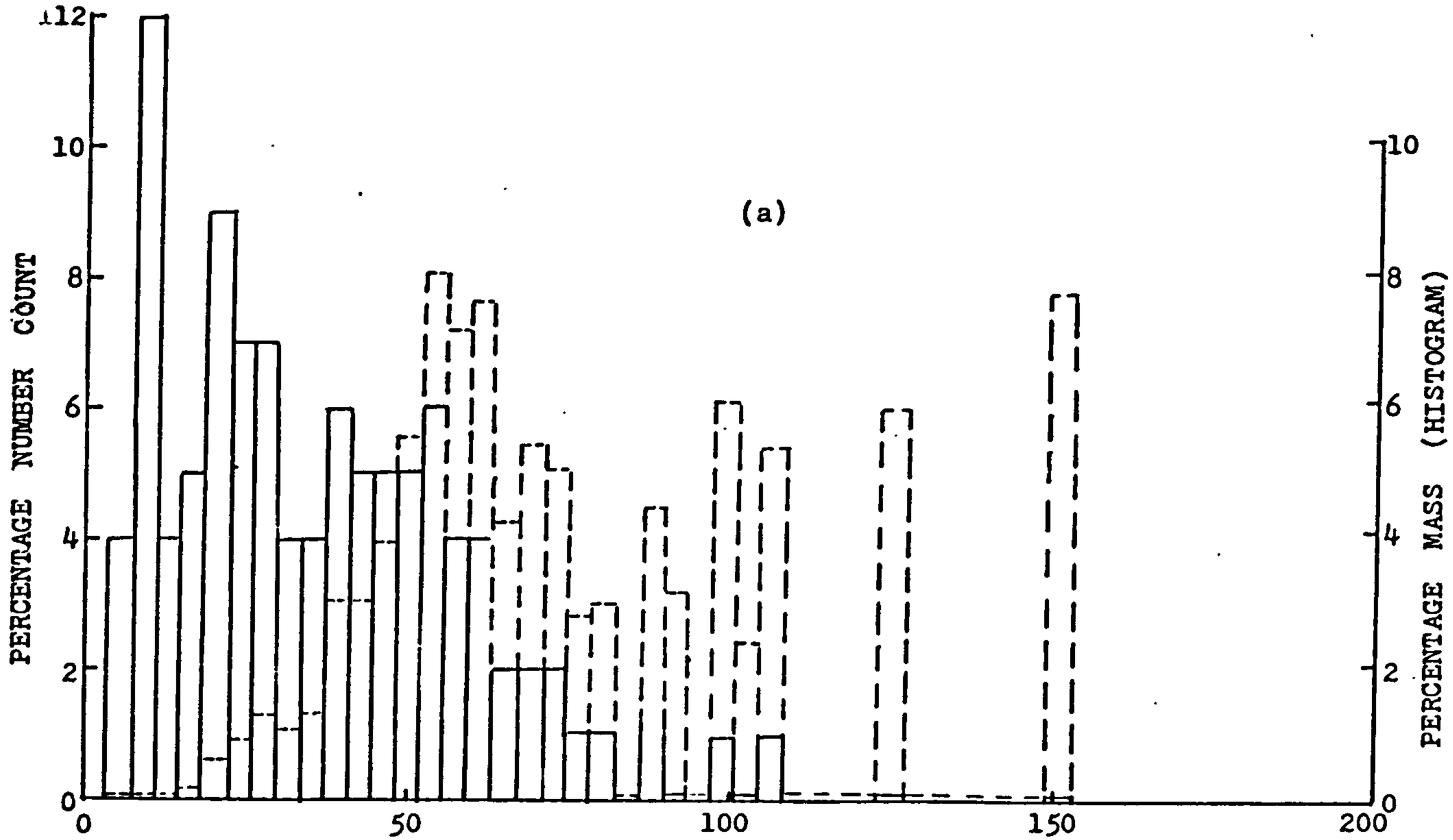


FIG. 7.6 Number and mass frequency distribution for test condition DW1(a) and DW2(b).
———:Original number frequency; - - - - - :Mass frequency (weighted)

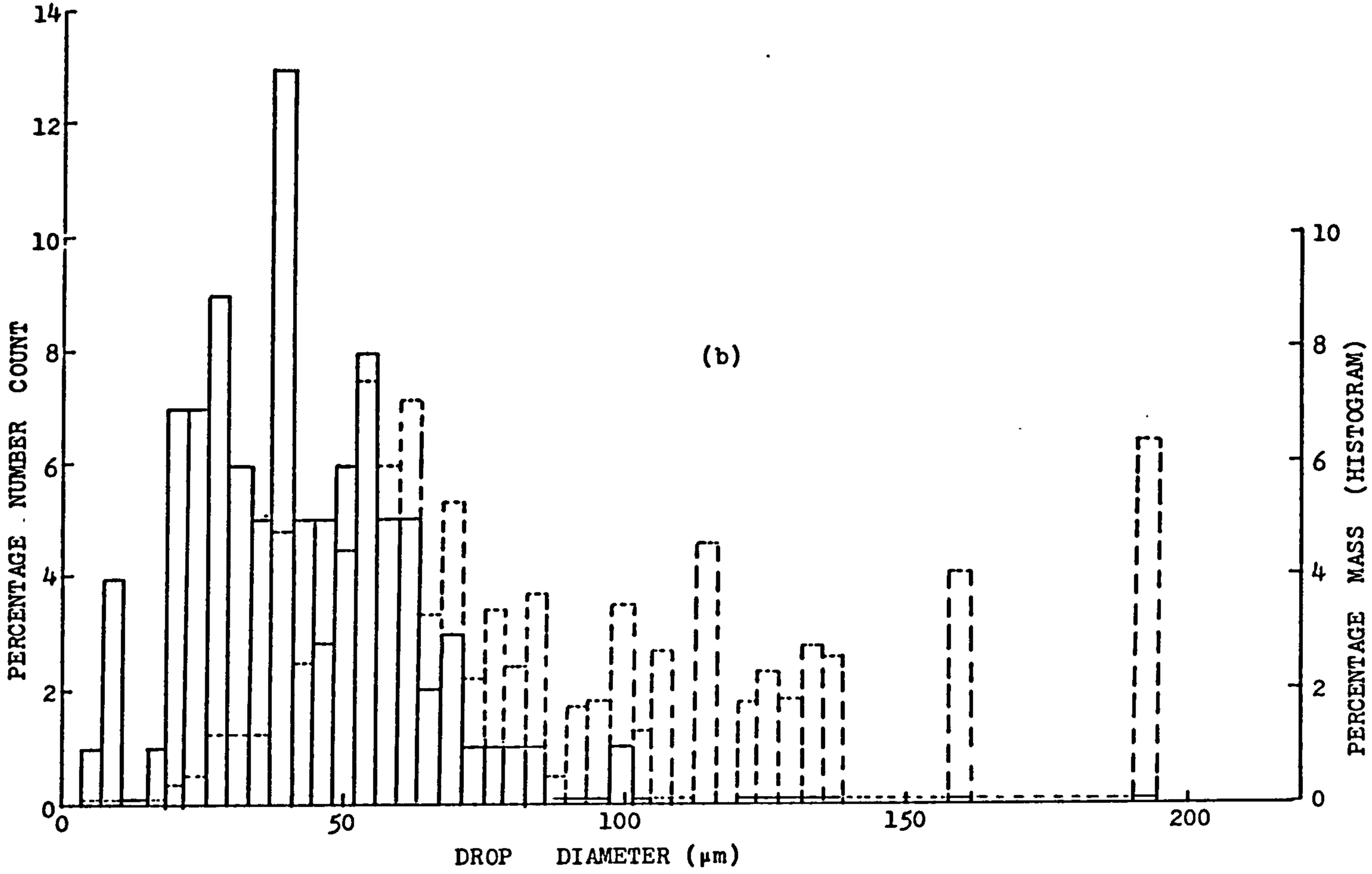

(b)
PERCENTAGE NUMBER COUNT
PERCENTAGE MASS (HISTOGRAM)
DROP DIAMETER (μm)
0
2
4
6
8
10
12
14
0
50
100
150
200

FIG. 7.6 (contd.)

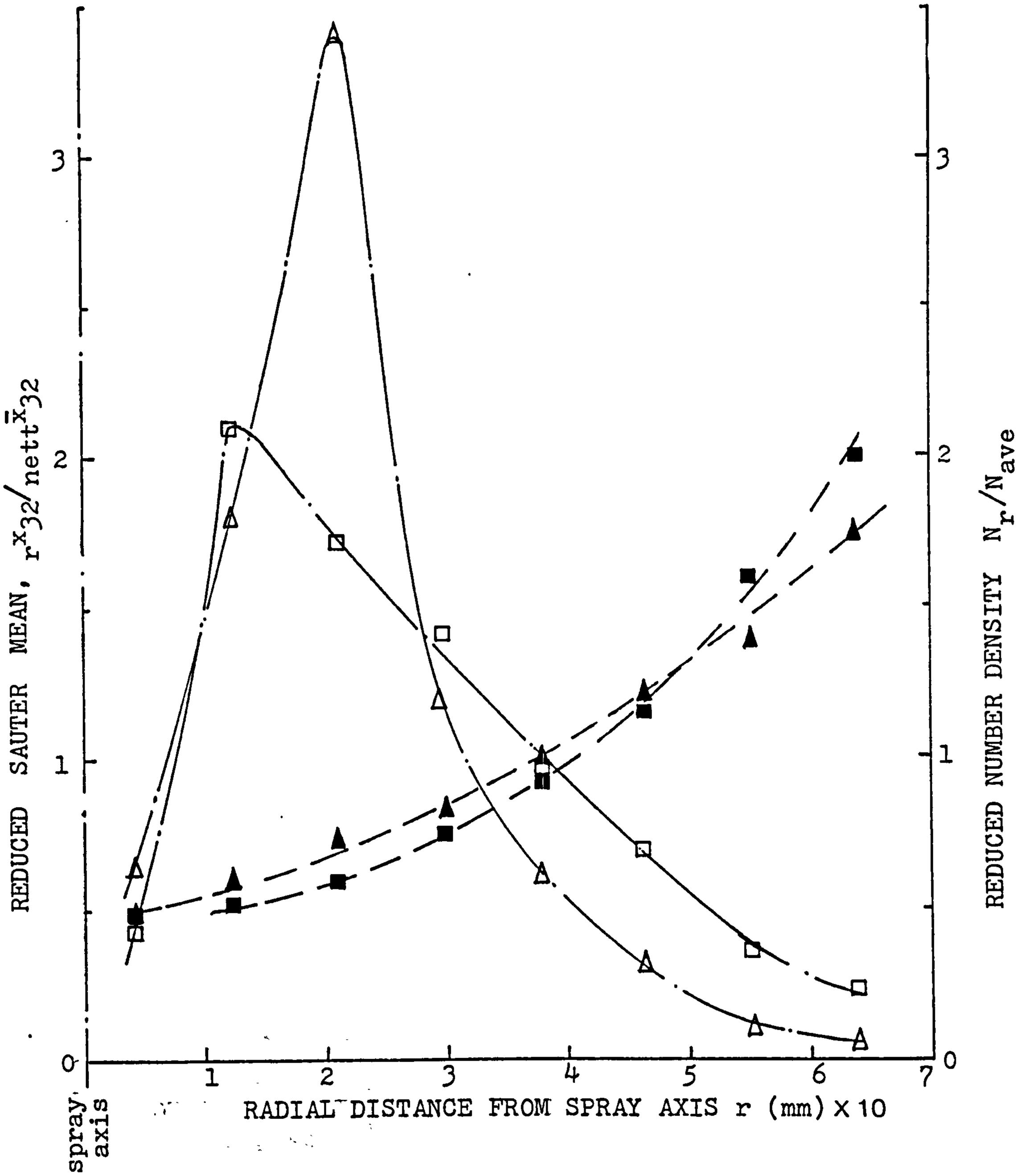


FIG. 7.7: Relationship between Sauter mean diameter(▲,■) and drop number density (Δ,□) and radial distance from spray axis for the Delavan-Watson atomiser.

$\dot{m}_a/\dot{m}_w$ = 0.53 : Δ, ▲
0.24 : □, ■

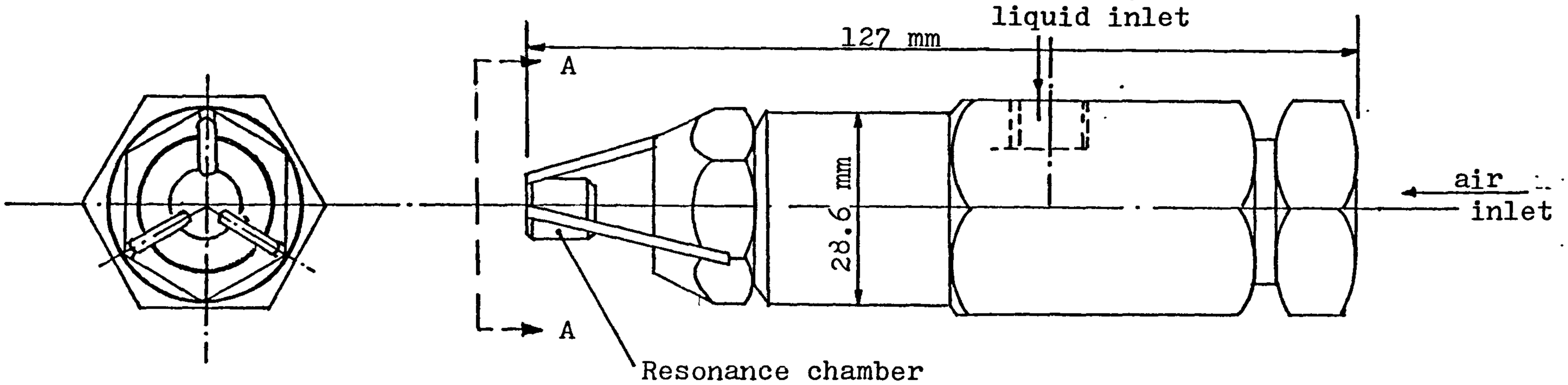


FIG. 7.8: Illustration of ultrasonic atomiser.

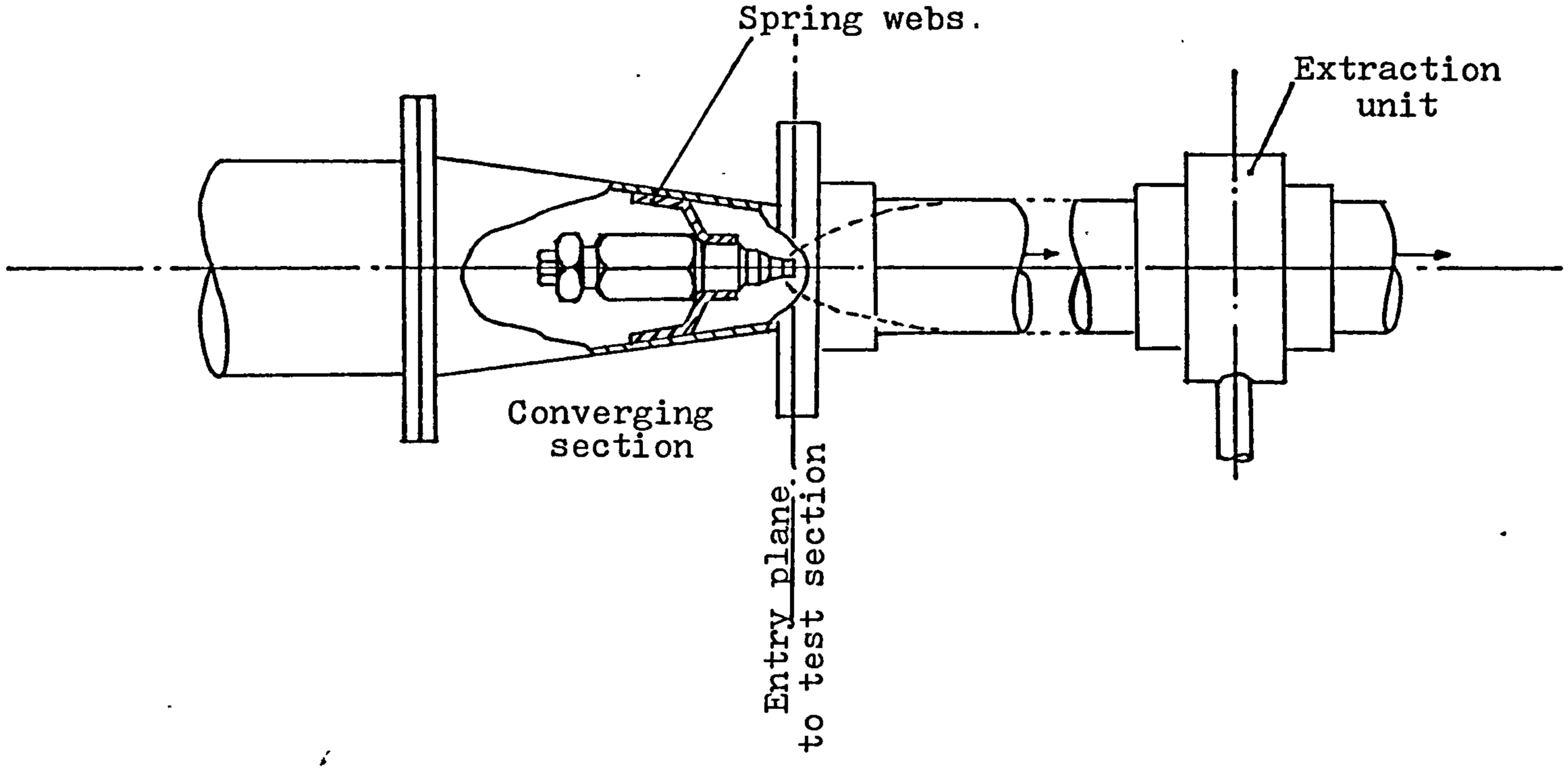


FIG. 7.9: Illustration of ultrasonic atomiser mounted in converging section of two-phase rig.

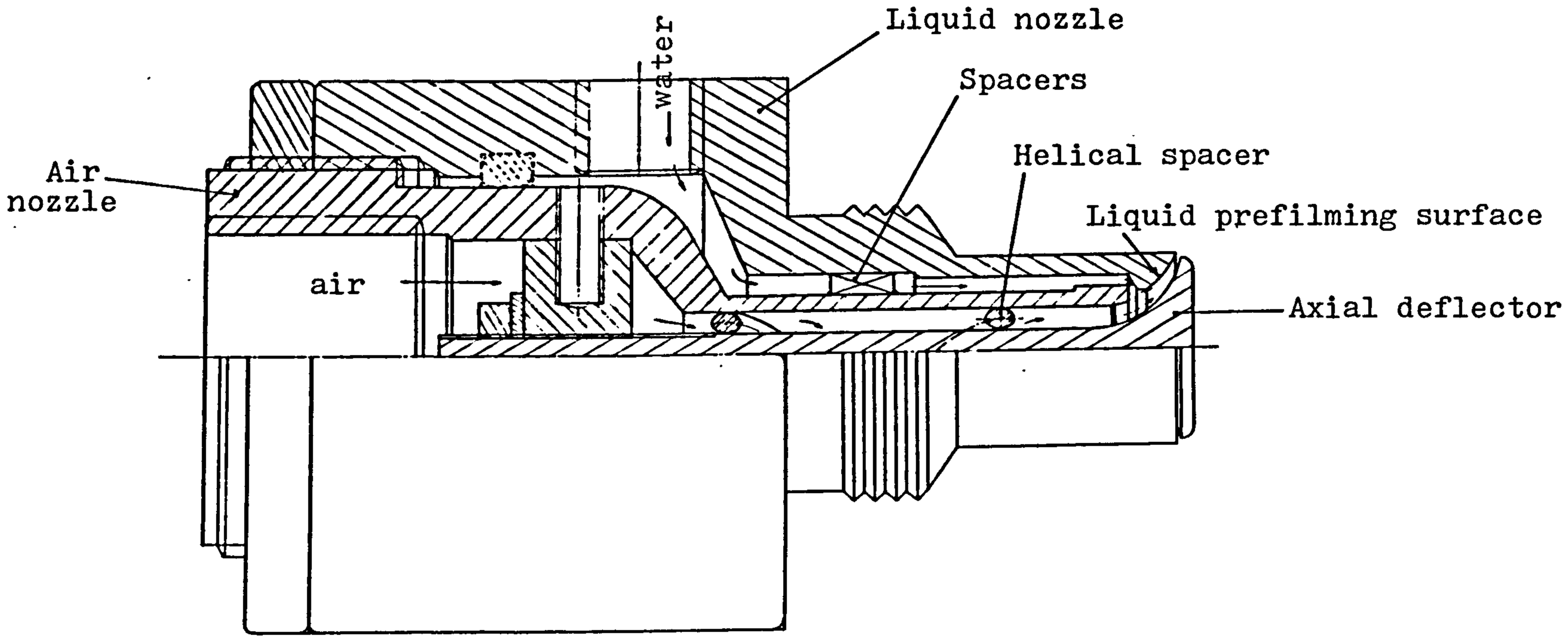


FIG. 7.10: Twin-fluid nozzle of air-blast atomiser.
(Dotted line indicates modifications)

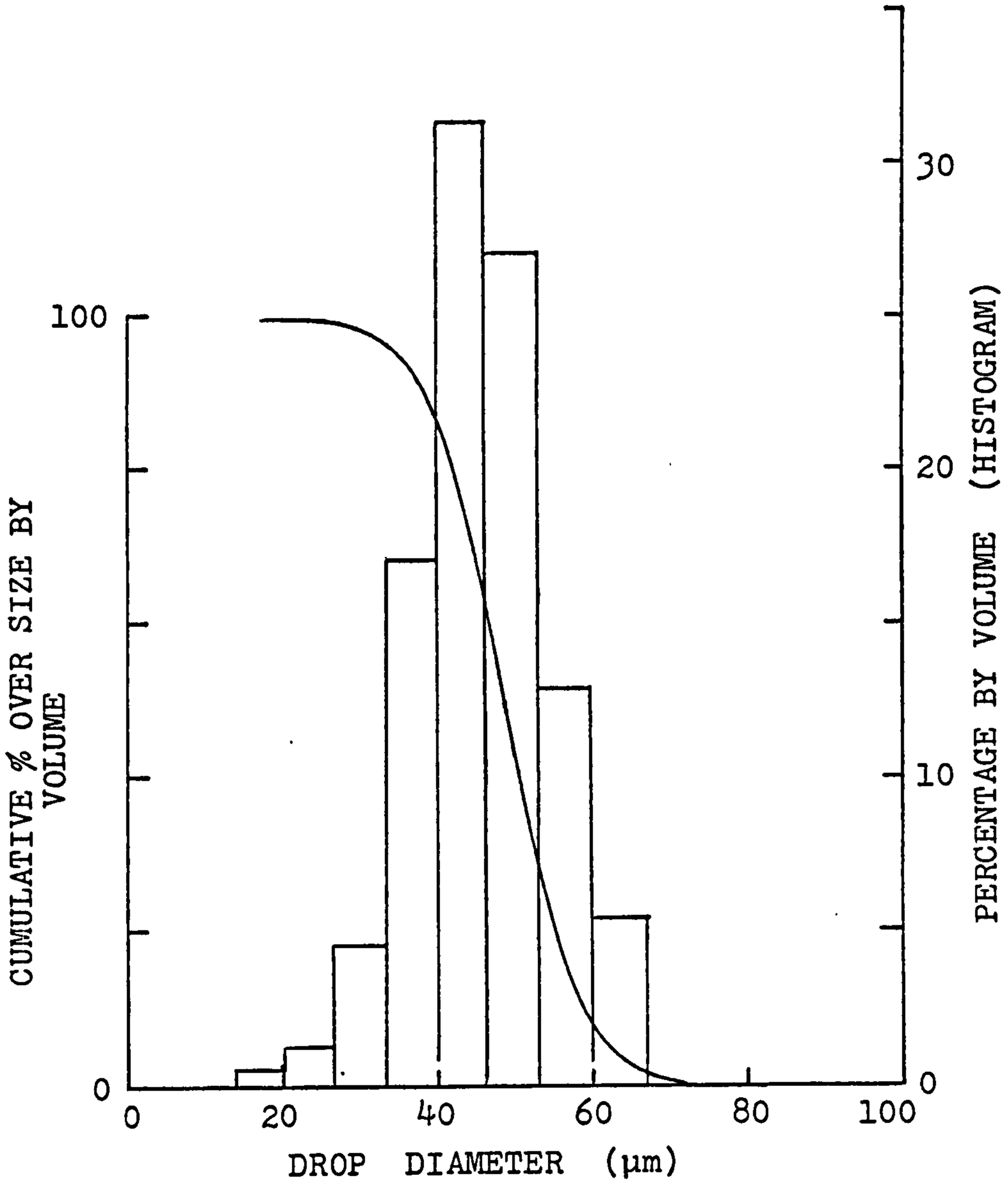


FIG. 7.11: Drop size distributions for test condition AG of prototype air-blast atomiser.

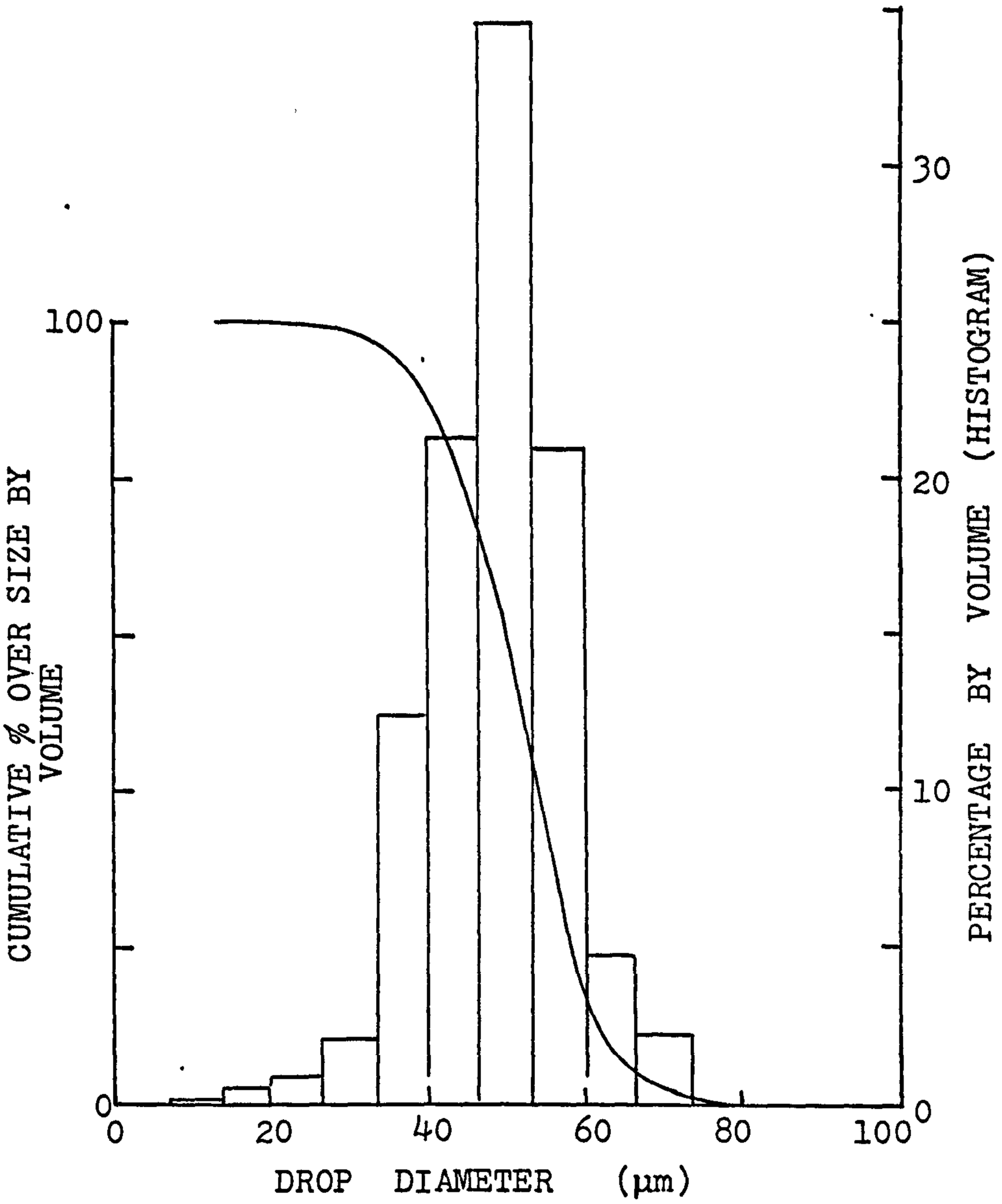


FIG. 7.12: Drop size distributions for test condition AH of prototype air-blast atomiser.

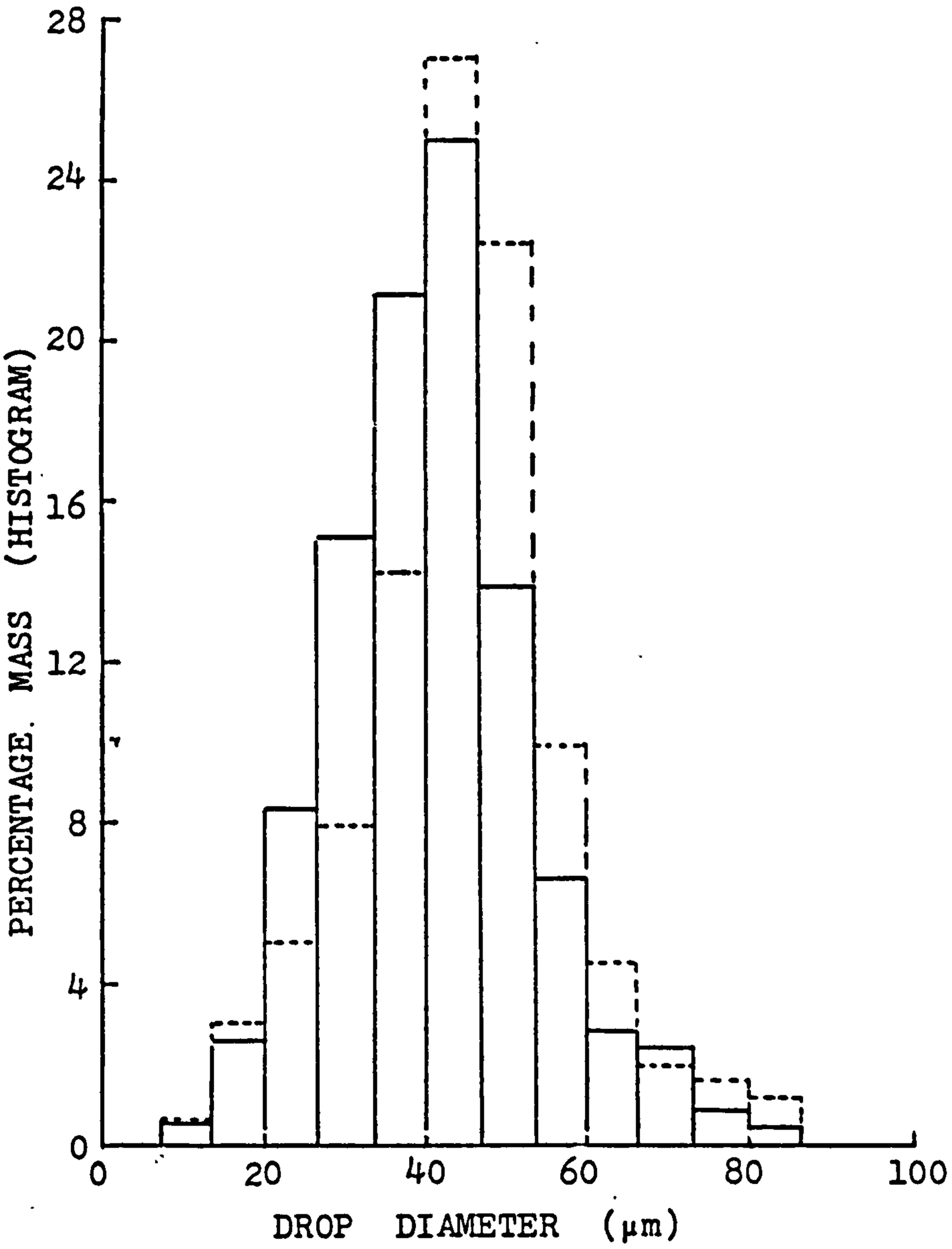


FIG. 7.13 Mass frequency distribution for air-blast atomiser units 1 and 3 for test conditions AI and AL respectively.

———: Test condition AI

------: Test condition AL

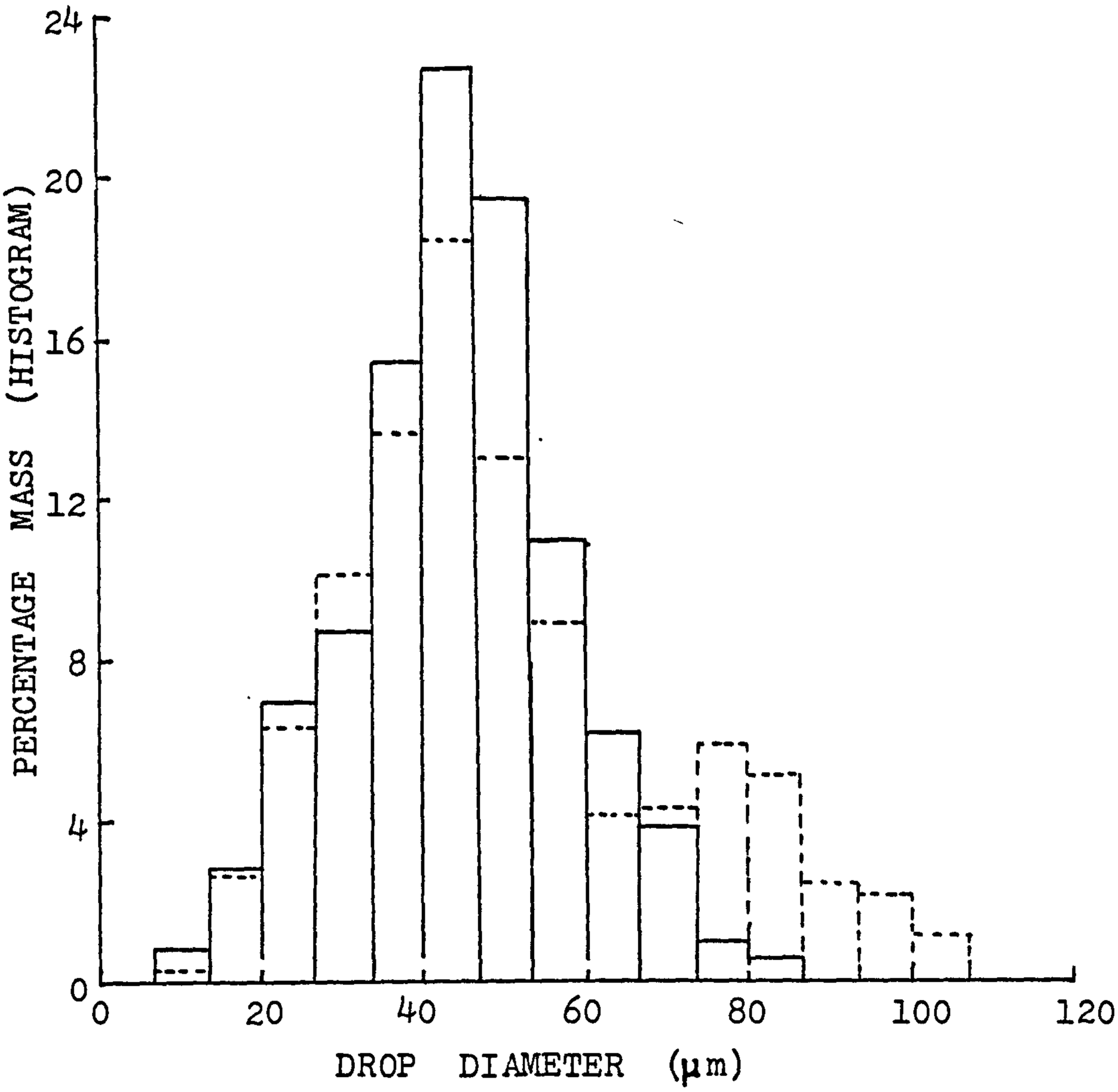


FIG. 7.14 Mass frequency distribution for air-blast atomiser unit 1 for test conditions AJ and AK.

———:Test condition AJ

------:Test condition AK

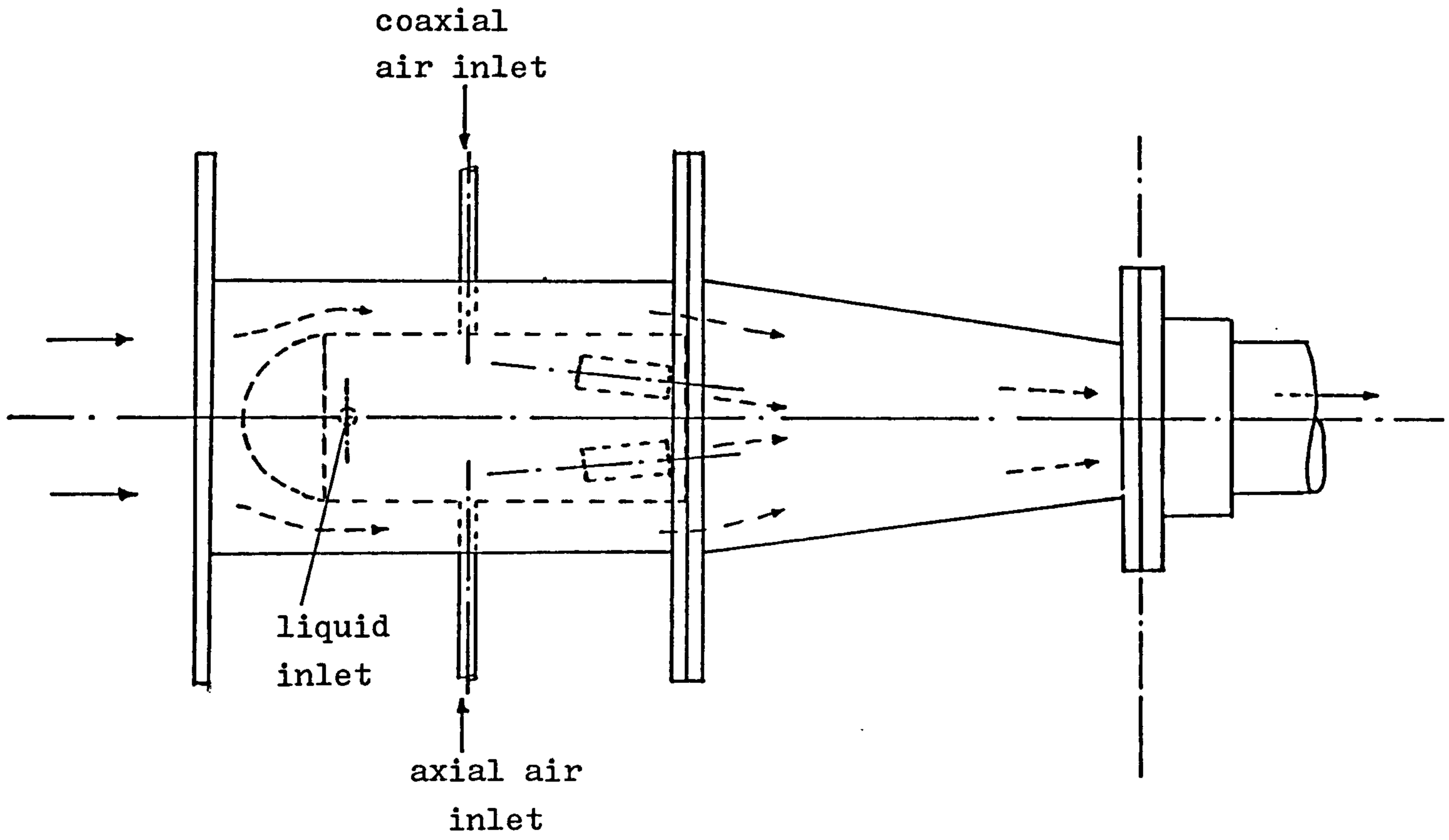


FIG. 7.15: Illustration of atomiser assembly in mixing chamber.

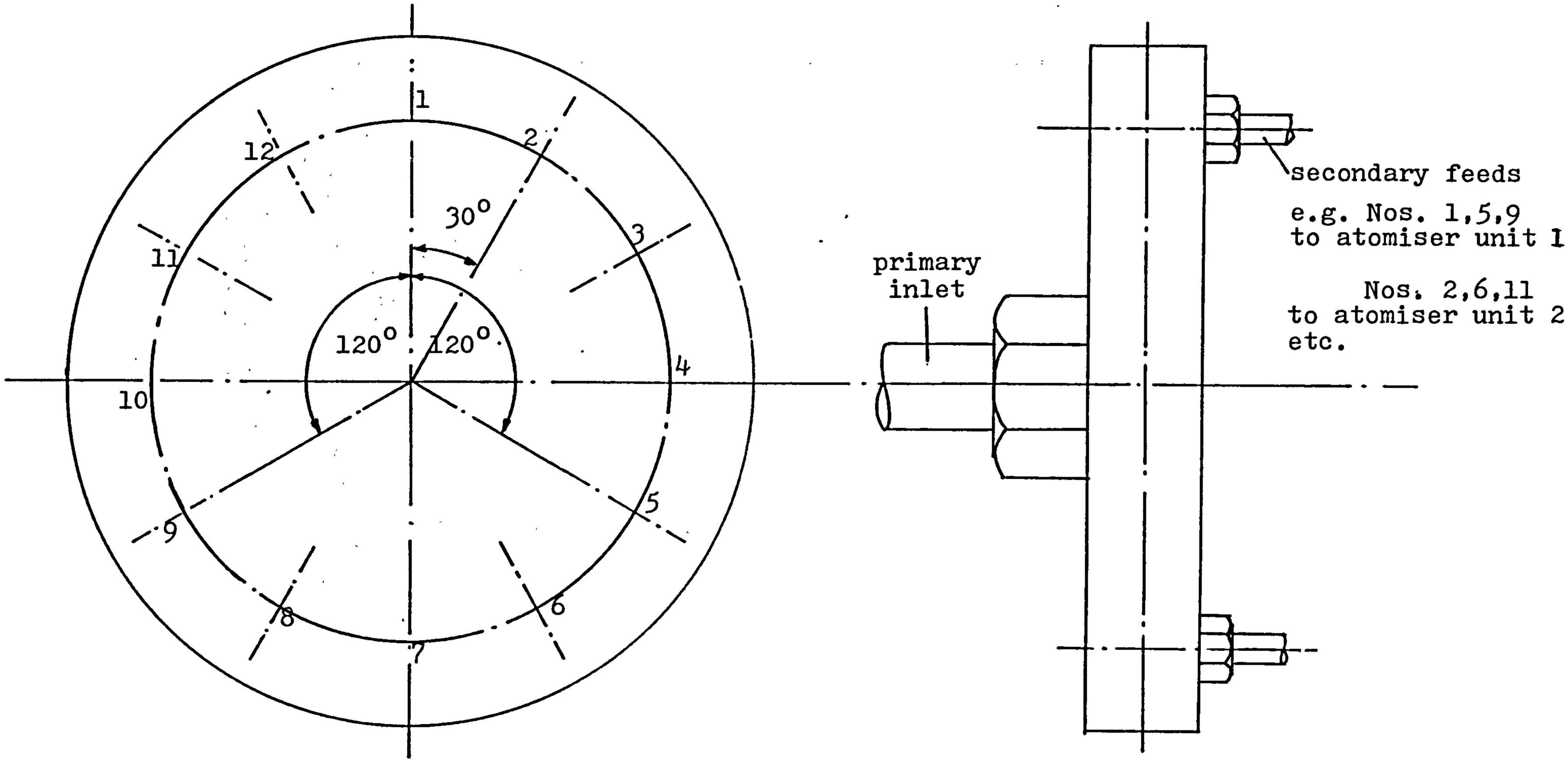


FIG. 7.16: Illustration of water redistribution chamber.

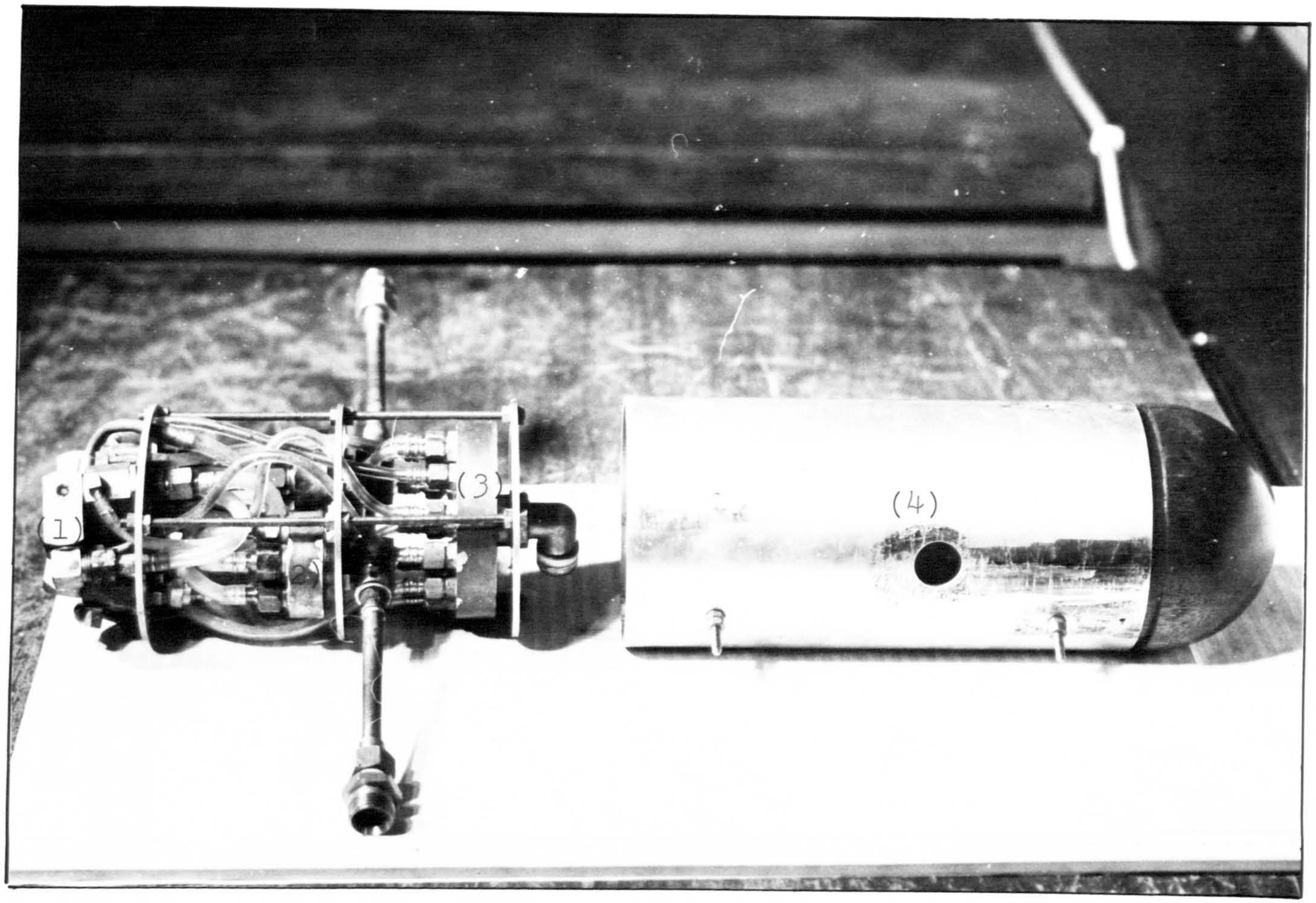


FIG. 7.17 Illustration of atomiser assembly (uncovered). Numbers referred to are:- (1) air-blast atomisers; (2) air re-distribution chambers; (3) water redistribution chamber and (4) outer casing.

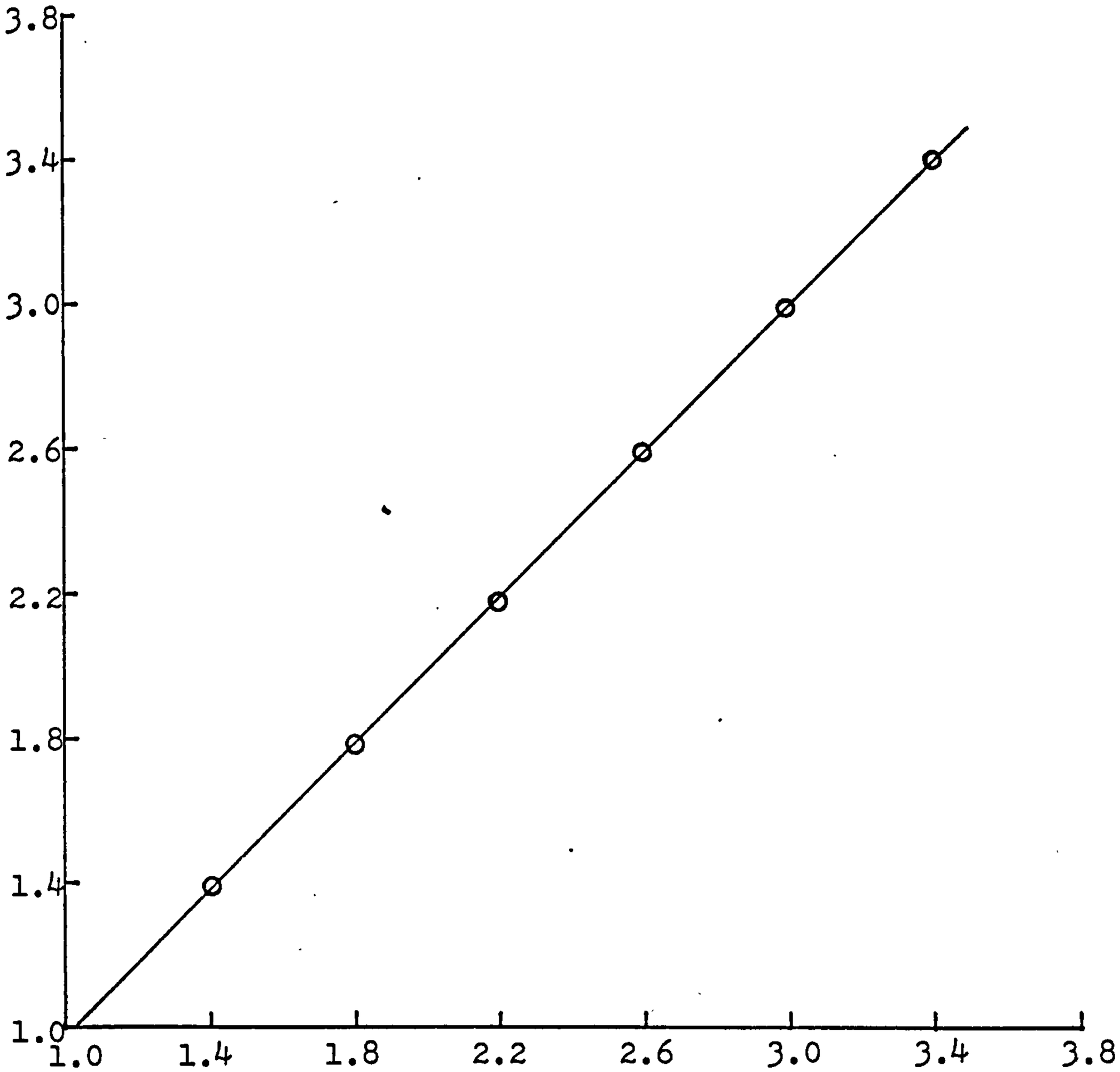
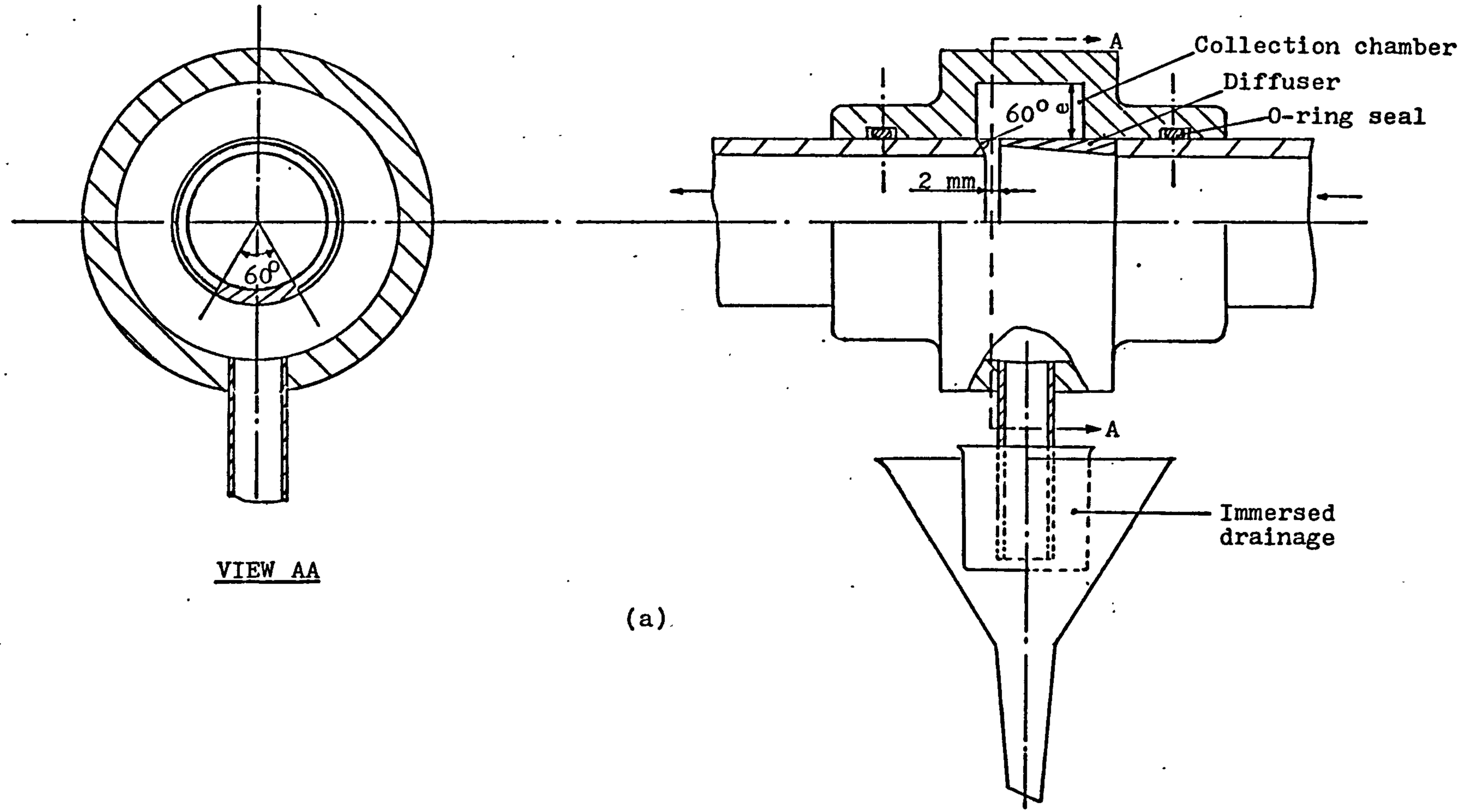
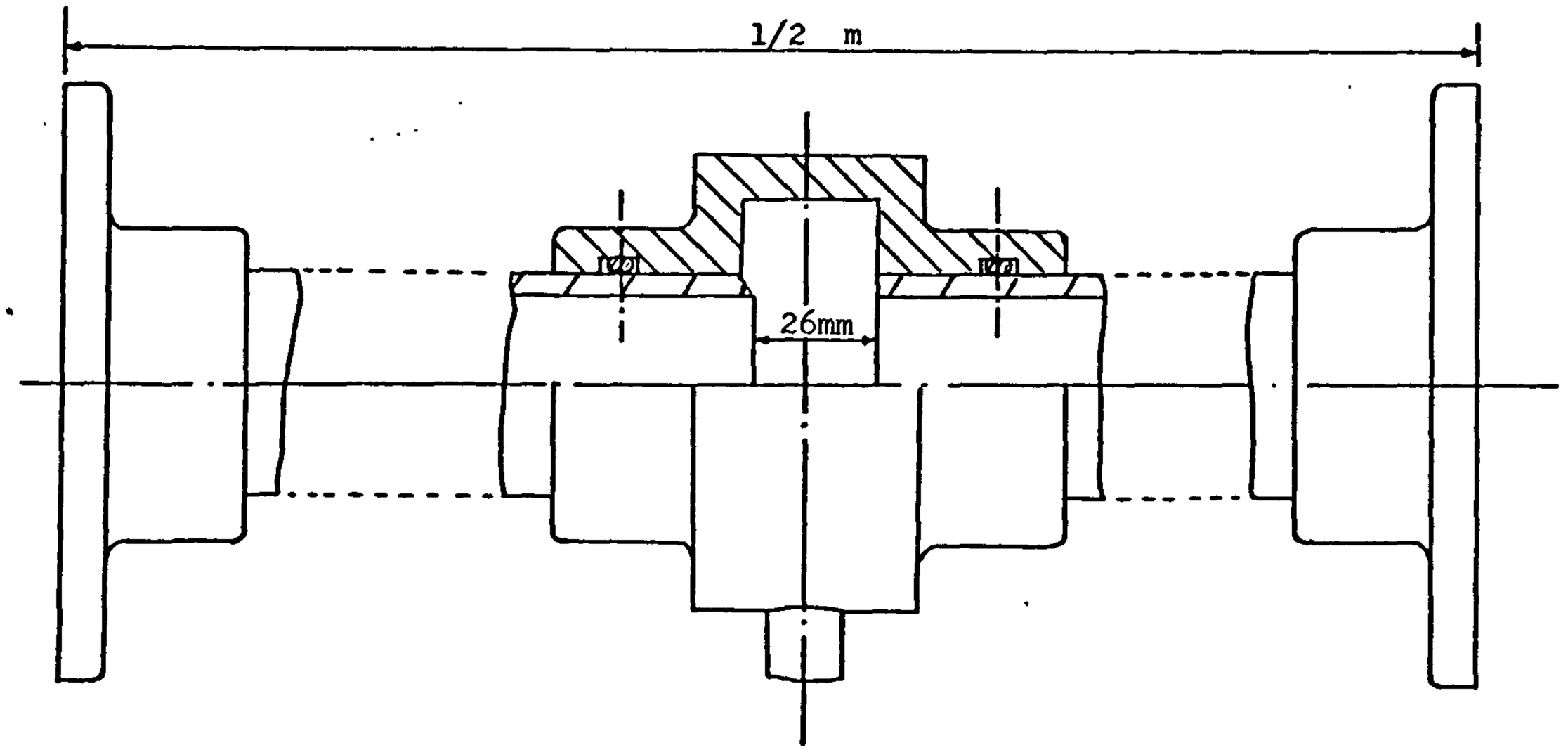


FIG. 7.18 Relationship between measured volumetric flow rate and rotameter reading for the 5 l/min maximum scale unit.



(a)

FIG. 7.19 Illustration of liquid extraction unit.



(b)

FIG. 7.19 (contd.)

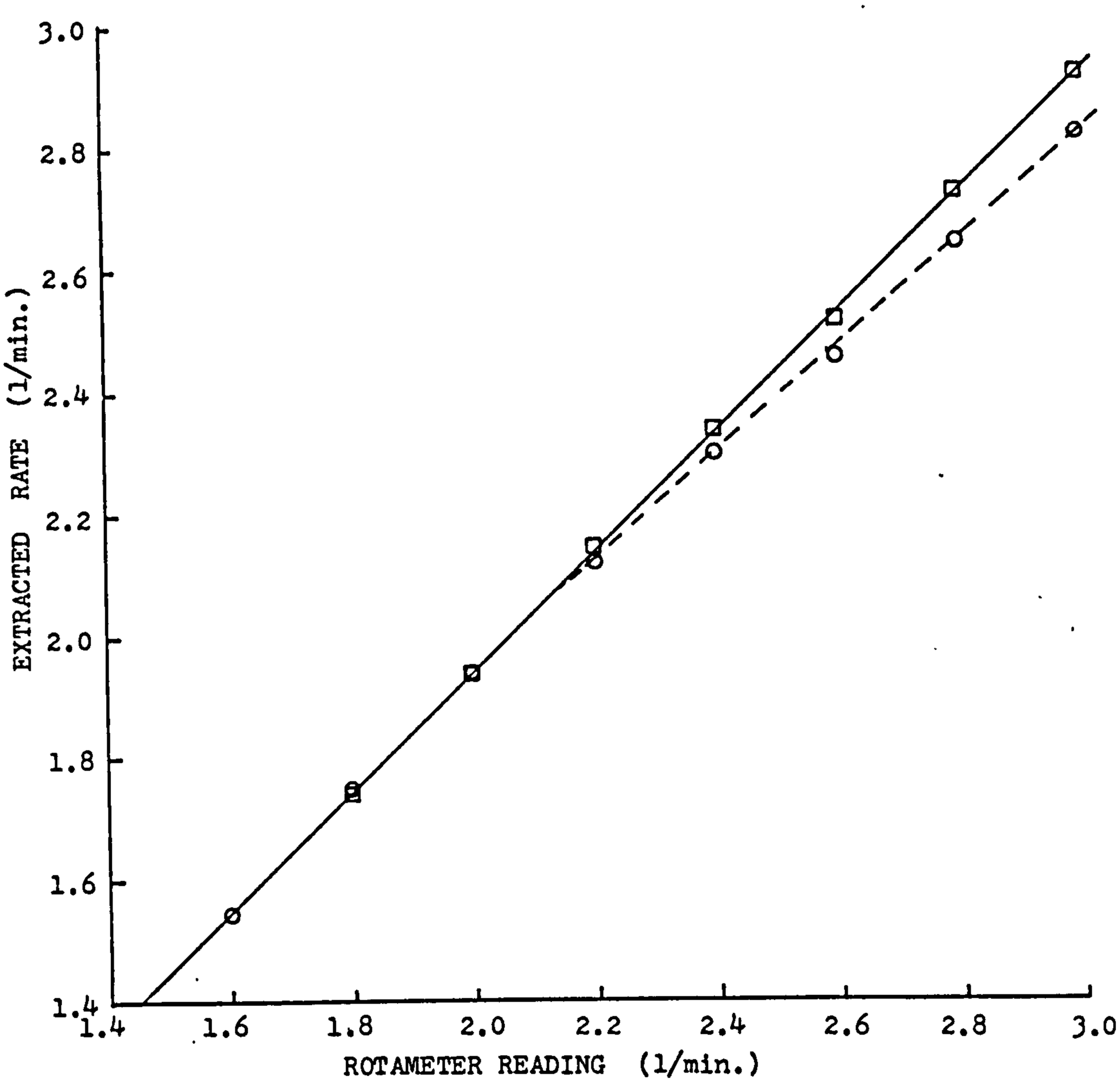


FIG. 7.20 Relationship between extracted and injected liquid rates. Symbols referred to are:-

○ : with immersion extraction;

□ : without immersion extraction.

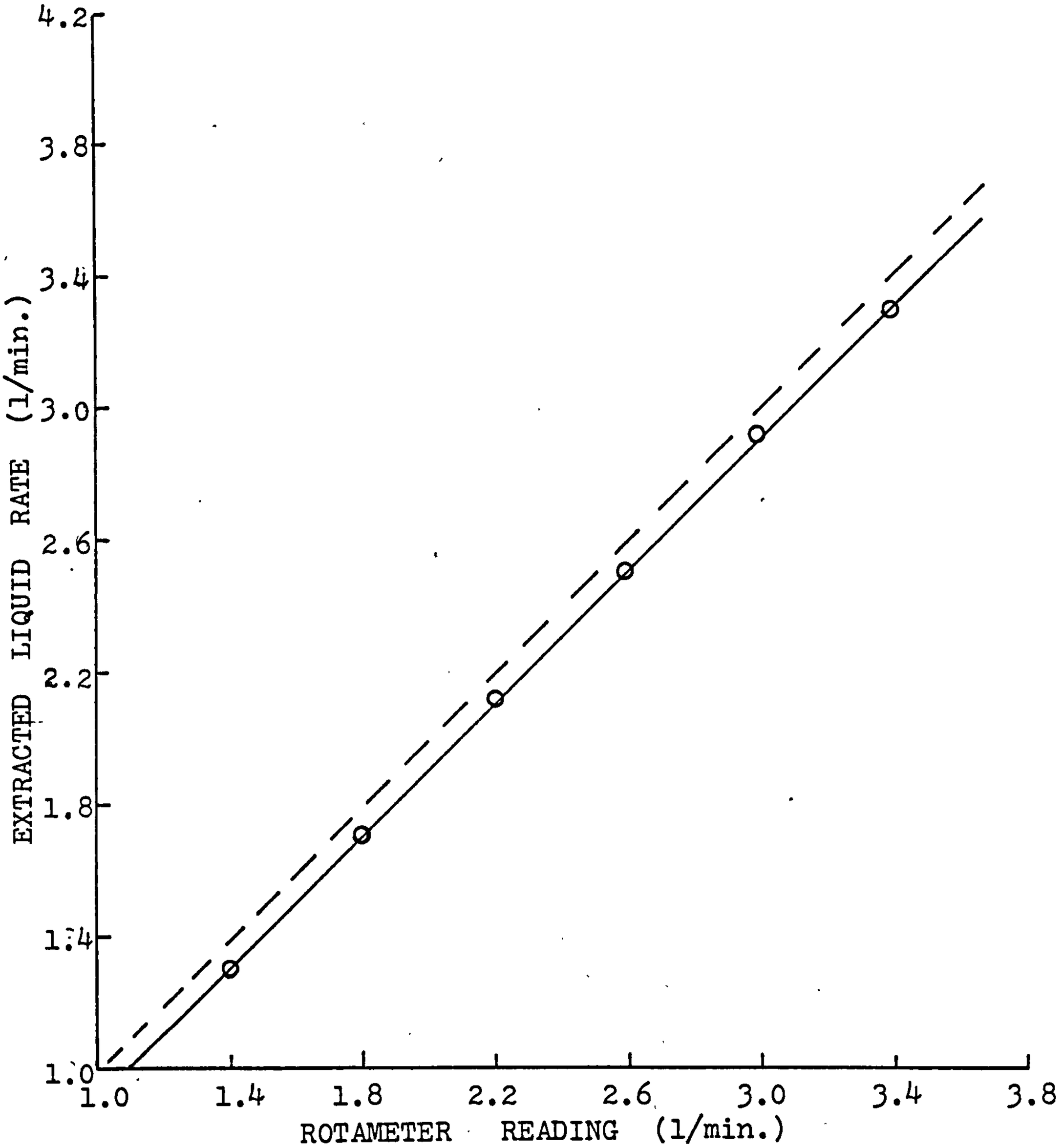


FIG. 7.21 Performance of extraction unit with enlarged collection chamber and immersion arrangement.

--- --: Zero entrainment line.

o : Current measurements.

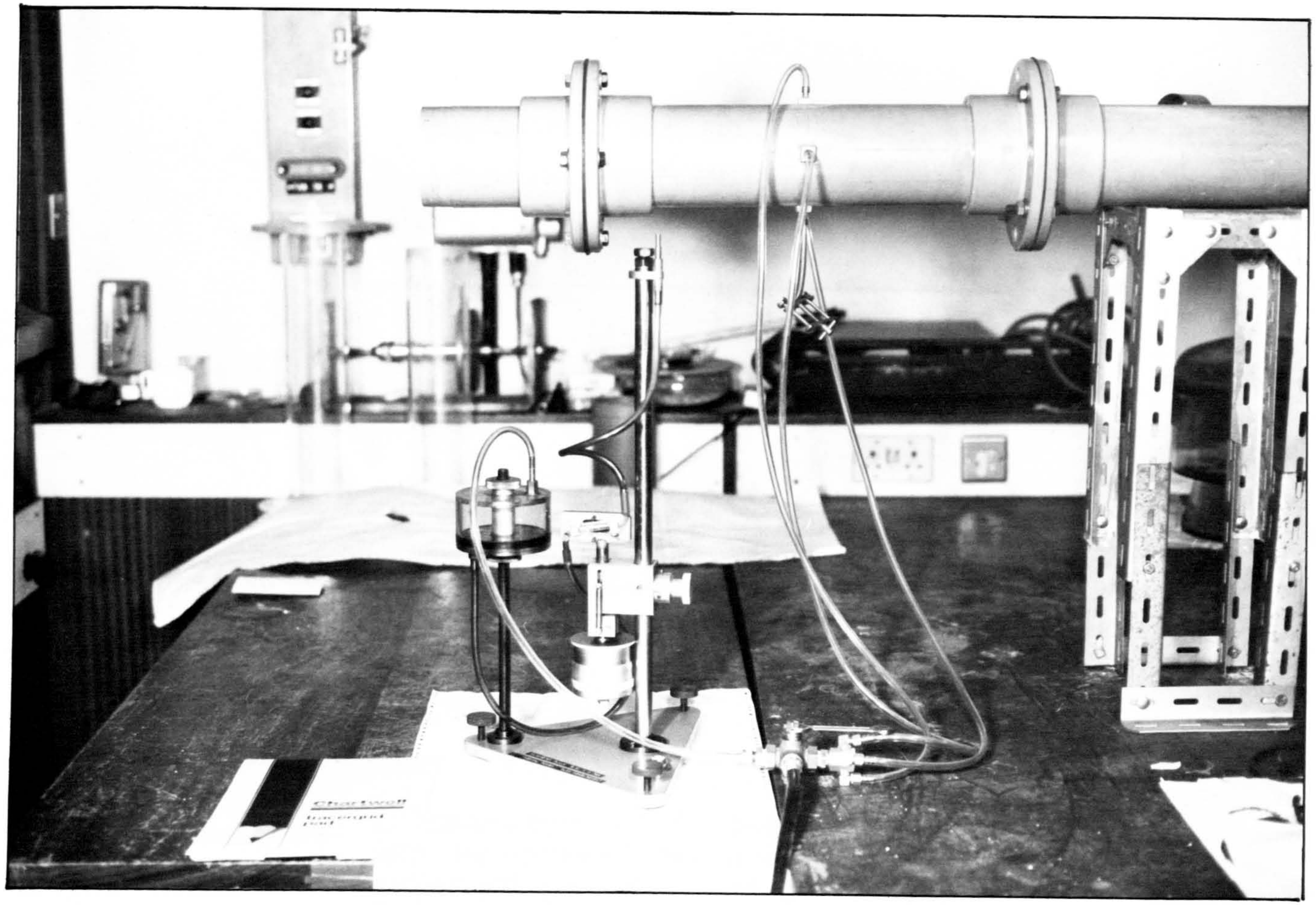


FIG. 7.22 Measurement of wall-static pressure.

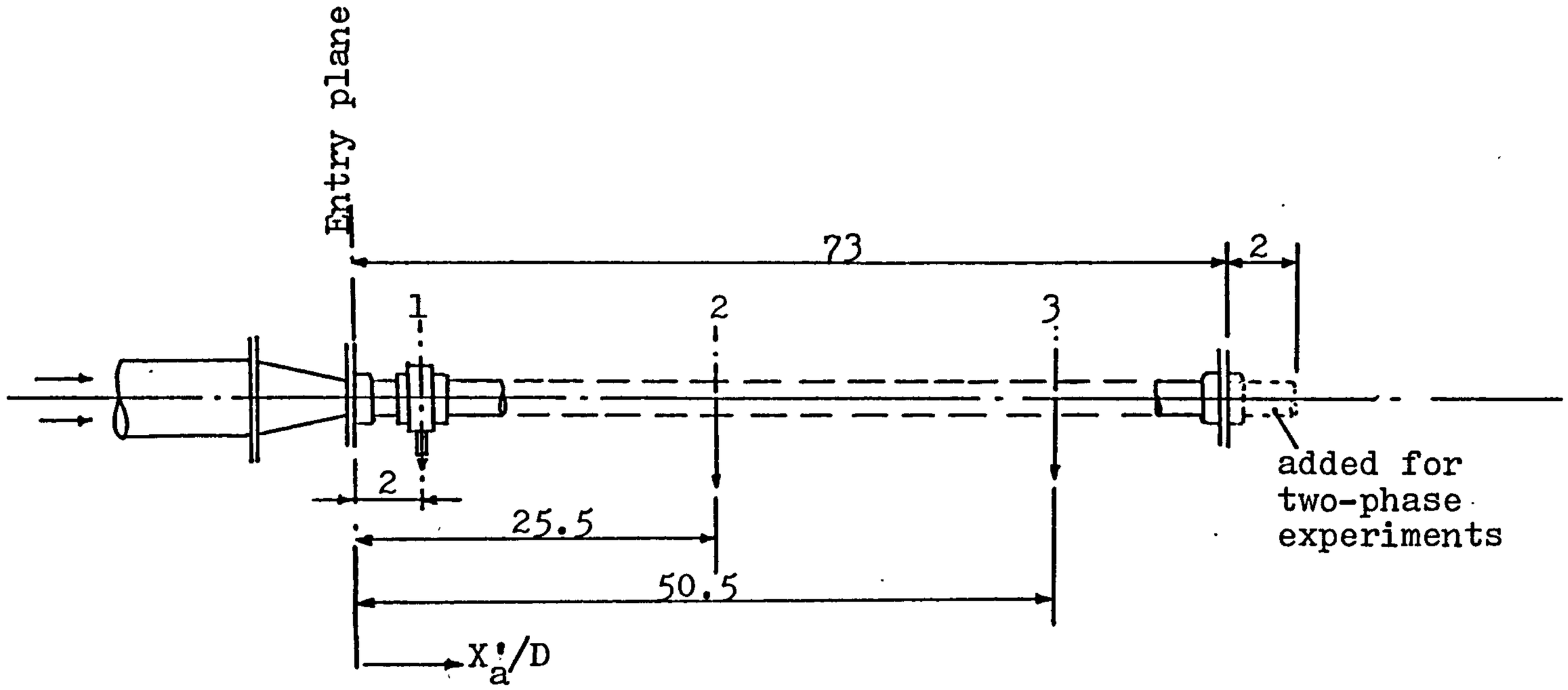


FIG. 7.23: Illustration of test-section geometry for single- and two-phase pressure drop measurements. Numbers referred to are axial locations of extraction units for two-phase flow measurements.

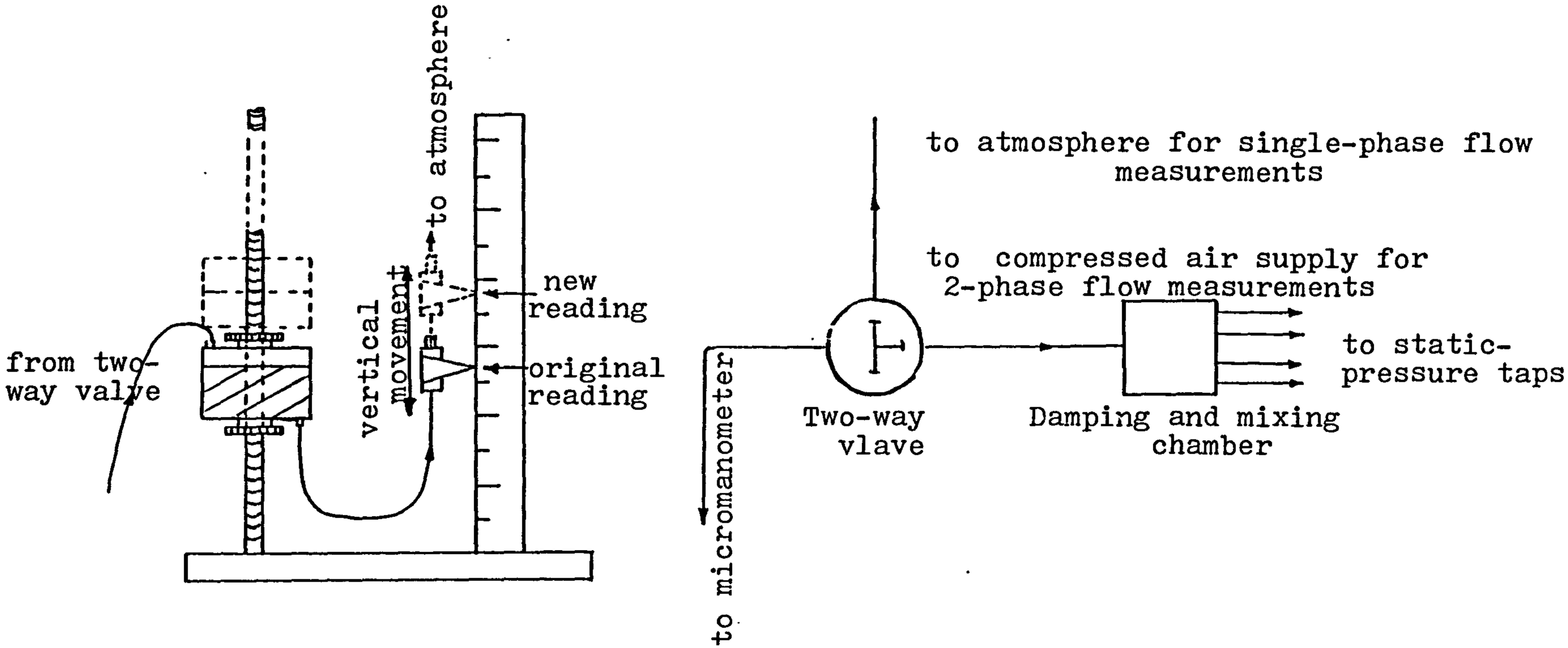


FIG. 7.24 Schematic of micromamometric pressure drop measurement system

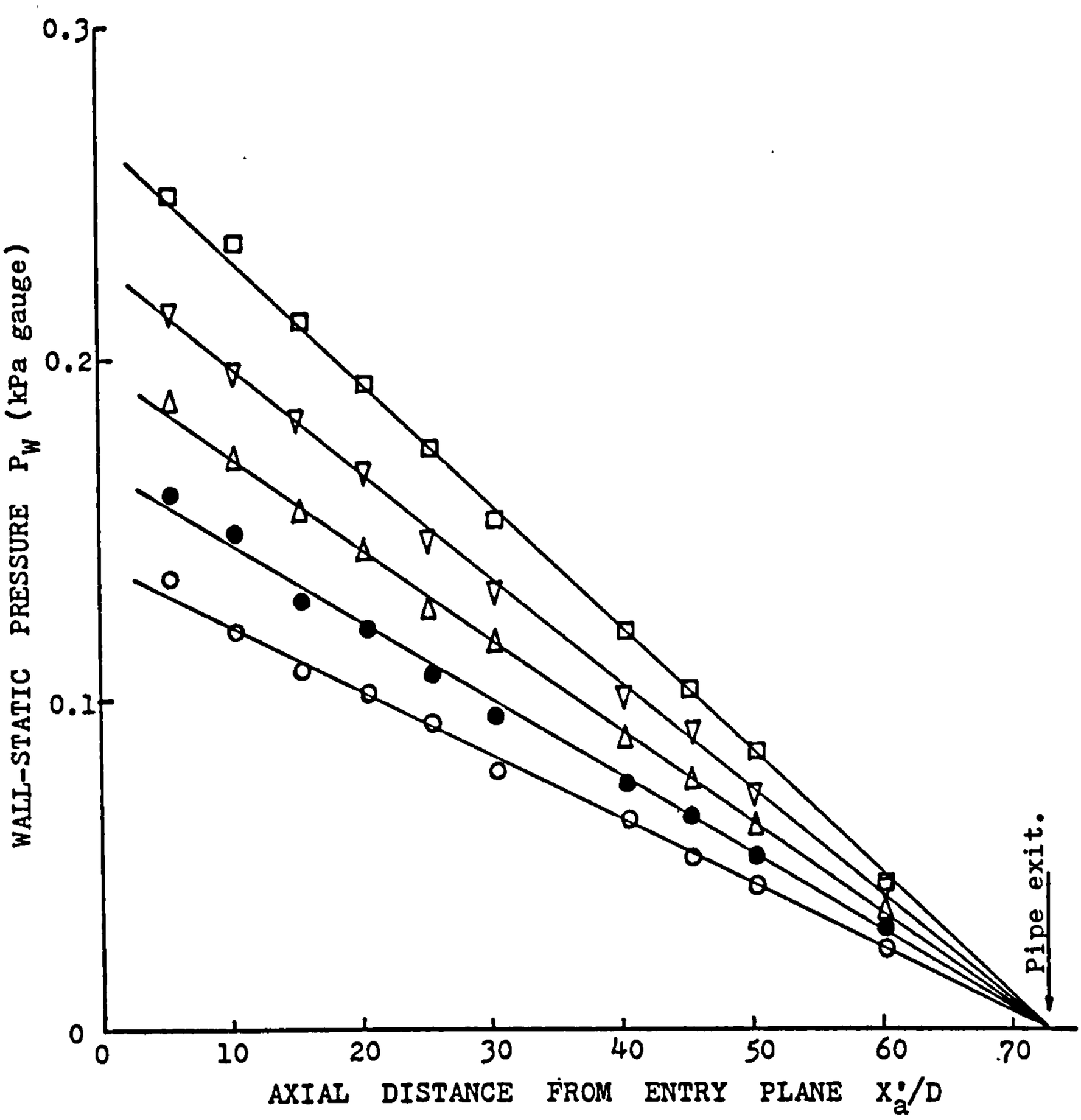


FIG. 7.25· Illustration of pressure drop with pipe length for single phase flow for Re_{D_4} from $8x10^4$: ○; $9x10^4$: ●; $10x10^4$: Δ; $11x10^4$: ∇ and $12x10^4$: □.

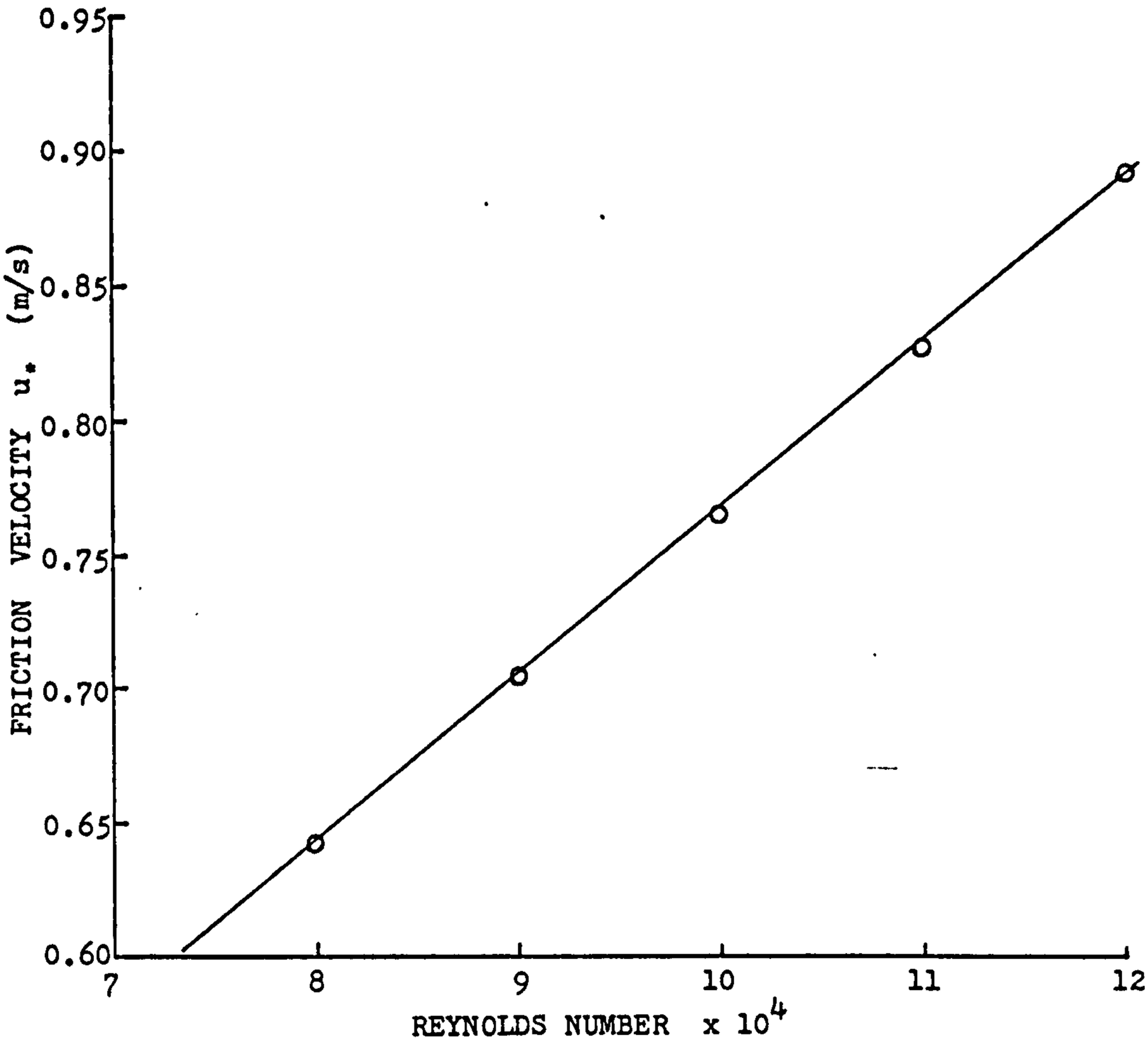


FIG. 7.26 Relationship between friction velocity and Re_D for single-phase (air only) flow.

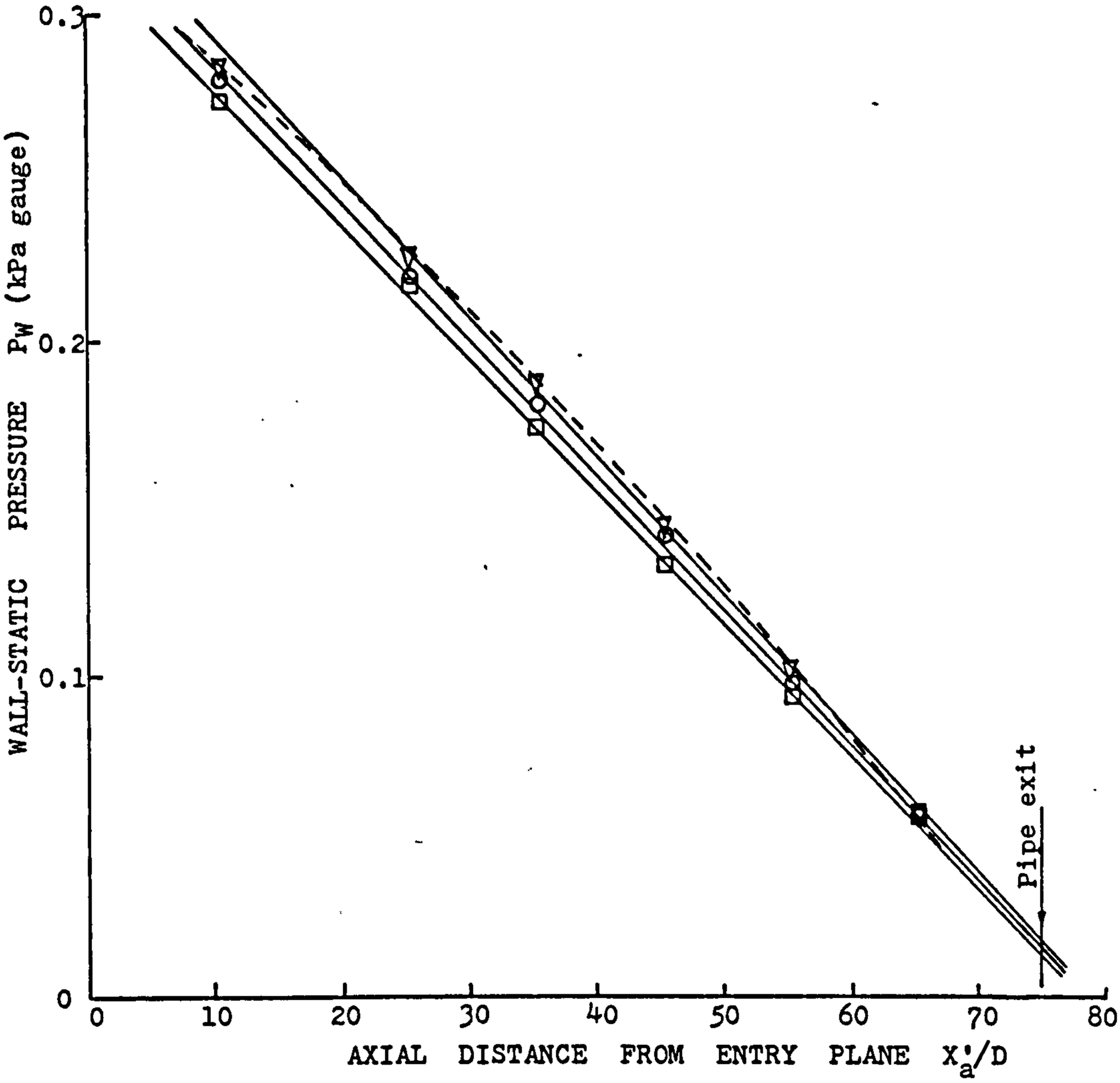


FIG. 7.27 Illustration of pressure drop with pipe length for two-phase flow for test conditions A: □ ; C: ○ and T: ▽ at Reynolds number of 10^5.

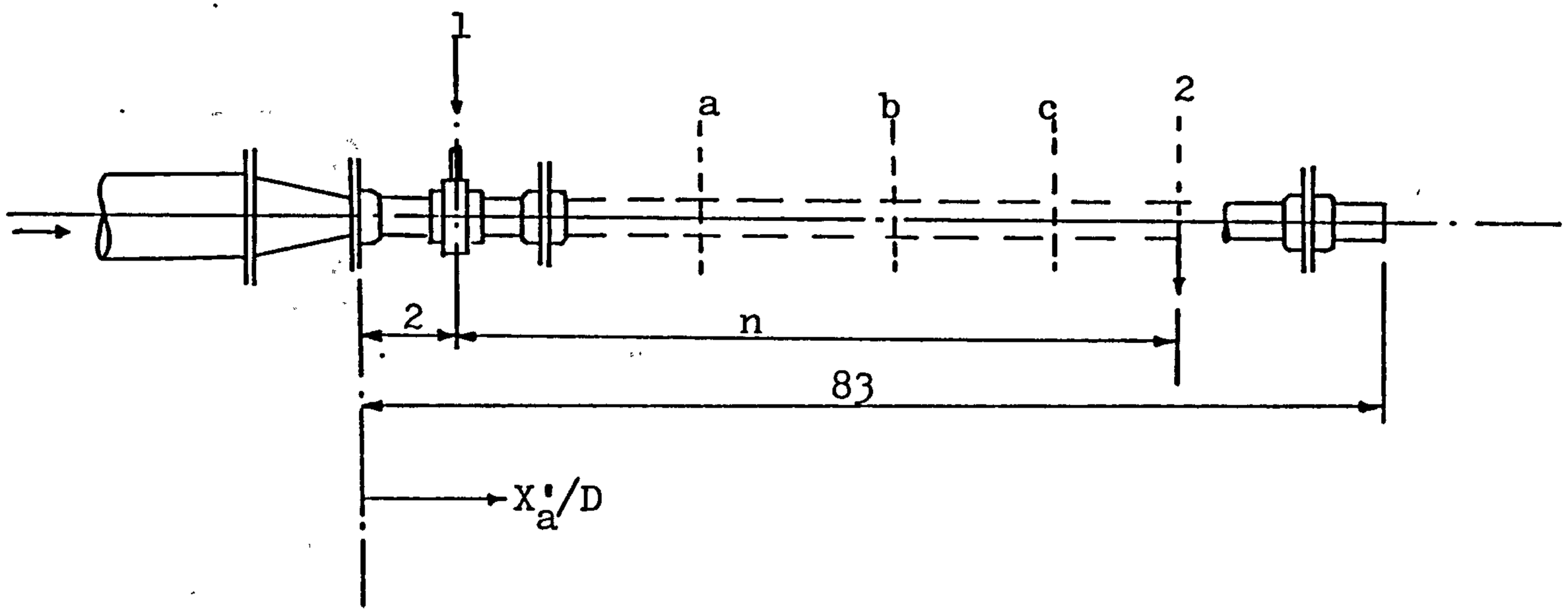


FIG. 8.1: Illustration of test length for entrainment studies. Numbers and letters referred to are 1:- injection unit; 2:- extraction unit; a, b, c:- static pressure tappings and n equal to one of the following values: 15, 25, 45 and 65.

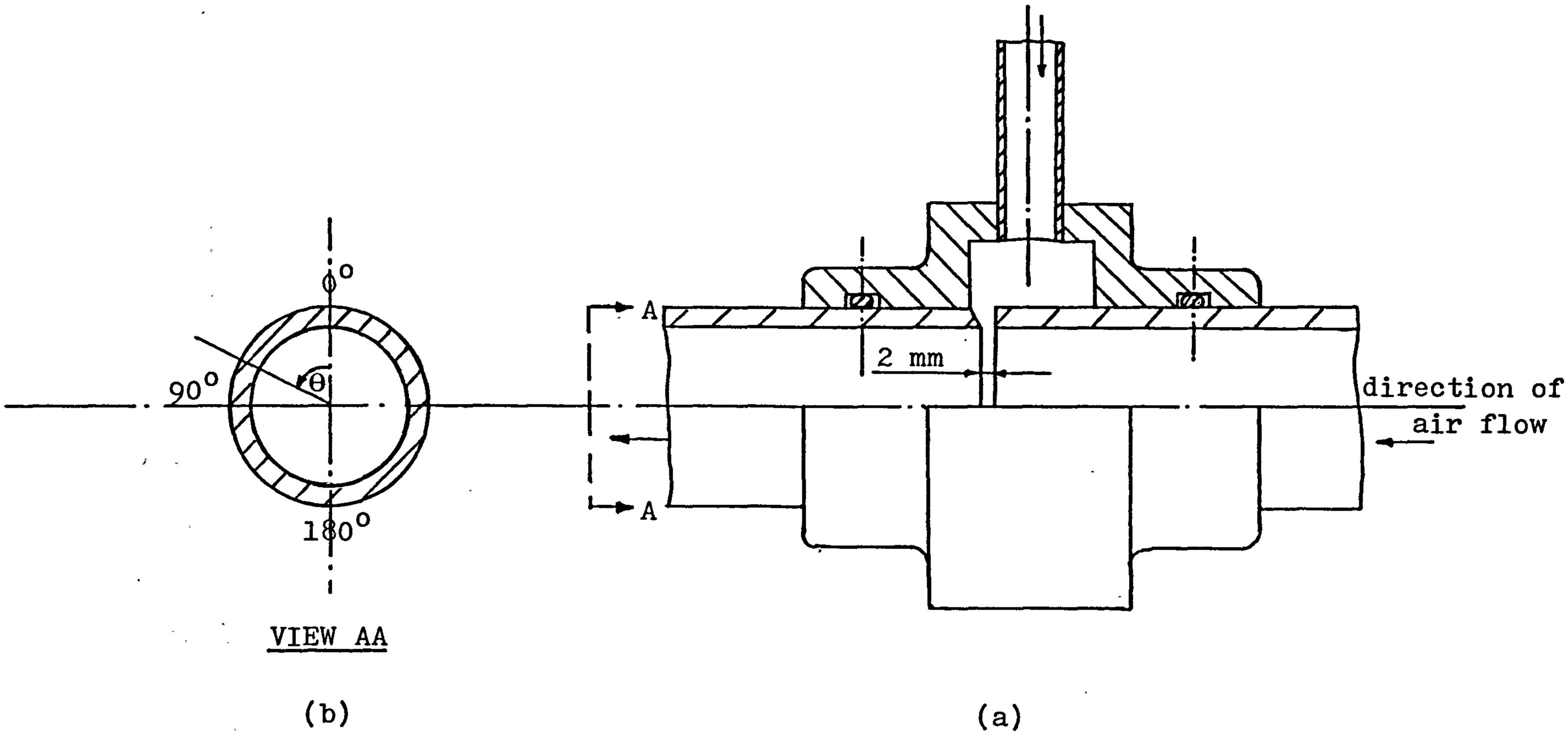


FIG 8.2 Illustration of wall injection unit.

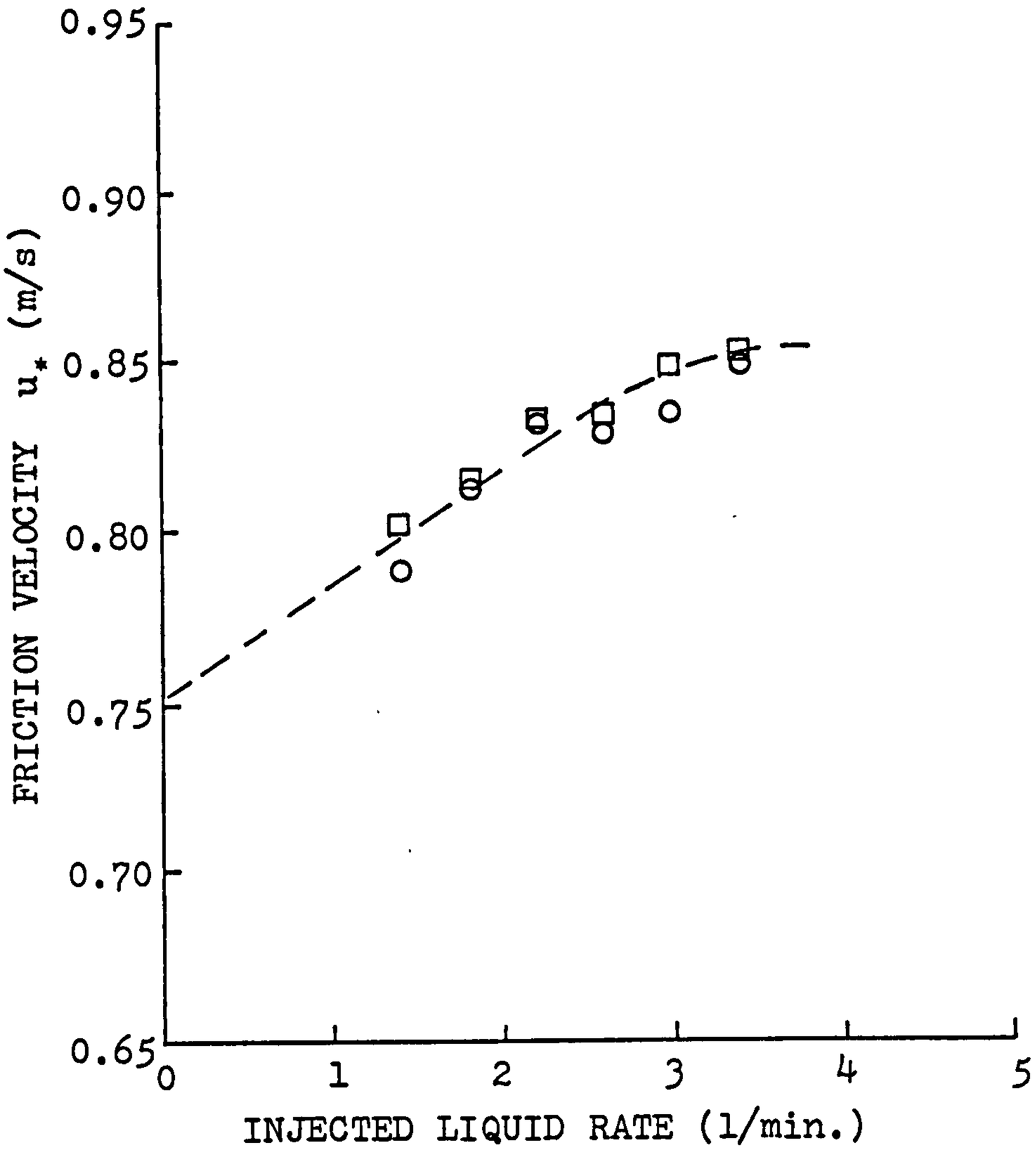


FIG. 8.3 Relationship between friction velocity, u_* and injected liquid rate for test conditions T81 to T86 (O) and T91 to T96 (□).

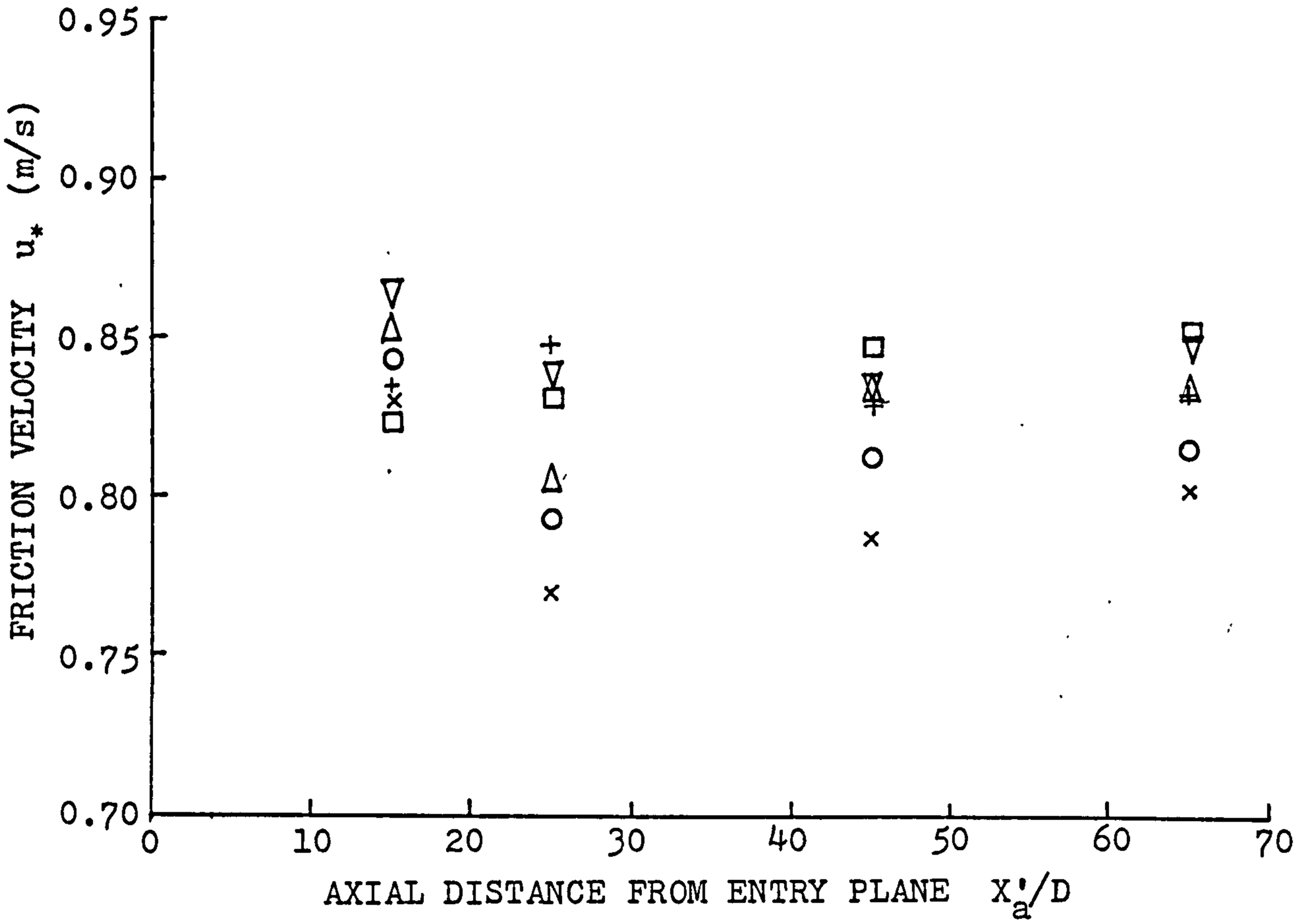


FIG. 8.4 Relationship between friction velocity and axial position of extraction unit relative injection slot for liquid flow rates of 1.4 l/min (X), 1.8 l/min (O), 2.2 l/min (Δ), 2.6 l/min (+), 3.0 l/min (∇) and 3.4 l/min (□).

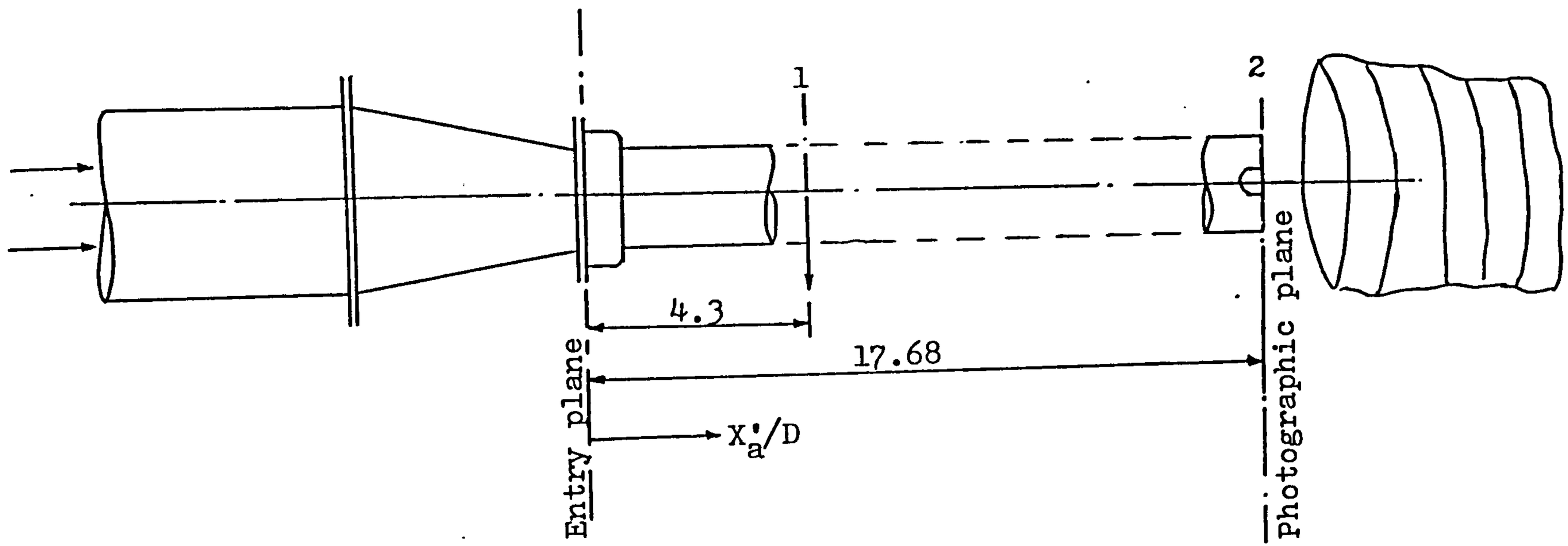


FIG. 8.5: Test section geometry for photographic study of re-entrainment effects.

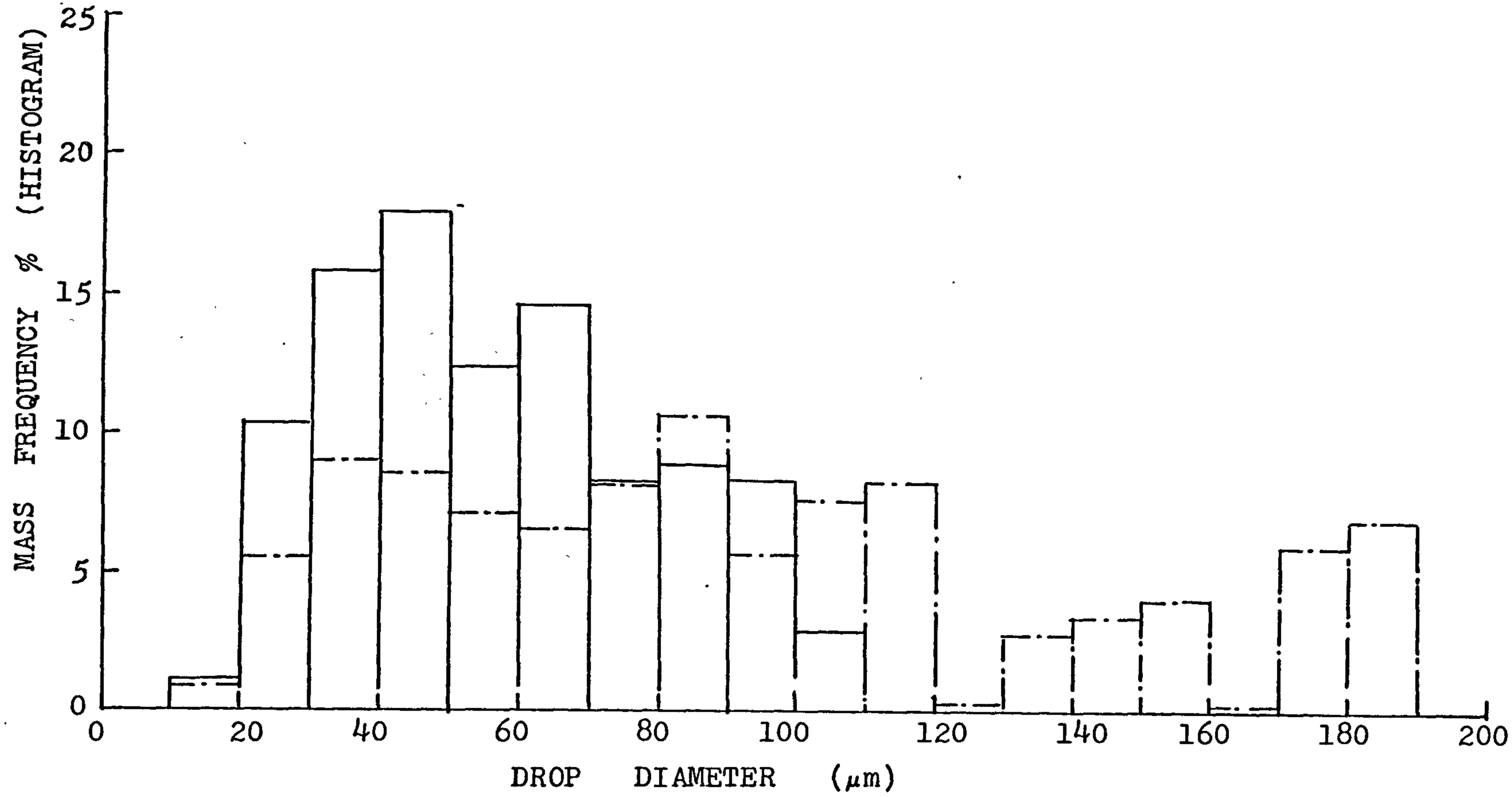


FIG. 8.6 Mass frequency distribution at station 2 for condition A.

——— : with upstream extraction.

—·—·— : without upstream extraction.

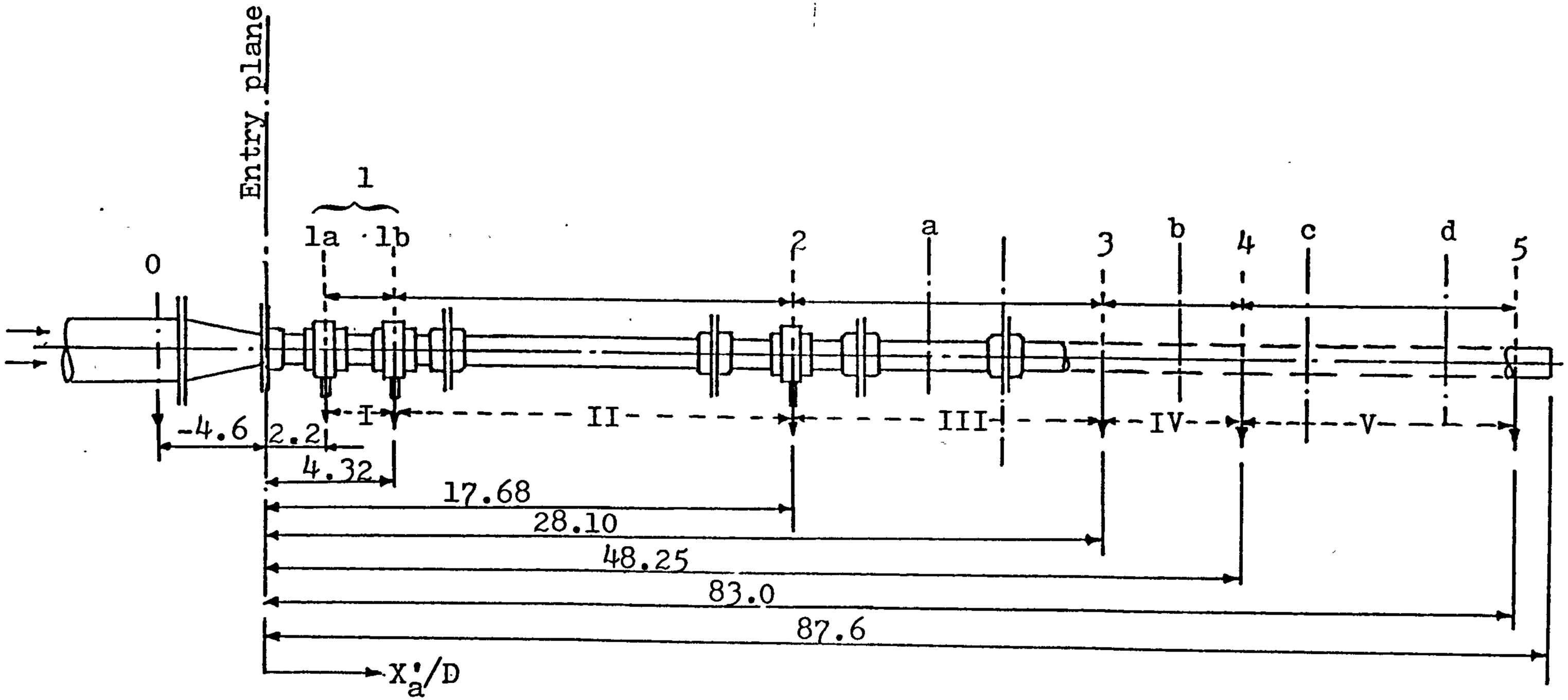
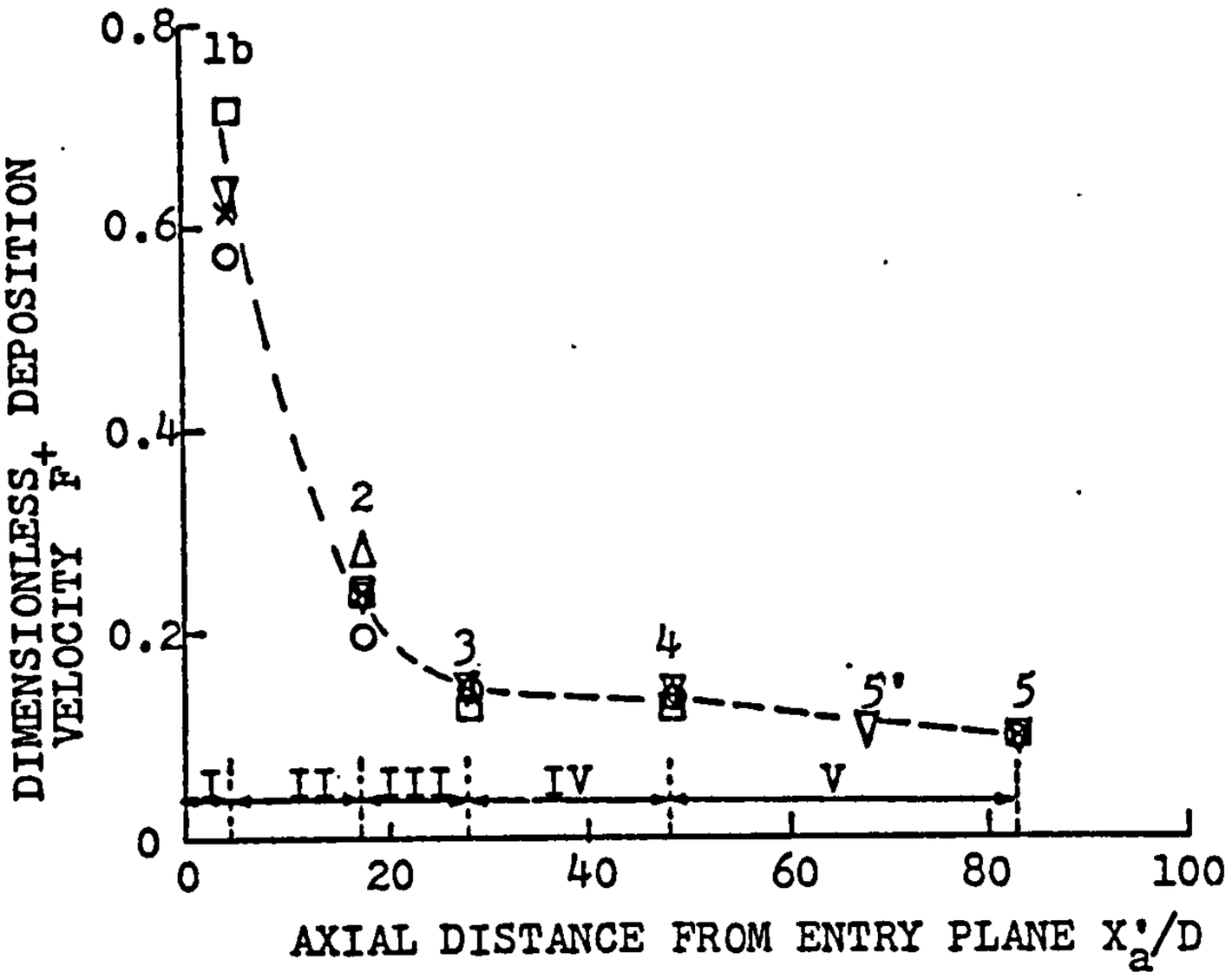
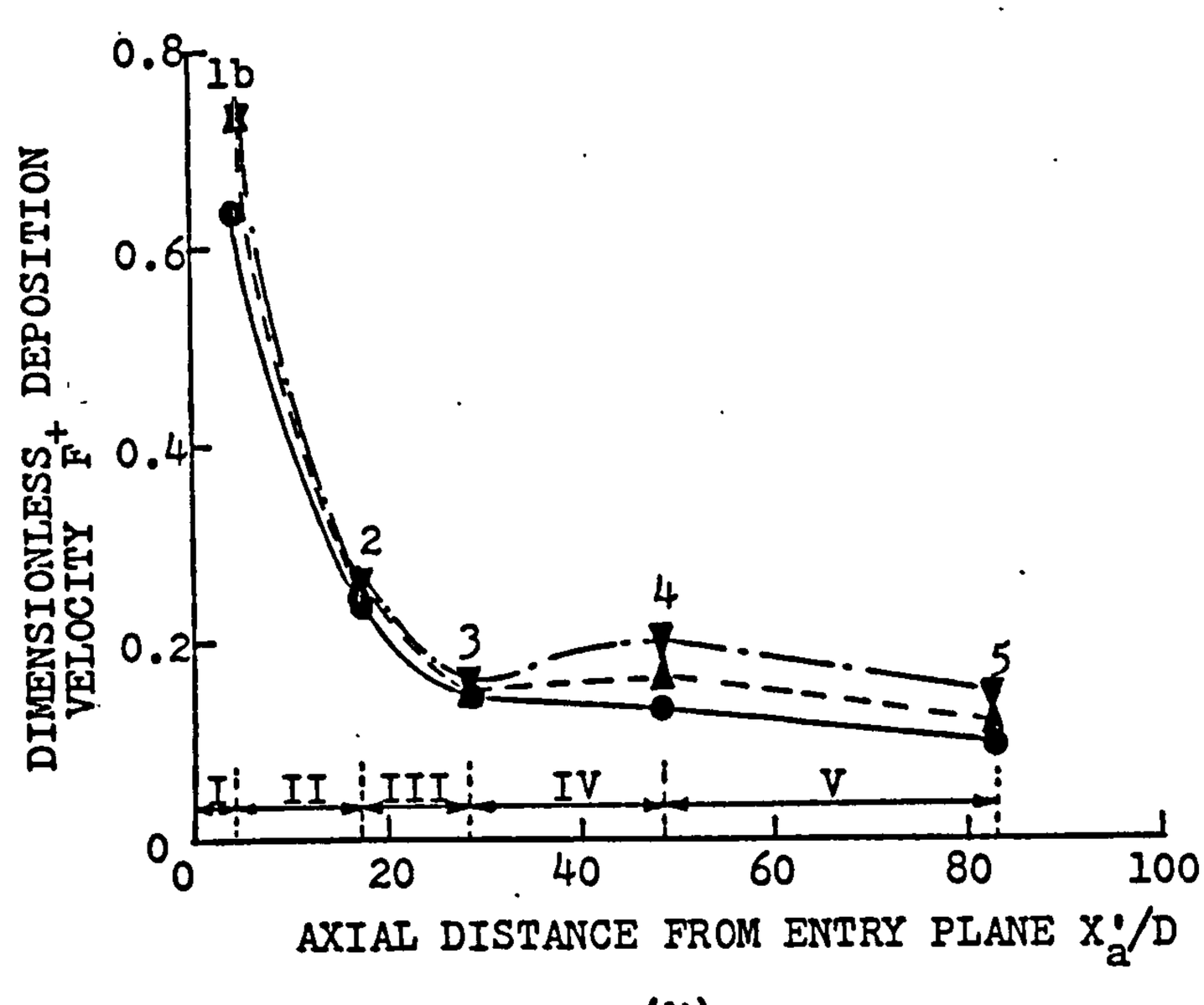


FIG. 8.7: Test section geometry for agglomeration and deposition studies. Numbers and letters referred to are: a, b, c, d:- pressure tappings; I, II, III, IV and V:- deposition sections and 0, 1(or 1a, 1b), 2, 3, 4&5:- extraction stations.

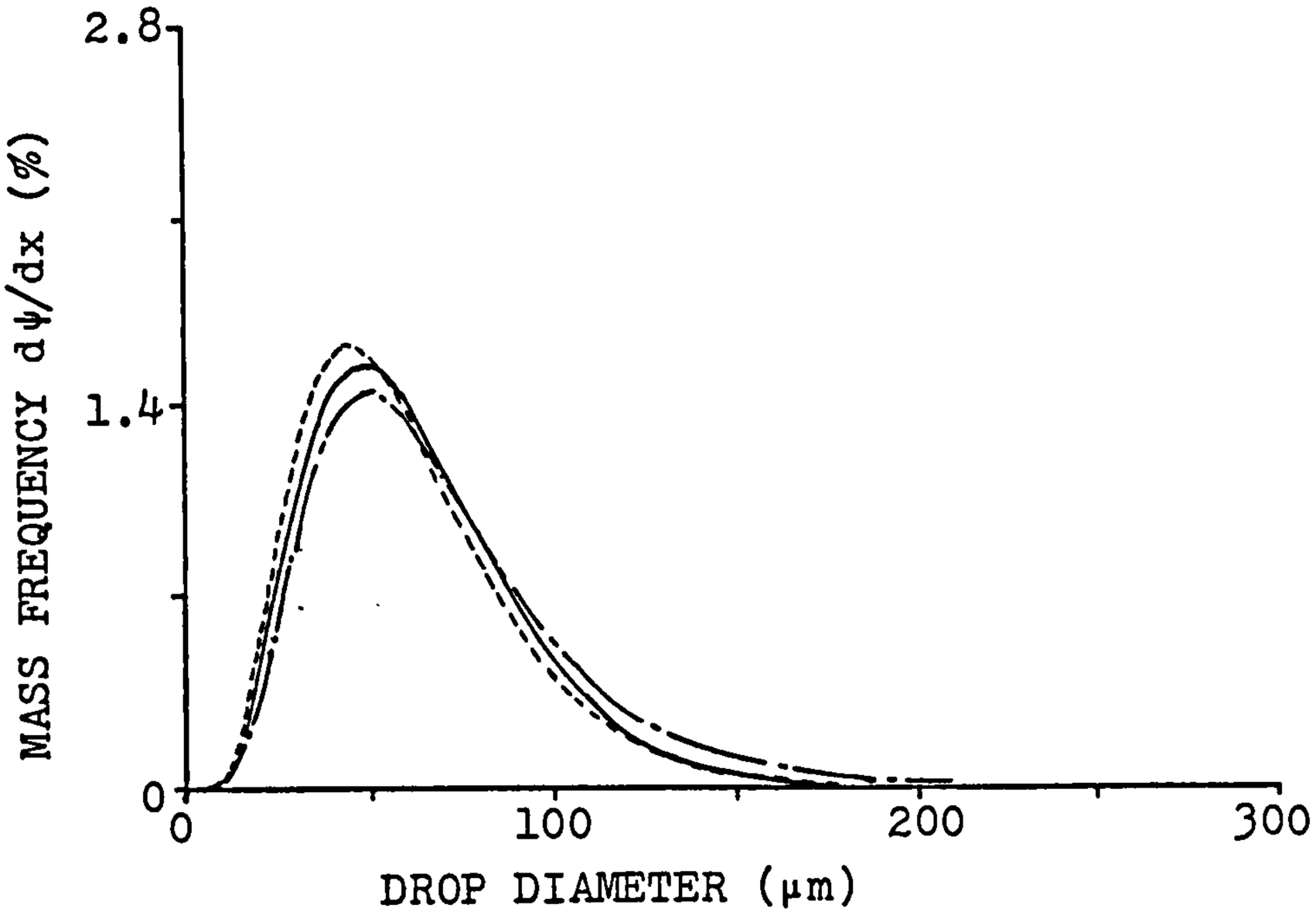


(a)

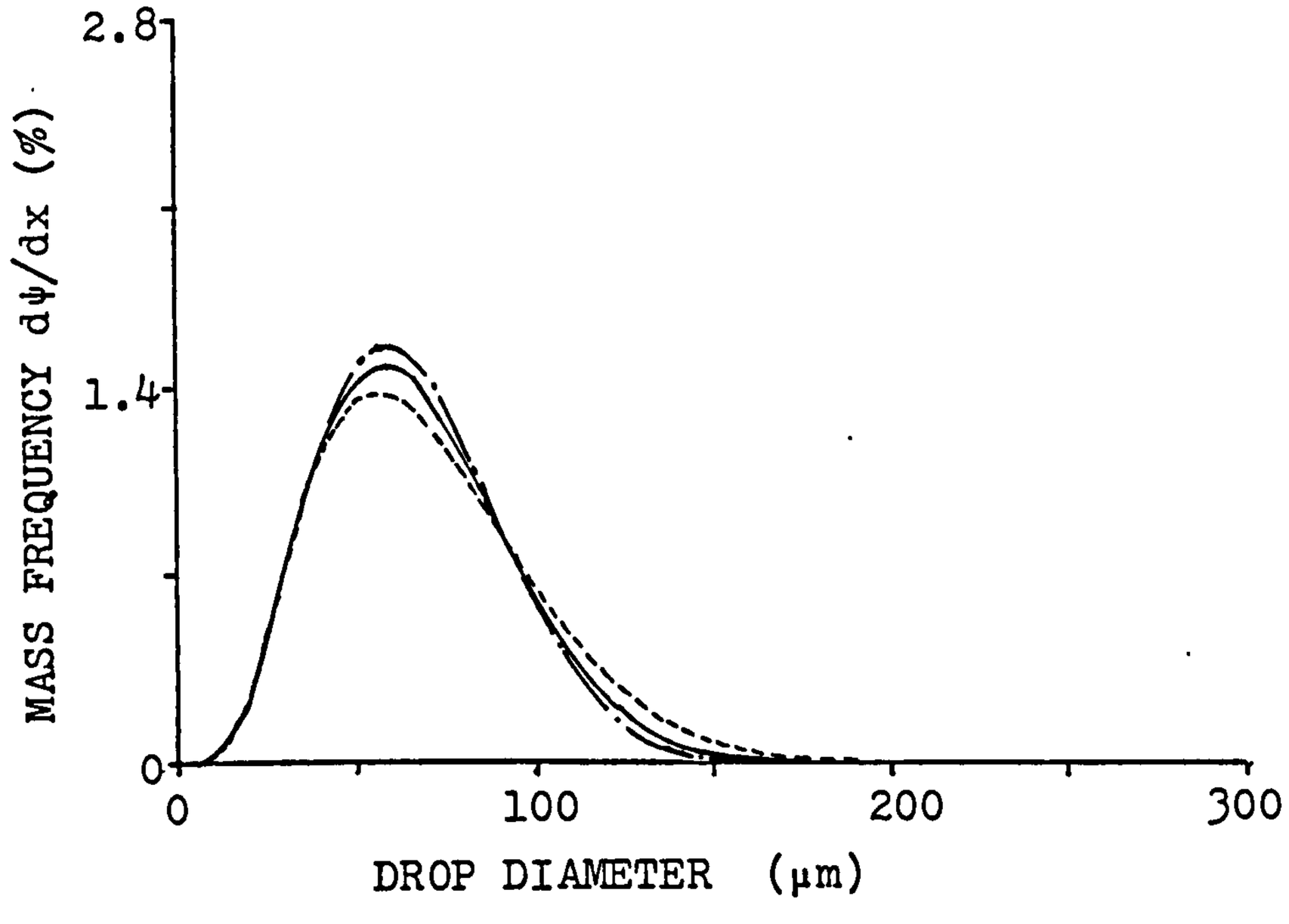


(b)

FIG. 8.8 Relationship between dimensionless deposition velocity and axial position of extraction stations (denoted by numbers) for data batches T11R: Δ; T13: □; T14: O; T18: ∇; T19: X and averaged values for test condition A: ●; B: ▲ and C: ▼ . I to V denote pipe sections.



(a)

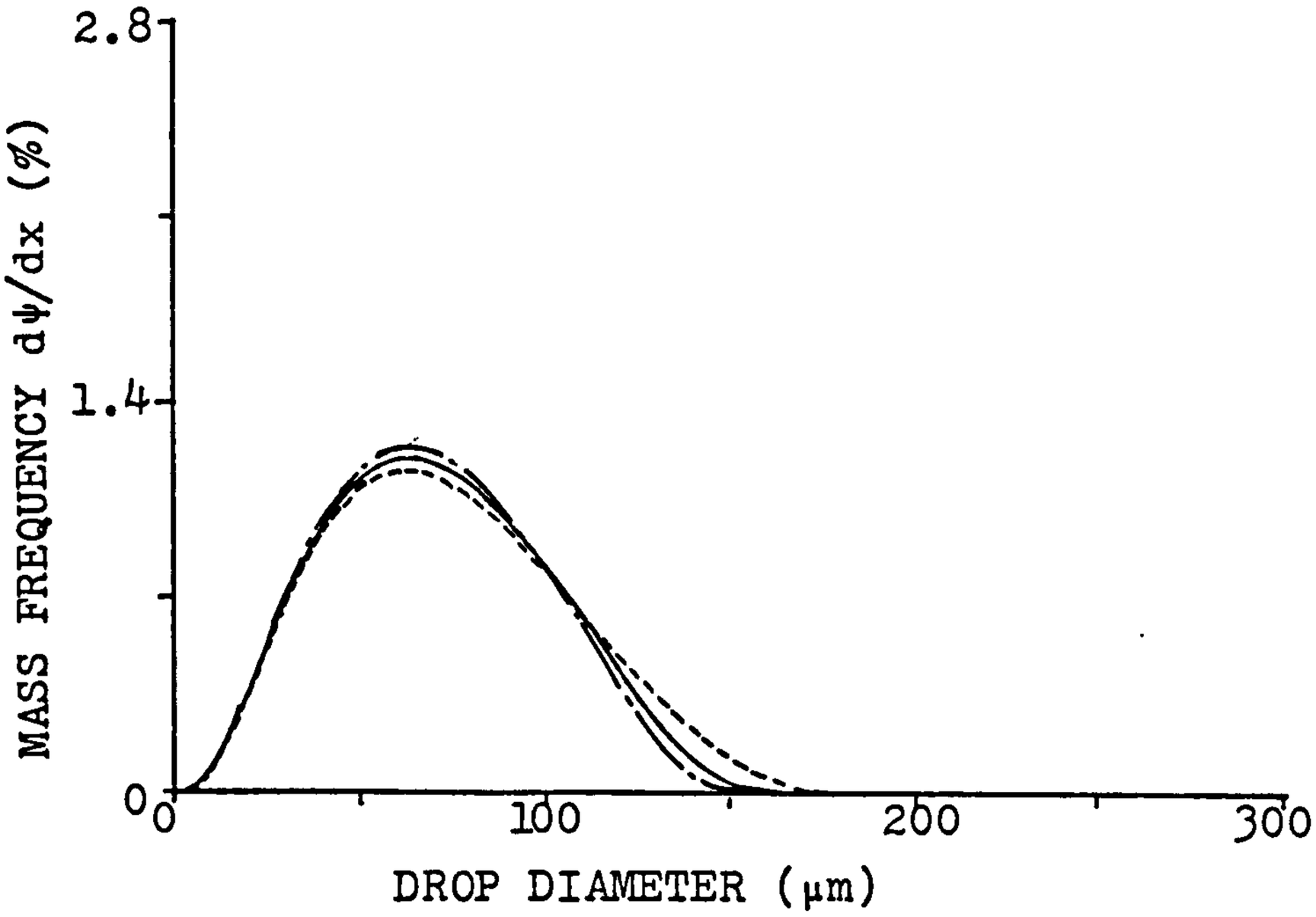


(b)

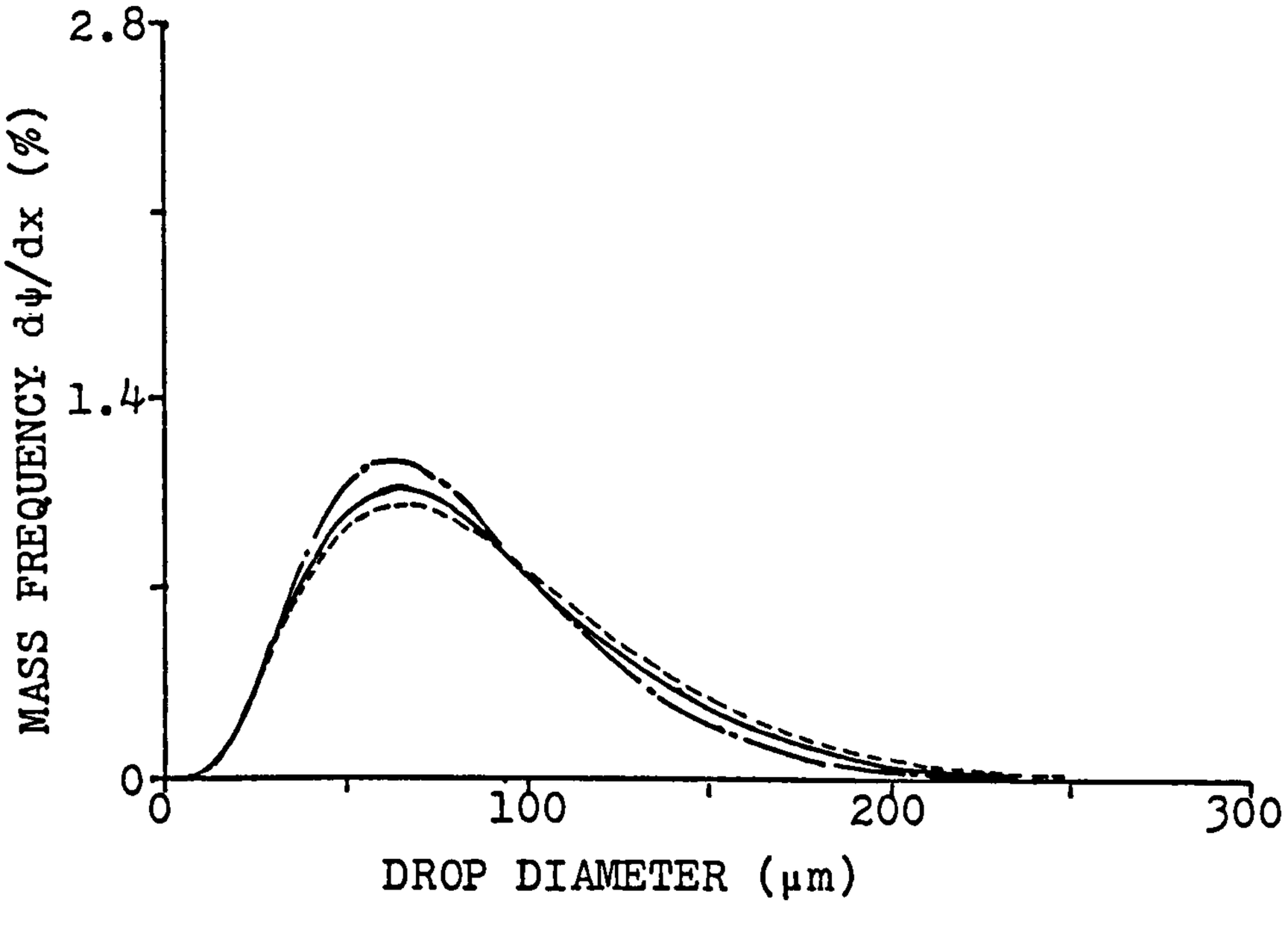
FIG. 8.9 Mass frequency distribution at station 2 at r/R = 0.04 for condition A: (a); A1: (b); B: (c) and C: (d). Lines represented are: - - - - -: first set of measurements

-·—·—: repeat

———: combined results.



(c)



(d)

FIG. 8.9 (contd.)

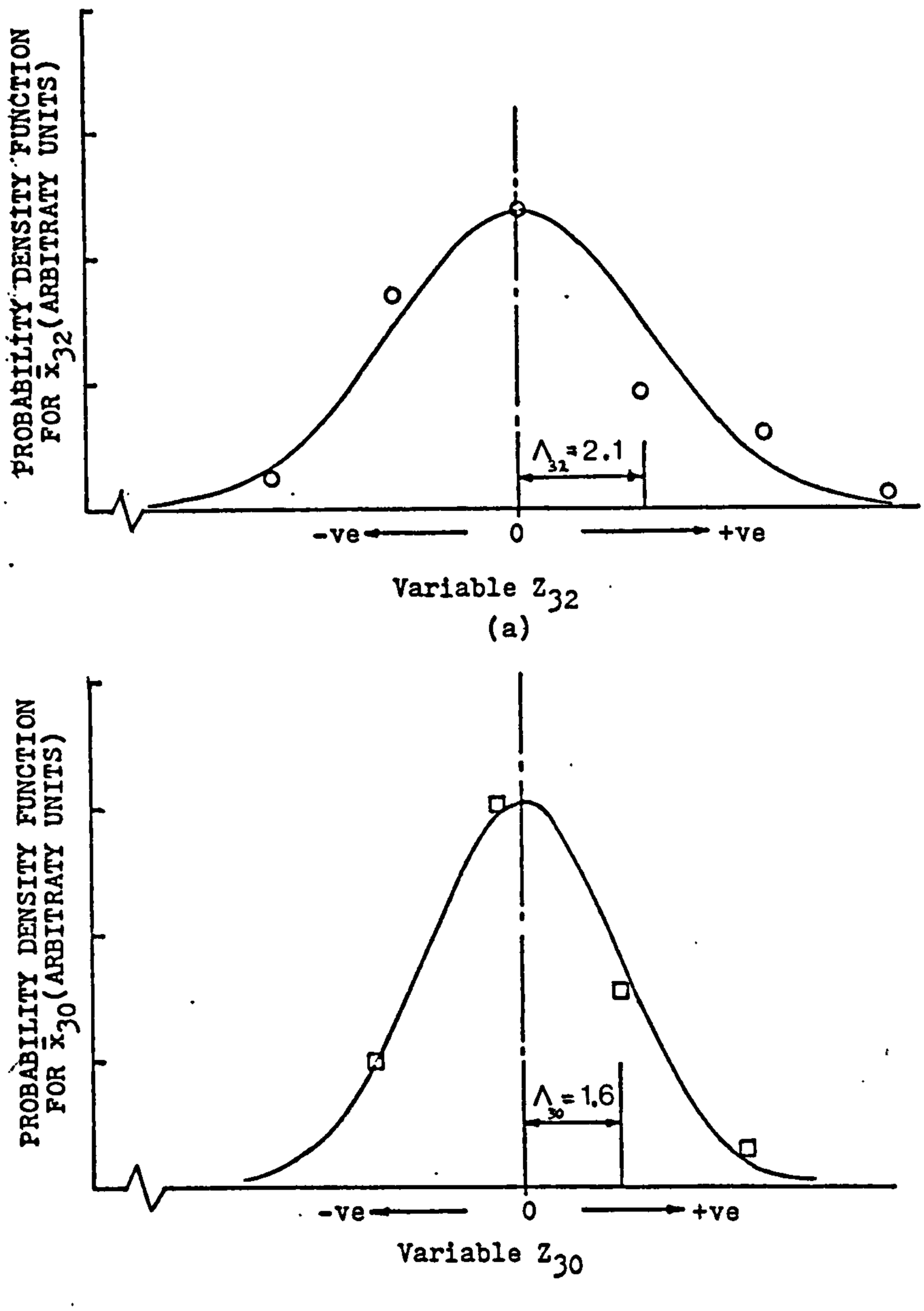


FIG. 8.10: Empirical distribution of Sauter mean, ${}_N\bar{x}_{32}$: , (a) and mass mean, ${}_N\bar{x}_{30}$: , (b) from 96 samples of average size N=5 plotted against standard normal variate Z_{32} or Z_{30} defined respectively as:-

$Z_{32}=({}_N\bar{x}_{32}-\omega_{32})\sqrt{N}/\Lambda_{32}$ and $Z_{30}=({}_N\bar{x}_{30}-\omega_{30})\sqrt{N}/\Lambda_{30}$

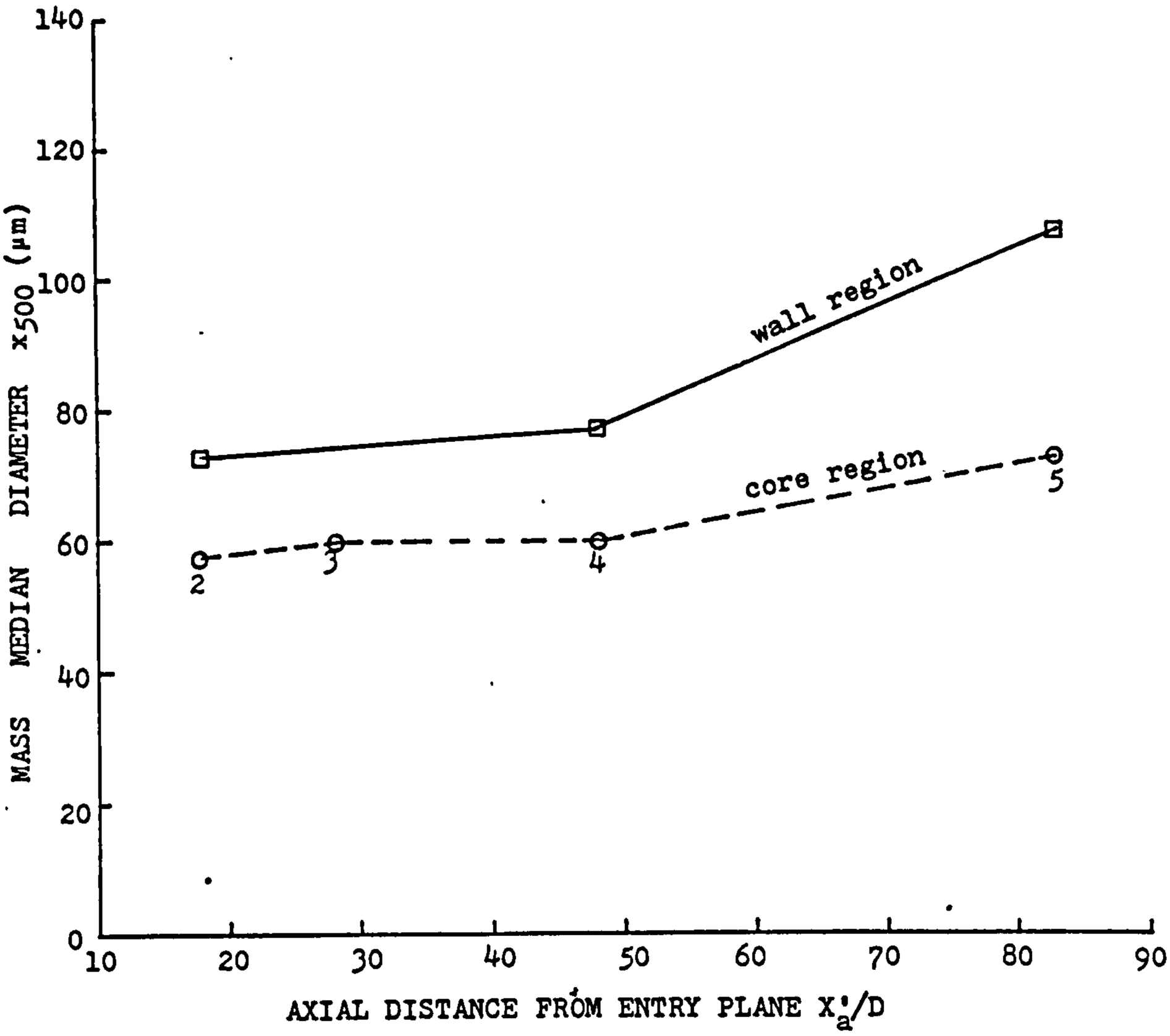


FIG. 8.11 Variation of mass median diameter with distance from the entry plane for test condition A.

○ : r/R = 0.04

□ : r/R = 0.88

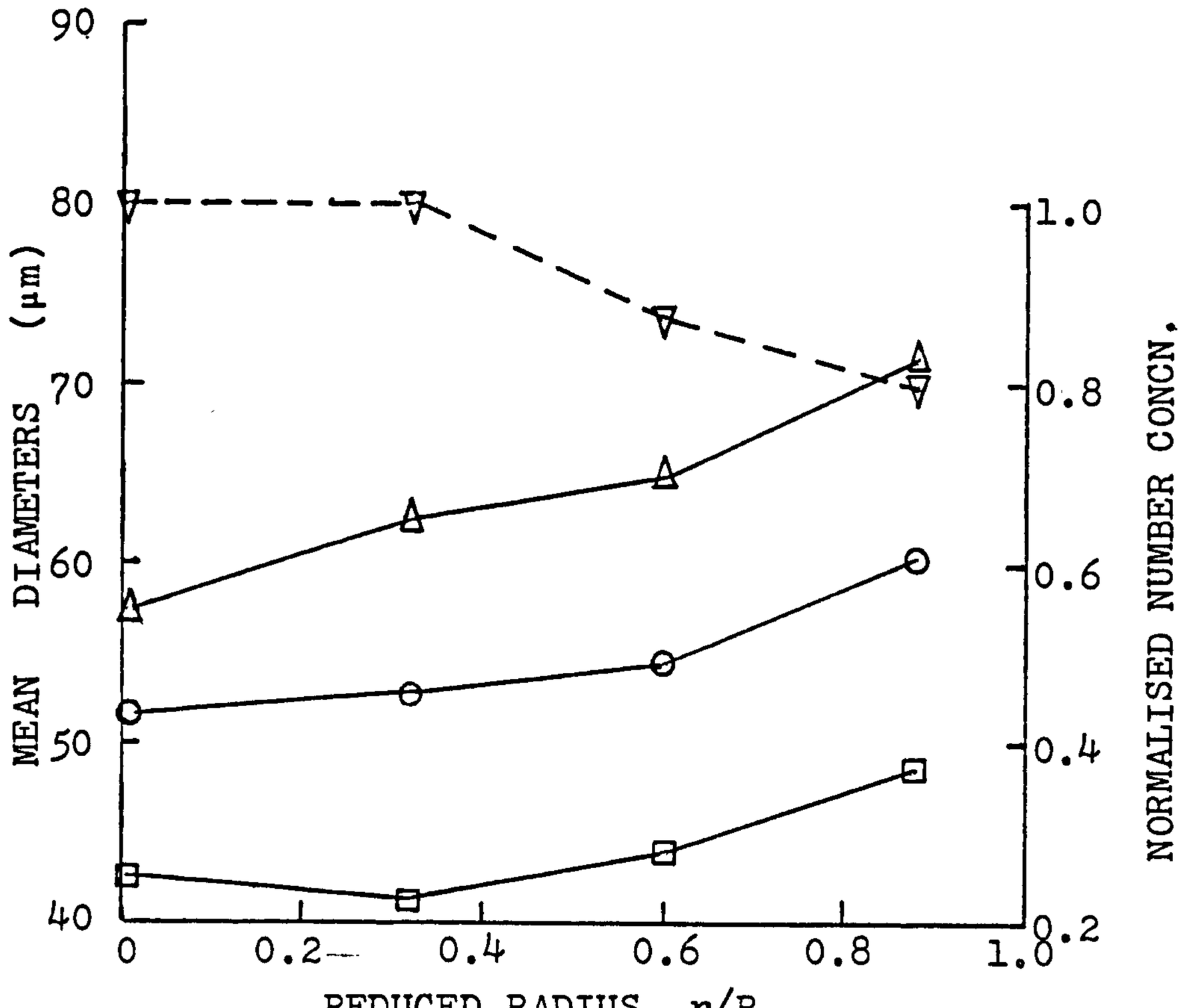


FIG. 8.12 Radial variation of mean diameters as well as normalised average number count at extraction station 2 for condition A.

Δ : mass median diameter (computed from least squares fit of the ULDF).

∇ : normalised average number count.

○ : Sauter mean, $\bar{x}_{32}$ from original data.

□ : mass mean, $\bar{x}_{30}$ from original data.

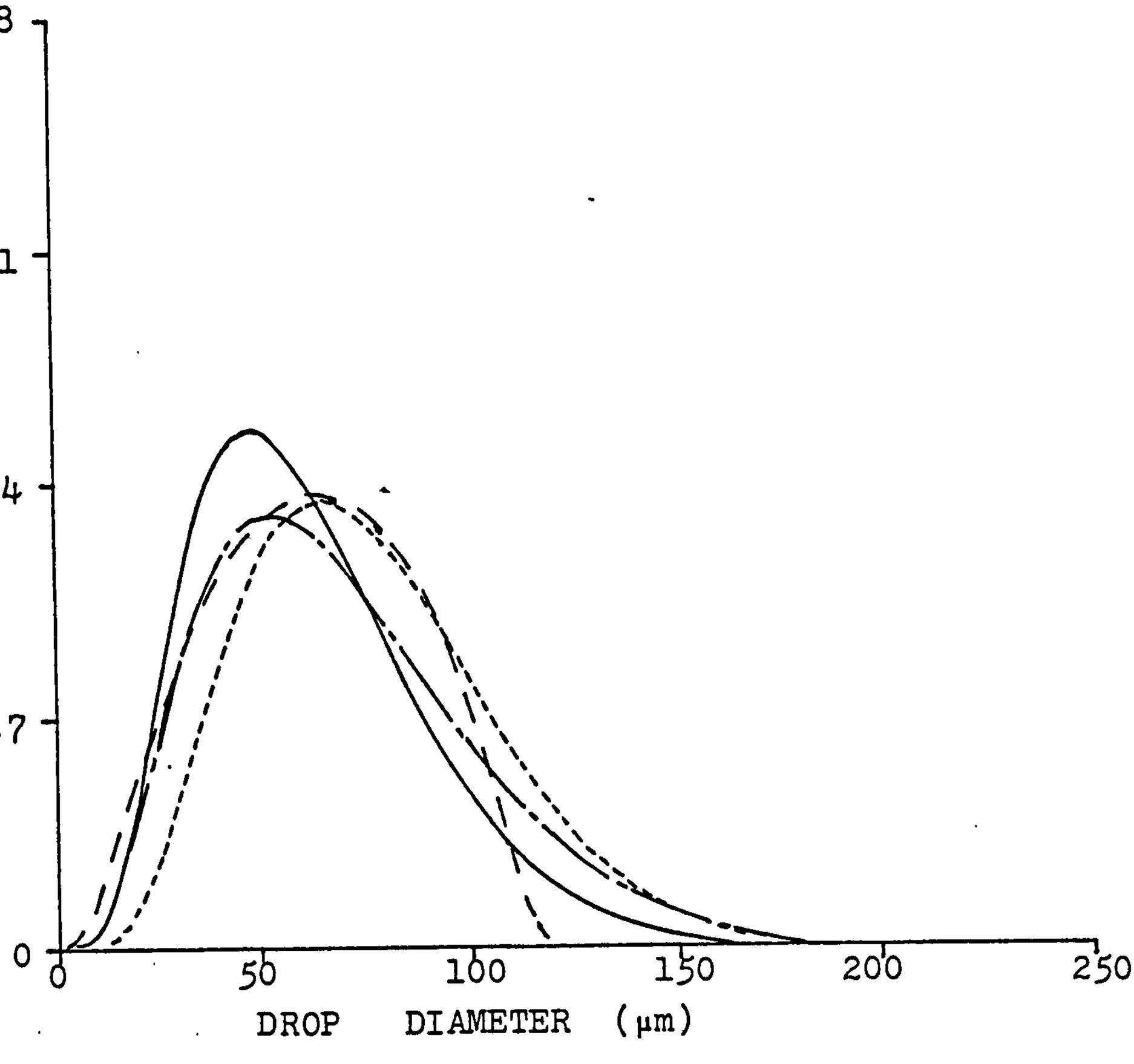


FIG. 8.13 Radial variation of mass frequency distribution at extraction station 2 for flow condition A.

——— :r/R = 0.04

— — — :r/R = 0.32

—·——·— :r/R = 0.60

·-·-·-·-· :r/R = 0.88

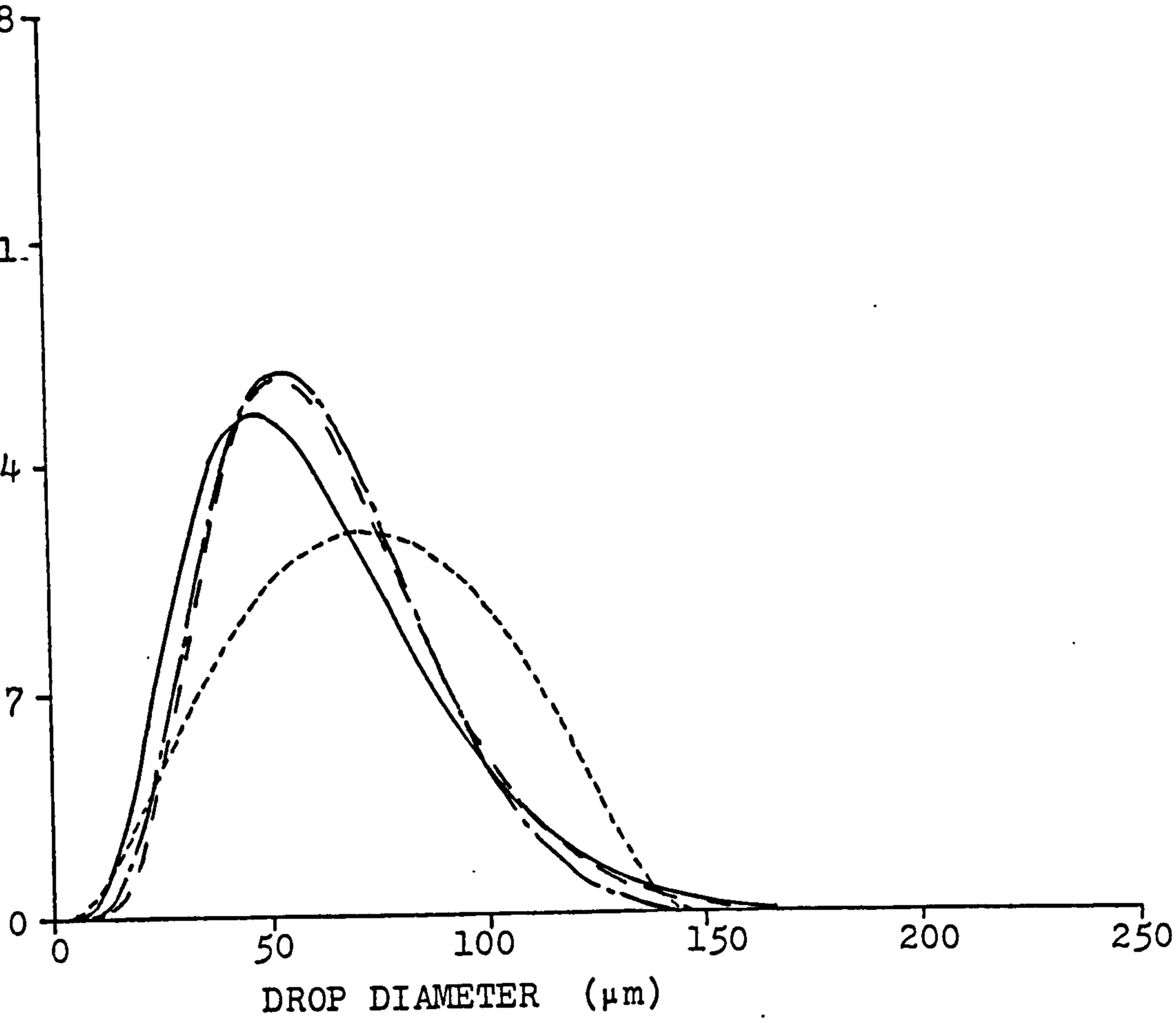


FIG. 8.14 Axial variation of mass frequency distribution for flow condition A at r/R = 0.04 (core region).

———— :Extraction station 2 (also reference drop-size distribution).

– – – – :Extraction station 3.

—·——·— :Extraction station 4.

·····:Extraction station 5.

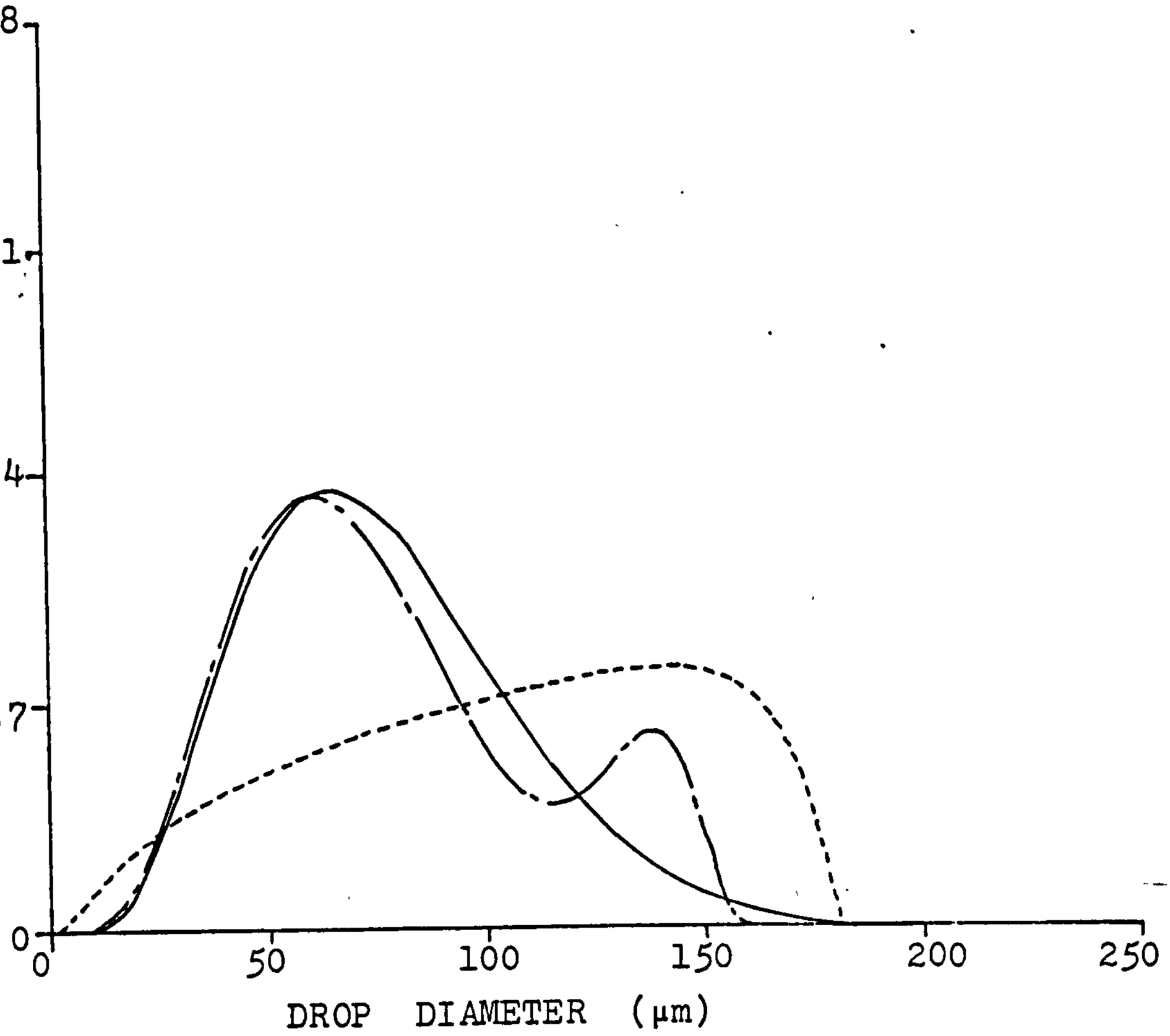


FIG. 8.15 Axial variation of mass frequency distribution for flow condition A at r/R = 0.88. (wall region).

———:Extraction station 2

—·—·—:Extraction station 4

--------:Extraction station 5

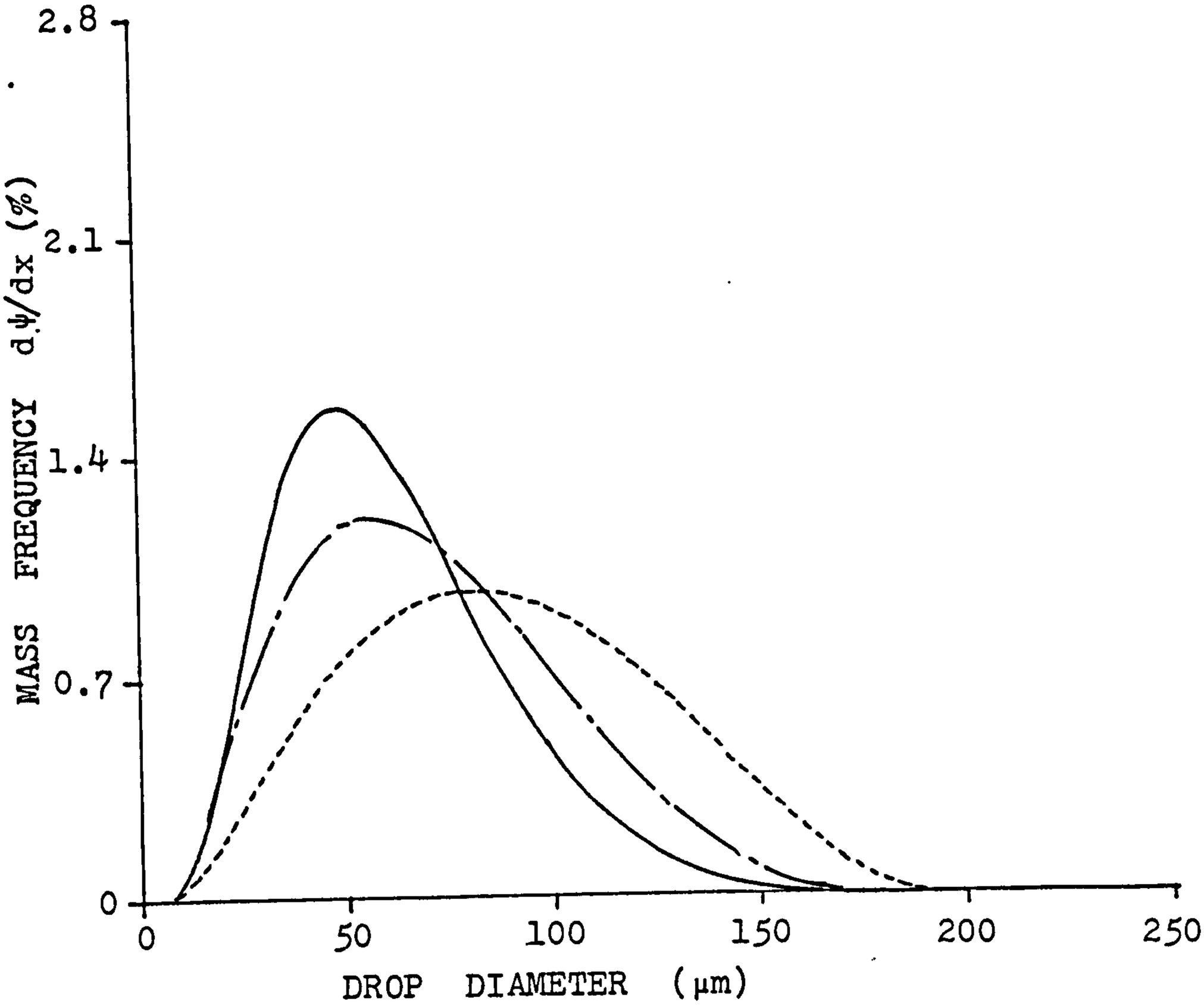


FIG. 8.16 Vertical variation of mass frequency distribution for condition A at extraction station 2 only.

·····: r/R=0.7 and θ=0

—·—·—: r/R=0.7 and θ=180°

————: r/R=0

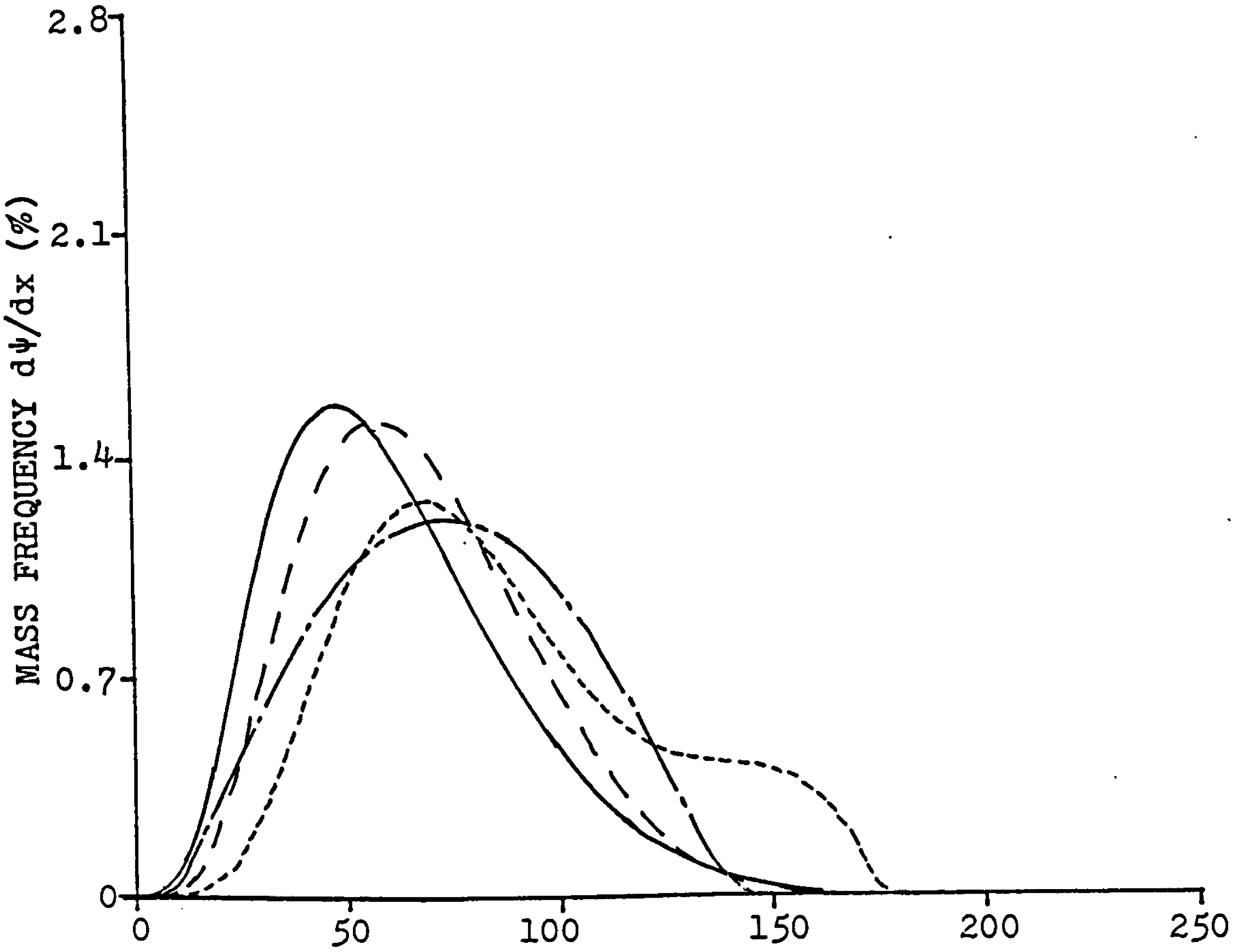


FIG. 8.17 Axial variation of mass frequency distribution for condition A1 compared with condition A.

———:Extraction station 2, condition A.
– – – –:Extraction station 2, condition A1.
———·—:Extraction station 5, condition A.
.....:Extraction station 5, condition A1.

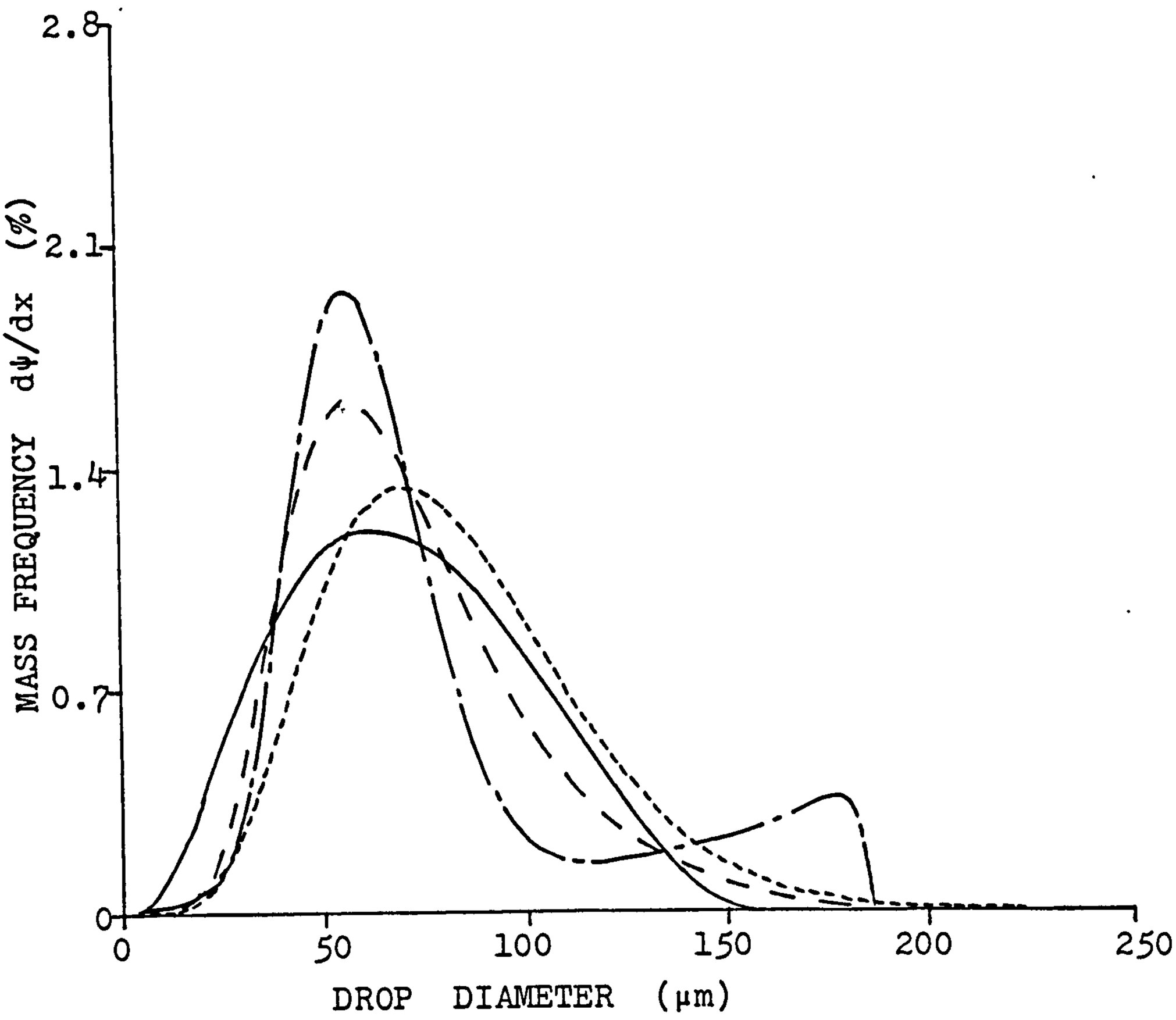


FIG. 8.18 Axial variation of mass frequency distribution for flow condition B at r/R=0.04.
————:Extraction station 2
– – – –:Extraction station 3
—·——·—:Extraction station 4
·····:Extraction station 5

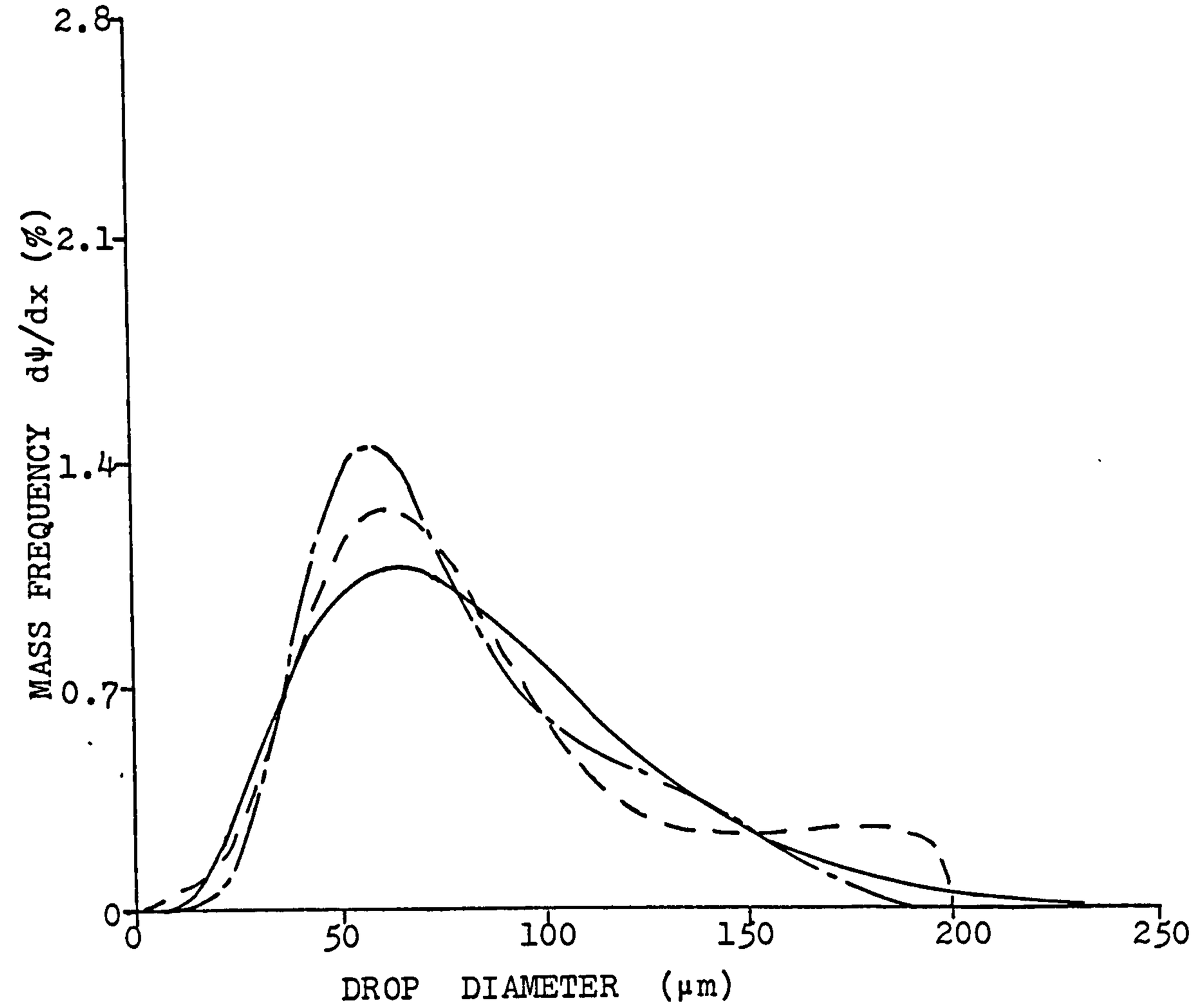


FIG. 8.19 Axial variation of mass frequency distribution for flow condition B at r/R=0.04.

————:Extraction station 2

— — — —:Extraction station 3

— · — · —:Extraction station 4

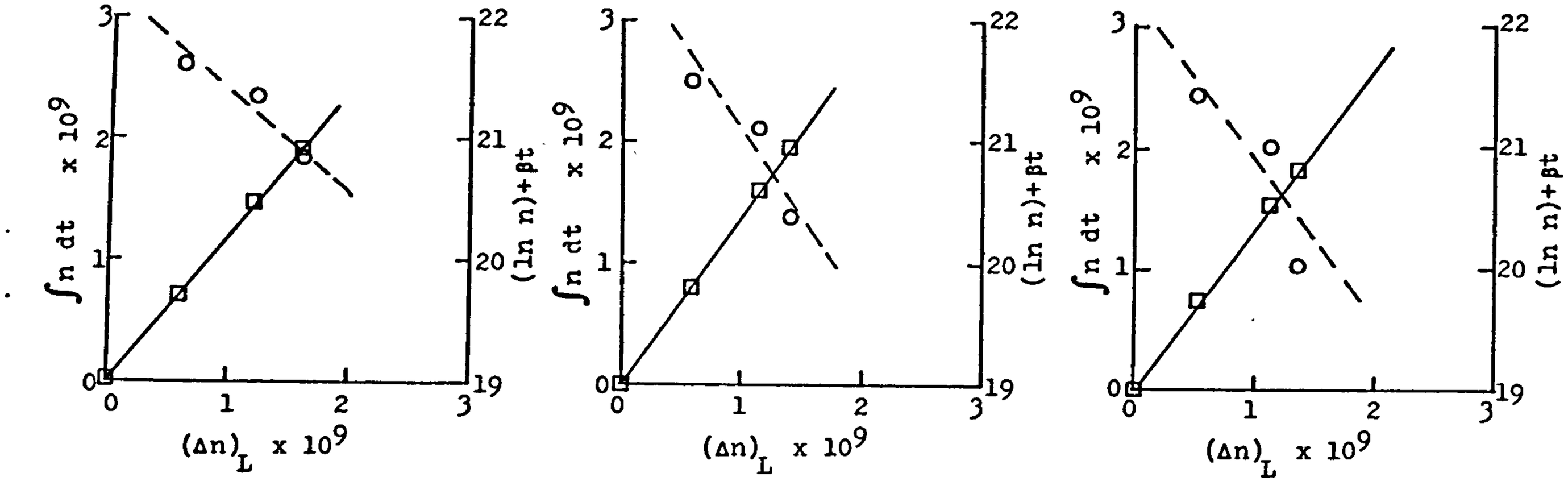


FIG. 8.20 Relevant plots for establishing values of deposition coefficient, β and coagulation coefficient, K for test conditions A, B and C.

□ : $\int n\,dt$ against $(\Delta n)_L$

○ : $(\ln n)+\beta t$ against $(\Delta n)_L$

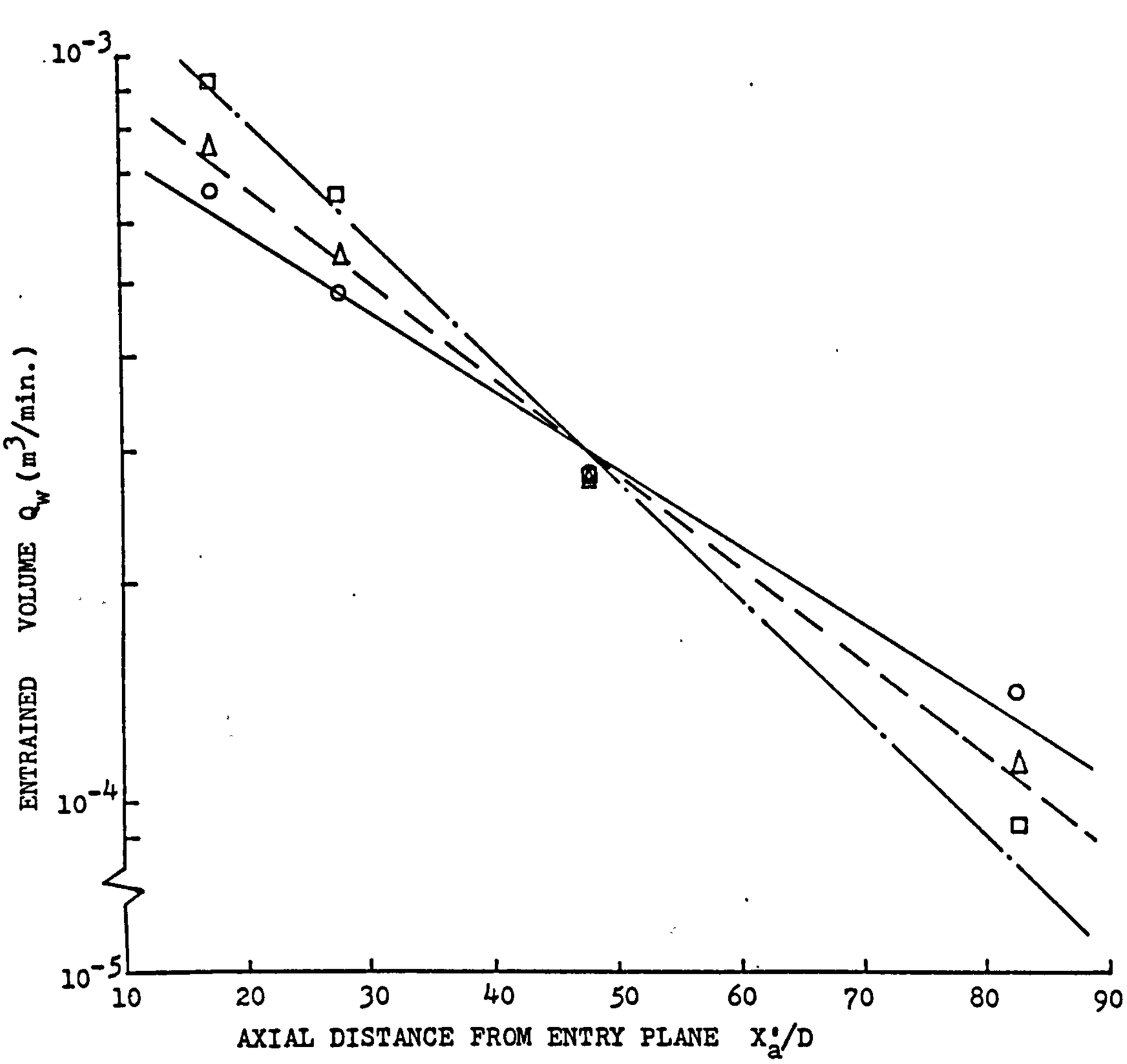


FIG. 8.21 Entrained flow rate with distance downstream of entry plane for Condition A: ——, O, B: - - - -, Δ and C: —·—·—, □.

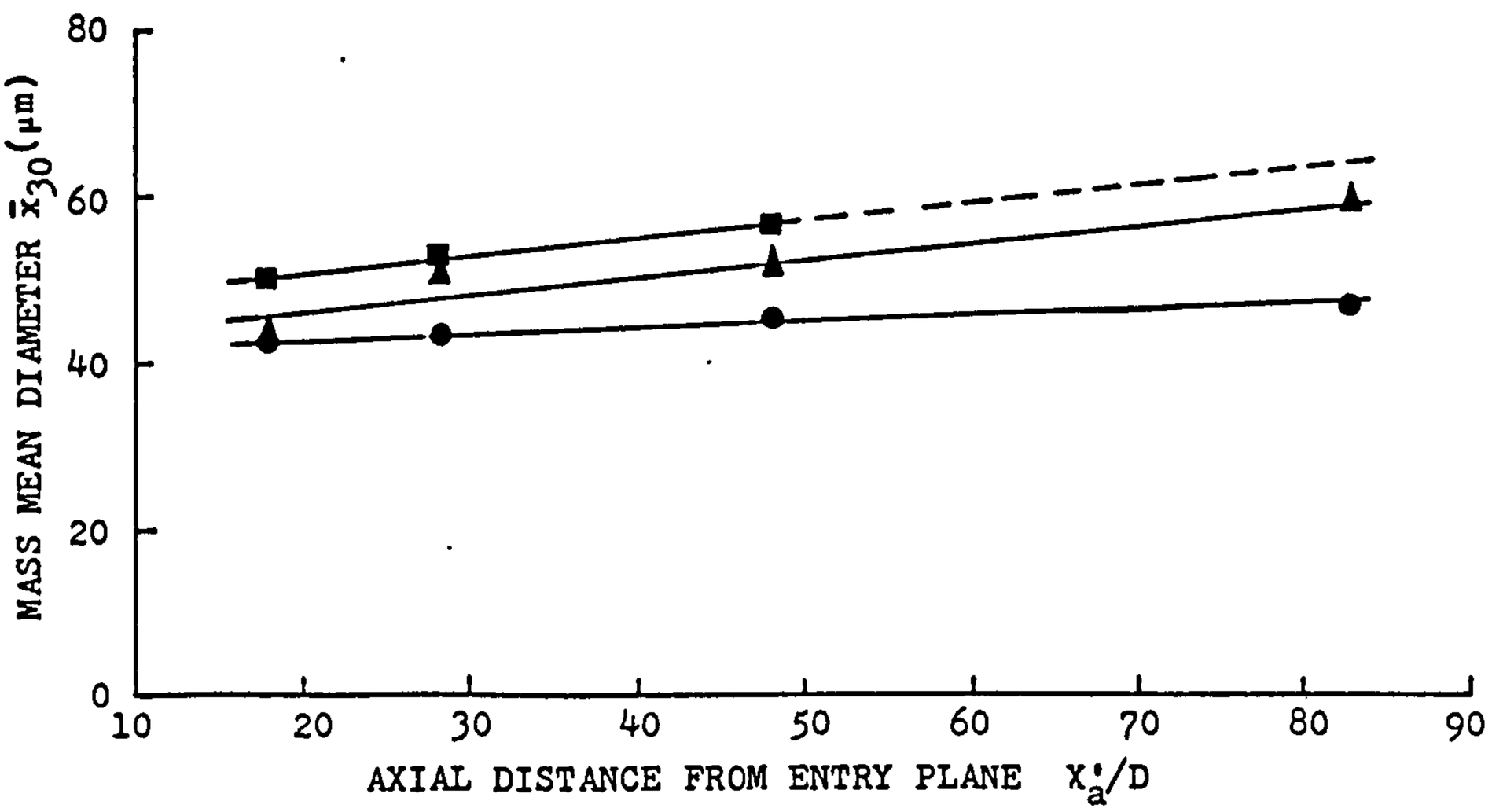


FIG. 8.22 Axial variation of mass mean diameter at r/R = 0.04 for conditions A: ●, B: ▲ and C: ■.

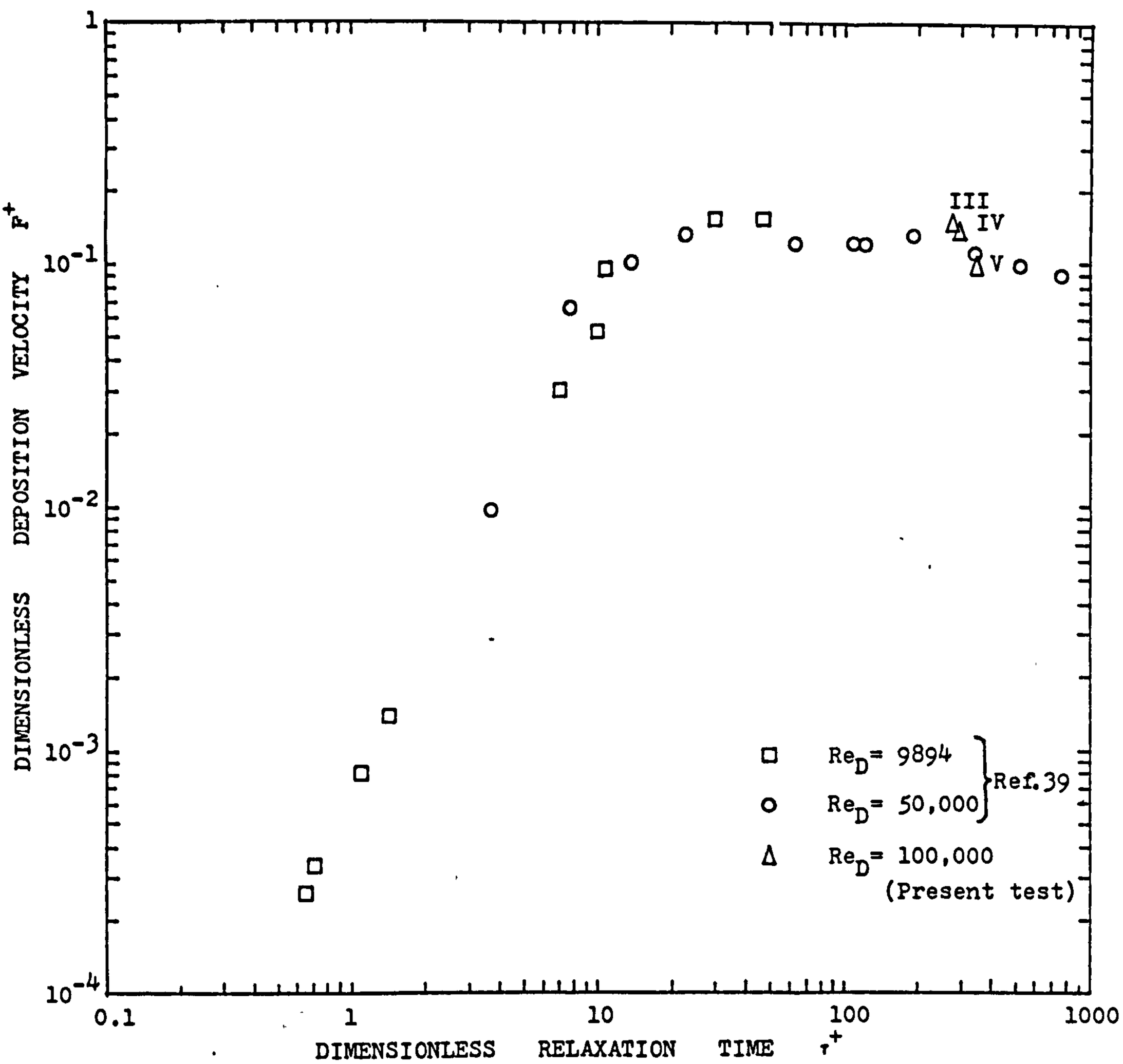


FIG. 8.23 Relationship between dimensionless deposition velocity and dimensionless particle relaxation time compared with ref. (39). Number besides data point denotes pipe section.

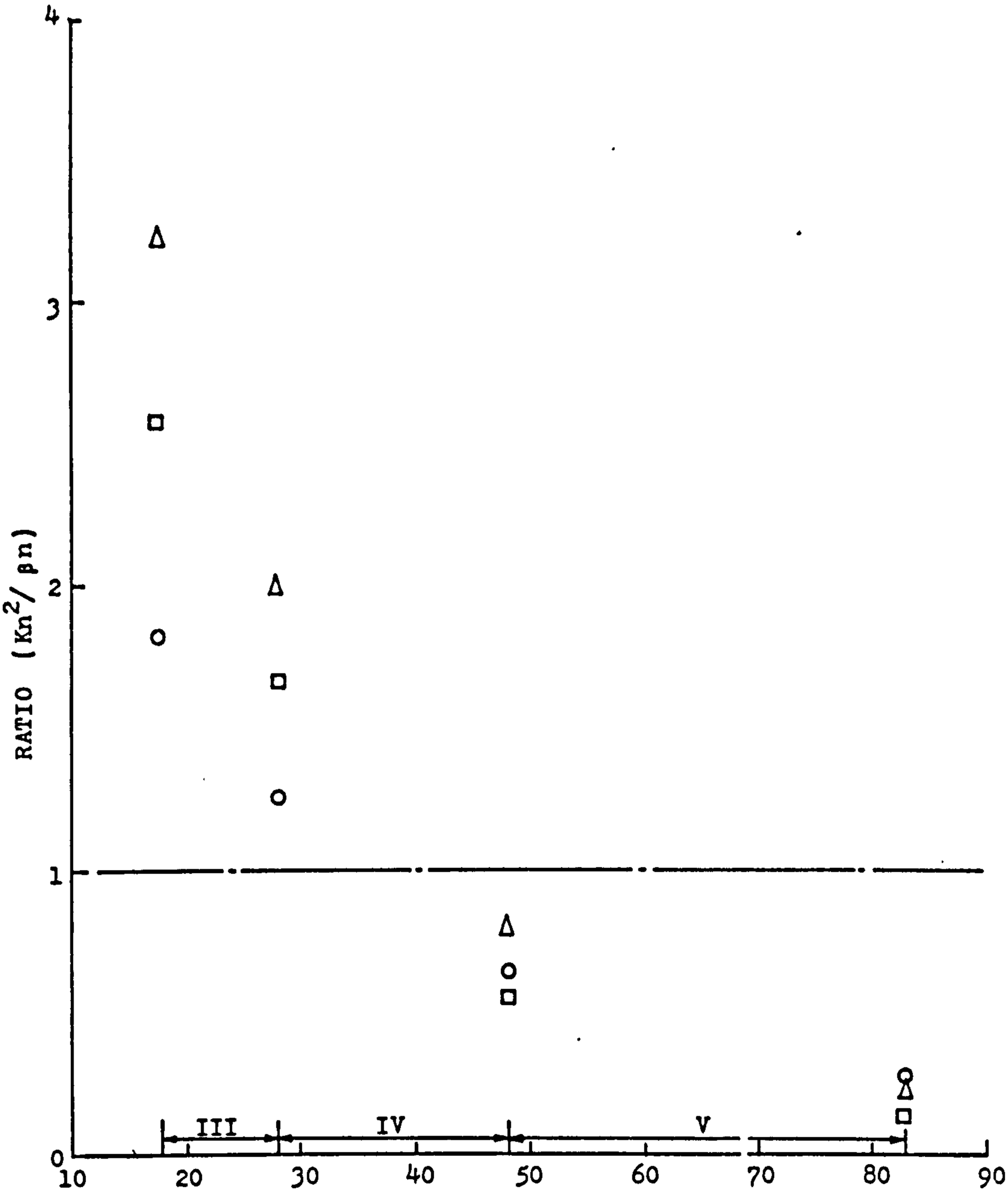


FIG. 8.24 Relationship between the ratio of rate of agglomeration to rate of deposition ($Kn^2/\beta n$) and axial distance from entry plane for conditions A: ○, B: △ and C: □. III, IV and V are respectively the pipe sections shown in Fig. 8.7.

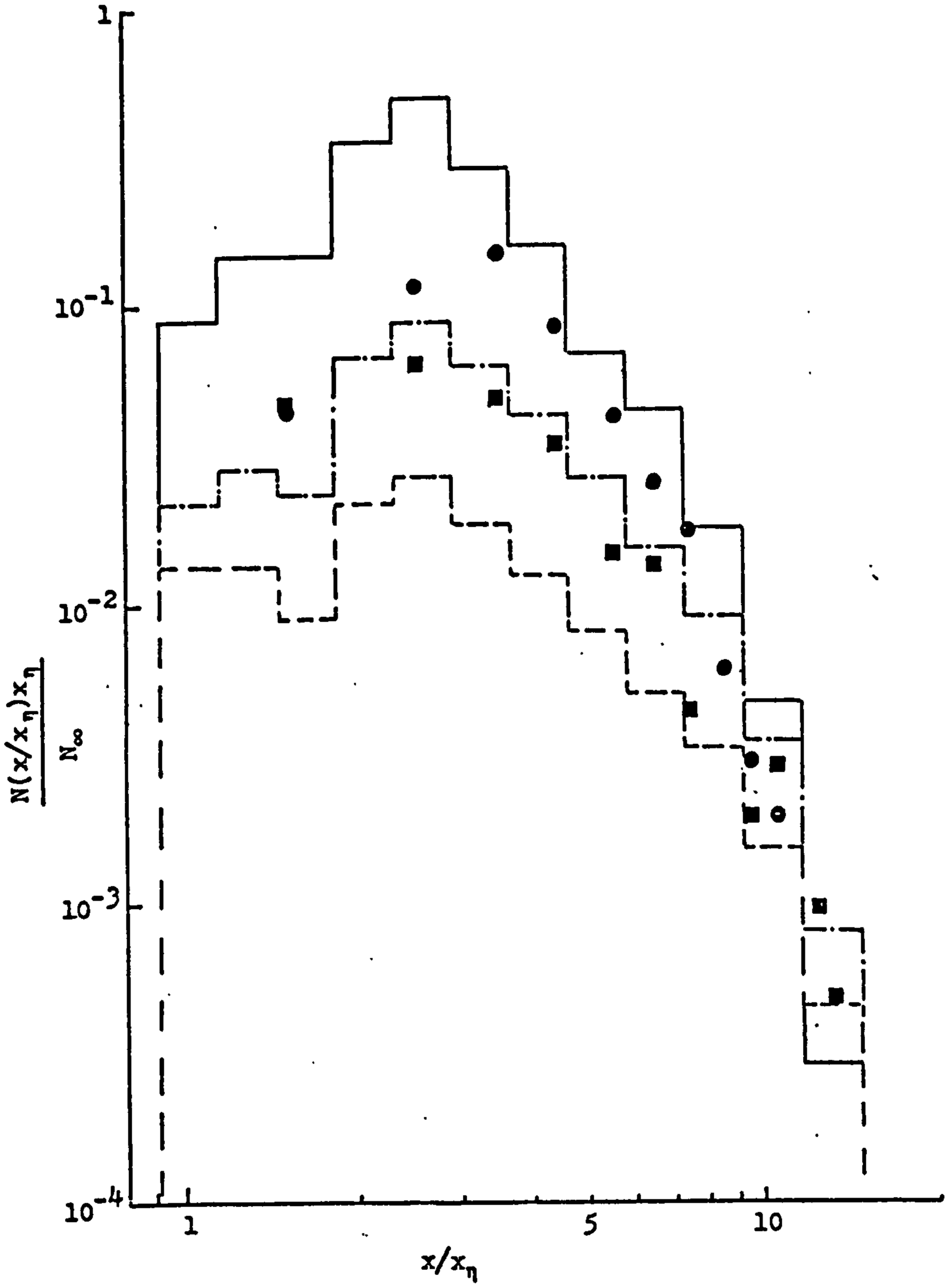


FIG. 8.25: Comparison of analytical and experimental forms of the drop number density distribution for r/R=0.04.

———: $X'_a/D = 0$ (station 2) Starting spectrum.

—·—·—: $X'_a/D = 30$ (station 4) } Analytical

– – – –: $X'_a/D = 65$ (station 5) }

● : $X'_a/D = 30$ } Experimental

■ : $X'_a/D = 65$ }

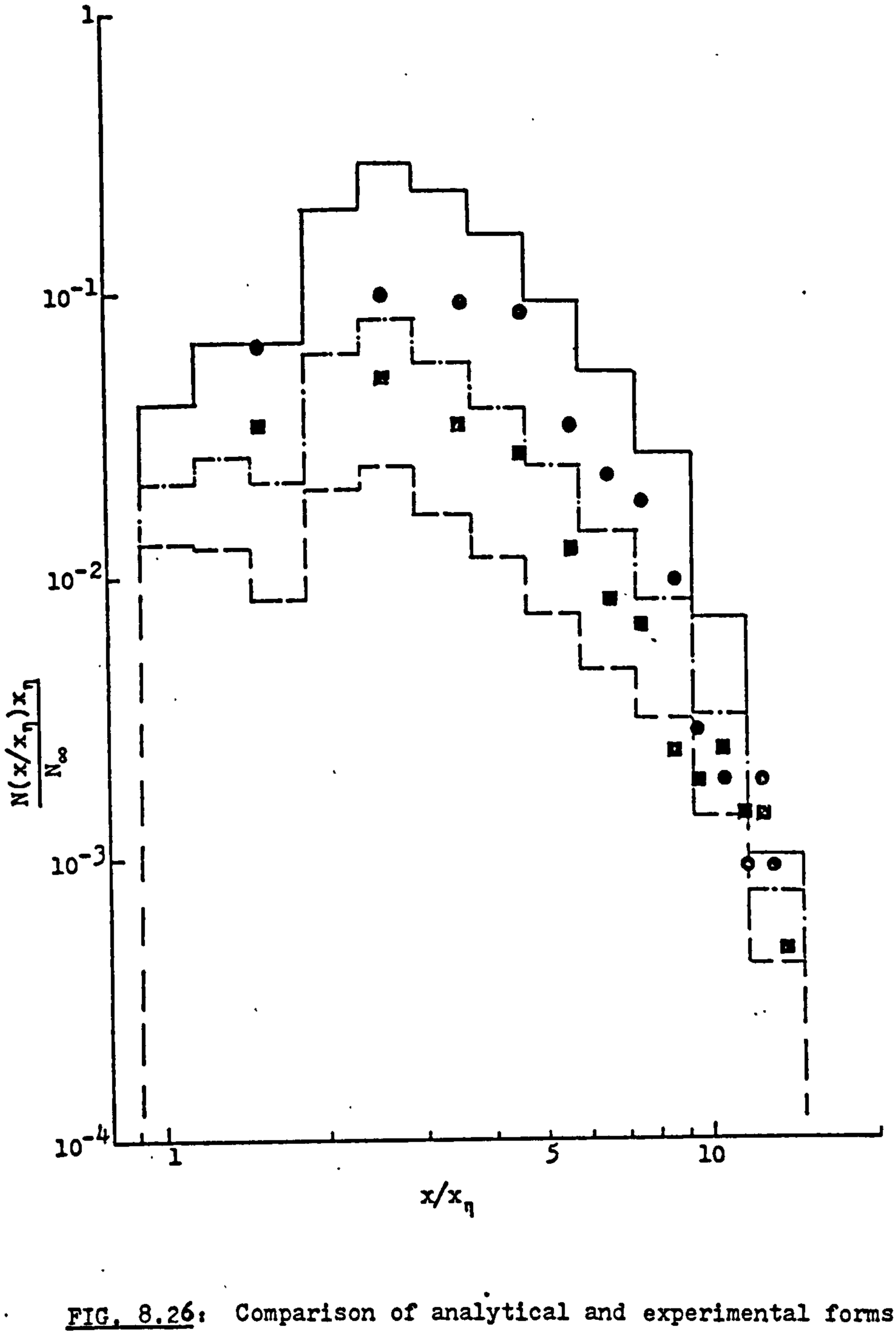


FIG. 8.26: Comparison of analytical and experimental forms of the drop number density distribution for r/R=0.88.

——— : X'_a/D = 0 (station 2) Starting spectrum.

-·—·- : X'_a/D = 30 (station 4) } Analytical

- - - - - : X'_a/D = 65 (station 5) }

● : X'_a/D = 30 } Experimental

■ : X'_a/D = 65 }

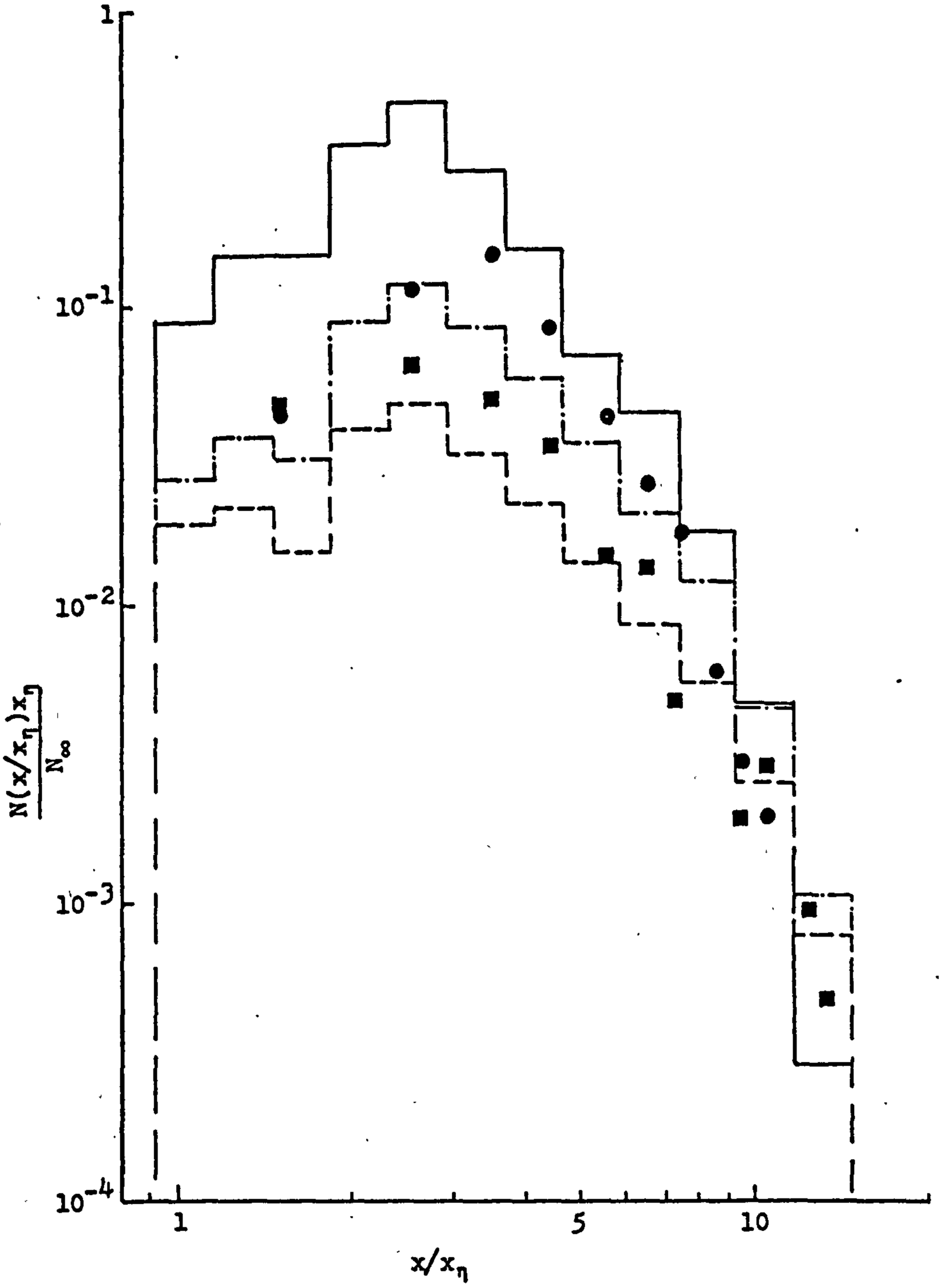


FIG. 8.27: Comparison of analytical and experimental forms of the drop number density distribution with reduced deposition for r/R=0.04.

———: $X'_a/D = 0$ (station 2) Starting spectrum.

—·——: $X'_a/D = 30$ (station 4) } Analytical

-------: $X'_a/D = 65$ (station 5) }

● : $X'_a/D = 30$ } Experimental

■ : $X'_a/D = 65$ }

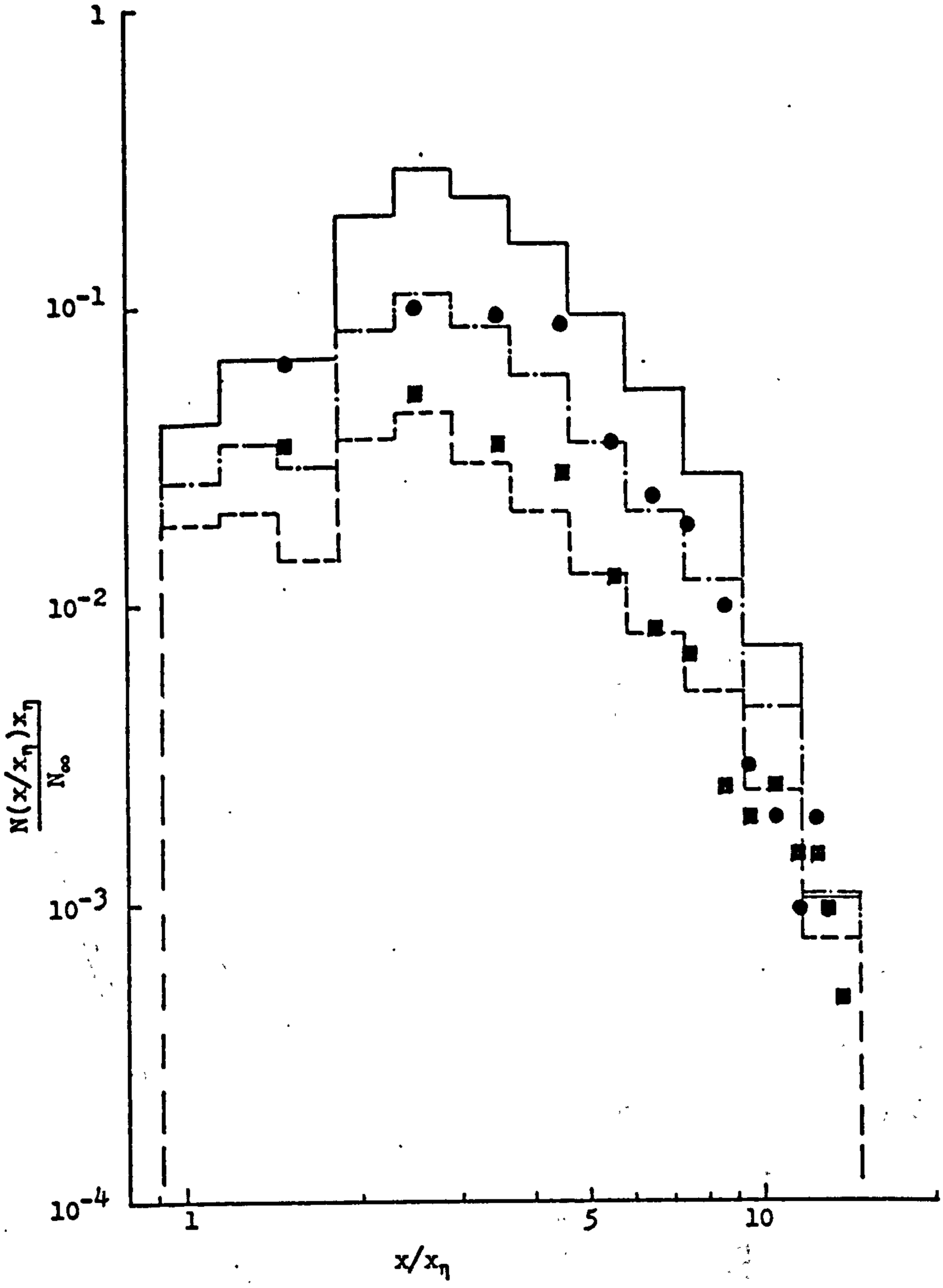


FIG. 8.28: Comparison of analytical and experimental forms of the drop number density distribution with reduced deposition for r/R=0.88.

———: X'_a/D = 0 (station 2) Starting spectrum.

—·—·—: X'_a/D = 30 (station 4) } Analytical

— — —: X'_a/D = 65 (station 5) }

● : X'_a/D = 30 } Experimental

■ : X'_a/D = 65 }

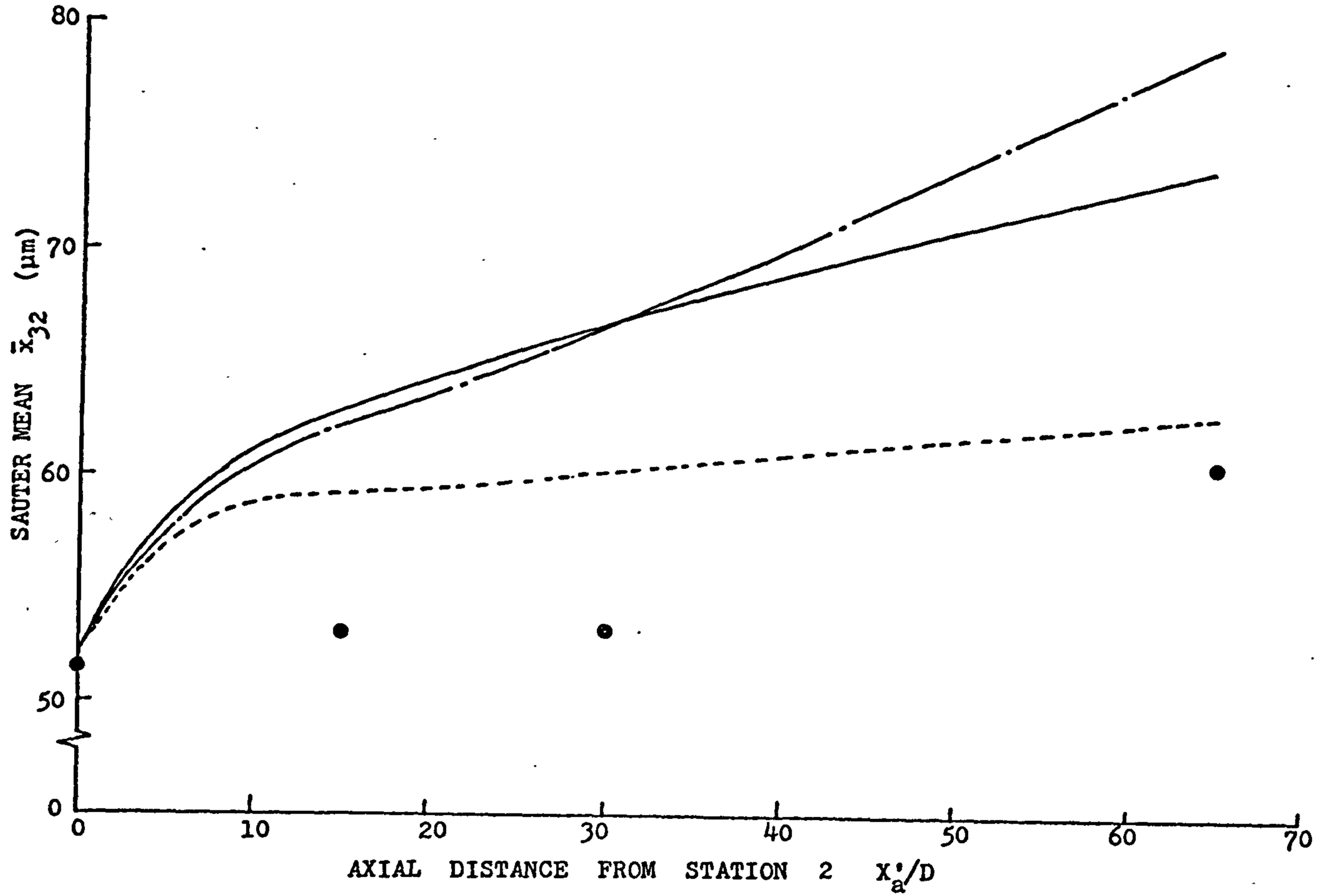


FIG. 8.29: Axial variation of analytical and experimental Sauter mean diameter for r/R= 0.04.

- ..... deposition only
- —·—·— coagulation only
- ——— coagulation and deposition

} Analytical

- ● experimental

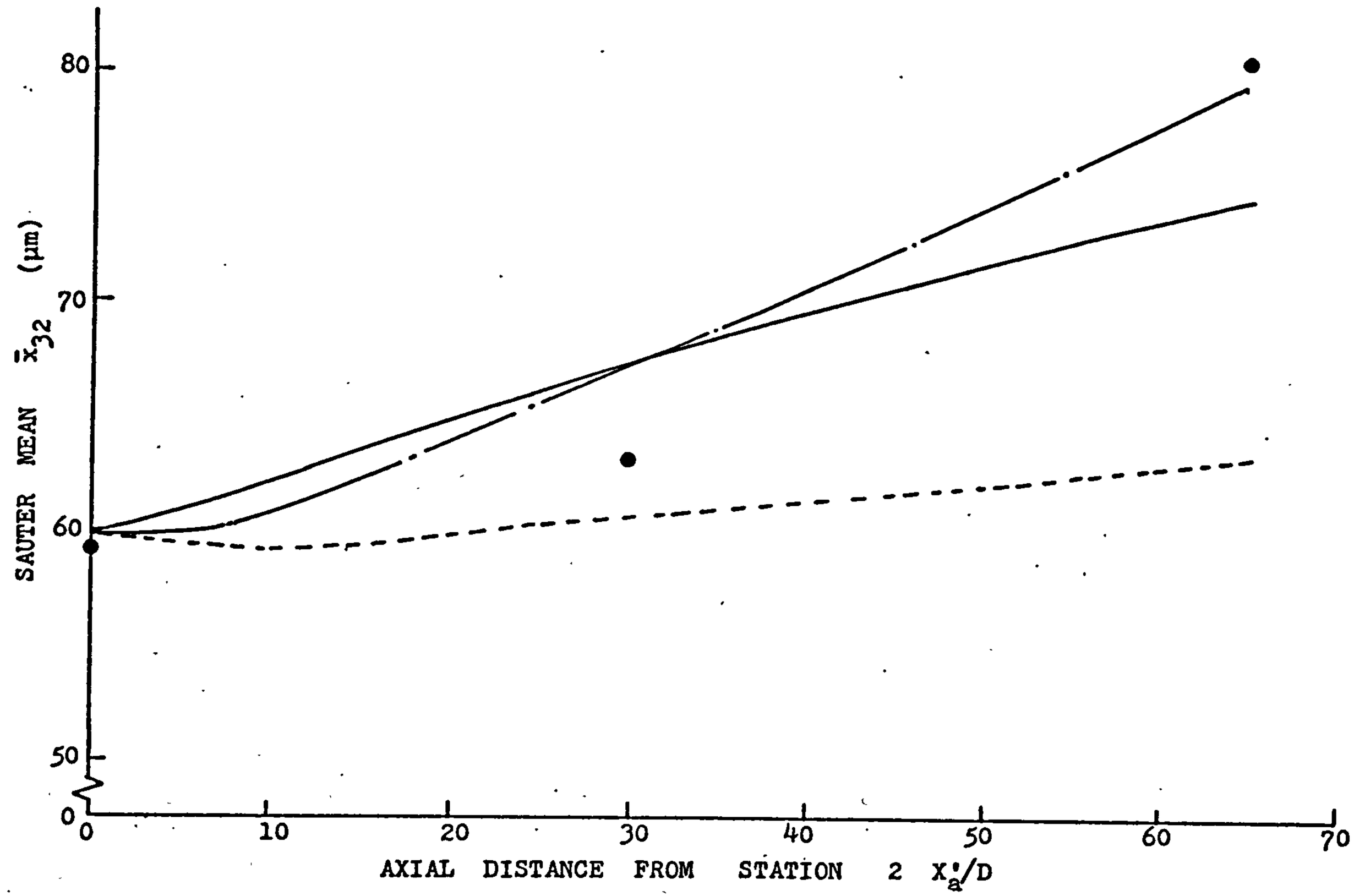


FIG. 8.30: Axial variation of analytical and experimental Sauter mean diameter for r/R=0.88.

- ------- deposition only
- —·—·— coagulation only
- ——— coagulation and deposition

} Analytical

- ● experimental